Report AFRPL-TR-76-60

PROJECT DAME - FLIGHT AND SIMULATION TESTING OF A
MODIFIED BOMB DUMMY UNIT

J. D. Burton
Rockwell International Corporation
Rocketdyne - McGregor
P. O. Box 548
McGregor, Texas 76657

October 1976

Final Report

DDC
RECEIVED
DEC 13 1976
A

FOREWORD

This report was submitted by Rockwell International Corporation, Rocketdyne-McGregor Division, P.O. Box 548, McGregor, Texas 76657, under Contract No. F04611-72-C-0049, Job Order No. 314812ME with the Air Force Rocket Propulsion Laboratory, Edwards, CA 93523.

This report has been reviewed by the Information Office/DOZ and is releasable to the National Technical Information Service (NTIS). It will be available to the general public, including foreign nations. This technical report is UNCLASSIFIED and suitable for public release.

MICHAEL E. BOND, 1LT, USAF
Project Engineer

LEE G. MEYER, GS-14, Chief
Air-Launch Propulsion Section

FOR THE COMMANDER

CHARLES R. COOKE, Director
Solid Rocket Division

NOTICES

"When U. S. Government drawings, specifications, or other data are used for any purpose other than a definitely related Government procurement operation, the Government thereby incurs no responsibility nor any obligation whatsoever, and the fact that the Government may have formulated, furnished, or in any way supplied the said drawings, specifications, or other data, is not to be regarded by implication or otherwise, or in any manner licensing the holder or any other person or corporation, or conveying any rights or permission to manufacture, use, or sell any patented invention that may in any way be related thereto."

REPORT DOCUMENTATION PAGE

READ INSTRUCTIONS
BEFORE COMPLETING FORM

1. REPORT NUMBER	2. GOVT ACCESSION NO.	3. RECIPIENT'S CATALOG NUMBER
AFRPL-TR-76-60		

4. TITLE (and Subtitle)	5. TYPE OF REPORT & PERIOD COVERED
PROJECT DAME - FLIGHT AND SIMULATION TESTING OF A MODIFIED BOMB DUMMY UNIT	Final Report. September 1972 to June 1976
	6. PERFORMING ORG. REPORT NUMBER

7. AUTHOR(s)	8. CONTRACT OR GRANT NUMBER(s)
J. D. Burton	F04611-72-C-0049

9. PERFORMING ORGANIZATION NAME AND ADDRESS	10. PROGRAM ELEMENT, PROJECT, TASK AREA & WORK UNIT NUMBERS
Rockwell International Corporation, Rocketdyne Division, P. O. Box 548 McGregor, TX 76657	

11. CONTROLLING OFFICE NAME AND ADDRESS	12. REPORT DATE
Air Force Rocket Propulsion Laboratory Edwards AFB, CA 93523	October 1976
	13. NUMBER OF PAGES
	358 + xx

14. MONITORING AGENCY NAME & ADDRESS(if different from Controlling Office)	15. SECURITY CLASS. (of this report)
	Unclassified
	15a. DECLASSIFICATION/DOWNGRADING SCHEDULE

16. DISTRIBUTION STATEMENT (of this Report)

Approved for Public Release; Distribution Unlimited

17. DISTRIBUTION STATEMENT (of the abstract entered in Block 20, if different from Report)

18. SUPPLEMENTARY NOTES

19. KEY WORDS (Continue on reverse side if necessary and identify by block number)

*FLIGHT TESTING; *SIMULATION; *SOLID PROPELLANT ROCKET ENGINES; VIBRATION; STRESSES; STRAINS; SENSORS; DATA ACQUISITION; QUALIFICATION TESTS

20. ABSTRACT (Continue on reverse side if necessary and identify by block number)

Results of a program to determine thermal and vibrational environments imposed on an air-launched propulsion system during captive carriage on high-performance aircraft are presented. Fabrication, instrumentation, ground and flight testing, and analysis of the bomb dummy unit used in the tests and implications, from data obtained, for motor qualification testing of tactical missiles are discussed. The 20 flight tests and three series of ground simulation tests to which the bomb dummy unit was subjected are described, and data obtained from each are presented.

DD FORM 1473 EDITION OF 1 NOV 65 IS OBSOLETE
1 JAN 73

408358

CONTENTS

CONTENTS

(Continued)

CONTENTS
(Continued)

FIGURES

FIGURES

(Continued)

FIGURES

(Continued)

FIGURES

(Continued)

FIGURES

(Continued)

xvi

FIGURES

(Continued)

TABLES

TABLES

(Continued)

INTRODUCTION

Project DAME (Determination of Aircraft/Missile Environment) was
initiated by the Air Force Rocket Propulsion Laboratory (AFRPL) several
years ago to determine the thermal and vibrational environments imposed
on an air-launched missile propulsion system during captive carriage on
high-performance aircraft. The primary impetus to start the program
resulted from an AFRPL survey showing a universal feeling throughout
the propulsion industry that existing military specifications and stand-
ards describing qualification testing were unrealistic. A qualifica-
tion specification that is erroneous with respect to severity may result
in a compromise in weapon system performance or excessive test costs.
Rocket motors qualified under inadequate environmental conditions may not
be able to withstand actual mission conditions. This may cause opera-
tional and logistics problems and endanger lives and equipment. On the
other hand, a rocket motor designed for unrealistically high environmen-
tal loads will lack performance and cost effectiveness. Additional cost
is sometimes incurred during design in an attempt to provide a motor that
will withstand loads to be imposed during simulation testing rather than
loads to be encountered in use.

The method of simulation testing is also important. Accelerometer
data from instrumented aircraft stores were used to generate the vibra-
tional test levels shown in MIL-STD-810B. The method of testing, how-
ever, is ill-defined; and, in a majority of the qualification tests
conducted on weapon systems, there is generally little commonality
between the simulation test environment and the aircraft captive-carry
environment.

Advances in developing load sensors that can be implanted in propel-
lant have provided new methods of determining environmentally imposed
stress, strain, and shear loads. Project DAME was designed to utilize

these advances and provide some of the data required to establish more realistic test specifications. The aerodynamically shaped Bomb Dummy Unit (BDU) used for Project DAME was modified to contain 150 pounds of inert propellant; stress sensors, strain gages, shear gages, and thermistors embedded in the propellant; accelerometers; surface-mounted thermocouples; semi-conductor strain gages on the launcher lugs and sway braces; and a complete data acquisition system.

An F-111 aircraft was selected as the test bed because of its superior air speed at both high and low altitudes. The flight profiles for Project DAME included: M = 0.70 at 35,000 feet, M = 0.9 at 500 feet above ground level using terrain-following radar (TFR), and M = 2.0 at 40,000 feet. Test history chronology is shown in Figure 1.

Lockheed Propulsion Company designed and fabricated the instrumented inert propellant grain. Propellant gage outputs were estimated based on flight regimes provided by the Air Force. These predicted loads and the actual flight loads were compared by Dr. Harold Leeming during the program to verify that gage outputs were believable and to determine the accuracy of the prediction techniques used. General Dynamics predicted the vibration loads and aerodynamic heating to be experienced during the flight test program. Rocketdyne, McGregor, Texas, conducted ground simulation and calibration tests with the all-up flight vehicle.

The test program began with vibration of the entire flight vehicle using sine inputs to calibrate the system and to check responses of the gages. Random vibrational loads and aerodynamic heat input levels provided by General Dynamics were then applied. A second series of ground simulation tests was run in mid-program to obtain preliminary comparisons with earlier tests based on prediction. Aeroheat was simulated using a circulating air system. Gage responses were recorded on the flight vehicle tape recorder as well as on a ground station. Simulation

2
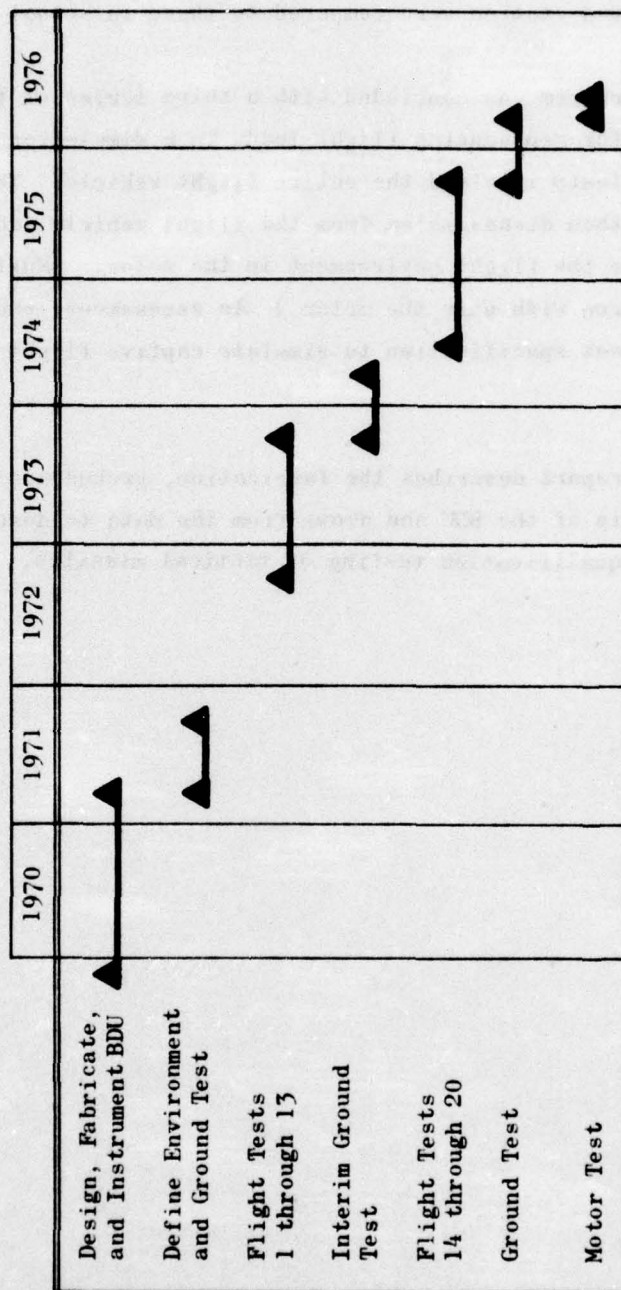
Figure 1. Chronological History of the BDU

test gage responses recorded on the flight vehicle tape recorder and on the ground station were compared to those in actual flight.

The program was concluded with a third series of tests to determine the means for reproducing flight loads in a simulation test. The first series of tests involved the entire flight vehicle. The inert rocket motor was then disassembled from the flight vehicle and tests were run to simulate the flight environment in the motor. (Most qualification tests are run with only the motor.) An assessment leading to a qualification test specification to simulate captive flight loads was then made.

This report describes the fabrication, ground and flight testing, and analysis of the BDU and draws from the data to describe implications for motor qualification testing of tactical missiles.

TEST VEHICLE

DESCRIPTION

The BDU contains 150 pounds of inert HTPB propellant in a simple center-perforated grain, 17.5 inches long with a diameter of 13.5 inches.

The original configuration of the BDU aft section is shown in Figure 2. This basic structure was modified to allow a propellant grain to be cast into Section B. To apply gage-calibration pressure steps to the grain, pressure-tight end closures were installed. An air-tight system also helps prevent grain damage from moisture or other atmospheric contaminants. A sketch of the modified BDU is shown in Figure 3.

The circular port grain, 17.5 inches long with a nominal web fraction of 0.75, had a bore diameter of 3.5 inches at the head end, tapering to 3.0 inches at the aft end. A 0.1-inch-thick layer of insulation was bonded directly to the aluminum case.

The grain was instrumented with strain, stress, and shear gages (see Figure 4). The clip-type strain gages use two semiconductors to form two active elements of a bridge circuit. Two clip gages (one to measure hoop strain and the other longitudinal strain) were mounted in the middle of the bore. Six Konigsberg Instrument P14B 150 psi range diaphragm gages were used to measure radial propellant-to-liner bond stress. Four embedded shear stress gages were used. These gages and their locations are described in the Instrumentation section.

Since propellant gage outputs are dependent on temperature, 20 thermistors were installed to measure temperatures in the immediate vicinity of the gages, at the case/liner interface (CLI), and throughout the grain.

5
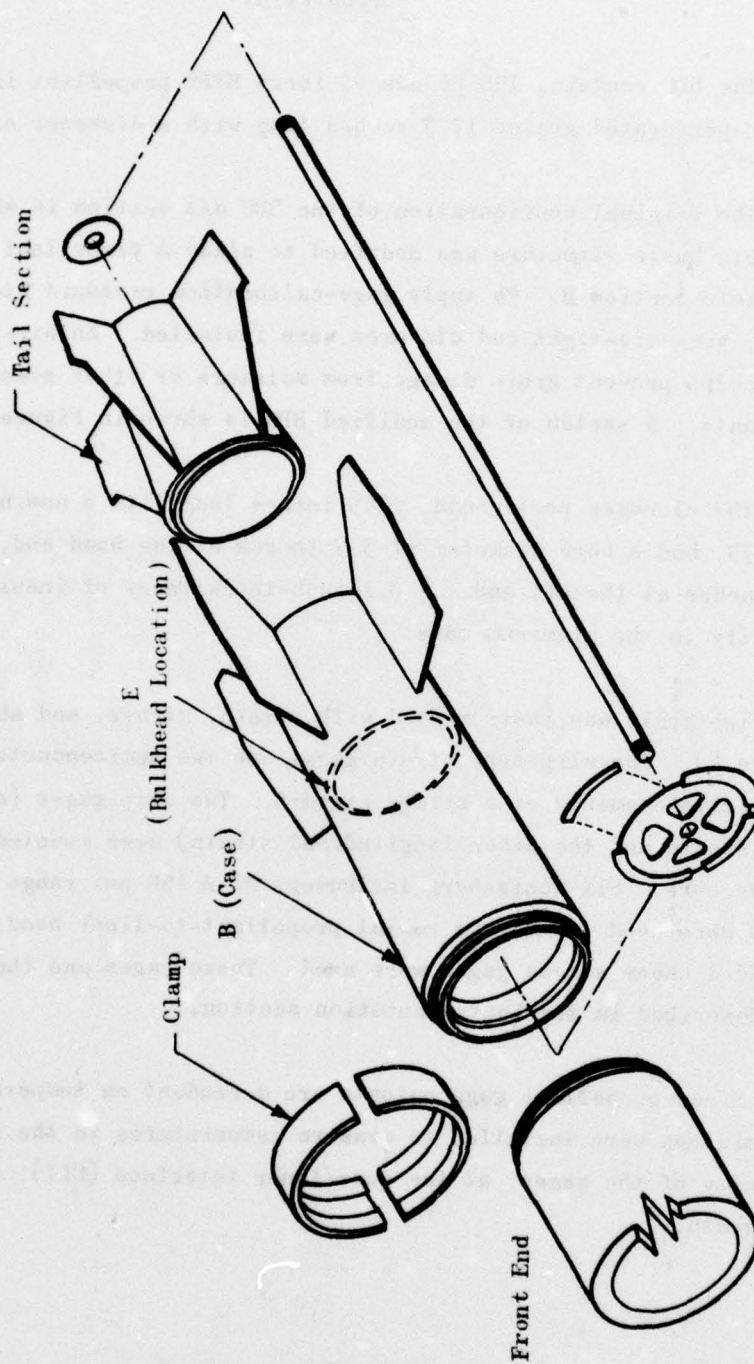
Figure 2. Original Bomb Dummy Unit Configuration

Tail Section

E (Bulkhead Location)

B (Case)

Clamp

Front End
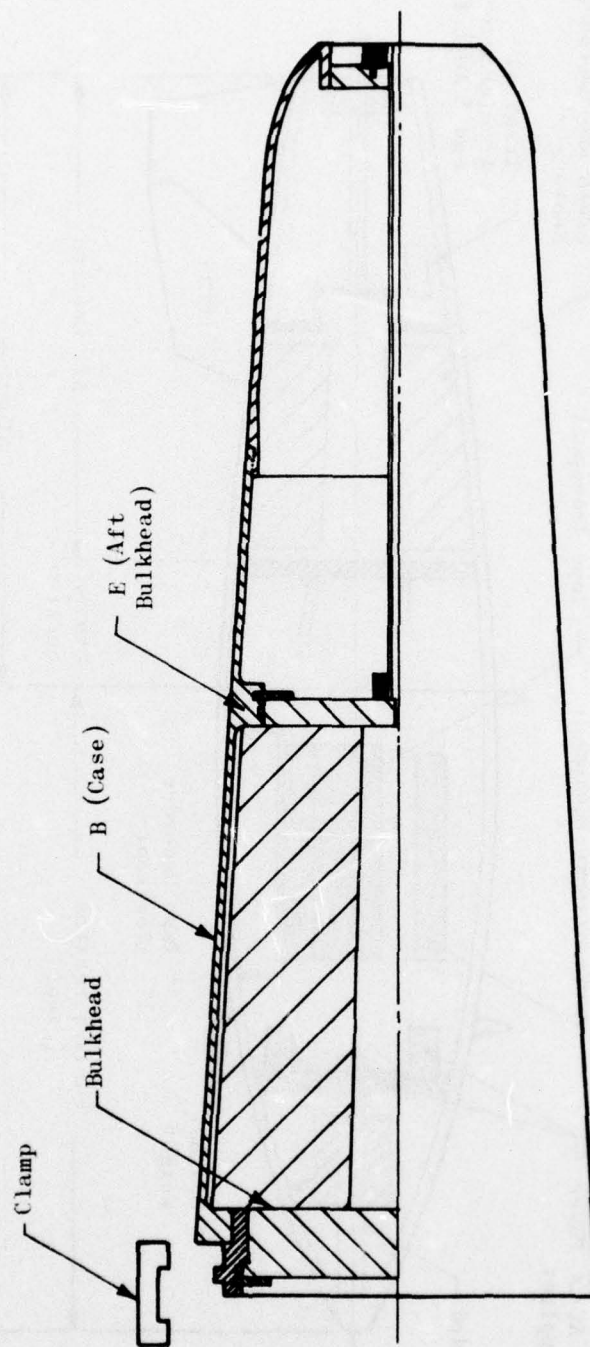
Figure 3. Modified Bomb Dummy Unit Configuration

7
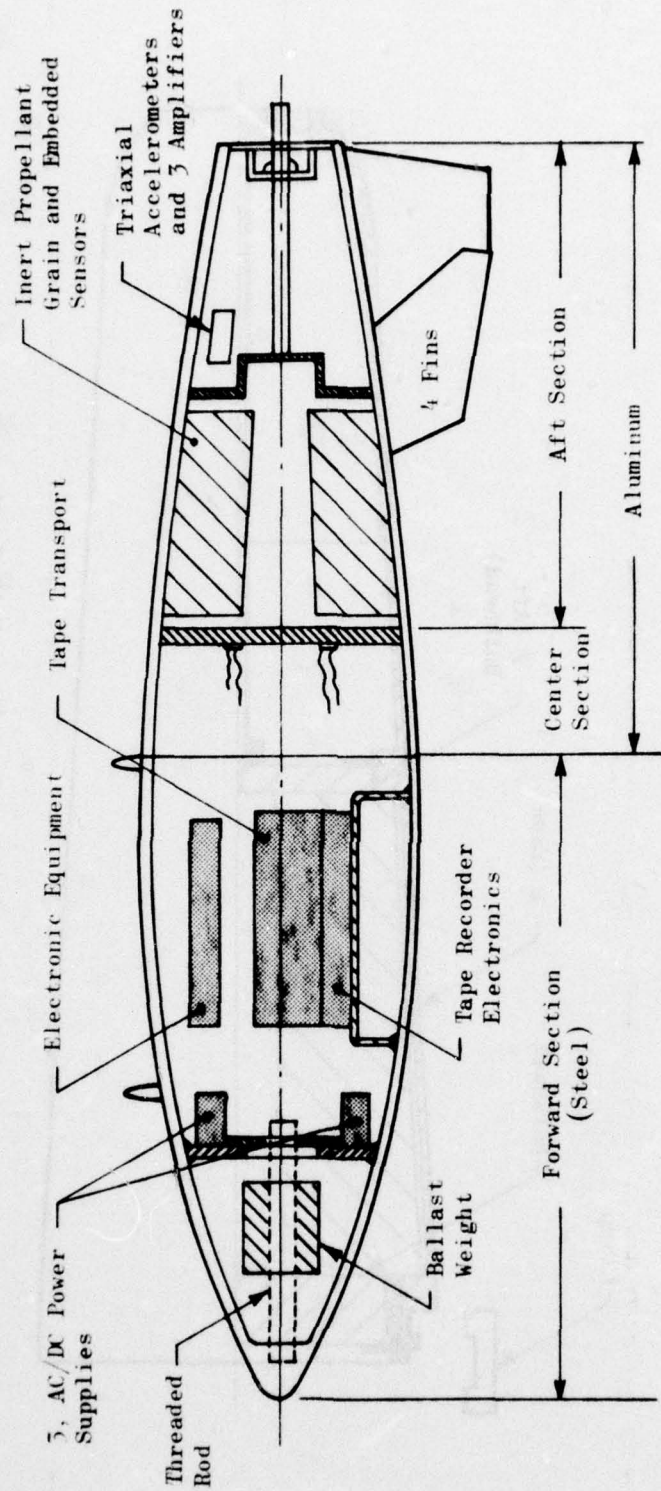
Figure 4. Sketch of Modified BDU-12/B Showing Principal Features

8

Propellant gages were calibrated over a temperature range of -65 to 200 F before they were embedded in the propellant and again after propellant cure. Gage response was checked before several flights by pressurizing the motor chamber cavity from the rear end of Section E (Ref. Figure 2) through the hollow tie bar with nitrogen from 0 to 50 psig.

In addition to the propellant transducers, numerous accelerometers and a system for measuring the load interchange between the BDU and the aircraft wing were installed. The flight load measuring system consisted of semiconductor strain gages applied to a MAU-12C launcher and to the BDU launch lugs.

The BDU was retained on the launcher by a stiff aft lug and a hinged forward lug. Stability was achieved with a pair of sway braces mounted between the lugs. The lugs were preloaded by the launcher sway brace set screws and were calibrated by applying known force vectors to the launcher/BDU assembly.

INERT PROPELLANT COMPOSITION AND PROPERTIES

The inert propellant in the BDU was LPC-667, an HTPB propellant developed by Lockheed Propulsion Company. The formulation and significant properties are given in Table 1.

Tab-end uniaxial test specimens tested at approximately 2% strain gave the relaxation modulus data shown in Figure 5 and the Log a_T shift factors shown in Figure 6. Some more recent indentation modulus values are also shown in Figures 5 and 6. Indentation data show modulus values approximately twice those of the earlier uniaxial test data; and after this material was exposed to a temperature of 150 F for 1 month, a considerably higher indentation modulus value was obtained. This indicated that the LPC-667 inert propellant would harden during the life of the BDU, resulting in increasing stresses.

9

TABLE 1. FORMULATION AND PHYSICAL PROPERTIES OF LPC-667

Formulation, wt %	
R-45/TDI Polymer/Curative	15.0
Fillers	
Aluminum	47.0
$(NH_4)_2SO_4$	35.0
IDP	3.0
Significant Physical Properties	
Block Density, lb/cu in.	0.0634
Coefficient of Linear Expansion, deg F^{-1}	4.25 to 4.50 x 10^{-5}
Poisson's Ratio	0.485--0.49
Stress Free Temperature, deg F	~ 170

PROPELLANT GRAIN STRESS ANALYSES

Stress analyses of the propellant grain were performed for loading conditions of internal pressure, steady-state temperatures, transverse dynamic accelerations, and aerodynamic heating. All calculations were made with finite element computer programs operating on a digital computer. Thermal and pressure calculations were performed with a finite element axisymmetric model consisting of 200 elements uniformly positioned in both axial and radial directions. Transverse dynamic solutions were computed with a plane strain model containing 162 elements in a 180-degree section, using symmetry conditions on the sector boundaries. These elements were positioned every 10 degrees with uniform radial divisions. Thermal and pressure problems were run with elastic properties; linear viscoelasticity was used in the dynamic computations. The results of the thermal analyses are shown as stress and deformation patterns in Figures 7 through 18. The asymmetry of these stress patterns is due to the taper in the grain configuration.
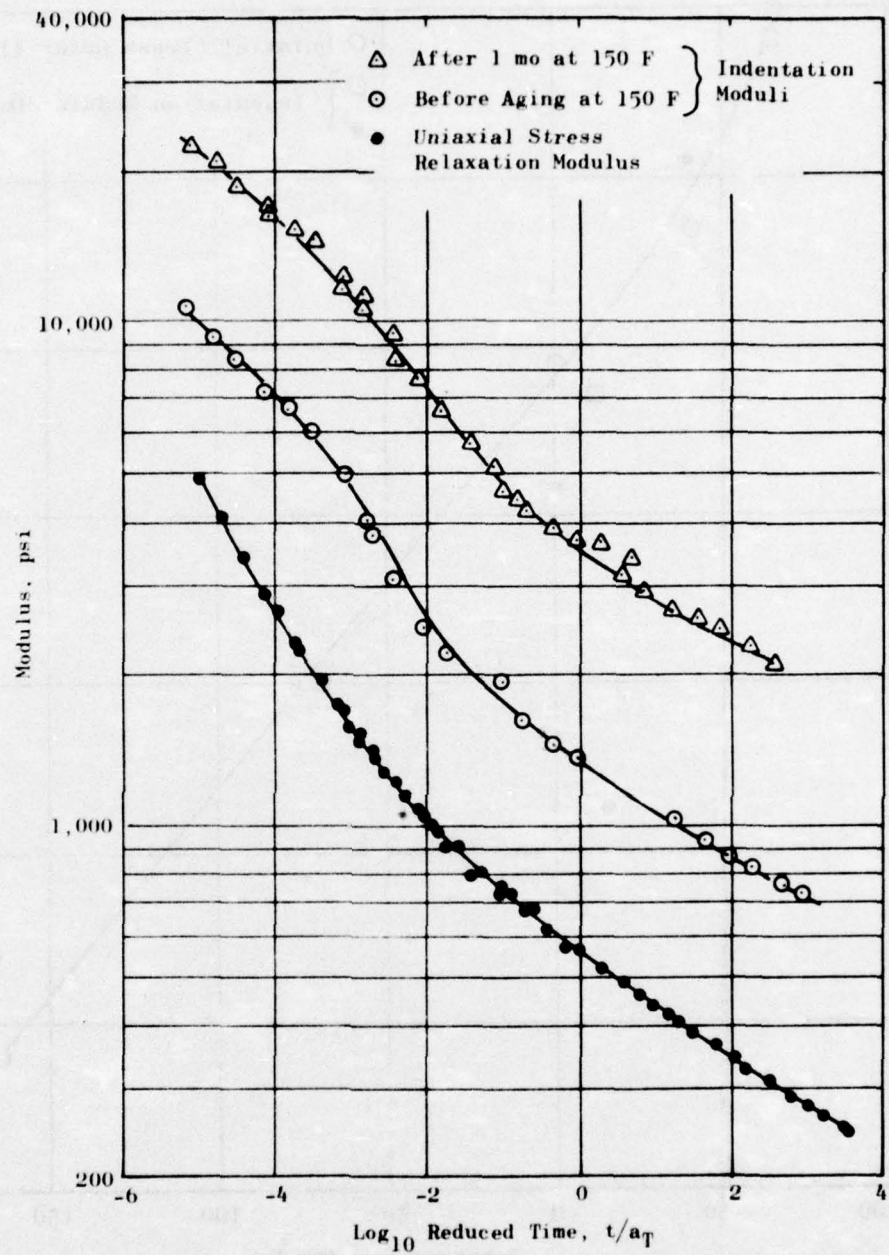
Figure 5. Uniaxial Stress Relaxation and Indentation Modulus
Data for Inert Propellant LPC-667

11
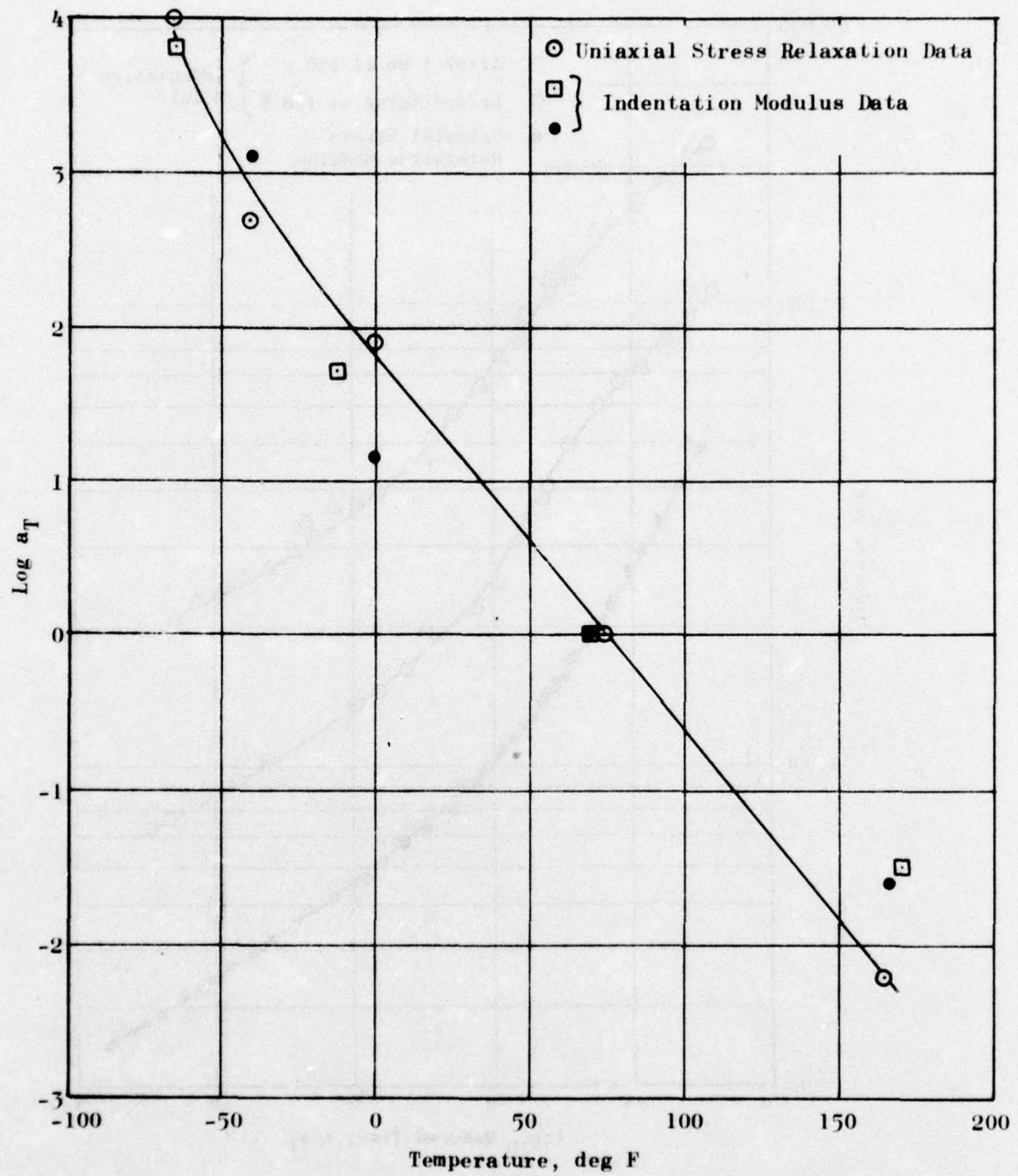
Figure 6. Log a_T vs Temperature, Inert Propellant LPC-667

12
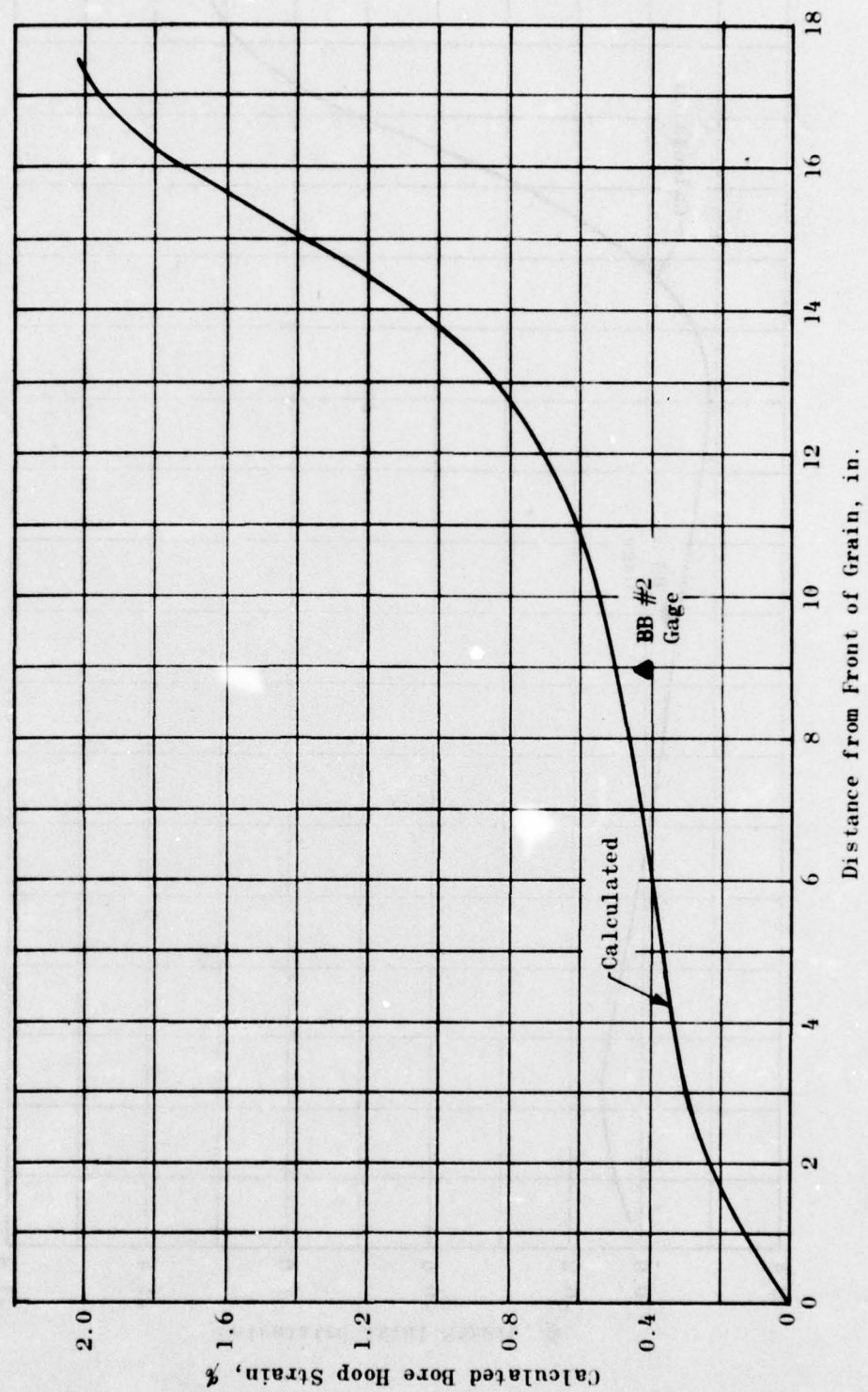
Figure 7. Bore Hoop Strain, 50 psi Internal Pressure

13
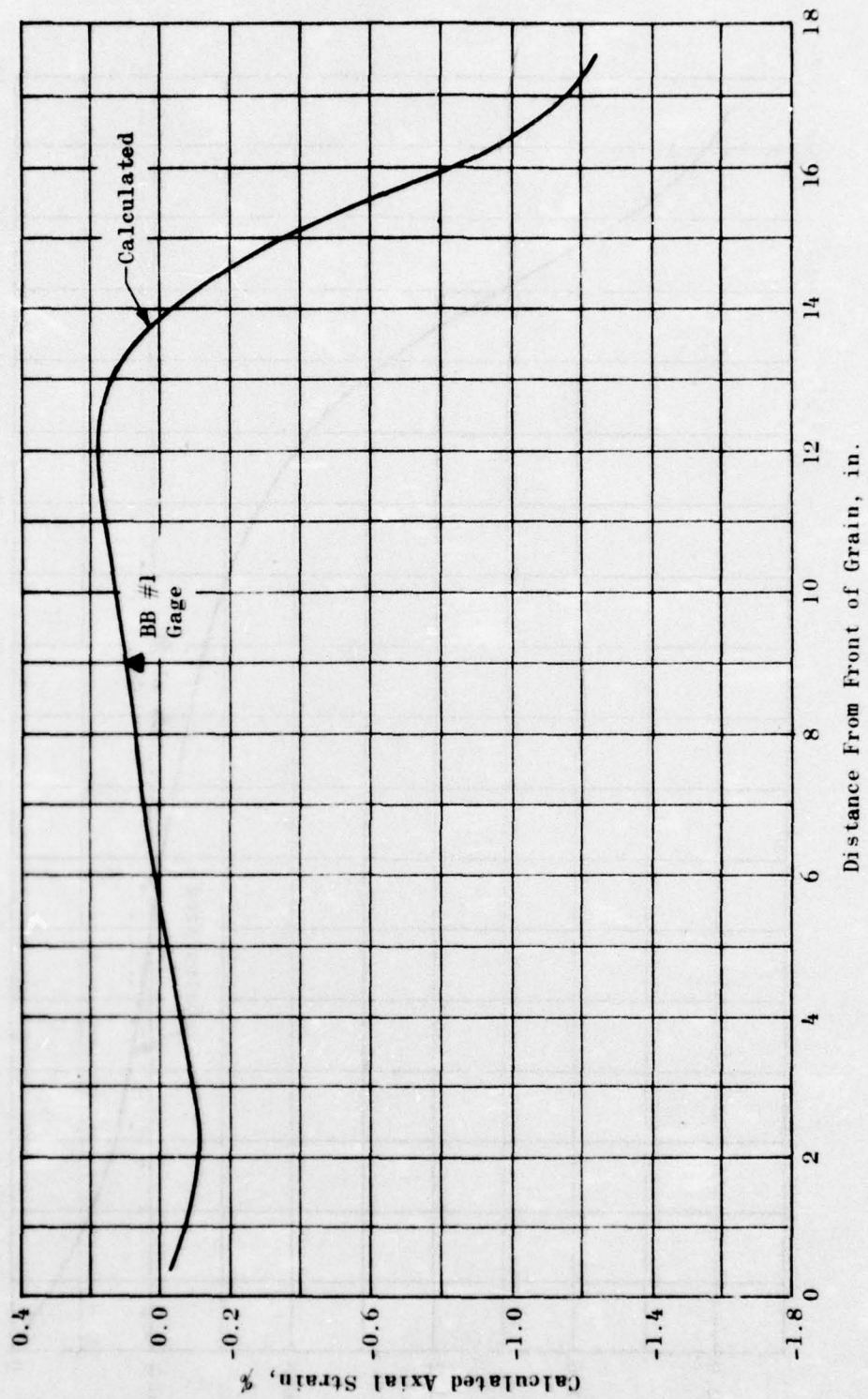
Figure 8. Bore Axial Strain, 50 psi Internal Pressure

14
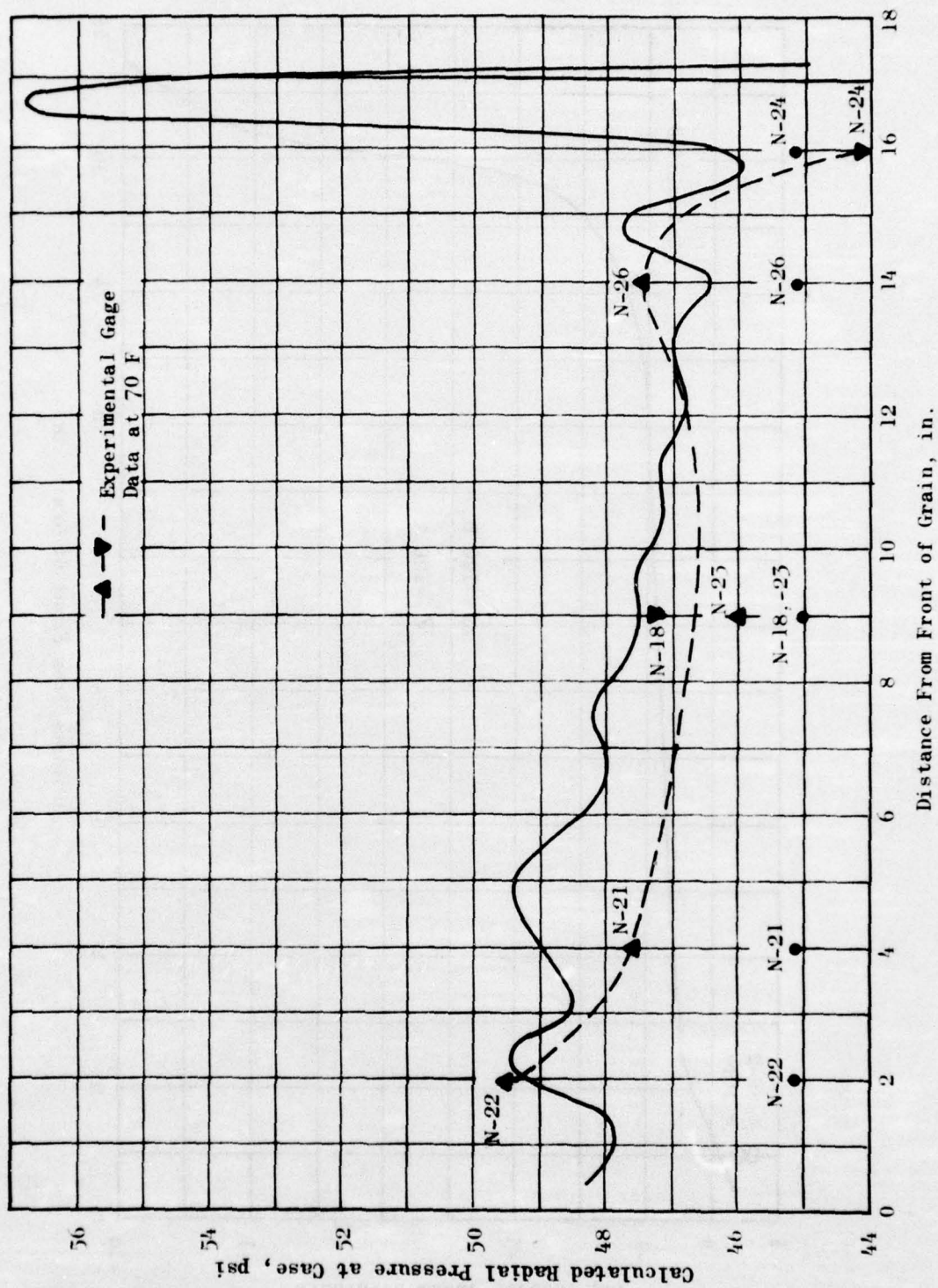
Figure 9. Radial Pressure at Case, 50 psi Internal Pressure

15
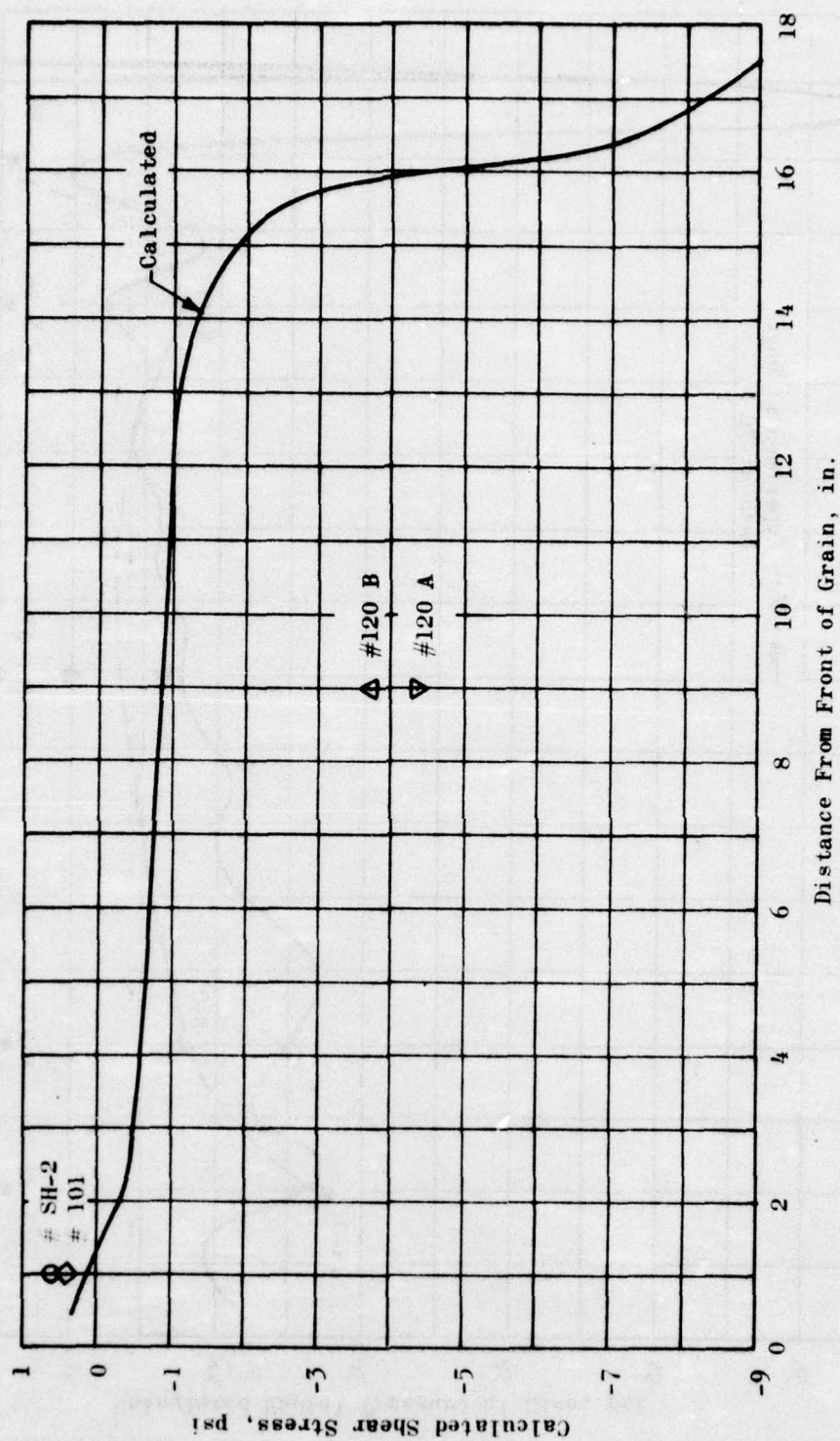
Figure 10. Interface Shear Stress, 50 psi Internal Pressure

16
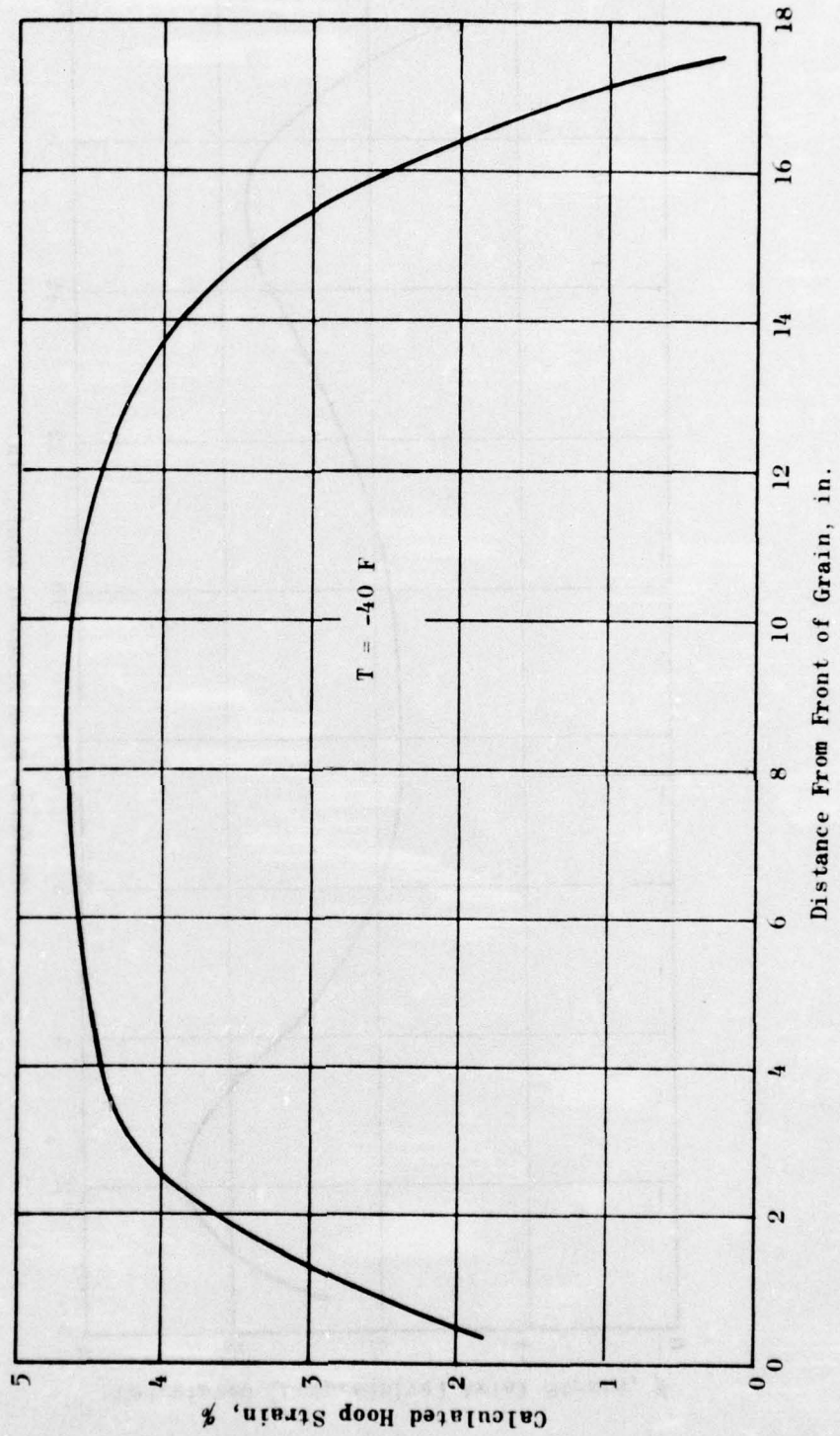
Figure 11. Bore Hoop Strain, Thermal Cooling

17
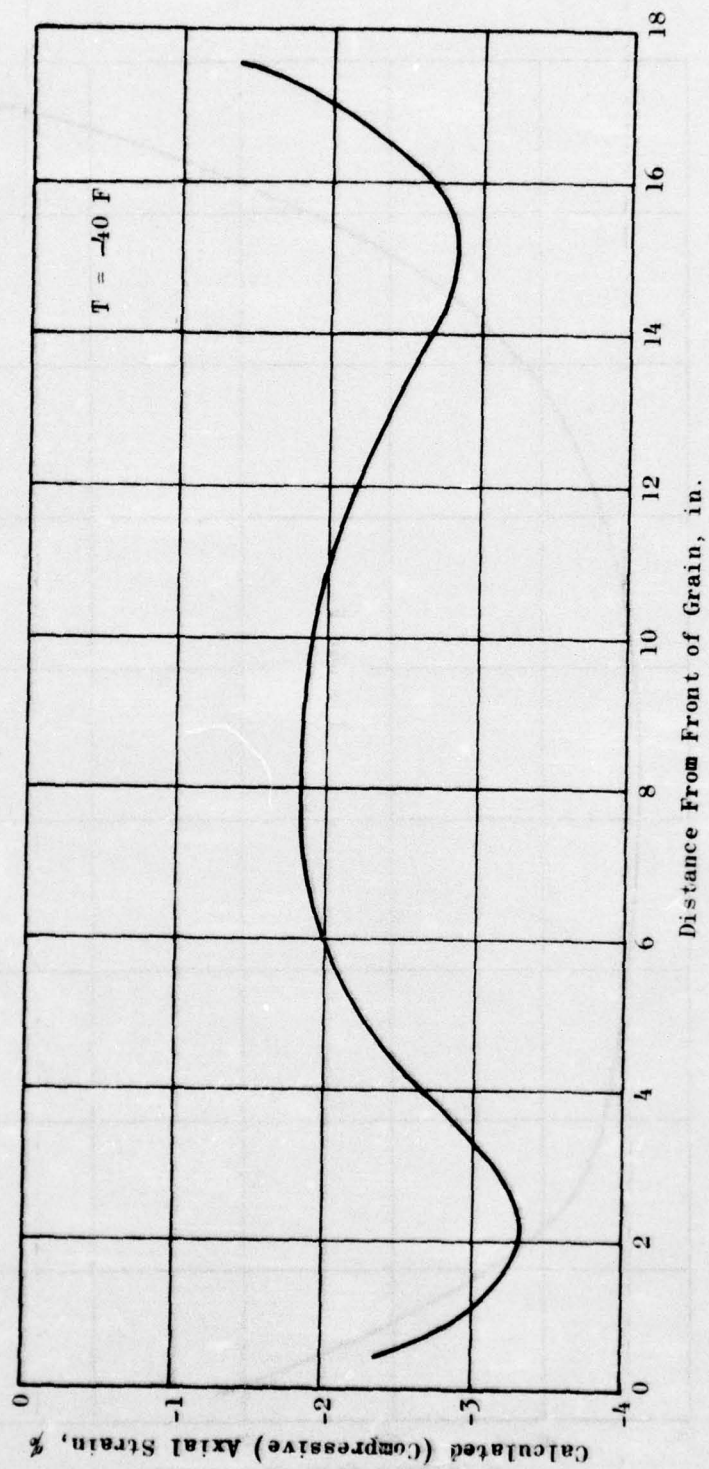
Figure 12. Bore Axial Strain, Thermal Cooling

18
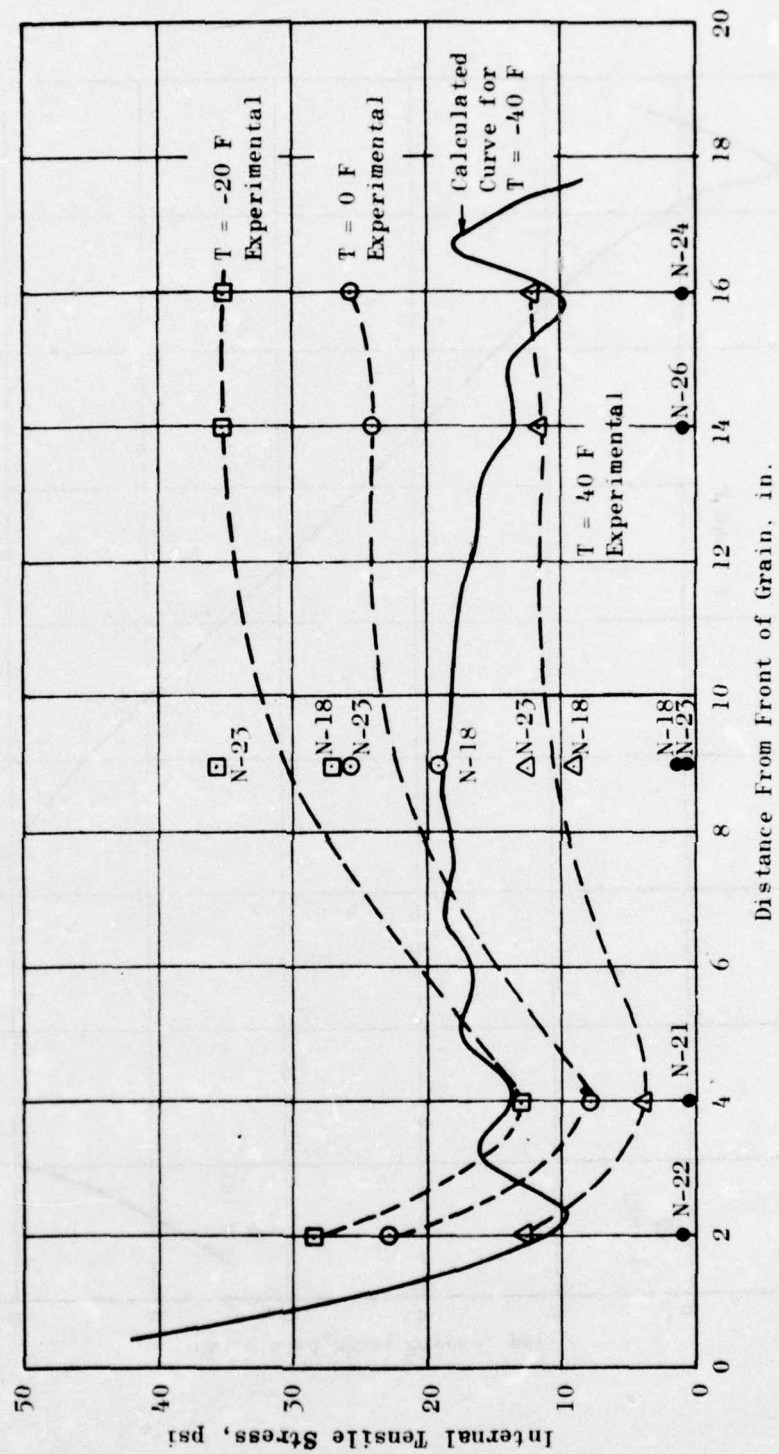
Figure 13. Interface Radial Stress, Thermal Cooling

19
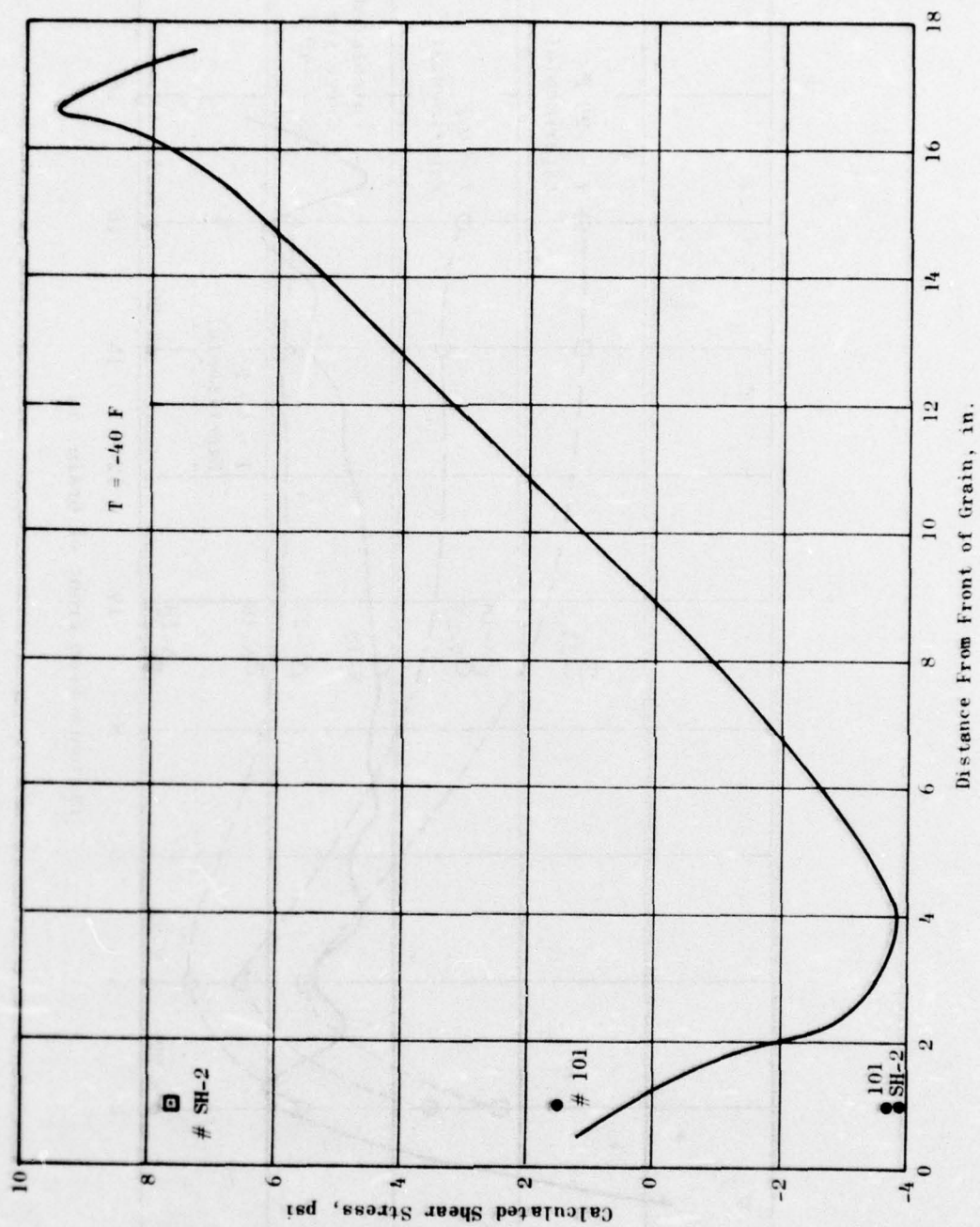
Figure 14. Interface Shear Stress, Thermal Cooling

20
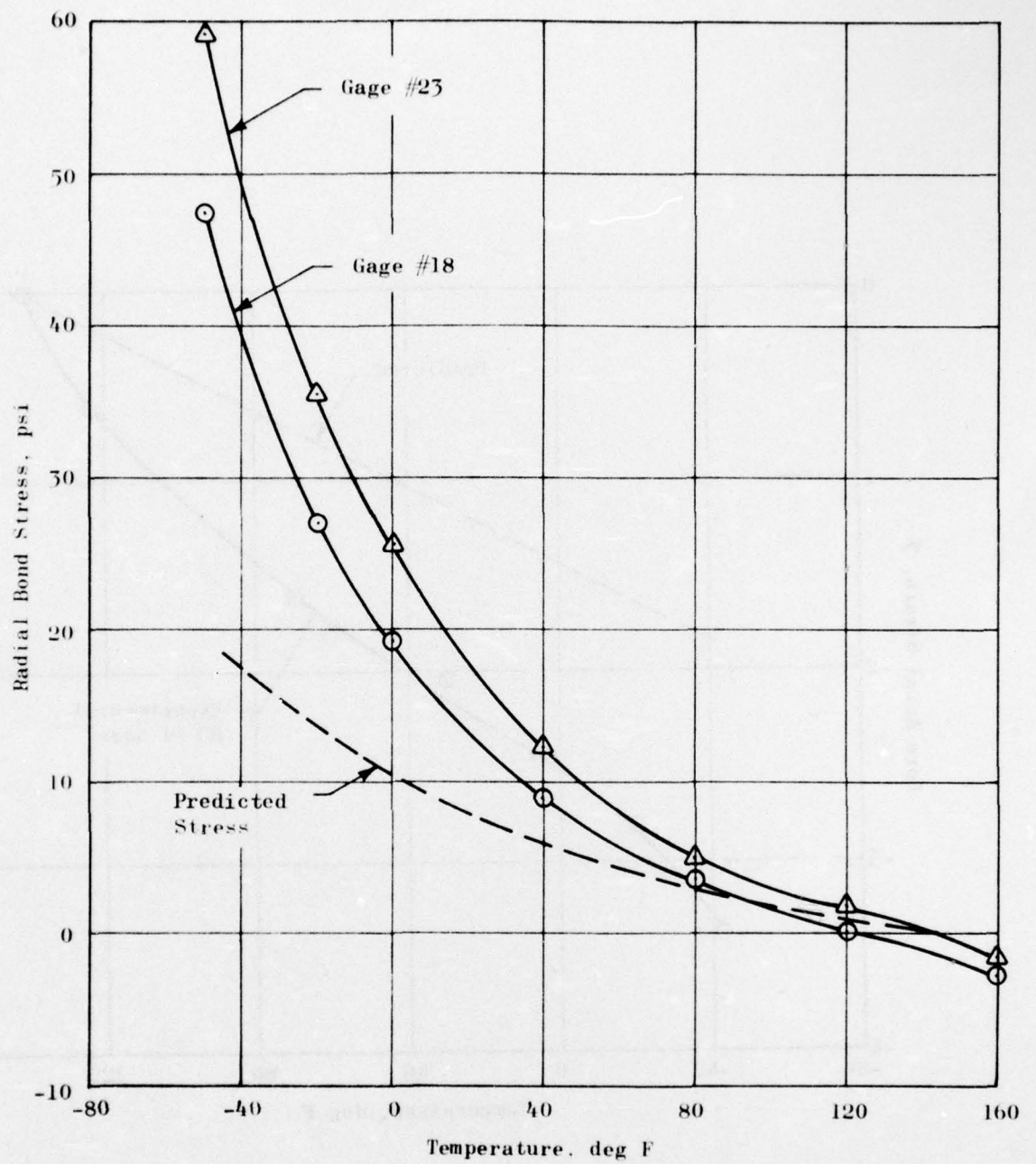
Figure 15. Predicted and Experimental Interface Radial Stress
vs Temperature, Midpoint of BDU Grain

21
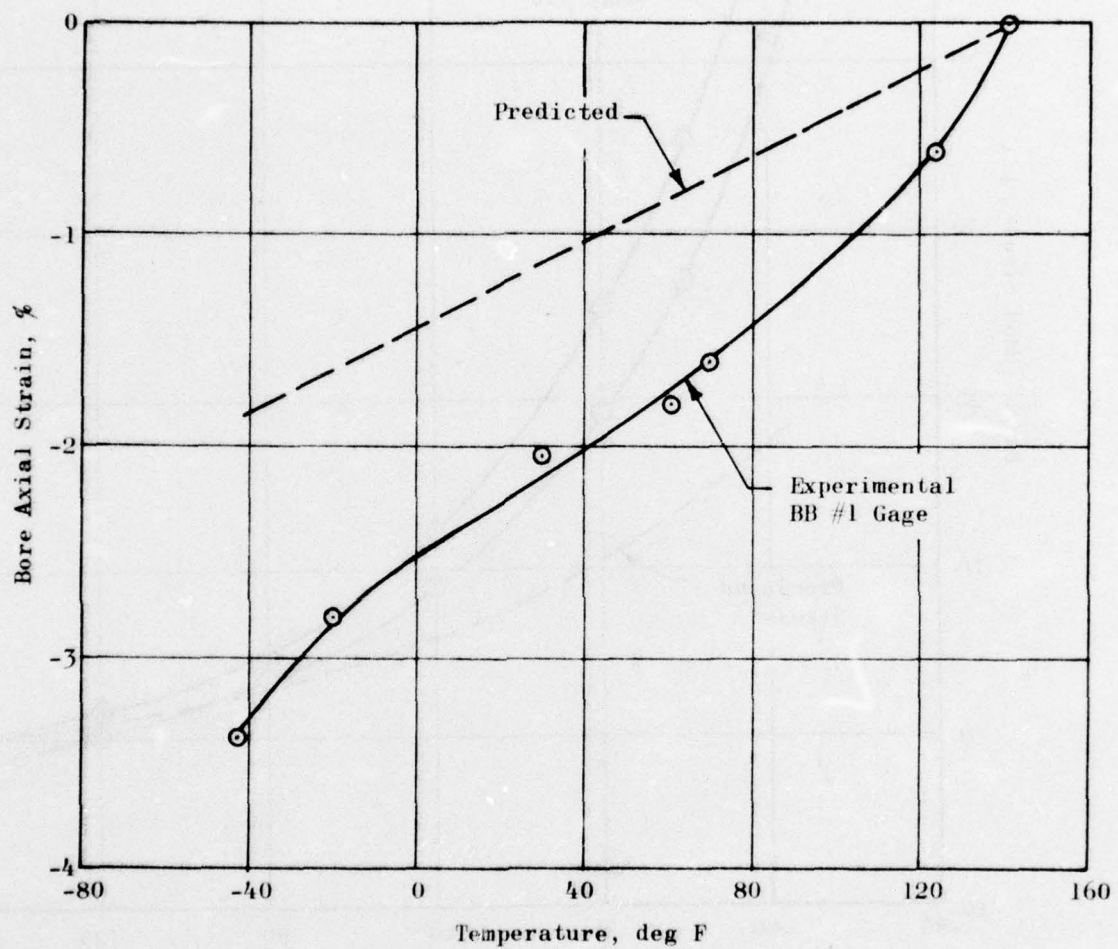
Figure 16. Predicted and Experimental Bore Axial Strains
vs Temperature, Midpoint of BDU Grain

22
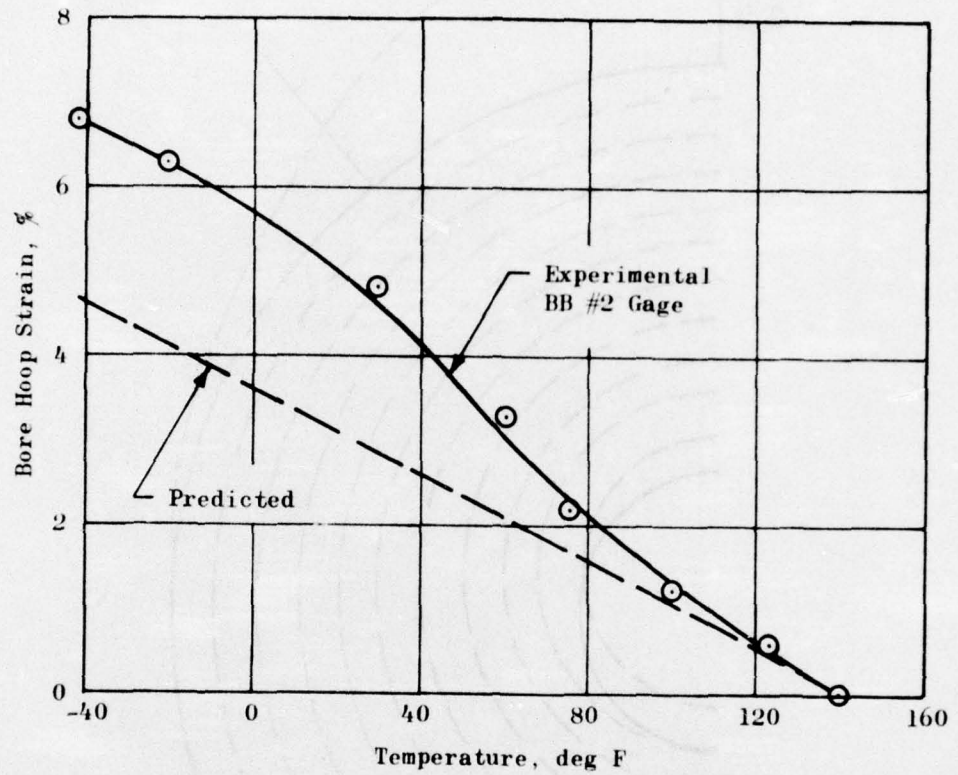
Figure 17. Predicted and Experimental Bore Hoop Strains
vs Temperature, Midpoint of BDU Grain

23
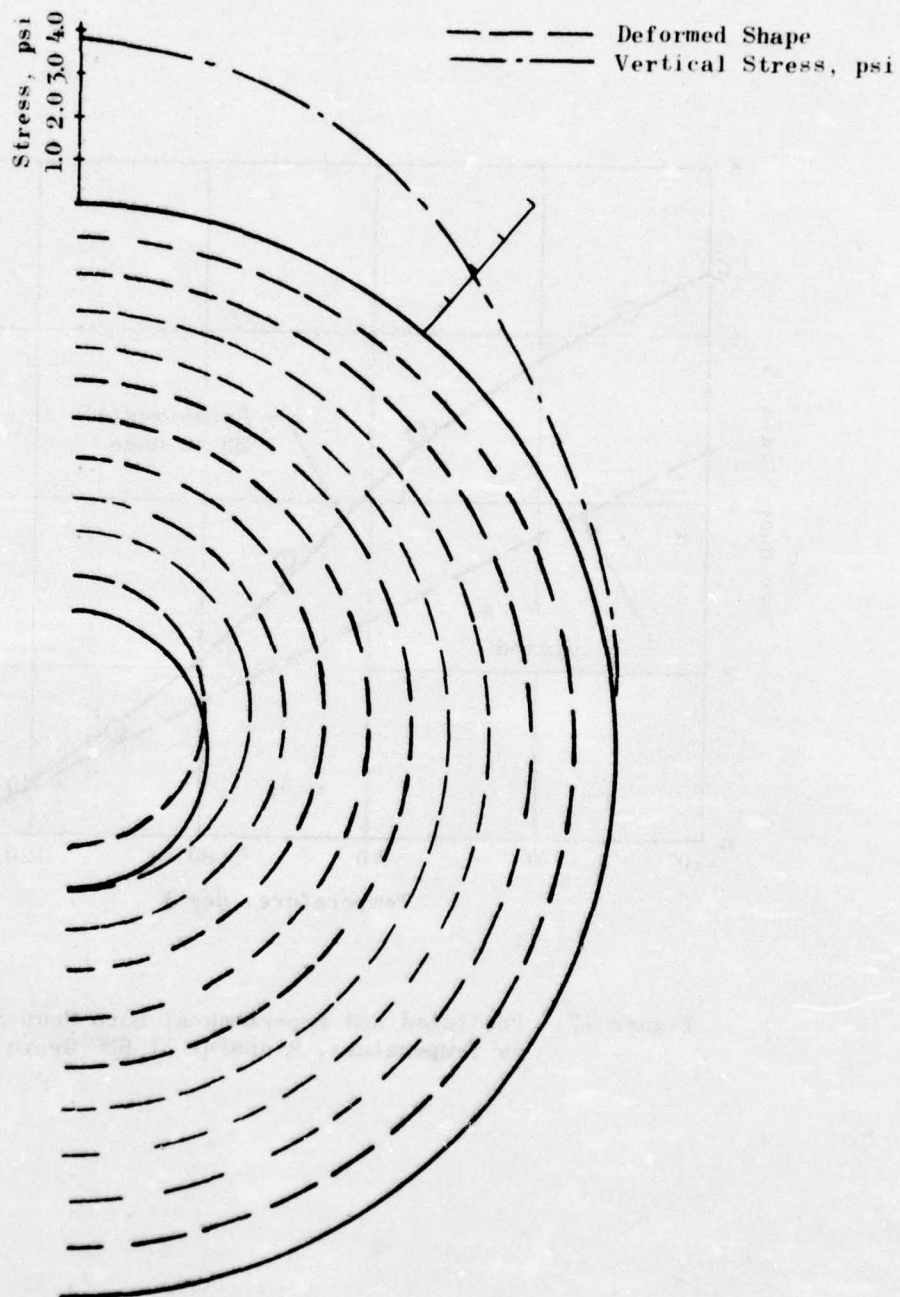
Figure 18. Deformation and Bond Stress Under Transverse
Dynamic Loads of 10 g at 300 Hz

24

Under some loading conditions the stresses exhibit an oscillatory pattern that is not a real phenomenon but a consequence of the periodicity of the element spacing. Actual stresses follow the mean value of the oscillations.

Dynamic solutions were obtained for the conditions of applied sinusoidal displacements of several frequencies and magnitudes. Displacement magnitudes were adjusted to produce a 10-g peak acceleration at each frequency. Bond stresses under this loading are thus independent of frequency, having a magnitude of about 3.5 psi at the top and bottom grain boundary.

This corresponds to 2.7 psi for locations at a roll angle of 45° to the plane of transverse acceleration. (BDU normal stress gages were oriented in a plane 45° from vertical in flight configuration.) For linear response one would predict 0.27 psi bond stress for a 1-g vertical (Z-axis) acceleration.

Maximum displacement response to the dynamic loading does not occur at the same location for each frequency but tends to occur either at the top of the inner bore or at the 90-degree position in the center of the web. This displacement pattern is shown in Figure 18.

Results of the dynamic analyses are presented in Table 2. The input frequencies shown were chosen to coincide with modal frequencies of the entire BDU assembly and do not represent modes of the propellant grain itself.

The aerodynamic heating analysis was made in two parts. The propellant modulus (see Figures 5 and 6) was determined at appropriate temperatures and loading times. For the aerodynamic heating analysis, the grain temperature distribution measured at the end of the high-altitude dash in Flight 10 was used (see Flight Tests Section). The peak bond stress was calculated to be 2.6 psi.

25

TABLE 2. DISPLACEMENT AND DISPLACEMENT AMPLIFICATION FOR 10 g TRANSVERSE DYNAMIC LOADING OF THE BDU GRAIN

Frequency, Hz	Input Displacement, in.	Maximum Amplification	Location
30	0.109	1.01	Midweb at 90°
64	0.024	1.01	Midweb at 90°
143	0.0048	1.01	Midweb at 90°
300	0.00109	1.09	Inner Bore
2000	0.0000245	2.1	Inner Bore

INSTRUMENTATION

BDU INSTRUMENTATION

Instruments used in the inert propellant grain were designed to measure the following parameters:

1. Bore hoop and axial strains
2. Radial temperature profile
3. Normal and shear stresses at the case-grain interface
4. Temperature

Bore strains were measured by flexible metal clip gages, Figure 19, mounted on the bore of the grain by means of short pins embedded in the propellant. The strain in the inert propellant at the clip gage locations was not sufficient to produce cracking, even with the increase in strain produced by the embedded pins.

Temperatures were measured by means of VECO "thinistors," extremely thin, unprotected thermistors with a very rapid temperature response. The thermistors were installed adjacent to each of the stress and strain sensors, and a temperature rake (Figure 20) manufactured from cured inert LPC-667 propellant was also used to measure the gradient in the grain.

Normal interface stresses in the grain were monitored by Konigsberg P14B 150 psi diaphragm-type pressure sensors. These devices were bonded to the inside of the insulation layer coated on the case wall. Interface shear stresses were monitored by several types of shear sensors: Two shear cubes containing semi-conductor strain gage elements as shown in Figure 21a, two shear cubes containing 120-ohm foil-type strain gage elements (Figure 21b), and a shear gage using a bending beam-type arrangement as shown in Figure 21c.

27

oll Semiconductor Strain Gages

0.006

0.25 in.

0.12 in.

.25 in.

Clip Gage

Adhesive

Mounting Pin

Propellant
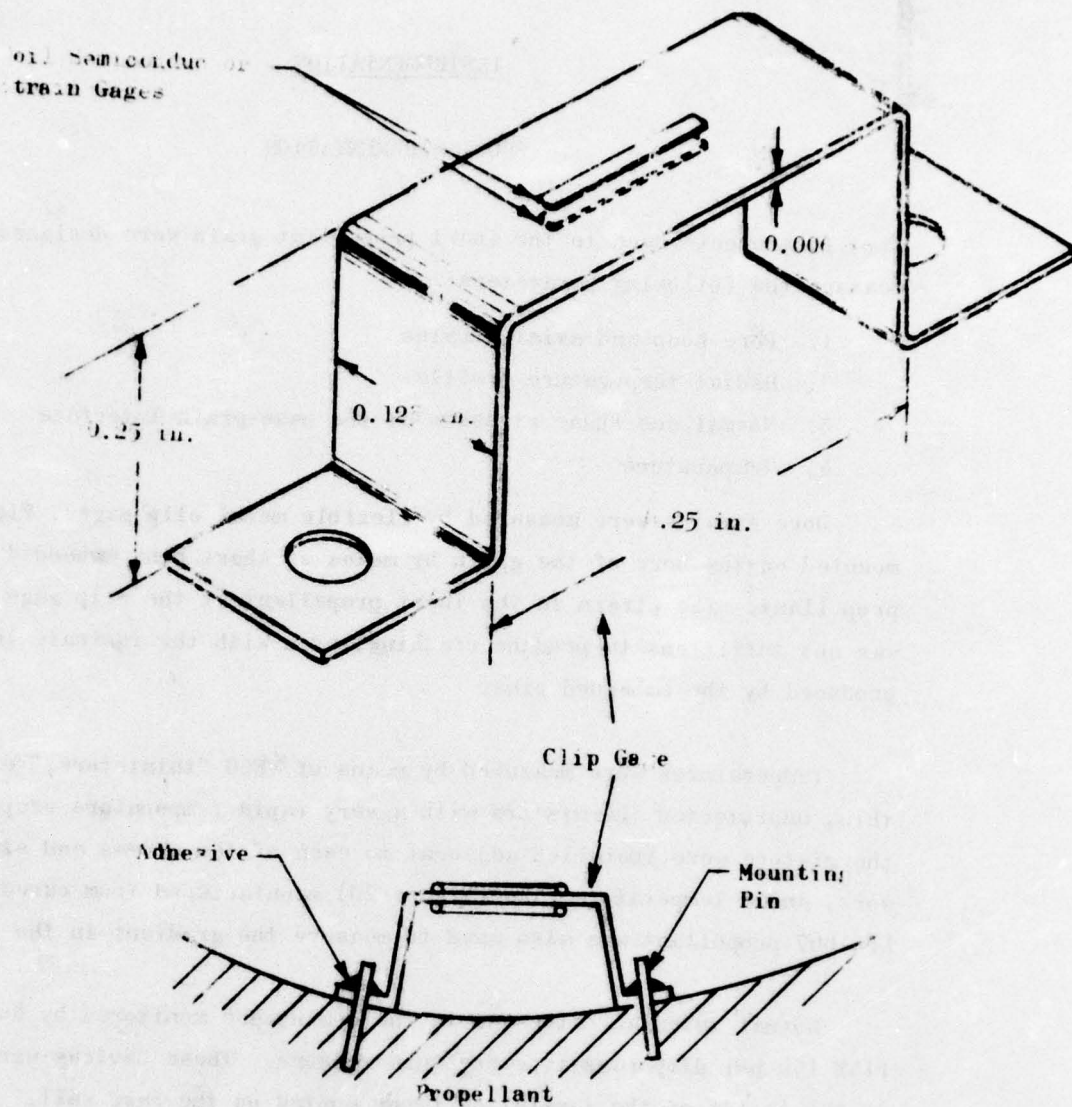
Figure 19. Clip-Type Surface Strain Gages Mounted on Bore of BDU
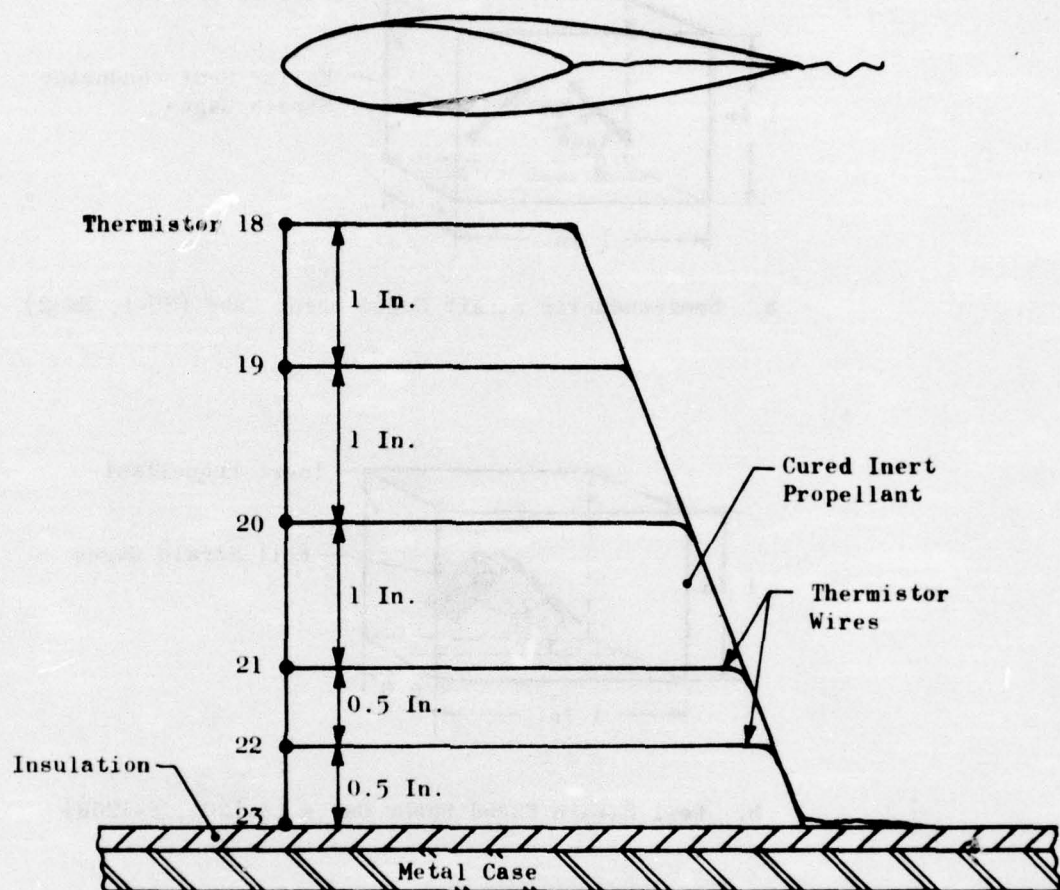
Figure 20. Thermocouple Rake for Strain Radial
Temperature Profile

29
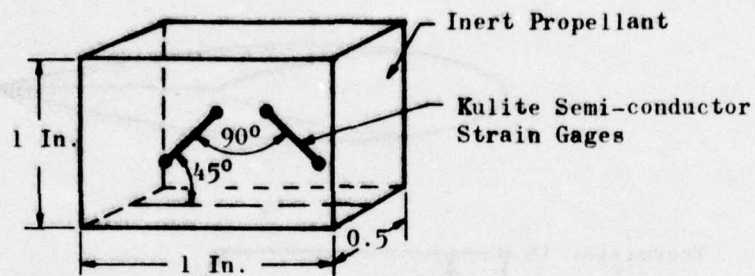
a. Semiconductor Strain Gaged Shear Cube (SH-1, SH-2)
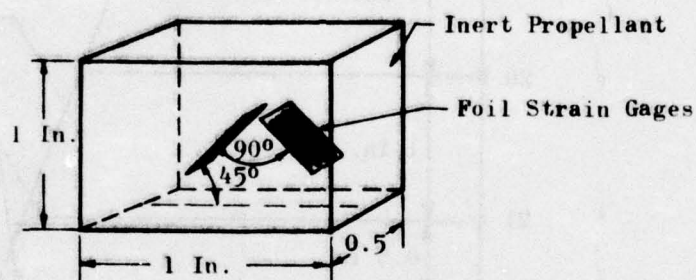
b. Foil Strain Gaged Shear Cubes (S-120A, S-120B)
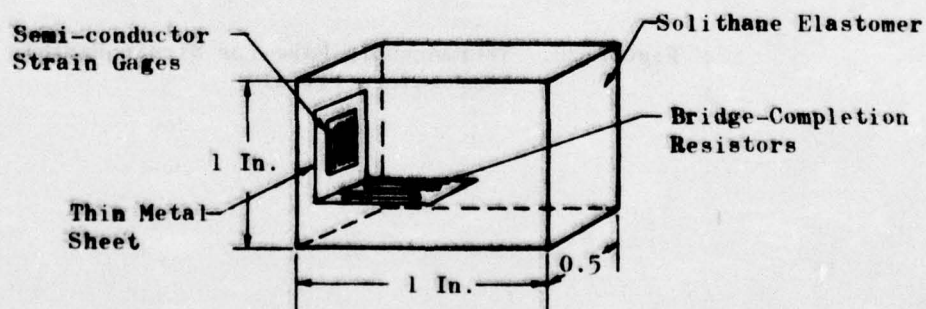
c. Bending Beam Type Shear Sensor (SH-101)

Figure 21. Shear Sensors Used in BDU

GAGE LOCATIONS

The instrumentation plan for the grain was designed to use two planes of embedded sensors as shown in Figure 22. In this manner, it was expected that sufficient data under conditions of yawing, pitching, and vibration (and combinations of these parameters), would be obtained during the flights. In addition, the instrumentation plan was slightly redundant so a number of the gages could fail during the life of the BDU without impairing the performance of the BDU as a whole.
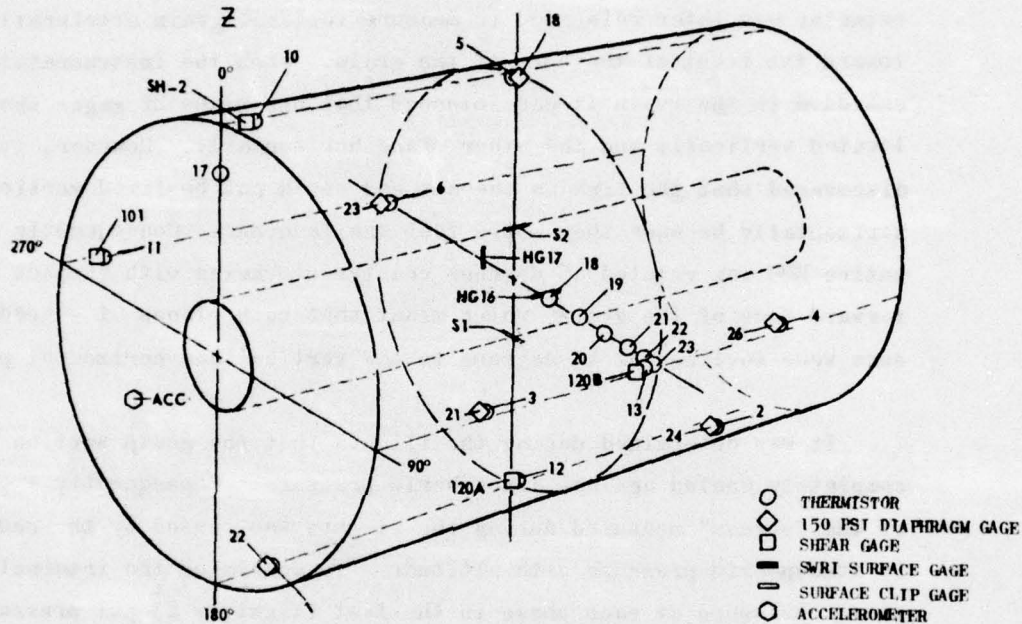
Figure 22. BDU Grain Instrument Locations

The thermistors did gradually fail during the life of the BDU and one shear cube, SH-1, failed when the mandrel was withdrawn from the grain after casting, leaving only one of the sensitive shear cubes, which remained operative for the majority of the test flights. The shear gages with foil sensing elements operated successfully throughout the flights, but their sensitivity was barely adequate for the thermal stresses in the grain. Only one normal 150-psi diaphragm stress sensor malfunctioned during the life of the BDU. Gage N-18 became defective in one sensing element,

and was subsequently rewired as a half-bridge gage. In this configuration, changes in pressure could readily be measured, as could vibrational stresses during flight. However, the zero stress temperature function for this modified gage was not known, with the result that thermal stresses it recorded were in error during the later test flights.

A CEC-type accelerometer was mounted on the front face of the grain to measure fore and aft grain accelerations in flight. Because of the small amplitudes of these fore and aft grain accelerations, this accelerometer was later relocated to measure vertical grain accelerations toward the front of the bore of the grain. When the instrumentation was embedded in the grain it was intended that one plane of gages should be located vertically and the other plane horizontally. However, it was discovered that the fins on the aft end could not be fixed vertically and horizontally because they would foul the launcher. Consequently the entire BDU was rotated 45 degrees counter-clockwise with respect to the forward face of the grain, which meant that both planes of embedded sensors were inclined at 45 degrees to the vertical and horizontal planes.

It was determined during the flights that the grain section was not completely sealed against atmospheric pressure. Consequently a portion of the "stress" measured during the flights was caused by the reduction in atmospheric pressure with altitude. To determine the internal atmospheric pressure at each phase in the test flight, a 25-psi pressure gage was bonded to the front face of the grain. Thermal stress in the grain was ascertained by subtracting this change in atmospheric pressure from the total change in stress at the gage location.

THERMISTOR CALIBRATION

The thermistors were connected with three resistors to form a bridge circuit (Figure 23) that was supplied from the 28-volt regulated voltage supply through a dropping resistor. The circuit for the grain thermistors

32

27 K Ω

VECO FN3C22
Thermistor

28 v

1 K Ω

E_O

1 K Ω

1 K Ω

100 K Ω

VECO FN3C23
Thermistor

28 v

5 K Ω

E_O

0.5 K Ω

5 K Ω
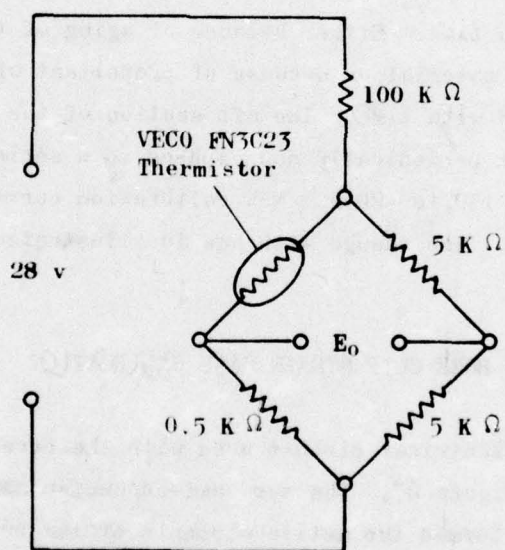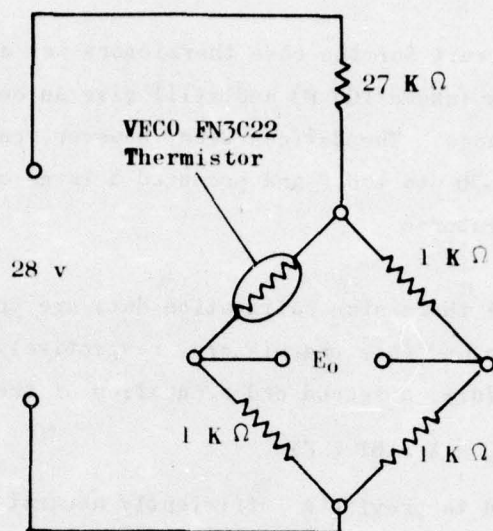
Figure 23.   Thermistor Circuits

33

was arranged to give an output between approximately 50 and 250 milli-volts for the expected temperature range of 160 to -70 F.

The circuit for the case thermistors was arranged to measure high temperatures (above 100 F) and still give an output in the 0- to 300-millivolt range. The devices were, however, calibrated over the entire range from -70 to 160 F and produced a large output (1.0 volt) at the lower temperatures.

Typical thermistor calibration data are presented in Figures 24 and 25 for grain and case thermistors, respectively. The curves are not linear; in fact, a second order equation of the type

$$E_o = A + BT + CT^2$$

was required to provide a sufficiently accurate fit.

One additional problem concerned the change in thermistor circuit output with time. Either because of aging of the exposed semi-conductor thermistor material or because of propellant attack, the thermistor output changed with time. The aft section of the BDU was placed in a storage box periodically and exposed to a series of different temperatures from 150 to -20 F. New calibration curves were obtained from these data. The change with age is illustrated in Figure 26 for Thermistor 2.

PROPELLANT BORE CLIP STRAIN GAGE CALIBRATION

The electrical circuit used with the bore-mounted clip gages is shown in Figure 27. The two semi-conductor strain gages mounted on the clip gage formed two active elements of the bridge circuit, and the bridge was supplied from the 28-volt regulated supply through a 13K ohm resistor.
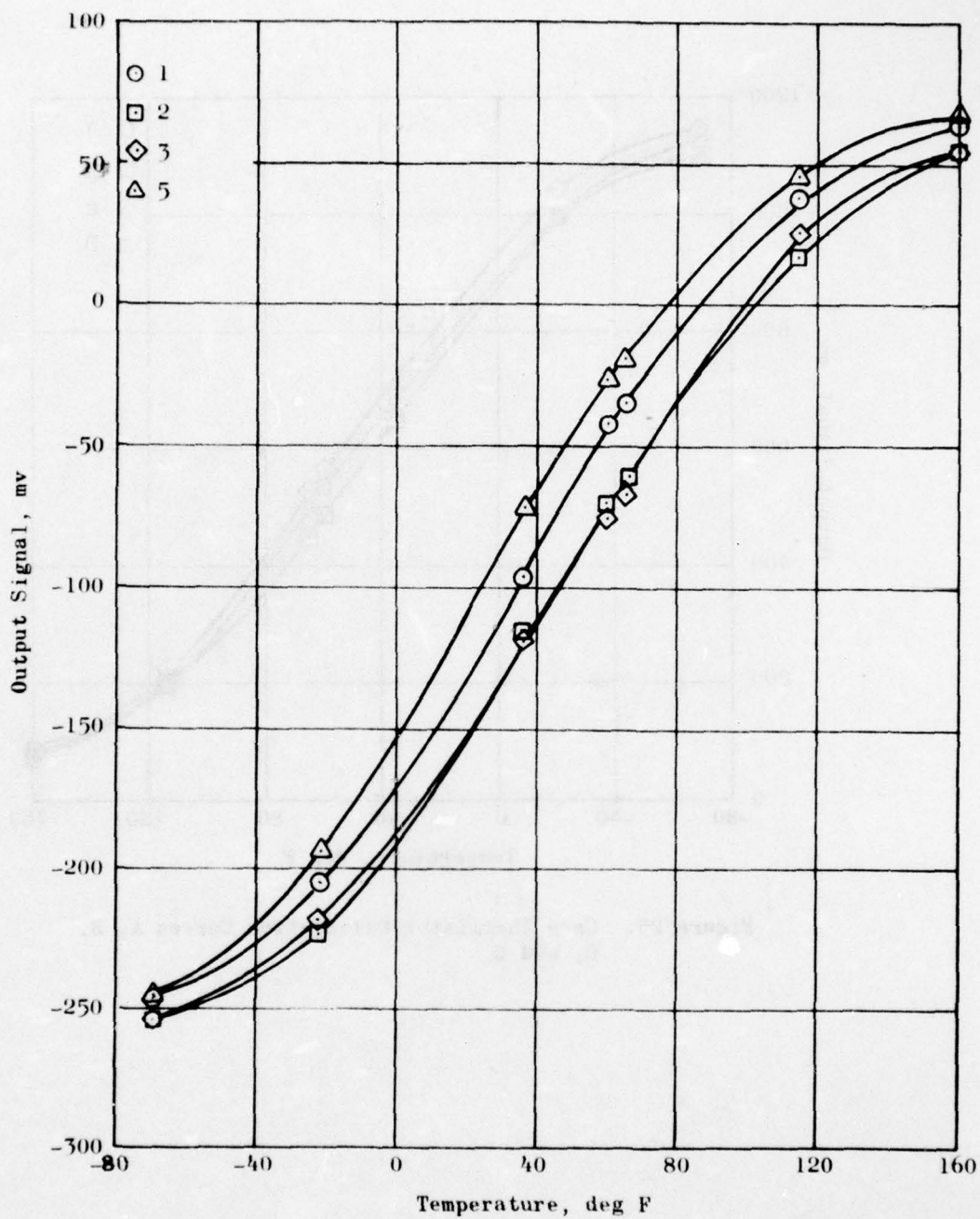
Figure 24. Thermistor Calibration Curves 1, 2, 3, and 5
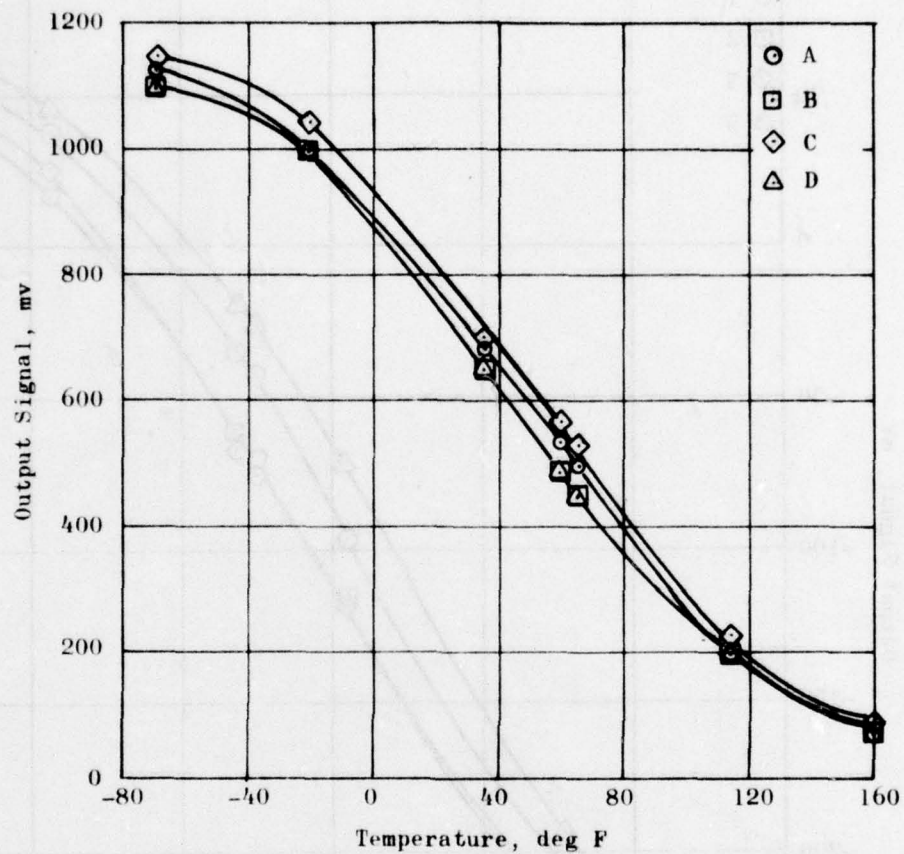
Figure 25. Case Thermistor Calibration Curves A, B, C, and D
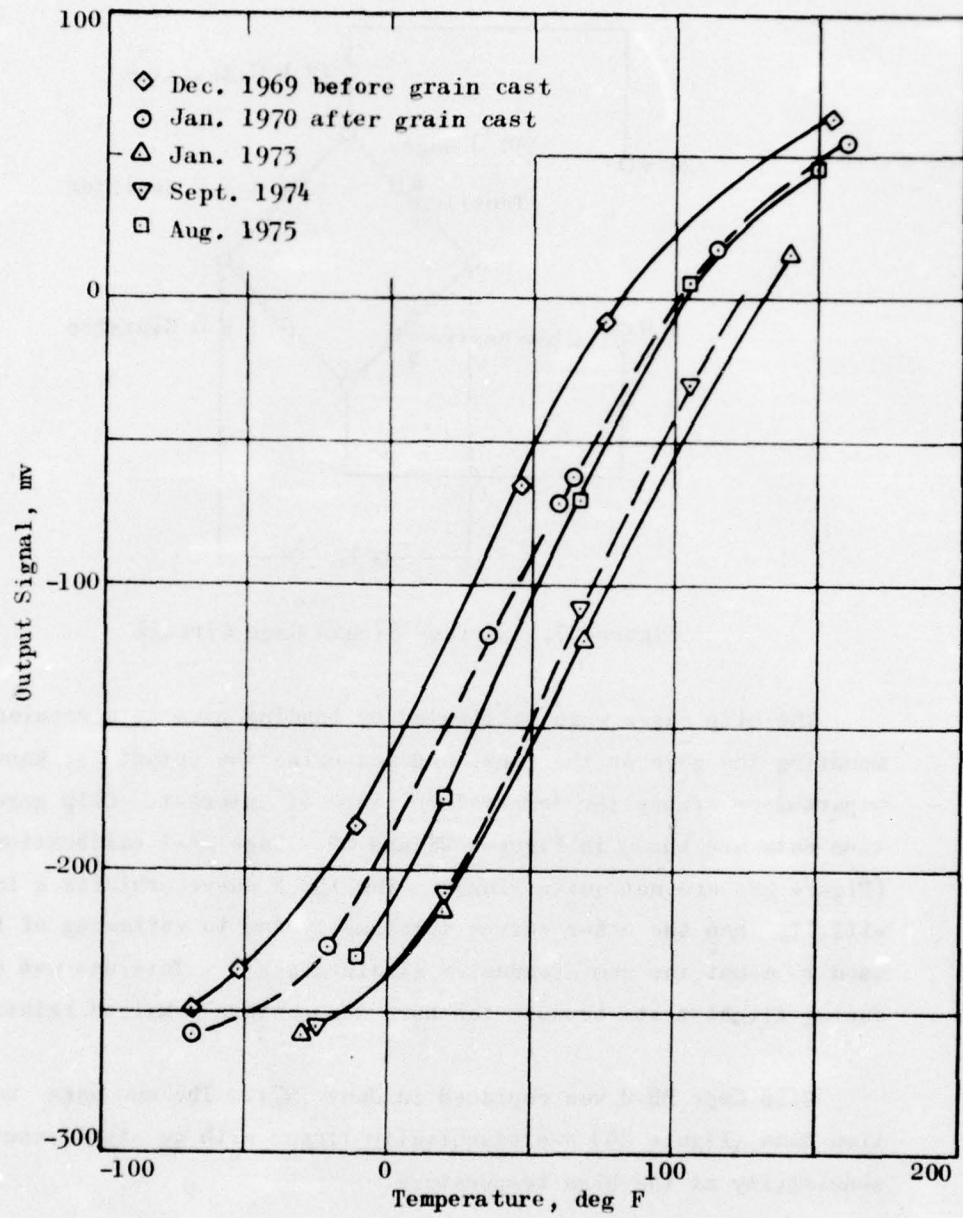
Figure 26.   Thermistor 2,   Output vs Temperature
Showing Changes with Age of BDU

37
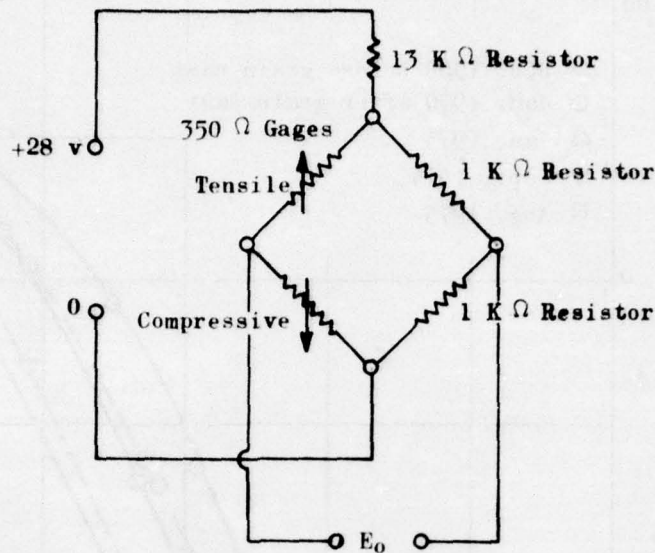
Figure 27. Surface Strain Gage Circuit

The clip gages were calibrated by bonding pins to a vernier caliper, mounting the gage on the pins, and measuring the output for known pin separations across the temperature range of interest. Clip gage calibration data are shown in Figures 28 and 29. Gage BB-1 calibration data (Figure 28) are not quite linear. The 150 F curve exhibits a lower sensitivity than the other curves (presumably due to softening of the epoxy used to mount the semi-conductor strain gages). This was not a problem during flight tests because the bore temperature remained relatively low.

Clip Gage BB-2 was replaced in June 1971. The new gage calibration data (Figure 29) are essentially linear with no significant loss in sensitivity at the high temperature.

38
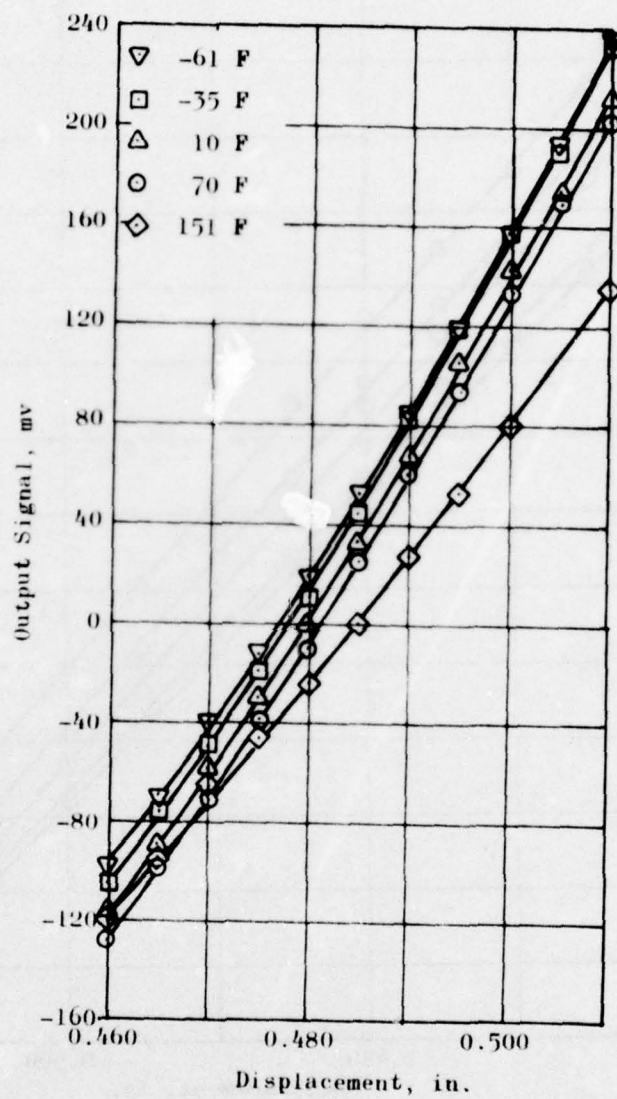
Figure 28. Surface Clip Gage 1 Calibration Data

39
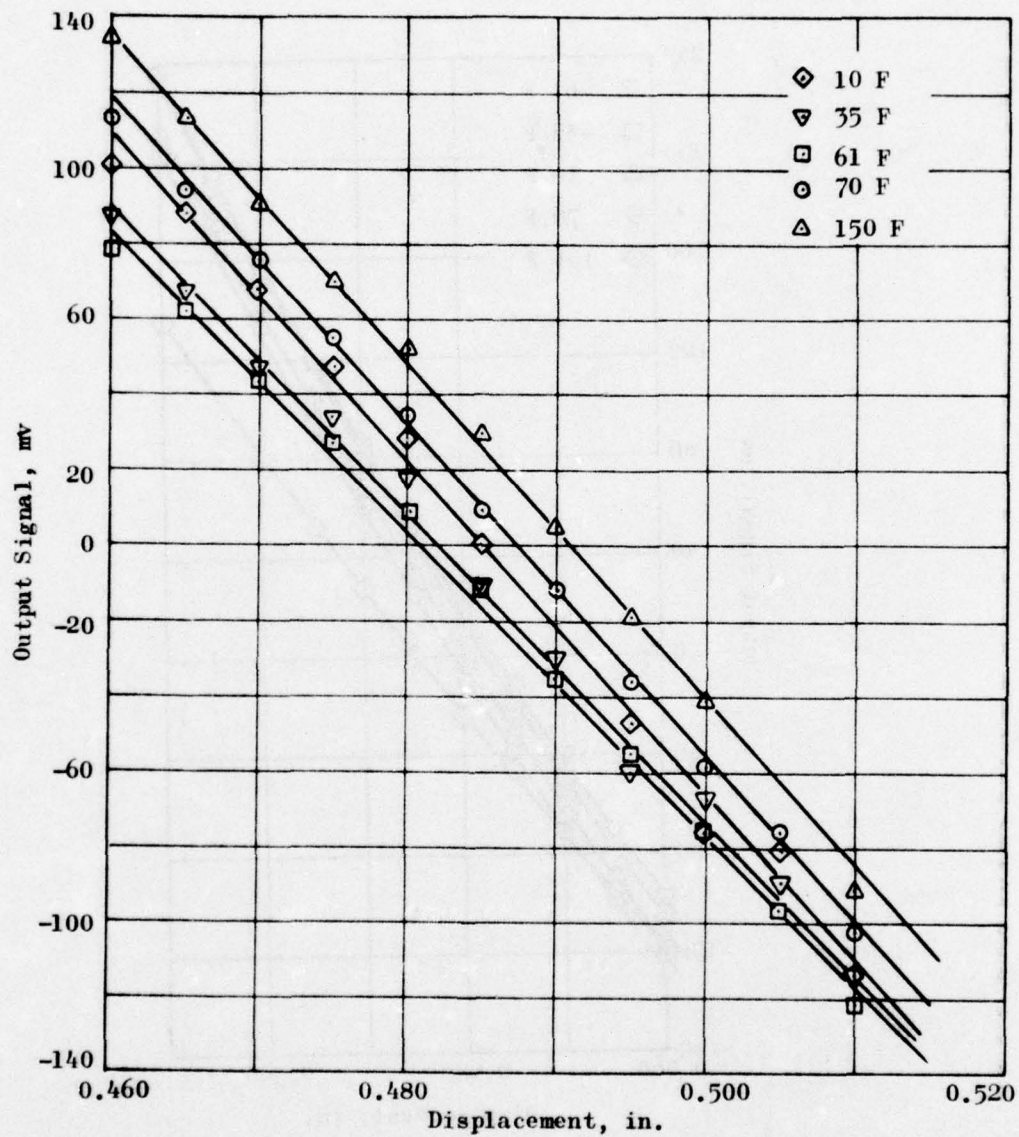
Figure 29. Surface Clip Gage 2 Calibration Data

40

Figures 30 and 31 show clip gage output during isothermal tests from 150 to -40 F. Clip Gage BB-2 reading hoop strain in the bore showed a change from the initial reading in 1970 to the 1971 tests, but thereafter no significant change in gage output was observed. Gage BB-1 measuring bore axial strain showed no significant changes during the entire life of the BDU.

NORMAL STRESS SENSOR CALIBRATION

The Konigsberg P14B normal stress gages contained four semi-conductor strain gage elements, two on each side of the diaphragm, wired to form a four-active-arm bridge circuit as shown in Figure 32. A dropping resistor of approximately 3.6K ohms was used with a 28-volt power supply. Various series and shunt resistors were used in the circuit to give a low zero shift with temperature and an almost constant sensitivity. Each gage was individually temperature-compensated and its circuit was, therefore, slightly different from circuits of the other gages.

Normal stress sensors were calibrated with the gages bonded in place inside the case and surrounded by inert propellant of approximately 1.5-inch radius. Pressure steps were applied to the gage-propellant systems, and gage output signals were recorded. By conducting the pressure calibration tests at a series of temperatures, the gage zero shift and sensitivity to pressure were obtained across the temperature range from 154 to -68 F.

Figure 33 shows the complete calibration data obtained for Gage 18 at temperatures between 154 and -68 F and pressures from 0 to 50 psi. Data for the other five gages were similar. Because the output signal-pressure data are linear they may be described in terms of the output signal at zero pressure (the normal zero signal) and the slope of the line (gage sensitivity, mv/psi). Thermal zero signals for the six gages are plotted as functions of temperature in Figure 34; gage sensitivities vs temperature are plotted in Figure 35.

41
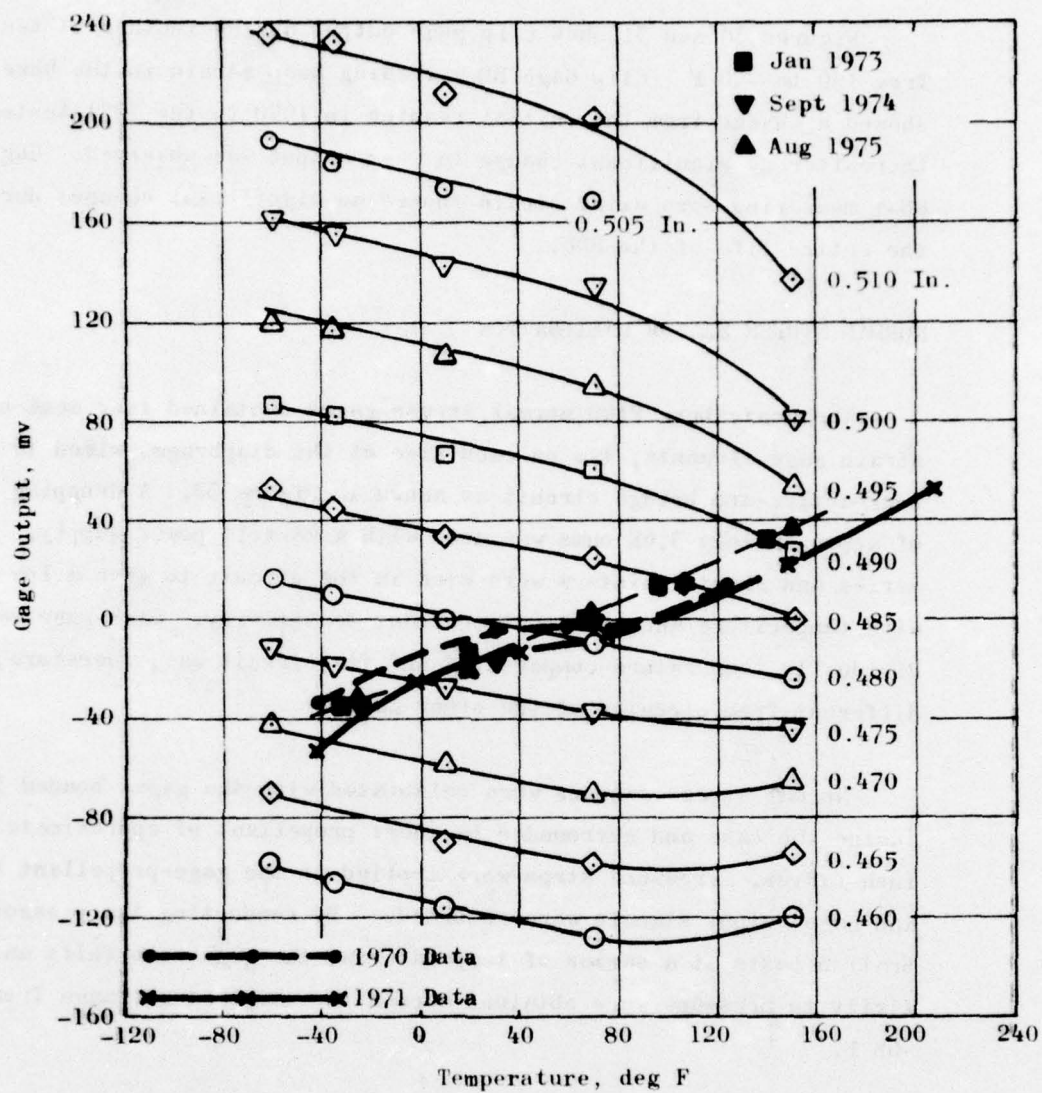
Figure 30. Surface Clip Gage BB-1 Data from Isothermal
Tests
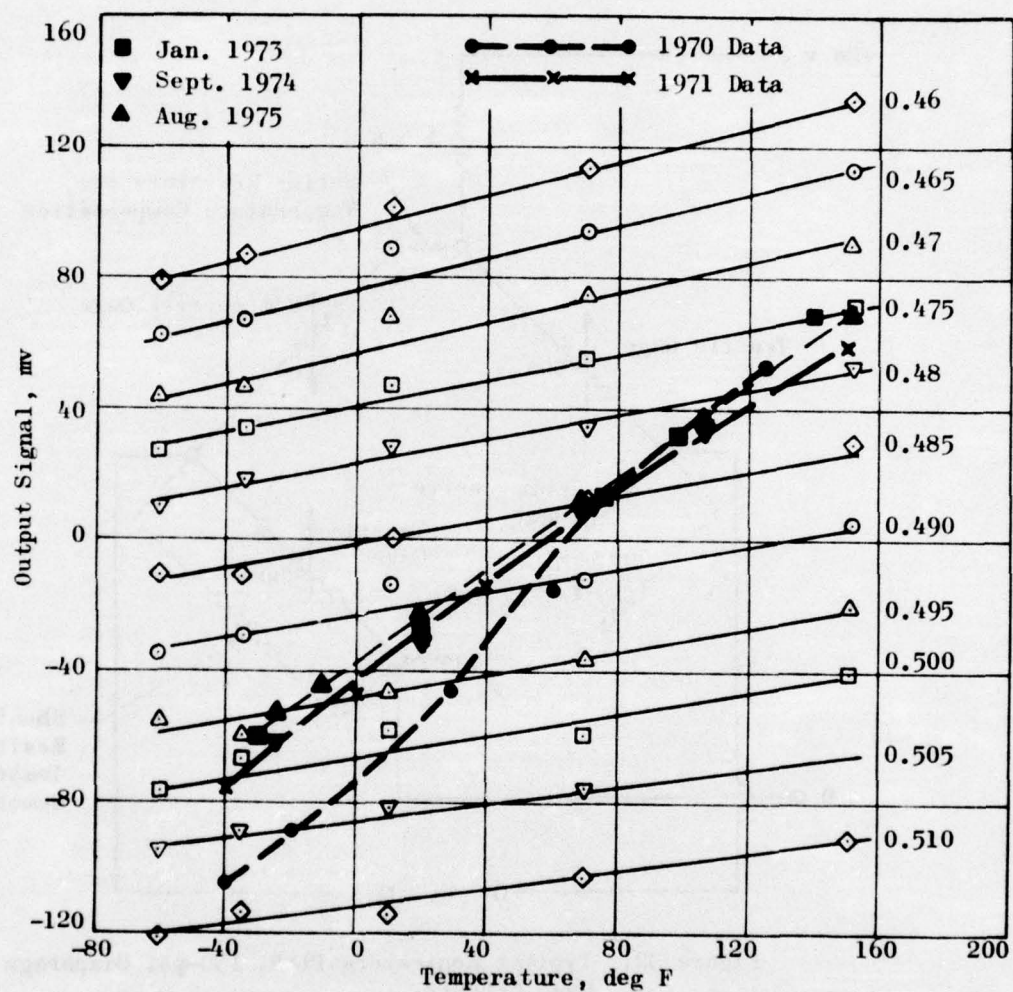
Figure 31. Surface Clip Gage BB-2 Data from Isothermal Tests
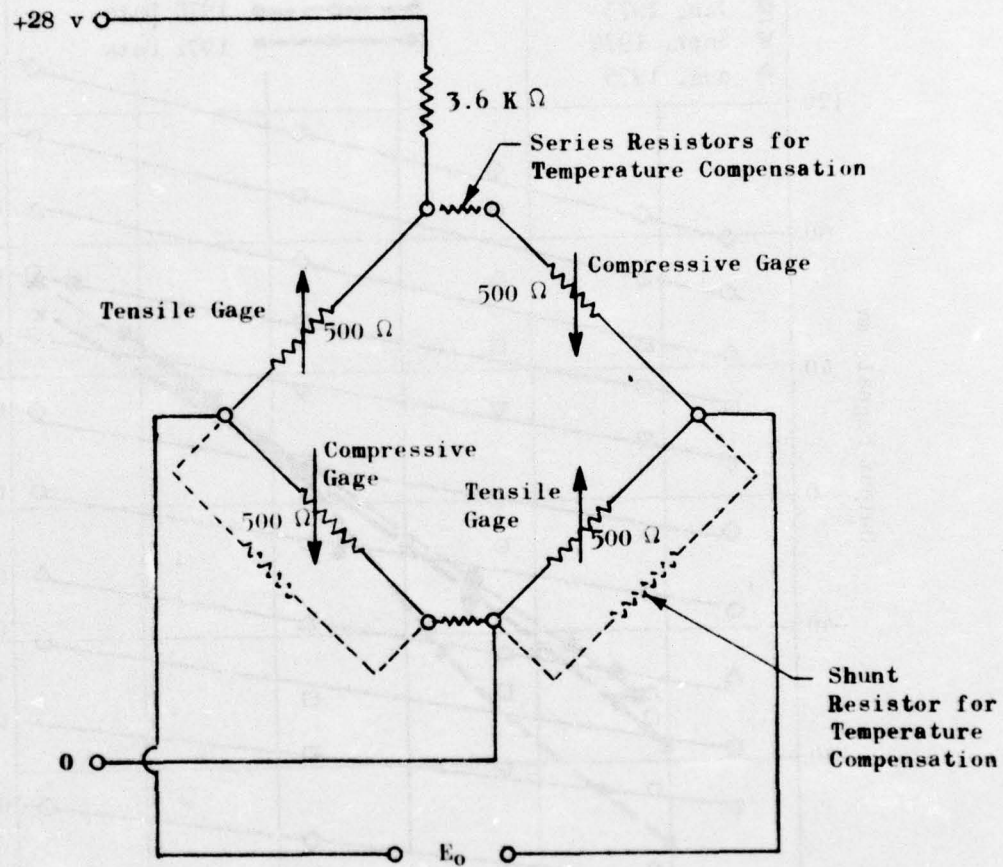
Figure 32. Typical Konigsberg P14B, 150-psi Diaphragm Gage Circuit
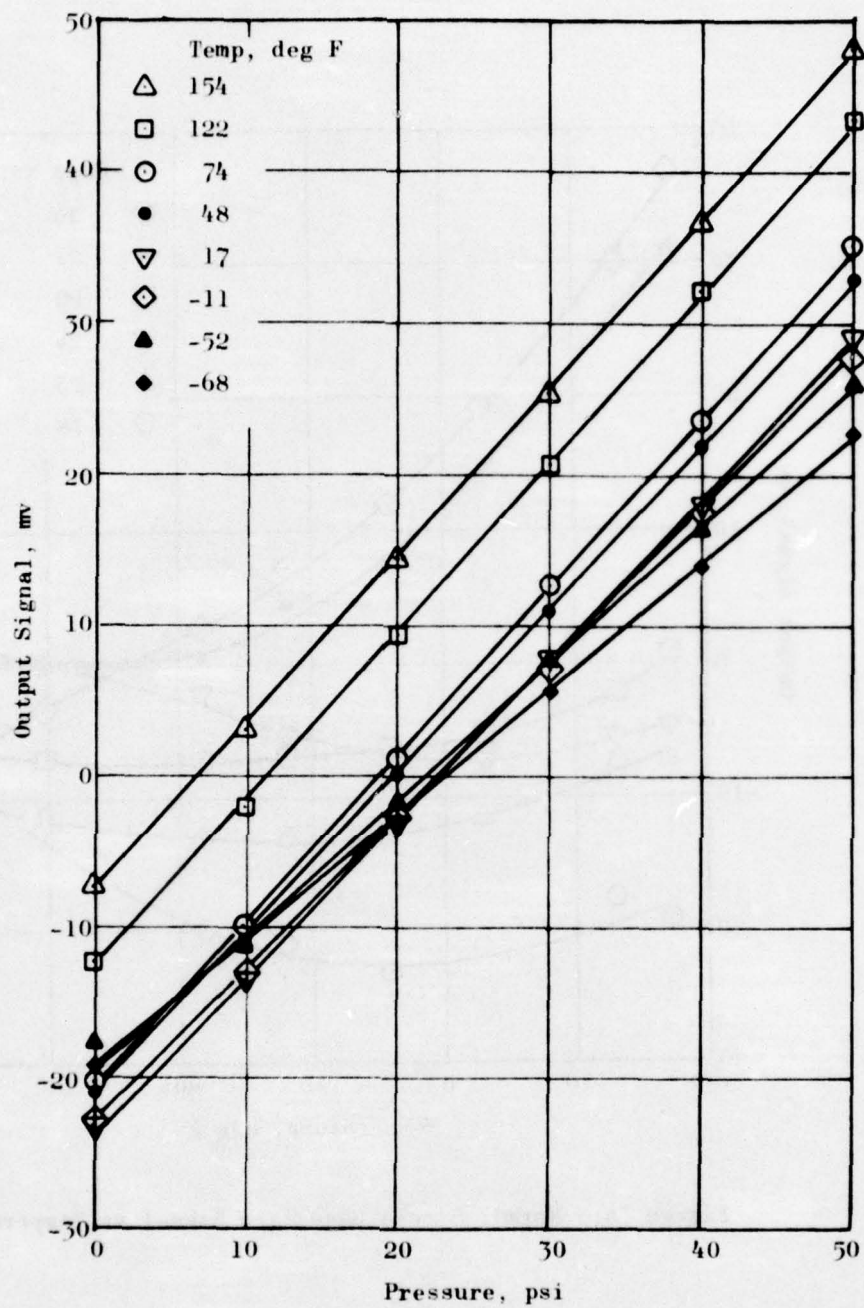
Figure 33. Pressure Calibration Data for 150-psi Normal
Stress Gage 18
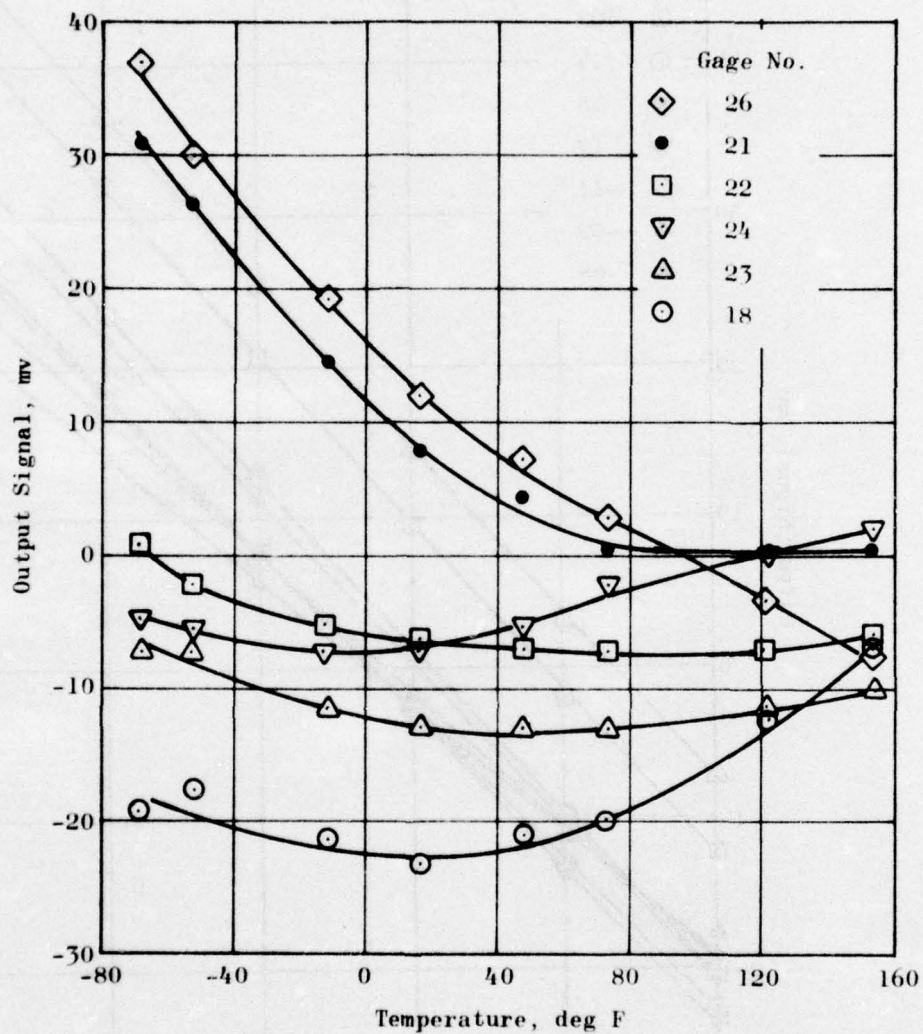
Figure 34. Normal Stress Gage Zero Signal vs Temperature

46
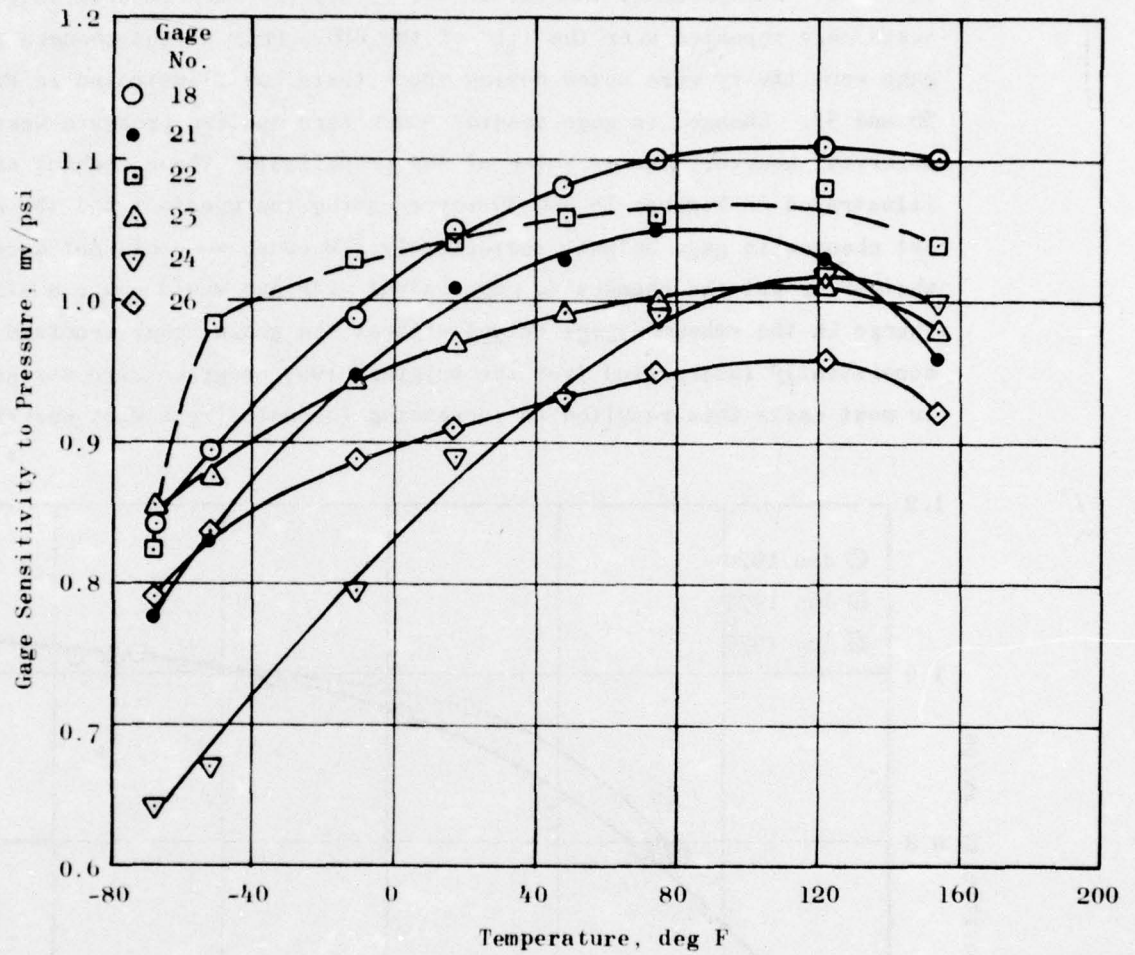
Figure 35. Normal Stress Gage Sensitivities to Pressure
vs Temperature

47

Following casting of the grain in 1969, the unit was subjected to a series of in-situ step pressure calibration tests at temperatures from 150 to -65 F. Periodically thereafter these step-pressure in-situ calibration tests were repeated over the life of the BDU. Only slight changes in gage sensitivity were noted during these tests, as illustrated in Figures 36 and 37. Changes in gage reading under zero applied pressure were observed, however, due to aging of the propellant. These changes are illustrated in Figures 38 and 39 representing the greatest and the smallest changes in gage output, respectively. Because we could not determine whether or not the changes in gage output with age would cause a similar change in the embedded gage output without the grain, gage readings were consistently interpreted from the original 1969 no-grain zero stress curves. In most cases this resulted in increasing thermal stress with age that would
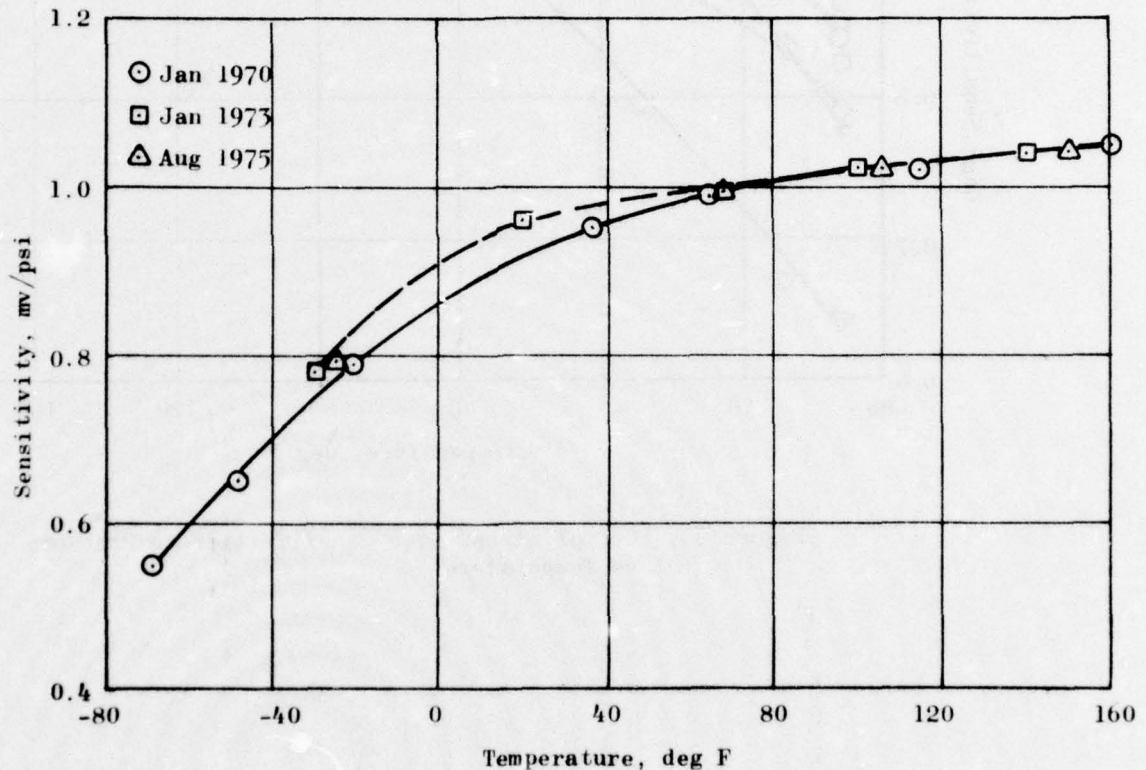
Figure 36. Normal Gage N-21 Sensitivity vs Temperature
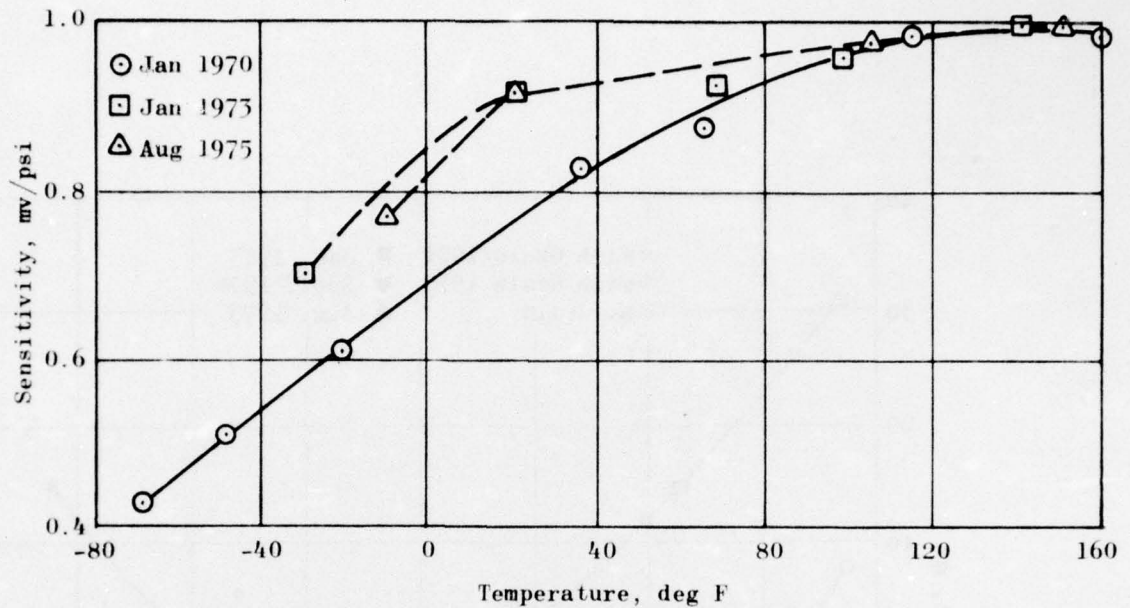
Figure 37. Normal Gage N-23 Sensitivity vs Temperature

be expected from a propellant hardening with time. However, a hardening propellant would be expected to produce a smaller gage sensitivity at low temperatures, which is contrary to the data shown in Figures 36 and 37.

SHEAR STRESS GAGE CALIBRATION

Bridge circuits for the three types of shear gages used are shown in Figure 40. All three circuits were powered through dropping resistors from the 28-volt supply line. No temperature-compensating devices were used with the shear gage circuits.

The shear gages were calibrated while cast in a double overlap shear fixture. Constant-load creep tests were performed at constant temperatures between 150 and -47 F.

49
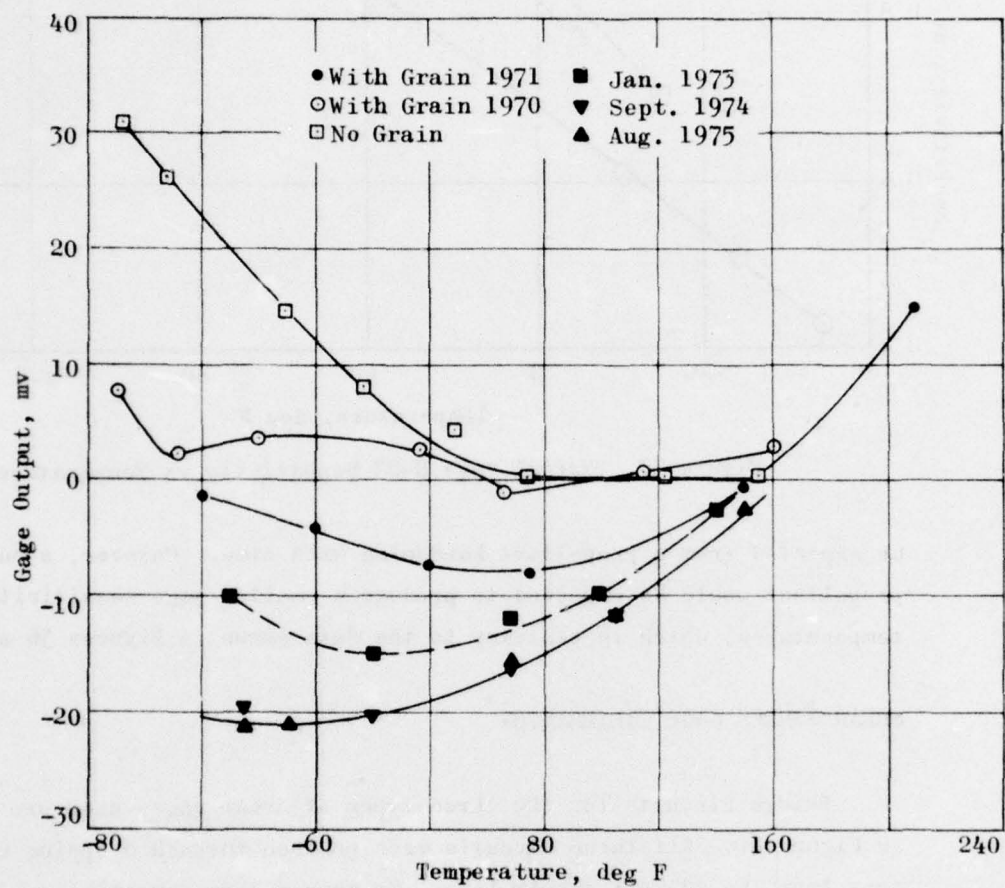
Figure 38. Normal Stress Gage N-21, Output vs
Temperature
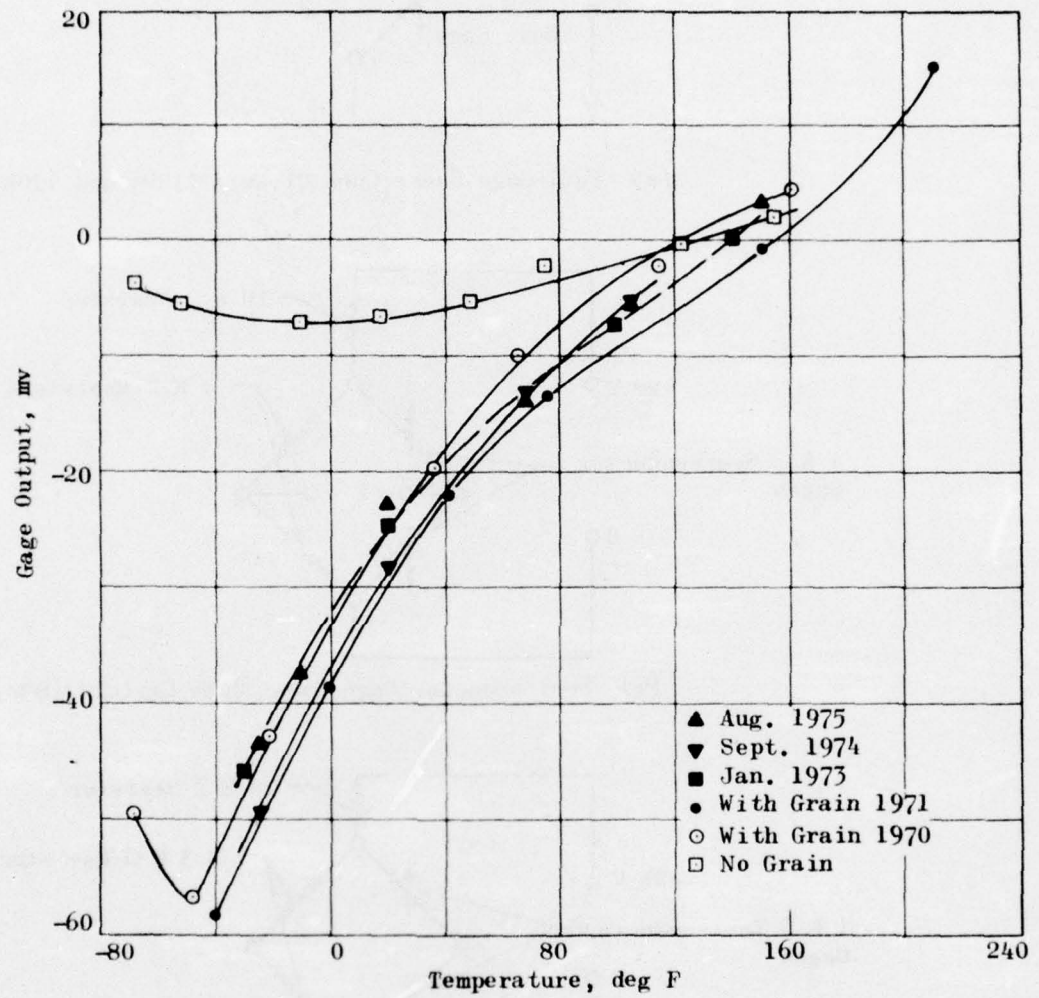
Figure 39. Normal Stress Gage N-24, Output vs
Temperature

51
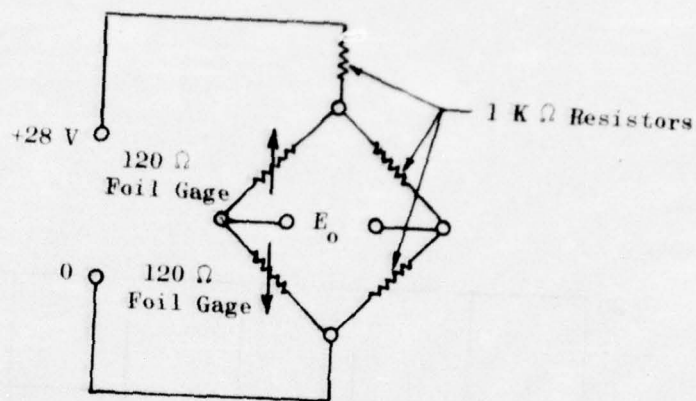
(a) Foil Gage Shear Cube Circuit (120A and 120B)
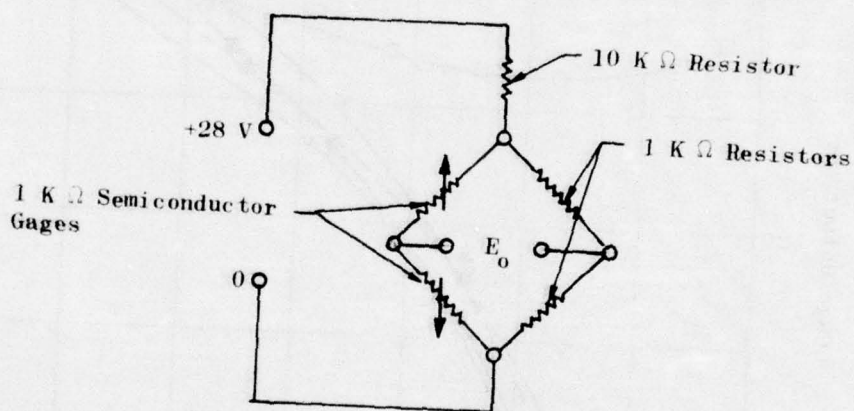
(b) Semiconductor Gage Shear Cube Circuit (SH2)
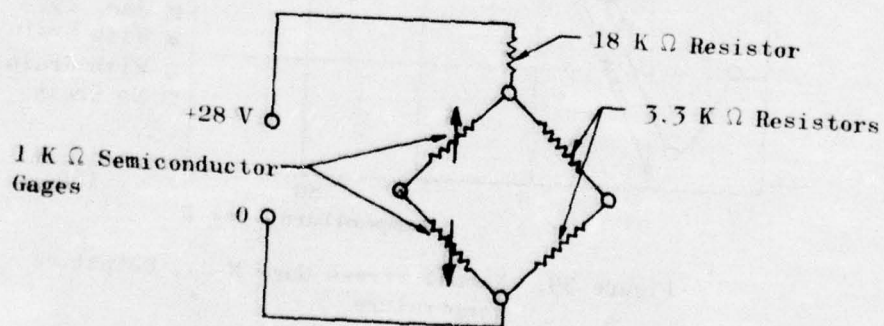
(c) Bending Beam Shear Gage Circuit (#101)

Figure 40. Shear Gage Circuits

52

Unlike the normal stress gages that have an almost constant sensitivity across the temperature range, the shear gage response to stress varied markedly with temperature and with time. Therefore, although the gage zero signals are primarily functions of temperature, shear gage sensitivities had to be plotted against log reduced time. Zero load signals for the four gages are plotted against temperature in Figure 41. Zero shift for the shear gages using semi-conductor elements (101 and SH-2) is greater than that for the foil gage Shear Cubes 120A and 120B. (Zero shift of Gage SH-2 was adjusted to the 100-millivolt offset so that gage output readings in flight would be within a $\pm$ 100-millivolt range.)

Shear gage sensitivities are given against log reduced time in Figures 42 and 43, which show that shear gage data were not as precise and repeatable as data from the other gages. Semiconductor-gaged sensors SH-2 and 101 produced the best calibration data. SH-2 was useful across the whole temperature range; whereas Gage 101 yielded poor data above 96 F. The presence of the metal foil in Gage 101 produced a much larger signal attenuation at low temperatures than was obtained with Shear Cube SH-2.

Sensitivity data obtained from Gages 120A and 120B showed considerable scatter and irregularity. Two causes of the data scatter were determined:

1. Zero drift in the digital millivoltmeter used to measure gage output
2. Temperature changes due to self heating of the gages

Zero drift of the meter caused the data scatter at short times. This is particularly evident in data from Shear Gage 120B. The drift was only 1 to 2 millivolts, but this was a significant fraction of the output signal.

53
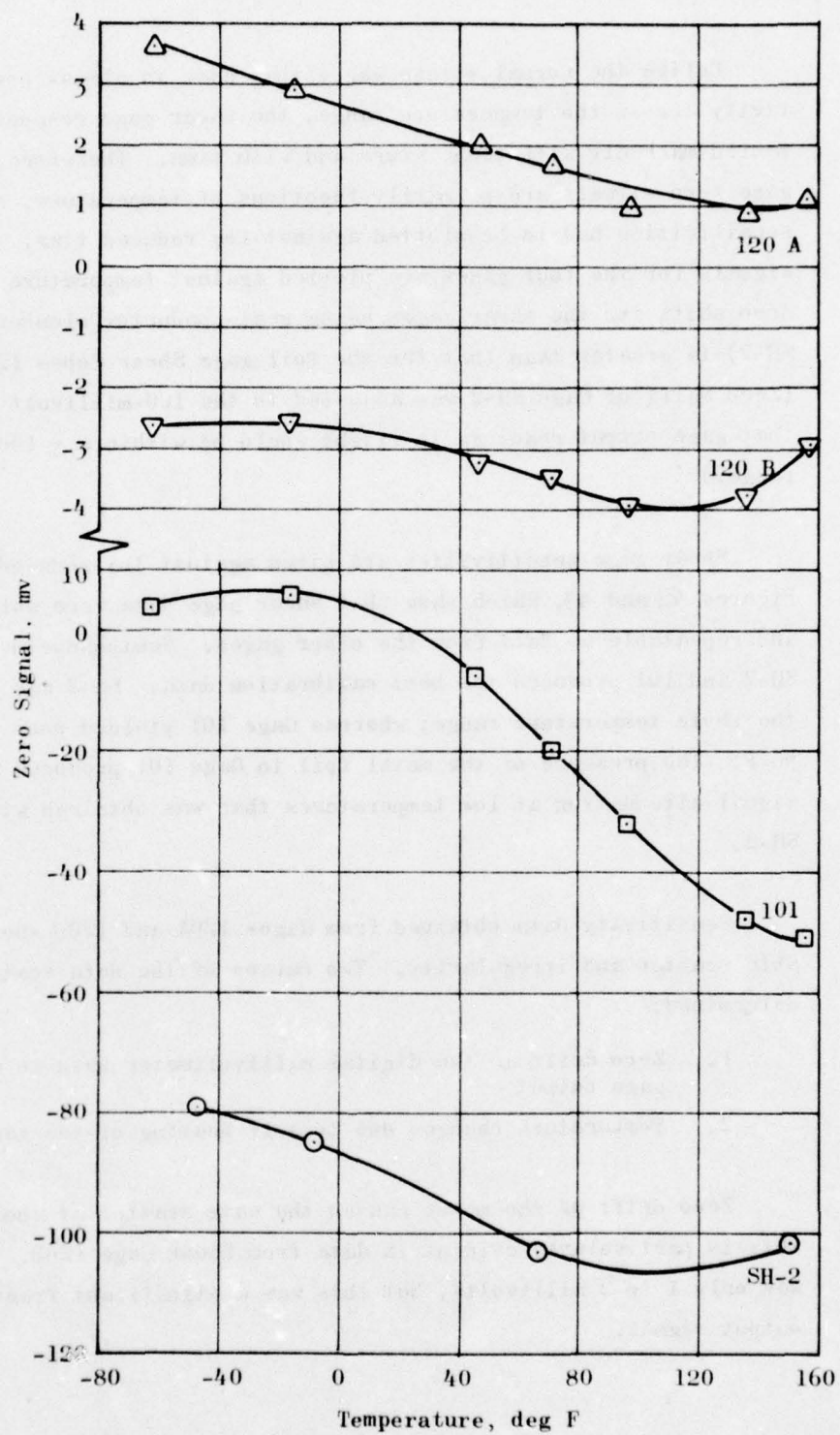
Figure 41. Gage Signal vs Temperature
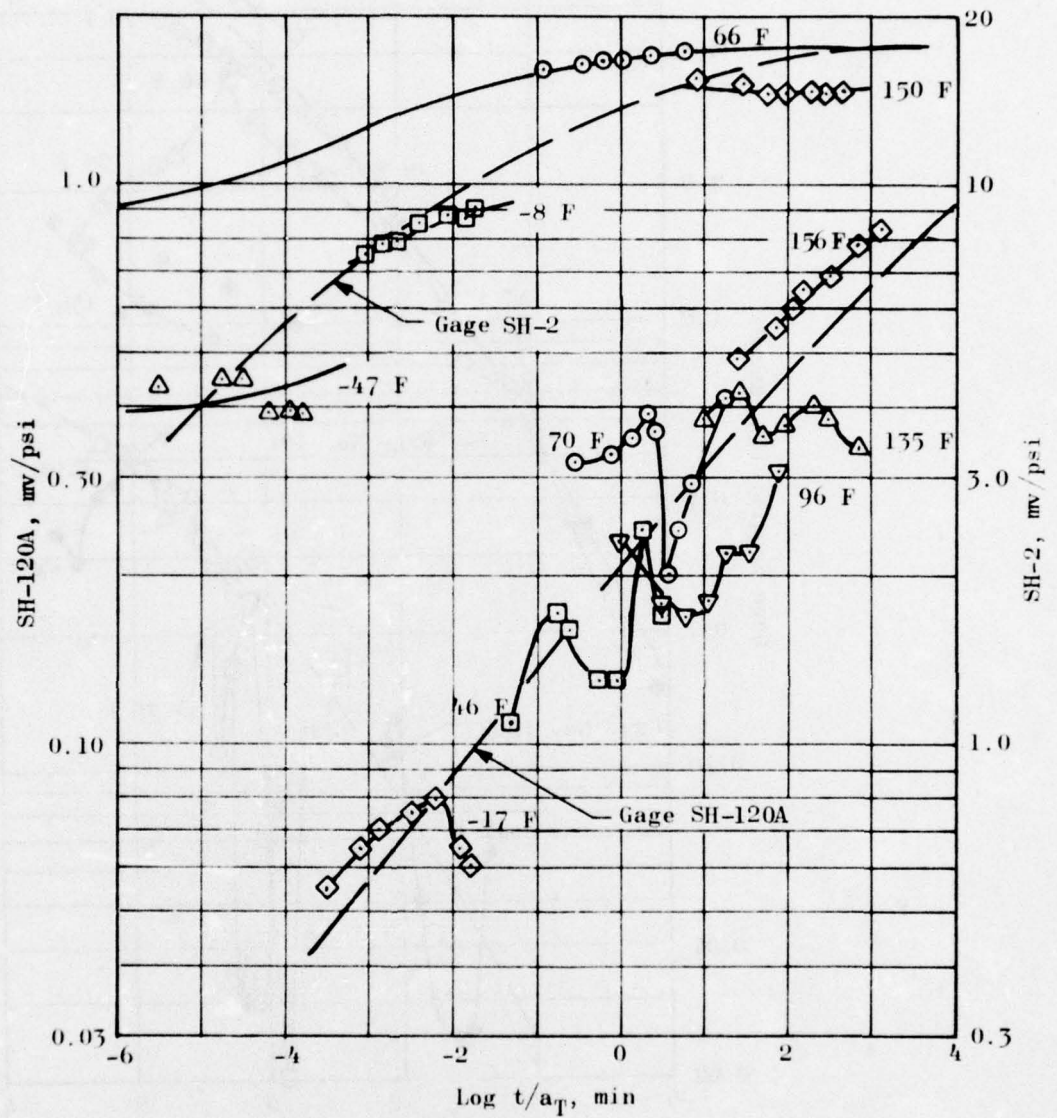
Figure 42. Shear Gages SH-2 and SH-120A, Response vs Log
Reduced Time
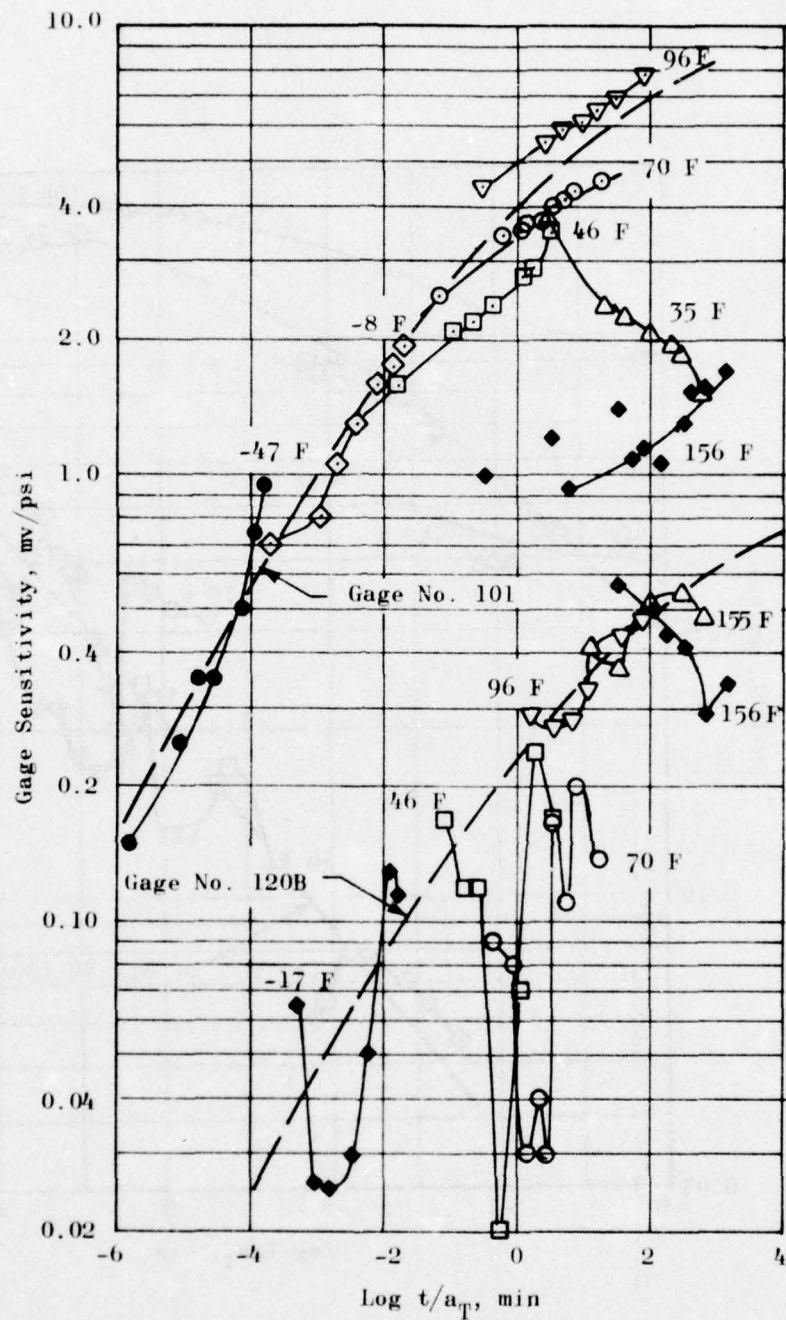
Figure 43. Shear Gages 101 and 120B, Response vs Log
Reduced Time

56

The dashed curves shown in Figures 42 and 43 are the suggested calibration curves, based on available data, for the shear gage.

Figures 44 and 45 show isothermal shear gage outputs for SH-2 and SH-120A, respectively, as measured at different times during the life of the BDU. There appears to be no consistent trend in data for Gage SH-2, which became defective by 1974. Data for SH-120A, however, show the greatest change in the early years 1970 through 1973, after which gage reading remained reasonably constant.

Results of step pressure tests on Gages SH-120A and -120B at 70 F over the life of the BDU are shown in Figure 46. These data reveal little change in sensitivity.

Additional calibration data are presented in Appendices A and B.
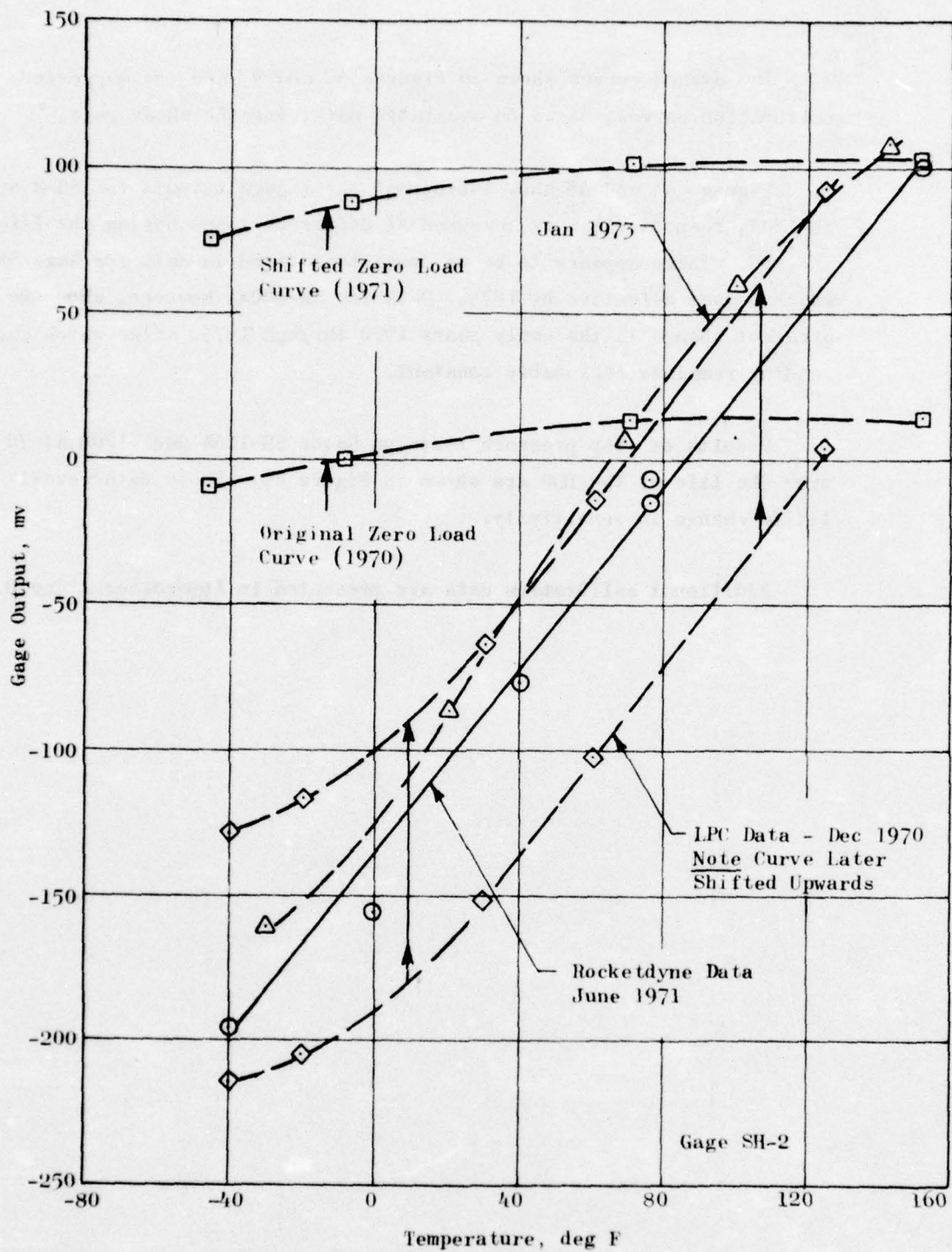
Figure 44. Shear Stress Gage SH-2, Output vs Temperature

58
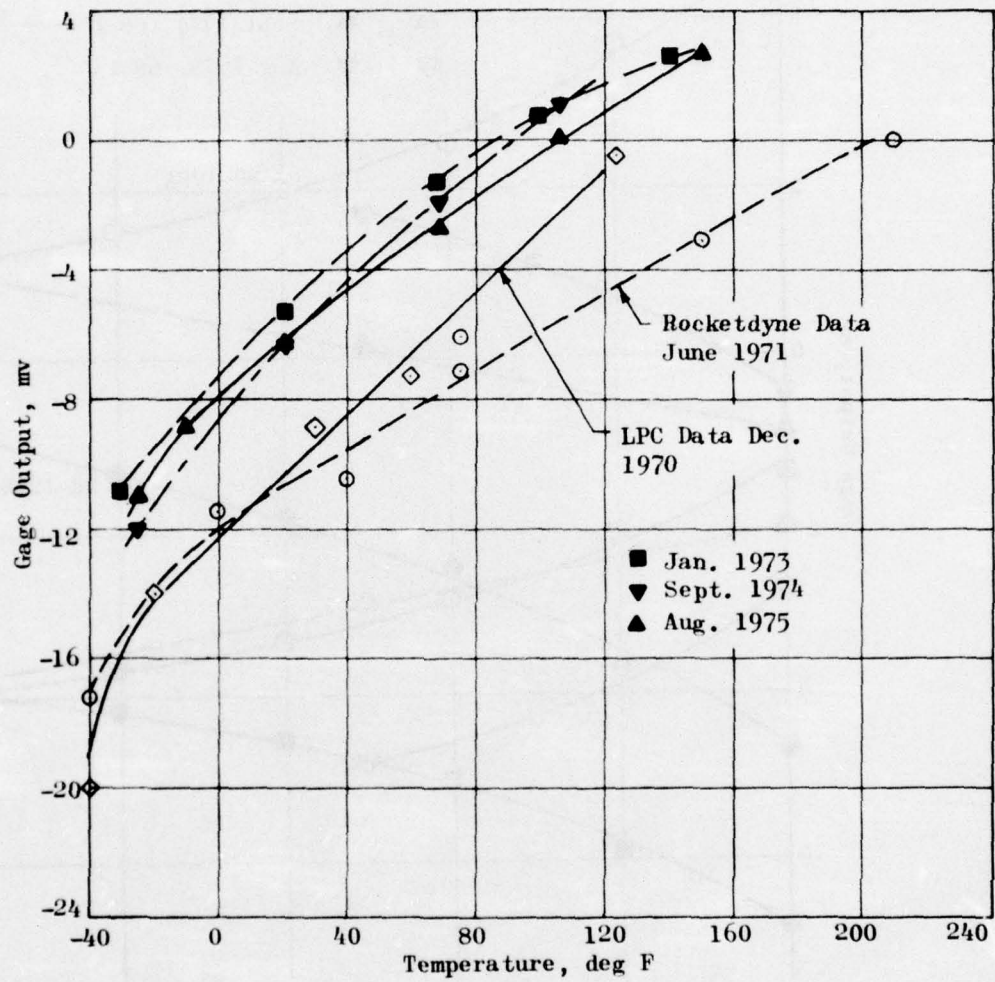
Figure 45. Shear Stress Gage SH-120A, Output vs
Temperature

59
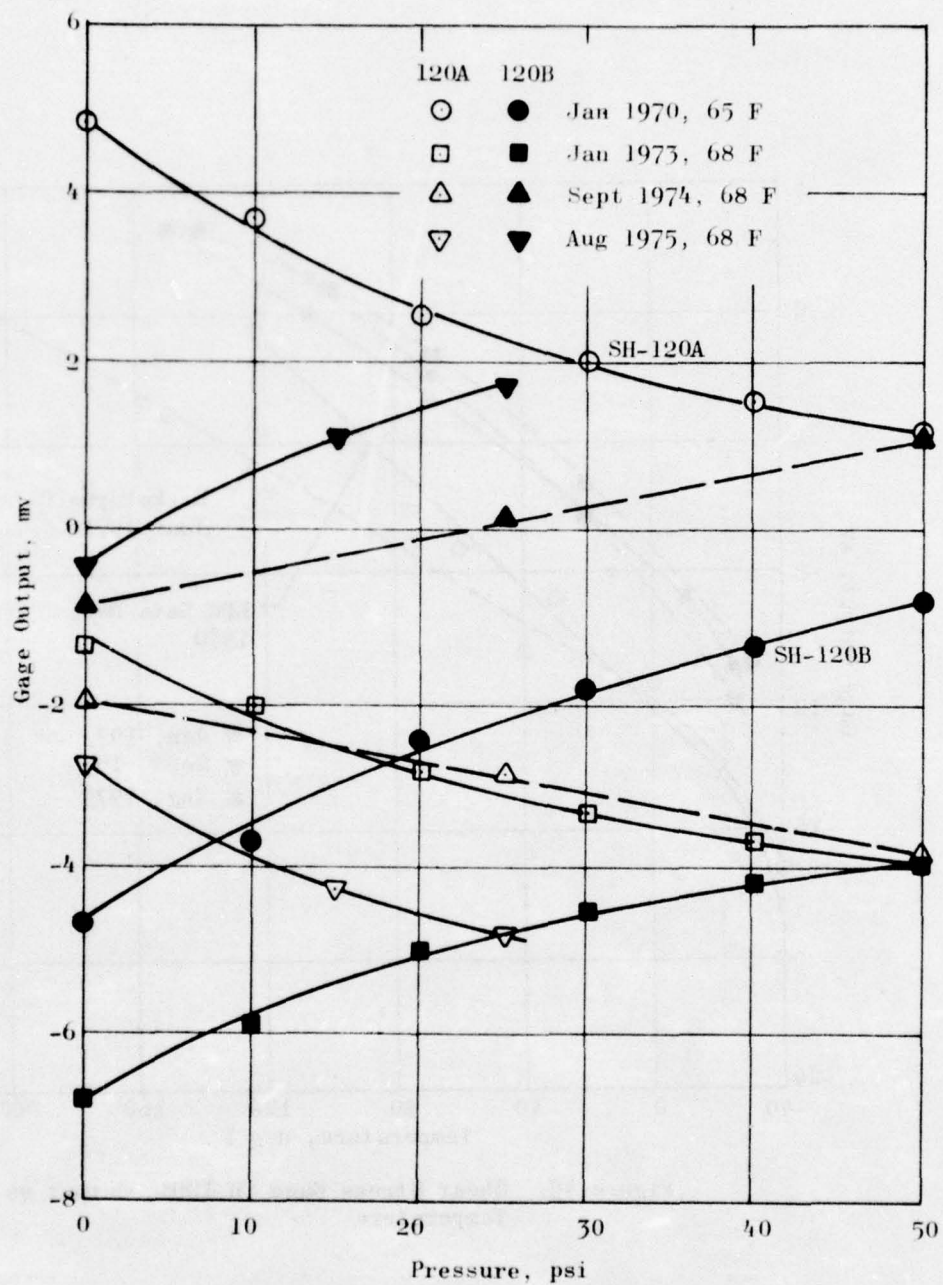
Figure 46. Shear Gages SH-120A and SH-120B, Output vs Pressure at 70 F

60

LAUNCHER INSTRUMENTATION

Locations of instrumentation on the BDU motor and a flow diagram indicating the monitoring system are charted in Figure 47. Wires and strain gages on several components were broken during flight testing and handling. Repairs made after Flight 11 included installation of new strain gages on the BDU forward and aft launch lugs and on the aft sway brace of the launcher.

Subsequent to gage installation, the instrumented launcher and the launch lugs were placed in a conditioning chamber and subjected to temperatures ranging from -20 to 180 F. Bridge output data were recorded over this range to design temperature compensation networks for the bridges. After the temperature-compensating resistors were installed, temperature sensitivities for the instrumented launcher and lugs were measured. Lug instrumentation was calibrated using static loads.

The instrumented launcher assembly was then checked using static loads at ambient temperature. To accomplish this, the BDU was suspended from a loading frame through the instrumented launcher. Transverse loads (both vertical and longitudinal) were then applied by hydraulic actuators through the center of gravity of the BDU. Longitudinal loads were applied by an actuator pressing on the nose of the BDU. Static load sensitivities on three of the five instrumented launcher channels were checked. Load interaction with the sway braces precluded resolution of component response.

The accelerometers attached to the metal hardware on the BDU were recalibrated. This involved removing the triaxial accelerometers at the center of gravity and at the aft end and the uniaxial accelerometers under the forward and aft lugs and vibrating them on a calibrated shaker over the frequency range of 20 to 2000 Hertz. The accelerometers were then re-installed in the BDU. Frayed cables were replaced and all connectors cleaned. Leakage checks revealed the cables were acceptable.

61
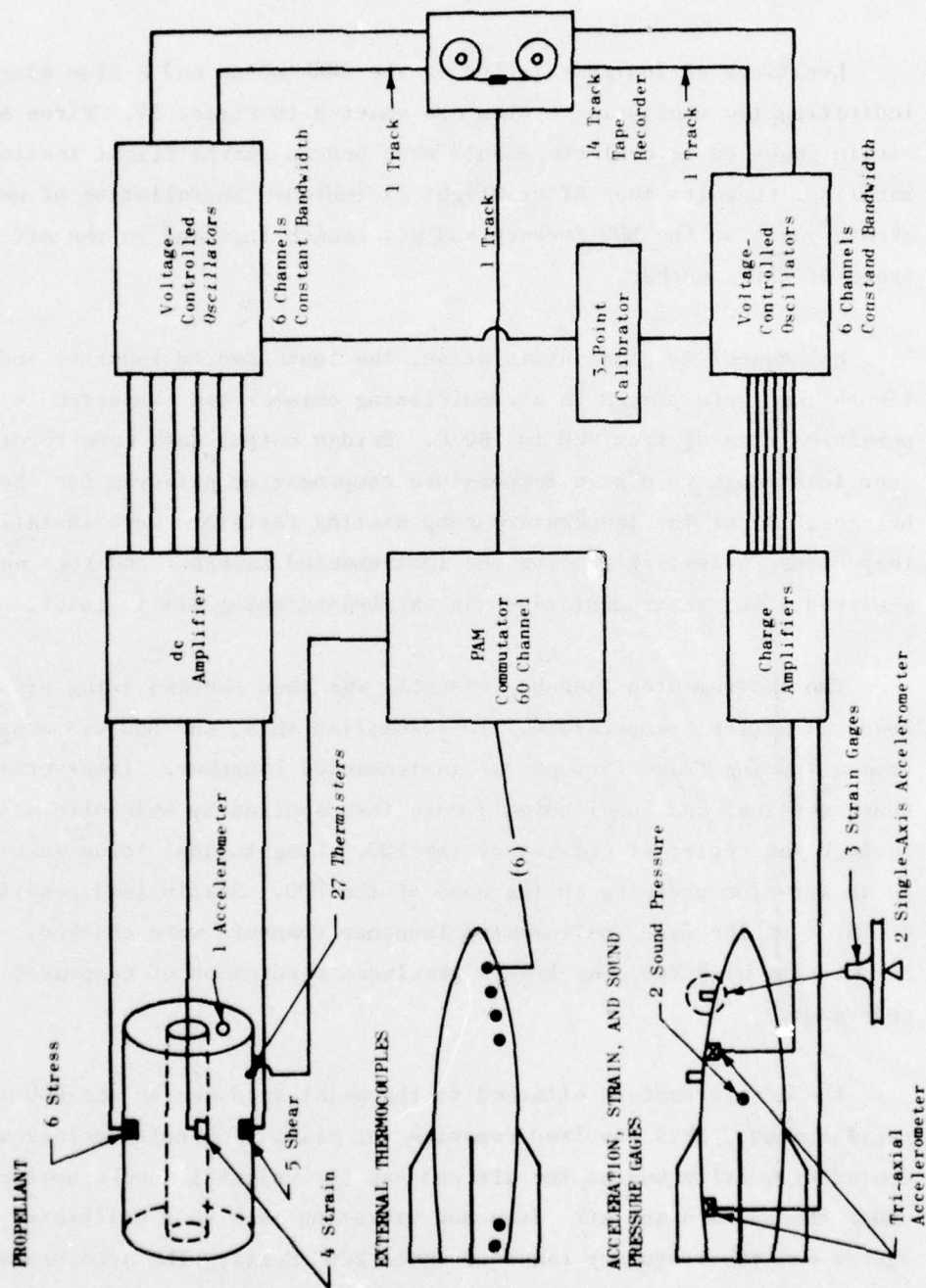
Figure 47. BDU Instrumentation and Monitoring System

507-T154-1005

62

Discrepancies had been observed in the ac data measured during Flights 9 and 11 on Track 7 compared with Tracks 3 and 10. Consequently, fidelity of the channels transmitting high-gain ac data to Track 7 on the tape was checked. Signals from a sine wave generator were superimposed on the output from particular propellant instruments using $1/2$ μf capacitance coupling. The signals were then passed through normal flight signal conditioning equipment and were reviewed using the ground-support discriminators (i.e., output from voltage-controlled oscillators). From these tests it was determined that Track 7 was operational. The source of the discrepancy between the low-gain data on Tracks 3 and 10 and the high-gain data on Track 7 was attributed to noise on each track which did not correlate to gage signal.

INSTRUMENTATION PACKAGE

A schematic of the BDU instrumentation is shown in Figure 48. Since the flight tape recorder held insufficient tape for continuous recording it was operated intermittently to obtain the desired data. All channels of propellant sensors were recorded on the flight recorder. Data from selected sensors (Table 3) were redundantly recorded on Rocketdyne's ground test equipment during all vibration cycles. (Locations of these instruments are shown in Figure 22.) In addition to propellant gages, accelerometers were installed for definition of total test vehicle response.

DATA ACQUISITION SYSTEM   PROPELLANT GRAIN
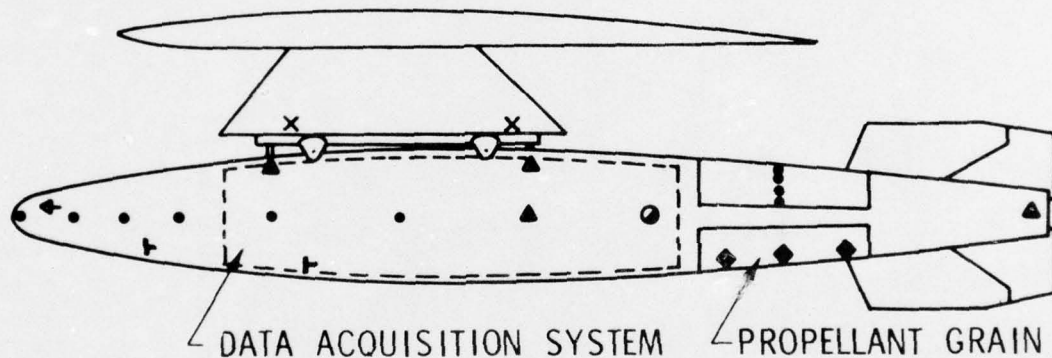
▲ ACCELEROMETERS	9
• THERMISTORS	~50
← STATIC PRESSURE	4
× FORCE TRANSDUCERS	5
◐ MICROPHONES	2
◆ STRESS/STRAIN GAGES	9
⊢ HEAT FLUX GAGES	13

507-T154-1002

Figure 48. BDU Instrumentation

64

TABLE 3. INSTRUMENTATION RECORD

Pin No.	Gage	Gage Major Active Axis	Adjacent Thermistor	Axis	
				Z	X
1 and 2	Stress #18	Z	5	X	X
5 and 6	Stress #22	Z	1	X	
7 and 8	Stress #23	X	6	X	X
11 and 12	Stress #26	X	2		X
16 and 17	Strain #17 (SWRI)	Hoop	15	X	X
18 and 19	Strain #17 (Clip)	Hoop	15	X	X
22 and 23	Strain A (Case) (Delete Requirement)	Hoop	--		
25 and 26	Shear #101 (Semi-conductor)	X	11		X
27 and 26	Shear #SH-2 (Semi-conductor)	Z	10	X	X
29 and 30	Shear #120A	Z	12	X	X
31 and 32	Shear #120B	X	13	X	X
33 and 34	Accelerometer (Propellant)	Y_2	--	X	X
36 and 52	Strain #1 (Lug #1 Fwd)		--	X	X
37 and 52	Strain #2 (Lug #2 Aft)		--	X	X
38 and 52	Strain #2B (Lug #2 Aft)		--	X	X
39 and 52	Accelerometer (cg)	X	--	X	X
40 and 52	Accelerometer (cg) Triaxial	Y	--	X	X
41 and 52	Accelerometer (cg)	Z	--	X	X
45 and 46	Accelerometer (Aft End)	X	--	X	X
47 and 48	Accelerometer (Aft End) Triaxial	Y	--	X	X
49 and 50	Accelerometer (Aft End)	Z	--	X	X
42 and 52	Accelerometer (Lug #1)	Z	--	X	X
43 and 52	Accelerometer (Lug #2)	Z	--	X	X
3 and 4	Stress #21	X	3		*B-up
9 and 10	Stress #24	Z	2	*B-up	
14 and 15	Strain #16 (SWRI) (Do not record)		15		
20 and 21	Strain #2 (Clip)	Hoop	i5	XQ	X

* B-up: Recorded but data not reduced

Temperature outputs taken from the PAM system, decoded, and then recorded by Rocketdyne:

  Thermistors:

  (a) Adjacent to other gages:

  #1, #2, #5, #6, #10, #11, #12, #13, and #15.

  (b) Propellant grain profile:

  #18, #19, #20, #21, and #23.

  Thermocouples:

  6 case

Additional temperature outputs recorded by Rocketdyne:

  Thermistors:

  #16 - Forward face of grain
  #17 - Forward face of grain
  A - Case thermistor (propellant/case)
  B - Case thermistor (propellant/case)
  D - Case thermistor (propellant/case)

  Thermocouples: 15 total

  3 in tail section
  7 in fore body section
  1 in electronic package
  4 locations to be defined later

Ground instrumentation tie-in points were directly on the output of the sensor on all strain gages and directly on the output of the charge amplifiers of crystal accelerometers. It was believed that switching transients from the commutator used on the temperature sensors would make it advisable to parallel record from these units; therefore, temperature stations recorded on ground-station equipment were derived from a decommutator unit.

The connecting instrumentation cables for all gages, thermistors, and internal thermocouples were less than 20 feet long. The instrument take-off point, signal conditioning, and recording equipment are shown in Figure 49.
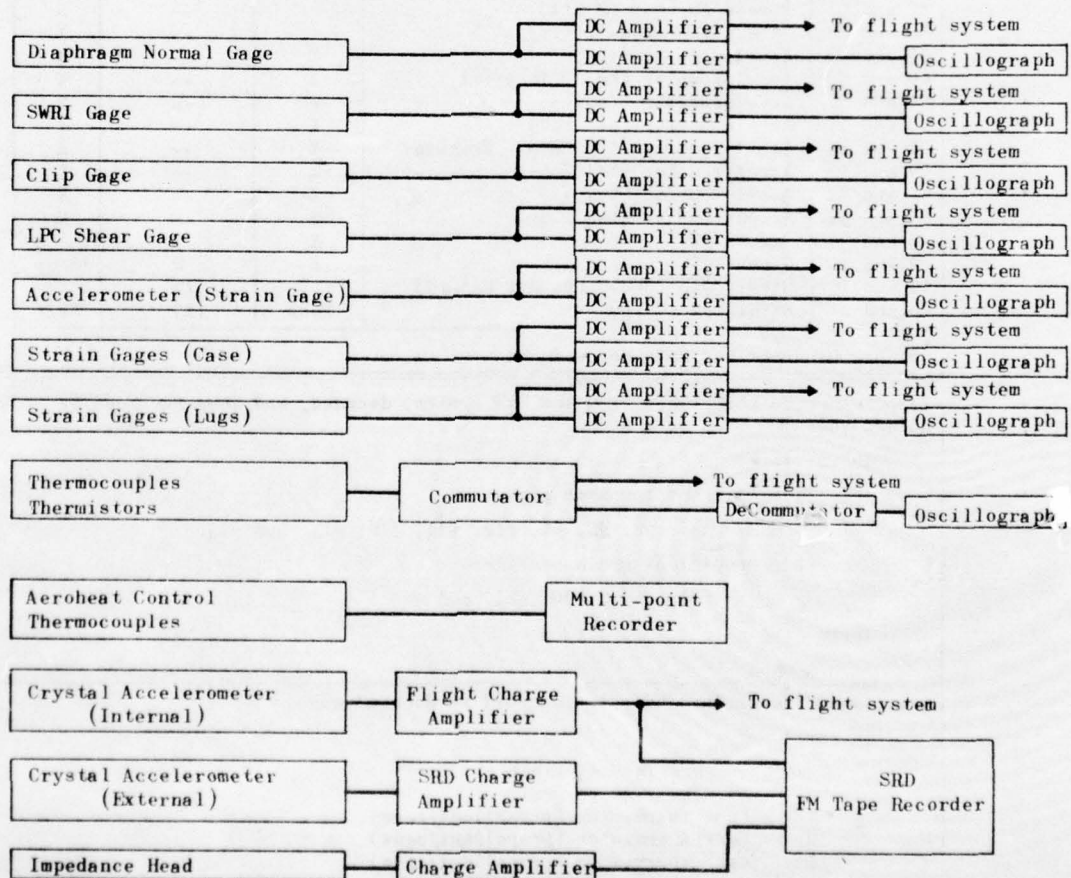
Figure 49. Recording Equipment Layout

After Flight 13, additional thermal and pressure sensors were added to the BDU to collect store aeroheating data for Arnold Engineering Development Center (AEDC). AEDC used these data to correlate supersonic wind tunnel tests of captive stores under AEDC Project V34A-29A, AFATL/AEDC Store Heating. The sensors, all located in the nose section of the BDU, included Gardon gages for heat flux measurement, thermocouples, and differential pressure transducers for the measurement of store pitch and yaw. All AEDC instrumentation was input to the flight recorder through the same commutator used by the propellant grain thermistors. As the flight profiles described in the following section were sufficient for AEDC's purpose, no changes in flight tests were required.

FLIGHT TESTING

TEST PLANS

At the start of Project DAME, six distinct flight segments for captive flight of the BDU on an F-111 aircraft were defined:

I.   Taxi, take-off, and landing

II. Climb to 50,000 feet in 9 minutes, accelerate from Mach 1.6 to Mach 2.5 in 6 minutes and maintain Mach 2.5 at 50,000 feet for 4 minutes (F-111D only)

III. Climb to 35,000 feet in 4 minutes, accelerate from Mach 0.9 to Mach 2.0 in 5 minutes, and maintain Mach 2.0 for 8 minutes

IV. Climb to 35,000 feet in 4 minutes and maintain Mach 0.8 for 30 minutes at 35,000 feet

V.   Fly terrain following radar (TFR) mission at 500 feet above ground level and Mach 0.9 for 30 minutes

VI. Climb to 12,000 feet in 2 minutes, accelerate from Mach 0.7 to Mach 1.5 in 5 minutes, and maintain Mach 1.5 for 4 minutes (F-111D only)

Most flight tests consolidated two or more of these segments to maximize the data collected. Flight endurance was generally limited by the capability of the flight recorder rather than aircraft fuel consumption. Flight test profiles are summarized in Table 4.

TEST AIRCRAFT

The F-111 aircraft was selected for these tests for its high performance characteristics and mission flexibility. All flight tests conducted were, in fact, typical missions for this type aircraft. Two aircraft (one FB-111A and one F-111D) were available for flight tests at Edwards AFB; however, incompatibility of the electrical systems of the F-111D and the BDU restricted all but three flights to the FB-111A.

69

TABLE 4. SUMMARY OF FLIGHT TEST PROFILES

MISSION SEGMENTS	FLT. NO.	1	2	3	4	5	6	7	8 [+]	9	10 [*]	11 [+]	12 [+]	13 [+]	14	15	16	17	18	19	20
I	T.O. and L.	●	●	●	●	●	●	●	●	●	●	●	●	●	●	●	●	●	●	●	●
III	M = 0.9 AT 35 K			●	●		●	●	-	●	●		-	-	●	●	●	▲			
	M = 2.0 AT 35 K - 40 K			●	●			●		●	●	●	-	-		●	●		●	●	●
IV	M = 0.7 AT 31 K	●	●	●	●	●			-				-	-		35K FOR 2 HR		●	●	●	
V	TFR 500-FT M = 0.9			●	●	●	●	●	-	●	●	●	-	-	●	●	●				
VI	M = 0.7 AT 12 K								-				-	-						●	
	M = 1.5 AT 12 K																				

- DATA NOT RECORDED
+ NO POWER
* SPECIAL TEST PROFILE
▲ M = 2.0 DASH ABORTED

70

Electrical modifications to the aircraft were necessary to provide power and flight-recorder control for the BDU and limited the flight to this one FB-111A. Since this aircraft was not exclusively dedicated to Project DAME some lengthy delays occurred when it was unavailable.

TEST PROCEDURES

The BDU instrumentation and the flight recorder were checked out before and after the BDU was loaded onto the aircraft. During the flight, the systems operator actuated the flight recorder according to a schedule of events and recorded pertinent flight conditions (Mach number, altitude, angle of attack, and total temperature) on the flight log. Depending on the event, the flight recorder was used either in 15-second intervals or run continuously (as during acceleration to supersonic flight) to gather rapidly changing data. Selected events recorded on the tape were reduced to produce oscillographs and digitized data. All data were reduced in-house at the AFRPL, and the processed data were forwarded to Rocketdyne for analysis.

FLIGHT DATA ACQUISITION PROBLEMS

Difficulties in either the BDU or the aircraft were encountered in 10 of the 20 flight tests conducted. On five of these flights (6, 7, 8, 12, 13) no data were recorded because of lack of power to the tape recorder. Only limited data were obtained on Flights 1, 2, 4, and 5 because of bad gage connections and/or intermittent function of the tape recorder. Flight 17 was aborted in flight due to an aircraft malfunction.

The most critical area in data acquisition was the flight recorder. A maximum of 15 minutes recording time limited the number and duration of events recorded for each flight. As the recorder was inaccessible from the cockpit, no in-flight maintenance could be performed if the recorder malfunctioned or the tape supply was exhausted.

71

INTERNAL INSTRUMENTATION RESPONSE

Individual flights are described and data obtained are summarized on the following pages.

FLIGHT 1 – 20 SEPTEMBER 1972

The first BDU test flight consisted of: take-off, climb to 35,000 feet, and cruise at Mach 0.71 for 30 minutes. Flight conditions are summarized in Table 5. Temperature data are shown in Figure 50. Case/liner interface (CLI) temperature fell from an initial 100 F at take-off to 3 F during cruise. Figures 51 through 53 show combined thermal and pressure (due to altitude) change induced responses from the normal stress, bore strain, and shear stress sensors, respectively. Normal stress changes between 10 (N-24) and 24 psi (N-26) were obtained and a 1% change in bore hoop strain was measured by Clip Gage BB-2. Only data from Shear Gage SH-2 appeared rational, resulting in the plot shown in Figure 53.

No dynamic data were measured during this first test flight.

TABLE 5. FLIGHT 1 CONDITIONS

Starting Time	Time Lapse, min	Altitude, ft	Mach No.	Flight Segment
3:09:15	0	2,300	0	I
3:20:10	10:55	2,300	0	I
3:23:40	14:25	2,300	0.21	IV
3:41:35	32:20	35,000	0.71	↓
3:56:35	47:20	35,000	0.71	
4:11:35	62.20	35,000	0.71	IV
4:27:41	78:26	3,000	0.20	I

72
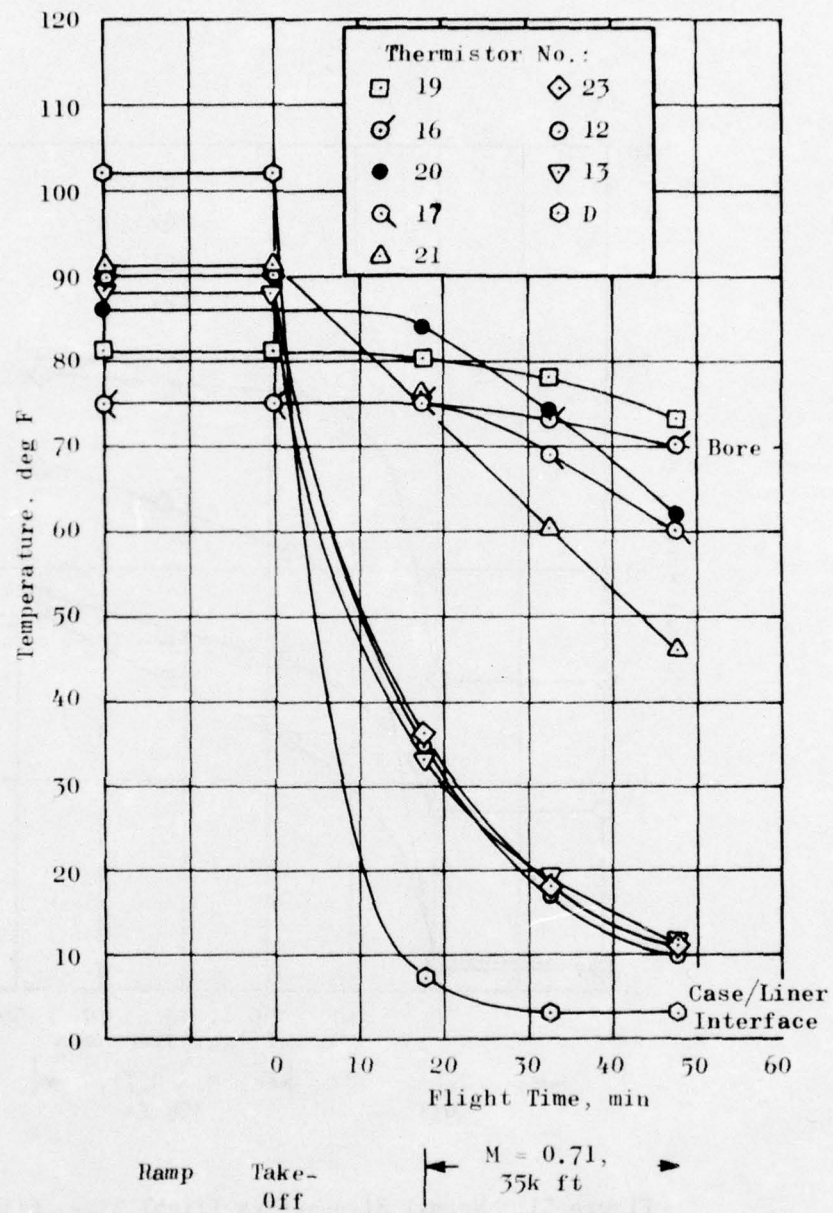
Figure 50. "Rationalized" Temperature Data for Flight 1
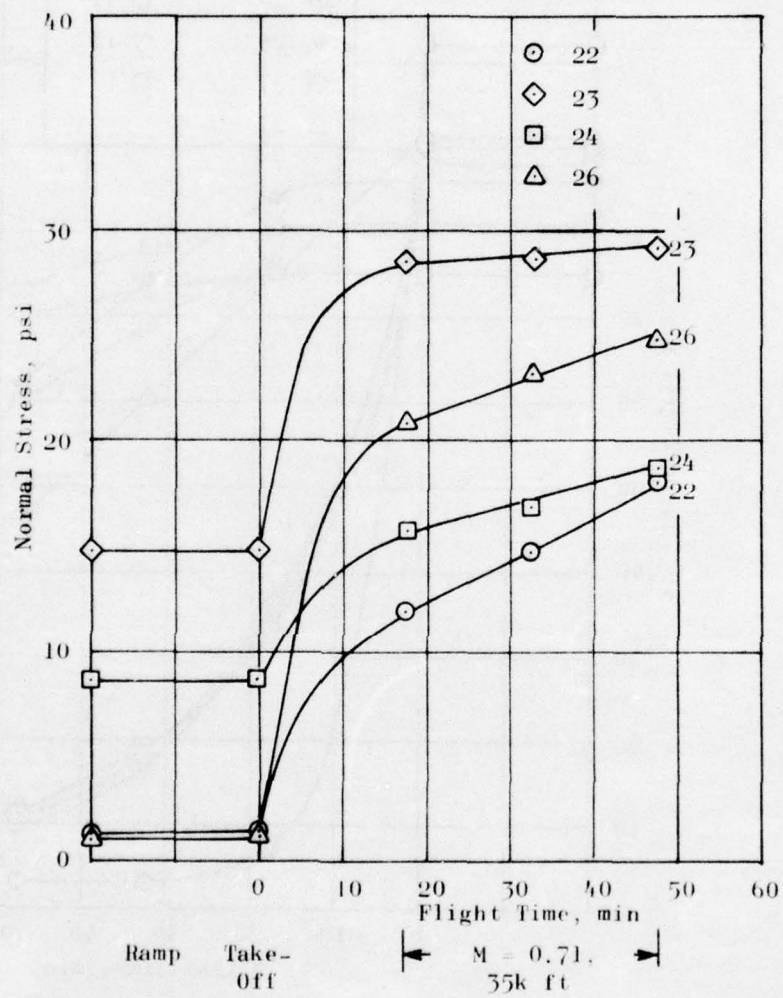
Figure 51. Normal Stresses vs Flight Time, Flight 1

74
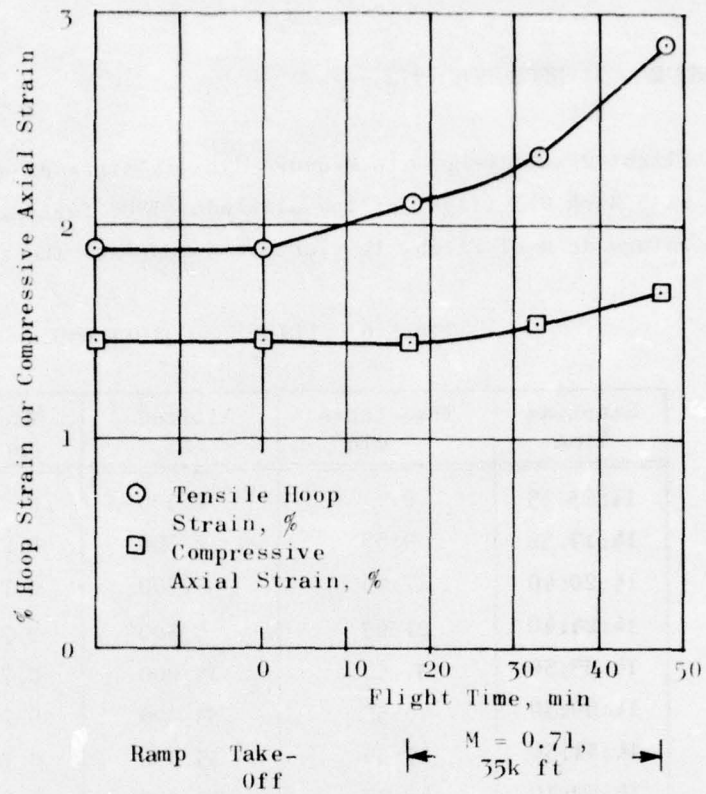
Figure 52. Hoop and Axial Bore Strains
vs Flight Time, Flight 1
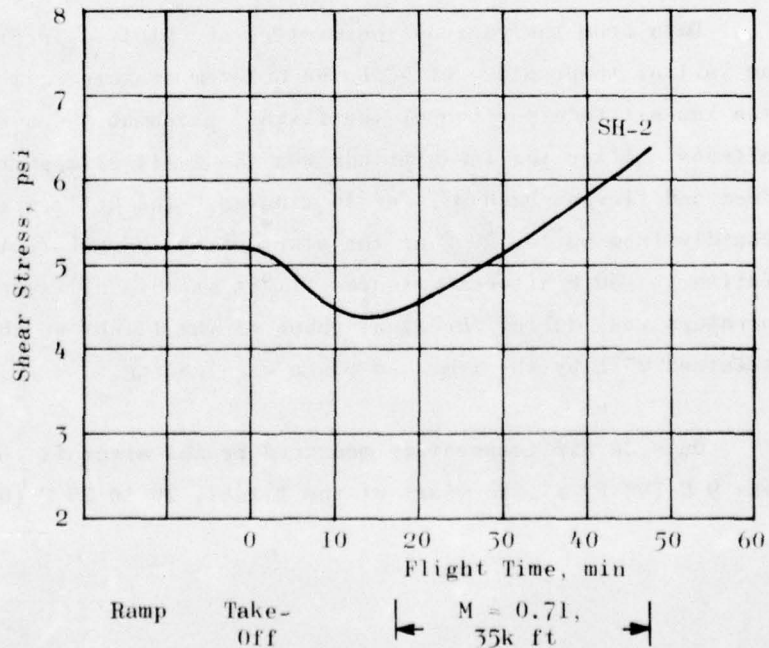
Figure 53. Thermal Shear Stress Data from Gage SH-2
vs Flight Time, Flight 1

FLIGHT 2 - 11 DECEMBER 1972

Flight 2 was designed to measure dynamic stresses and strains associated with Mach 0.7 flight at low altitude (1800 feet) and to confirm the temperature data of Flight 1. Table 6 summarizes the flight conditions.

TABLE 6. FLIGHT 2 CONDITIONS

Starting Time	Time Lapse, min	Altitude, ft	Mach No.	Flight Segment
14:03:35	0	2,300	0	I
14:13:30	9:55	2,300	0.2	I
14:20:40	17:05	4,300	0.7	Special Low Alt Cruise
14:24:40	21:05	4,300	0.7	
14:35:30	31:55	35,000	0.7	IV
14:50:30	46:55	35,000	0.7	
14:51:30	47:55	35,000	0.7	
14:52:10	48:35	35,000	0.7	IV
5:10:35	67:00	3,200	0.2	I

Data from the various thermistors are plotted in Figure 54. From an initial temperature of 40 F the CLI temperature climbed to 60 F during the low-altitude portion of the flight, presumably due to aeroheating effects. After the low-altitude run the F-111 climbed rapidly to 35,000 feet and flew at Mach 0.7 for 15 minutes. The CLI temperature dropped rapidly from 60 to -20 F at the start of the 35,000-foot flight and had fallen to -30 F after 15 minutes flight at this altitude. The CLI temperature rose during the final phase of the flight so that it had attained 25 F by the time the plane was landing.

Outside air temperature measured by the aircraft instrumentation was 9 C (48 F) at the start of the flight, 20 to 25 C (68 to 77 F) during

76
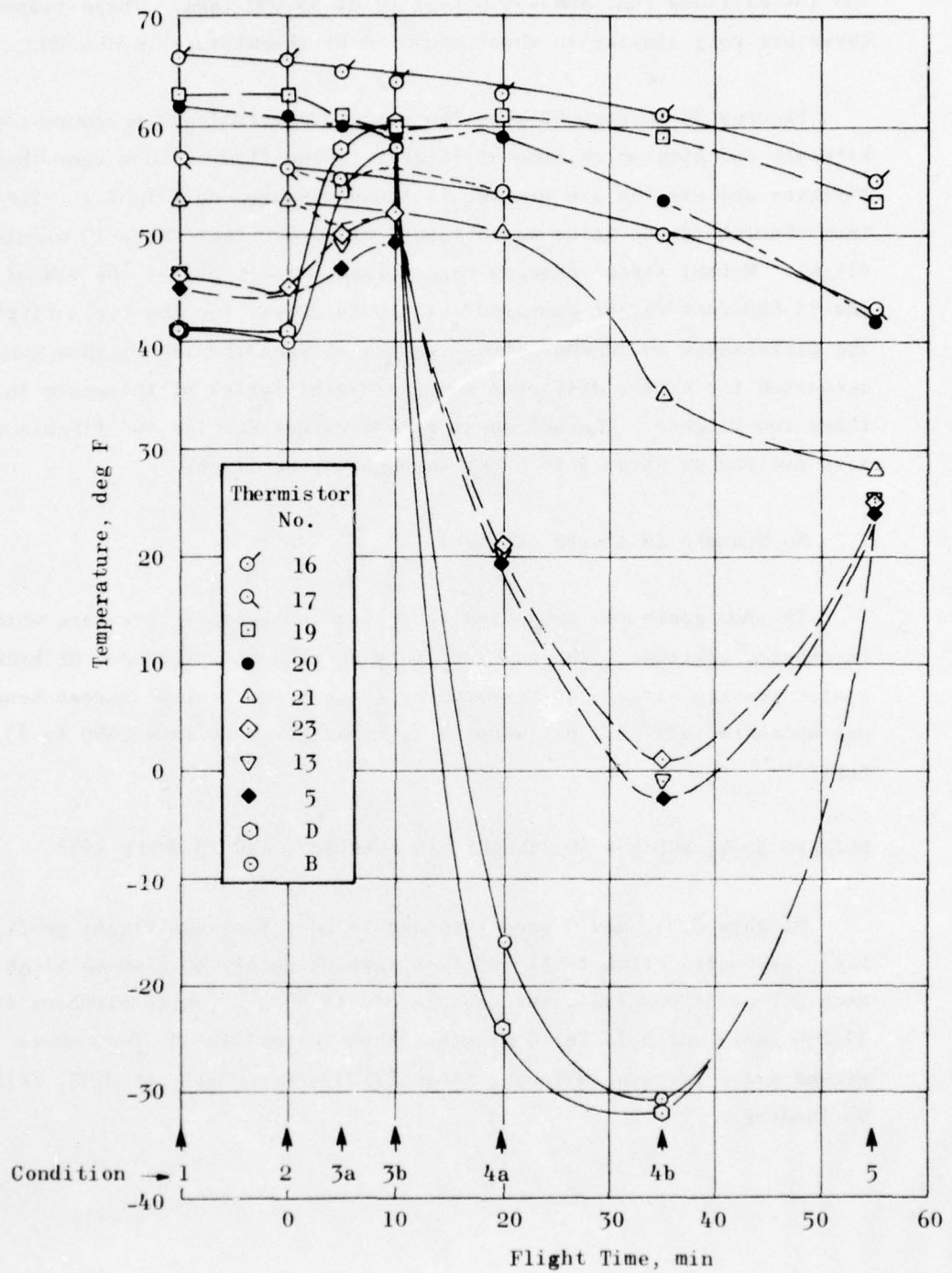
Figure 54.   BDU Temperature History, Test.Flight 2
(Revised Thermistor Calibrations)

the low-altitude run, and -35 C (-31 F) at 35,000 feet. These temperatures are very similar to those measured by thermistors in the BDU.

Figures 55 through 57 show the combined thermal and pressure-induced stresses and strains vs time of flight. These figures show that thermal stresses and strains are similar to those measured on Flight 1. The maximum thermal stress value was obtained at 35,000 feet after 15 minutes flight. Normal stress changes ranged from 6 to 16 psi at the end of the 35,000-foot flight compared with 10 to 22 psi for the first flight. The differences in thermal stress values between the two flights can be accounted for by the different temperature histories of the grain in these two flights. Thermal shear stress values for the two flights are also similar at about 5 to 6 psi throughout the flight.

No dynamic data were obtained.

The BDU grain was subjected to a lower ambient air pressure with increasing altitude. The value of this decrease in pressure, or hydrostatic tensile stress, as measured by the embedded normal stress sensors was approximately 10.2 psi when the aircraft climbed from 2500 to 35,000 feet.

FLIGHTS 3, 4, AND 5 - 30 JANUARY, 16 FEBRUARY, AND 19 MARCH 1973

Flights 3, 4, and 5 were intended to have the same flight profile, i.e., take-off, climb to 31,000 feet, approximately 30 minutes flight at Mach 0.7 at 31,000 feet, then accelerate to Mach 2 (while climbing to 35,000 feet) and hold for 5 minutes, then descend to 500 feet above ground and a terrain-following radar (TFR) mission at Mach 0.95, followed by landing.
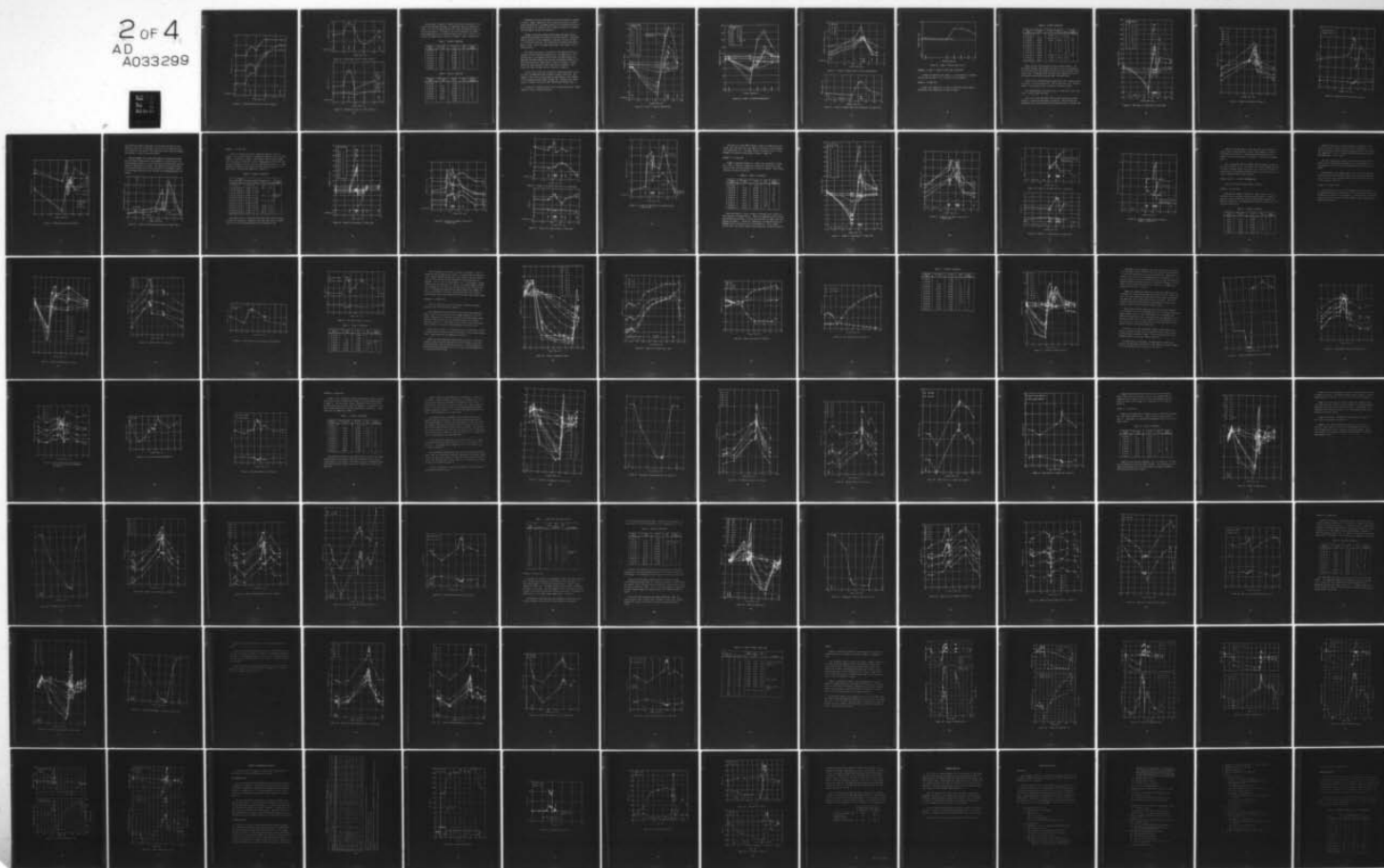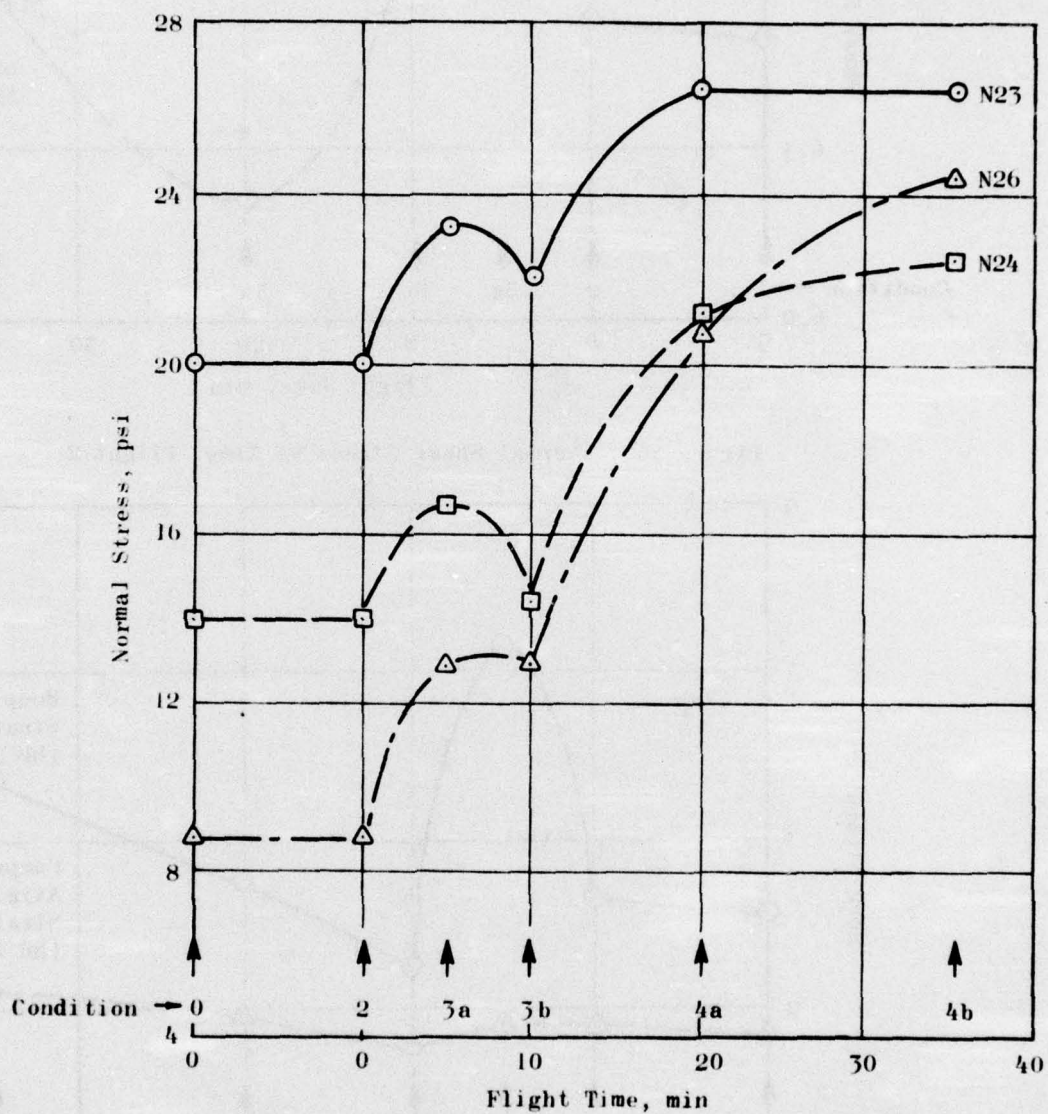
Figure 55. Normal Thermal Stresses vs Time, Flight 2
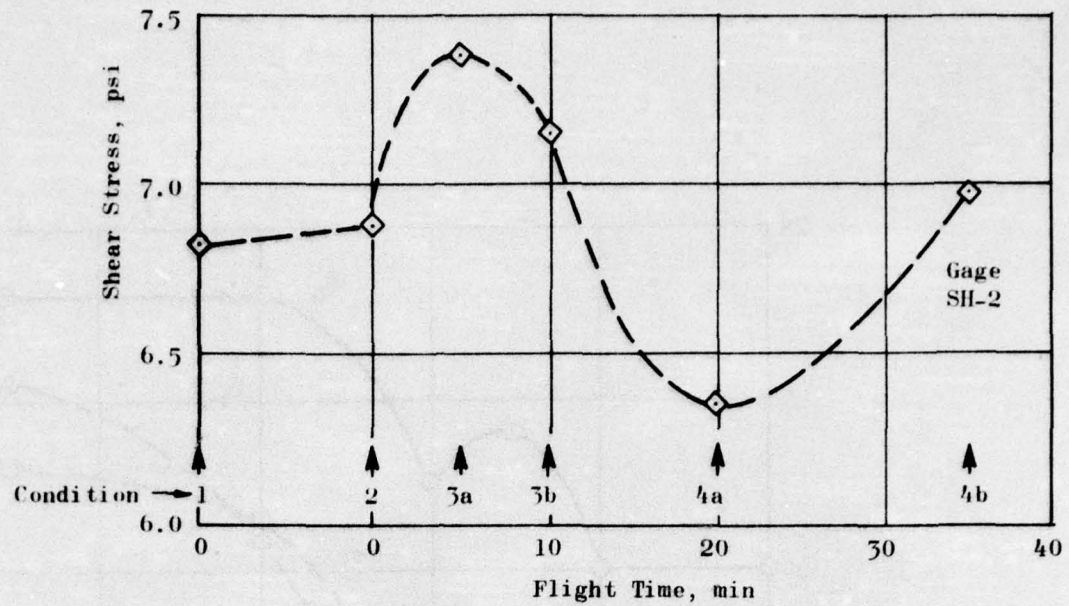
Figure 56. Thermal Shear Stress vs Time, Flight 2
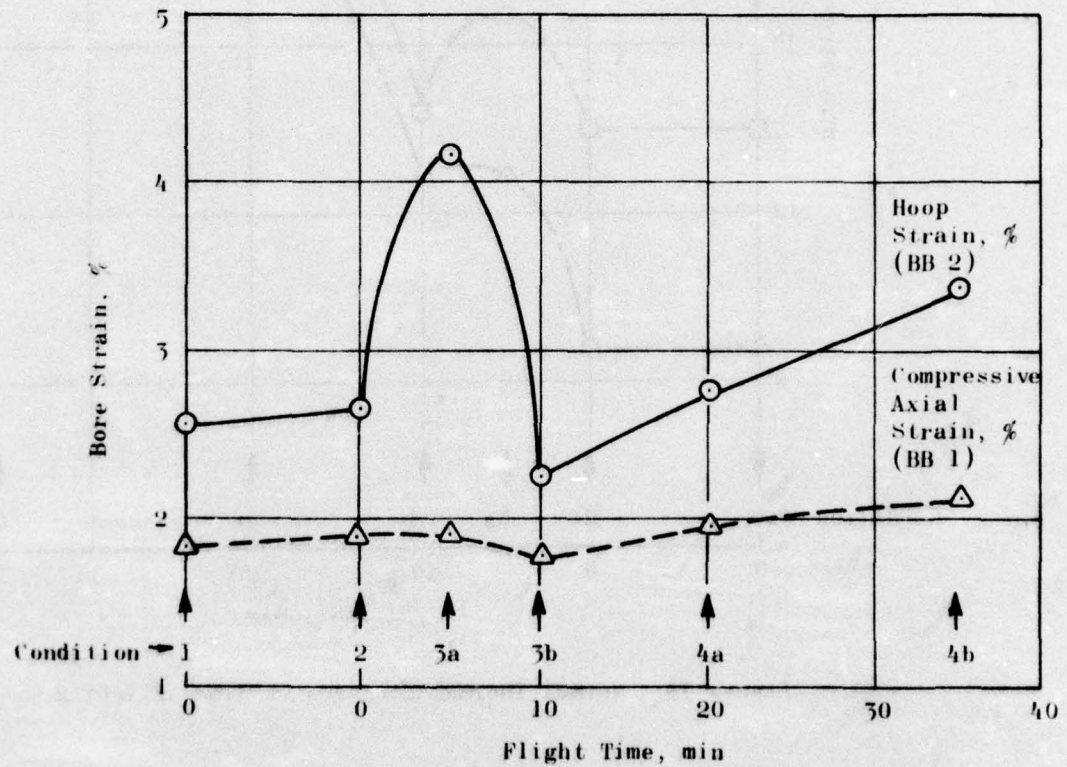
Figure 57. Thermal Bore Strains vs Time, Flight 2

80

During Flight 3, however, an engine stall when accelerating to Mach 2 led to considerable buffeting. No temperature data were obtained on Flight 4 due to an equipment malfunction so that the gage data could not be analyzed properly. On Flight 5, the dc data from Track 10 (normal stress gage data) were not recorded because of an error in wiring. Conditions for Flights 3 and 5 are given in Tables 7 and 8, respectively.

TABLE 7. FLIGHT 3 CONDITIONS

Starting Time	Time Lapse, min	Altitude, ft	Mach No.	Flight Segment
13:11:40	0	2,300	0	I
13:14:00	2:20	2,300	0.22	IV
13:44:00	32:20	31,000	0.7	IV
13:51:40	40:00	35,000	2.0	III
13:54:48	43:08	35,000	2.0	III
13:55:52	44:12	35,000	2.0	III
14:05:50	54:10	4,000	0.5	V
14:12:50	71:10	2,300	0.2	I

TABLE 8. FLIGHT 5 CONDITIONS

Starting Time	Time Lapse, min	Altitude, ft	Mach No.	Flight Segment
14:23:30	0	2,300	0	I
14:27:00	04:00	2,300	0.2	IV
14:37:00	14:00	31,000	0.7	IV
15:06:00	43:00	35,000	2.0	III
15:10:15	47:15	35,000	2.0	III
15:15:20	52:20	35,000	0.9	III
15:19:30	56:30	2,300	0.2	I
		2,300	0	I

81

Temperature profiles from Flights 3 and 5 are presented in Figures 58 and 59. Higher temperatures were recorded at the end of the Mach 2 flight during Flight 3, presumably because of the extended acceleration period caused by the compressor stall. However, both sets of temperature data appear rational and consistent.

Thermal- and pressure-change-induced normal and shear stresses measured during Flight 3 are plotted in Figures 60 and 61. These data show an increase in stress magnitude as the grain cooled in the Mach 0.7, 31,000-foot Condition. An increase due to aeroheat during Mach 2, dash is noted. Most of the gages showed peak stress changes from 8 to 30 psi tension.

The normal stress gage in the middle of the grain (N-23) did not increase in stress during the aeroheat test. An examination of the problem later in the program disclosed that the output signal from Gage N-23 "bottomed" against the limits of the amplifier inputs ($\pm$ 50 millivolts) during the flight tests so that the increase in stresses during the latter portions of the flight were not measured. Early flight test data from Gage N-23 are, therefore, incorrect.

Flight 3 shear stress data, Figure 61, showed peak shear stresses of 12 psi from Gage SH-2 under the Mach 2 aeroheat conditions. The change in shear stress during flight was approximately 4 psi compared to 3 psi measured during Flight 5 (Figure 62). Absolute shear stress values for Flight 5 were lower than those measured during Flight 3.

No data were obtained from the bore clip gages during these flights because of poor or broken connections.
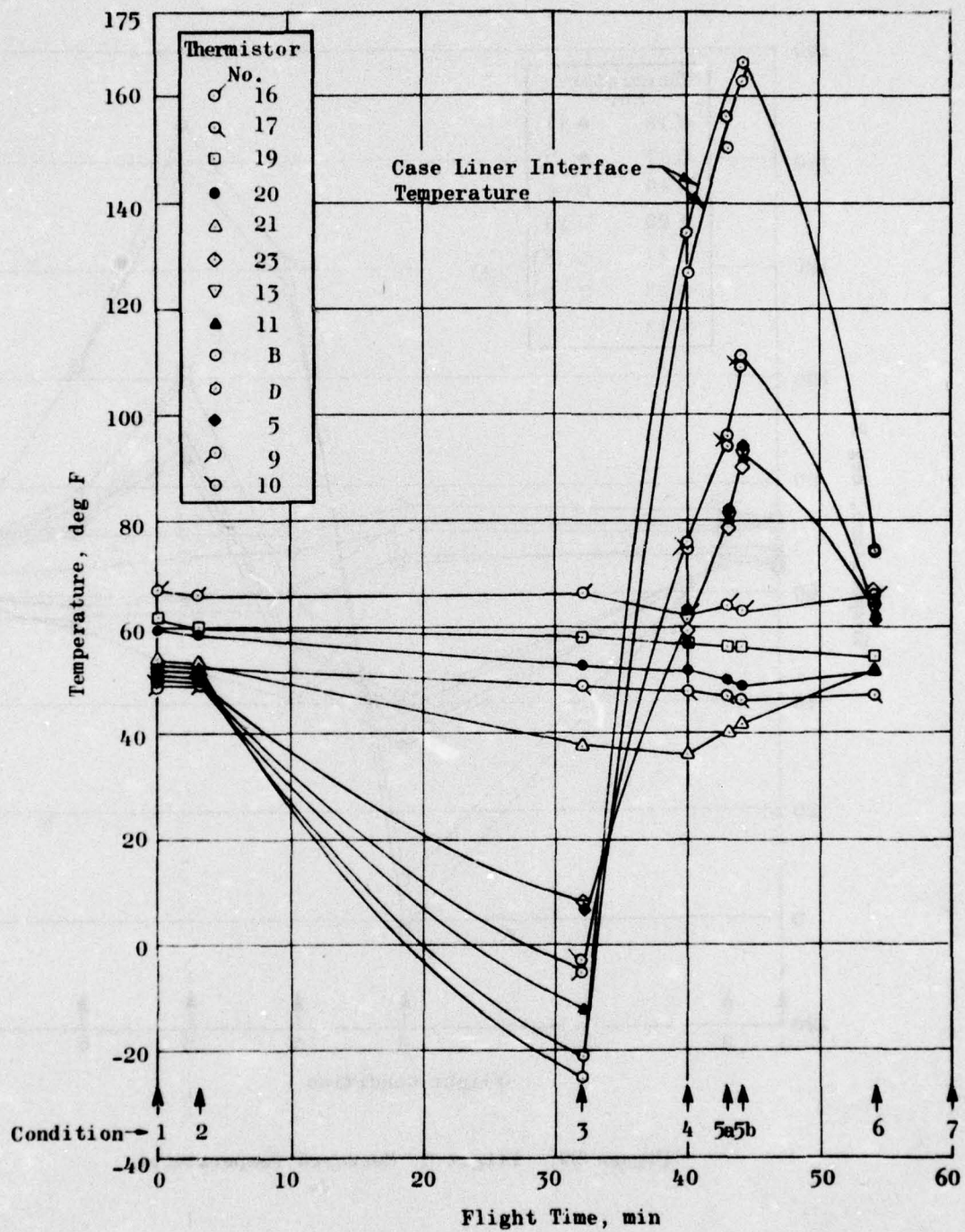
Figure 58. Flight 3, Measured Temperatures

83
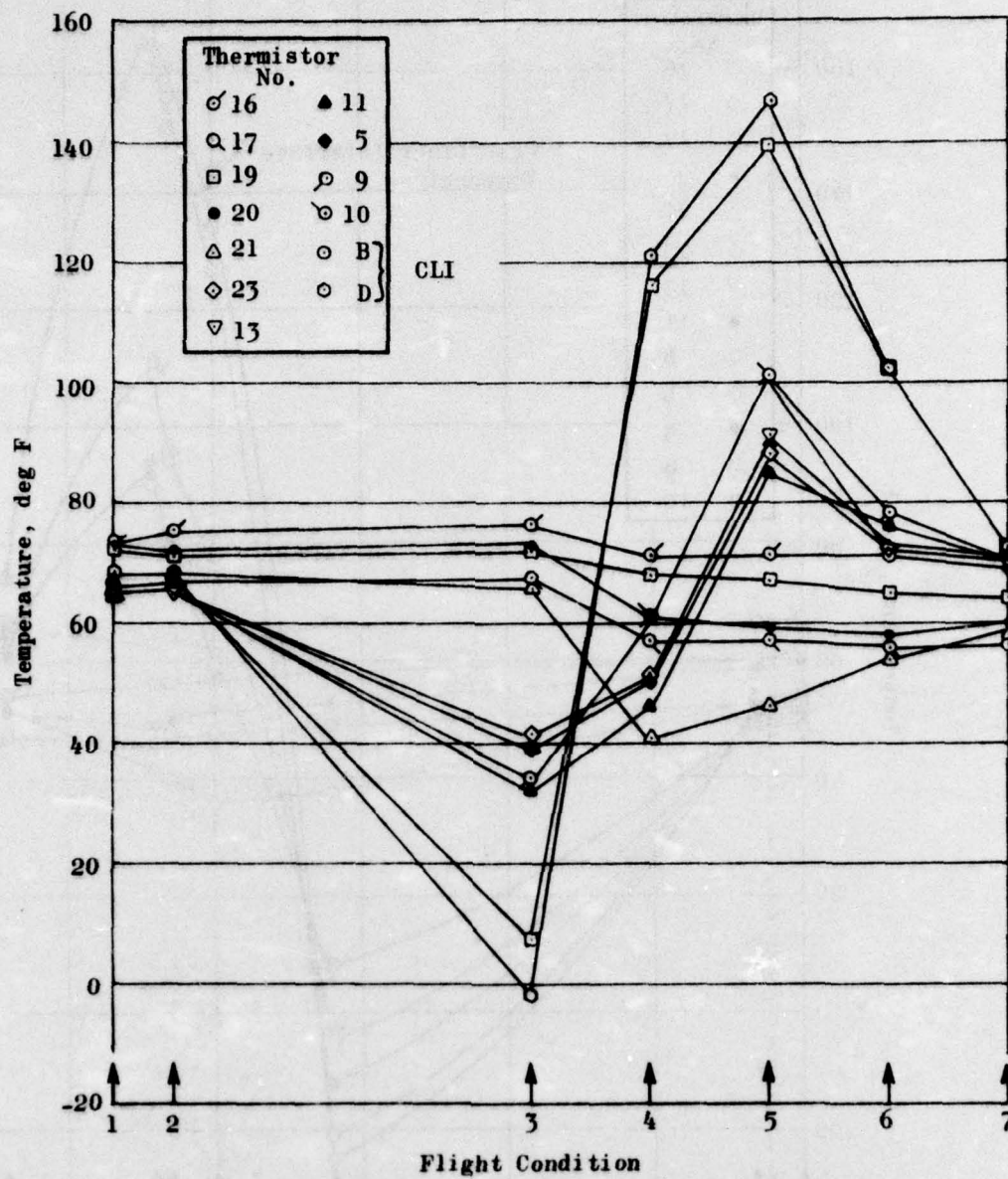
Figure 59. Flight 5, Measured Temperatures

84
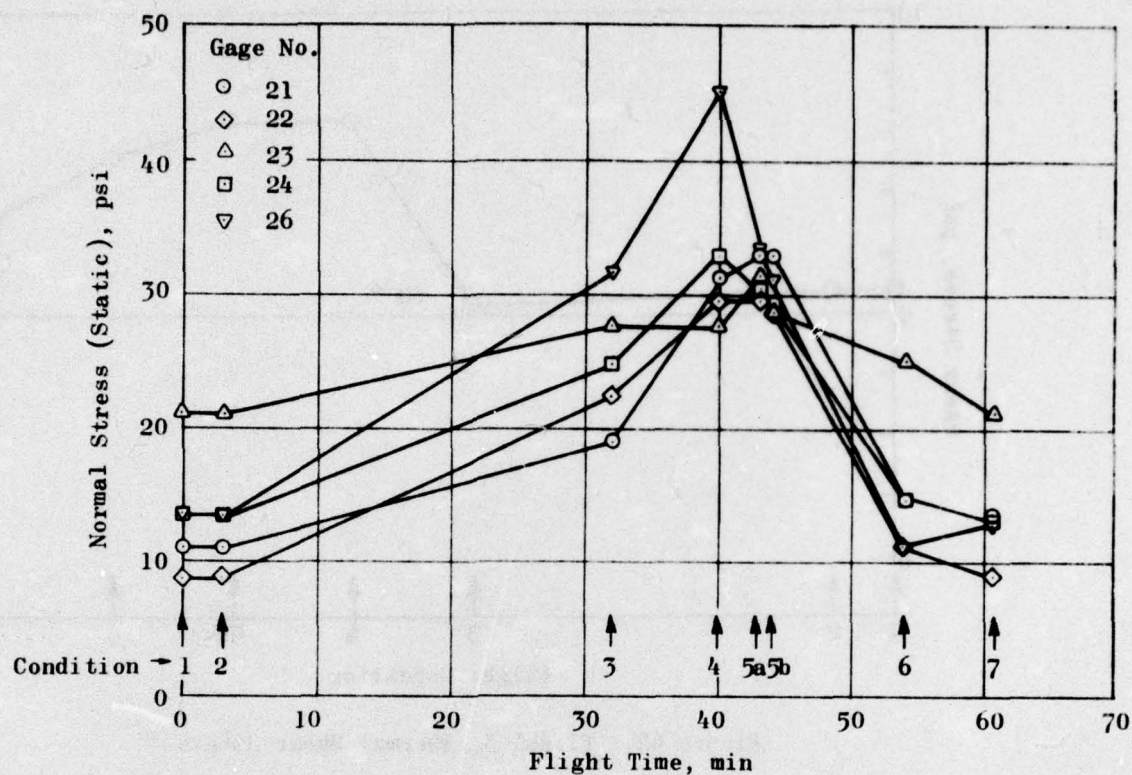
Figure 60. Flight 3, Thermal Normal Stresses (Hand Reduced)
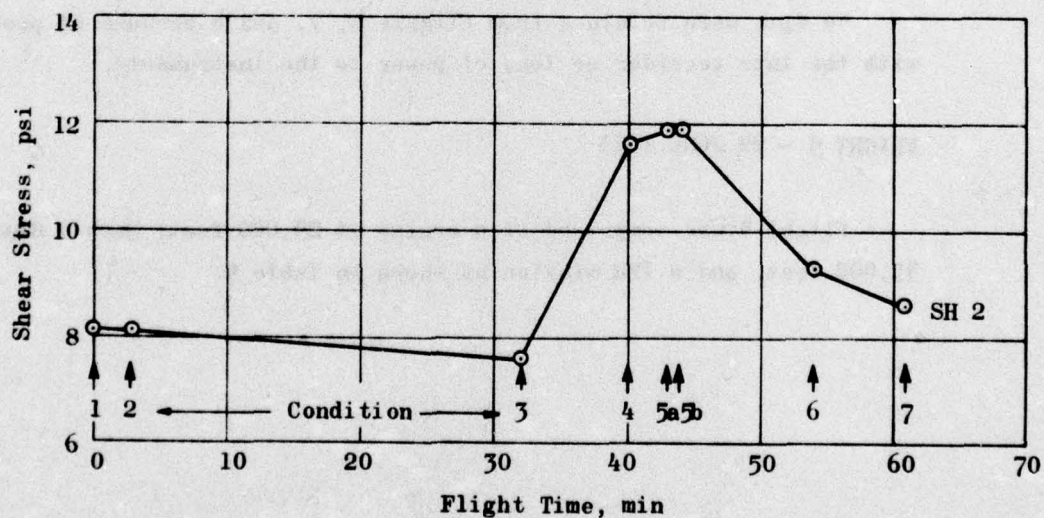
Figure 61. Flight 3, Thermal Shear Stress (Measured with Gage SH-2)

85
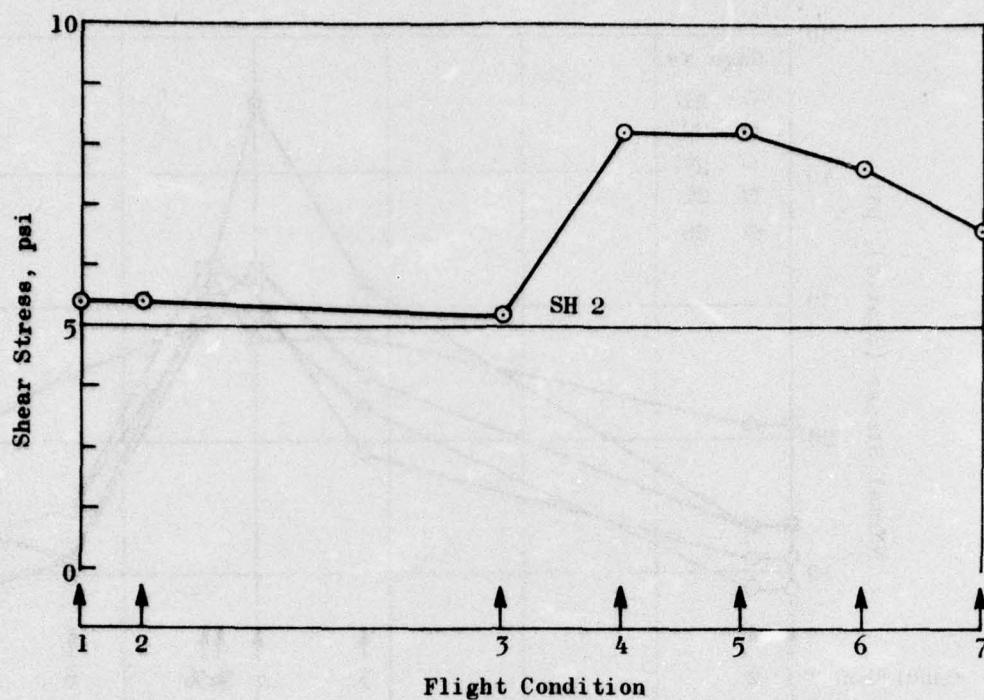
Figure 62.   Flight 5, Thermal Shear Stress

FLIGHTS 6, 7, AND 8 – 24 MAY, 15 JUNE, AND 18 JUNE 1973

No data were obtained from Flights 6, 7, and 8 because of problems with the tape recorder or loss of power to the instruments.

FLIGHT 9 – 22 JUNE 1973

Flight 9 was comprised of a cruise at 29,000 feet, Mach 2 dash at 35,000 feet, and a TFR mission as shown in Table 9.

86

TABLE 9. FLIGHT 9 CONDITIONS

Starting Time	Time Lapse, min	Altitude, ft	Mach No.	P_{atm}	Flight Segment
12:52:40	0	2,300	0	13.5	I
13:28:04	35:24	29,000	0.8	4.2	IV
13:36:00	43:20	35,000	2.02	1.6	III
13:37:00	44:20				
13:38:00	45:20				
13:39:00	46:20				
13:40:00	47:20	↓	↓		↓
13:41:00	48:20	--	--	↓	
13:42:00	49:20	19,000	0.8	6.4	III
13:45:45	53:05	2,700	0.95	10.0	V
14:01:40	69:0	2,300	0	13.5	I

Figure 63 shows the temperatures measured during Flight 9. The data appear rational with minimum temperatures of 30 F and maximum of 170 F occurring after the 29,000-foot cruise and after the Mach 2 dash, respectively. A high Case/Liner Interface (CLI) temperature of 145 F was recorded during the low-altitude Mach 0.95 TFR mission.

Normal stresses measured during Flight 9 are shown in Figure 64 and are similar to earlier flight data. The N-23 data were still incorrect because of overloading of the $\pm$ 50 millivolt amplifier output.

Bore hoop and axial strain data, shown in Figure 65, are also similar to earlier flight test data.

Shear stress data from three shear sensors were monitored during Flight 9, yielding the data shown in Figure 66. Data from SH-2 and SH-120B are very similar; whereas data from SH-101 shows a similar trend
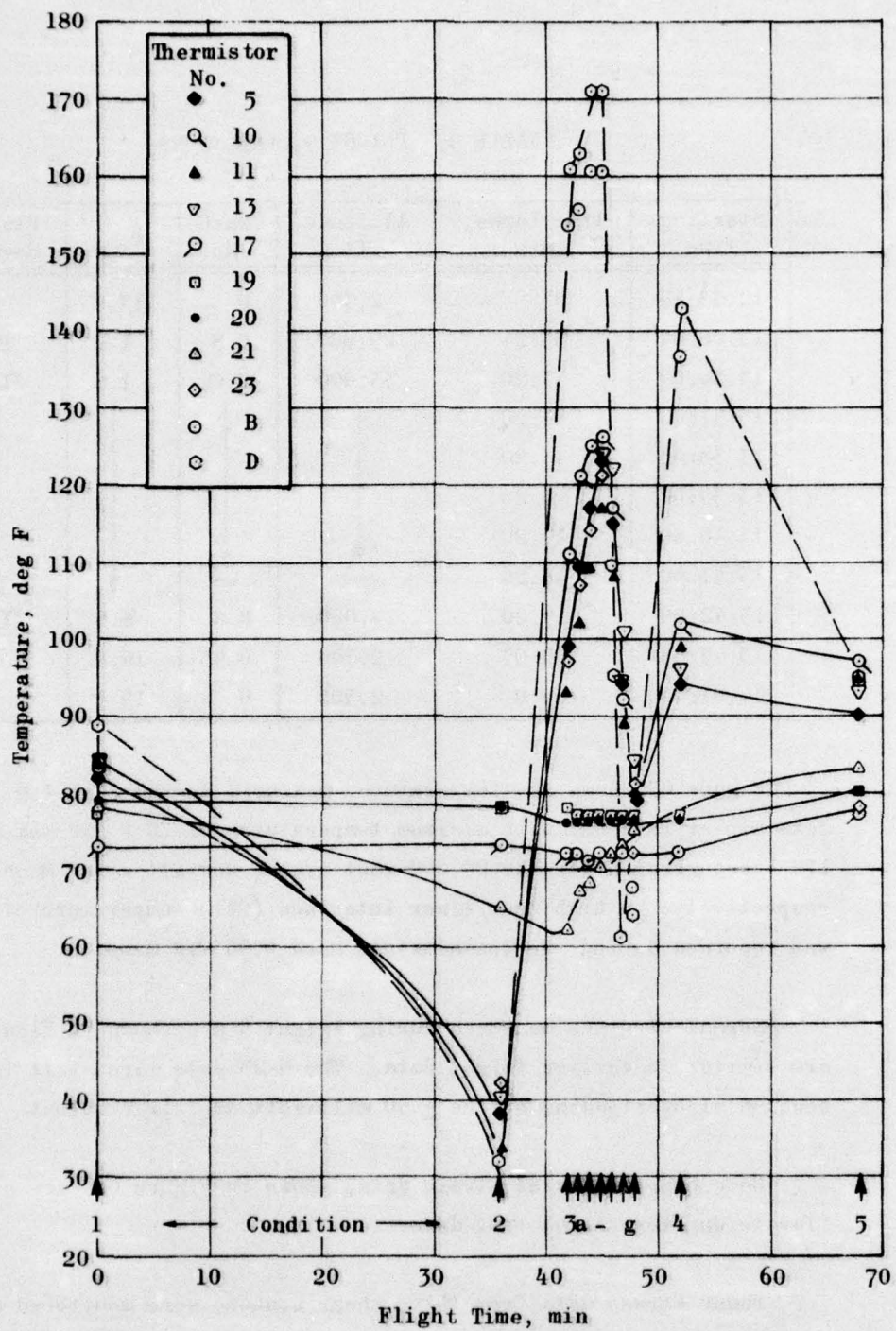
Figure 63. BDU Flight 9, Temperature vs Flight Time

88
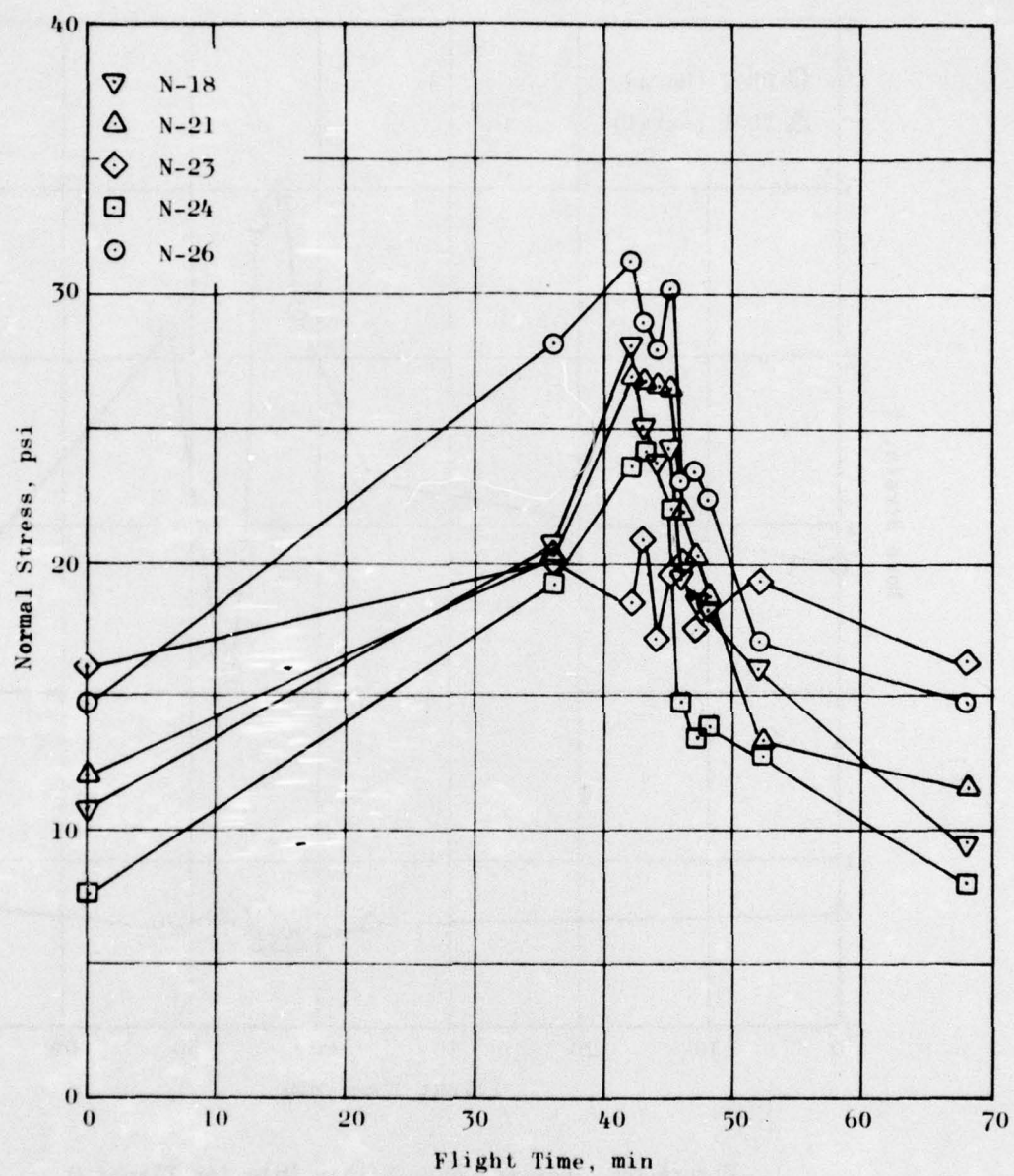
Figure 64. Normal Stress Data for Flight 9

89
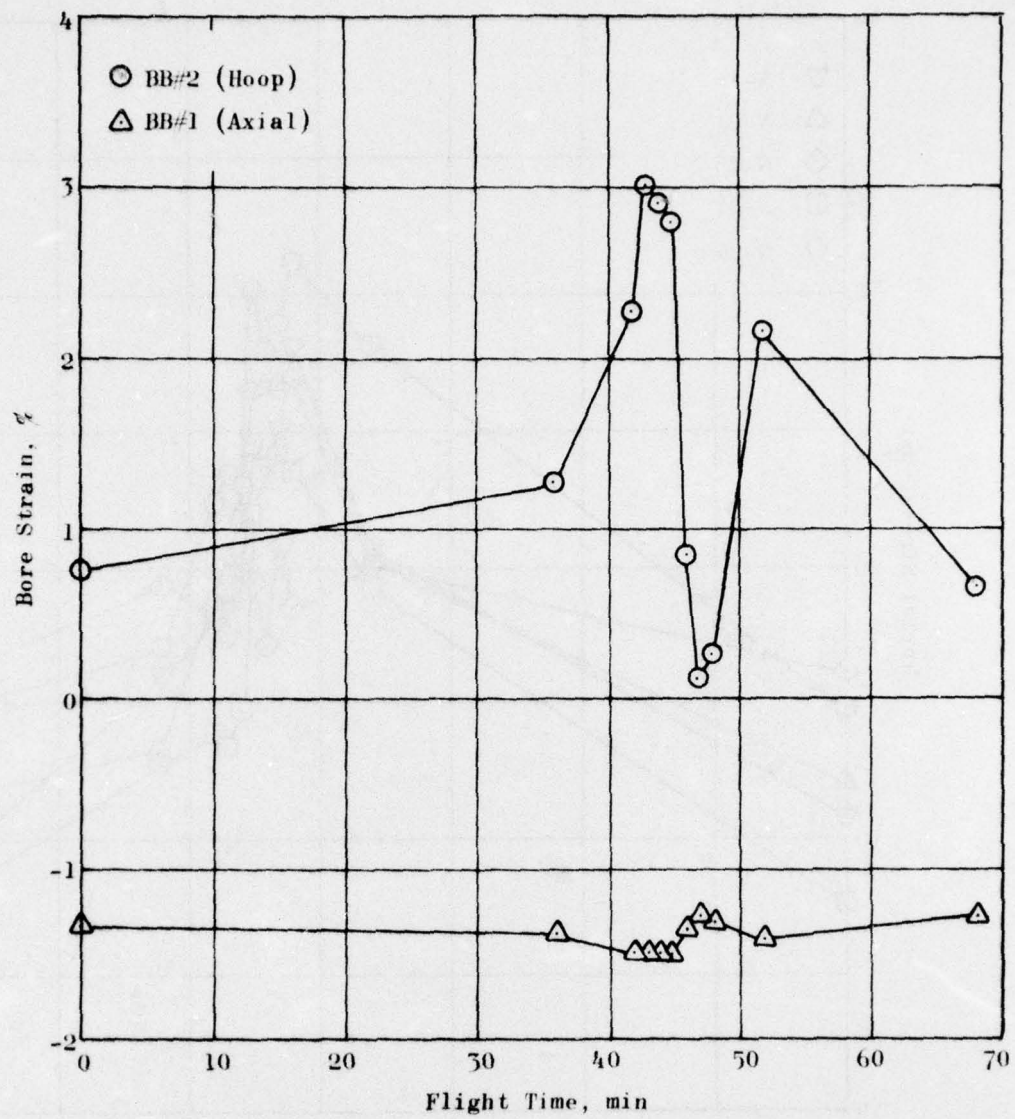
Figure 65. Revised Bore Strain Data for Flight 9
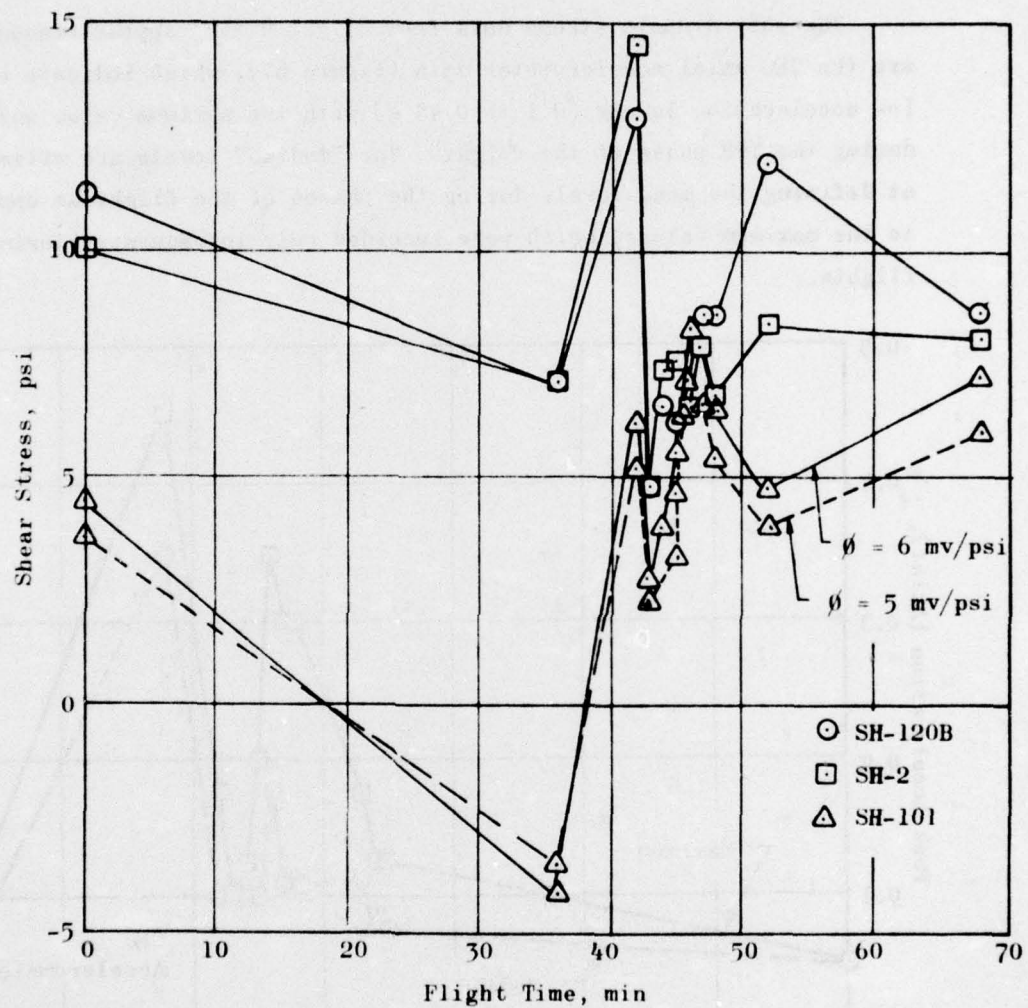
Figure 66. Shear Stress Data for Flight 9

but a different range of magnitudes. Since SH-101 and SH-2 are both located at the front of the grain, their shear stress-flight time profiles should be very similar. The differences between them are probably attributable to errors in data from SH-101.

The only dynamic stress data from Flight 9 that appear reasonable are the CEC axial accelerometer data (Figure 67), which indicate very low acceleration levels (0.1 to 0.45 g) with the maximum value occurring during the TFR phase of the flight. The "median" levels are attempts at defining the mean levels during the phases of the flight as opposed to the maximum values, which were recorded only infrequently during the flights.
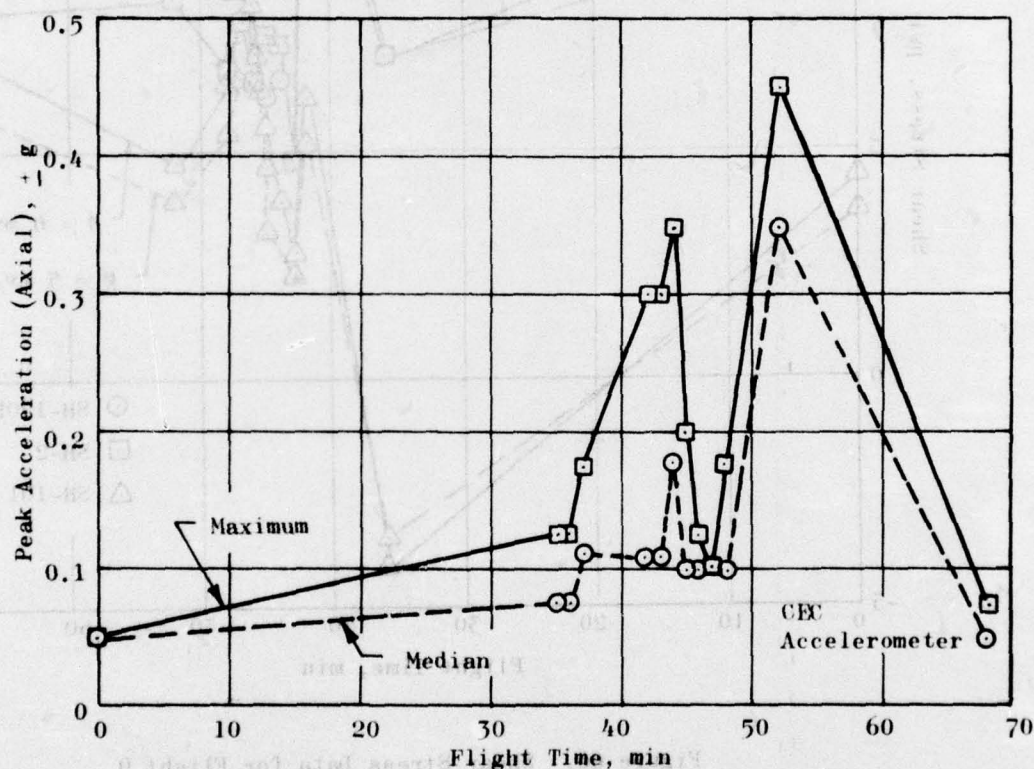
Figure 67.   Flight 9, Peak Axial Accelerations vs Flight Time

92

FLIGHT 10 - 12 JULY 1973

Flight 10 followed a different flight plan than all other test flights. After take-off the F-111 performed a supersonic low-level dash ending in a right turn, climbed to 30,000 feet, and performed a right roll, finishing at 14,000 feet. After climbing again to 30,000 feet the aircraft performed a left roll that was completed at 8,000 feet. It then performed a landing attempt followed by the real landing and roll out. These flight conditions are summarized in Table 10.

TABLE 10.   FLIGHT 10 CONDITIONS

Starting Time	Time Lapse, min	Altitude, ft	Mach No.	Temperature, deg F	P atm	Flight Segment
53:00	0	2,300	0	92.12	13.5	I
1:07:30	14:30	2,800	0.52	89.6	12.7	
1:14:35	21:35	3,500	1.06			
1:16:56	23:56	4,000	1.10			
1:17:45	24:45	11,800	0.72	50.72	8.4	Special Tests
1:23:20	30:20	30,300	0.87			
1:24:55	31:55	14,000	0.93	43.34	6.8	
1:26:55	33:55	25,000	0.88			
1:28:15	35:15	7,800	0.92	35.42	8.5	
1:33:13	40:13	3,850	0.26	84.02	12.8	
1:40:25	47:25	2,500	0.2	92.12	13.4	
1:50:40	53:00	2,300	0	92.12	13.5	I

Temperature, stress, and strain data from Flight 10 are presented in Figures 68 through 72. Temperature data show that high CLI temperatures of 160 F were obtained during the short supersonic dash.

93
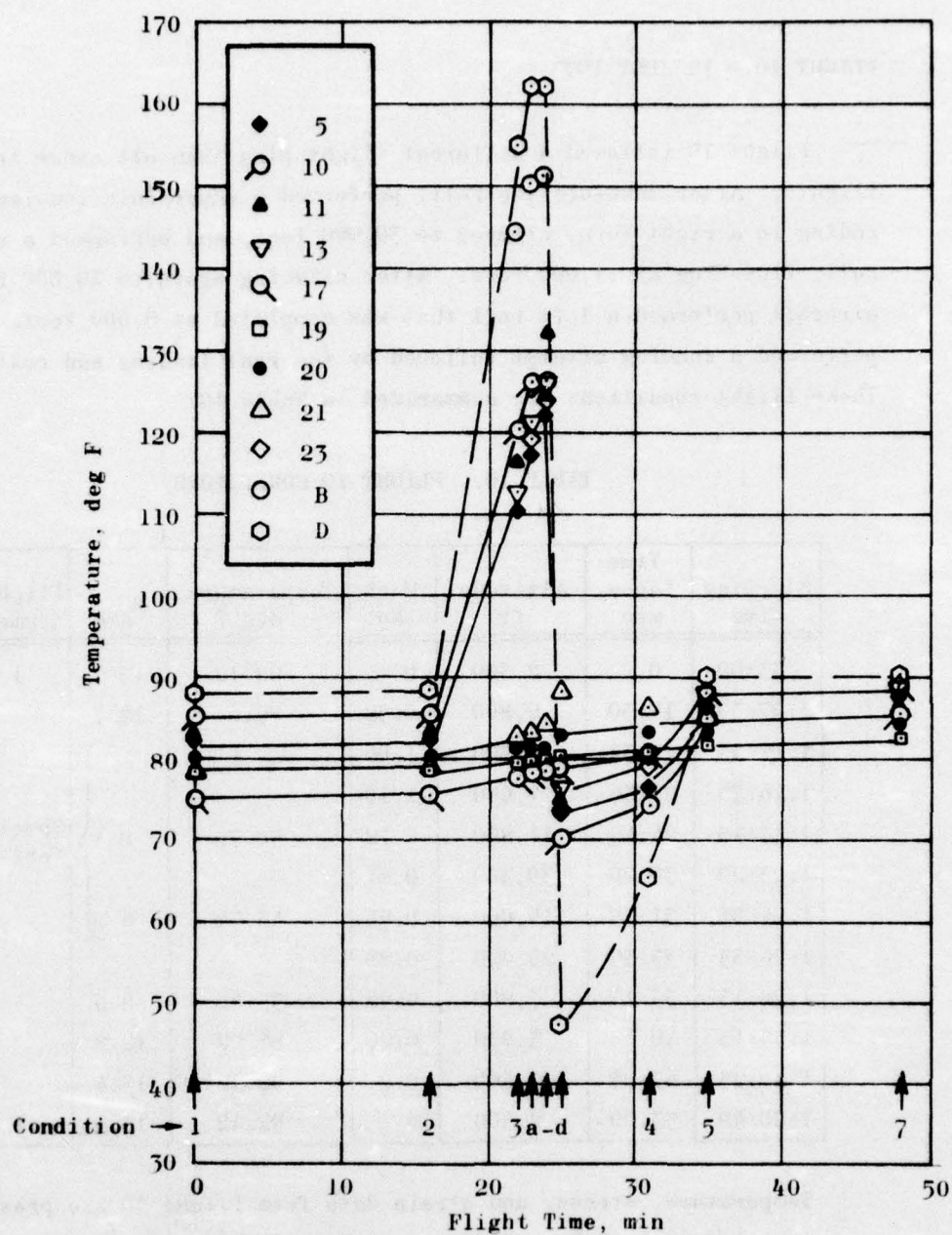
Figure 68. Flight 10, Temperature vs Flight Time
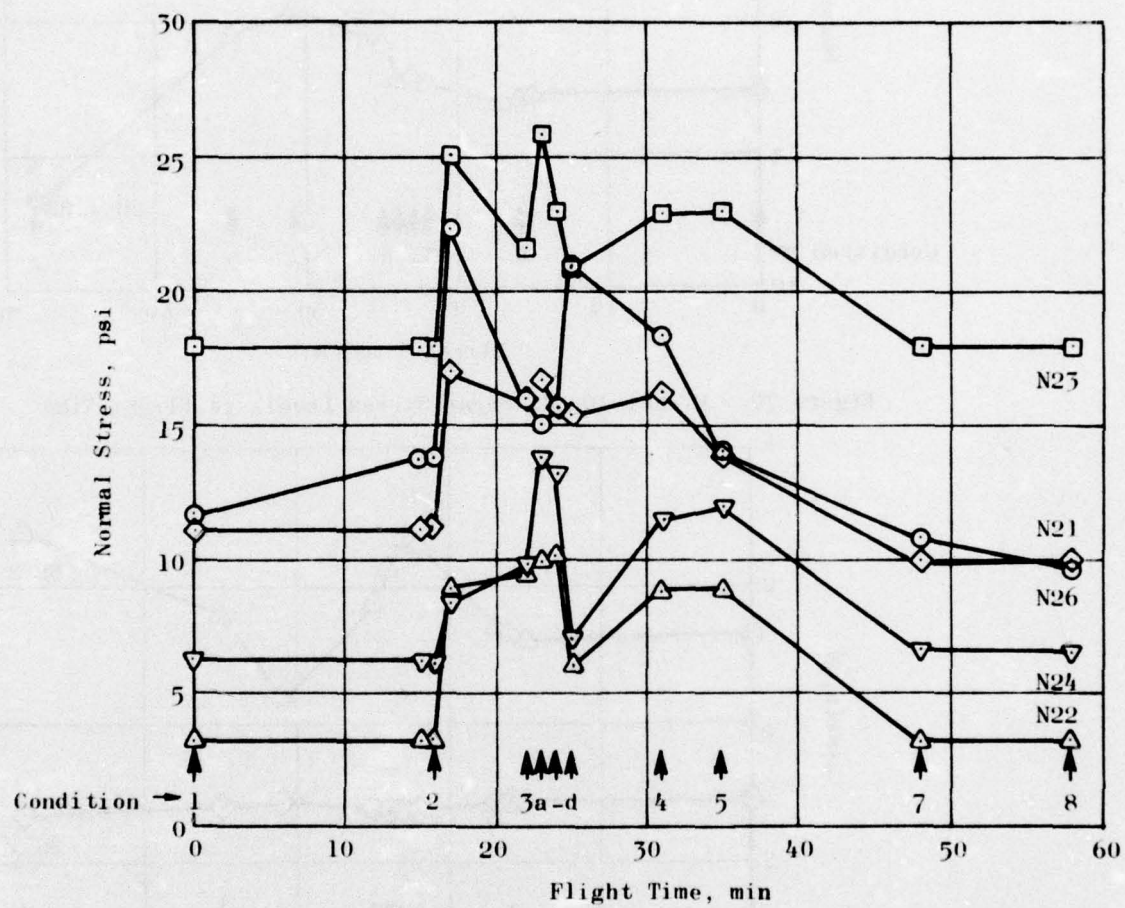
Figure 69.   Flight 10, dc Normal Stress Levels
vs Flight Time

95
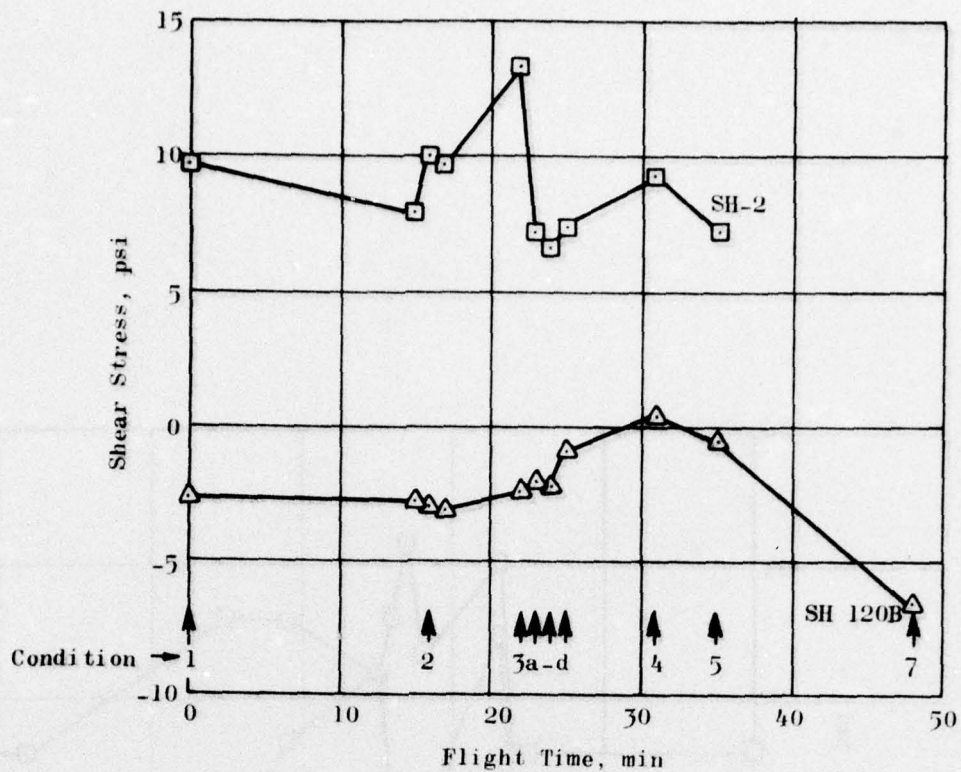
Figure 70.   Flight 10, dc Shear Stress Levels vs Flight Time
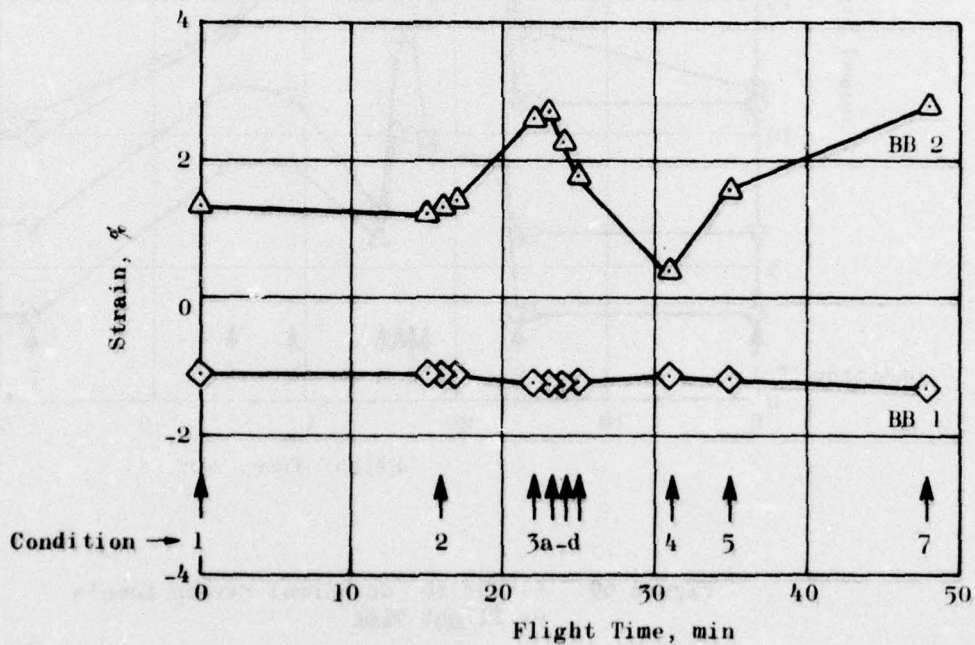
Figure 71.   Flight 10, dc Bore Strains vs Flight Time

96
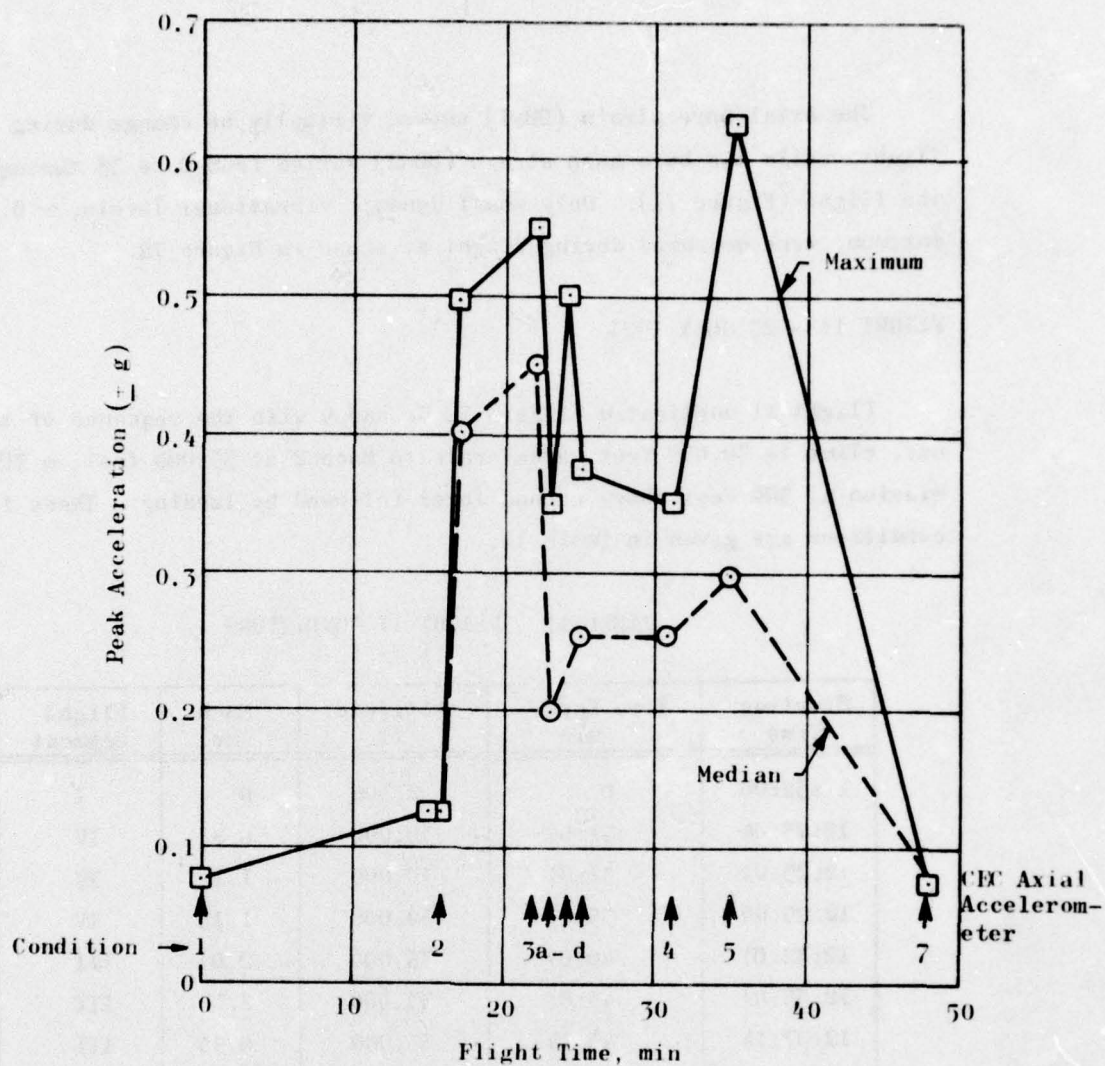
Figure 72. Flight 10, Peak Axial Accelerometer Values
vs Flight Time

The axial bore strain (BB-1) showed virtually no change during the flight; while the bore hoop strain (BB-2) varied from 0 to 3% throughout the flight (Figure 71). Only small dynamic vibrational levels, ~ 0.5 g maximum, were measured during flight as shown in Figure 72.

FLIGHT 11 - 27 JULY 1973

Flight 11 duplicated Flights 3, 5, and 9 with the sequence of take-off, climb to 30,000 feet, accelerate to Mach 2 at 35,000 feet, a TFR mission at 500 feet above ground level followed by landing. These flight conditions are given in Table 11.

TABLE 11.   FLIGHT 11 CONDITIONS

Starting Time	Time Lapse, min	Altitude, ft	Mach No.	Flight Segment
11:52:00	0	2,300	0	I
12:23:04	31:04	30,000	0.8	IV
12:23:21	31:21	30,000	1.1	IV
12:25:00	33:00	30,000	1.15	IV
12:32:01	40:01	35,000	2.0	III
12:35:01	43:01	35,000	2.0	III
12:37:14	45:14	35,000	0.95	III
12:41:35	49:35	2,950	0.95	V
12:42:35	50:35	2,950	0.95	V
12:56:30	64:30	2,300	0	I

Data from Flight 11, given in Figures 73 through 77, are similar to those obtained in Flights 9 and 11. Higher CLI temperatures (up to 180 F) were measured during Flight 11 at the end of the Mach 2 flight; 170 F was obtained on Flight 9. Similar CLI temperatures were obtained during the TFR phase (143 F for Flight 9, 146 F for Flight 11). The dc normal stresses show very similar trends as may be observed in Figures 64 and 74.
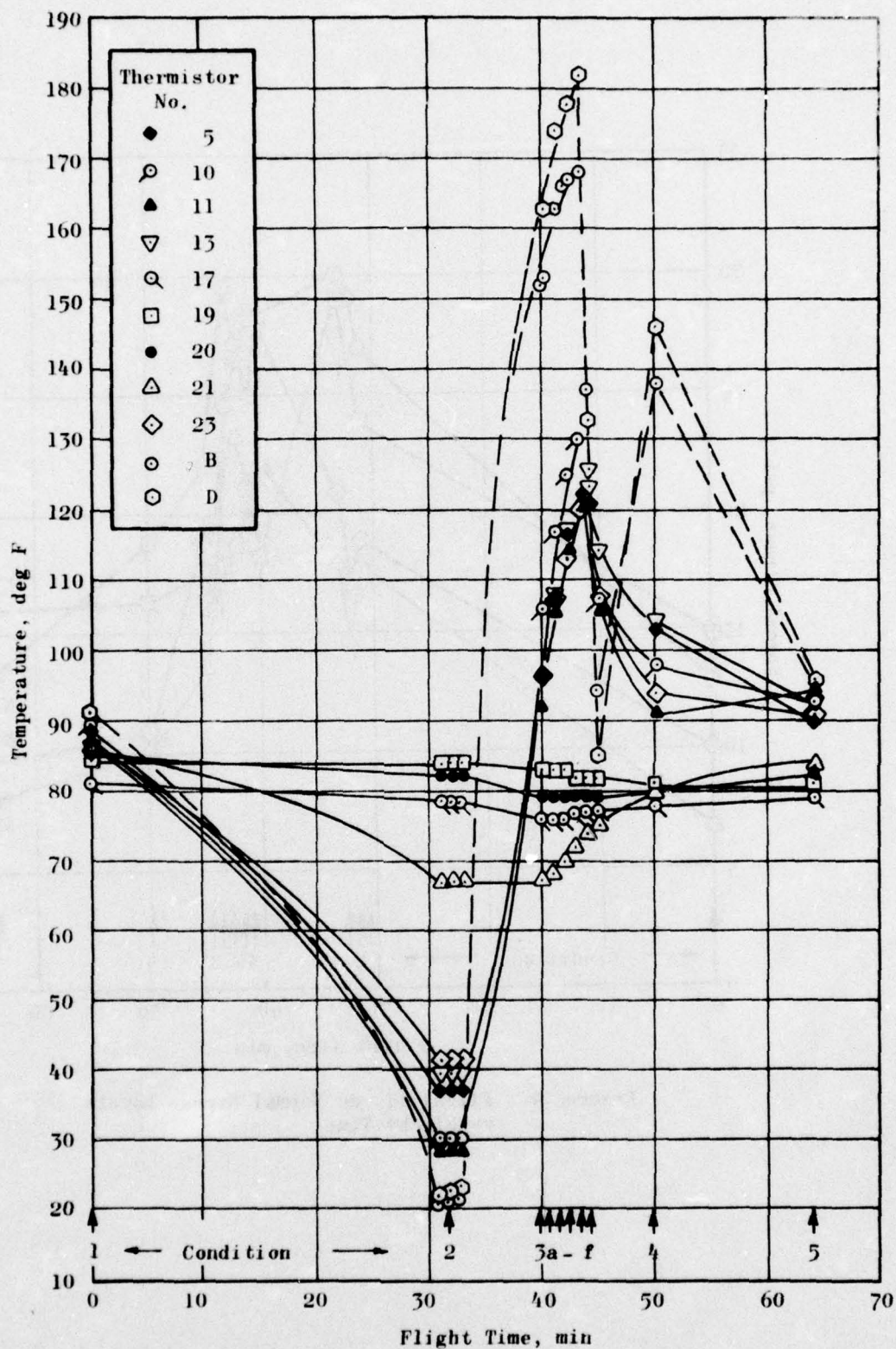
Figure 73. Flight 11, Temperatures vs Flight Time

99
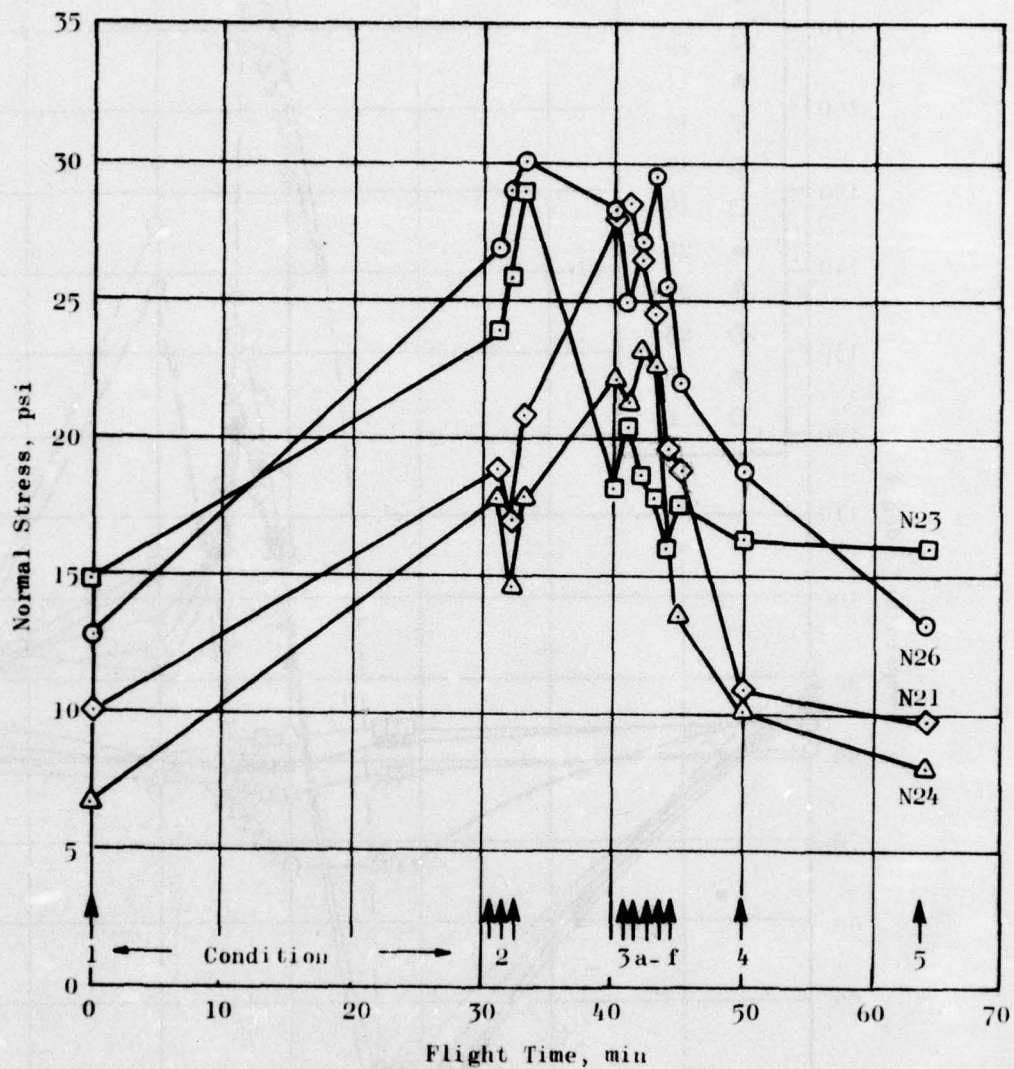
Figure 74. Flight 11, dc Normal Stress Levels vs Flight Time

100
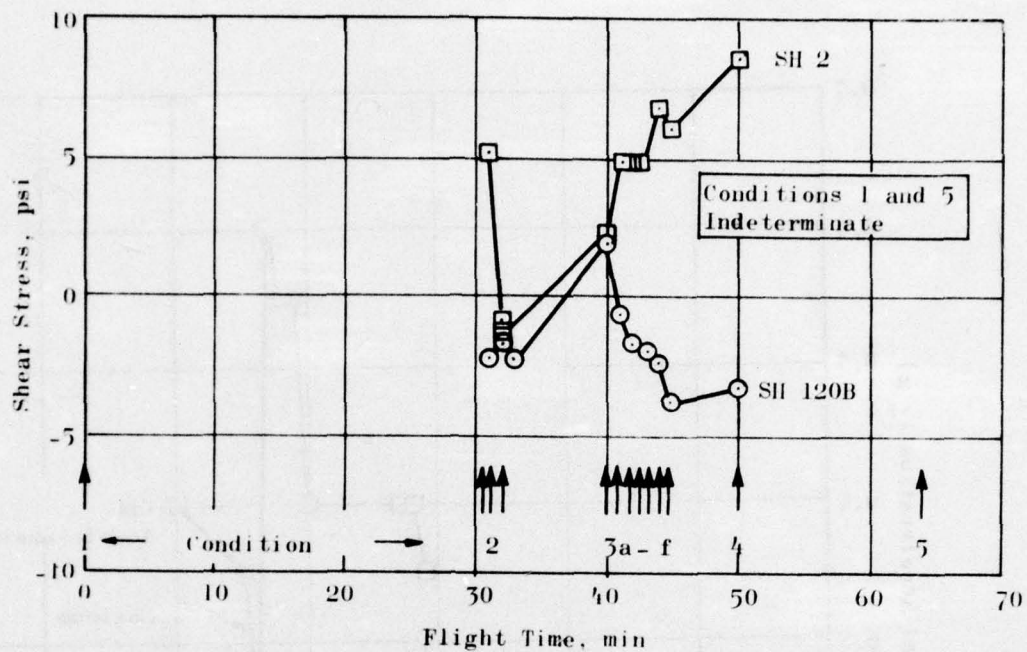
Figure 75. Flight 11, dc Shear Stresses vs Flight Time
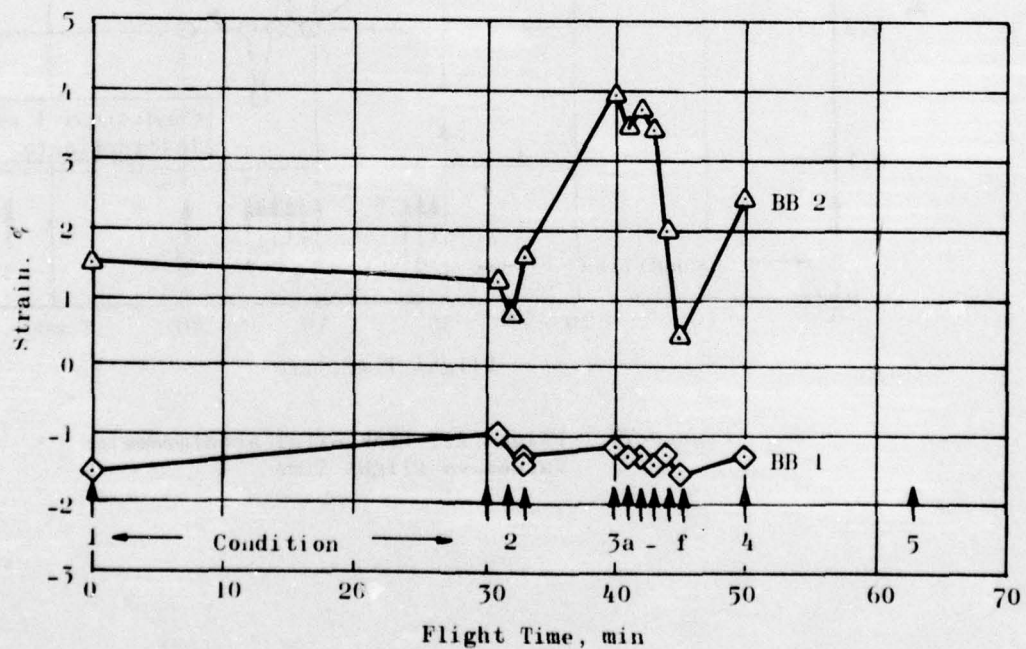
Figure 76. Flight 11, dc Bore Strains vs Flight Time

101
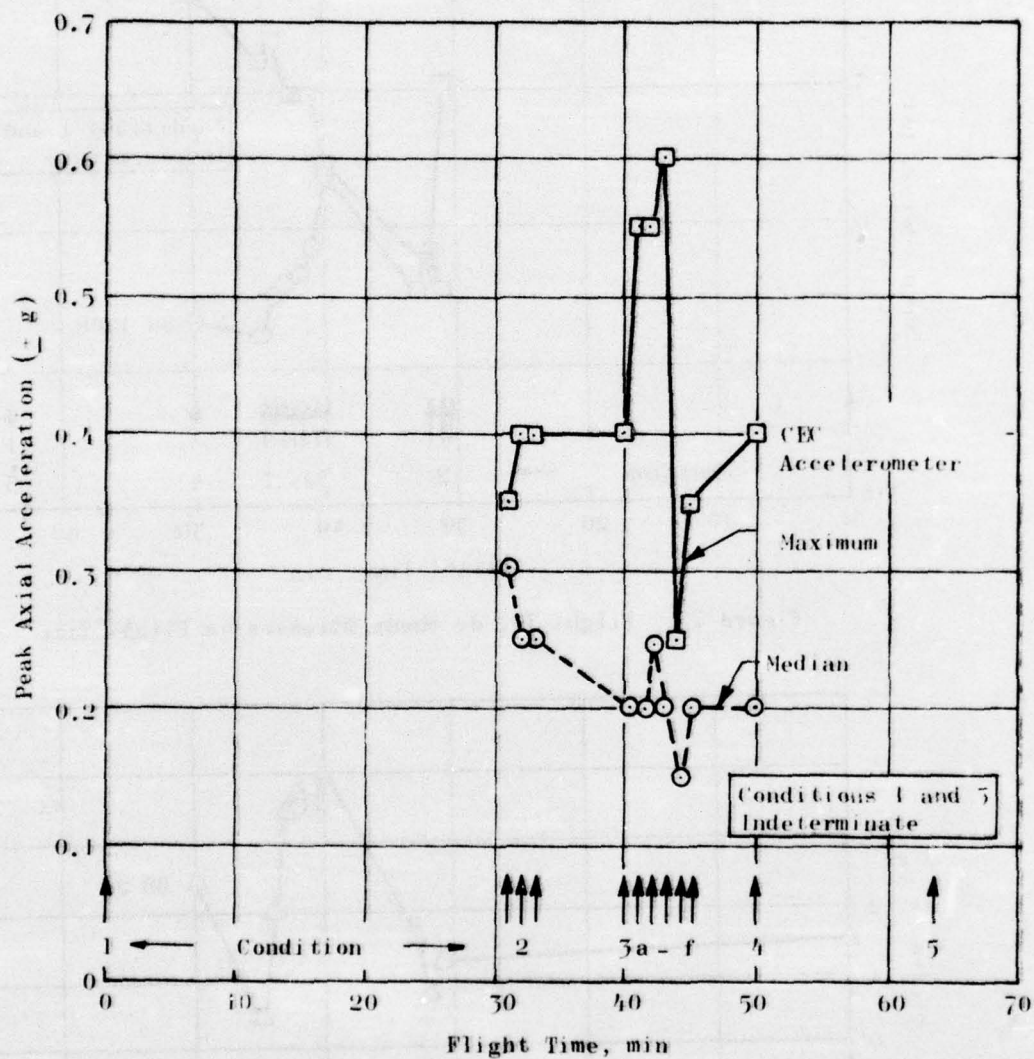
Figure 77. Flight 11, Peak Axial Accelerometer
Values vs Flight Time

Flight 11 shear gage data for some conditions were unreadable because of tape recorder problems so that a clear comparison with data from Flight 9 is difficult. Strain gage data from Flights 9 and 11 (Figures 65 and 76) are similar, with Flight 11 strains being slightly higher.

Axial accelerometer data for Flights 9 and 11 (Figures 67 and 77) show that the Mach 2 portion of Flight 11 was slightly rougher than that of Flight 9 although similar low g levels were observed (0.6 and 0.45 g, respectively). Accelerometer data for Flight 11, were not obtained because of problems with the tape recorder.

FLIGHTS 12 AND 13 - 24 AND 25 SEPTEMBER 1973

No data were measured during Flights 12 and 13.

FLIGHT 14 - 18 JULY 1974

Conditions for Flight 14 are given in Table 12 where it will be noted that they are similar to those of Flights 9 and 11. However, a shorter cruise at 30,000 feet was flown and the Mach 2 dash was performed at 40,000 feet. The TFR phase was performed at Mach 0.95 at 500 feet above ground level.

TABLE 12. FLIGHT 14 CONDITIONS

Starting Time	Time Lapse, min	Altitude, ft	Mach No.	Flight Segment
01:45	0	2,300	0	I
26:15	24:30	30,000	0.8	IV
29:00	27:15	30,000	1.10	IV
35:31	33:46	40,000	2.02	III
39:31	37:46	40,000	2.02	III
62:40	60:55	2,800	0.95	V
98:40	96:55	2,300	0	I

103

Measured flight data are shown on Figures 78 through 81. The shorter soak time at 30,000 feet produced a CLI temperature of 25 F; while the supersonic dash at 40,000 feet produced only a 125 F maximum CLI temperature. In fact, the Mach 0.95 TFR flight developed equally high temperatures in this flight.

The lower temperatures produced correspondingly smaller thermal stresses (Figure 79 and 80) and thermal bore strains (Figure 81). A large amount of noise on the tape invalidated the dynamic data on this flight.

Although peak stress change values of 18 psi were obtained under aeroheat conditions during Mach 2 flight, these values were obtained for a short time only. The hoop strain at the bore increased by only 2% under aeroheat conditions.

FLIGHT 15 - 22 AUGUST 1974

Flight 15 had the objective of determining environmental loads during prolonged flight at 35,000 feet. After take-off, the FB-111 flew at 7000 feet at Mach 0.85 for 20 minutes. It then climbed to 35,000 feet and flew for 2 hours at Mach 0.7 before landing. These conditions are summarized in Table 13.

104

Figure 78.   Flight 14 Temperatures vs Time
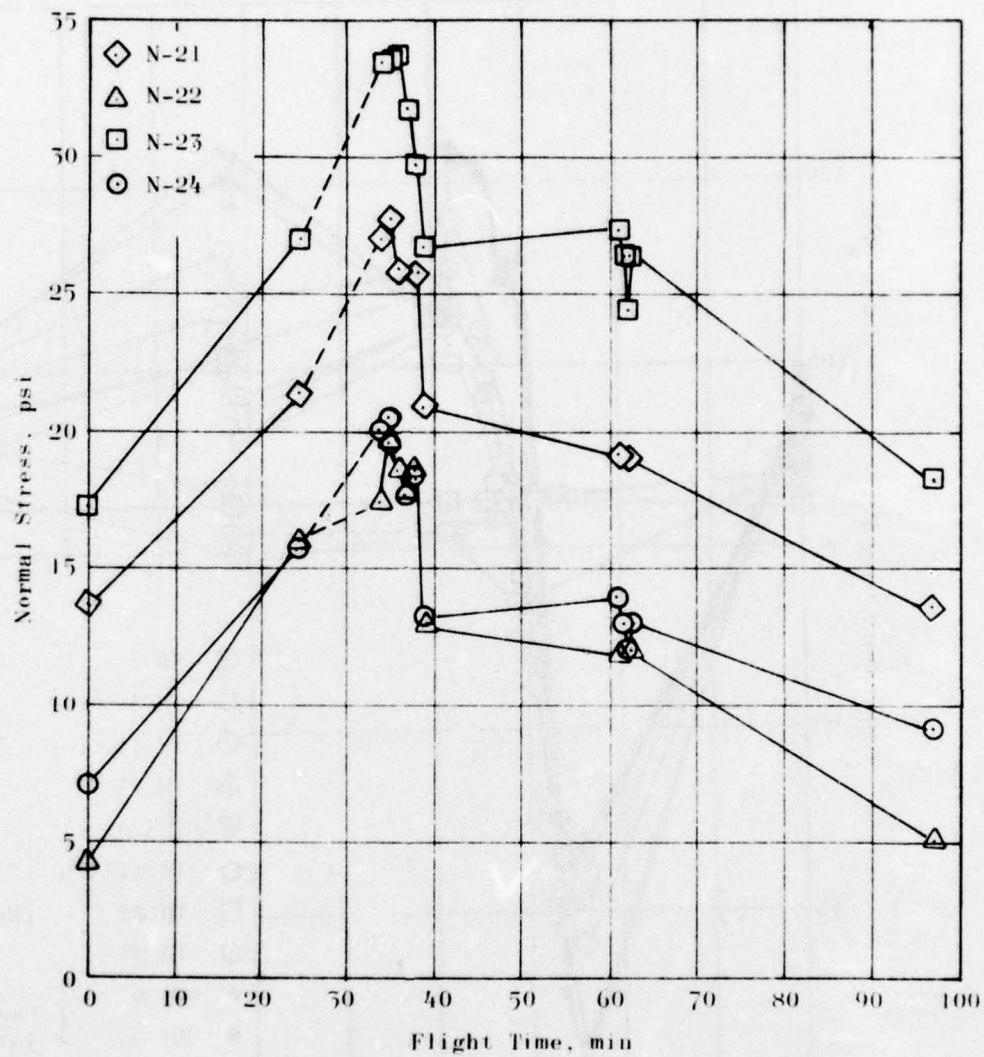
Figure 79. Normal Stresses for Flight 14
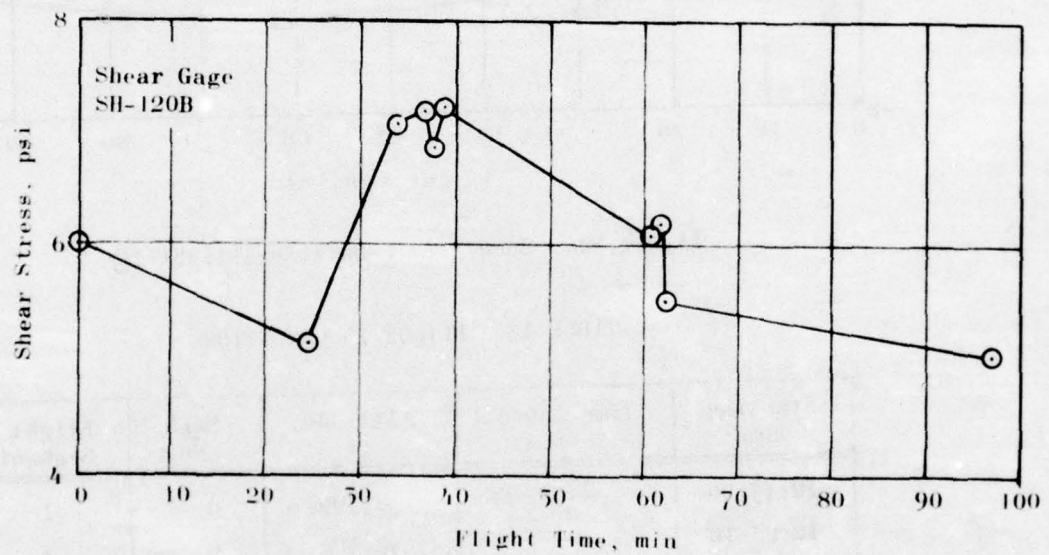
Figure 80.   Shear Stress Data for Flight 14 from SH-120B

107
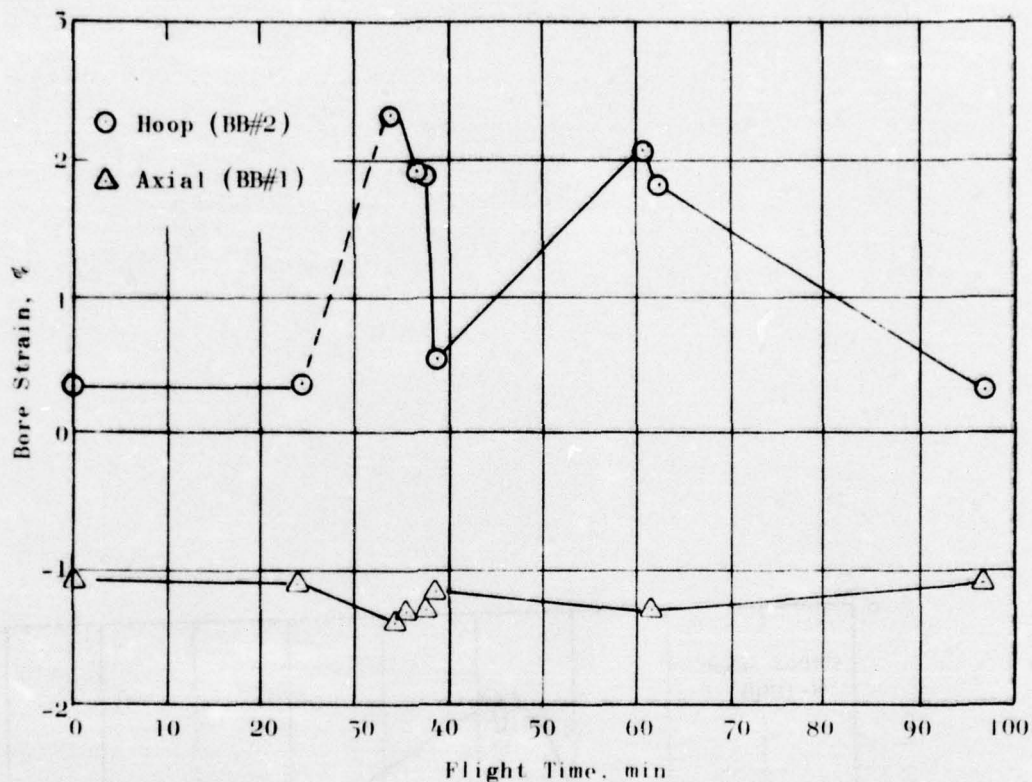
Figure 81.   Bore Strain Data for Flight 14

TABLE 13.   FLIGHT 15 CONDITIONS

Starting Time	Time Lapse, min	Altitude, ft	Mach No.	Flight Segment
12:15:00	0	2,300	0	I
12:25:10	0	2,300	0	I
12:32:45	7:35	7,000	0.85 ⎫	Special
12:52:30	27:20	7,000	0.85 ⎬	Test
12:59:30	34:20	35,000	0.70	IV
14:59:45	154:35	35,000	0.70	IV
15:20:10	175:00	2,300	0	I

108

Data from Flight 15 are given in Figures 82 through 85. The CLI thermistor data in Figure 82 is suspect. It appears that the thermistor output signals equalled the amplifier input maximum at about 60 minutes into the flight so that the real maximum CLI temperatures were not measured. A lower limit of approximately -30 F, as in Flight 2, should probably have been measured. As expected, a prolonged flight at 35,000 feet produced the most significant thermal stresses and strains in the grain. A maximum dc thermal/pressure-change-induced stress change of 23 psi was measured at the end of the 2-hour flight. The bore hoop strain change reached a peak value of 4% at the end of the 2-hour flight.

FLIGHT 16 - 22 APRIL 1975

New bore thermistors and a pressure gage to measure atmospheric pressures were installed prior to Flight 16.

Oscillograph records from Flight 16 were played back through 625-Hertz filters to reduce the level of the high-frequency noise in the signal. Examination of the traces revealed a negligible dynamic signal. Only under TFR conditions was any measurable dynamic data recorded. These data consisted of small 300-Hertz oscillations, some low-frequency (18 to 20 Hertz) oscillations, and considerable 1100-Hertz noise.

Flight 16 was comprised of a Mach 0.9 cruise at 30,000 feet followed by a Mach 2 dash at 40,000 feet and a TFR flight at 500 feet above ground level. Flight conditions are summarized in Table 14.

Figure 86 shows temperatures measured during Flight 16. They are similar to those measured during earlier flights although the new thermistor calibration made the data more consistent. The CLI thermistors recorded a minimum temperature of 12 to 15 F and a maximum temperature of 117 F during the Mach 2 dash.
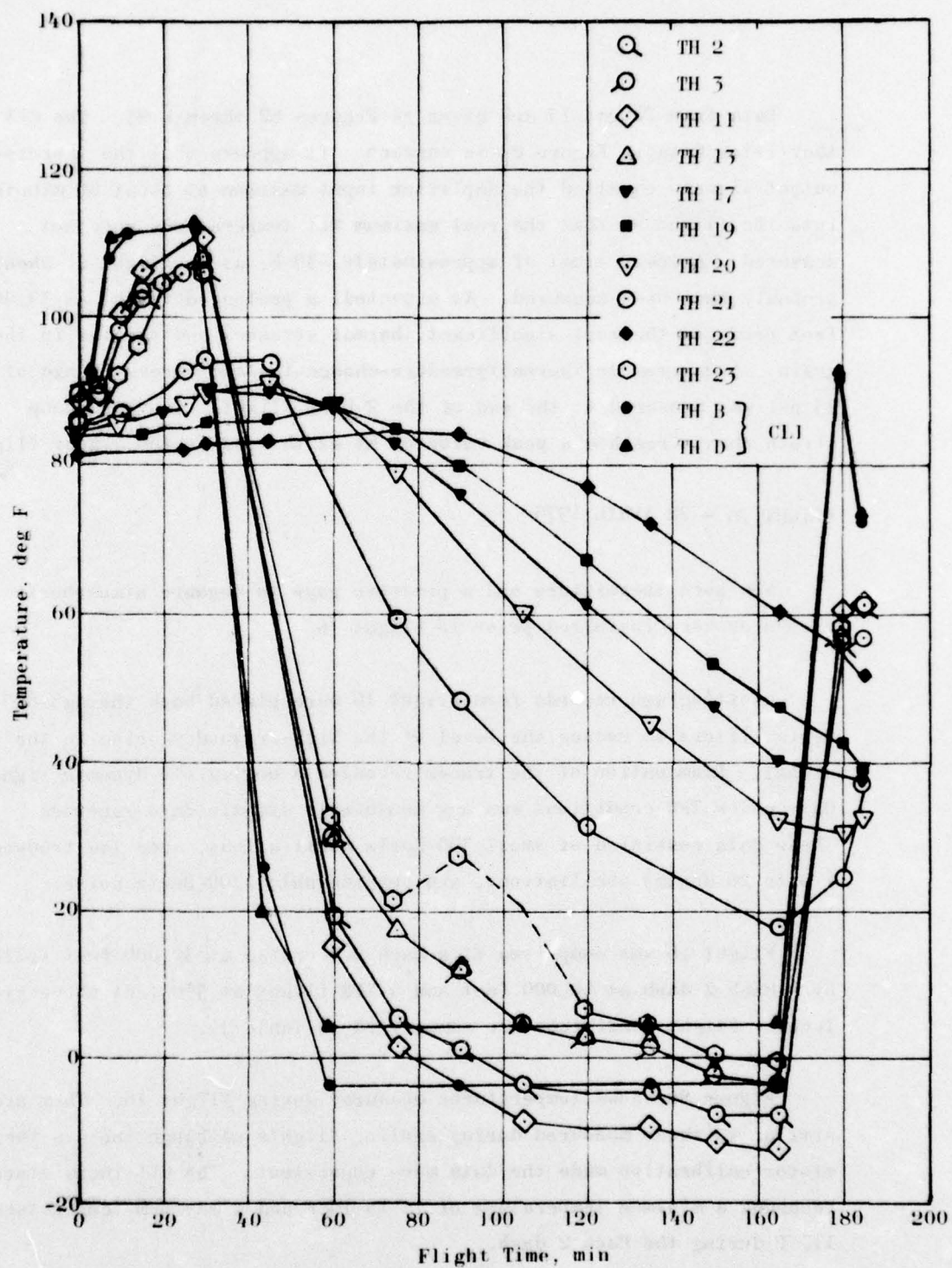
Figure 82. Flight 15 Temperature Data
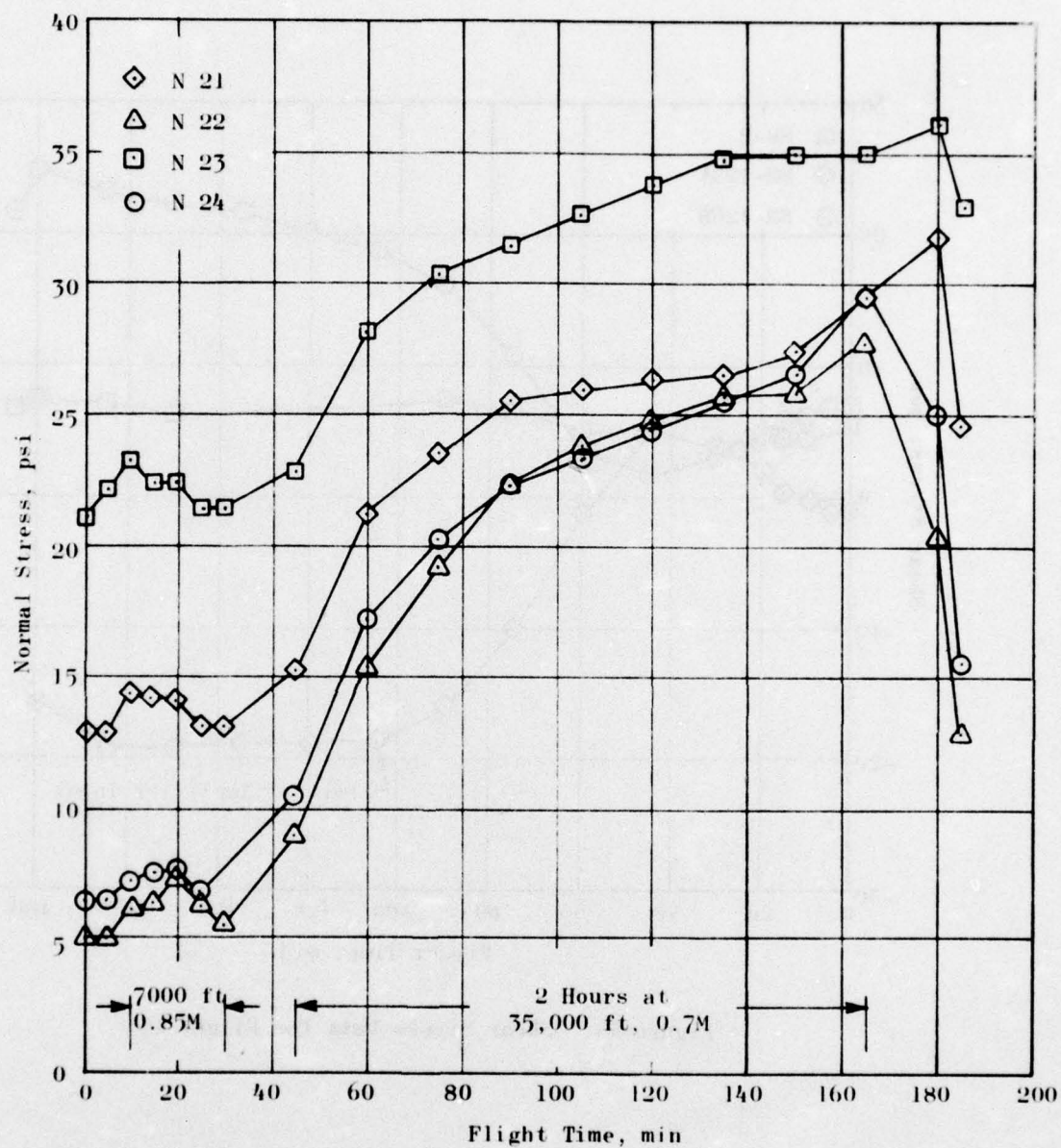
Figure 83.   Flight 15 dc Normal Stress Data

111
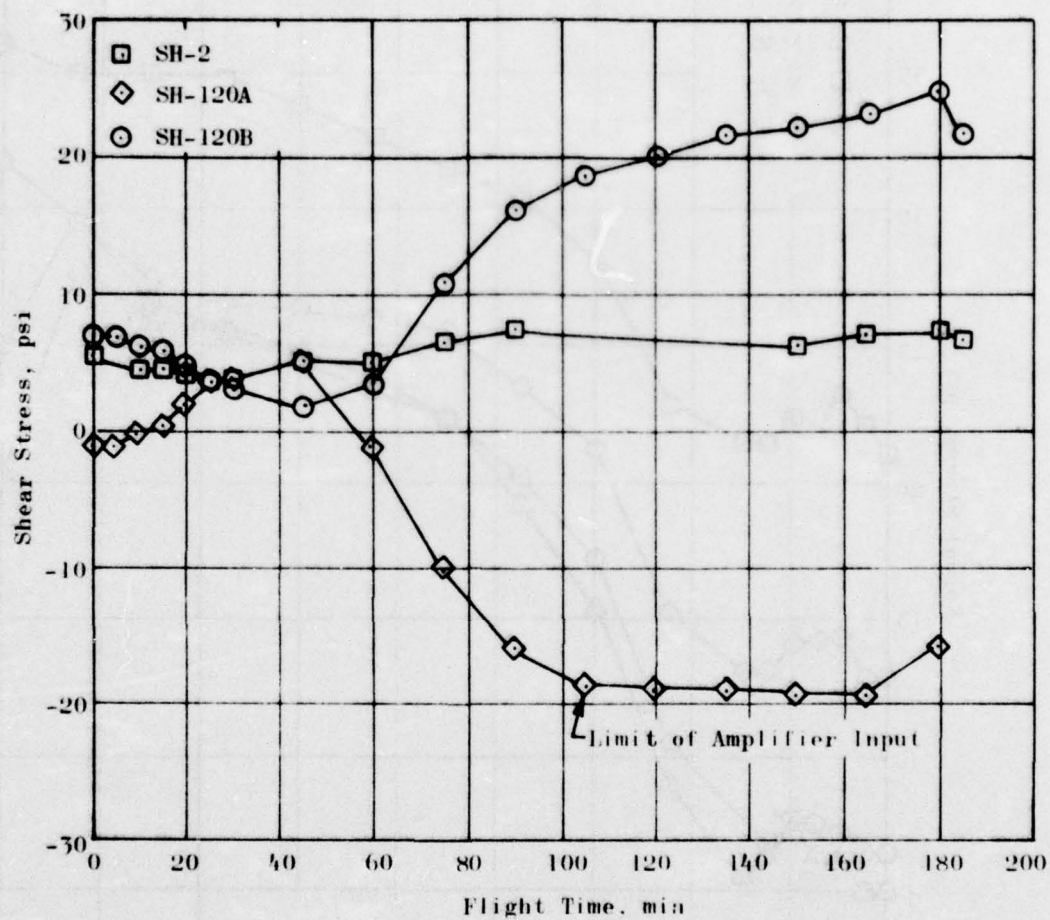
Figure 84. Shear Stress Data for Flight 15

112
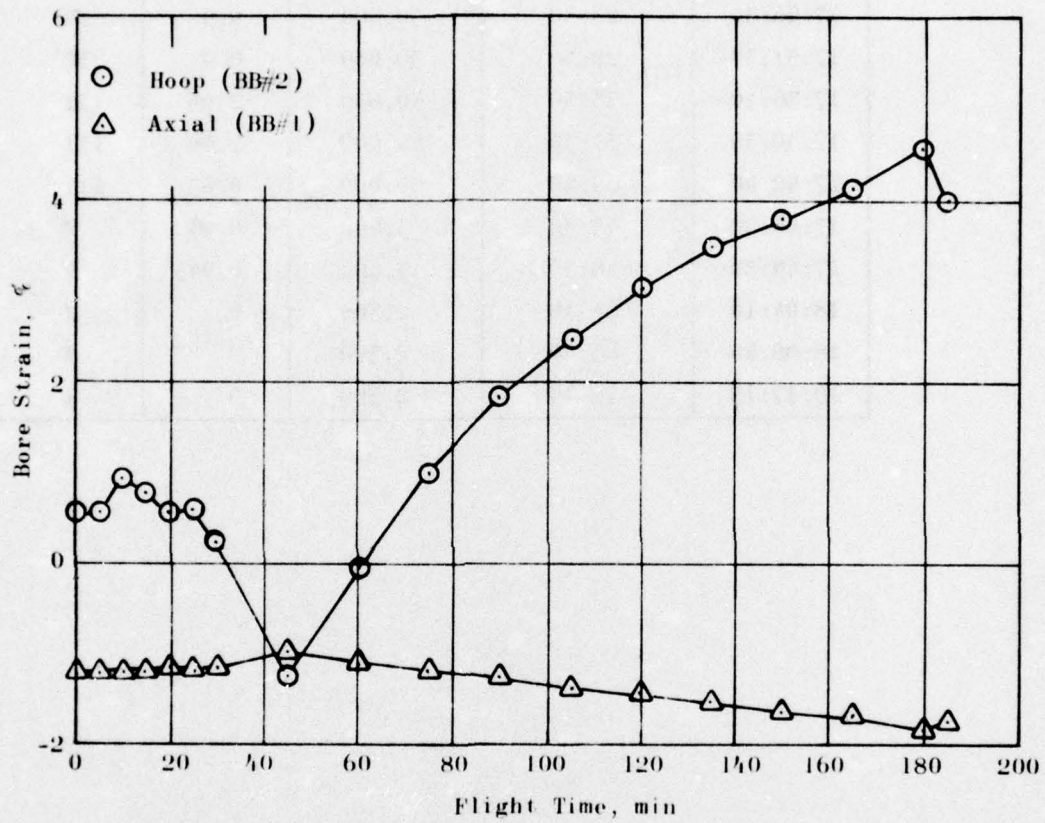
Figure 85. Bore Strain Data for Flight 15

TABLE 14. FLIGHT 16 CONDITIONS

Starting Time	Time Lapse, min	Altitude, ft	Mach No.	Flight Segment
17:02:30	0	2,300	0	I
17:03:00	0	2,300	0	I
17:16:30	13:30	30,000	0.9	IV
17:26:30	23:30	30,000	0.9	IV
17:31:30	28:30	30,000	0.9	IV
17:36:30	33:30	40,000	2.05	III
17:40:30	37:30	40,000	2.00	III
17:42:40	39:40	30,000	0.95	III
17:46:30	43:30	3,400	0.95	V
17:49:30	46:30	3,600	0.945	V
18:04:10	61:10	2,300	0	I
18:08:40	65:40	2,300	0	I
19:17:15	74:15	2,300	0	I

114
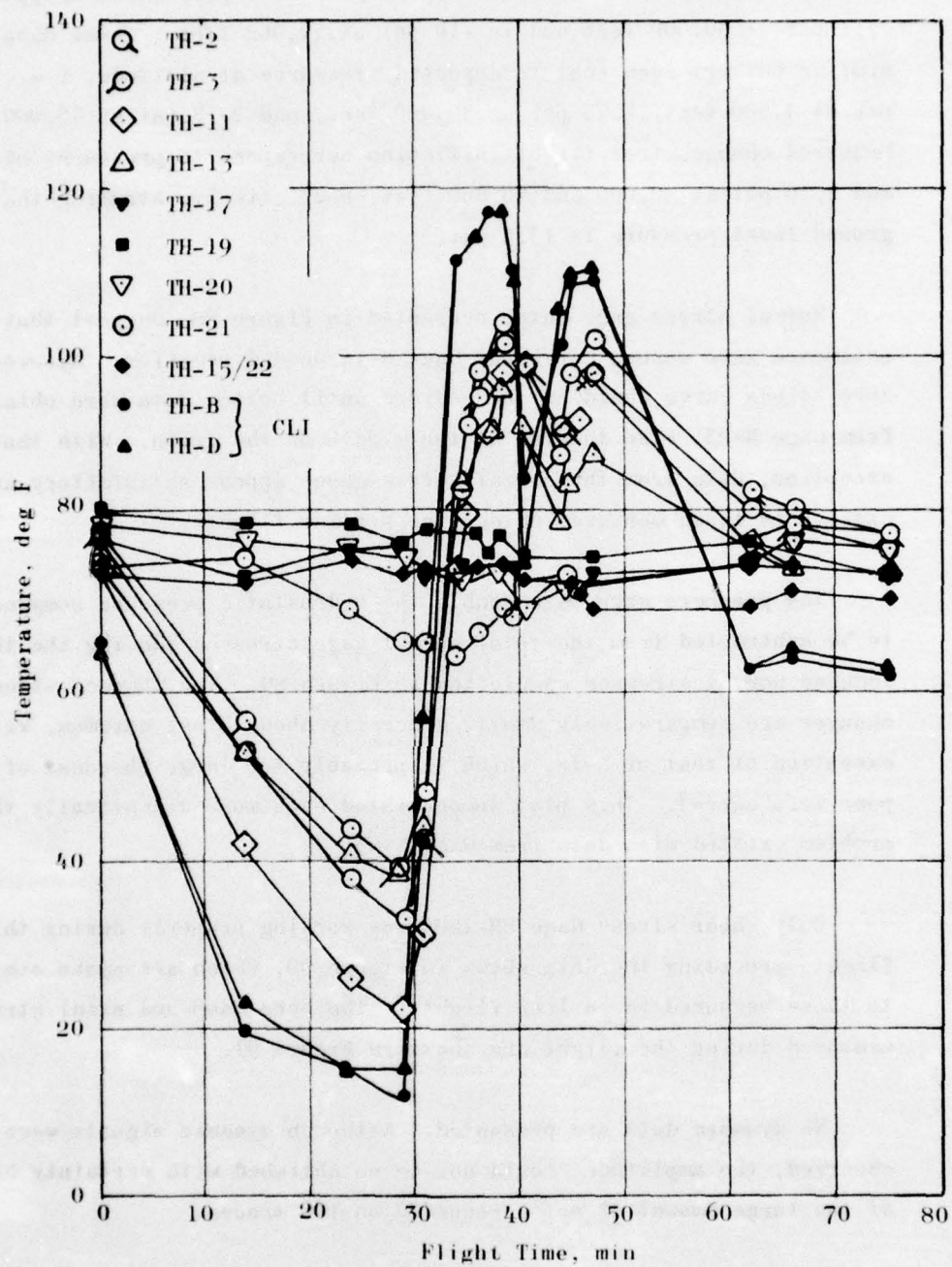
Figure 86. Flight 16, Temperature Data

Atmospheric pressure gage data are shown on Figure 87. At ground
level that gage initially showed a value of 1.06 psi, which dropped to
-7.1 psi at 30,000 feet and to -10 psi at 40,000 feet. These data are
similar but not identical to expected pressures at altitude, i.e., 13.17
psi at 3,500 feet, 4.45 psi at 30,000 feet, and 2.78 psi at 40,000 feet.
Measured changes from flight initiation correspond to pressures of 4.98
and 2.10 psi at 30,000 and 40,000 feet, respectively, assuming that
ground level pressure is 13.5 psi.

Normal stress gage data, presented in Figure 88, suggest that the
estimated zero stress curve for Gage N-18 needed revision. However, the
zero stress curve could not be revised until better data were obtained
from Gage N-23, also located at the middle of the grain. With that
exception, data from the normal stress gages appear satisfactory and
similar to those measured on earlier similar flights.

The pressure gage data enable the hydrostatic pressure component
to be subtracted from the total normal gage stresses leaving the thermally
induced normal stresses as plotted in Figure 89. The thermal stress
changes are comparatively small, generally about 5 psi maximum, with the
exception of that of N-18, which is probably too large (because of the
poor zero curve). This plot demonstrated even more dramatically that a
problem existed with data from Gage N-23.

Only shear stress Gage SH-120B was working properly during this
flight, providing the data shown in Figure 90, which are again similar
to those measured in earlier flights. The bore hoop and axial strain
measured during the flight are shown in Figure 91.

No dynamic data are presented. Although dynamic signals were
observed, the amplitudes could not be established with certainty because
of the large amount of noise recorded on the traces.

116
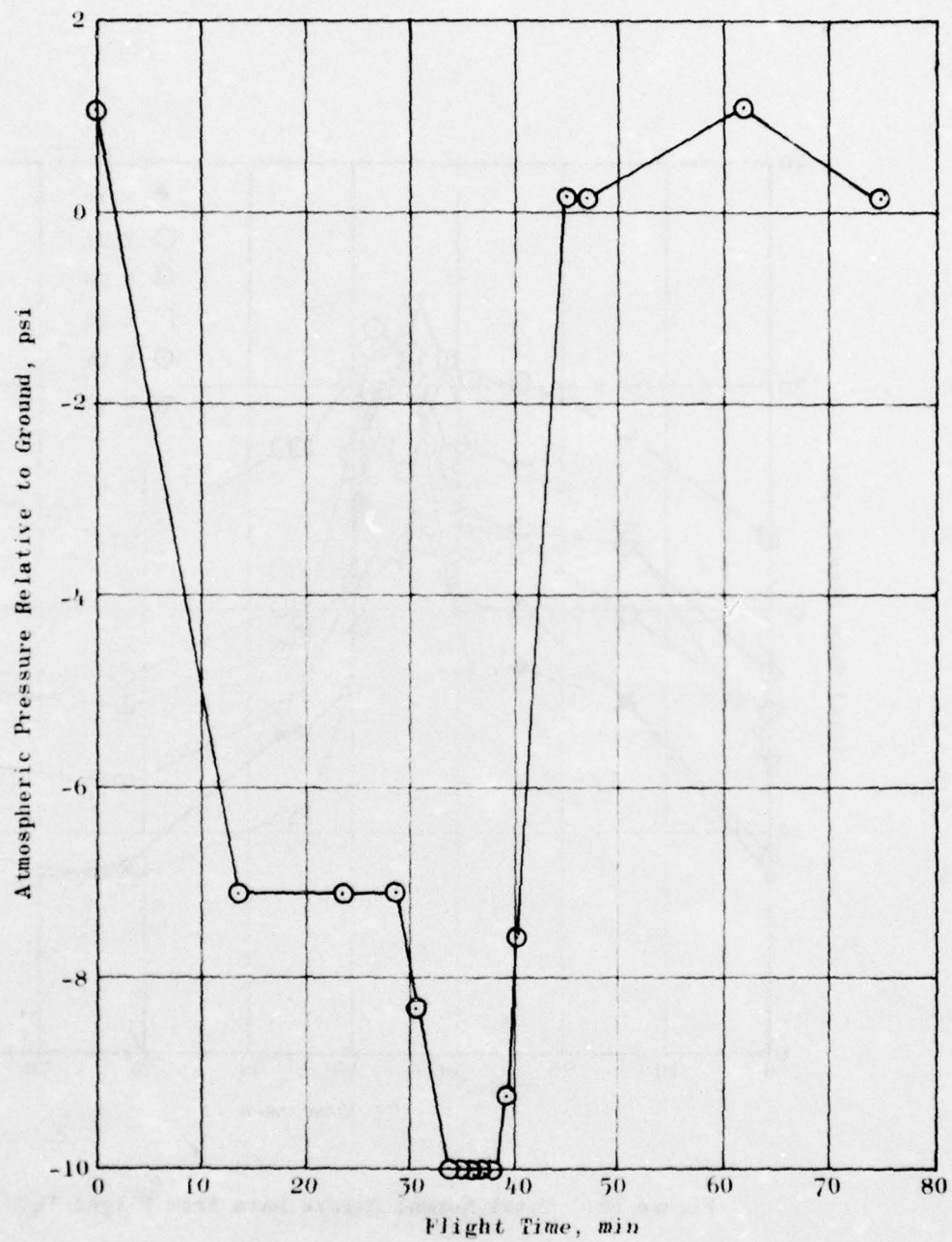
Figure 87.   Flight 16 Atmospheric Pressure Gage Data

117
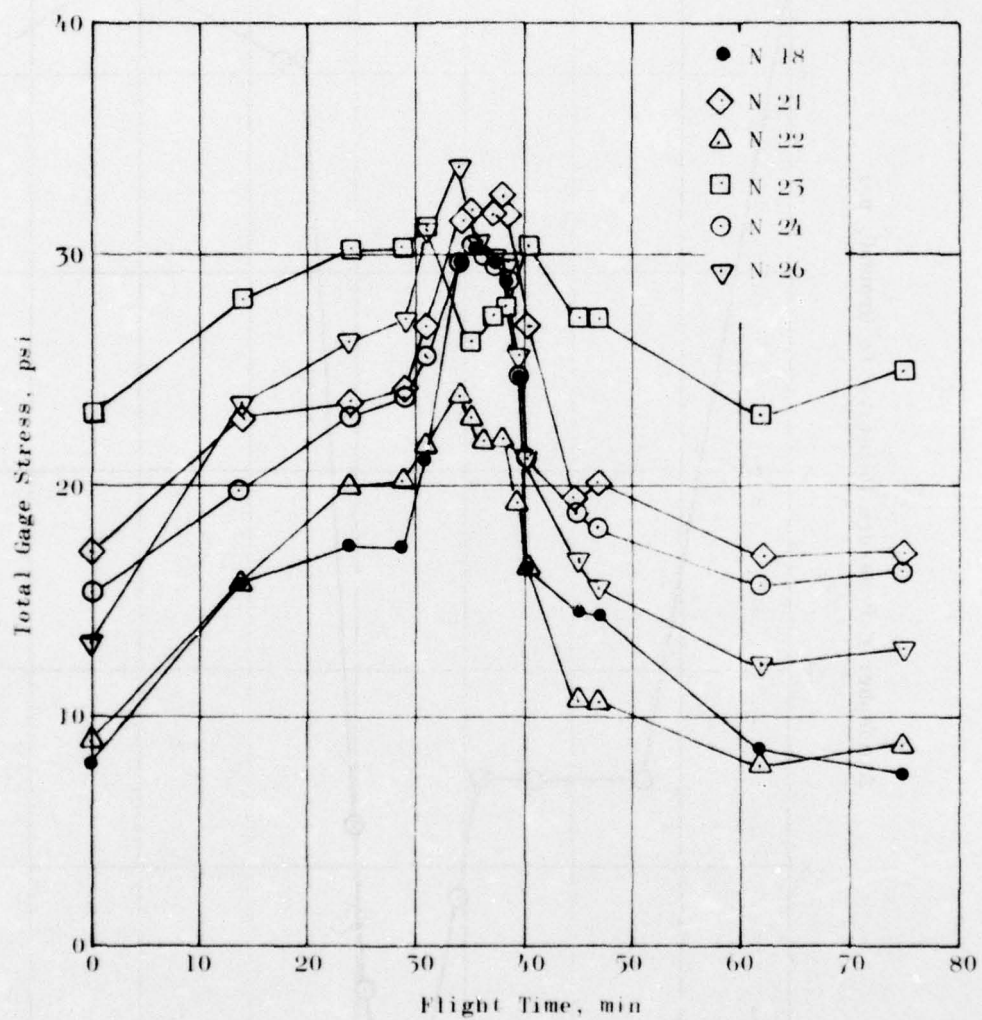
Figure 88. Total Normal Stress Data from Flight 16

118
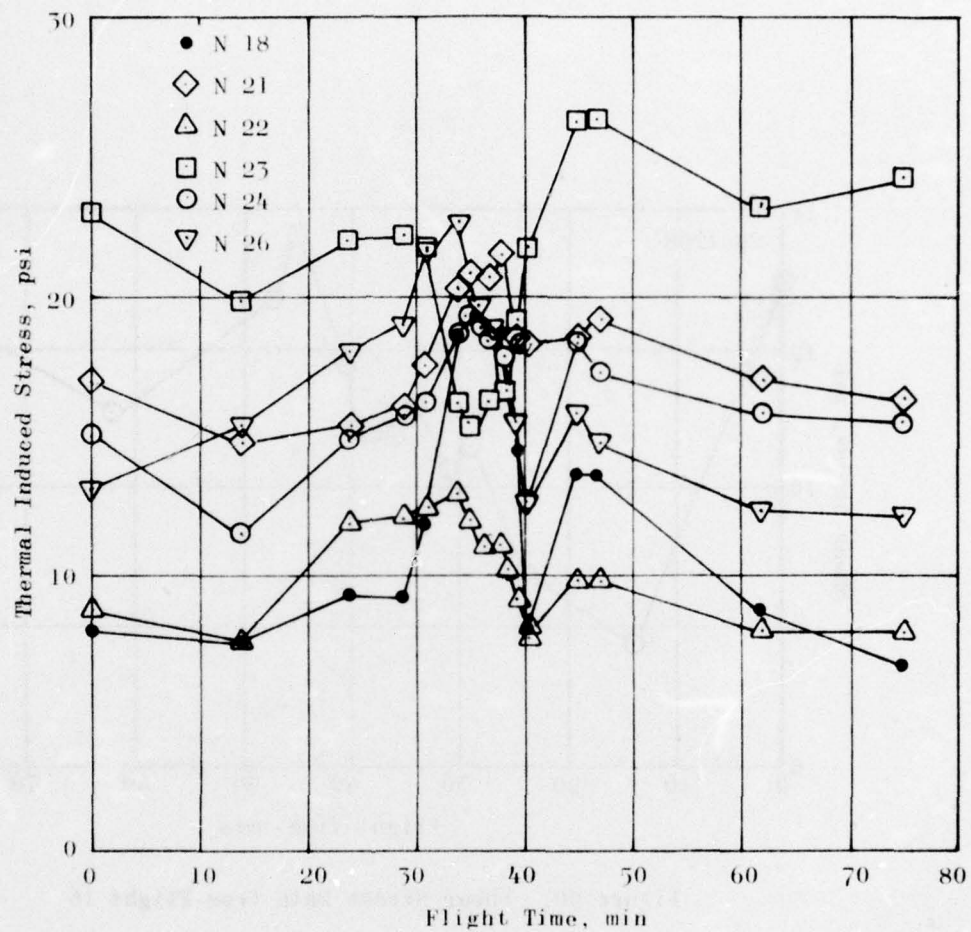
Figure 89. Thermal Stress Data from Flight 16
(Total dc Stress Minus Atmospheric
Pressures)

119
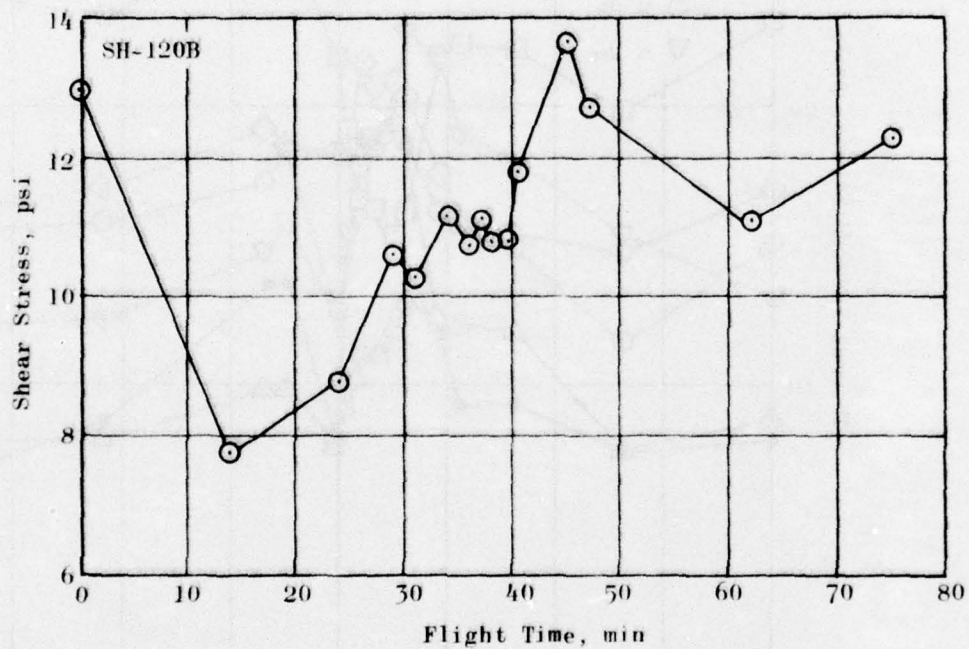
Figure 90. Shear Stress Data from Flight 16
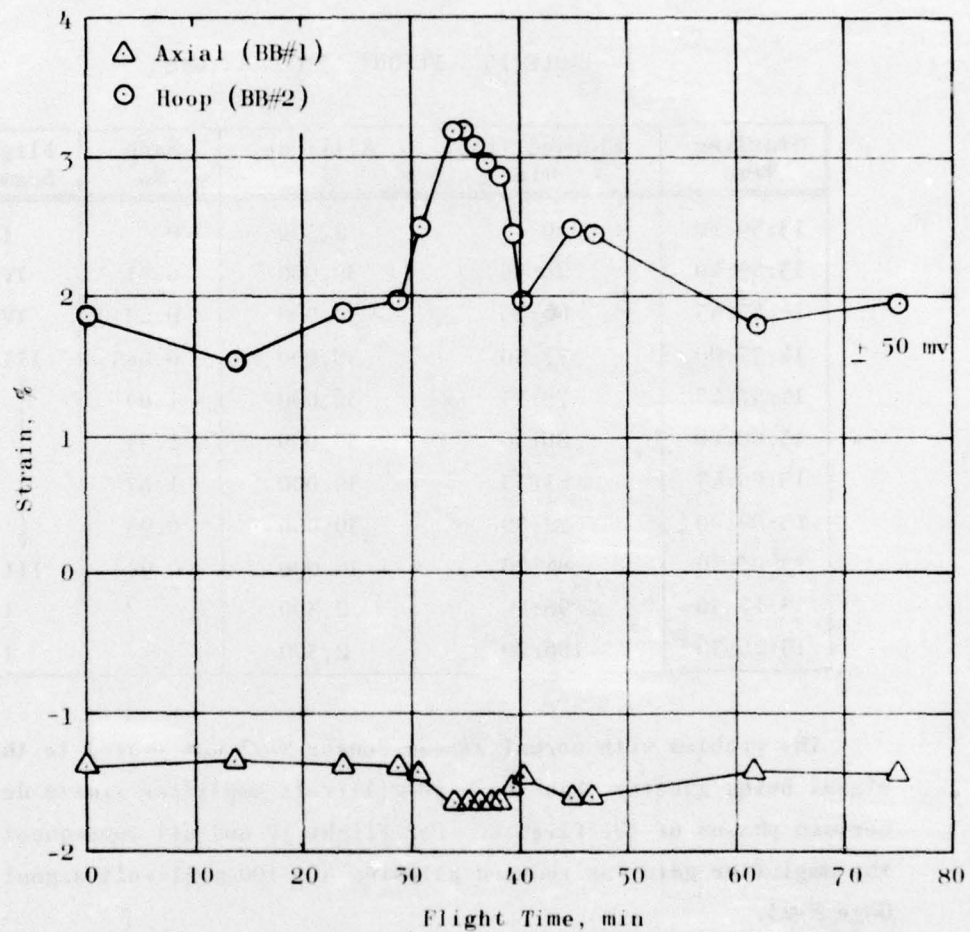
Figure 91. Bore Strain Data from Flight 16

FLIGHT 17 - 16 JULY 1975

Flight 17 was to have been similar to many earlier flights--take-off and subsonic cruise to 30,000 feet at Mach 0.7 followed by acceleration to Mach 2.0. The mission was, however, aborted at Mach 1.67 when fuel problems caused an aft center-of-gravity imbalance. Consequently, there were no high temperatures during the flight and no TFR mission. Flight conditions are summarized in Table 15.

TABLE 15. FLIGHT 17 CONDITIONS

Starting Time	Elapsed Time, min	Altitude, ft	Mach No.	Flight Segment
13:39:10	0	2,300	0	I
13:59:40	20:30	30,000	0.71	IV
14:45:45	66:35	30,000	0.69	IV
14:57:00	77:50	30,000	0.685	III
14:57:45	78:35	30,000	1.09	
15:00:00	80:50	30,000	1.55	
15:00:45	81:35	30,000	1.67	
15:02:00	82:50	30,000	0.95	
15:03:30	84:20	30,000	0.95	III
15:17:50	98:40	2,300		I
15:25:30	106:20	2,300		I

The problem with normal stress Sensor N-23 was traced to the output signal being greater than the $\pm$ 50-millivolt amplifier limits during certain phases of the flights. For Flight 17 and all subsequent flights the amplifier gain was reduced allowing a $\pm$ 100-millivolt signal from Gage N-23.

122

Figure 92 shows measured temperatures from Flight 17. The period of subsonic cruise (~ 78 minutes) produced low CLI temperatures on the order of 20 F. However, a maximum CLI temperature of only 112 F was measured before the flight was aborted at Mach 1.67. These temperature data were not as consistent as those usually obtained from the AFRPL computer reduction. However, it is unlikely that they introduced large errors into the measured stresses and strains.

Data obtained from the atmospheric pressure gage are presented in Figure 93; and, as in Flight 16, the pressure gage operated properly; but the measurement of -5.22 psi after 20.5 minutes of flight at 30,000 feet suggests that the grain was not vented to atmospheric pressure and that the internal pressure was reduced slowly by leakage. The minimum pressure at 30,000 feet was -10.28 psi, a change of -8.9 psi from ground level (compared with a change of -8.16 psi in Flight 16). The grain was vented to atmosphere in the remaining flights.

Total normal stress gage data are presented in Figure 94. (Gage N-23 provided good data during Flight 17, recording a high peak stress of 41 psi.) The thermal stress component of this total normal stress is shown in Figure 95.

Both SH-120A and SH-120B shear gages were working during Flight 17 and yielded the data shown in Figure 96. Both gages show similar trends in that the shear stress drops initially then climbs during the subsonic cruise and subsequent acceleration to Mach 1.67. These data are similar to those measured during Flight 16.

The bore hoop and axial strain data (Figure 97) are also similar to data measured during Flight 16.

123
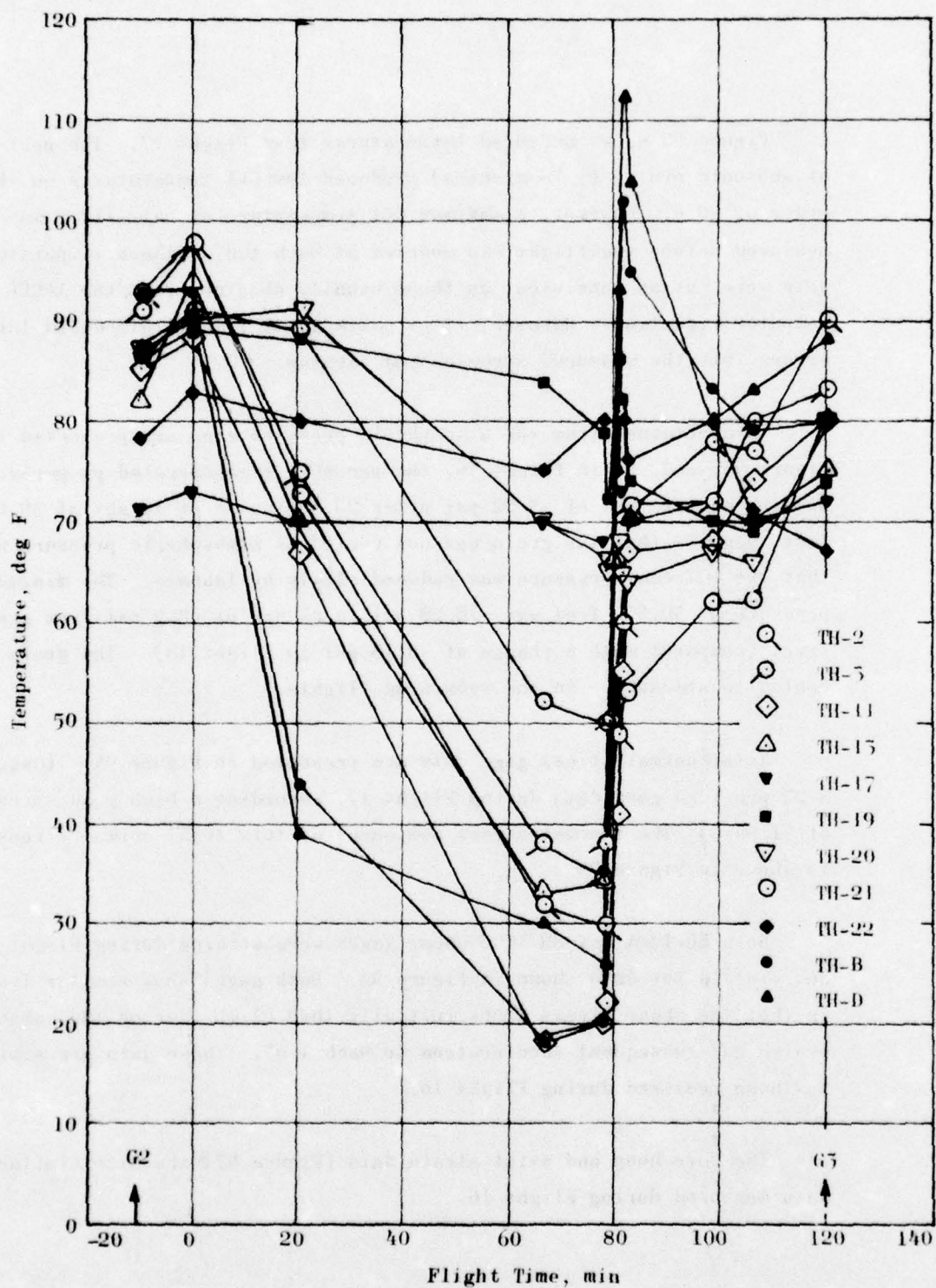
Figure 92. Flight 17 Temperatures vs Flight Time
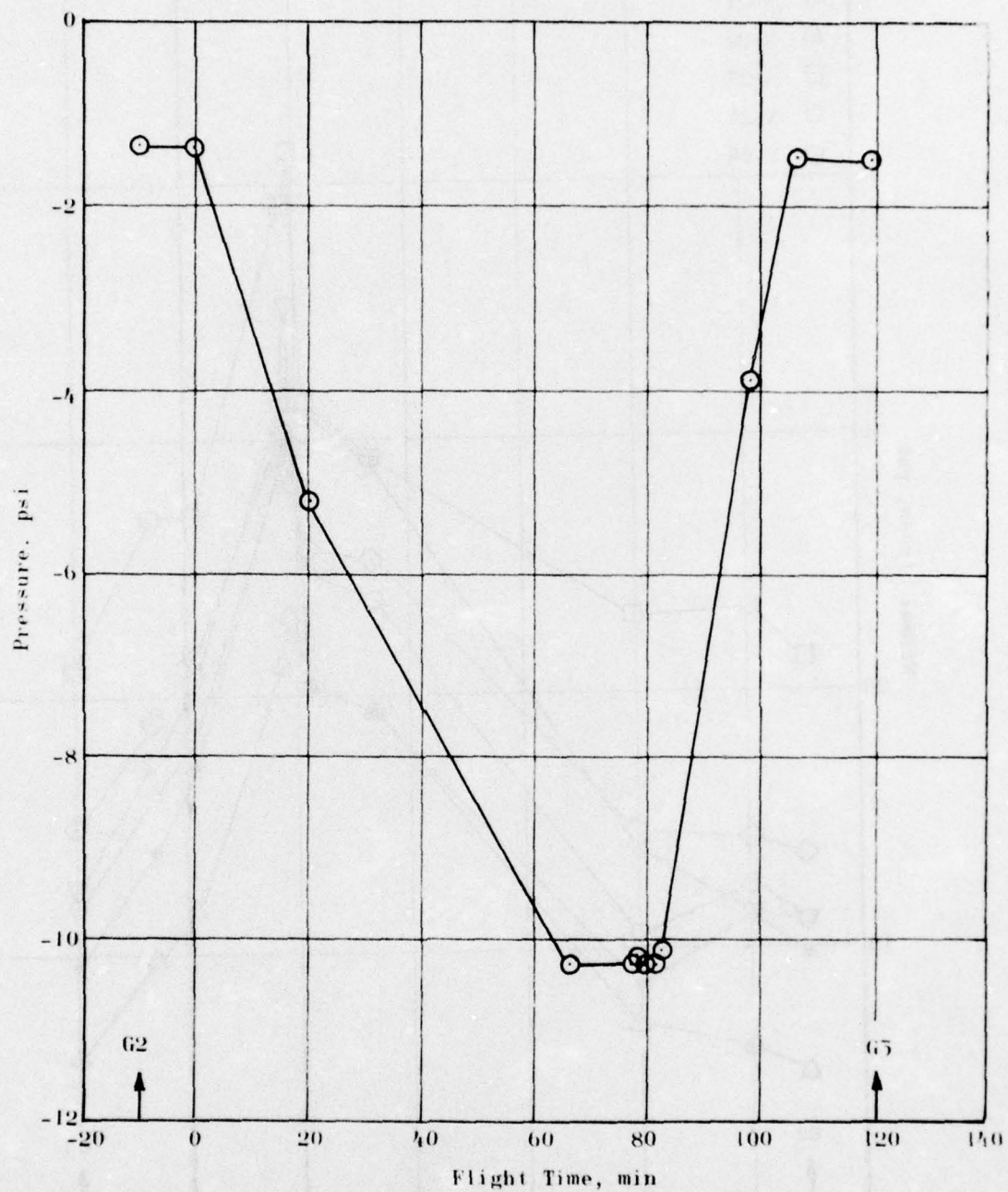
Figure 93.   Atmospheric Pressure Gage Data for Flight 17

125
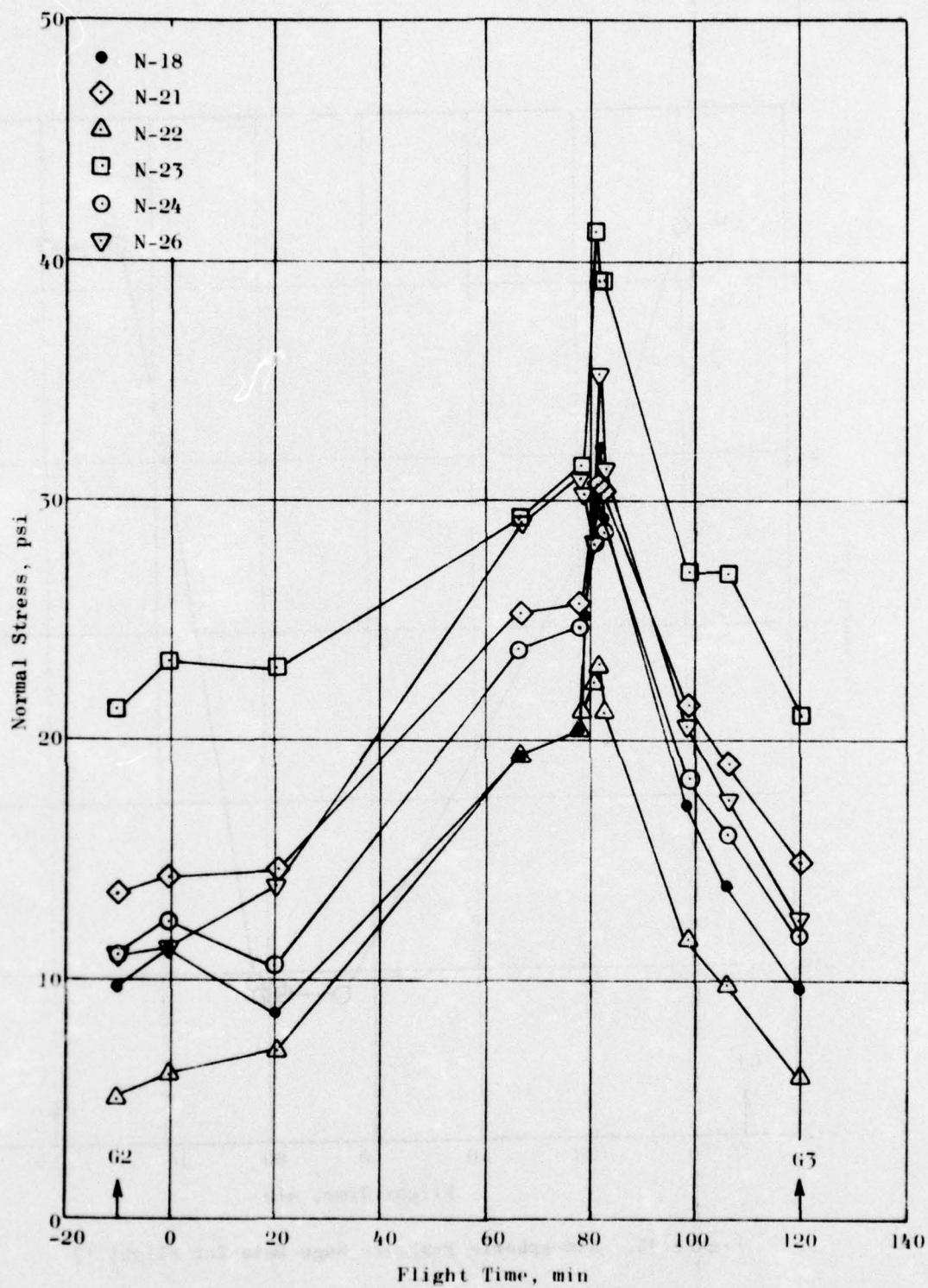
Figure 94. Total Normal Stresses for Flight 17

126
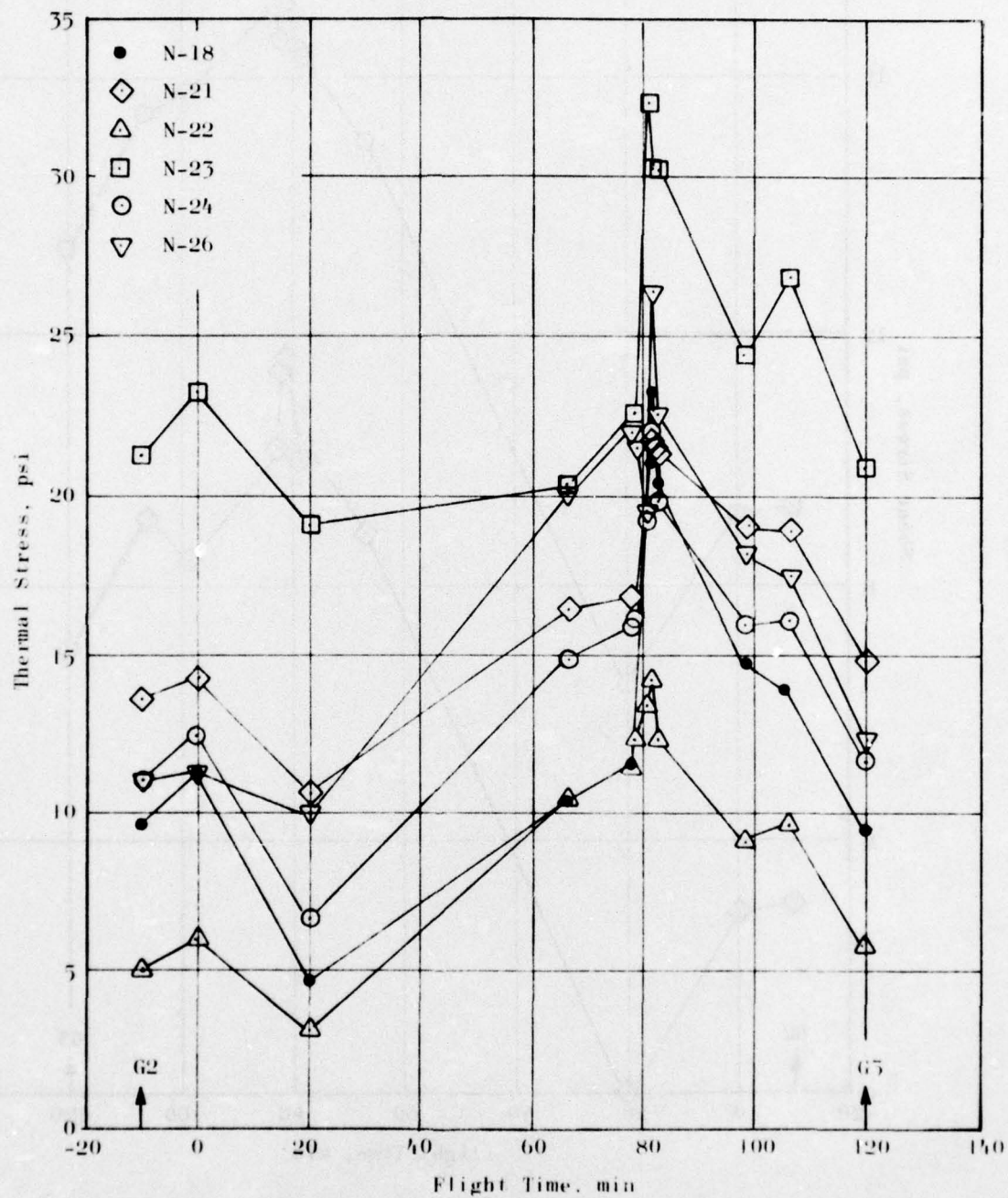
Figure 95.   Thermal Stresses for Flight 17

127
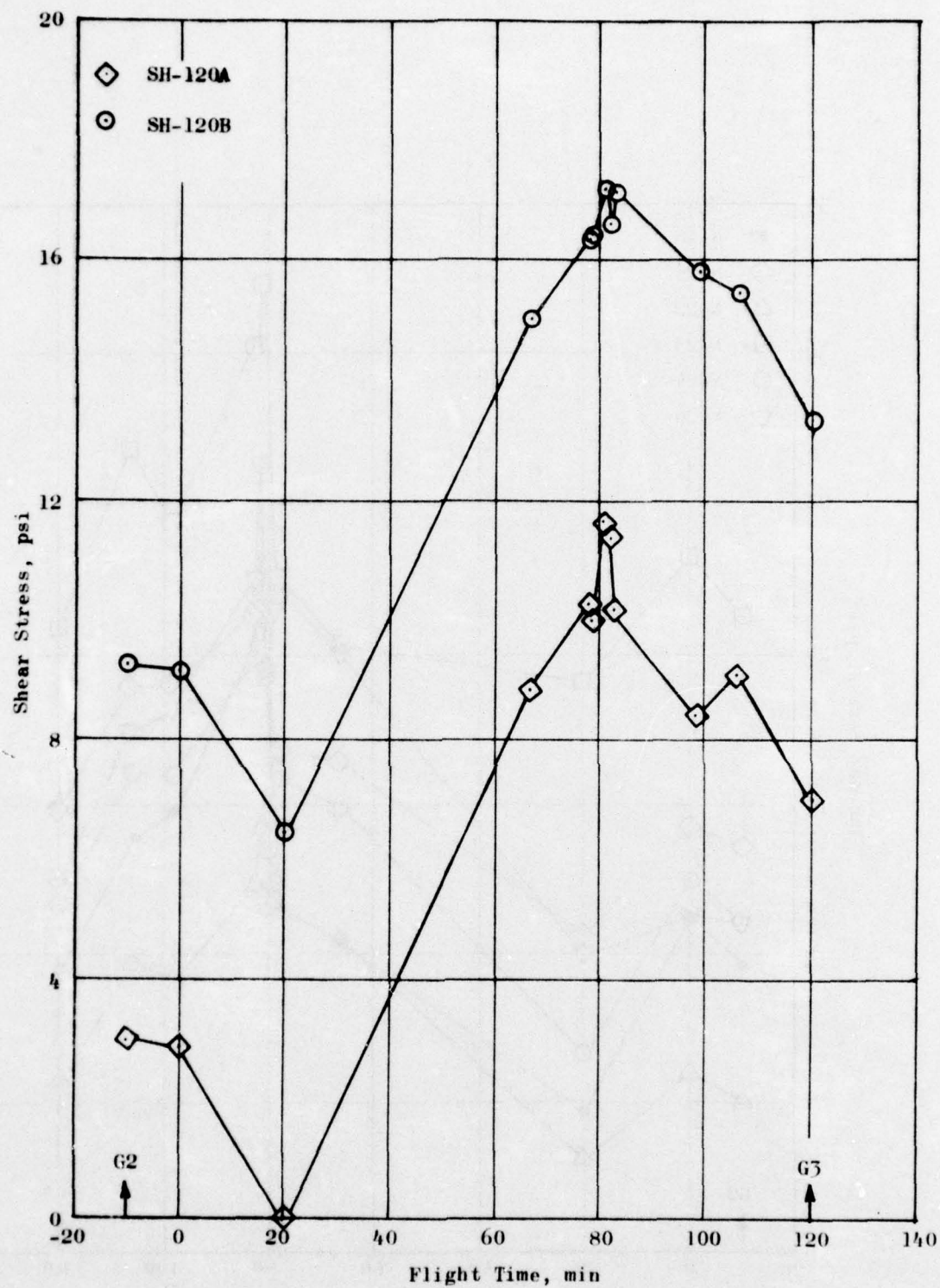
Figure 96. Shear Stresses vs Flight Time, Flight 17

128
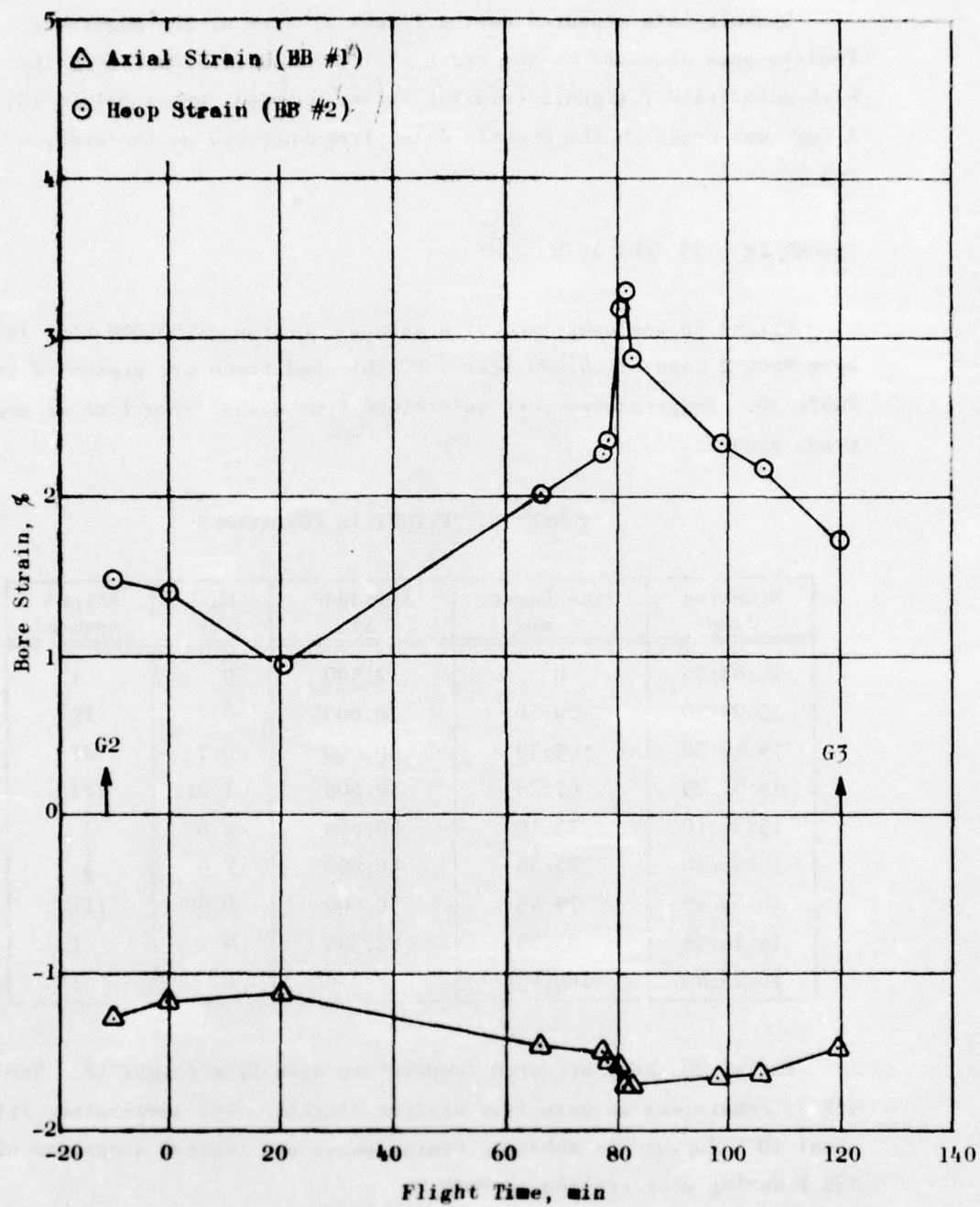
Figure 97. Bore Strains vs Flight Time, Flight 17

129

Dynamic data measured during Flight 17 were of *low magnitude*. Peak-to-peak stresses on the order of 1 psi were measured from the high-gain Track 7 signals (similar to those noted during Flight 16). A beat was noted in the dynamic data; frequency was on the order of 205 Hertz.

FLIGHT 18 – 25 JULY 1975

Flight 18 was comprised of a subsonic cruise at 30,000 feet followed by a Mach 2 dash at 40,000 feet. Flight conditions are presented in Table 16. Temperatures were determined from manual reduction of oscillograph records.

TABLE 16.   FLIGHT 18 CONDITIONS

Starting Time	Time Lapse, min	Altitude, ft	Mach No.	Flight Segment
14:43:00	0	2,300	0	I
15:03:30	20:30	30,000	0.7	IV
15:48:30	65:30	30,000	0.7	IV
15:50:25	67:25	30,000	1.01	III
15:56:10	73:10	40,000	2.0	
15:59:30	76:30	40,000	2.0	↓
16:02:45	79:45	30,000	0.90	III
16:16:55	93:55	2,300	0	I
16:25:45	102:45	2,300	0	I

Figure 98 shows measured temperature data from Flight 18. The data are as consistent as data from earlier flights. CLI temperature fell to about 10 F during the subsonic cruise phase and reached a maximum of 138 F during acceleration to Mach 2.

130
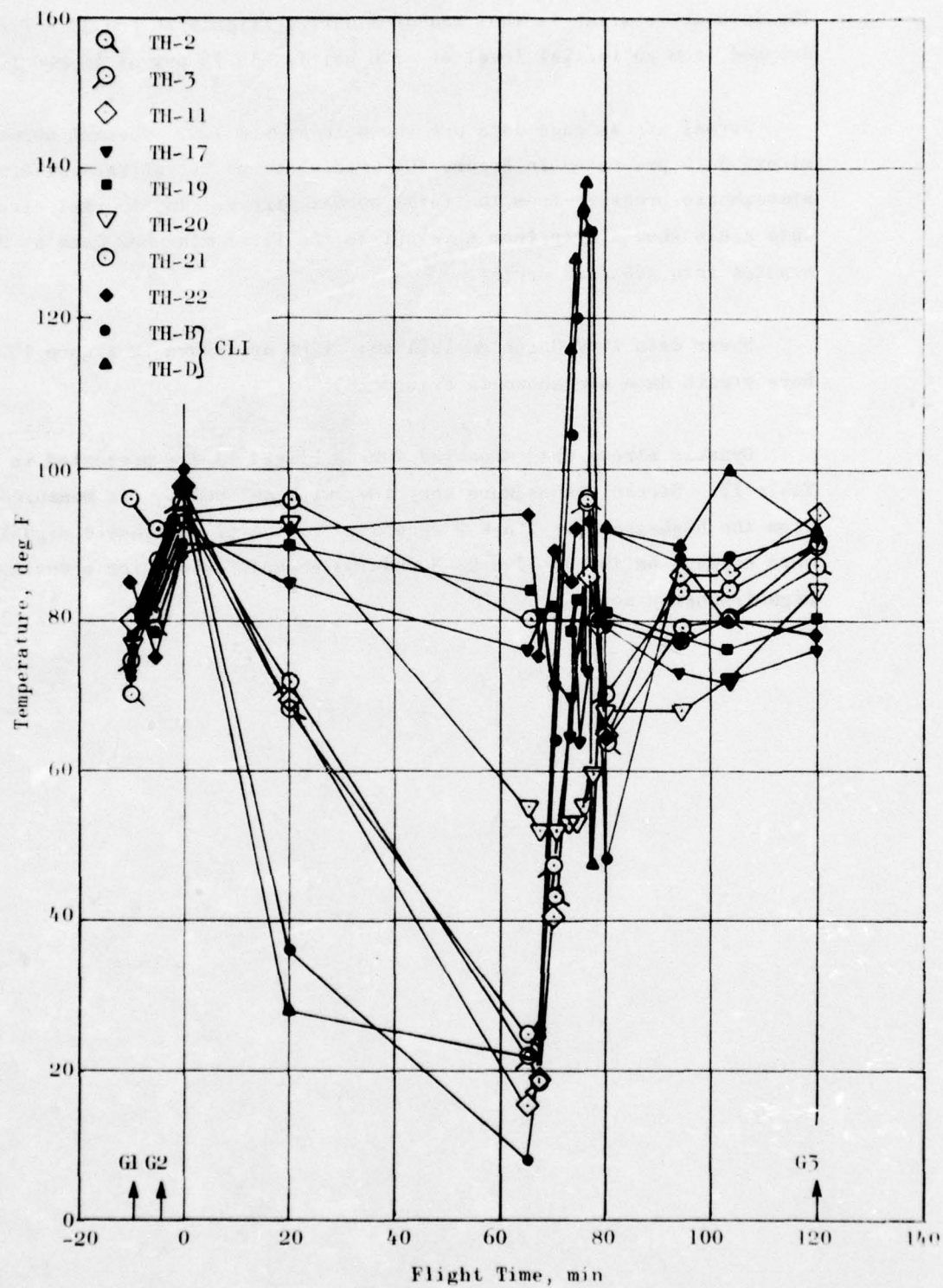
Figure 98. Flight 18 Temperatures

131

Figure 99 shows the atmospheric pressures recorded during the flight. The data are similar to that measured during Flights 16 and 17. Pressure dropped from an initial level of -1.6 psi to -10.75 psi at 40,000 feet.

Normal stress gage data are shown in Figure 100. Thermal normal stress data presented in Figure 101 were obtained by subtracting measured atmospheric pressure from the total normal stress. The thermal stress data again show a drop from take-off to the first measured data at 20.5 minutes into subsonic cruise.

Shear data from Gages SH-120A and -120B are shown in Figure 102. Bore strain data are shown in Figure 103.

Dynamic stress data measured during Flight 18 are presented in Table 17. Stress values were very low, with maximum levels measured from the high-grain ac Track 7 records. Virtually no dynamic signals were evident on the dc (Tracks 3 and 10) records except for occasional high-frequency noise.
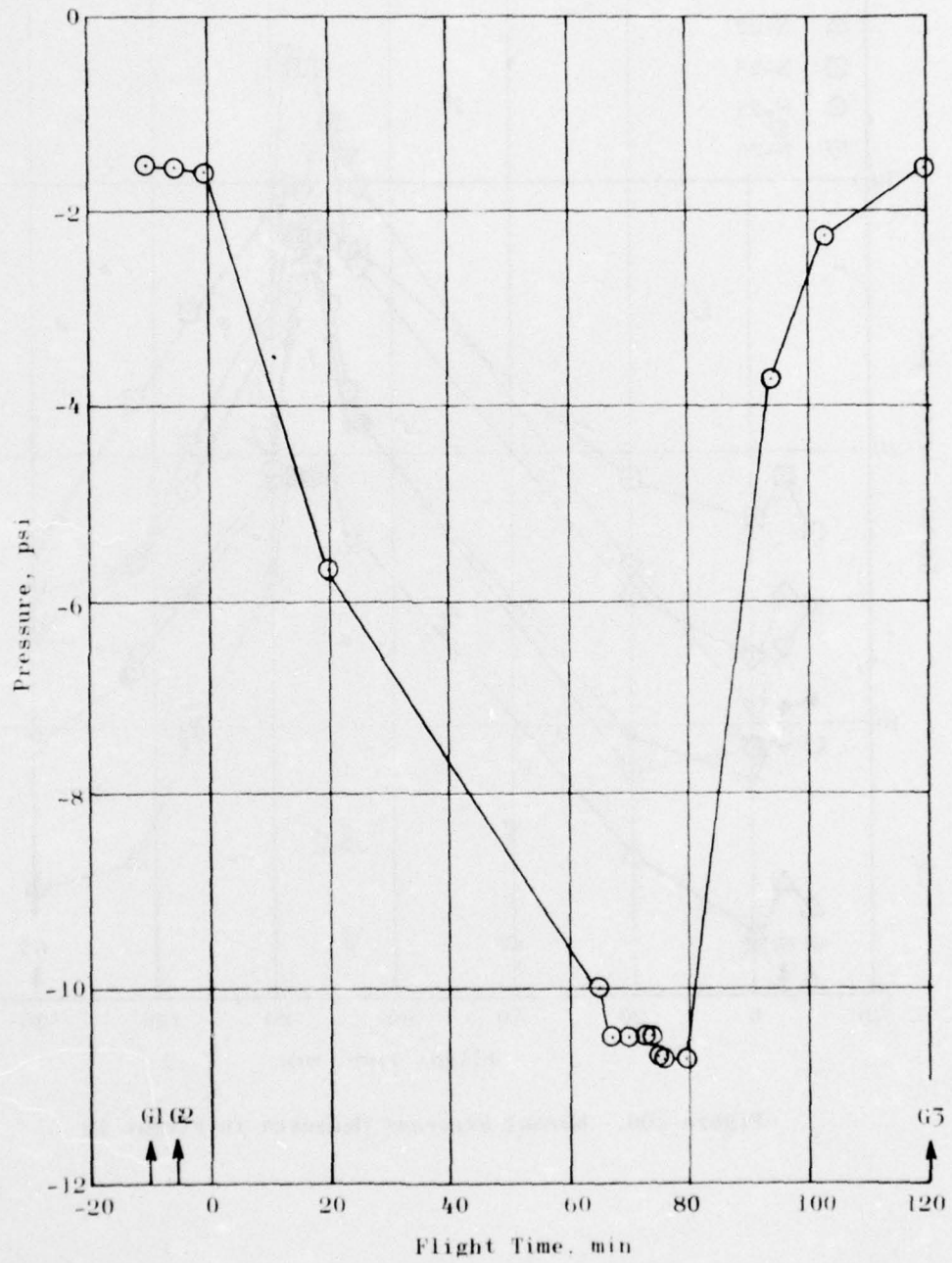
Figure 99. Atmospheric Pressure Data for Flight 18

133
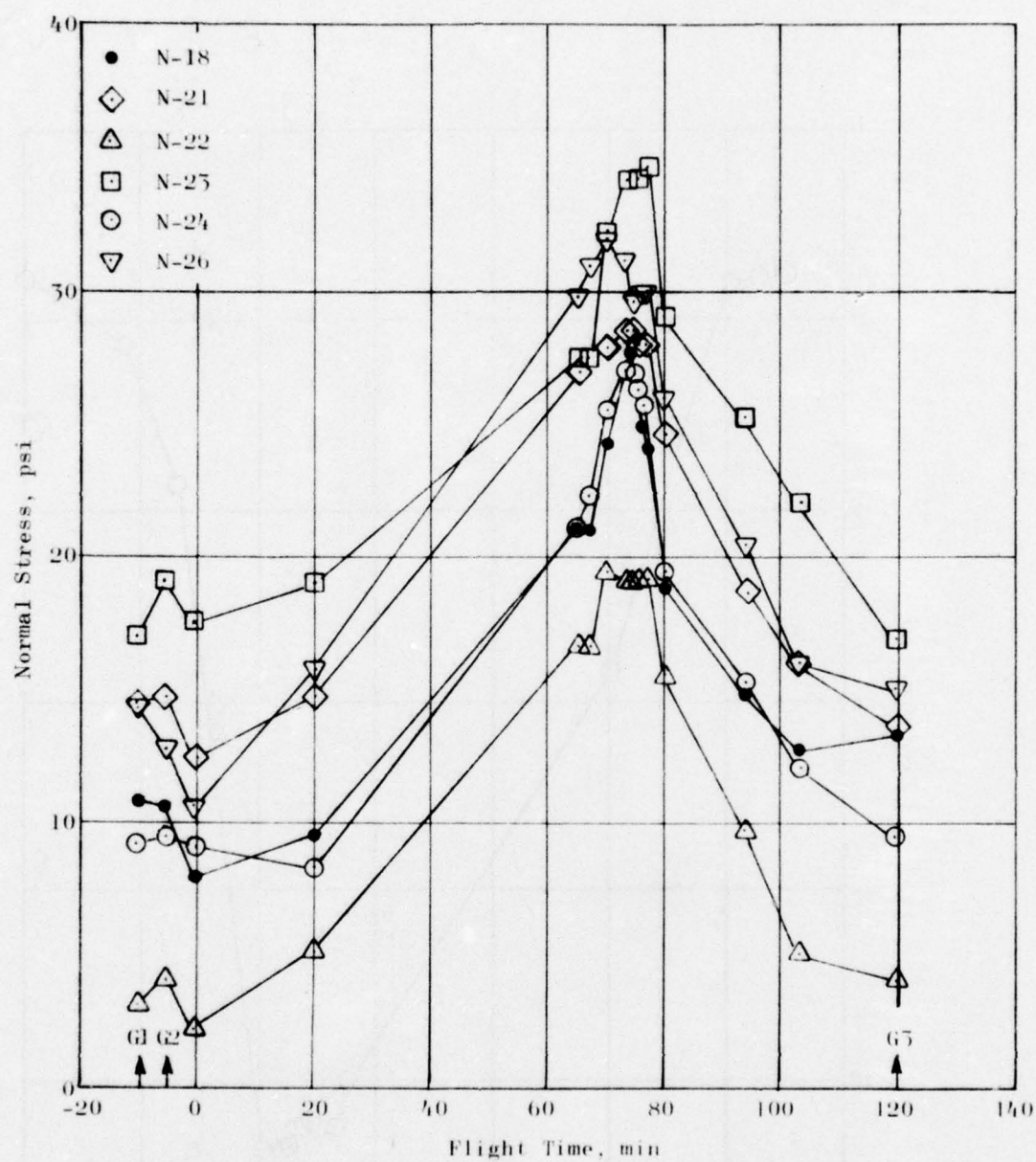
Figure 160. Normal Stresses Measured in Flight 18

134
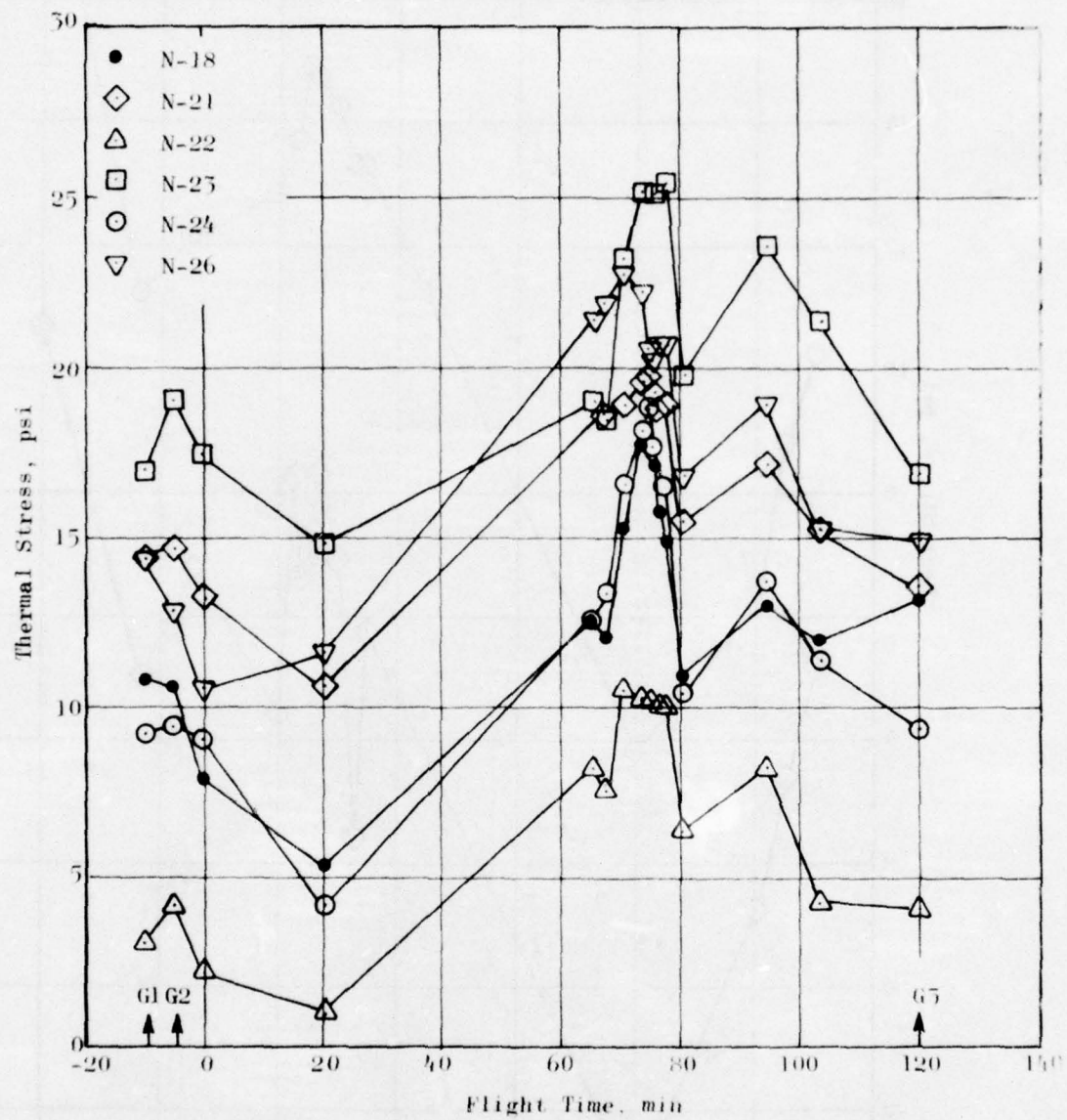
Figure 101. Measured Thermal Normal Stresses, Flight 18
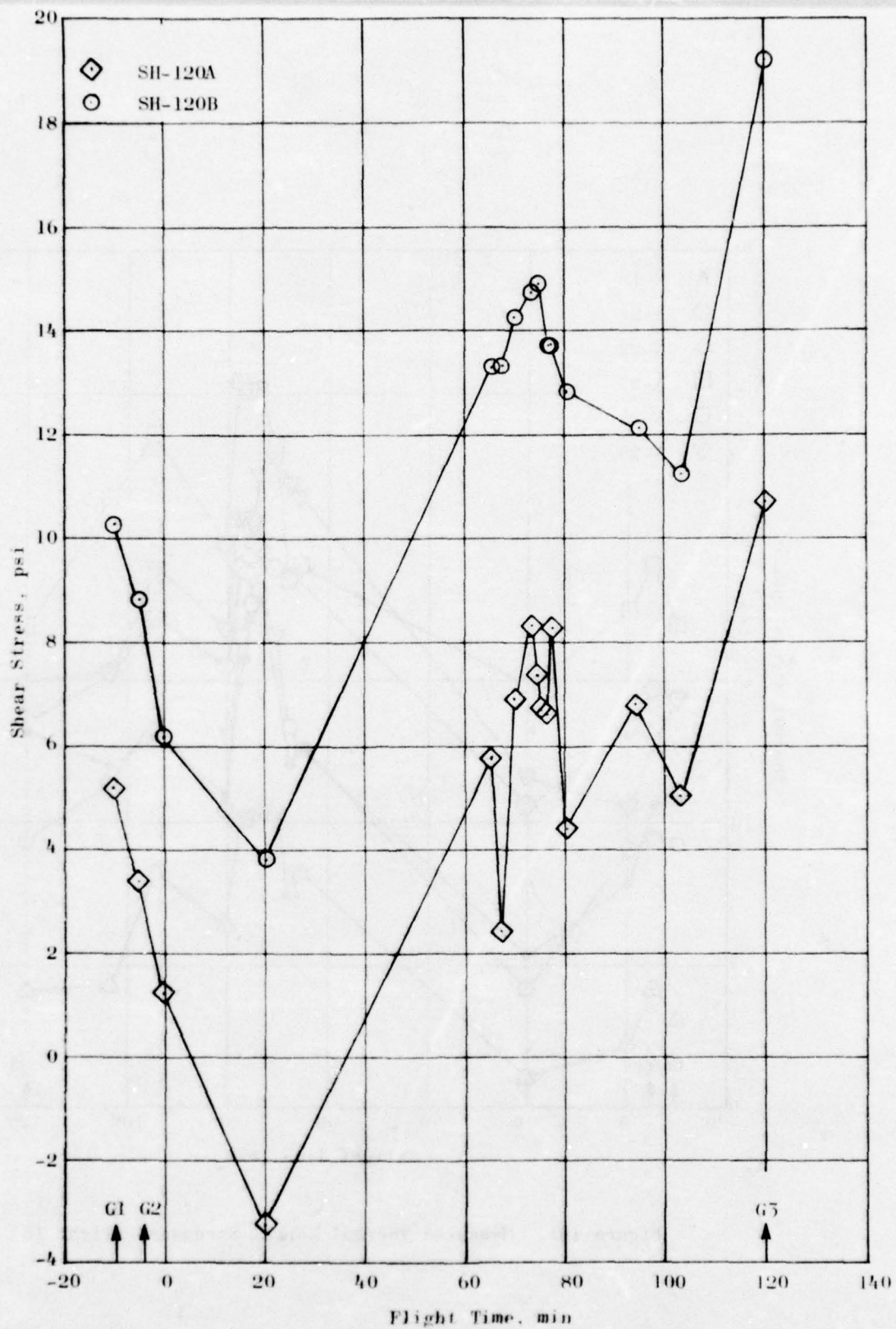
Figure 102. Shear Stresses Measured During Flight 18

136
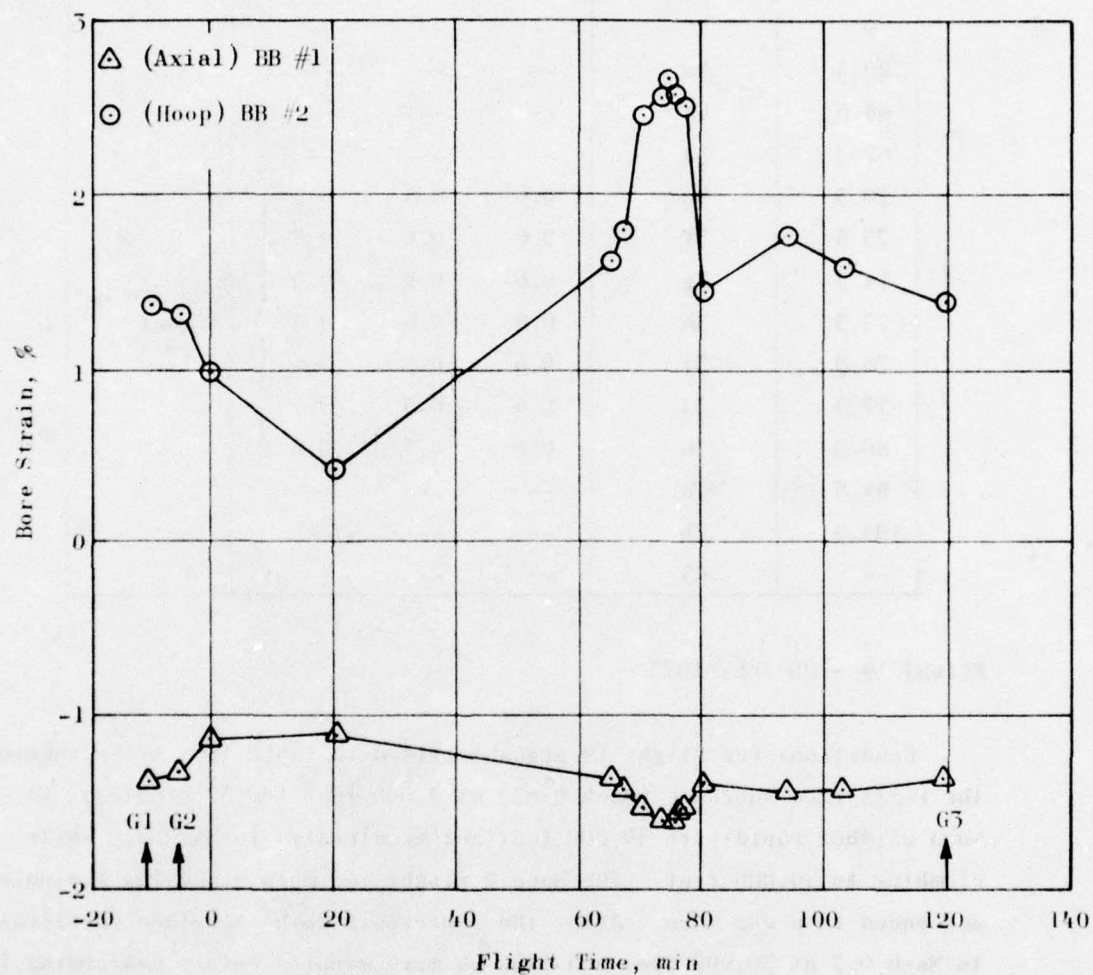
Figure 103. Bore Strains Measured During Flight 18

TABLE 17. DYNAMIC TEST DATA FROM FLIGHT 18

Time, min	Condition	N18	N23 psi (Pk-Pk)	N24	Comments
--	G1	--	--	--	
--	G2	--	--	--	
0	1	--	--	--	
20.5	4a	--	--	--	
65.5	4d	--	--	--	
67.5	3a	--	--	--	
70.5	3c	0.6	0.5	0.5	
73.5	3f	0.6	0.6	0.5	
74.5	3g	0.6	0.6	0.5	200/300 Hz
75.5	3h	0.6	0.6	0.5	Signal
76.5	3i	0.6	0.5	0.4	
77.5	3j	0.6	0.5	0.4	
80.5	3k	0.8	0.7	0.8	
94.5	7a	--	--	--	
103.5	7b	--	--	--	
--	G3	--	--	--	

FLIGHT 19 - 29 JULY 1975

Conditions for Flight 19 are summarized in Table 18. After take-off the F-111 flew subsonic (Mach 0.87) at 7,000 feet for 32 minutes. It then climbed rapidly to 30,000 feet and accelerated to Mach 2.0 while climbing to 40,000 feet. The Mach 2 flight was maintained for 4 minutes and ended in a 2-g turn. After the supersonic dash the plane decelerated to Mach 0.7 at 30,000 feet and flew 44 more minutes before descending for landing after a total flight time of approximately 124 minutes.

The modified flight plan gave rise to moderate aeroheating at the low-level subsonic condition and to fairly high case temperature

138

($\sim$ 150 F) during the supersonic dash. In addition, the 44-minute sub-
sonic flight at 30,000 feet produced low case temperatures of $\sim$ 10 F.

TABLE 18.   FLIGHT 19 CONDITIONS

Starting Time	Time Lapse, min	Altitude, ft	Mach No.	Flight Segment
13:24:00	0	2,300	0	I
13:45:20	21:20	7,000	0.865	Special Test
13:56:00	32:00	7,000	0.87	
14:05:00	41:00	30,000	1.0	III
14:11:00	47:00	40,000	2.0	III
14:15:30	51:30	40,000	2.0	III
14:15:45	51:45	41,000	1.8	III
14:20:00	56:00	30,000	0.7	IV
15:05:00	101:00	30,000	0.7	IV
15:28:20	124:20	2,300	--	I
15:36:45	132:45	2,300	--	I

Measured temperatures from Flight 19 are presented in Figure 104.
These data were obtained by manual analysis of oscillograph records of
the PAM data.   The atmospheric pressure data are presented in Figure 105.

Figure 106 shows combined thermal and altitude-induced normal
stresses measured during Flight 19.   Because the supersonic dash preceded
the subsonic cruise, the total stresses developed in the grain were lower
than those in previous flights.   This is even more apparent in Figure 107.
All gages showed comparatively small thermal stress changes during the
flight.

Figure 108 shows shear data from Gages SH-120A and -120B.   Bore
strain data are shown in Figure 109.   No dynamic stresses were obtained.
Maximum hoop strains on the order of 2% were developed during the
flight.

139
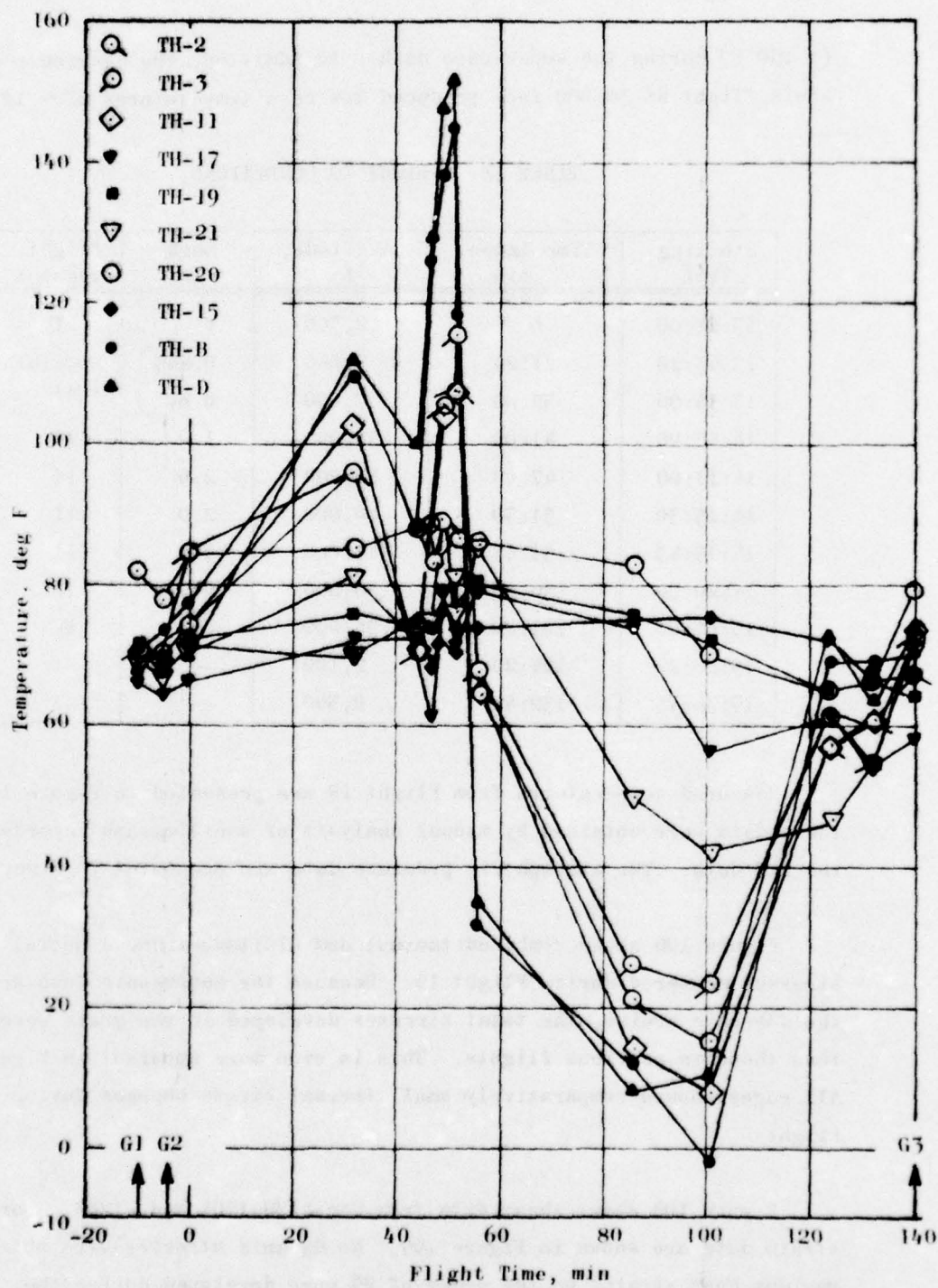
Figure 104. Flight 19 Temperatures

140
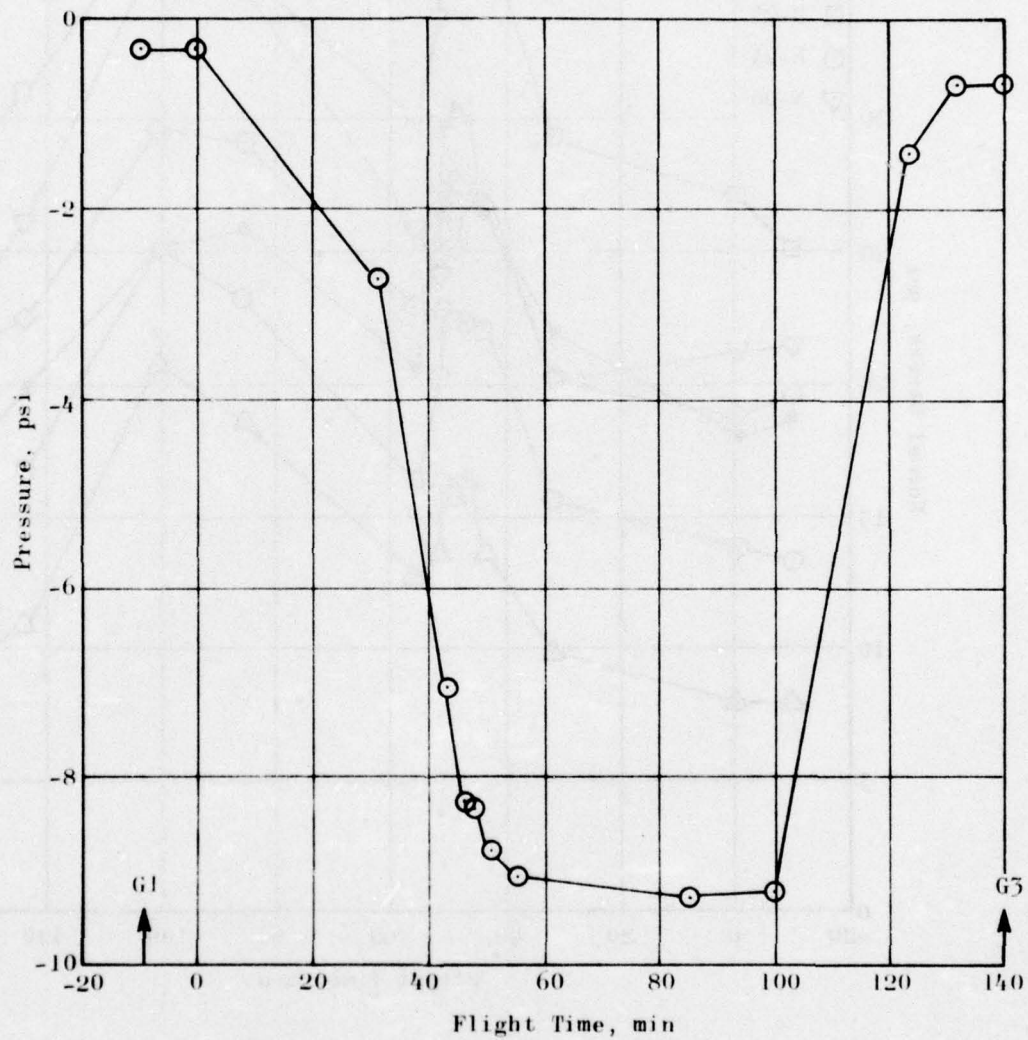
Figure 105. Atmospheric Pressure Data for Flight 19
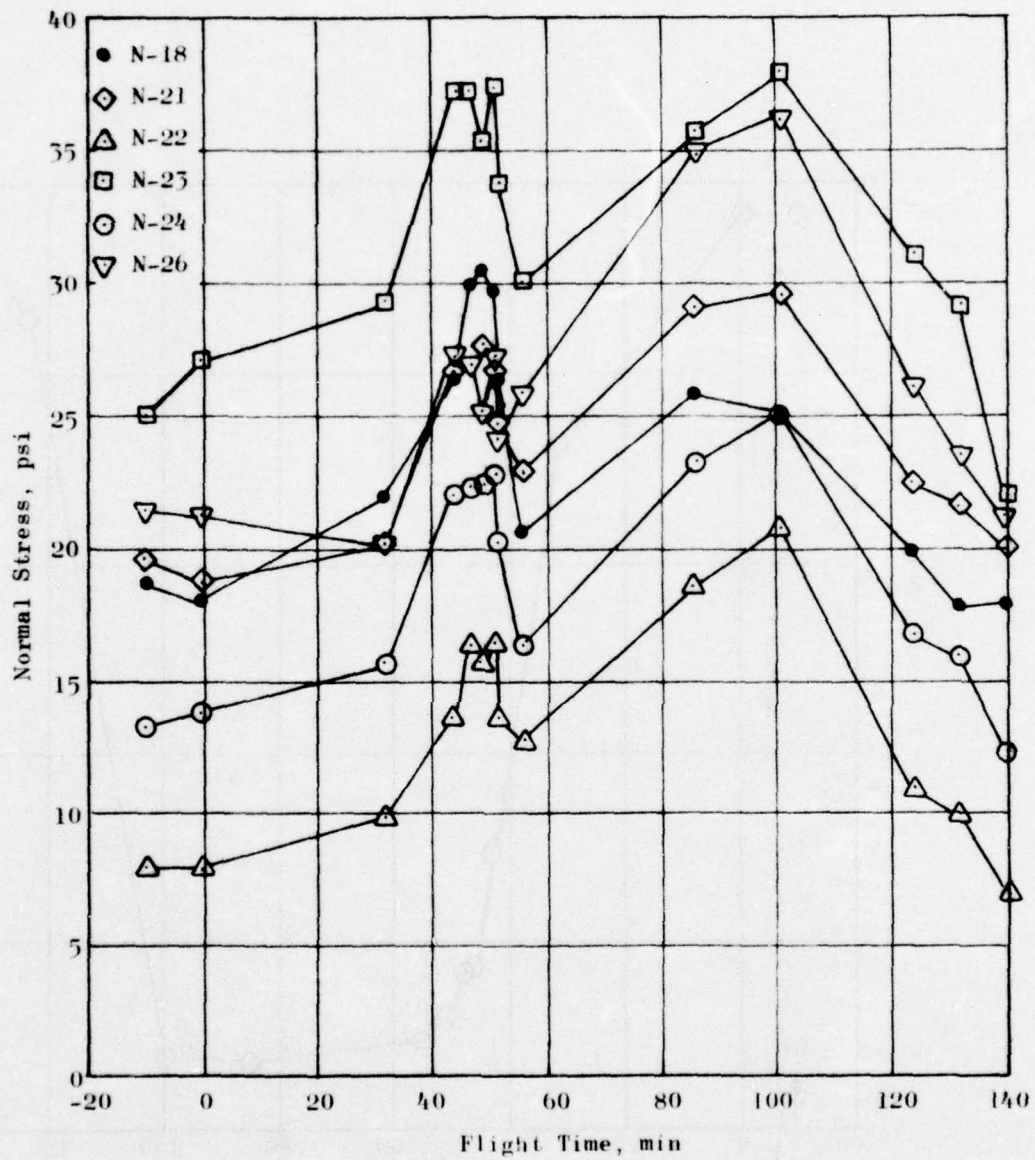
Figure 106.   Normal Stresses Measured in Flight 19

142
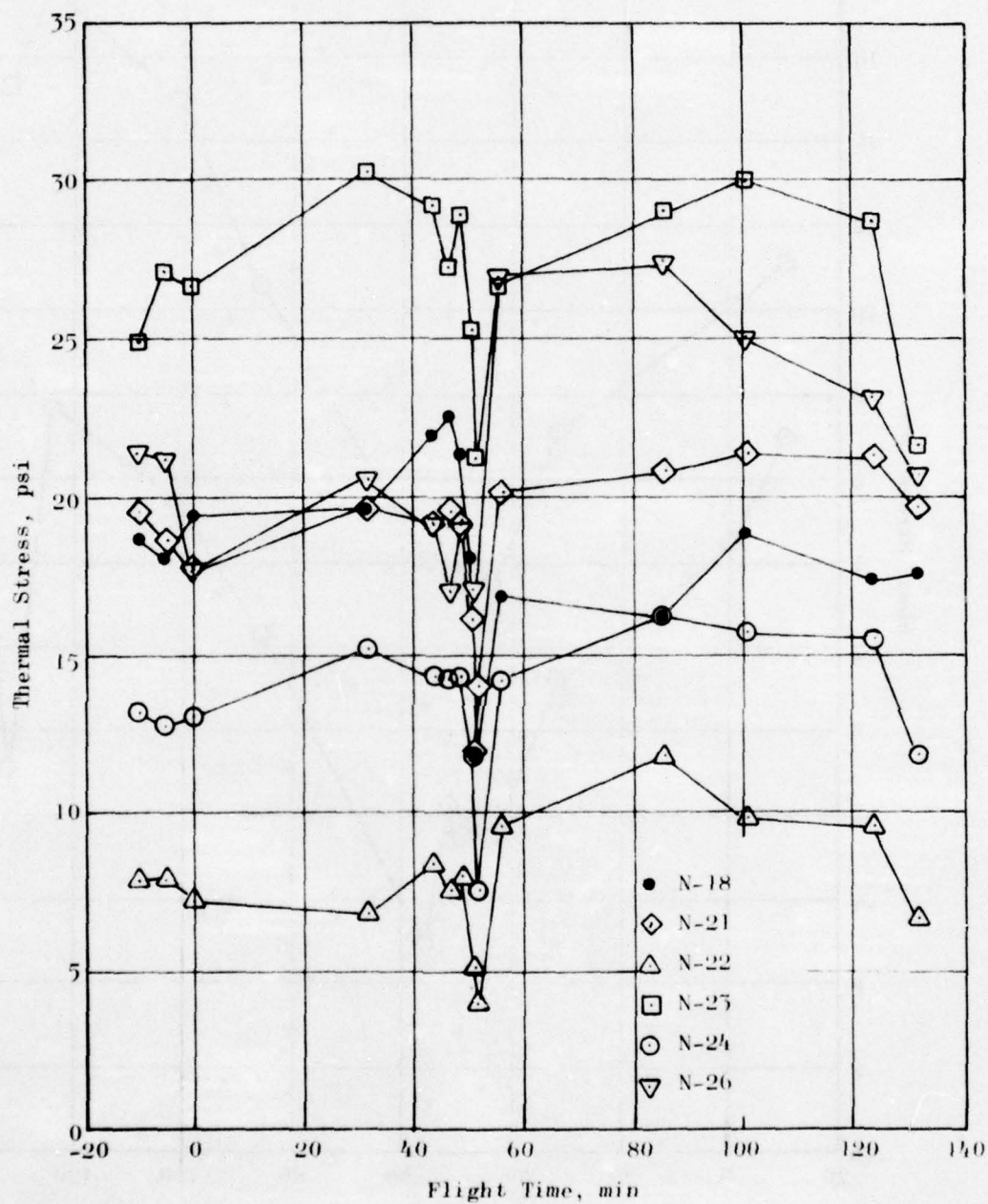
Figure 107. Measured Thermal Normal Stresses, Flight 19
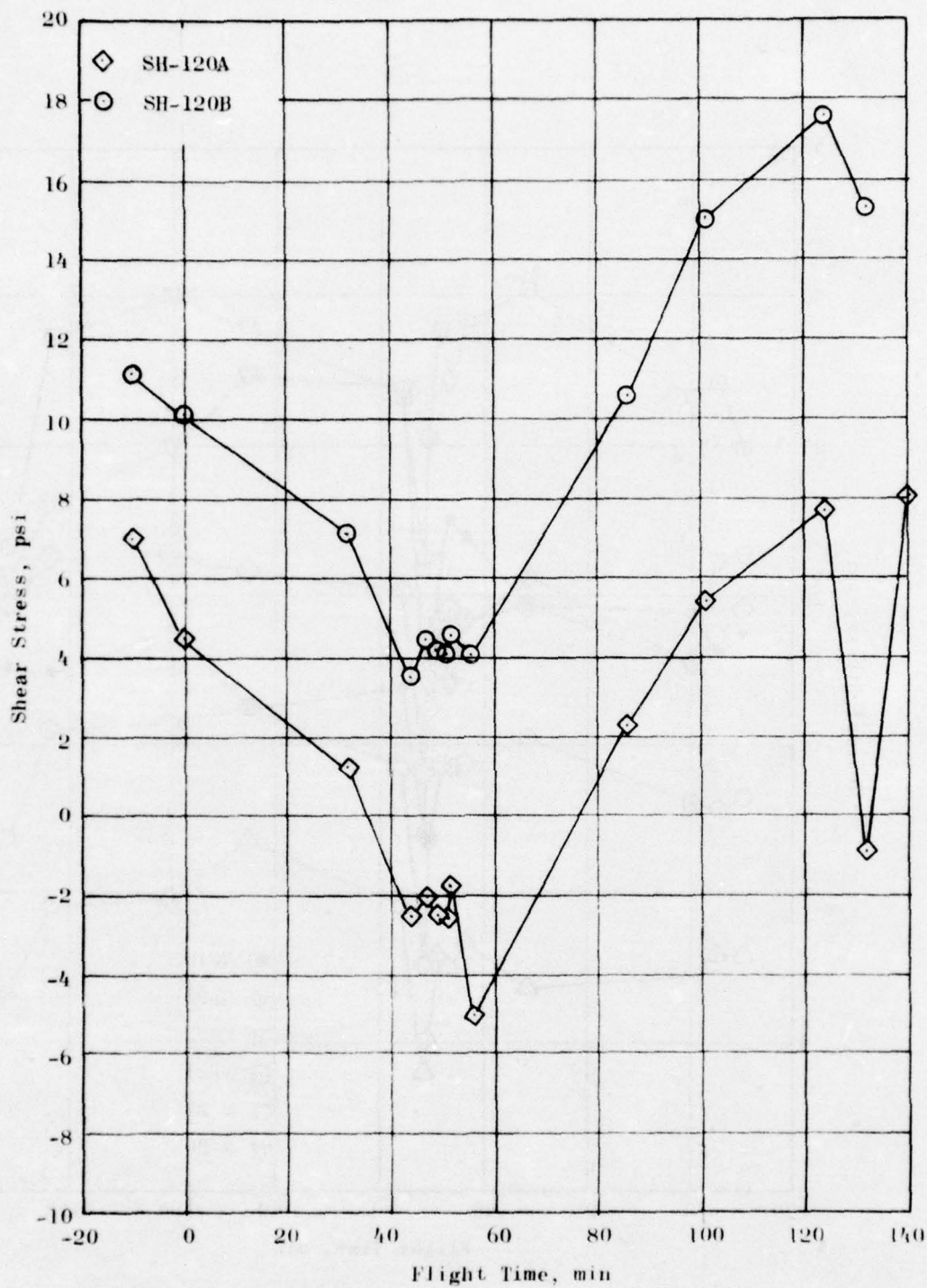
Figure 108.   Shear Stress Measured During Flight 19
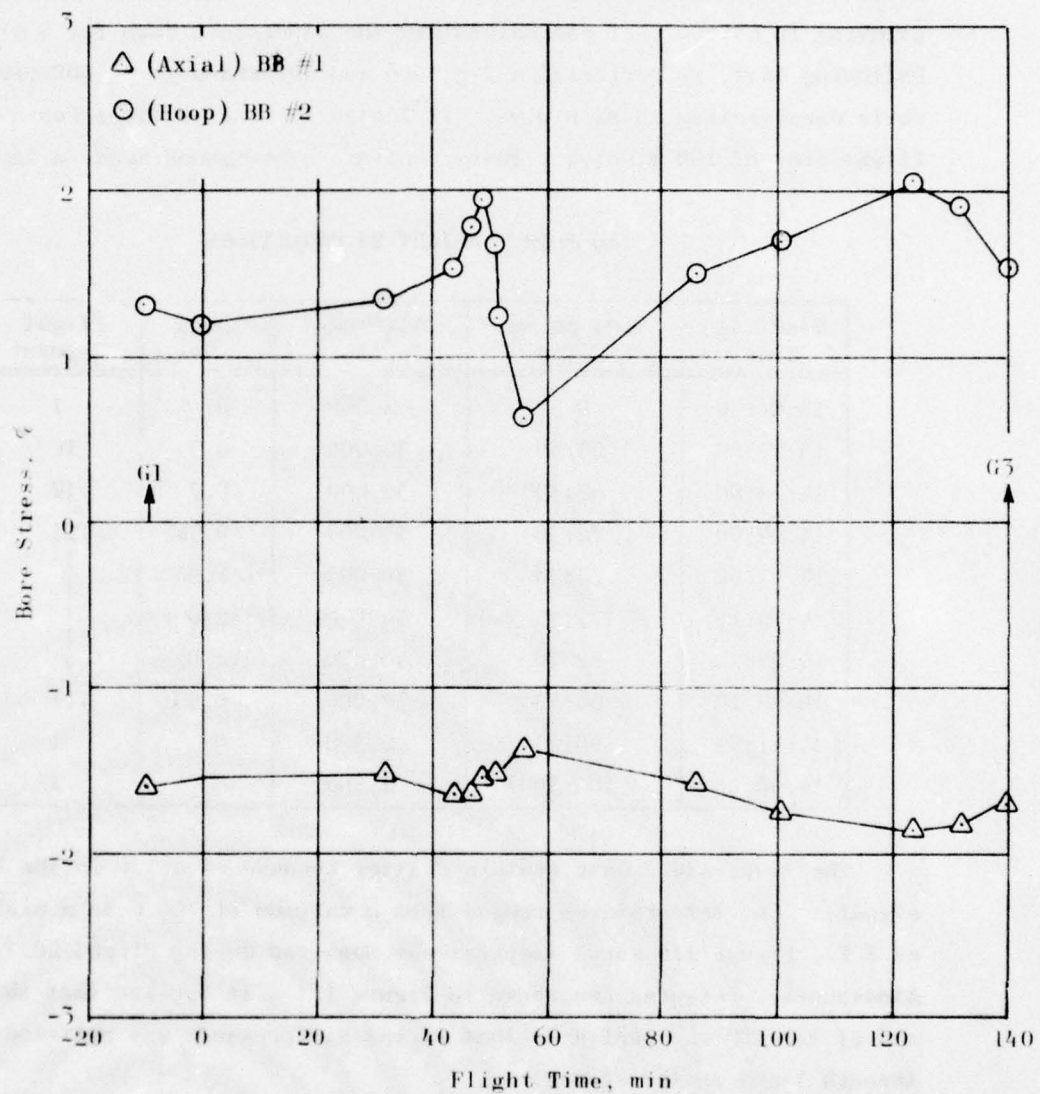
Figure 109.   Bore Stress Measured During Flight 19

145

FLIGHT 20 - 4 AUGUST 1975

Flight 20 returned to a more typical format. After take-off the aircraft climbed to 30,000 feet over a period of 25 minutes then cruised at Mach 0.7 for another 45 minutes. It then accelerated to Mach 2 while climbing to 40,000 feet and maintained the supersonic dash for 5 minutes. Following that, it performed a 2-g turn and descended to 30,000 feet while decelerating to Mach 0.95. It landed 14 minutes later for a total flight time of 100 minutes. These conditions are summarized in Table 19.

TABLE 19. FLIGHT 20 CONDITIONS

Starting Time	Time lapse, min	Altitude, ft	Mach No.	Flight Segment
13:01:30	0	2,300	0	I
13:27:00	25:30	30,000	0.7	IV
14:10:00	68:30	30,000	0.7	IV
14:14:00	72:30	30,000	0.91	III
14:17:00	75:30	30,000	1.5	↓
14:19:15	77:45	40,000	2.0	
14:24:20	82:50	40,000	2.02	↓
14:28:15	86:45	30,000	0.95	III
14:41:55	100:25	2,300	0	I
14:50:00	108:30	2,300	0	I

The temperature data contain scatter because of noise in the PAM signals. CLI temperatures ranged from a maximum of 140 F to a minimum of 8 F. Figure 110 shows temperatures measured during Flight 20. Atmospheric pressures are shown in Figure 111. It appears that the aft end of the BDU was sealed so that excess gas pressure was relieved slowly through leaks in the system.

146
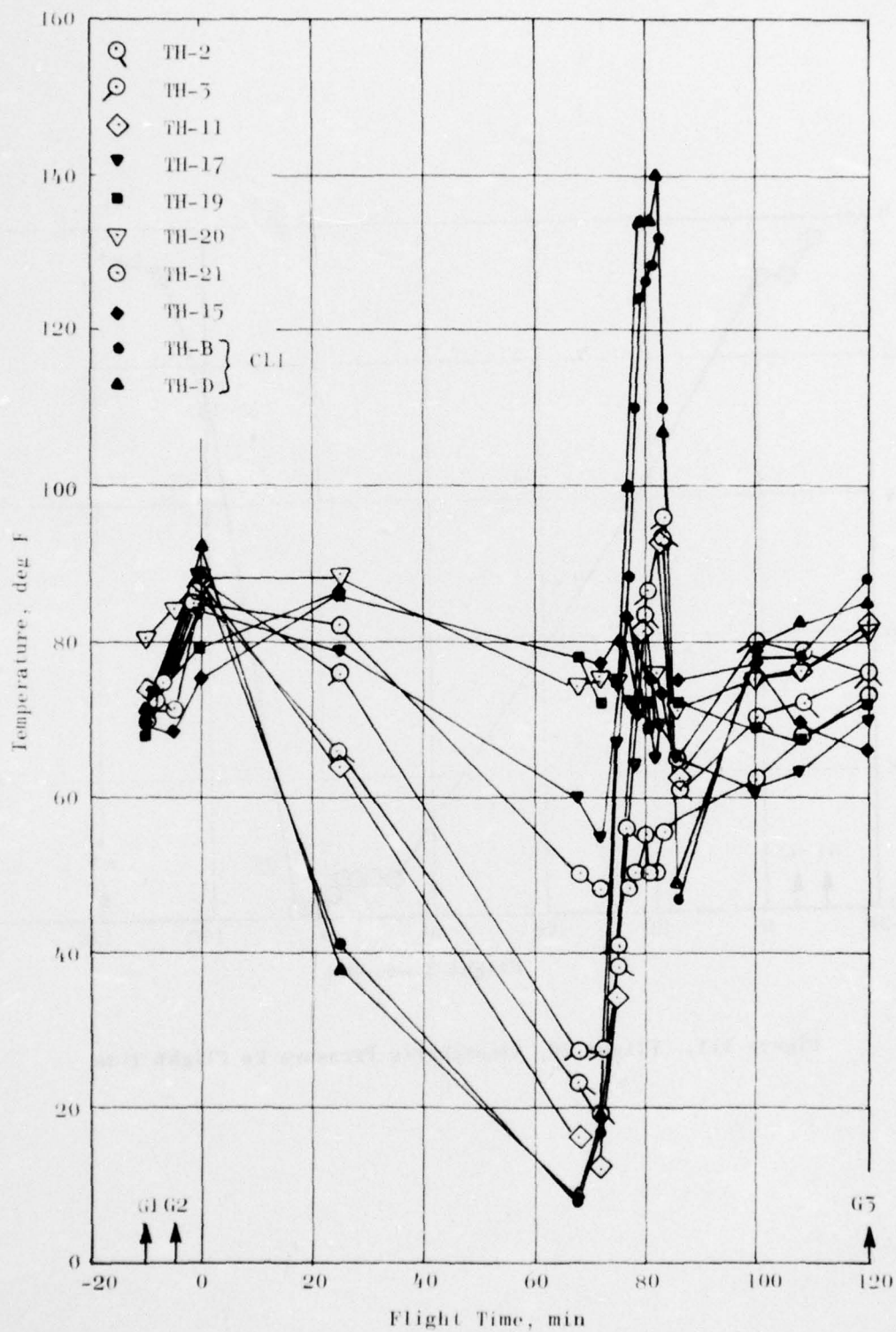
Figure 110.   Flight 20, Temperatures vs Flight Time

147
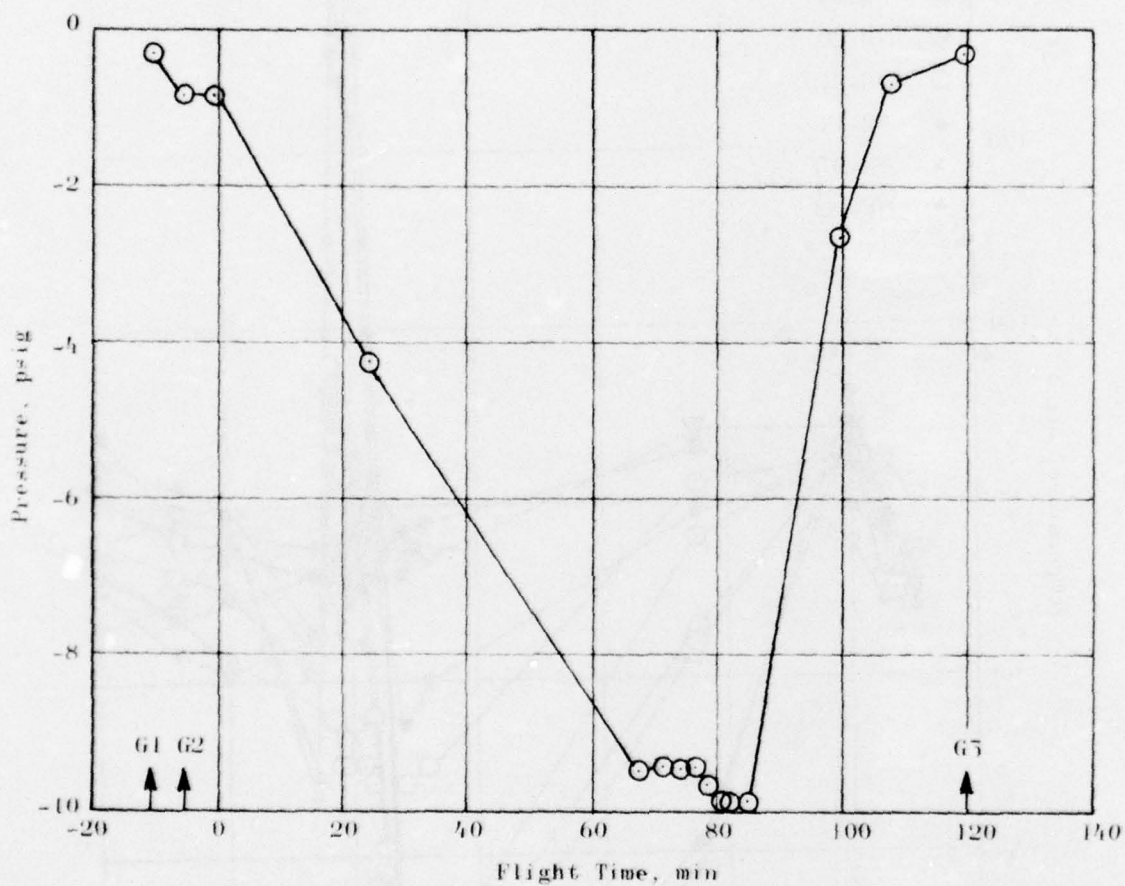
Figure 111.   Flight 20, Atmospheric Pressure vs Flight Time

148

Figure 112 shows the total normal stresses measured during the flight.

Figure 113 presents thermal normal stresses recorded during Flight 20. These data show an increase in thermal stress during the supersonic dash phase. Significantly different stresses may be introduced into an air-carried rocket motor depending on the sequence in which the maneuvers are performed.

Flight 20 shear stress data are presented in Figure 114; hoop and axial strain data are given in Figure 115. Dynamic stresses, given in Table 20, indicate small stress levels.
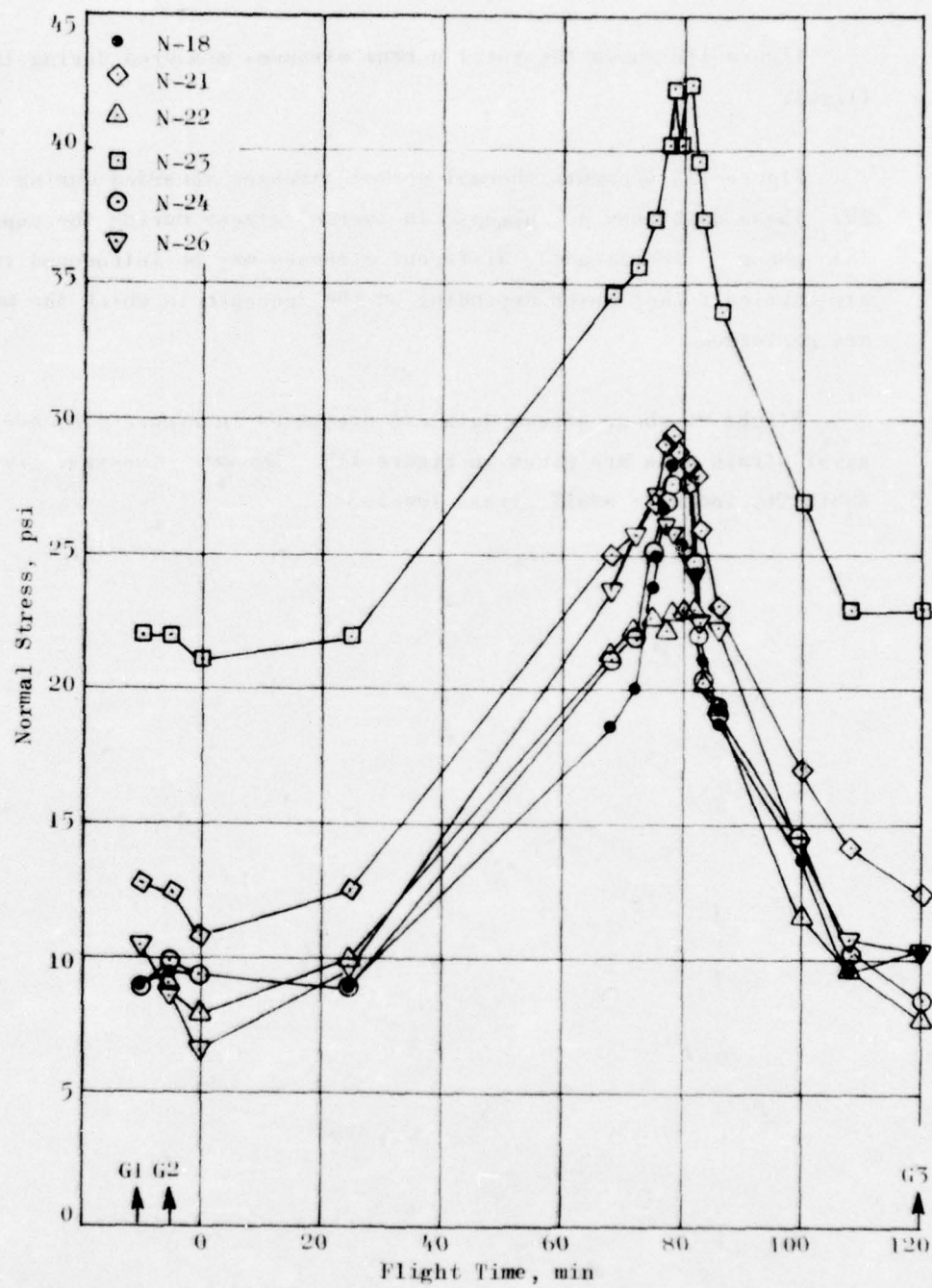
Figure 112. Flight 20, Total Normal Stresses vs Flight Time

150
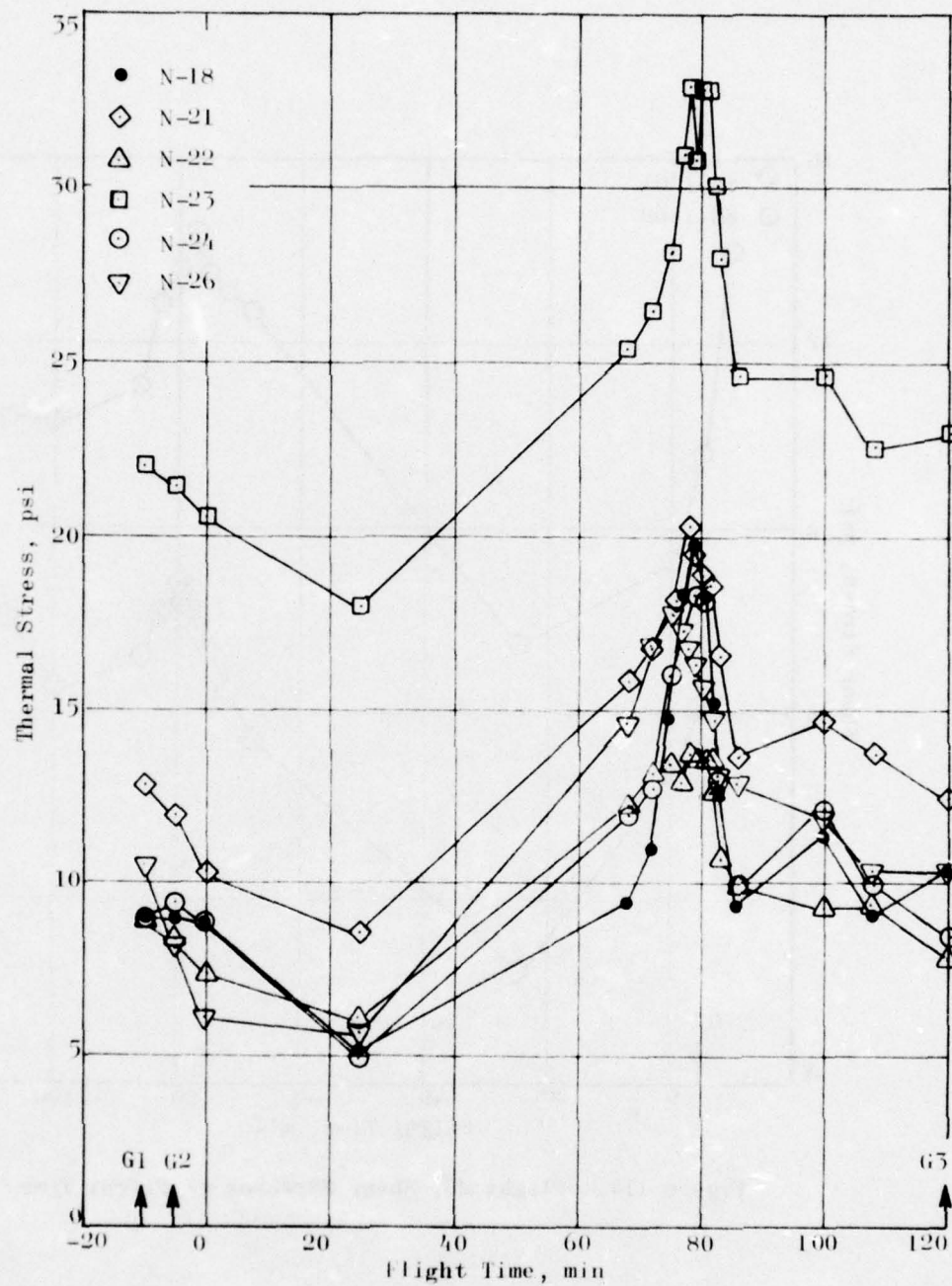
Figure 113. Flight 20, Thermal Normal Stresses vs Flight Time

151
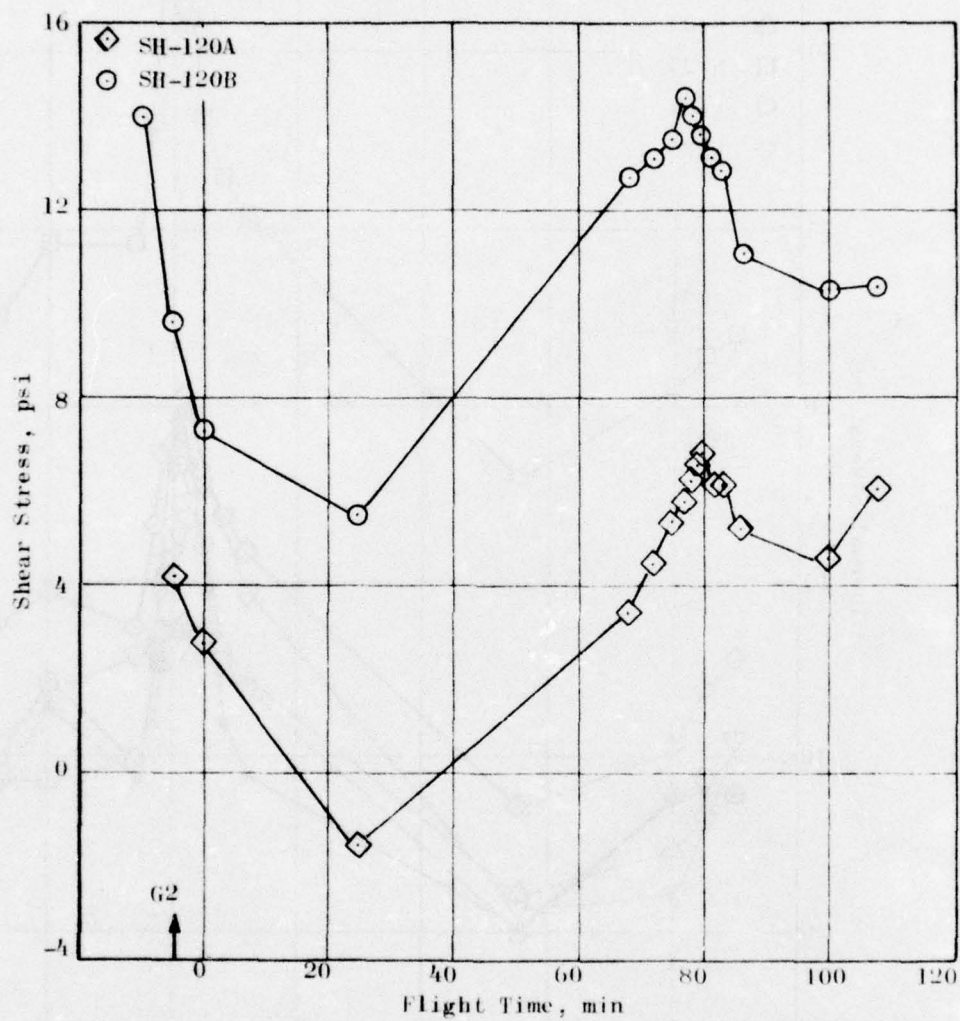
Figure 114.   Flight 20, Shear Stresses vs Flight Time
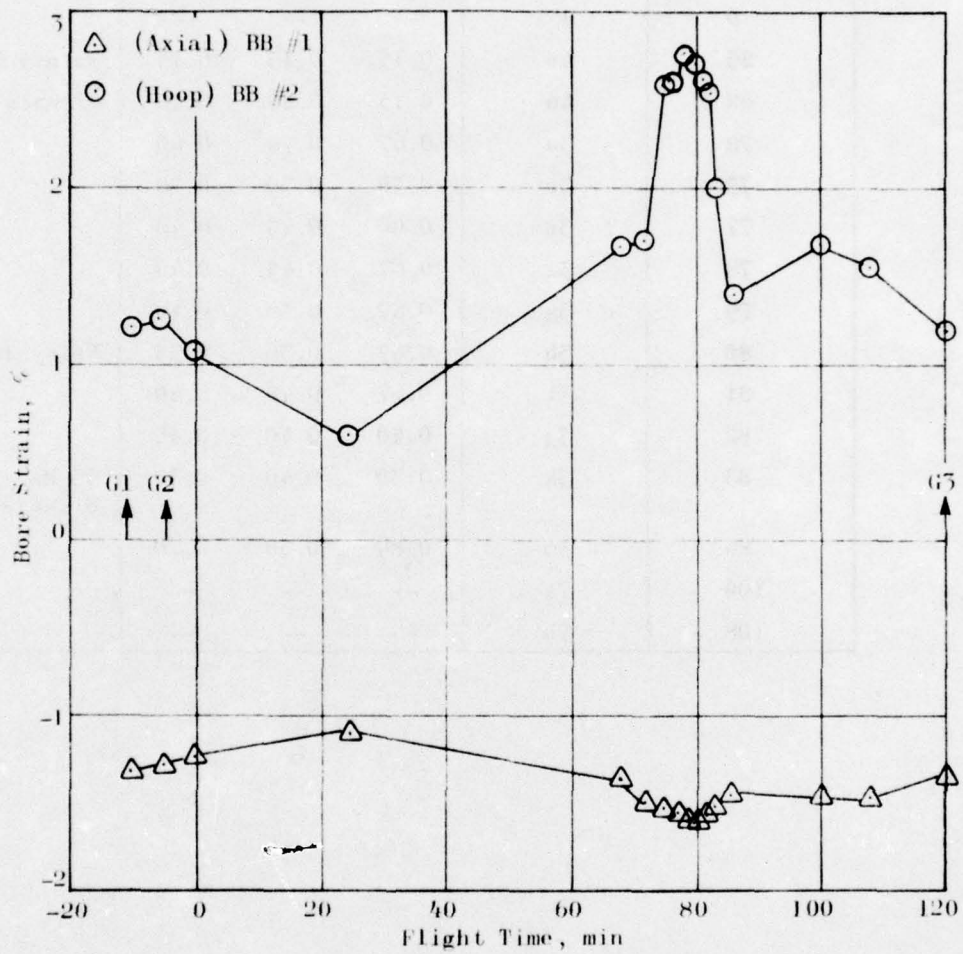
Figure 115.   Flight 20, Bore Strains vs Flight Time

153

TABLE 20. FLIGHT 20 DYNAMIC STRESS DATA

Flight Time, min	Condition	N18 N23 N24 Pk-Pk Dynamic Stress, psi			Comments
0	1	--	--	--	
25	4a	0.15	0.15	0.15	Mainly 200--300 Hz
68	4d	0.15	0.25	0.20	Signals
72	3a	0.67	0.70	0.60	"
75	3c	0.50	0.30	0.30	"
77	3e	0.60	0.45	0.40	"
78	3f	0.67	0.45	0.40	
79	3g	0.67	0.50	0.40	
80	3h	0.67	0.50	0.35	Noisy Traces
81	3i	0.67	0.40	0.40	
82	3j	0.40	0.40	0.45	
83	3k	0.30	0.40	0.30	50 Hz + 300 Hz Signals
86	3m	0.80	0.60	0.70	
100	7a	--	--	--	
108	7b	--	--	--	

154

SUMMARY

Because of questions raised as to the accuracy of the internal instrumentation prior to Flight 14, the latter flights are summarized below.

Since the major interest center is the change in grain response due to captive flight, an approach based on normalization of the stress/strain data was taken. Removing the pressure-change-induced load, normalizing the data, and averaging the stress gage responses yields a usable presentation of the flight-induced stress state. Data scatter in the normal gage response is probably higher than the distribution of stresses down the length of the motor.

Figures 116 through 122 depict selected temperatures, average normalized thermal bond stress, and inner bore hoop strain, all as functions of flight time, for Flights 14 through 20, respectively. Repeatability between flights is indicated by the consistency of the stress/strain ratio and the magnitudes of the changes observed.

As mentioned, dynamic stress signals during the severe flight conditions (Mach 2 and TFR) approached magnitudes of ± 1.0 psi but were usually even lower. This represents such a low level of response (less than 1% of gage full-scale response) that these must be treated as generally indicative rather than exact quantity.

155
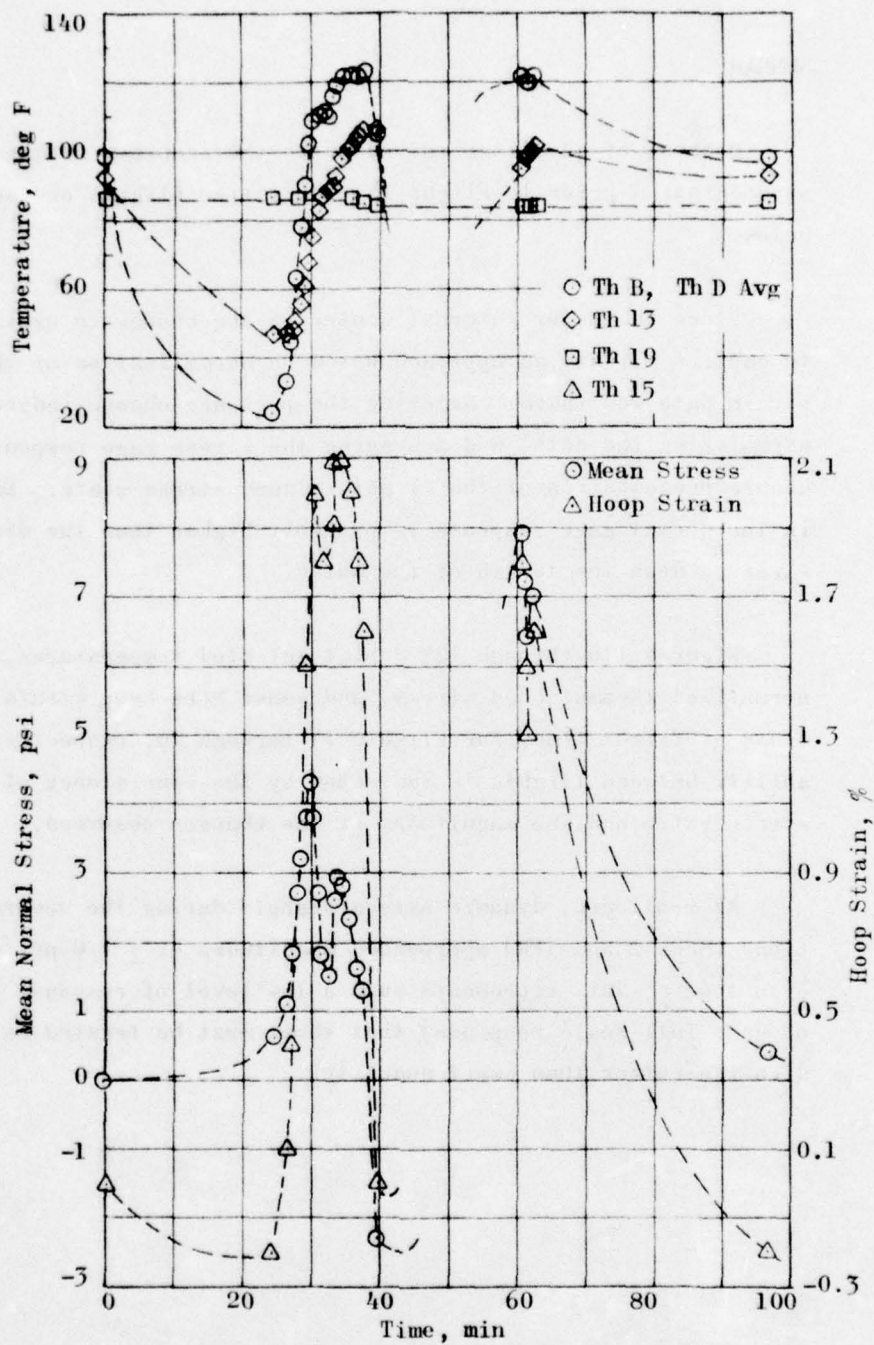
Figure 116.   Flight 14 Thermal History

156
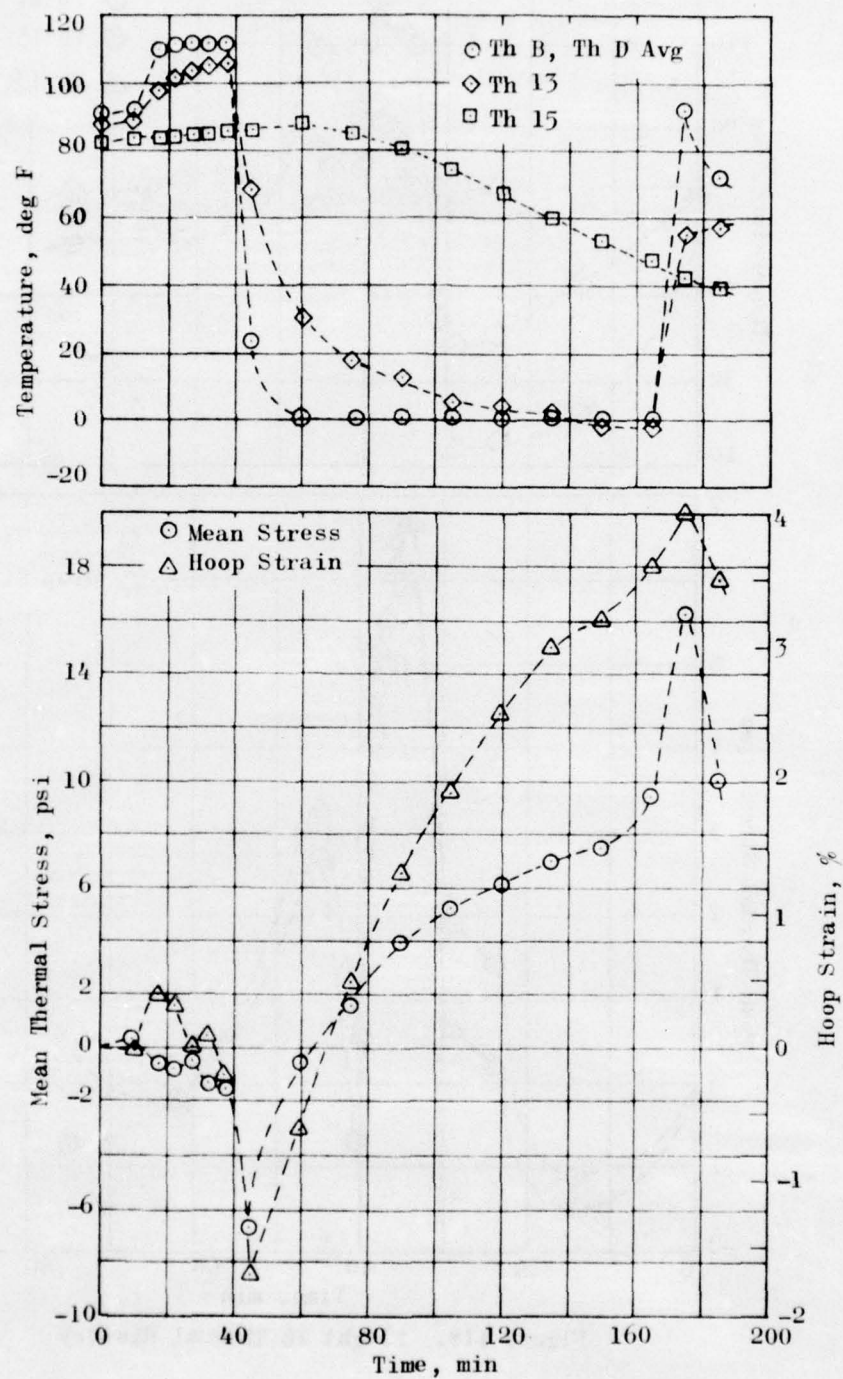
Figure 117. Flight 15 Thermal History

157
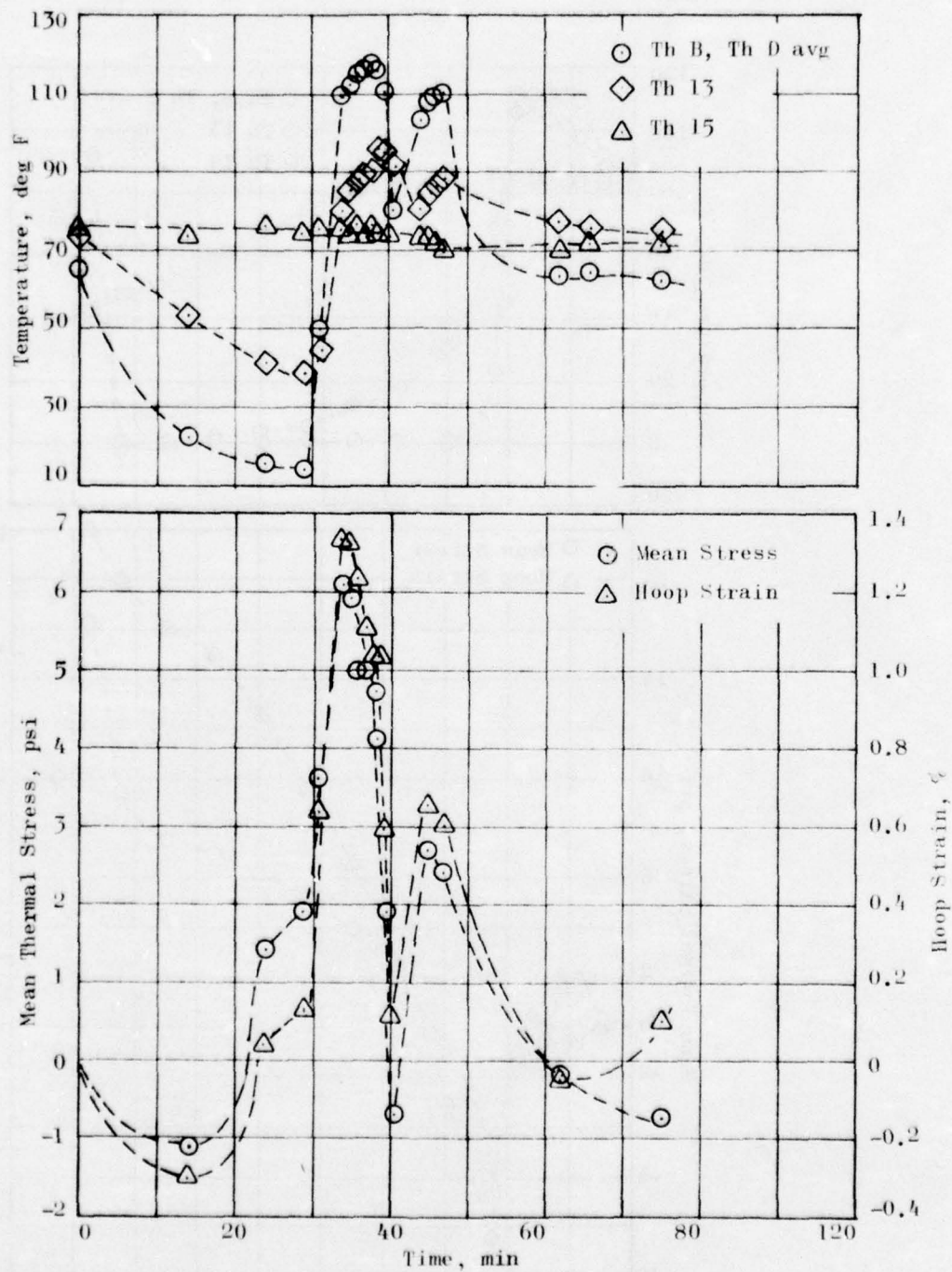
Figure 118. Flight 16 Thermal History
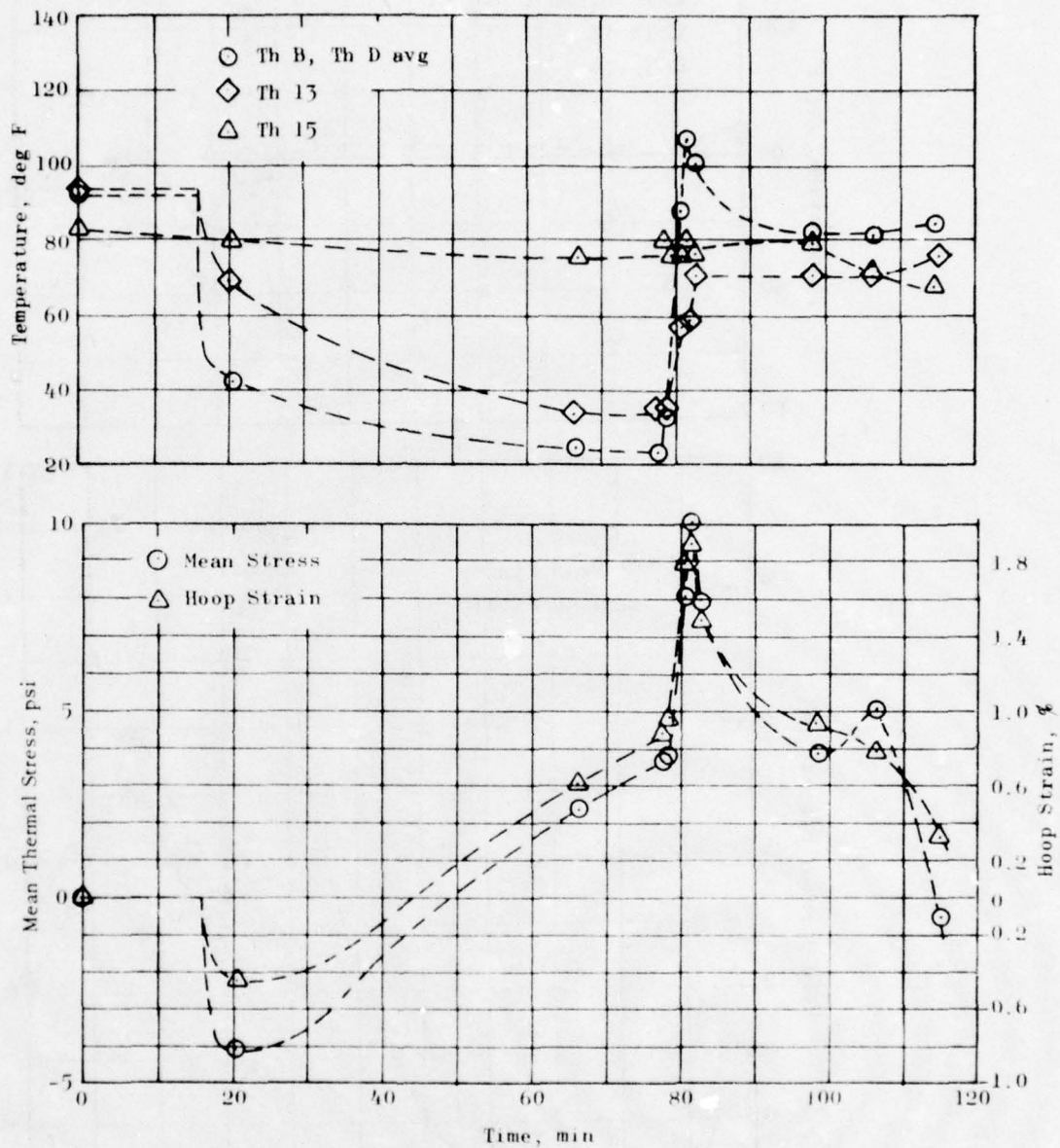
Figure 119. Flight 17 Thermal History

159
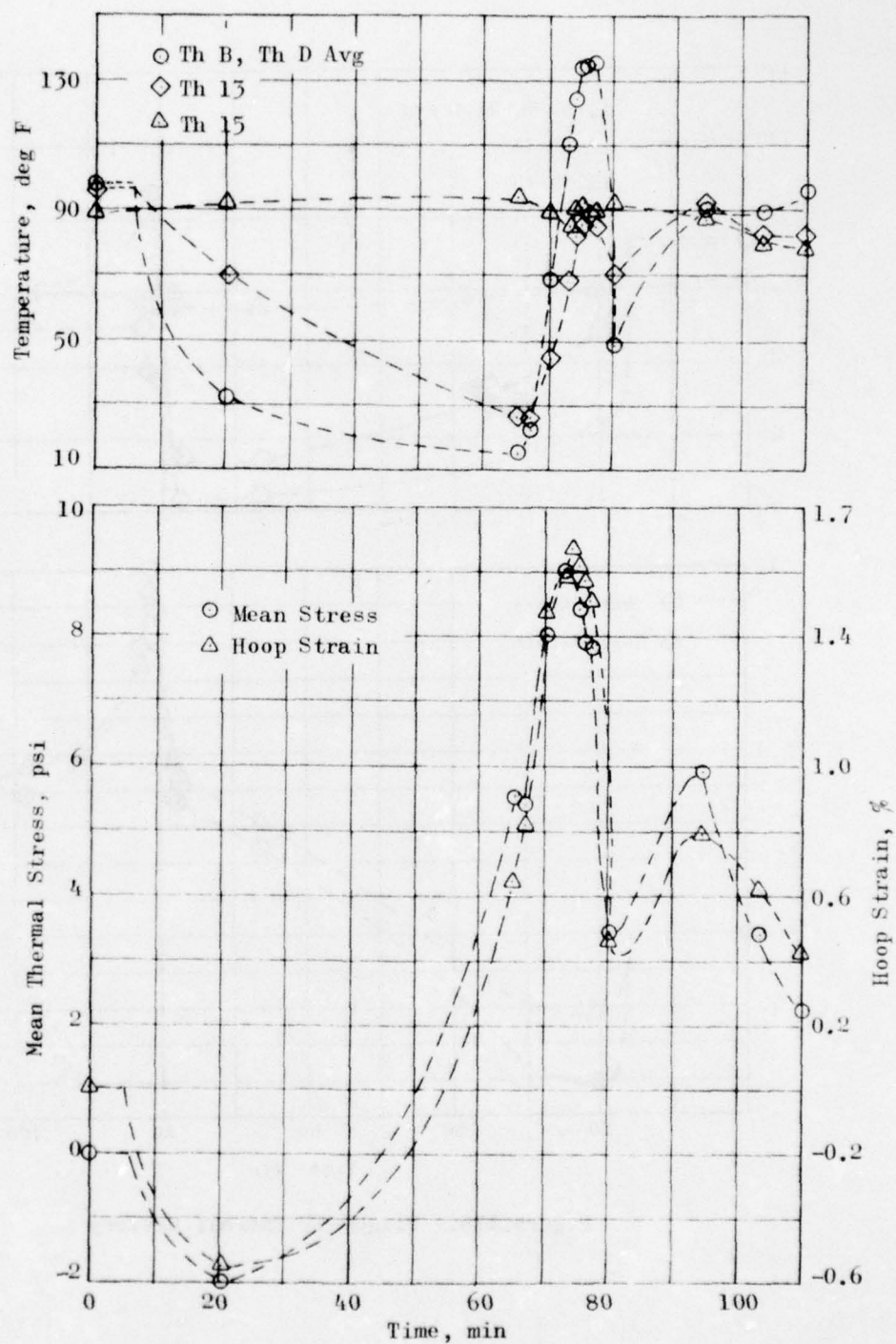
Figure 120. Flight 18 Thermal History

160
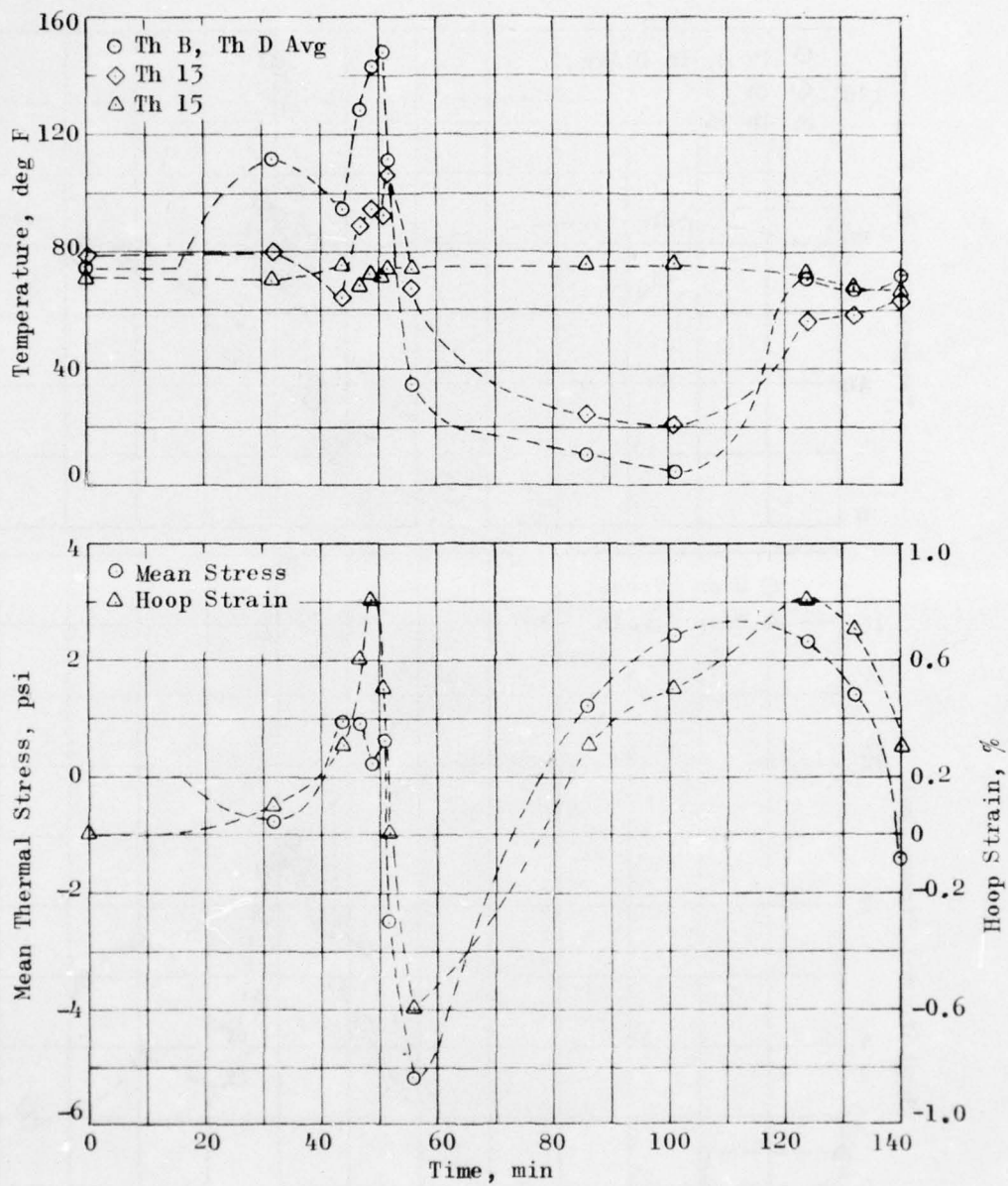
Figure 121. Flight 19 Thermal History

161
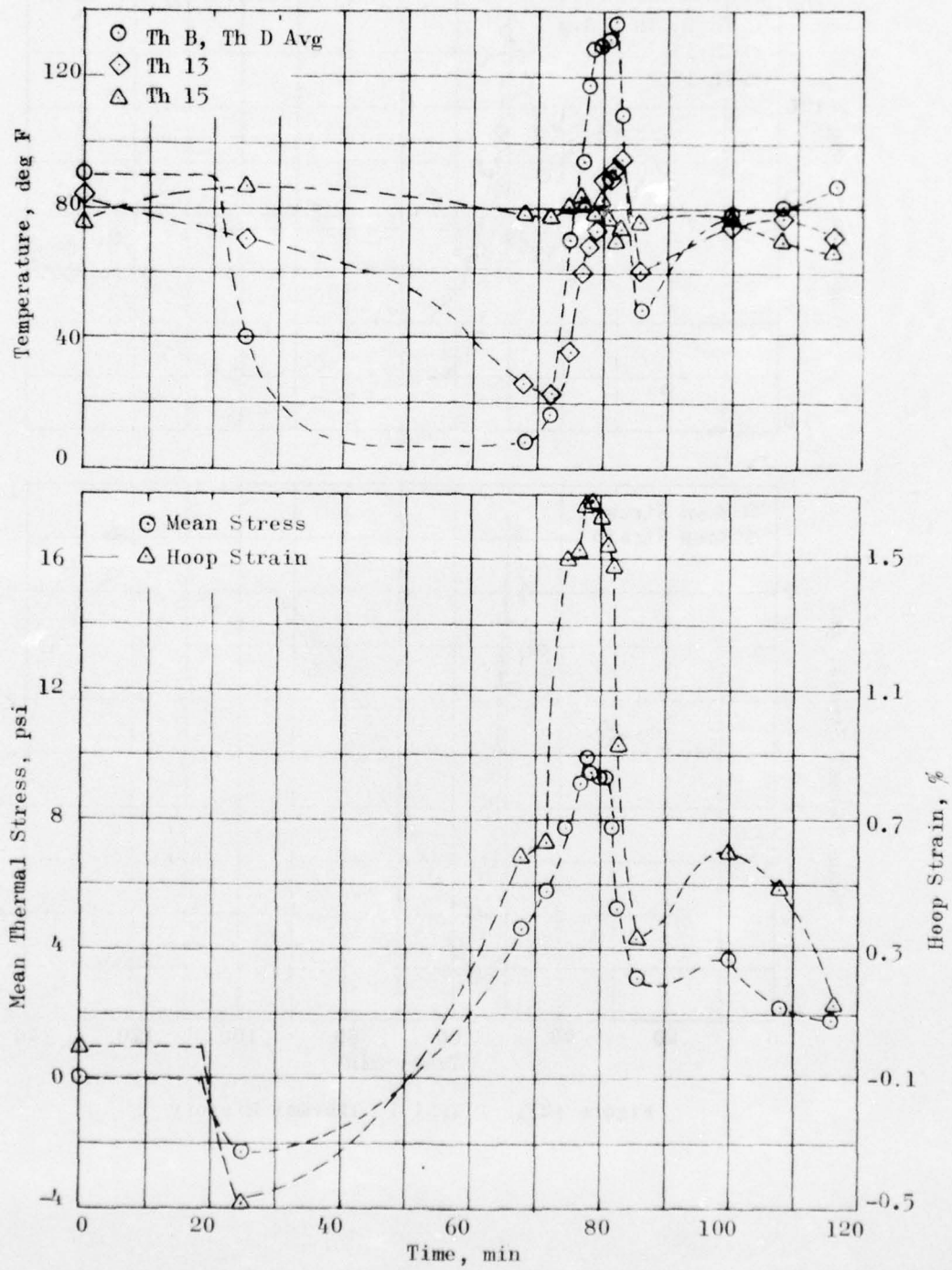
Figure 122. Flight 20 Thermal History

162

EXTERNAL INSTRUMENTATION RESPONSE

In addition to grain response, a large amount of dynamic data describing the external environment were recorded.

ACCELEROMETER DATA

The accelerometer data were analyzed using digital samples and performing Fourier analysis to obtain random response (power spectral density (PSD) vs frequency). A measure of the response in the area under the PSD vs frequency curve, i.e., the mean square g level at several accelerometer locations for significant flight conditions is given in Table 21.

The data are generally erratic due to recording, reduction, and analysis difficulties. Data from the latter flights (15, ff) are more reliable than those from earlier flights. It is obvious that the supersonic dash and TFR generate the largest vibrations. The differences between these two conditions are not significant. Data from the Y-axis accelerometers were not reduced since the indicated signal on the oscillographs was very low compared to that for the translational (Z, X) axes.

LAUNCHER LUG DATA

Because of frictional contact between the sway braces and motor case, the sway brace and aft lug bending calibration were indeterminate. The key response of lug tension was measured, however. This response reflects the effects of tightening the sway braces and the non-linear behavior due to the frictional contact with the motor. Plots of forward and aft lug tension for the various flight conditions are shown in Figures 123 through 127 for Flights 15 through 18 and 20. Lug load induced by installation was measured on Flights 17 and 18. For Flight 17,

163

TABLE 21. ACCELEROMETER RESPONSE DATA[1] - MEAN SQUARE g-LEVEL - g's

Gage/Axis Location	Flight/Segment													
	9-III	9-V	Special Test 10[3]	11[4]-III	11[4]-V	15-IV	16-IV	16-III	16-V	17-IV	18-IV	18-III	20-IV	20-III
Aft End - X[2]	3.1	7.7	5.2	4.6	1.6	--	0.3	1.0	3.2	0.1	0.1	1.1	0.1	1.2
Aft End - Z[2]	1.4	3.5	2.4	2.0	3.6	1.3	0.7	1.2	4.9	0.2	0.2	1.3	0.2	1.7
CG - X	0.9	1.5	0.7	0.1	0.1	--	0.2	4.6	1.2	0.2	0.0	0.4	0.2	3.7
CG - Y	0.6	0.9	--	3.8	0.1	--	--	--	--	--	--	--	--	--
CG - Z	0.5	0.6	0.6	--	--	--	0.8	1.9	2.4	0.2	0.2	1.2	0.2	1.1
Fwd Lug - Z	2.5	2.5	2.2	3.0	12.5	--	0.6	2.5	2.7	0.1	0.1	2.5	0.1	2.5
Aft Lug - Z	0.4	1.1	0.4	0.7	1.9	--	2.9	6.5	6.9	0.5	0.5	5.7	0.5	5.5
Grain - Z[5]	--	--	--	--	--	0.005	0.005	0.02	0.4	0.02	0.02	0.02	0.01	0.05

[1] Typical PSD plots of these data are shown in the Ground Simulation discussion.

[2] Gage oriented 45° to missile coordinate system

[3] Special Test - M = 1.1 at ~ 4000 ft MSL altitude

[4] Several bad accelerometer connections were found following Flight 11. Data up to and including Flight 11 are suspect.

[5] Accelerometer originally installed in Y-axis--re-installed in Z-axis before Flight 15.

164
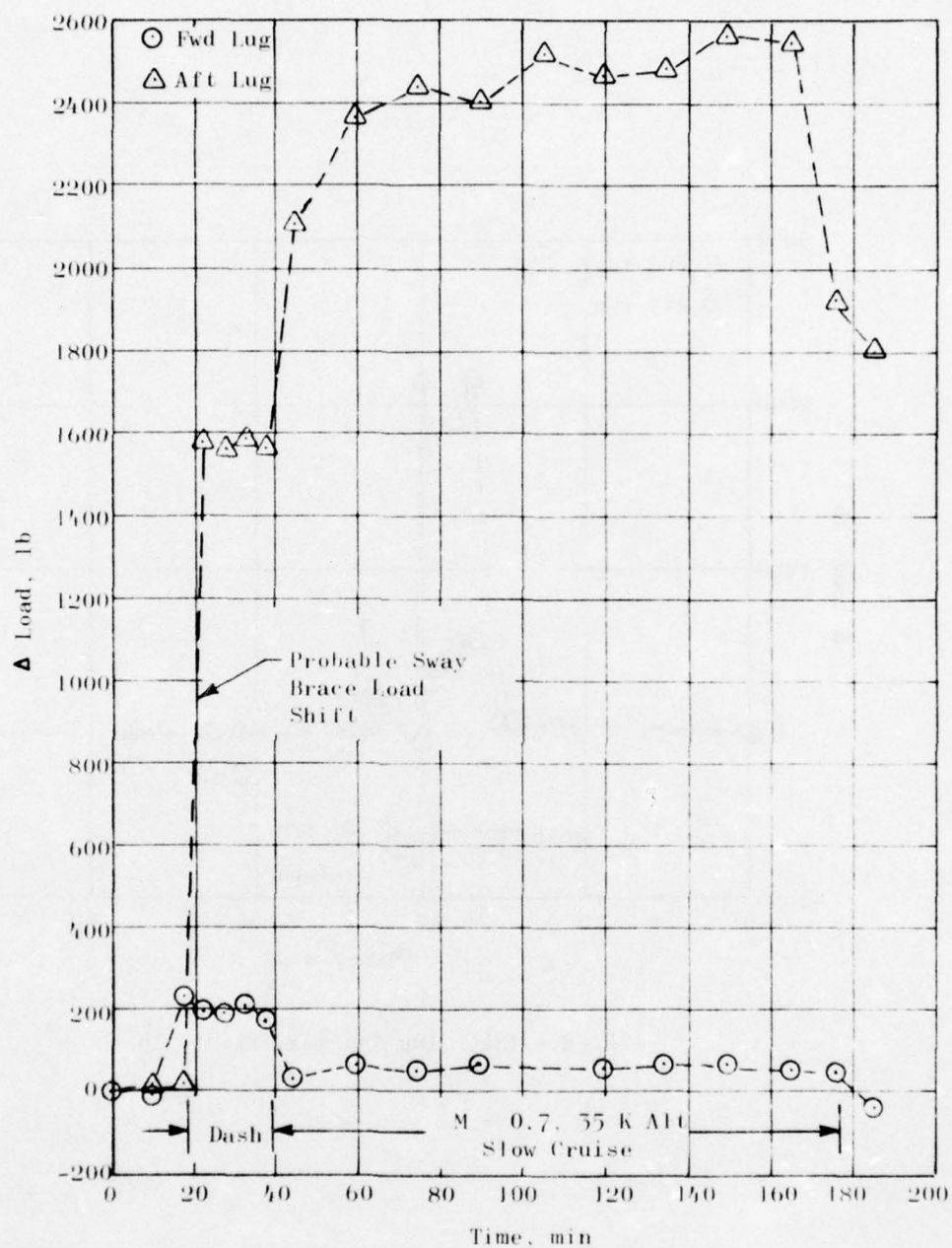
Figure 123. Lug Tension, Flight 15
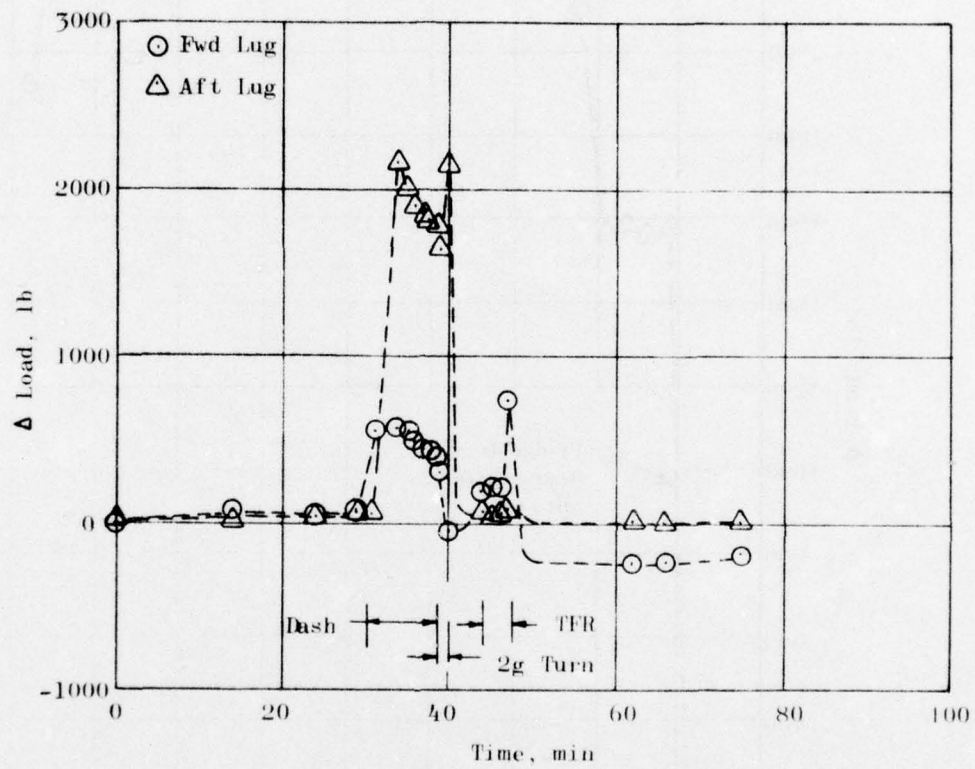
Figure 124. Lug Tension, Flight 16

166
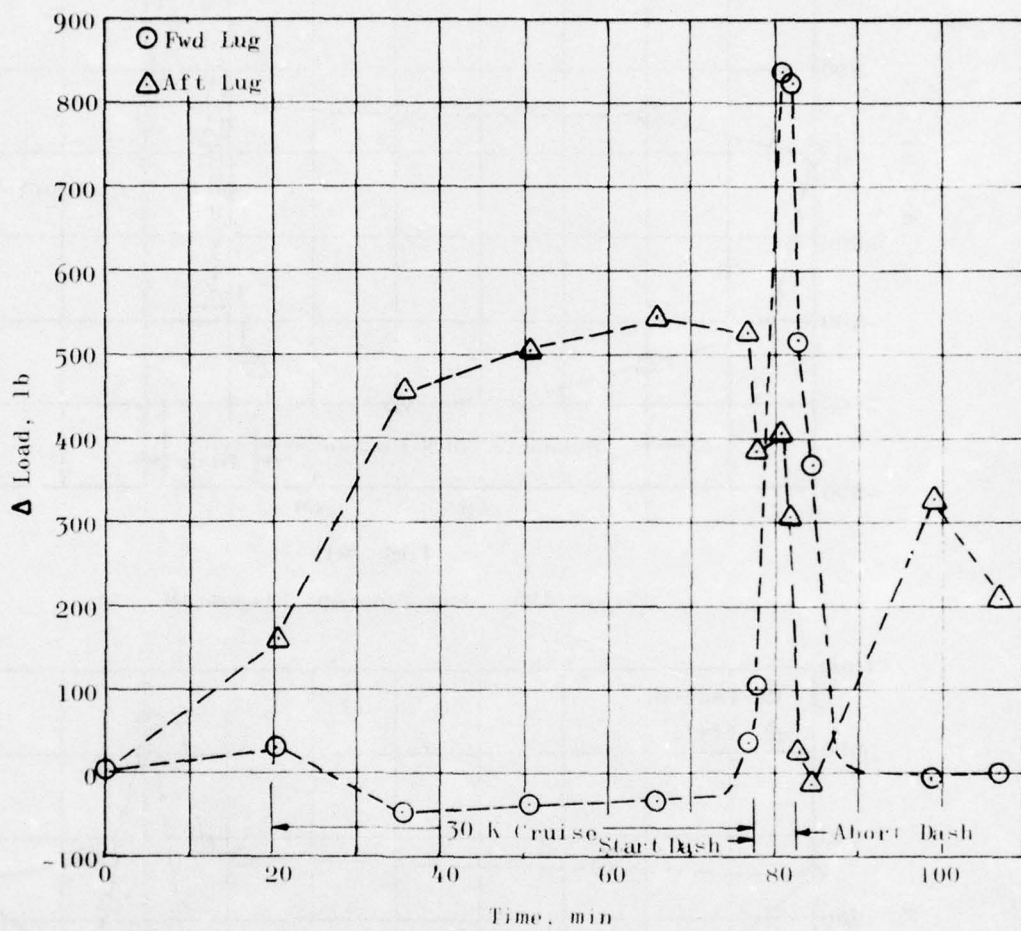
Figure 125.   Lug Tension, Flight 17

167
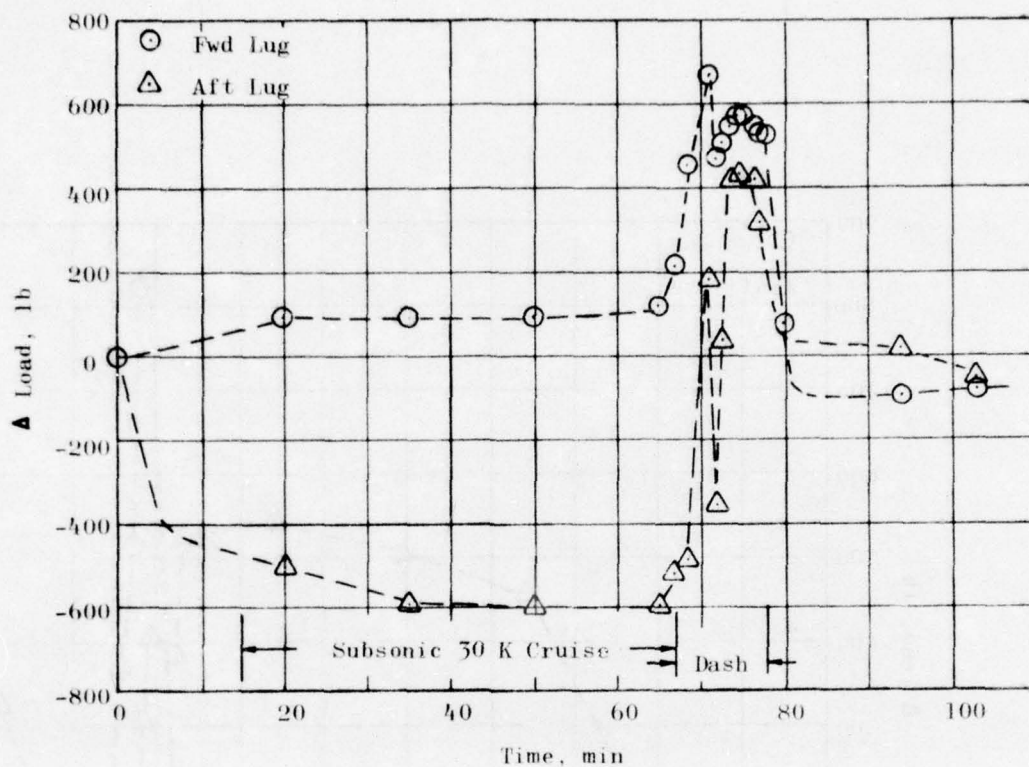
Figure 126. Lug Tension, Flight 18
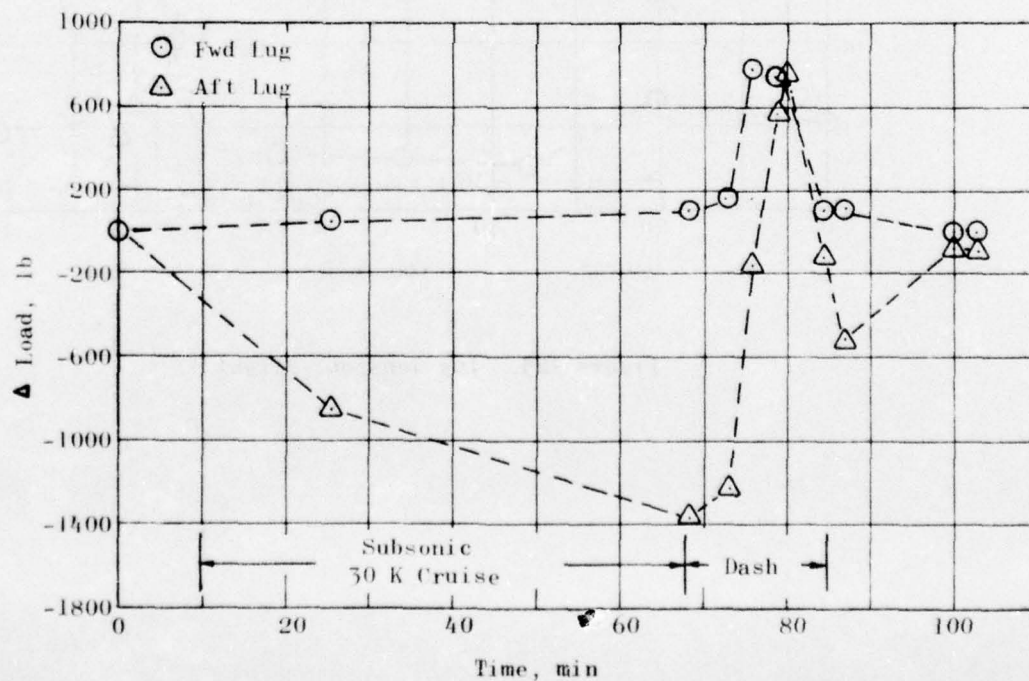
Figure 127. Lug Tension, Flight 20

168

tightening the sway braces resulted in 3200 pounds, tension, in the forward lug and about 1600 pounds, tension, in the aft lug. For Flight 18, the corresponding induced loads were about 2600 and 3400 pounds, respectively. During Flight 15, an 1800-pound shift in the aft lug tensile load was recorded. This shift is attributed to an in-flight shift of the motor/sway brace interface. Noise levels in the reduced data on the order of $\pm$ 150 pounds for the forward lug and $\pm$ 300 pounds for the aft lug were of the same or greater order than those for the dynamic response of the lugs.

As in the case of the other test data, a large range in observed response occurred between flights and flight conditions. This phenomena was closely related to the initial tightening of the sway braces, which produced the most significant load on the lugs. A generalization of the response observed throughout the tests of the BDU is as summarized below:

	Lug Tensile Load, lb	
	Forward Lug	Aft Lug
Loading from Hanging BDU	3000	2500
Flight Load (Mach 2 - Dash)	800	1600
Dynamic Load in Flight	<200	<500

GROUND SIMULATION

Three series of ground simulation tests were conducted. The flight vehicle and MAU-12C aircraft ejector rack were mounted on a vibration machine using a rigid mount between the shaker and aircraft rack to simulate aircraft input. During preflight simulation the entire flight unit was vibrated using (1) sine inputs to calibrate the system and to check responses of the gages and (2) random vibrational loads and aerodynamic heat input levels predicted by General Dynamics.

After 13 flights on an F-111 aircraft, the BDU was returned to Rocketdyne for repairs, recalibration, and additional ground simulation testing to obtain preliminary comparisons with the earlier tests based on prediction. Responses of the gages in the interim simulation tests were also compared to those obtained in actual flight.

The final series (postflight) of tests were conducted to establish the degree to which the captive-flight environment can be simulated in ground test equipment using grain response as the evaluation criterion.

The three series of tests are discussed on the following pages.

171

PREFLIGHT SIMULATION

TEST PLAN

A preliminary test plan was established and approved before testing was begun. Random vibration and aeroheat requirements were based on the flight prediction environments.

Other prerequisites used in developing the testing sequence were: (1) minimize number of difficult and hazardous BDU handling operations, (2) delay the aeroheating cycles until last, and (3) provide maximum possibility of data gathering at both ground and flight recording stations. Minimal handling of the BDU reduced the chances of damaging instrumentation. By holding all aeroheat cycles until near the end of the checkout test cycle, the maximum data were obtained before the BDU was subjected to potential heating damage. The actual test sequence was:

1. Initial Functional Checks
   a. Pressure check 10 and 20 psig
   b. Thermal check
      (1) 70 F stability
      (2) 20 F stability check
      (3) 20--100 F gradient and stability check

2. Z Axis (Vertical)
   a. Hard-mount sine sweep vibration with impedance head
      (1) Calibrate system
      (2) Perform 10 to 2000 Hertz sinusoidal survey
      (3) Make X-Y plots of all specified channels
      (4) Process oscillograph records
   b. Hard-mount random vibration with impedance head
      (1) Multiple random vibrations with increasing power
          input were run until either the impedance head
          load limit was reached or the required random

172

vibration level was achieved. If the impedance head limit was reached first the impedance heads were to have been replaced with steel blocks. The impedance head load limit (5000 pounds max) was not reached during this test step; therefore, impedance heads were used in all vibration tests.

    (2) Reload flight recorder

    (3) Perform random vibration

    (4) Make PSD plots as specified

    (5) Process oscillograph records

c. Replace hard-mount with launcher and reload flight recorder

d. Soft-mount sine vibration with impedance heads

    (1) Calibrate system

    (2) Perform 10 to 2000 Hertz sinusoidal survey

    (3) Make X-Y plots of all specified channels

3. X Axis

a. Soft-mount sine sweep vibration with impedance heads

    (1) Calibrate system

    (2) Perform 10 to 2000 Hertz sinusoidal survey

    (3) Make X-Y plots of specified data channels

b. Replace launcher with hard rack mount and reload flight recorder

c. Hard-mount sine sweep vibration with impedance heads

    (1) Calibrate system

    (2) Perform 10 to 2000 Hertz sinusoidal survey

    (3) Make X-Y plots of specified data channels and process oscillograph records

d. Hard-mount with impedance heads (random)

    (1) Perform random vibration

    (2) Make PSD plots as specified

    (3) Process oscillograph records

    (4) Continue making any X-Y plots from previous tests as specified

    (5) Reload flight recorder

173

4. Thermal soak unit for flight recorder system checkout

5. Instrument sway braces and lugs

6. Thermal calibration

7. Static load calibrate Z, X, and Y axes

8. X Axis

    a. Calibrate system

    b. Perform 10 to 2000 Hz sinusoidal survey

    c. Make X-Y plots of specified channels and process oscillograph record

    d. Set up and conduct aeroheat only

        (1) Record temperature vs time as specified

        (2) Reload flight recorder

    e. Soft-mount with impedance heads

        (1) Perform random vibration in conjunction with aeroheat

        (2) Process oscillograph records

        (3) Make PSD plots as specified

        (4) Reload flight recorder

9. Z Axis (Vertical)

    a. Calibrate system

    b. Perform 10 to 2000 Hz sinusoidal survey

    c. Make X-Y plots of specified channels and process oscillograph record

    d. Soft-mount with impedance heads

        (1) Perform random vibration in conjunction with aeroheat

        (2) Process oscillograph records

        (3) Make PSD plots as specified

10. Ship BDU to AFRPL for flight test preparation

TEST CYCLES, DATA, AND DISCUSSION

Functional Checks

The initial tests were conducted to perform three types of functional checks on the instrumentation. The first was to record the response of the instruments to existing internal pressure, 10 psig, then to 20 psig and compare the two sets of data. The second check was to record selected responses to three different temperature levels, 20, 75, and 100 F. The third test was conducted on the vibrator to verify that the instruments and recording system were functioning.

Static pressure was not checked because of a low-level pressure leak around the bulkhead electrical connectors. Instead pressure was held at 10 and 20 psig by regulating the pressure source. Resulting data are shown in Tables 22 and 23.

TABLE 22. PRESSURE CHECK AT 20 F UNIT TEMPERATURE

Gage No.	Gage Readings, mv		
	0 psig	10 psig	20 psig
Stress #18	− 46	− 38	− 28
Stress #21	− 4	+ 4	+ 12
Stress #22	− 20	− 11	− 1
Stress #23	− 35	− 27	− 19
Stress #24	+ 23	+ 14	+ 6
Stress #26	− 7	+ 1	+ 9
Strain #17	− 22	− 22	− 22
Strain #1	+ 13	+ 12	+ 12
Strain #2	+ 75	+ 73	+ 72
Shear #101	+109	+109	+112
Shear #SH-2	+158	+161	+169
Shear #120A	− 6	− 8	− 8
Shear #120B	+ 1	0	0
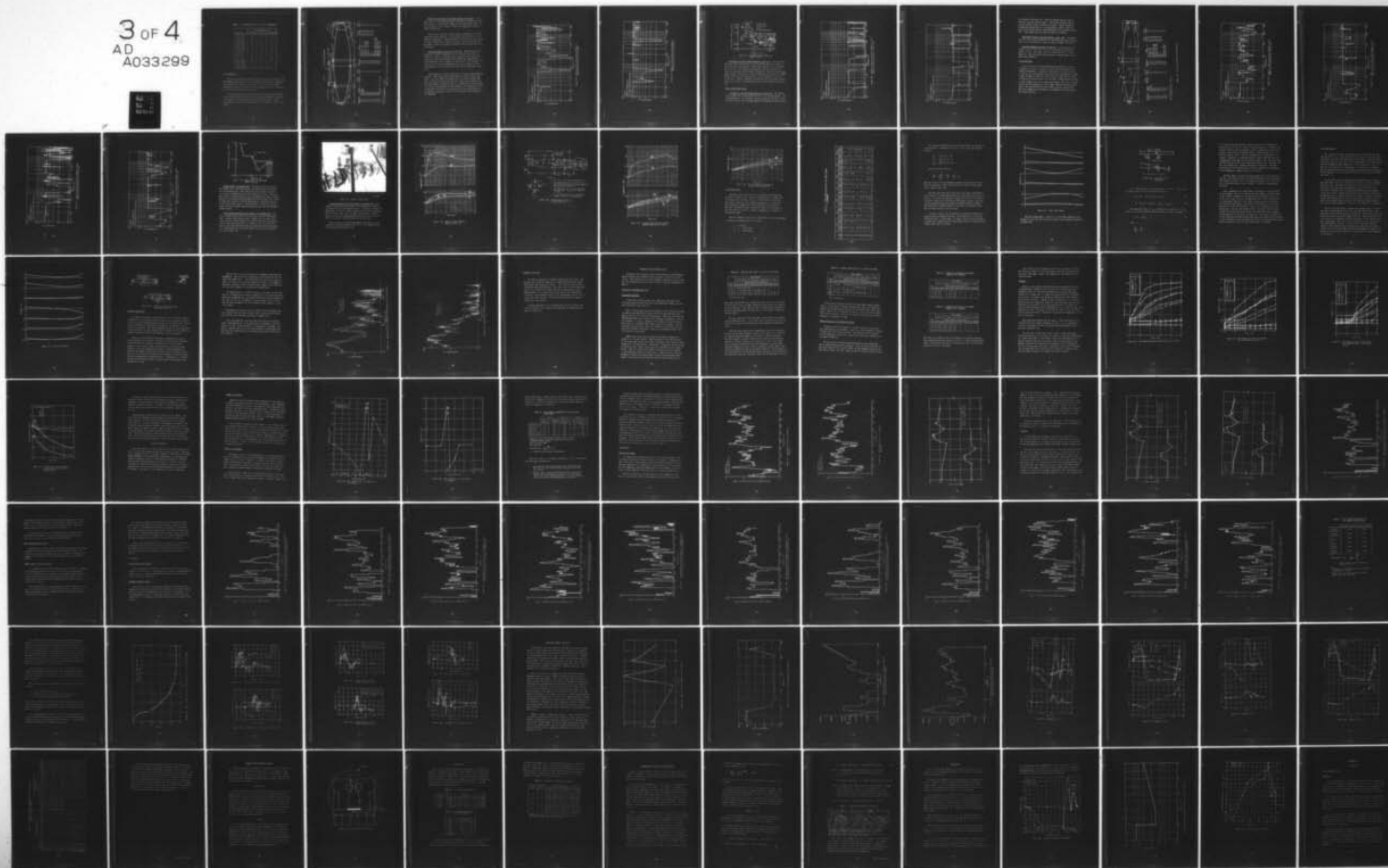
TABLE 23. PRESSURE CHECK AT 75 F UNIT TEMPERATURE

Gage No.	Gage Readings, mv		
	0 psig	10 psig	20 psig
Stress #18	- 30	- 19	- 9
Stress #21	- 5	+ 4	+ 13
Stress #22	- 13	- 3	+ 7
Stress #23	- 23	- 14	- 4
Stress #24	+ 8	0	- 9
Stress #26	- 5	+ 4	+ 13
Strain #17	- 17	- 17	- 16
Strain #1	- 4	- 4	- 3
Strain #2	+127	+125	+124
Shear #101	+ 46	+ 48	+ 50
Shear #SH-2	+ 64	+ 71	+ 77
Shear #120A	- 1	- 2	- 3
Shear #120B	- 7	- 6	- 5

Z Axis (Vertical)

One of the initial concerns was transmissibility and control of the BDU during vibration with what was thought to be a very soft mounting system when using the MAU-12A/C launcher. For this reason a hard mounting system was included in the test program. The first vibration test was with the hard mounting system.

Besides the instrumentation shown earlier in the propellant grain section, additional accelerometers, Figure 128, were placed on the unit to define the vibration mode(s) of the total test vehicle. These accelerometer locations were maintained for all vibration tests in the Z axis.

176

Channel*	Gage	Plug Pin No.	Active Axis
A-1	Launcher		Z
A-2	Launcher		Z
A-3	Case		Z
A-4	Case		X
A-5	Case		Z
A-6	Case		Z
A-7	Case		X
A-8	Case		Z
A-9	Case		Z
A-10	Case		Z
A-11	Case		X
A-12	Triaxial – CG	39, 52	X

Channel*	Gage	Plug Pin No.	Active Axis
A-13	Triaxial – CG	40, 52	Y
A-14	Triaxial – CG	41, 51	Z
A-15	Triaxial – Aft End	45, 52	X
A-16	Triaxial – Aft End	47, 52	Y
A-17	Triaxial – Aft End	49, 52	Z
A-18	Lug 1	42, 52	Z
A-19	Lug 2	45, 52	Z
A-20	CEC	33, 34	Y
A-21	Impedance Head Forward		Z
F-22	Impedance Head Forward		Z
A-23	Impedance Head Aft		Z
F-24	Impedance Head Aft		Z

* A – Accelerometer, F – Force

Figure 128. Location of External Instrumentation

177

Hard-Mount Sine Sweep with Impedance Head, 30 June 1971. A 1-g input level was maintained during the sweep from 10 to 2000 Hz at 0.63 octaves/minute. Accelerometer channels 5 and 8 were used as dual controls during the sweep. Replots of these two channels are shown in Figures 129 and 130.

Data revealed that some of the internal instruments were showing impacting between components. The on-board flight recorder was also running intermittently. During coordination discussions it was decided to conduct subsequent testing at 0.5-g input. NWC also modified the attachment of the tape recorder to minimize vibration chattering within its carriage.

Hard-Mount Random Vibration, 1 July 1971. Random vibration was conducted at ambient temperature with the scheduled input shown in Figure 131. However, the BDU was generating sufficient energy from shaker input below about 1000 Hz that no additional shaker energy was required above this frequency to complete the total spectrum. The duration of the test was determined by the time necessary to obtain both ground-station and on-board recording systems data, about 3 minutes.

Random data were reduced in analog form through an ASD-80 spectral analyzer. These data revealed high responses between 1250 and 1750 Hertz. Since all shaker excitation power at frequencies above 1000 Hertz had already been filtered out, the response was clearly resulting from sympathetic harmonics that are a characteristic of the mechanical system. The amplitudes of these harmonics were reducible by lowering the power density at certain frequencies (such as 300 Hertz), but it appeared the harmonics could not be eliminated without mechanical rearrangement.

178
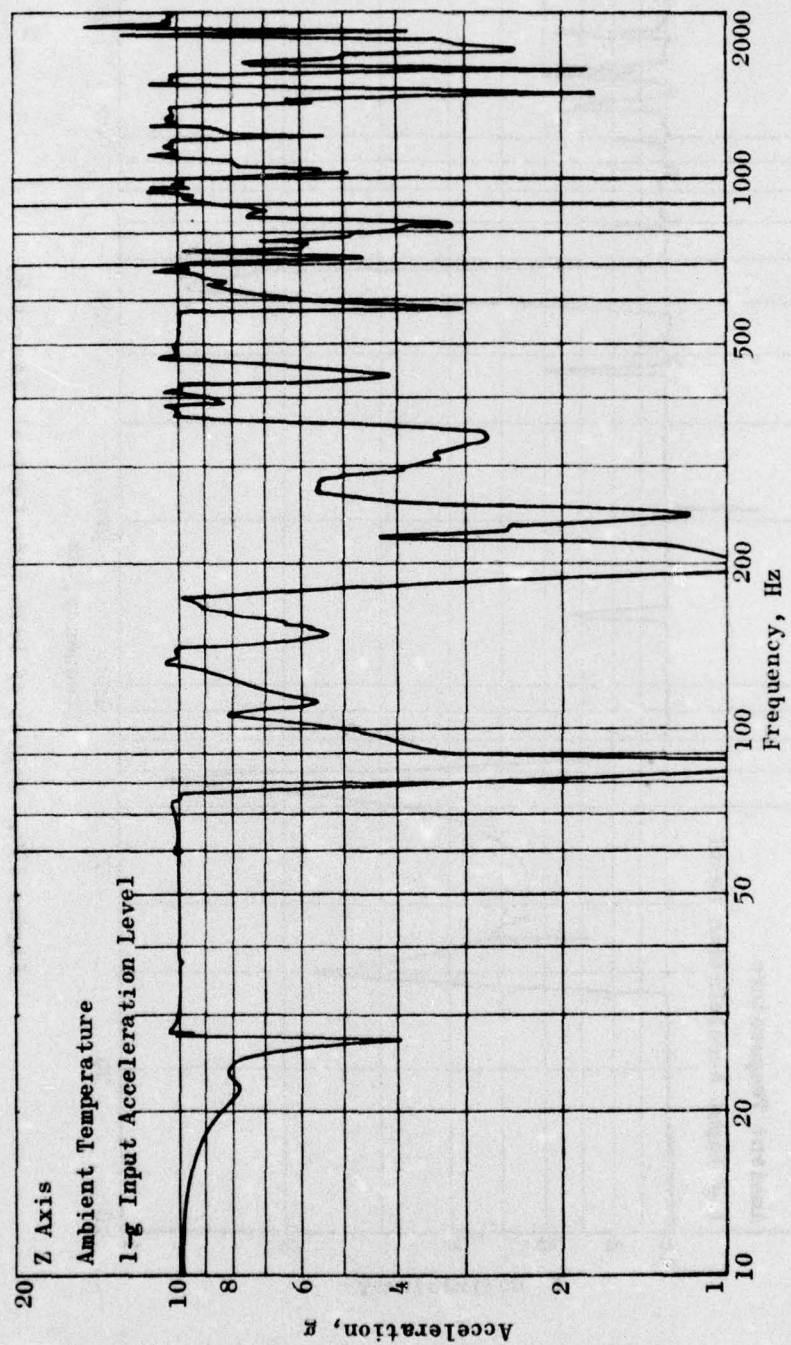
Figure 129. Replot of Data from Control Channel 5,
Hard-Mount Sine Sweep, 30 June 1971

179
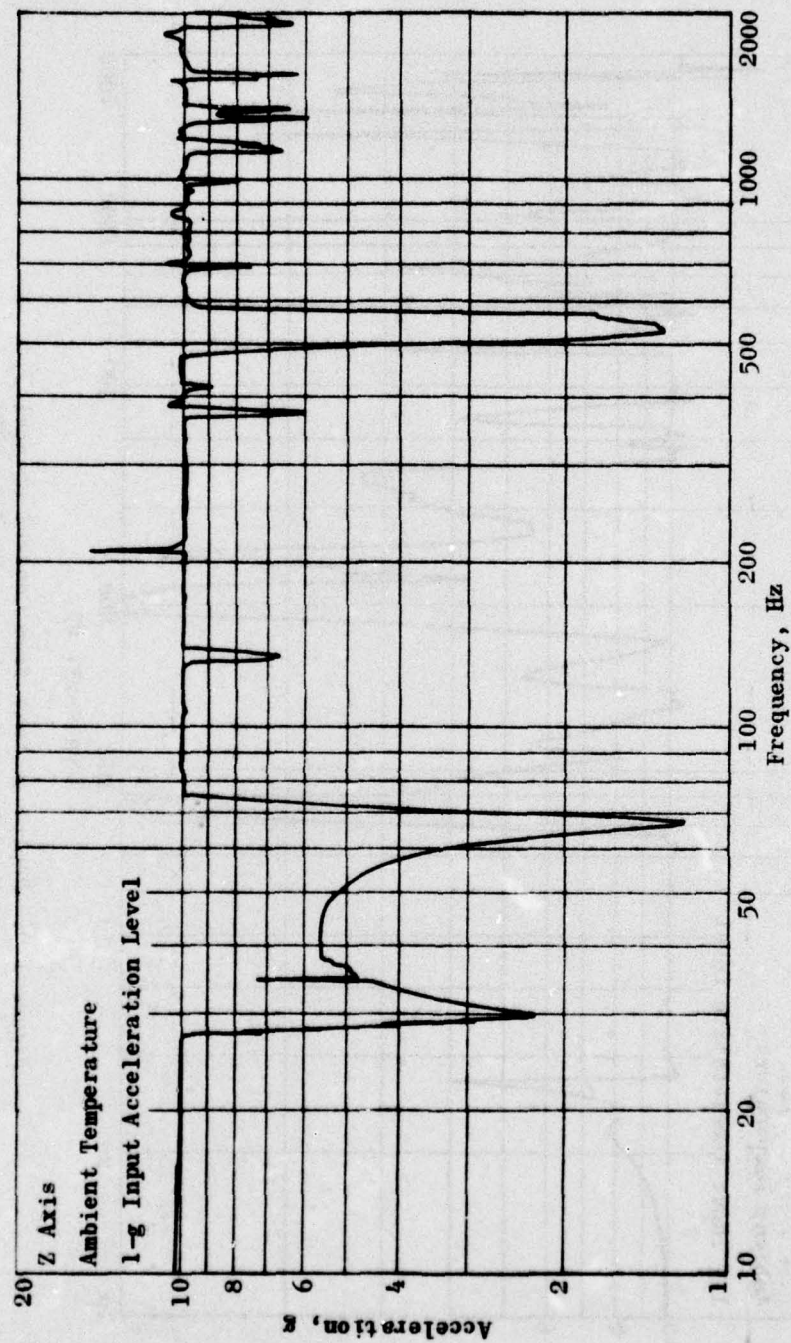
Figure 130. Replot of Data from Control Channel 8, Hard-Mount Sine Sweep, 30 June 1971

180
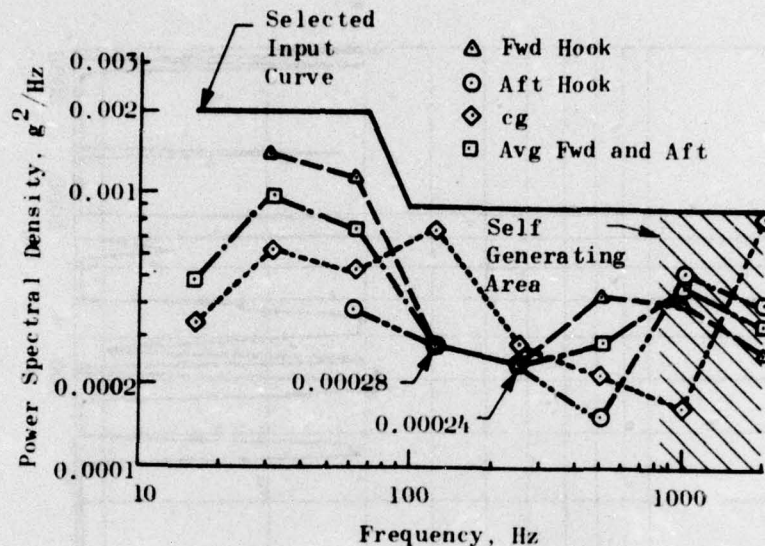
Figure 131. Hard-Mount Random Vibration
Input, Z Axis

Soft-Mount 0.5-g Sine Sweep Vibration, 6 July 1971. The soft-mount
0.5-g sine sweep vibration more closely simulated the actual flight test
due to the use of the launcher. Dual control channels were used during
this test also. One difference between this test and the other sine
tests was the input g level, Figures 132 and 133. Because of the loading
amplification on the previous 1-g test and difficulties with the on-board
flight recorder at this loading level, a 0.5-g loading level was used
on this test. However, problems still existed with the on-board recorder,
and it was returned to the manufacturer for a quick check before the next
test.

X Axis Tests (Transverse)

Soft-Mount 0.5-g Sine Sweep Vibration, 13 July 1971. The reduced
g level input load was maintained for X-axis sine vibration sweeps. The
instrumentation in the propellant section remained the same due to lack
of access; however, the externally applied instrumentation was relocated

181
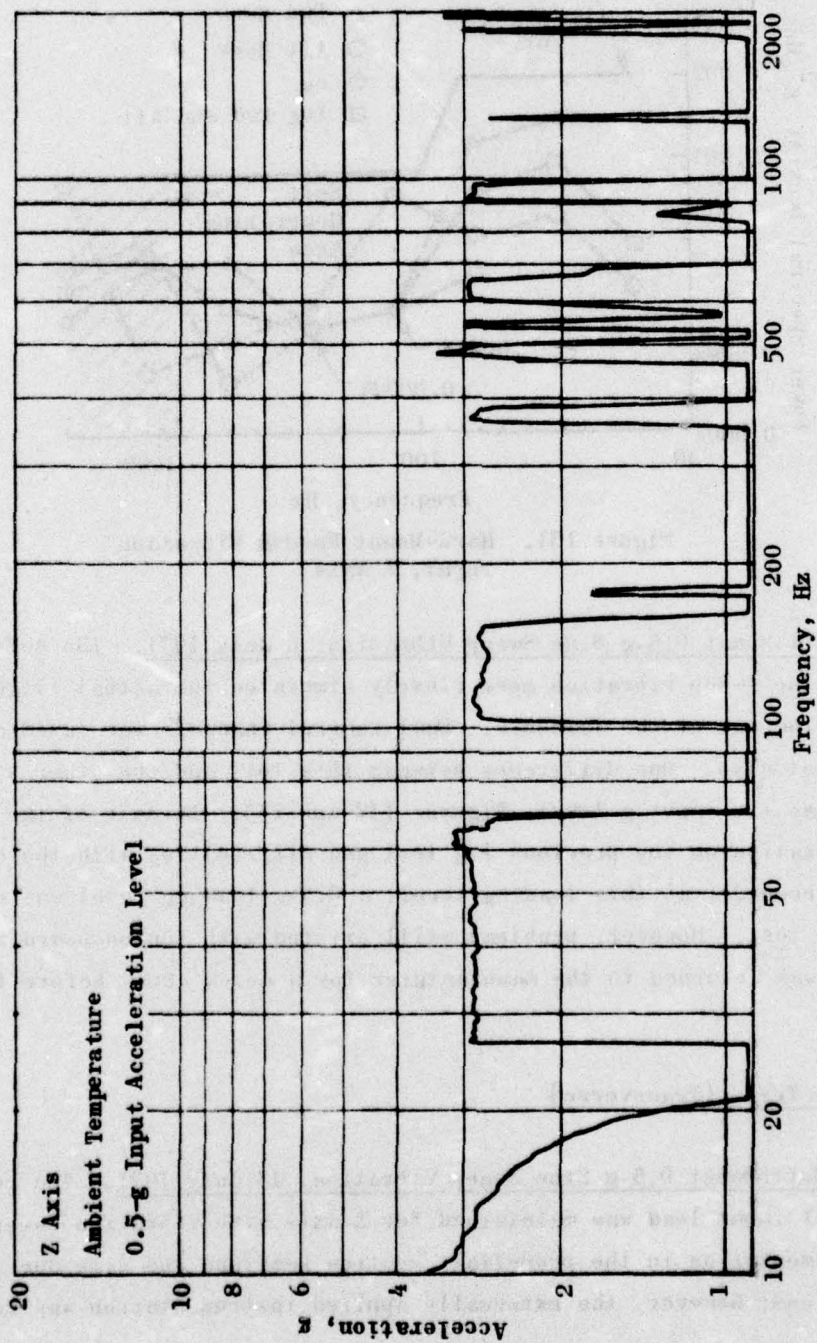
Figure 132. Replot of Data from Control Channel 5, Soft-
Mount Sine Sweep Vibration, 6 July 1971

182
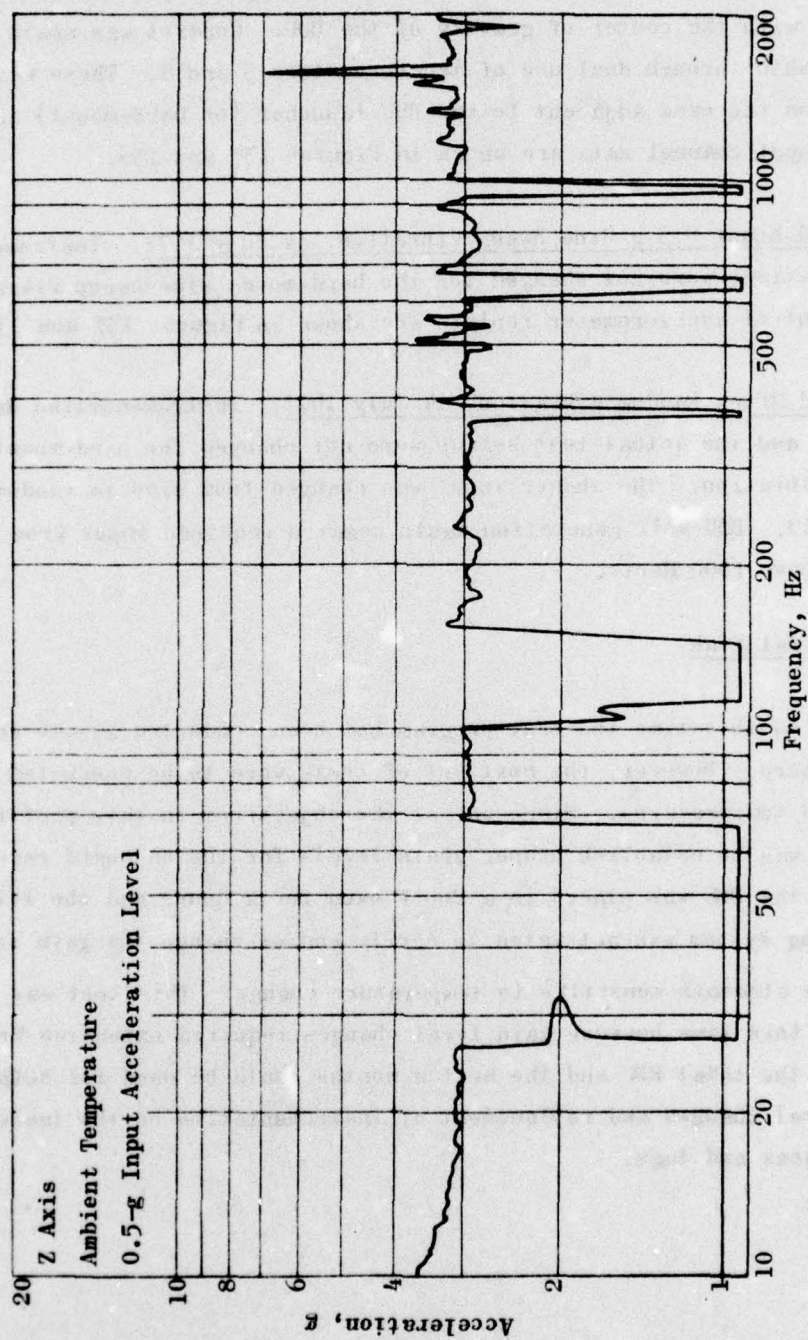
Figure 133. Replot of Data from Control Channel 8, Soft-Mount Sine Sweep Vibration, 6 July 1971

in accordance with Figure 134. Only one impedance head was used in this axis since the vibrator input to the tooling was positioned to coincide with the center of gravity of the BDU. Control was again accomplished through dual use of Accelerometers 5 and 8. These were located on the case adjacent to the BDU/launcher (or hard-mount) interface. Input channel data are shown in Figures 135 and 136.

Hard-Mount 0.5-g Sine Sweep Vibration, 14 July 1971. Instrumentation locations were not changed for the hard-mount sine sweep vibration. Input control accelerometer replots are shown in Figures 137 and 138.

Hard-Mount Random Vibration, 14 July 1971. Instrumentation data channels and the actual test set-up were not changed for hard-mount random vibration. The shaker input was changed from sine to random. Figure 139. BDU self generation again negated required input from the shaker above 1000 Hertz.

BDU Thermal Soak

Up to this time the test program had been conducted at ambient temperature. However, the next set of tests were to be conducted at elevated temperatures. Since one of the objectives in this preflight testing was to establish proper grain levels for the on-board recording system, the BDU was placed in a 200 F oven for 2 hours and the flight recording system was activated to verify and/or change the gain settings on those elements sensitive to temperature change. This test was scheduled at this time because gain level changes required extensive breakdown of the total BDU and the next 2 months could be used for both gain level changes and replacement of instrumentation on the launcher sway braces and lugs.
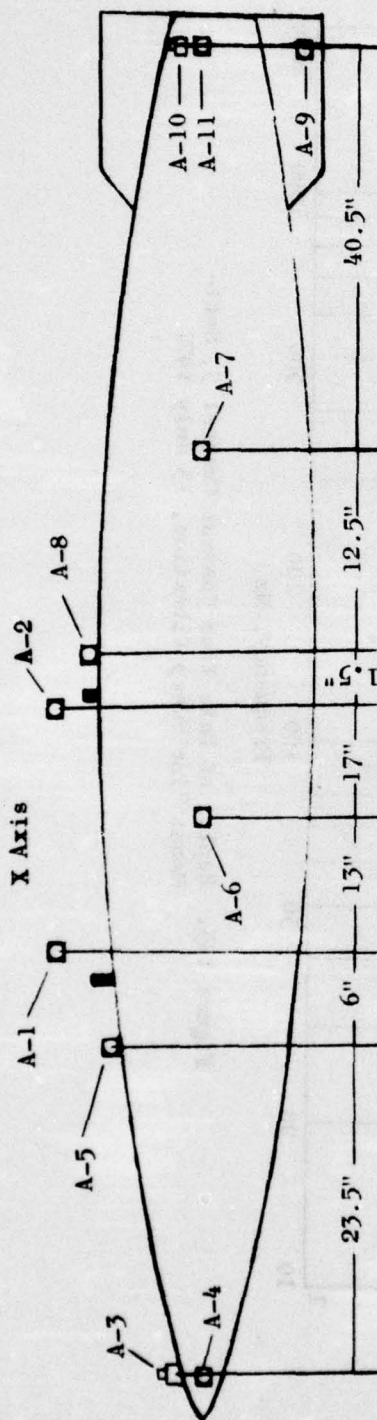
Channel*	Gage	Plug Pin No.	Active Axis
A-1	Control		X
A-2	Control		X
A-3	Case		Z
A-4	Case		X
A-5	Case		X
A-6	Case		X
A-7	Case		X
A-8	Case		X
A-9	Case		X
A-10	Case		Z
A-11	Case		X

Channel*	Gage	Plug Pin No.	Active Axis
A-12	Triaxial CG	39, 52	X
A-13	Triaxial CG	40, 52	Y
A-14	Triaxial CG	41, 52	Z
A-15	Triaxial Aft End	45, 46	X
A-16	Triaxial Aft End	47, 48	Y
A-17	Triaxial Aft End	49, 50	Z
A-18	Lug 1	42, 52	Z
A-19	Lug 2	33, 34	Y
A-20	CEC	33, 34	Y
A-21	Impedance Head 1	33, 34	X
F-22	Impedance Head 1		X

* A - Acceleration, F - Force

Figure 134. Relocated External Instrumentation
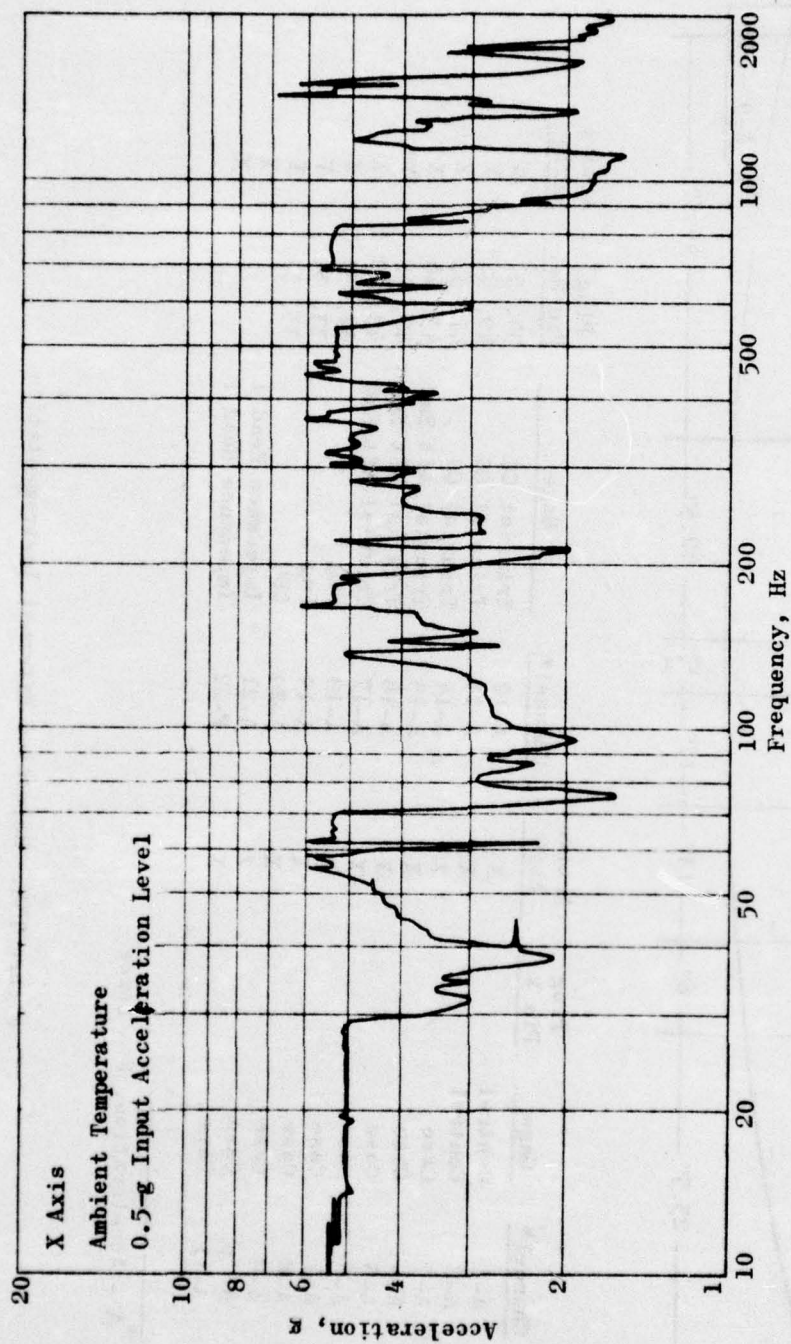
Figure 135. Replot of Data from Control Channel 5, Soft-Mount Sine Sweep Vibration, 13 July 1971

186
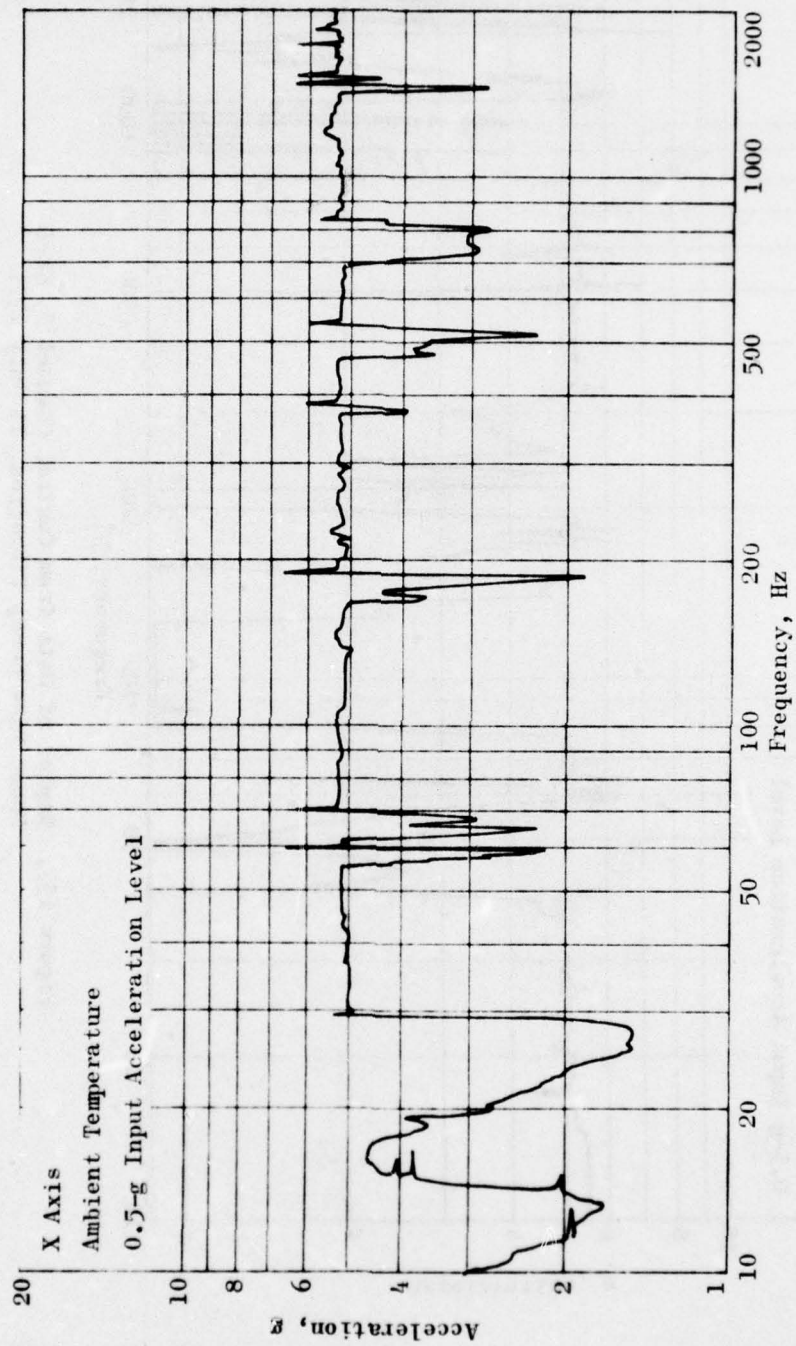
Figure 136.   Replot of Data from Control Channel 8, Soft-Mount Sine Sweep Vibration, 13 July 1971

187
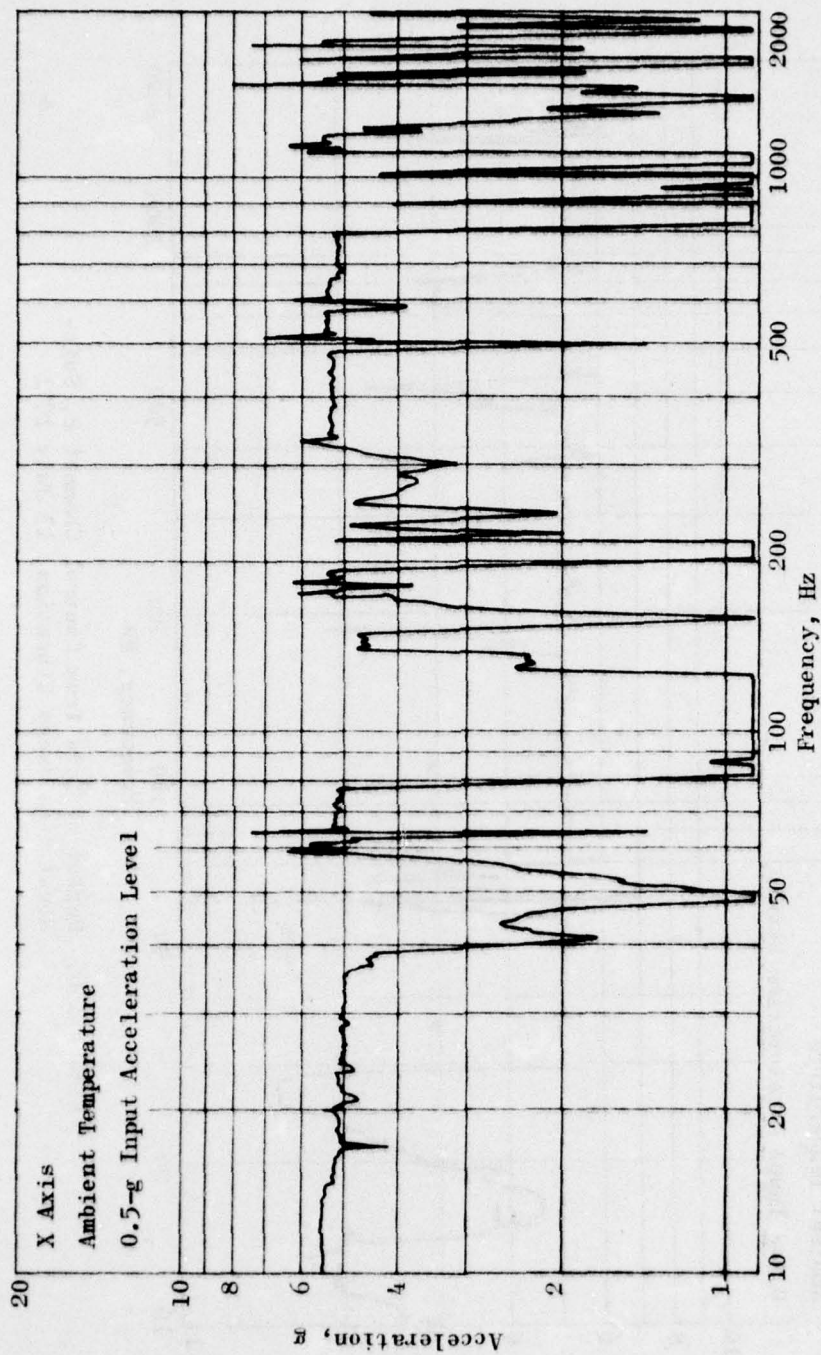
Figure 137. Replot of Data from Control Channel 5, Hard-Mount Sine Sweep Vibration, 14 July 1971

188
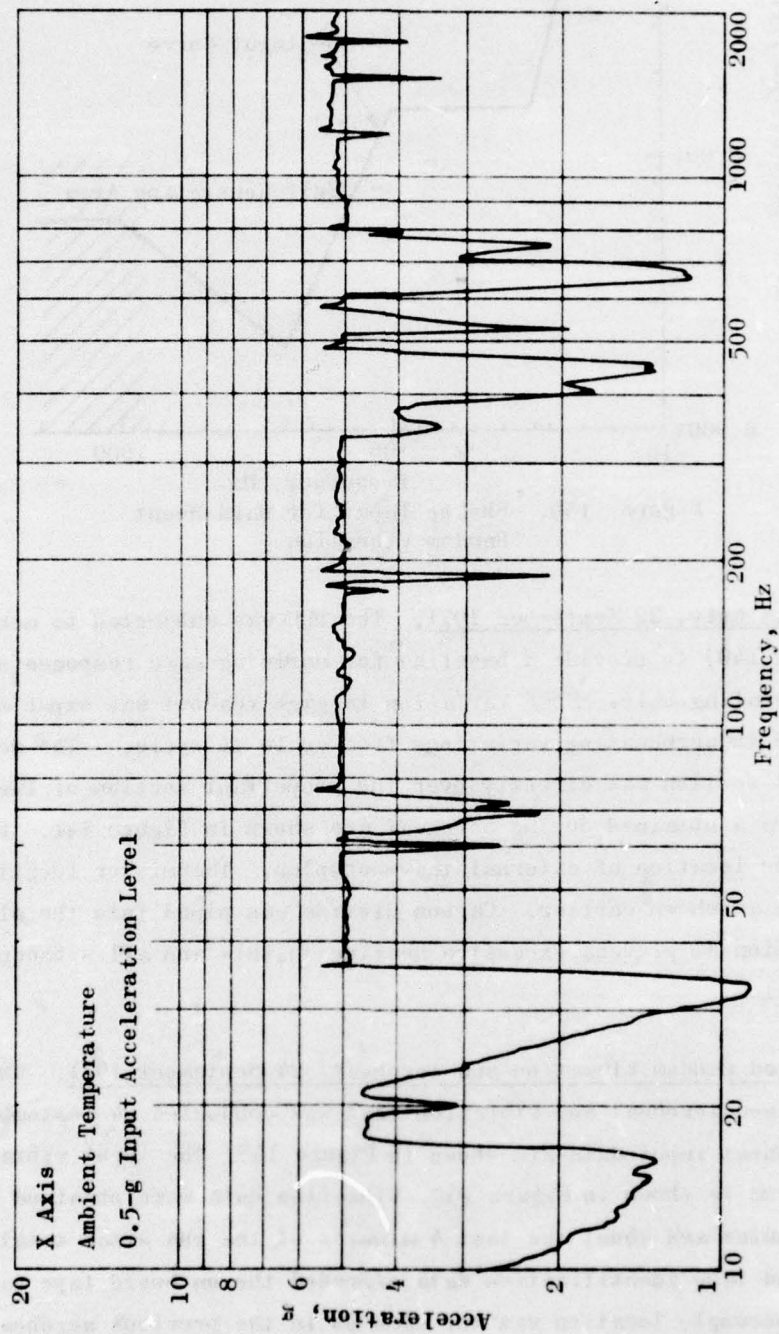
Figure 138. Replot of Data from Control Channel 8, Hard-Mount Sine Sweep Vibration, 14 July 1971

189
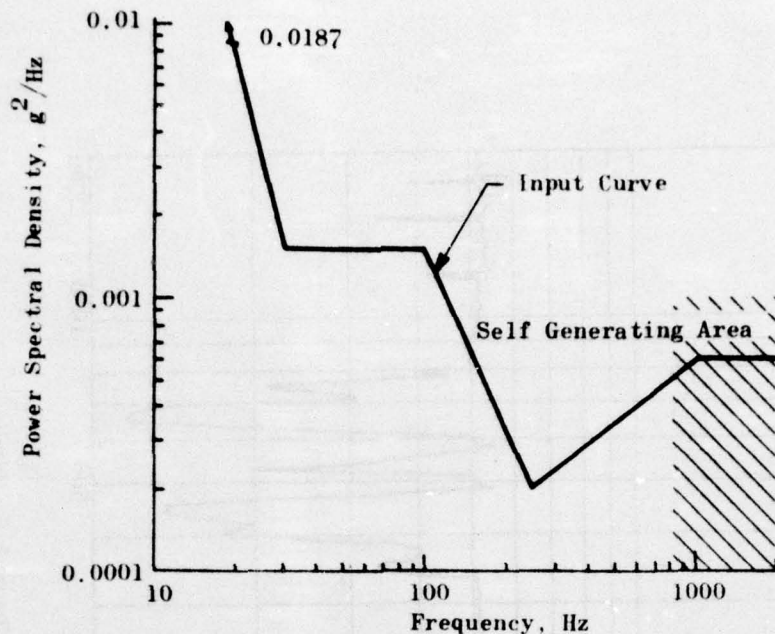
Figure 139. Shaker Input for Hard-Mount
Random Vibration

Aeroheat Only, 22 September 1971. The BDU was subjected to aero-
heat (Figure 140) to provide a baseline for defining gage response(s)
due to aeroheating only. Some variation in gage readout was expected
to occur due to aeroheating variations from cycle to cycle.   The aero-
heat control section was directly over the propellant section of the BDU.
Replots of data obtained during aeroheat are shown in Figure 141. Figure
142 shows the location of external thermocouples. Thermistor location
was the same as shown earlier. Carbon dioxide was piped into the elec-
tronics section to prevent excessive heating on this and all subsequent
aeroheat cycles.

Combined Random Vibration and Aeroheat, 24 September 1971.   The
first combined aeroheat and vibration test was conducted 24 September
1971. Aeroheat input data are shown in Figure 143. The input vibra-
tion spectrum is shown in Figure 139. Vibration data were obtained the
first 4 minutes and about the last 4 minutes of the run since total
run time and tape identification data exceeded the on-board tape capac-
ity. Thermocouple location was the same as in the previous aeroheat-
only cycle, Figure 142.

190
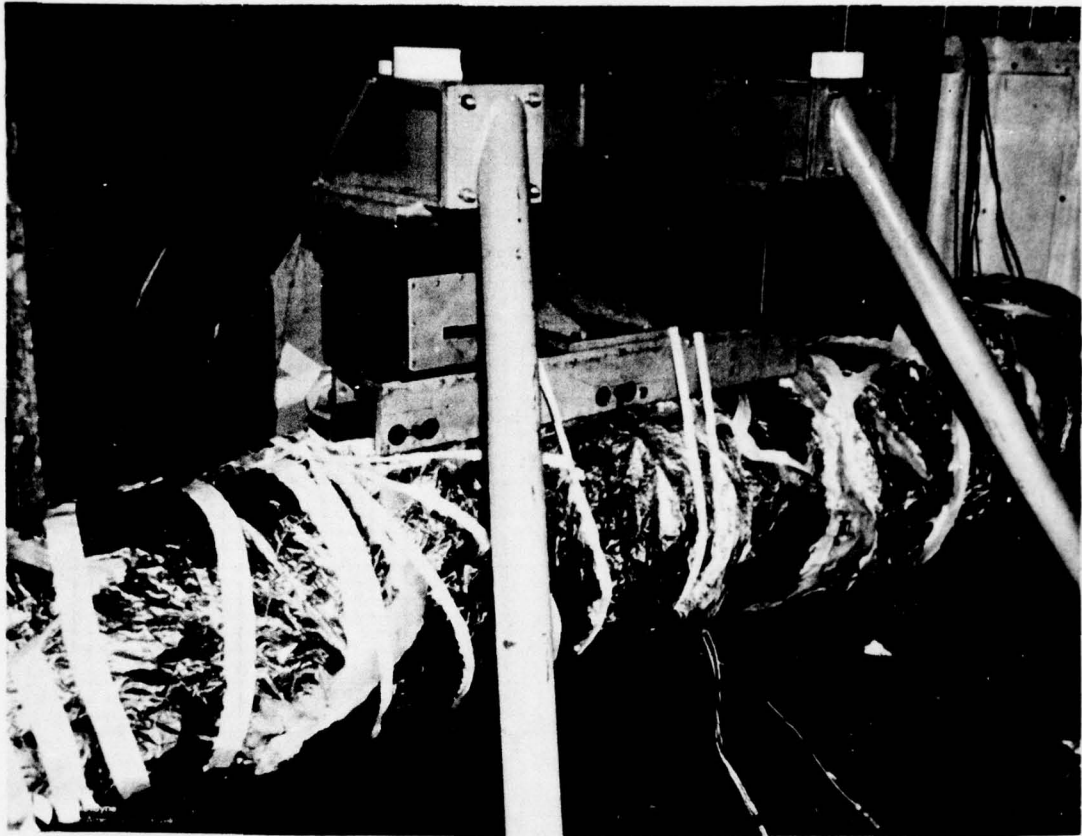
71-789

Figure 140. Aeroheat Setup for BDU

Combined Random Vibration and Aeroheat, 28 September 1971. The
combined random vibration and aeroheat on 28 September 1971 completed
the planned tests for verifying the integrity of the BDU for flight test.
Thermocouple locations are shown in Figure 142; resulting case aeroheat
data are shown in Figure 144. The input vibration curve is shown in
Figure 131. The data accumulation plan on this test was the same as
that of the previous combined aeroheat and vibration cycle.

Spectral analysis of several data channels early and late in the
aeroheat run shows the response of the unit was only slightly altered
by the temperature gradient and rise.

191
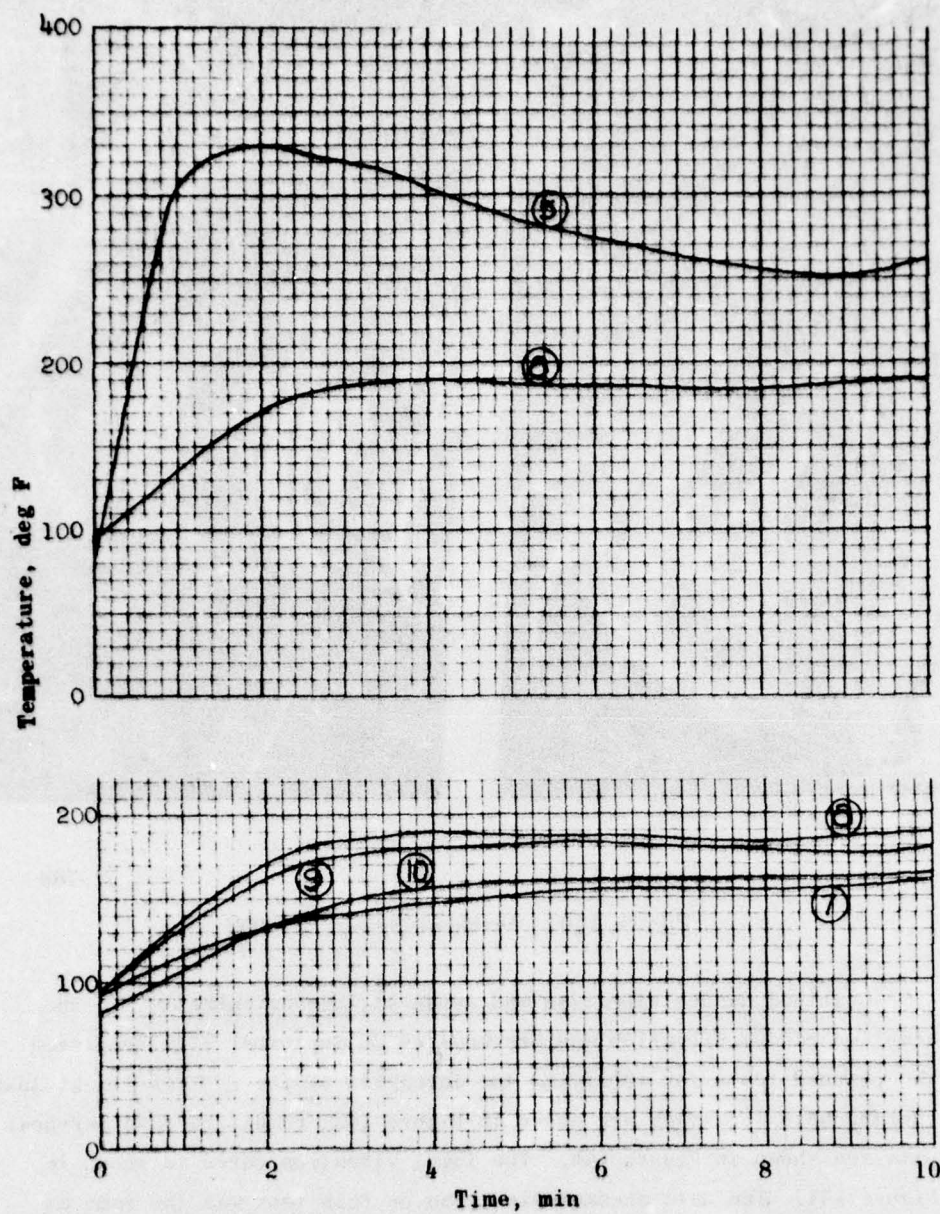
Figure 141. Replots of Data Obtained
During Aeroheat Only
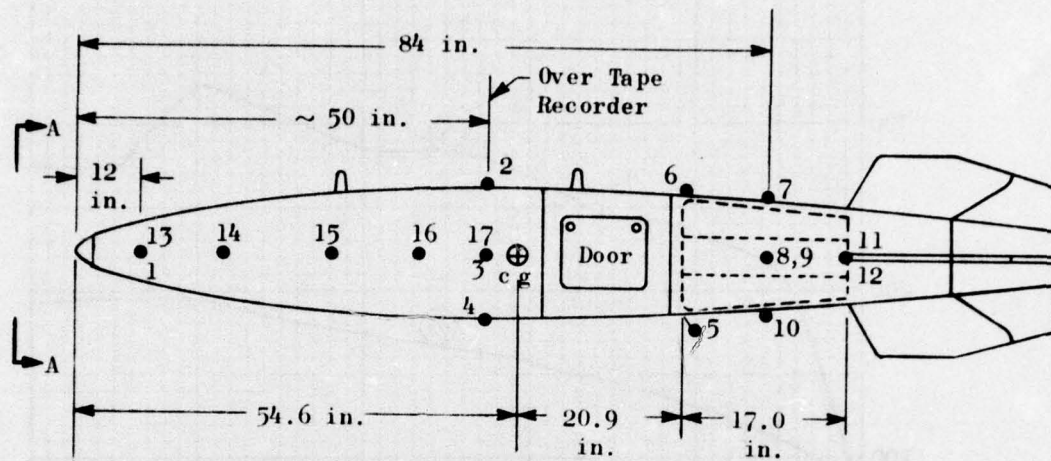
Notes:

1. T.C.'s 7, 8, 9, 10 are control T.C.'s.

2. Five additional T.C.'s (13, 14, 15, 16, and 17) will be located directly opposite NWC installed internal T.C.

3. One additional T.C. will be located on tape recorder. Max temp for this T.C. is 100 F.

4. T.C.'s 5 and 12 will be ~ 1 inch from surface to measure air temperature.
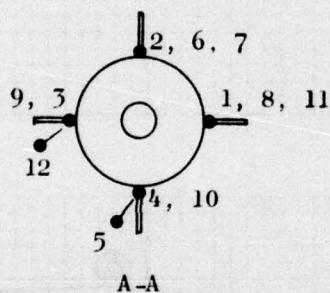
Figure 142. Thermocouple Location for Aeroheat Cycle(s)

193
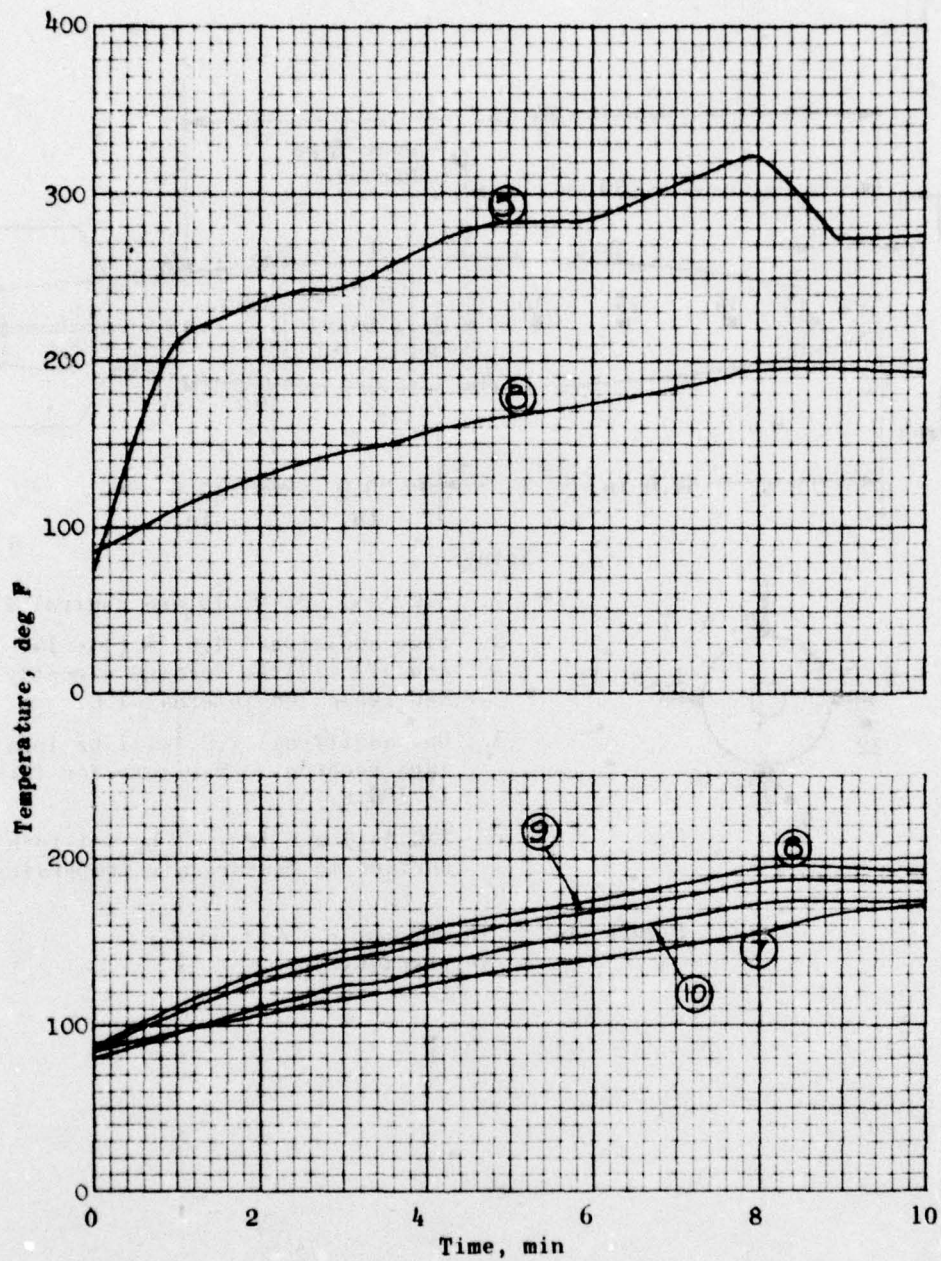
Figure 143. Aeroheat Input Data for Combined
Random Vibration and Aeroheat

194
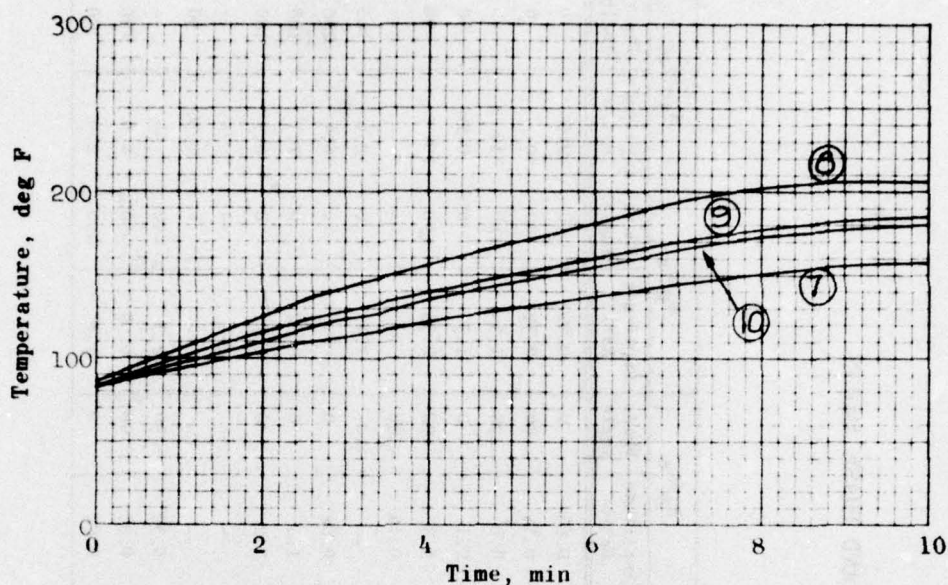
Figure 144. Data from Random Vibration and
Aeroheat, 28 September 1971

Z-AXIS MODE SHAPES

During a review of the ratios of accelerometers Rocketdyne had
attached to the BDU, it was found that complex motion was experienced
during the Z-axis vibration testing. The accelerometer ratios and
phase angles (related to Accelerometer 8, which was used with A-5 in
dual control) were summarized at what appeared to be resonant fre-
quencies. The data are shown in Table 24. Some of the data that ap-
pear more directly related to resonance conditions were replotted to
display mode shapes.

From the standpoint that the test vehicle was excited by and assumed
to respond to sinusoidal motion, for input:

$$x = A \sin(\omega t)$$
$$\dot{x} = v = A\omega \cos(\omega t)$$
$$\ddot{x} = a = A\omega^2 \sin(\omega t)$$

195

TABLE 24. Z AXIS AMPLITUDE RATIOS AND PHASE ANGLES IN DEGREES

Frequency, Hz	A_1/A_8		A_2/A_8		A_3/A_8		A_4/A_8		A_5/A_8		A_6/A_8		A_{10}/A_{14}	
	Amplitude Ratio	Phase Angle	Amplitude Ratio	Phase Angle	Amplitude Ratio	Phase Angle	Amplitude Ratio	Phase Angle	Amplitude Ratio	Phase Angle	Amplitude Ratio	Phase Angle	Amplitude Ratio	Phase Angle
19	0.73	0	0.84	0	0.36	0	0.14	0	0.63	0	0.96	-90	2.5	0
25	0.42	90	0.36	0	9.0	90	0.17	90	0.34	90	0.59	90	10+	0
27	5.3	90	1.92	0	9.6	90	0.79	0	5.0	90	1.5	180	>10	--
45	1.65	0	1.1	0	3.1	0	0.31	0	2.1	0	1.3	0	0.28	90
60	4.1	-90	0.33	-90	10+	-90	1.6	0	5.5	-90	0.38	-90	10+	-90
72	0.35	-90	0.62	0	0.17	-90	0.16	90	0.14	-180	--	--	--	--
83	--	--	--	--	--	--	--	--	--	--	1.4	0	2.0	180
92	0.56	0	0.52	0	--	--	0.8	-180	0.62	0	--	--	6.4	180
96	0.46	0	0.38	0	2.45	0	--	--	1.4	0	0.62	0	1.7	180
126	1.25	0	2.15	90	8.7	-90	0.33	90	3.2	0	0.72	0	6.9	180
140	0.57	0	--	--	4.3	-90	1.3	90	--	--	--	--	--	--
150	0.82	0	--	--	--	--	2.1	0	--	--	--	--	0.36	90
165	0.5	0	0.69	0	1.35	-180	3.7	-90	0.32	-90	2.5	-90	--	--
170	0.94	0	1.8	0	3.5	-180	--	--	0.95	-90	0.99	-90	4.0	180
210	1.0	90	2.0	90	2.5	-180	0.31	0	0.22	0	4.1	-90	2.0	90

The response displacement and acceleration might lag the input by a phase angle φ. (Resonance occurs at $\varphi = 90°$.) Then the response would be

$$x_R = A_R \sin (\omega t + \varphi)$$

$$\dot{x}_R = A_R \omega \cos (\omega t + \varphi)$$

$$\ddot{x}_R = A_R \omega^2 \sin (\omega t + \varphi)$$

The ratios would then give

$$\frac{\ddot{x}_R}{\ddot{x}} = \frac{A_R \omega^2}{A \omega^2} = \frac{A_R}{A} = \frac{x_R}{x} \quad \text{at } \varphi$$

Thus the ratios of the accelerometer signals served as ratios of displacement amplitude. These ratios were used to plot the mode shape curves shown in Figure 145.

The mode shape curves were referenced to an input accelerometer, A-8, attached to the BDU approximately 8.5 inches behind the center of gravity. This particular method of display was chosen to facilitate a convenient comparison of the measured BDU dynamic response to the analytical predictions previously made by Lockheed Propulsion Company. The BDU/launcher assembly response is defined by the impedance head data described earlier in this section.

As shown in Figure 145, the normalized displacement amplitude is plotted along the length of the BDU. The forward end is to the left and the aft end is to the right. It appears that there were two basic response modes, typified by the "beam tipping" mode at 27 Hertz and the "beam flexure" mode at 60 Hertz.
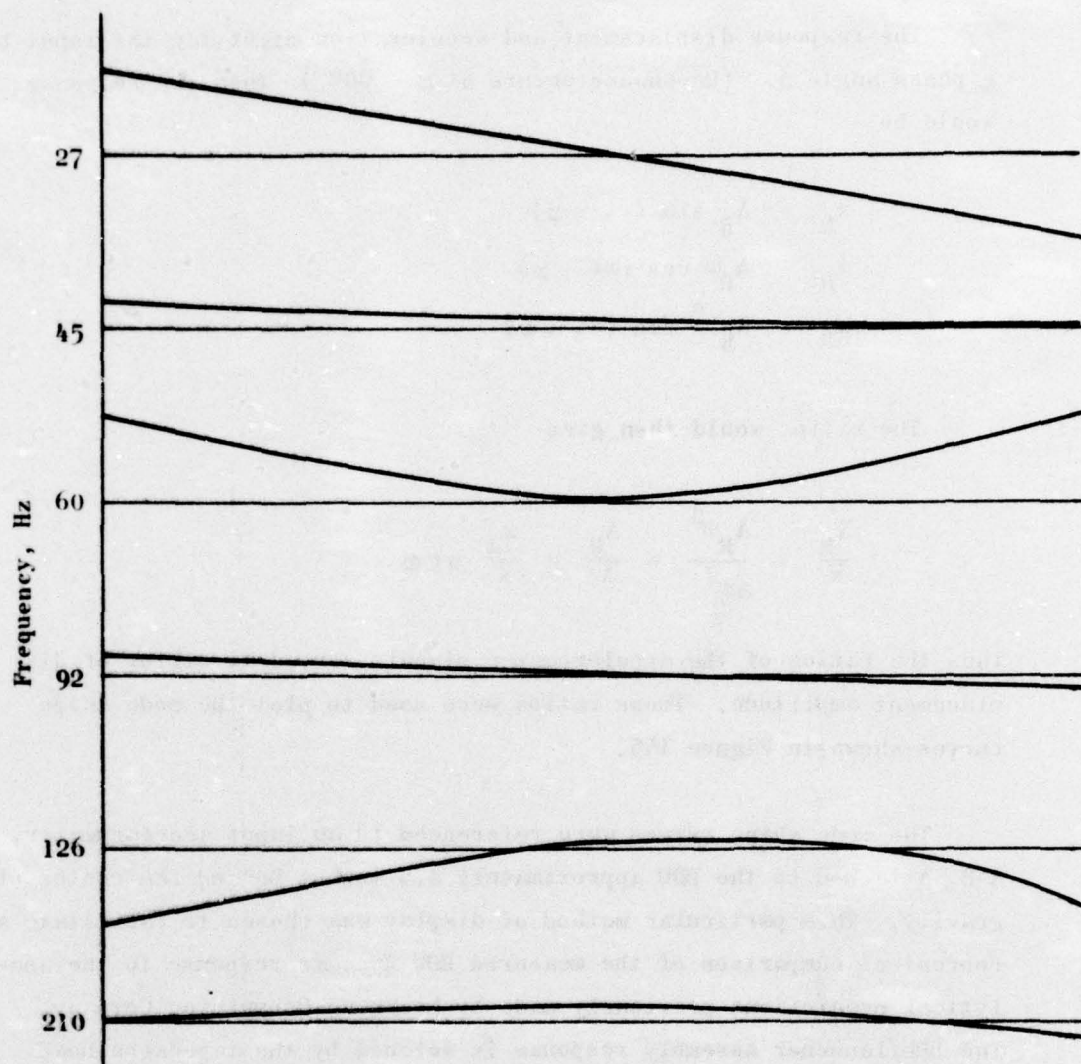
Figure 145. Z-Axis Mode Shapes

The beam tipping mode is typical of a stiff beam supported by two springs (in this case the fore and aft ends of the launcher) as sketched in Figure 146.

(a) Model Beam

(b) Generalized Coordinates
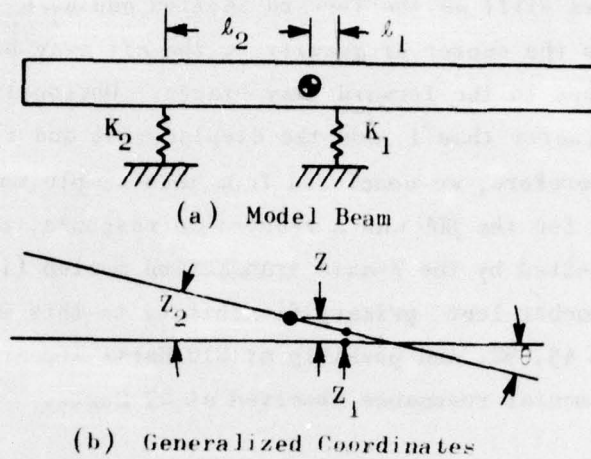
Figure 146. Simplified Stiff
Beam Model

It is observed that the two generalized coordinates, x and θ, may
be used to derive the two equations shown below:

$$m\ddot{Z} + (K_1 + K_2)\, Z - (K_1\, \ell_1 - K_2\, \ell_2)\, \theta = 0 \tag{1}$$

$$I\ddot{\theta} + (K_1\, \ell_1^2 + K_2\, \ell_2^2)\, \theta - (K_1\, \ell_1 - K_2\, \ell_2)\, Z = 0 \tag{2}$$

The combination $(K_1\, \ell_1 - K_2\, \ell_2)$ couples these equations. If this
term is set to zero, then the equations would no longer be coupled. If

$$K_1\, \ell_1 - K_2\, \ell_2 = 0 \tag{3}$$

then

$$\frac{K_1}{K_2} = \frac{\ell_2}{\ell_1} \tag{4}$$

But in the case of the BDU tests, the aft section of the launcher was very nearly as stiff as the forward section and $K_1/K_2 \approx 1$. However, the distance from the center of gravity to the aft sway braces was 0.6 inch and 20.6 inches to the forward sway braces. Obviously ℓ_2/ℓ_1 was substantially greater than 1, and the displacement and tipping modes were coupled. Therefore, we concluded from this simple model that the beam tipping mode for the BDU was a reasonable response, that this mode could indeed be excited by the Z-axis translation motion (i.e., coupling), and that the launcher lent primary flexibility to this mode. The modes occurring at 45, 92, and possibly at 210 Hertz appeared to be harmonics of the fundamental resonance observed at 27 Hertz.

The mode shape occurring at 60 Hertz appeared to be the beam bending mode. The linear nature of the forward end deflections substantiated the stiffness of that section. Flexing would appear to be in the thinner section toward the aft end. A harmonic occurred at approximately 126 Hertz.

Other components were contributing to and being excited by the BDU Z-axis response. The fins on the aft end, for example, responsed loudly at the 27-Hertz frequency. At 165 Hertz, X-axis response was excited by the Z-axis input such that the amplitude ratio at the forward end was 3.7, and greater than 10 at the center of gravity and on the aft fins. The triaxial accelerometers showed Y-axis excitation up to 1 g at frequencies of 27, 66, and 170 Hertz. Y-axis cross response was not too significant. However, the response in the X axis was at times as high as that in the direction being driven. The magnitude of this response, and the apparent low energy level required to excite this cross mode led to the conclusion that BDU motions along the X-axis should be the limiting criteria relating to adjusting data band widths for the acquisition system, and to evaluation of the structural requirements of the unit.

200

X-AXIS MODE SHAPES

The technique previously described was used to determine BDU mode shapes in the X-axis. Again, these modes are referenced to Accelerometer 8 attached to the BDU just behind the aft launch lug. Normalized output signals are shown in Figure 147. These shapes appear to be variations of the same fundamental mode, amplified at certain frequencies (e.g., 25 Hertz) by the flexibility of the launcher. Nevertheless, it appeared that the beam flexure mode was the primary response modified by resonance of BDU components such as the launcher, fins, recorder, and instrumentation racks, etc.

In addition to the acceleration (or displacement) ratios taken to show mode shapes relative to control Accelerometer 8, transfer impedance plots were made. Instrument locations are shown in Figure 148. Unfortunately, the phase angle measurements for the F/A-7 and F/A-11 ratios were erroneous due to recording and playback head misalignment on the tape recorder. (Much time and effort were expended adjusting the alignment and most of the other data were recovered. However, the alignment was particularly tedious for the rapid surveys required to accommodate the on-board flight recorder.) The other phase angle channels were correct and the amplitude ratios were close enough for our purposes.

Review of the data showed a primary bell-ringing mode at 11.5 Hertz and other strong resonance modes at 60, 90, 180, and 600 Hertz. The mode shapes agree with those shown in Figure 147 and provide a more comprehensive overview of the BDU dynamic behavior. The measurement of motion relative to a different reference point more clearly elucidated the bell-ringing mode. The use of the force (measured at the input excitation point), and the response at several spots on the BDU, provided transfer coefficient data that the analyst may compare with stiffness coefficients in a finite element stiffness method dynamic (computerized) analysis, or more directly, may use to show the more flexible components of the system.

201
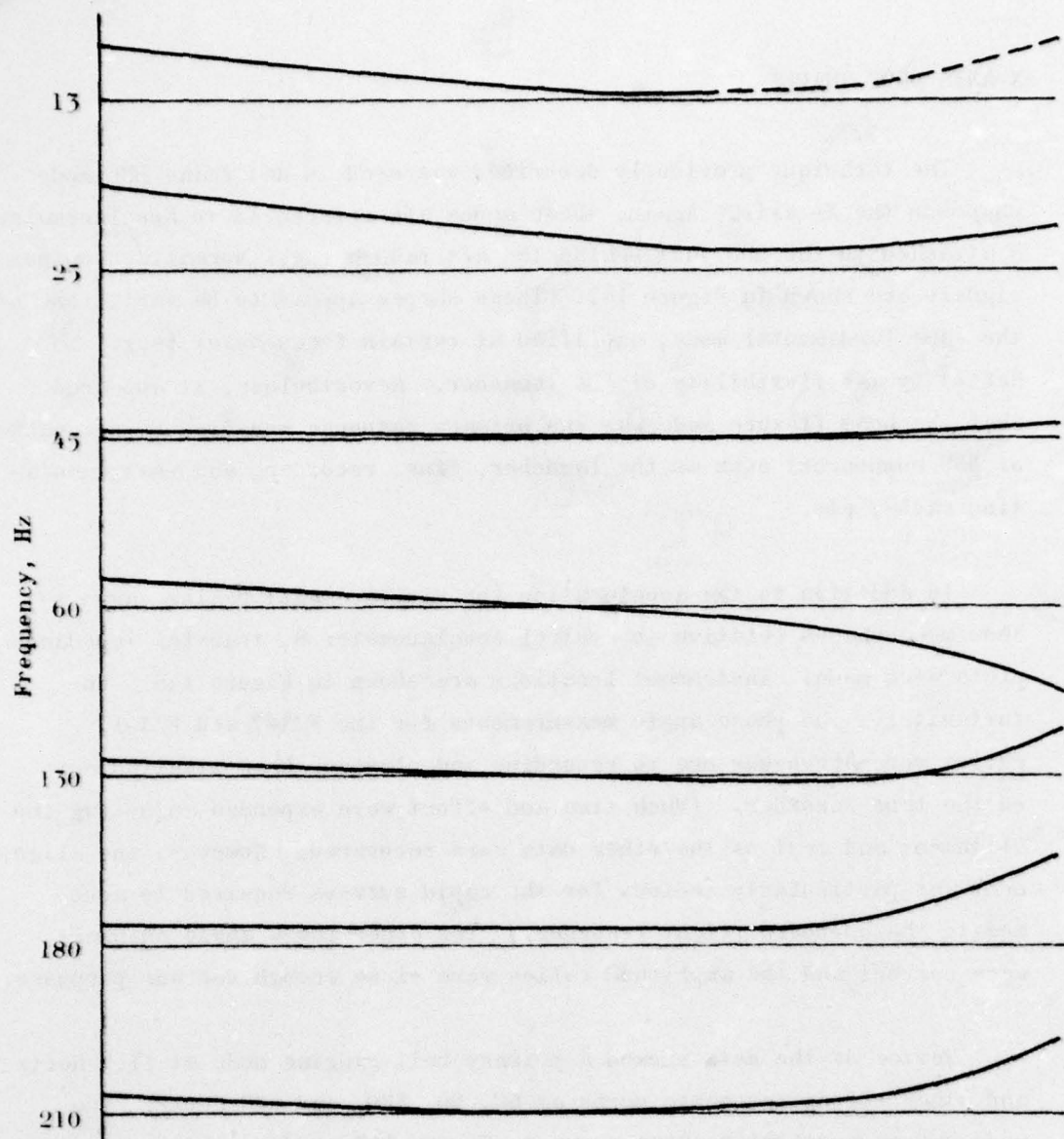
Figure 147. X-Axis Mode Shapes
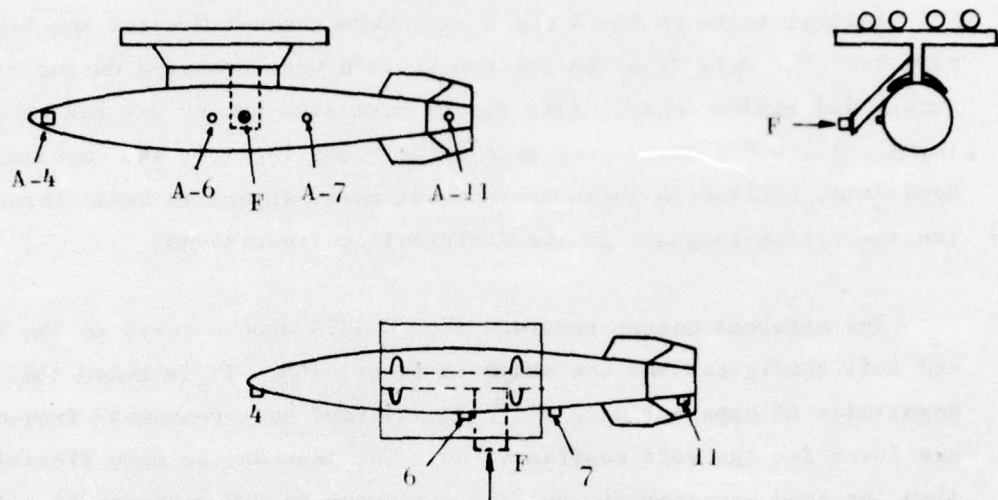
Figure 148.   Sketch of Transfer Impedance
Instrument Locations

LAUNCHER FLEXIBILITY

The BDU was attached to the vibration jig in two slightly different
arrangements for testing during this program. One arrangement ("hard")
used a stiff interconnecting member between the jig and the BDU. Attach-
ment to the BDU was accomplished by bolting into the BDU body at the
launch lug locations. The other arrangement ("soft") used the MAU-12A/C
launcher, bolted to the jig through clevis fittings as used on the F-111
pylon. The BDU was fitted to the launcher in the usual manner.

Adoption of the different arrangements stemmed from the need to
excite the BDU to the spectrum of frequencies between 10 and 2000 Hertz.
A MAU-12A/B launcher originally scheduled for use in the program
appeared to be so flexible that the BDU would be isolated from high
frequency loads input through that launcher. Since aerodynamically
induced high frequency loads could be experienced by the BDU in flight,
and since it was desired to simulate the environment in ground testing,
the hard arrangement was designed and built. Subsequently, a stiffened
launcher (the MAU-12A/C) became available and was used throughout the
experimental testing.

Initial tests in the X and Z axes were conducted using the hard arrangement. Data from the instrumentation were recorded during sine survey and random tests. (The Z-axis hard sine survey was run at 1-g input. All other tests were made using 0.5-g input.) The impedance head data, plotted in terms of apparent mass, appear to best characterize the system response in the different configurations.

The apparent masses recorded from Z-axis sine surveys in the hard and soft configurations are shown in Figure 149. It is noted that both magnitudes of apparent mass and resonant (and anti-resonant) frequencies are lower for the soft configuration. The launcher is more flexible than the hard arrangement, but the influence on BDU response is relatively small.

The apparent masses for X-axis sine survey tests in the hard and soft configurations are shown in Figure 150. The differences between the curves are less than those displayed in Figure 149.

It was concluded from these data that the differences in BDU response resulting from use of the hard and soft arrangement were small relative to other system complexities. Consequently, subsequent testing was conducted only in the soft (with launcher) configuration, and these data were analyzed and are discussed in more detail earlier in this section.
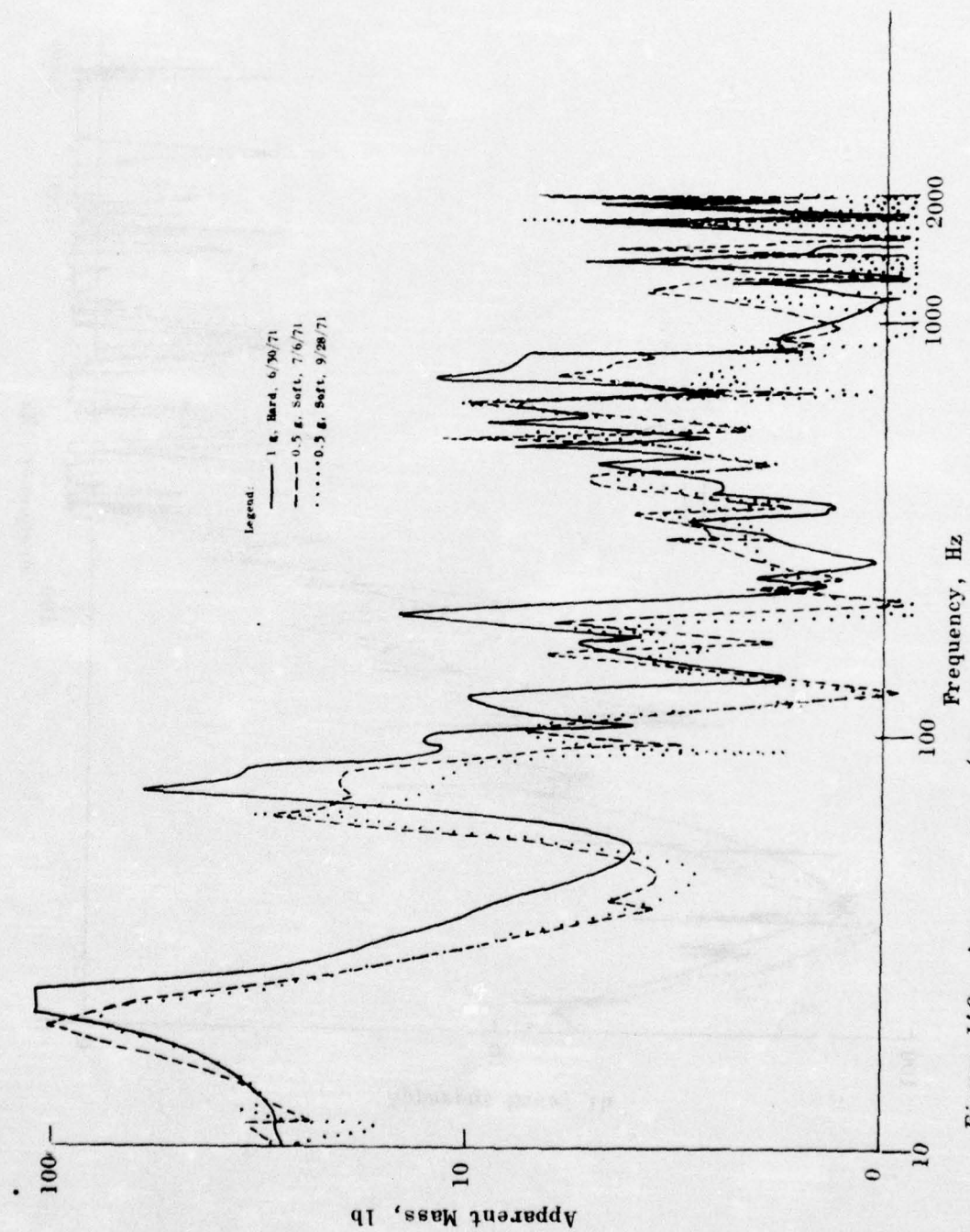
Figure 149. Apparent Mass (Aft Impedance Head) During Z-Axis Sine Surveys

205
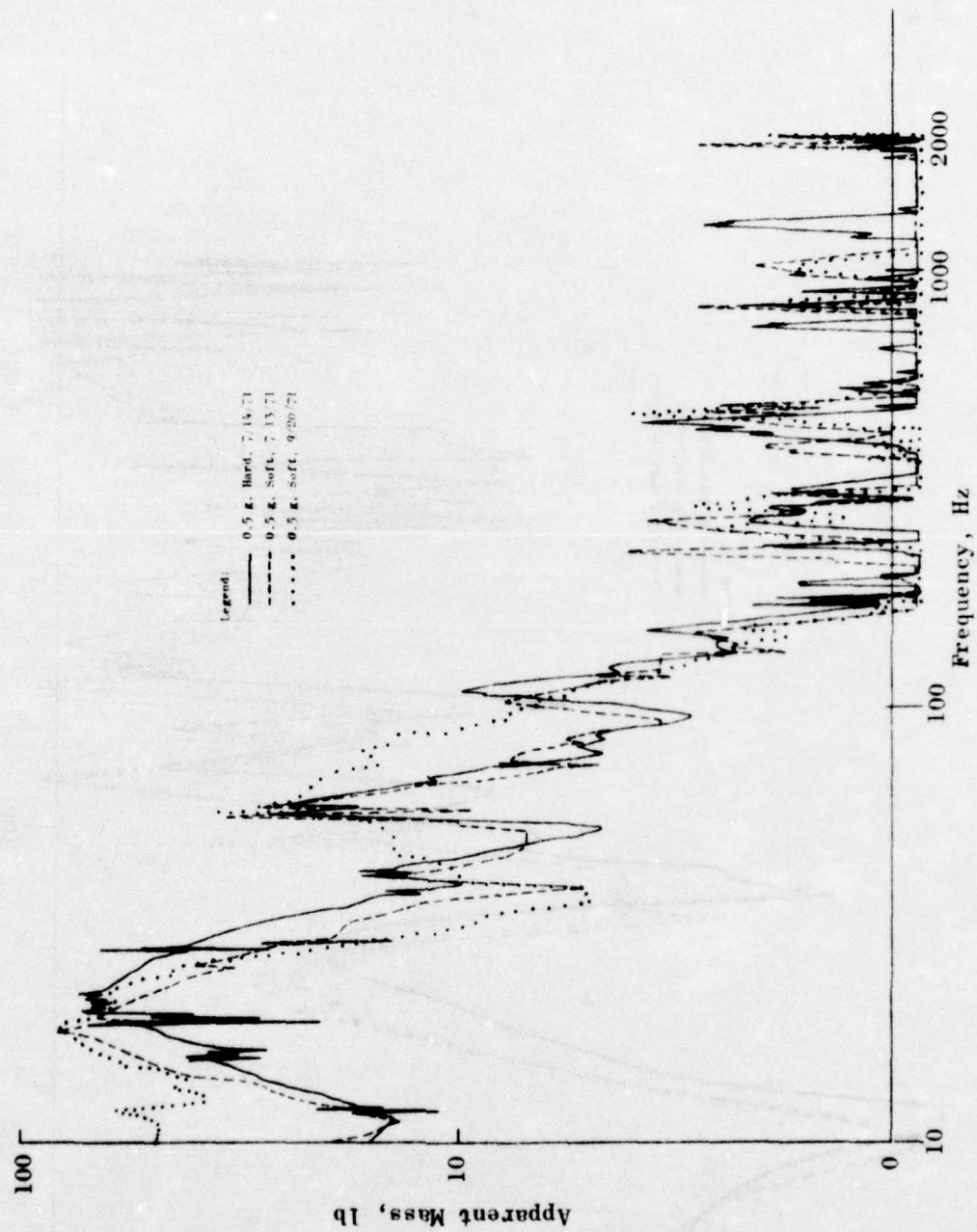
Figure 150. Apparent Mass During X-Axis Sine Surveys

AEROHEAT SIMULATION

The BDU was subjected to aeroheat during three test cycles. One aeroheat-only cycle was conducted to establish a baseline for future thermocouple and thermistor reference. The other two cycles were of combined aeroheat and vibration. The center section of the propellant grain was selected as the control section for the aeroheat cycles. Thermocouples 7, 8, 9, and 10 were on the case at the longitudinal centerline of the propellant grain; while thermocouple 5 was in the air stream just above the case. Data from the three tests are shown in Figures 141, 143, and 144.

Maximum differences in case temperatures were 30 to 50 F at the end of 10 minutes. Air temperature and maximum case temperature are shown in Figure 143.

PROPELLANT GRAIN RESPONSE DATA

Significant data obtained from the propellant grain instrumentation during vibration and simulated aeroheat testing are discussed in this section. The identification of the instruments and their location within the inert propellant grain are shown in Table 3, page 65, and Figure 22, page 31.

PROPELLANT INSTRUMENTATION DATA

Sinusoidal Vibration

A sine wave excitation survey was conducted in both the Z axis (vertical) and the X axis (horizontal and transverse to BDU) at an input acceleration level of 0.5 g.

Table 25 shows data from the sine survey in the Z axis and includes the peak-to-peak amplitudes obtained from the normal and shear stress gages and the two bore strain measuring gages. These data represent the maximum amplitudes noted at the various resonance frequencies. The lowest frequency ~ 11.5 Hz is apparently the frequency at which the whole BDU swings like a pendulum (Bell-ringer mode) on its support. This is primarily an X-axis motion, and very low normal stresses (0.15 to 0.25 psi) were obtained in this mode. There was no measurable shear stress in the axial or Y direction.

Higher stress levels were obtained at the higher resonant frequencies of ~ 25 and ≃ 100 Hz. Gage 22 situated at the 180° (bottom) of the forward end of the grain shows the largest stress values at both frequencies, 0.93 and 0.70 psi, respectively. Gage 24 at the rear bottom of the grain shows similar stress levels at 0.64 and 0.61 psi, respectively. Gage 18 located in the middle of the grain was not connected to the Rocketdyne recorder for these tests. Gages 21 and 26, which are arranged to measure the lateral normal stresses, gave extremely small outputs in the noise level during the vertical Z-axis vibration tests.

208

TABLE 25. VIBRATION DATA FROM 0.5 g Z-AXIS SINE SURVEY

Freq, Hz	Gage Number							
	21	22	24	26	101	SH-2	BB 1	BB 2
	Peak-to-Peak Stress/Strain							
	psi	psi	psi	psi	psi	psi	% Ax.	% Hoop
11/12	0.15	0.26	0.22	N	--	--	-	-
23/24	N*	0.93	0.64	N	0.42	0.20	N	N
97/105	N	0.70	0.61	N	0.38	0.31	N	0.014

*Noise level only

Shear gages 101 and SH-2 both showed small shear stresses in the axial or Y direction at the two higher frequencies when the BDU was vibrated in the Z direction. This indicates some coupling between the modes of vibration and demonstrates how difficult it is to obtain a simple pure vibration mode.

The bore strain measuring clip gages showed virtually no vibration strains during the tests. A very small value of 0.014% hoop strain was obtained at the 100 Hz frequency but no other measurable strains were noted.

Table 26 shows similar data obtained from the X axis sine survey. In this mode the lateral plane of normal stress gages, i.e., Gages 21, 24, and 26, showed the highest stress values as would be expected. Resonant frequencies noted in these lateral vibration tests were not identical to those obtained in the vertical test mode. Thus, there was no resonance detected at the 11/12 Hz frequency; and the lowest resonant frequency was 28 Hz, which is probably a similar mode to that obtained at 23/24 Hz in the Z axis mode of vibration. There appears to be no equivalent to the 100 Hz mode during vibrations in the X direction but additional peaks were obtained at 140, 220, and 280/300 Hz as noted.

TABLE 26. VIBRATION DATA FROM 0.5 g X-AXIS SINE SURVEY

Freq, Hz	Gage Number							
	21	22	24	26	101	SH-2	BB 1	BB 2
	Peak-to-Peak Stress/Strain							
	psi	psi	psi	psi	psi	psi	% Ax.	% Hoop
28	0.66		0.64	0.82	0.50	0.37	N*	0.0085
140	--	--	--	--	0.069	0.051	N	N
220	1.15	--	0.59	0.34	--	--	-	-
280/300	0.40	--	0.29	0.27	0.107	0.065	N	N

*Noise level only

At the lowest frequency of 28 Hz the shear gage readings suggest
that it is once again a coupled vibration mode, but at the higher fre-
quencies the measured shear stresses are much smaller and almost negli-
gible. There is also essentially no hoop or axial strain in the grain
bore during vibration, since only one value of the hoop strain could be
measured (i.e. 0.0085% at 28 Hz).

Random Vibration with Simulated Aeroheat

Random excitation was applied to the BDU in both the X and the Z
axes simultaneously with aeroheat. These tests were intended to simulate
a flight test as closely as possible. Data from the X-axis vibration
test are presented in Table 27, and data from the Z-axis vibration test
are given in Table 28.

The data consist of peak-to-peak amplitudes at the maximum data
points observed during the test sequence. Thus the results from the nor-
mal stress Gages 21, 24, and 26 in Table 27 show maximum values of nor-
mal stress of from 2 to 4 psi. Gages 21 and 26, which are located at the

210

TABLE 27. VIBRATION DATA FROM X AXIS RANDOM
VIBRATION PLUS AEROHEAT

Time, sec	Gage Number							
	21	22	24	26	101	SH-2	BB 1	BB 2
	Peak-to-Peak Stress/Strain							
	psi	psi	psi	psi	psi	psi	% Ax.	% Hoop
18.8	2.05	--	1.23	1.78	--	--	--	--
57.7	2.16	--	1.21	1.59	--	--	--	--
444.2	3.99	--	1.80	2.24	--	--	--	--

TABLE 28. VIBRATION DATA FROM Z AXIS RANDOM
VIBRATION PLUS AEROHEAT

Time, sec	Gage Number							
	21	22	24	26	101	SH-2	BB 1	BB 2
	Peak-to-Peak Stress/Strain							
	psi	psi	psi	psi	psi	psi	% Ax.	% Hoop
44.1	0.60	2.23	1.18	1.09	--	--	--	--
95.5	0.59	1.10	1.14	1.08	--	--	--	--
150.9	0.67	2.18	1.28	1.05	--	--	--	--

$90°$ points of the grain, show the maximum data as would be expected.
Some coupling between the X and the Z planes is evidenced by the magni-
tude of the response from Gage 24, which measures the vertical (Z) re-
sponse at the rear of the grain.

211

Data in Table 28 show maximum stress levels from Gages 22 and 24, but stresses at Gage 26 are not much smaller than those recorded by the two Z-axis plane gages. Again, this demonstrates the complexity of the vibration modes.

AEROHEAT

Results of the aeroheat vibration tests were presented in the preceding paragraph; thermal results from the tests are discussed here. Temperature data were obtained from thermistors located in the grain adjacent to the gages and in a temperature gradient block at the middle of the grain. In Figures 151 through 154, Thermistors B and D measured the case/liner interface temperature while Thermistors 1, 2, 5, and 10 measured the grain temperature inside the insulation layer near the gages. Thermistor 21 was located inside the propellant web at a distance of 1 inch from the insulation layer, and Thermistor 20 was located in line with Thermistor 21 and 1 inch deeper in the grain (2 inches inside the grain from the insulation layer). Thermistor 16 measured the temperature at the bore of the grain.

Data from three aeroheat runs are given. Figure 151 shows the temperature data from a simple aeroheat test alone, i.e., no simultaneous vibration; and Figures 152 and 153 show data obtained during the aeroheat plus vibration tests.

All three sets of data show similar results in that the maximum heating was obtained at the bottom of the grain as evidenced by Thermistors D, 1, and 2 all located at the bottom of the grain and Thermistors B, 5, and 10 located at the top of the grain. There is a difference in temperature of about 10 F between the bottom and the top of the grain at the end of the aeroheat test alone, a difference of 20 to 25 F in Figure 152, aeroheat plus Z axis vibration, and a difference of about 20 F in the data shown in Figure 153, aeroheat plus X-axis vibration.

212
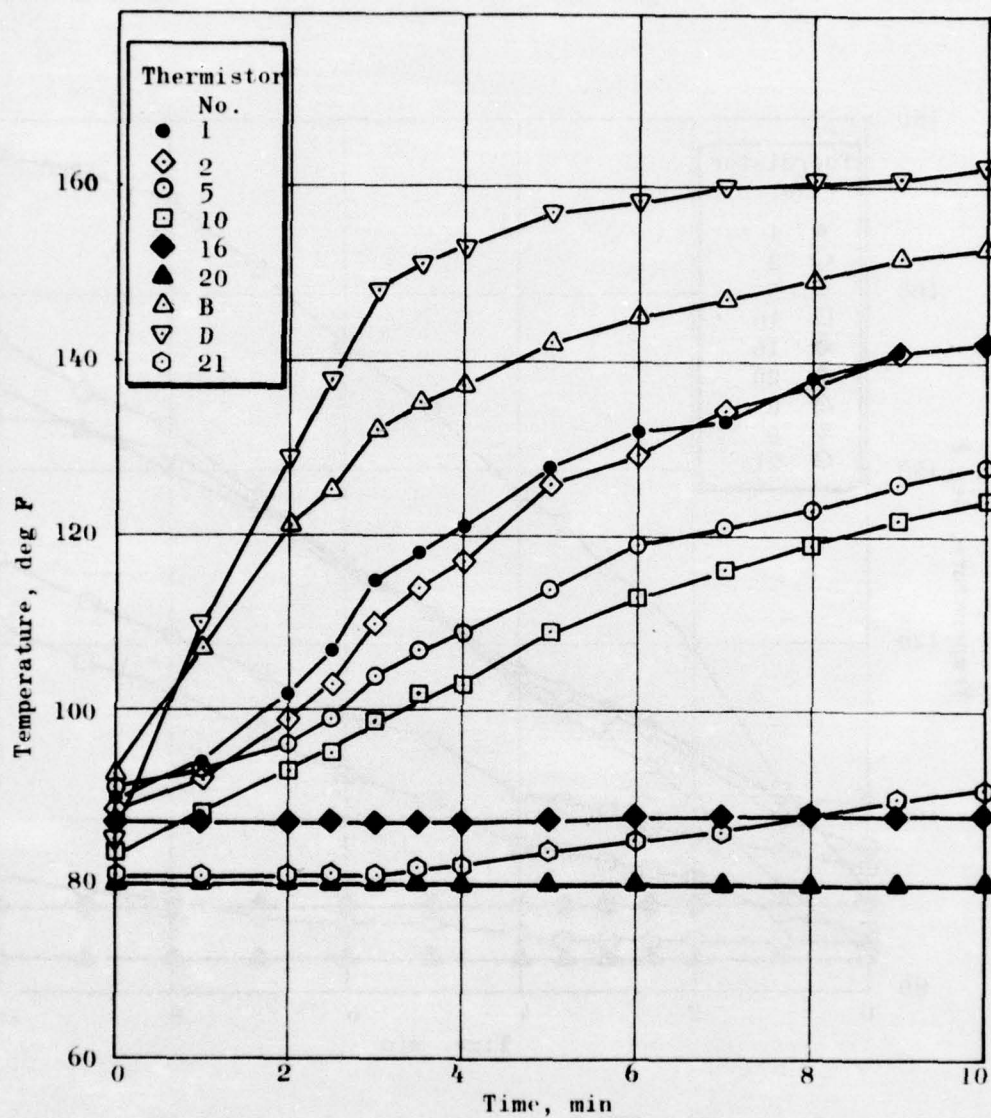
Figure 151. BDU Temperature Data from Aeroheat Test 9/22/71
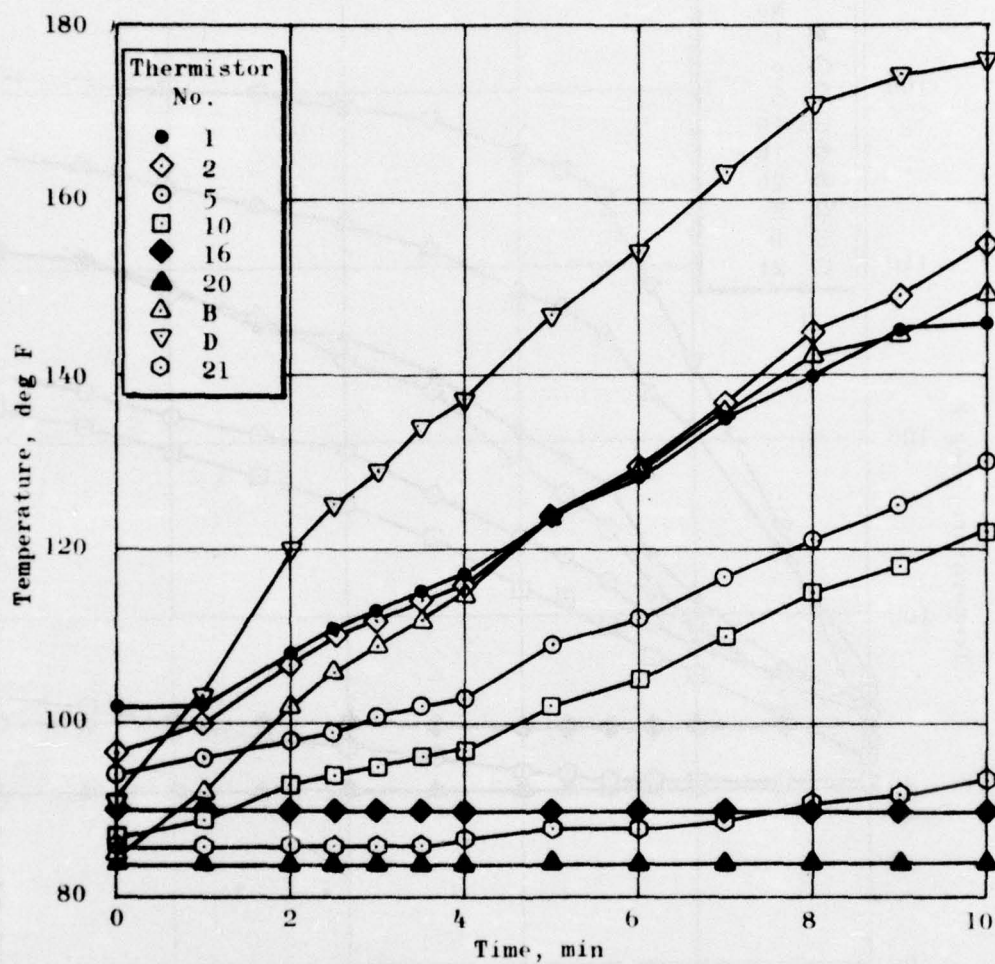
Figure 152.   BDU Temperature Data from Aeroheat
Plus Vibration Test 9/28/71

214
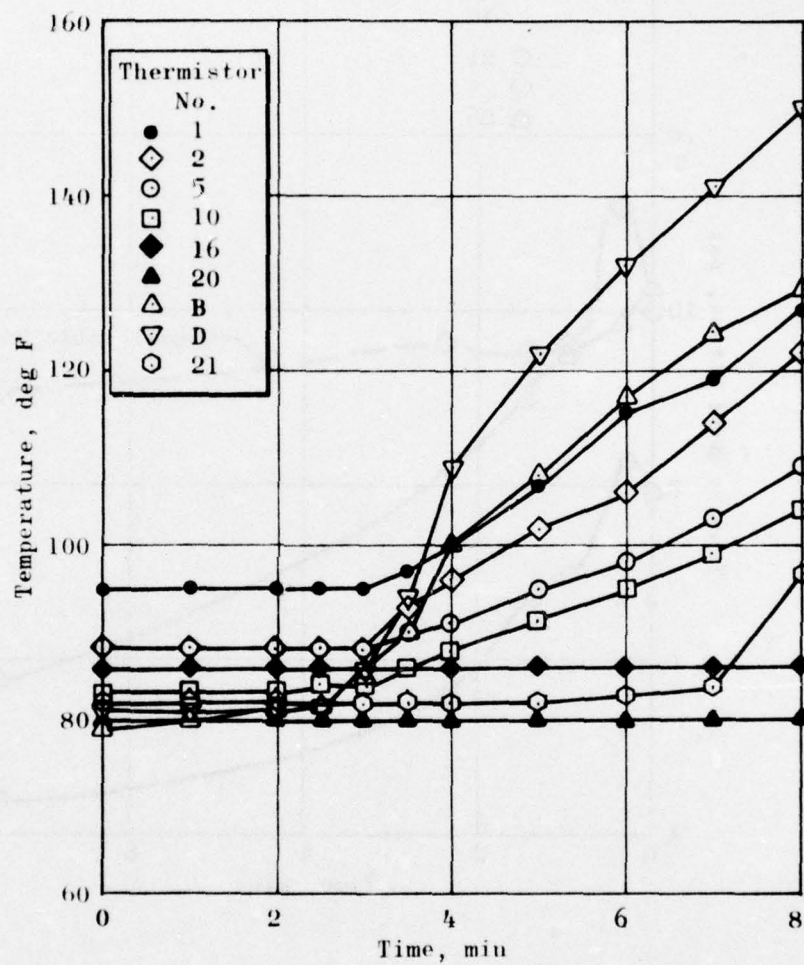
Figure 153. BDU Temperature Data from Aeroheat
Plus Vibration Test, X Axis Random,
9/24/71

215
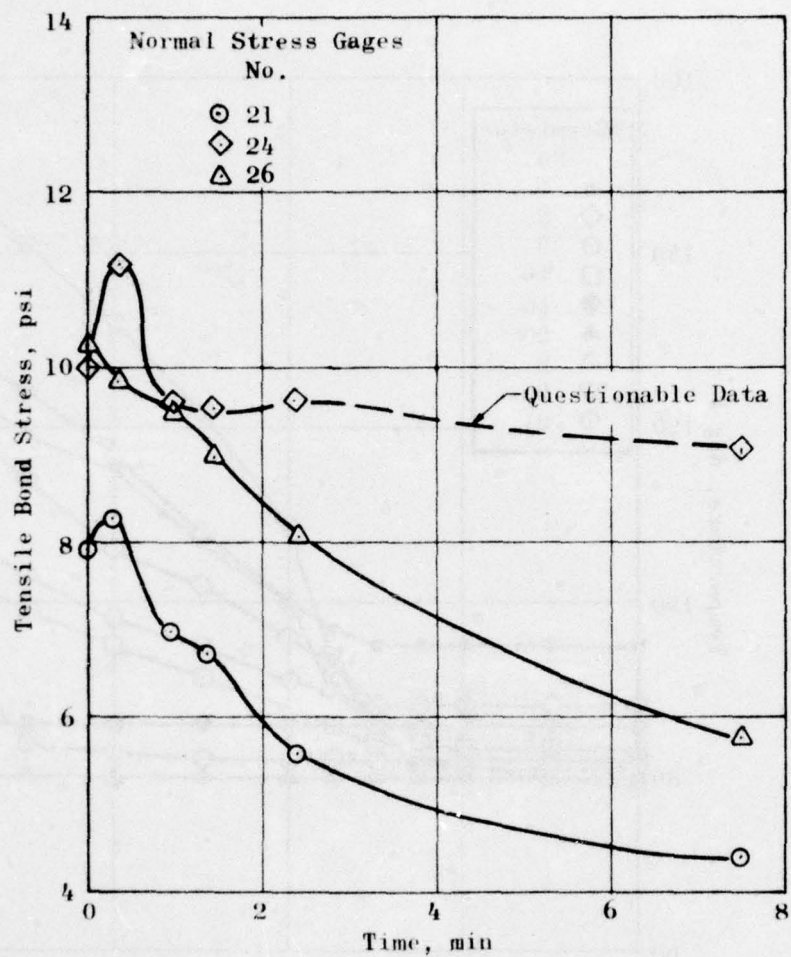
Figure 154.   Thermal Bond Stresses Measured
During Aeroheat Plus X Axis
Vibration Test

During the combined random vibration and simulated aeroheat, the propellant stress transducers were expected to display relatively small amplitude (vibration response) oscillations superimposed on larger (thermal response) variations. In order to record the amplified vibrator response, the signal reference base was manually adjusted during the test.

Data presented in Figure 154 were obtained in this manner. The curves show the thermally induced changes in the outputs from normal stress Gages 21, 24, and 26 during the aeroheat plus X-axis random vibration test. In the first minute of the aeroheat test Gages 21 and 24 showed a small increase in tensile stress after which the stresses became smaller for Gages 21 and 26. Gage 24 showed the initial increase as described above then showed a reduction in tensile stress for a short time. The final data point at 444.2 seconds indicated an increase in stress, but it is possible that this was merely an error in signs and that the stress actually decreased as in the case of the other two gages.

INTERIM SIMULATION

Data from Flights 9, 10, and 11 were used to establish random vibration levels and time-temperature histories for the new ground simulation tests. Mission profiles for Flights 9 and 11 are discussed in the FLIGHT TESTING SECTION. Two simulation test environments were constructed to represent pertinent features of these two mission profiles. Numerous simplifications and assumptions were necessary to establish the test environments. Practical considerations such as capabilities of the test equipment and test time prevented a precise duplication of the flight environment. Nevertheless, good simulation tests were established.

THERMAL ENVIRONMENT

Thermistor data from Flights 9 and 10 (Figures 155 and 156) were reviewed. The figures indicate a little difference in the temperatures recorded by Thermistors B and D. The median of these temperatures was used as a test objective for the simulation tests. To duplicate flight aeroheat conditions, it was only necessary to duplicate the case/liner interface (CLI) temperature history. That is, if CLI temperature as a function of time was the same in the test as in the flight, the grain thermal gradient histories were also the same.

Since ground test equipment cannot supply air at velocities encountered during flight it was not possible to attain identical convective heat transfer coefficients. Since heat flow rate through the case governs simulation accuracy, it was necessary to accentuate the temperature potential (the difference between the air and case temperatures) to compensate for the low convective coefficients in test. The equipment has high-capacity heaters and an air preheating loop so that rapid heating of the case was feasible. Absence of a precooling loop resulted in slower case cooling than desired.

VIBRATION ENVIRONMENT

The dynamic response of the BDU during captive flight was monitored by five accelerometers—a triaxial accelerometer monitoring major axis vibrations at the center of gravity; a triaxial accelerometer canted 45 degrees from the horizontal plane, located in the aft end; two single-axis accelerometers (oriented to vertical), located on the launch lugs; and a single-axis (longitudinal) accelerometer, mounted in the grain.

Data from three flights were reviewed and assimilated to determine input vibration levels for ground simulation of the flight tests. Selection of flights and flight conditions was based on aeroheat, dynamic, and
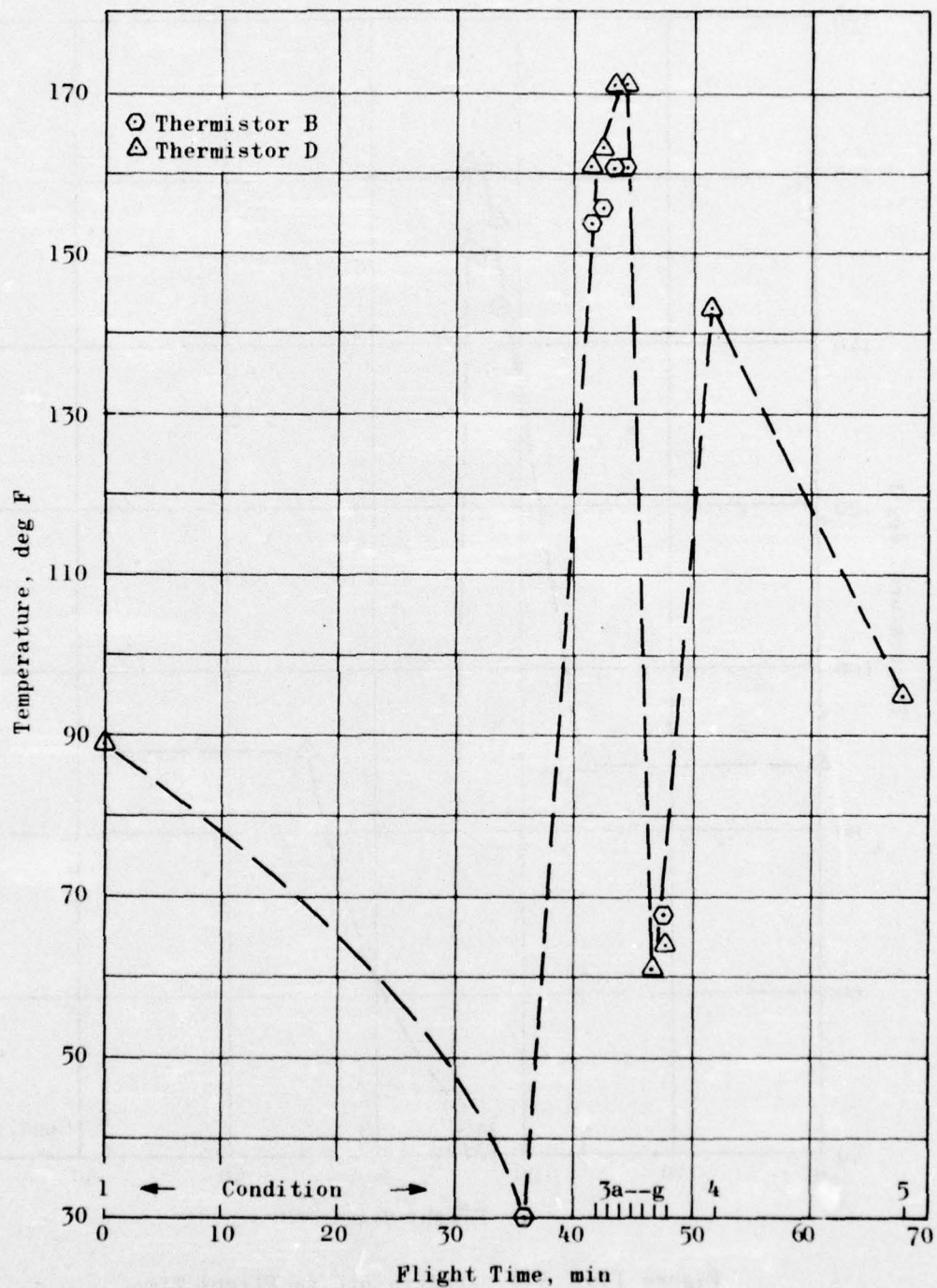
Figure 155. CLI Temperatures vs Flight Time
for Flight 9

219
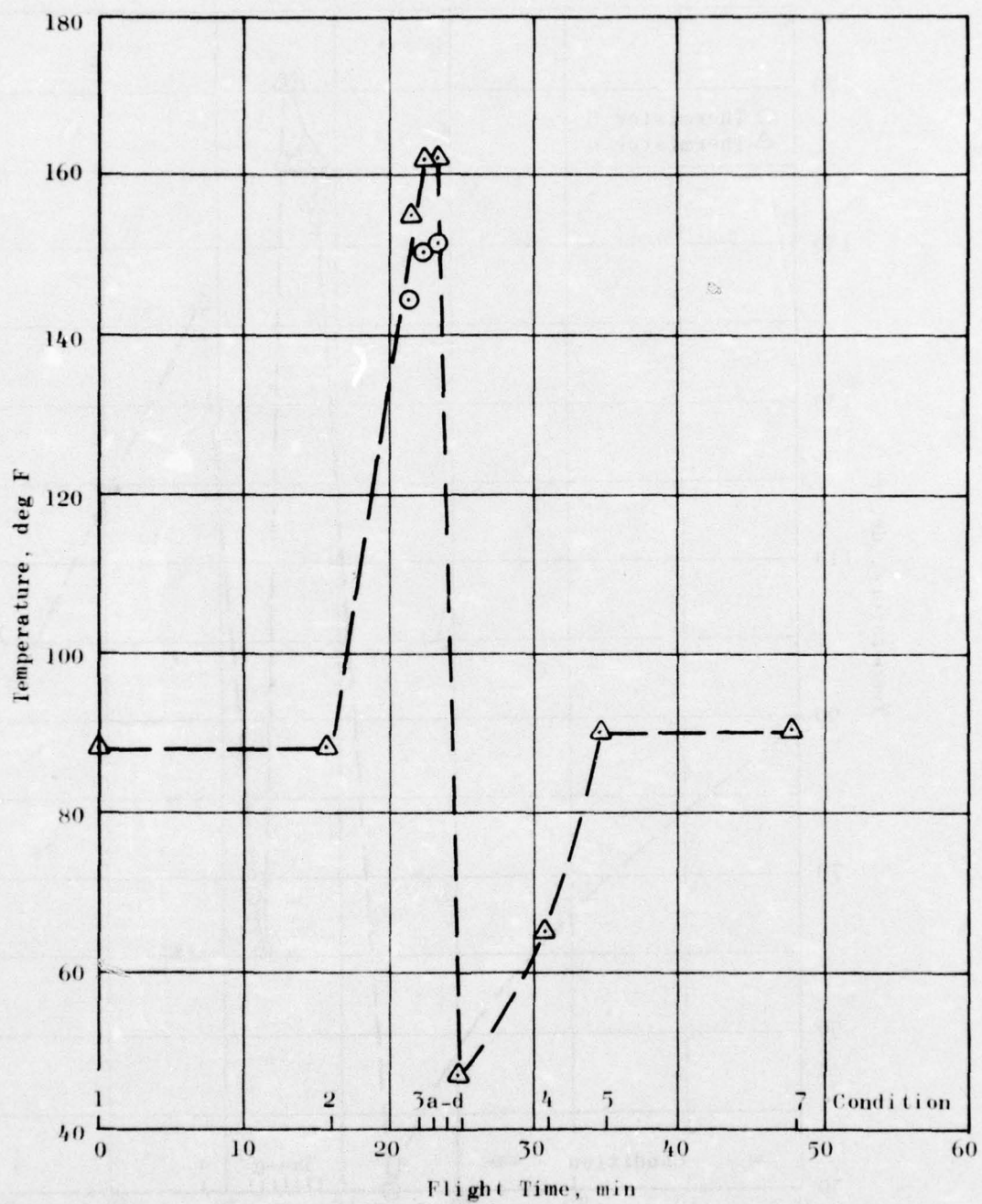
Figure 156. CLI Temperature vs Flight Time
for Flight 10

220

grain response data. Dynamic data for the X and Z axes (horizontal and vertical) are summarized in Table 29 in the form of mean square acceleration levels at each accelerometer for the various flight conditions chosen as candidates for simulation.

TABLE 29. MEAN SQUARE ACCELERATION (g^2) FOR CAPTIVE FLIGHT TESTS

	Flight 9		Flight 10	Flight 11	
	Condition 3 M = 2, 35,000 MSL	Condition 4 M = 0.95, TFR, 500 MSL	Condition 3 Dash to M = 1+, 12,000 MSL	Condition 3 (Same as Flight 9)	Condition 4
Aft End, X Axis[a]	1.35	3.27	2.35	1.88	4.00
Aft End, Z Axis[a]	3.08	7.68	5.20	4.59	1.62
cg[b], X Axis	0.72	1.09	0.72	0.05	0.06
cg[b], Z Axis	0.17	0.32	0.57	--[c]	--[c]
Fwd Lug, Z Axis	2.51	2.26	2.18	2.97	12.25[d]
Aft Lug, Z Axis[b]	0.40	1.14	0.44	0.74	1.85

[a]Major axes of accelerometer rotated 45 degrees to major axes of motor
[b]Readings were erratic. Postflight test inspection revealed defective connection to monitoring system.
[c]Data not reduced at AFRPL
[d]Questionable data

Mean Square Value $= \dfrac{1}{1000} \sum\limits_{i\,=\,1}^{1000} (x_i)^2$

x_i = digital data point (g) sampled at 4000 points/sec

Choice of control accelerometer--forward lug, Z axis--was based on the following considerations:

1. Since dynamic input during ground simulation was through the lugs, lug accelerometers were the logical sites for test control.

2. The aft lug accelerometer behaved erratically during the flights and was subsequently found to have a defective connection with the monitoring system. A similar problem was noted for the center-of-gravity accelerometer.

221

Replots of mean square acceleration density vs frequency are shown in Figures 157 and 158 for the forward lug (Z-axis orientation) accelerometers for Flights 9 and 1G, respectively. The most severe conditions for vibration were found to be those occurring during supersonic dash and TFR. Measured levels for Flights 9 and 11, Condition 3, and Flight 10, Condition 3, were similar. Therefore, a single power spectrum was designed for ground test vibration input.

For simulation testing, accelerometers and thermocouples were mounted to the exterior of the BDU to monitor and control the test environment. The BDU was mounted directly (without the instrumented launcher) to a large electrodynamic vibrator in the Z axis, and duct work was assembled around the BDU. The duct work was connected to the environmental control unit that provides the aerodynamic heat simulation. Two tests were then conducted. Random vibration was continued throughout the test while the time-temperature profile for each particular flight condition was applied. Data from external instrumentation were recorded using conventional ground equipment. The on-board flight recorder was switched on and off at frequent preselected intervals to acquire data from internal instrumentation. Test results are discussed in the following sections.

TEST RESULTS

Thermal Environment

CLI temperatures measured during the tests are shown in Figure 159. CLI data measured during flight testing are also shown. A comparison of these data reveals good agreement during the heating portions of the test. The peak temperature for simulation test of Mission 9 falls between the two CLI temperatures measured during flight as was intended. (Up to this point, the CLI temperature had been taken to be the case temperature.)

The aerocooling portion of the simulation tests lagged the flight data, as was expected. The test equipment used CO_2 for cooling and the

Condition 5
Track 8, Channel 5
Forward Lug, Z Axis

Log Mean Square Acceleration Density, g^2/Hz
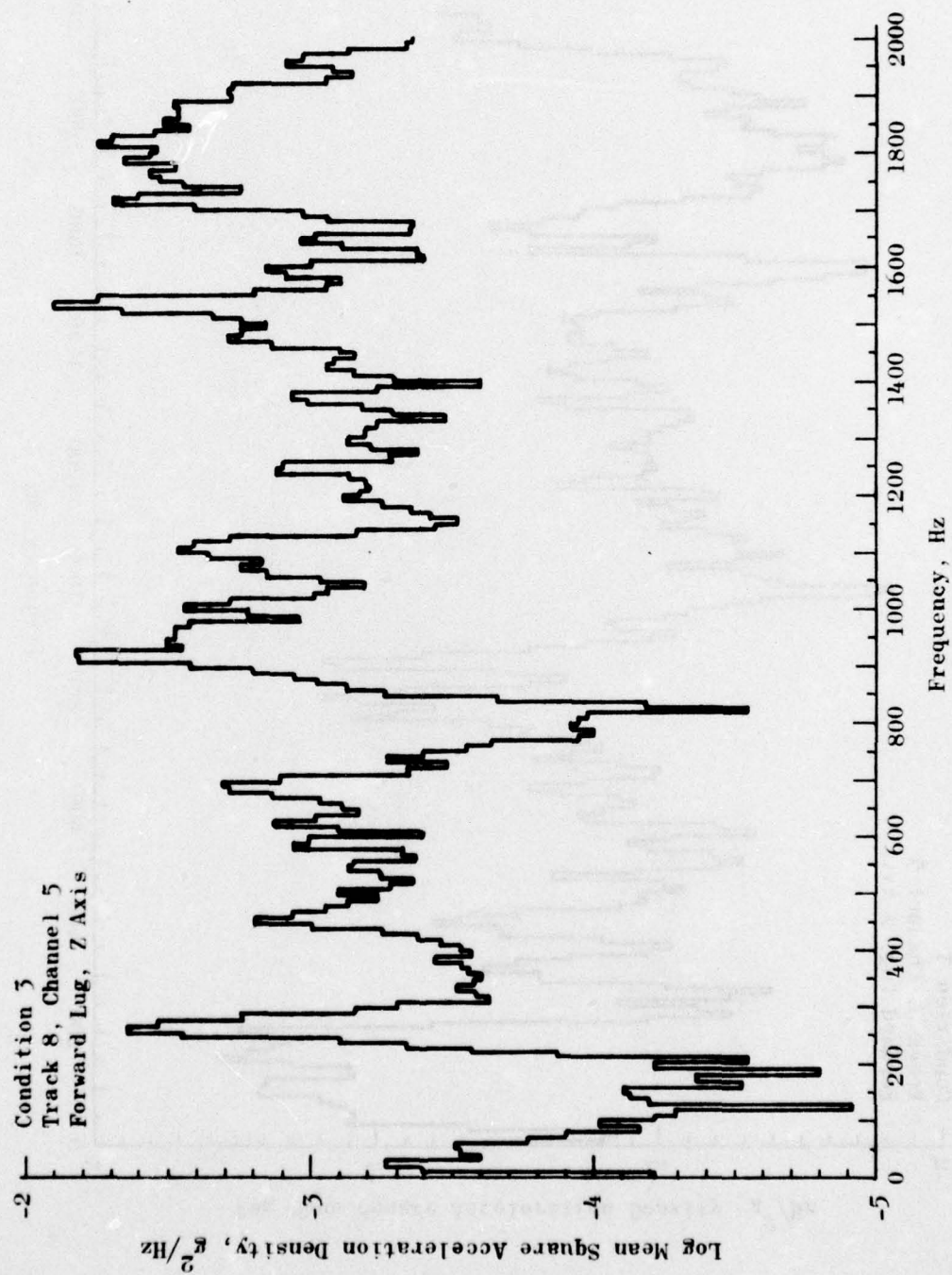
Frequency, Hz

Figure 157. Mean Square Density vs Frequency, Flight 9
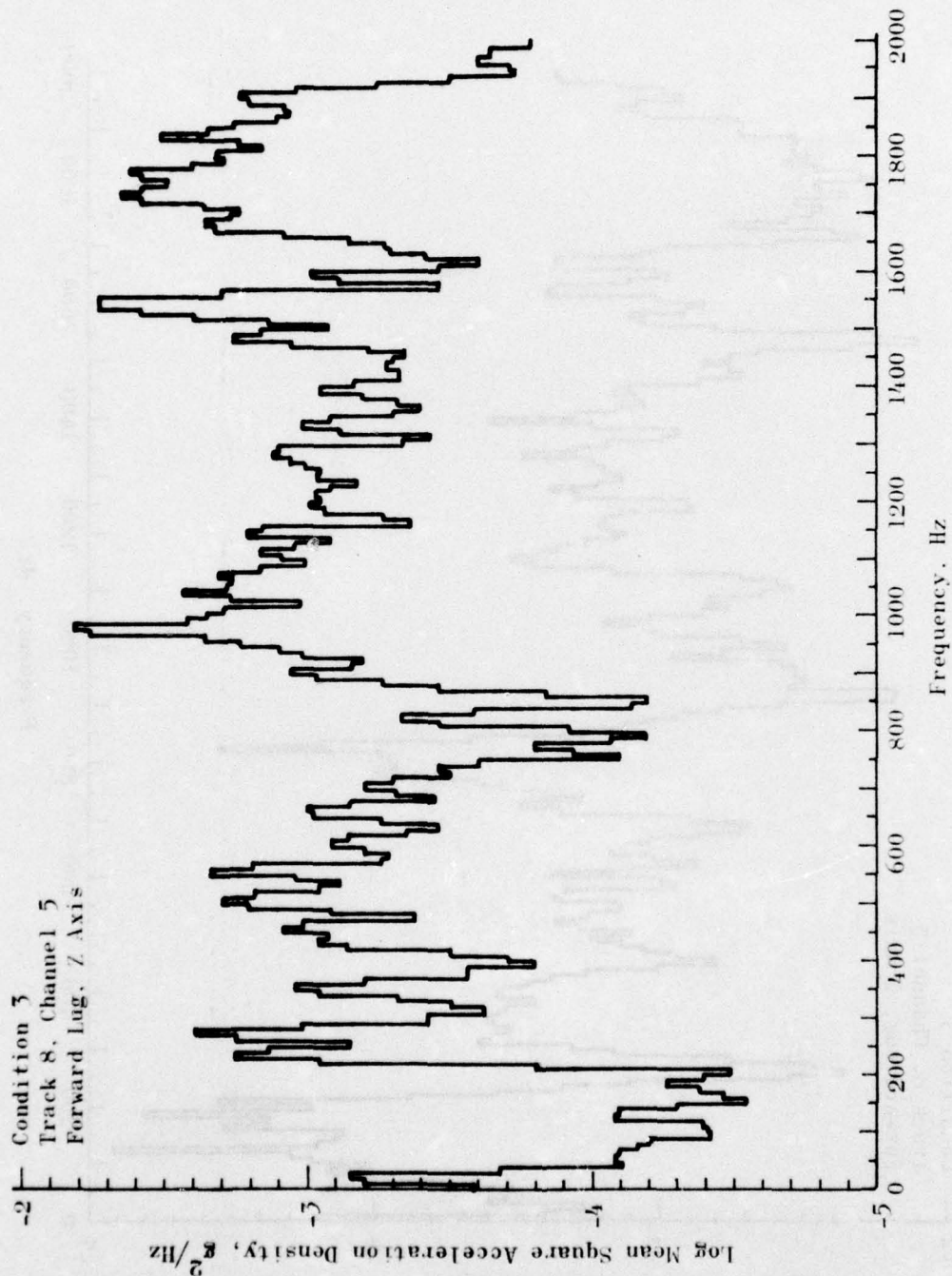
Figure 158. Mean Square Density vs Frequency,
Flight 10

224
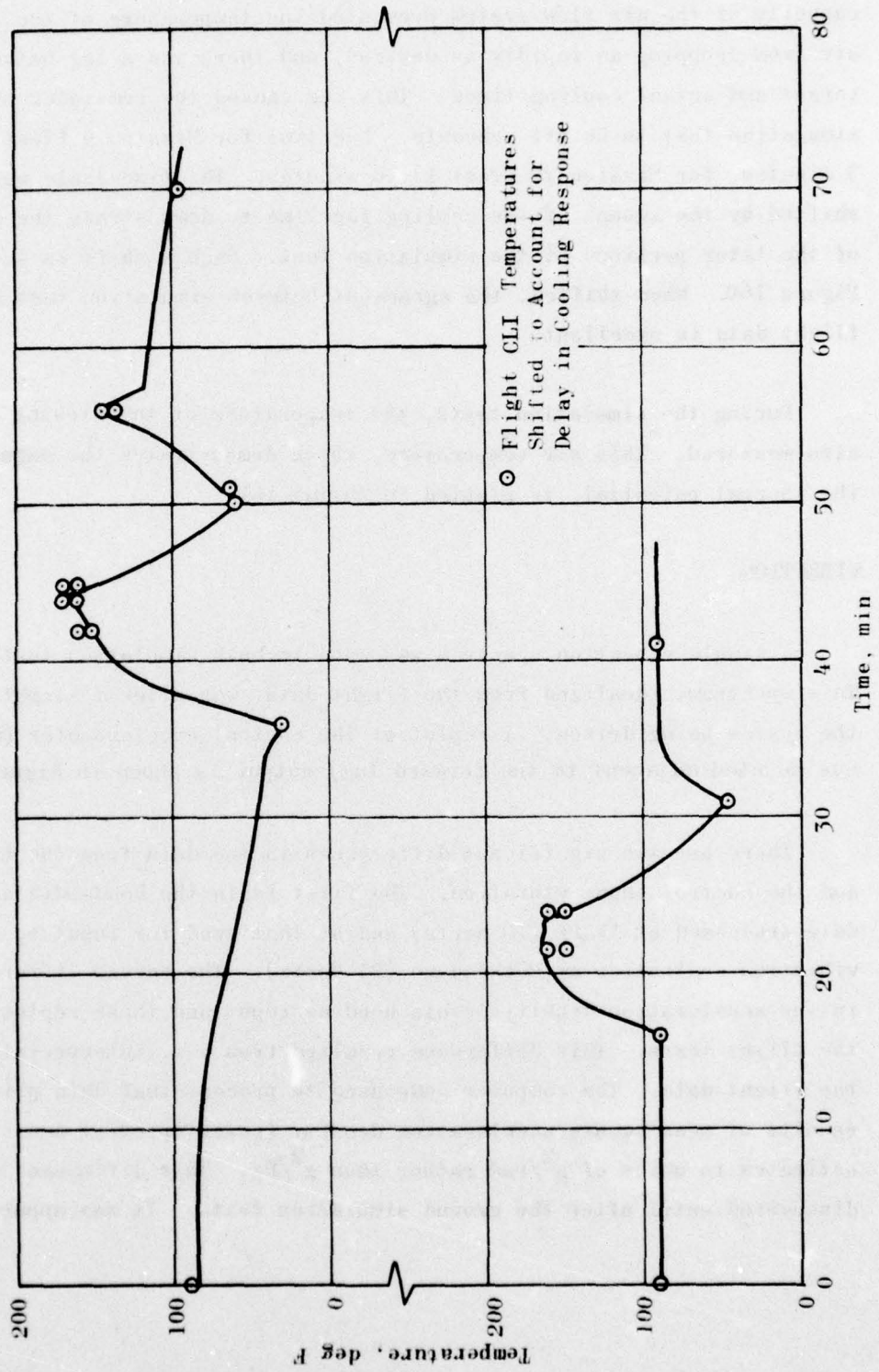
Figure 159. Test and Flight CLI Temperatures vs Time

valves used had insufficient capacity. This, coupled with the heating capacity of the air flow system prevented the temperature of the flowing air from dropping as rapidly as desired, and there was a lag between target and actual cooling times. This lag caused the remainder of the simulation test to be off schedule. Lag time for Mission 9 (Test 2) was 3 minutes, for Mission 10 (Test 1), 6 minutes. The time scale was shifted by the amount of the cooling lag time to demonstrate the quality of the later portions of the simulation test. Such a shift is shown in Figure 160. When shifted, the agreement between simulation test and flight data is excellent.

During the simulation tests, the temperature of the flowing air was also measured. This air temperature, which demonstrates the magnitude of the thermal potential, is plotted in Figure 161.

VIBRATION

A single vibration spectrum was used in both simulation tests. This spectrum, idealized from the flight data, was altered slightly by the system being driven. A replot of the control accelerometer (which was mounted adjacent to the forward lug) output is shown in Figure 162.

There are two significant differences in the data from the flights and the control input vibration. The first is in the bandwidth of the data processed at AFRPL (10 Hertz) and of that used for input to the vibration controller at Rocketdyne (25 Hertz). The second difference is in the acceleration density levels used as input and those replotted from the flight tests. This difference resulted from a misinterpretation of the flight data. The computer code used to process that data printed results of mean square acceleration density (power spectral density) estimates in units of g^2/rad rather than g^2/Hz. This difference was not discovered until after the ground simulation tests. It was apparent that

226
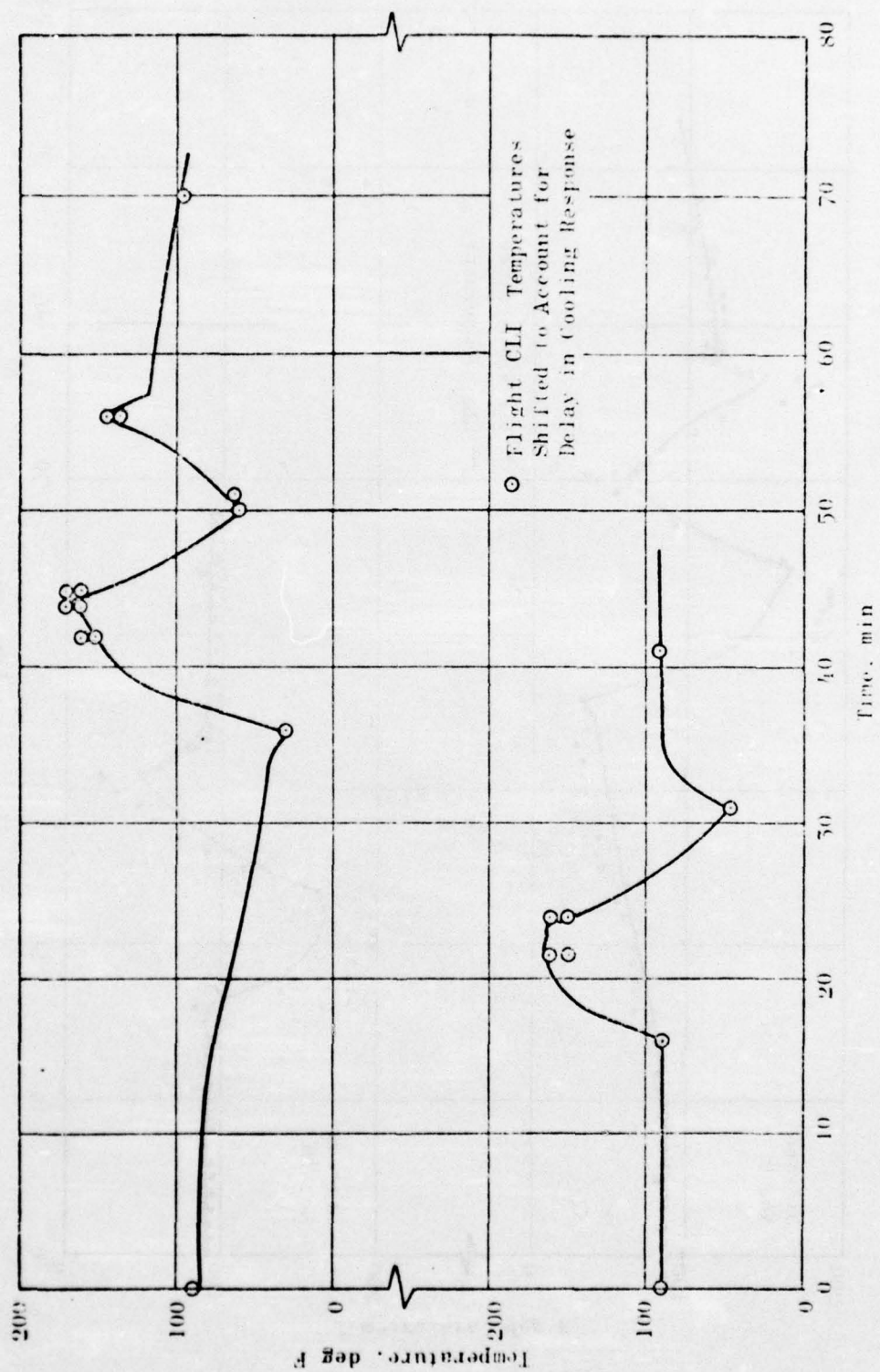
Figure 160. Actual and Shifted Flight CLI Temperatures vs Time

227
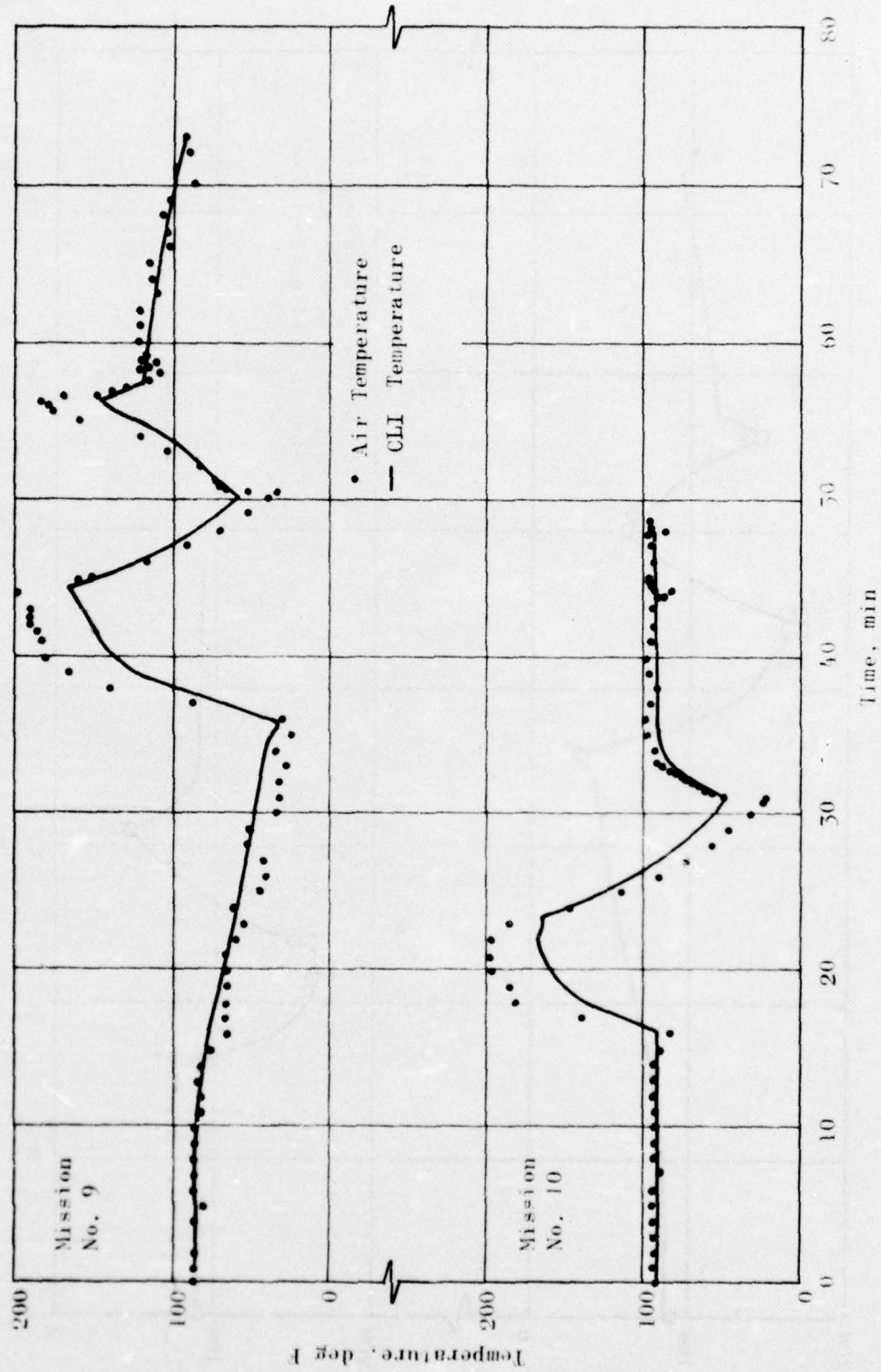
Figure 161. CLI Temperature vs Flight Time with
Air Temperature at Motor Station

228
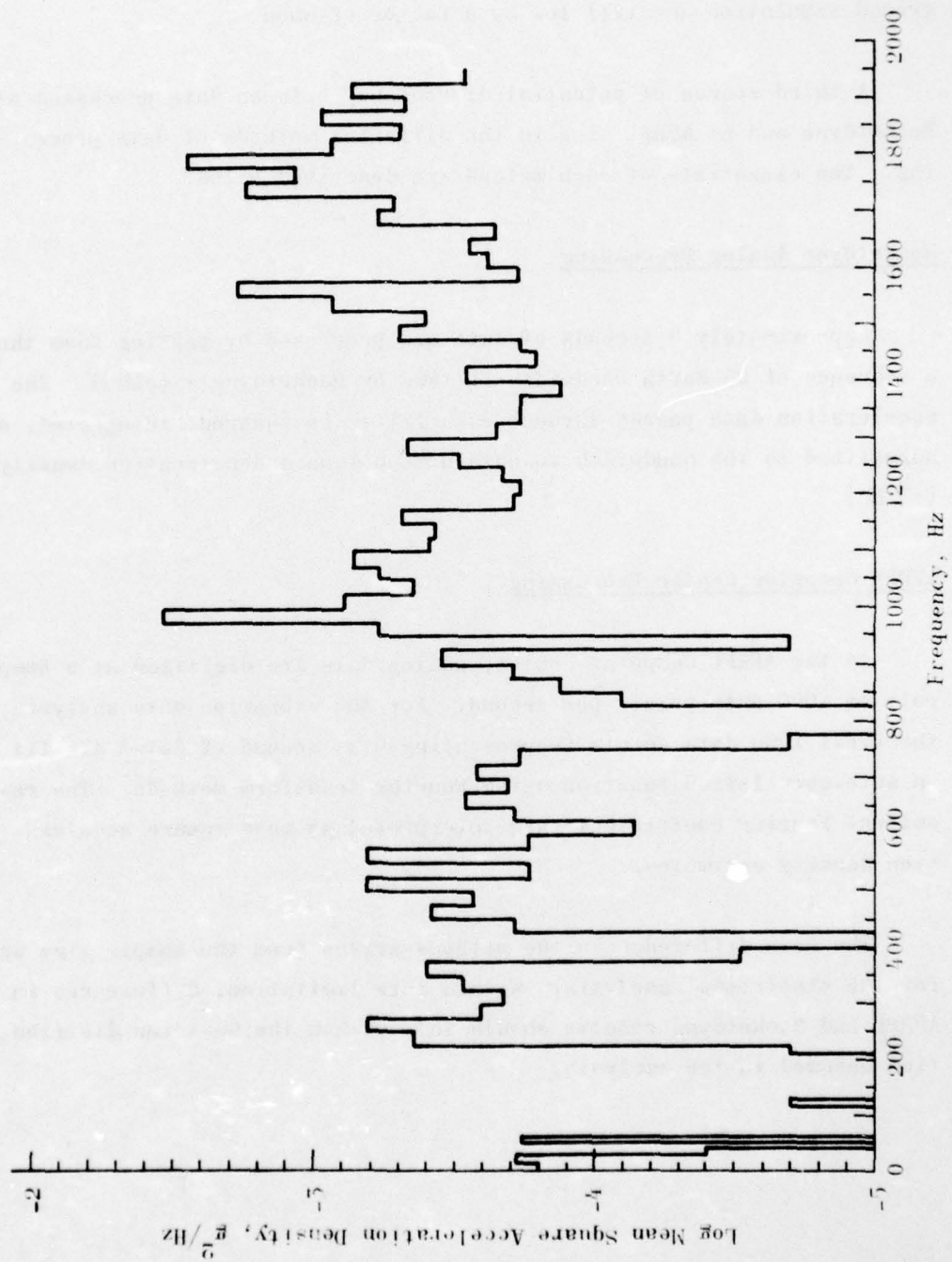
Figure 162. Mean Square Acceleration Density vs Frequency, Simulation Test 1, Fwd Lug Control Accelerometer (Rocketdyne Data)

the computer printout was lower than expected and comparison of oscillographs of the flight and vibration control analog outputs led to using a factor of 2 in setting up the control acceleration levels. Thus, the ground simulation was still low by a factor of about π.

A third source of potential discrepancy between data processed at Rocketdyne and at AFRPL lies in the different methods of data processing. The essentials of each method are described below.

Rocketdyne Analog Processing

Approximately 8 seconds of data are processed by passing them through a sequence of 25-Hertz bandwidth filters by Rocketdyne's method. The acceleration data passed through each filter is squared, integrated, and normalized to the bandwidth to obtain mean square acceleration density (g^2/Hz).

AFRPL Computer Center Processing

At the AFRPL Computer Center, analog data are digitized at a sampling rate of 4000 data points per second. For the vibration data analysis, the first 1000 data points (representing 0.25 second of data) are fit to an auto-correlation function using Fourier transform methods. The resultant Fourier coefficients are interpreted as mean square acceleration density estimates.

The main difference in the methods arises from the sample size used for the statistical analysis. Within this limitation, differences in AFRPL and Rocketdyne results should fall within the Gaussian distribution assumed in the analysis.

230

For subsequent comparison with flight data, Rocketdyne data taken at the center of gravity and aft lug are replotted in Figures 163 and 164. Replots of the AFRPL-processed data corresponding to the forward lug, center of gravity, and aft lug for Test 1 are shown in Figures 165, 166, and 167. Rocketdyne data from each of the three 2-axis accelerometers are shown for Test 2 in Figures 168, 169, and 170; AFRPL data from the same accelerometers are plotted in Figures 171, 172, and 173.

Cables to the accelerometer located in the aft end of the BDU were broken and no data were collected during the ground simulation test. For comparison with flight test data, the mean square acceleration values at each accelerometer for the ground simulation tests are shown in Table 30.

TEST RESULTS

Measured Propellant Stresses

Grain instrumentation output was recorded using the flight recorder during the simulation tests. Analog data in the form of oscillographs and digital tapes were produced and used for data reduction per the normal flight test analysis procedure.

Thermally Induced Stresses

Variations in stress levels during flight derive principally from temperature excursions occurring in the propellant section and the ambient pressure because the diaphragm gages are sealed to the atmosphere. In relating measured stresses to calculated response or between flight and ground tests, it is important to account for differences in what is being measured.
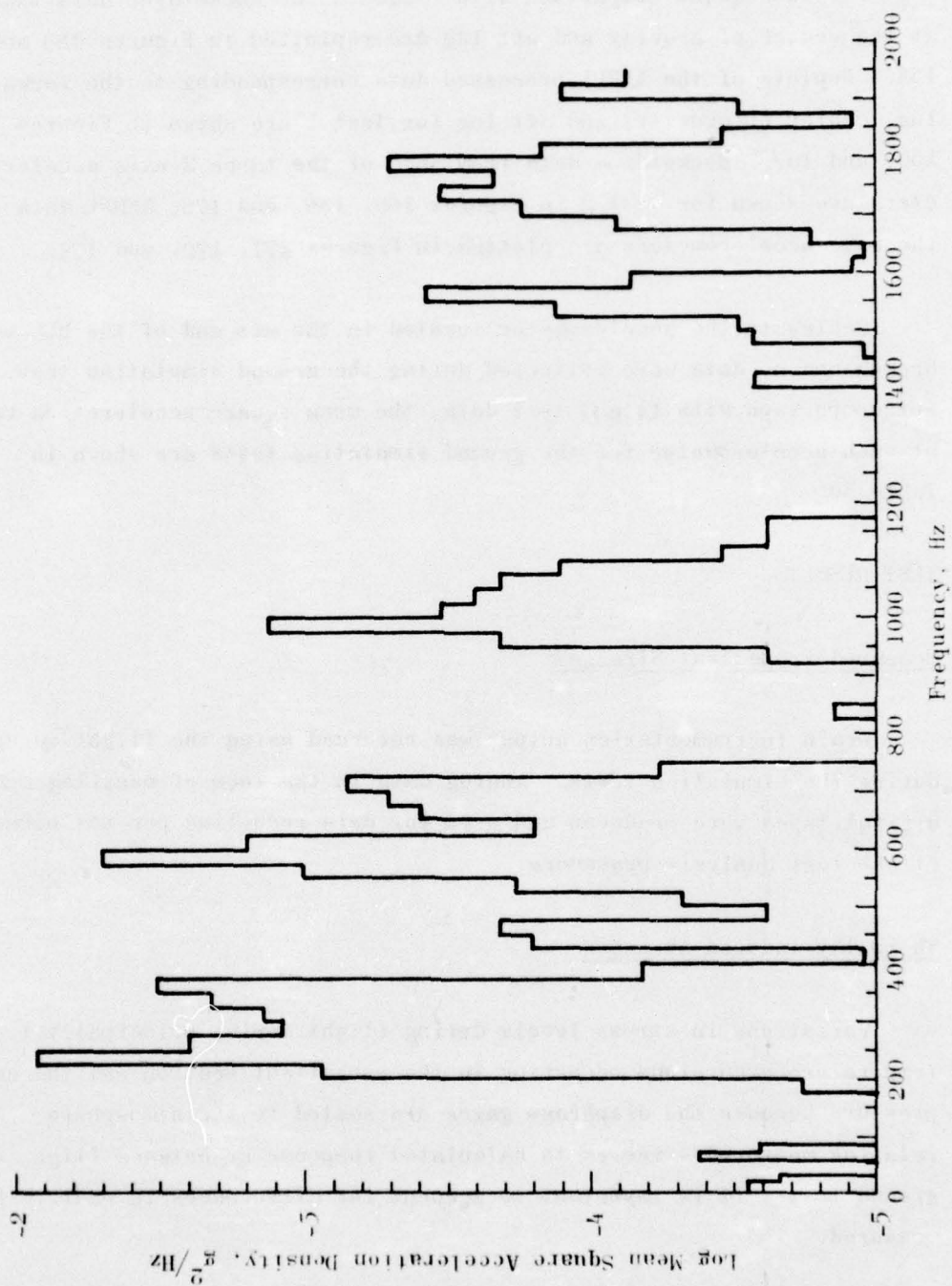
Figure 163; Mean Square Acceleration Density vs Frequency, Simulation
Test 1, °g Z-Axis Accelerometer (Rocketdyne Data)
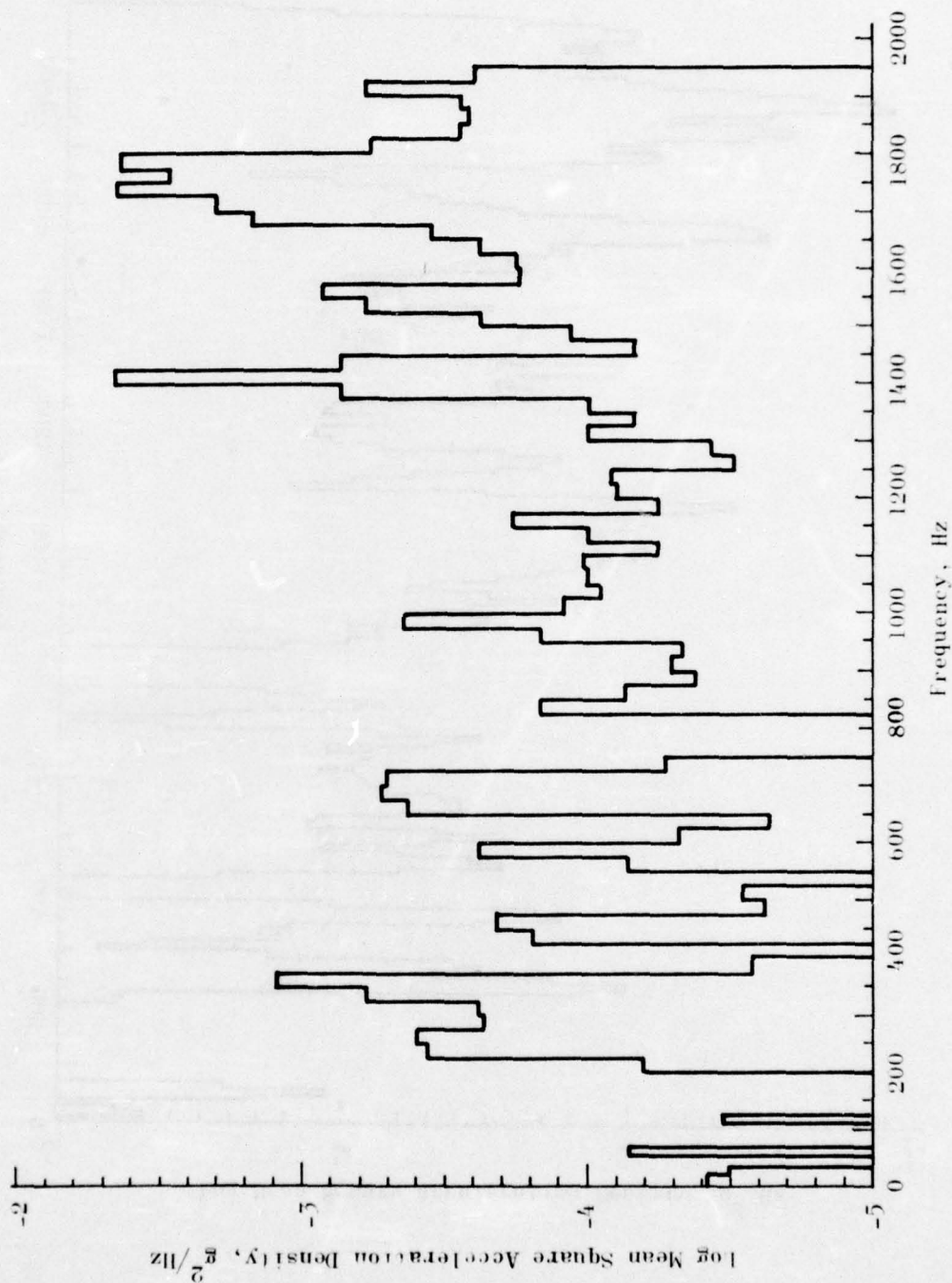
Figure 164. Mean Square Acceleration Density vs Frequency, Simulation
Test 1, Aft Lug Z-Axis Accelerometer (Rocketdyne Data)

233
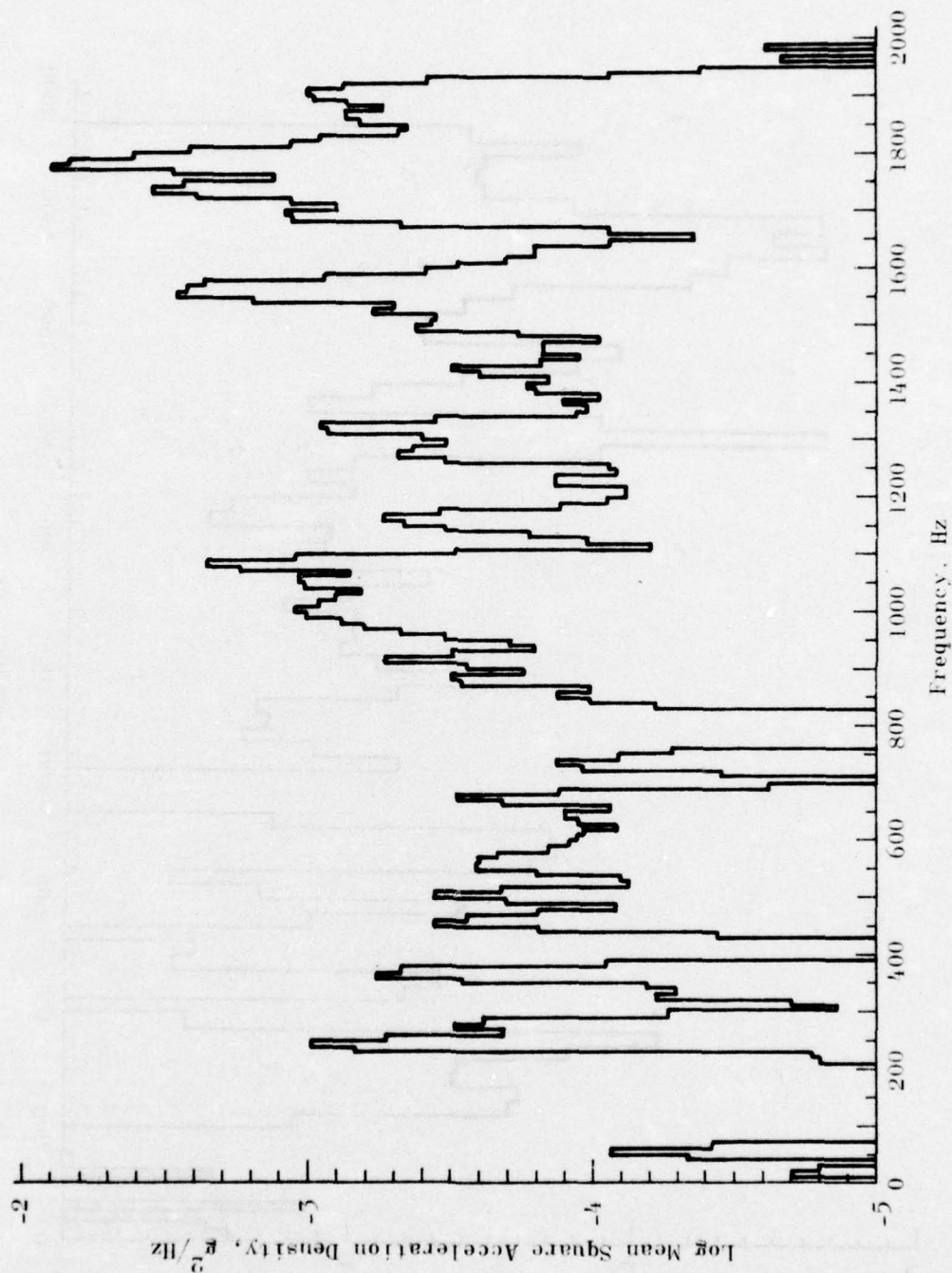
Figure 165. Mean Square Acceleration Density vs Frequency, Test 1, Cut 14, Fwd Lug Z-Axis Accelerometer (AFRPL Data)

234
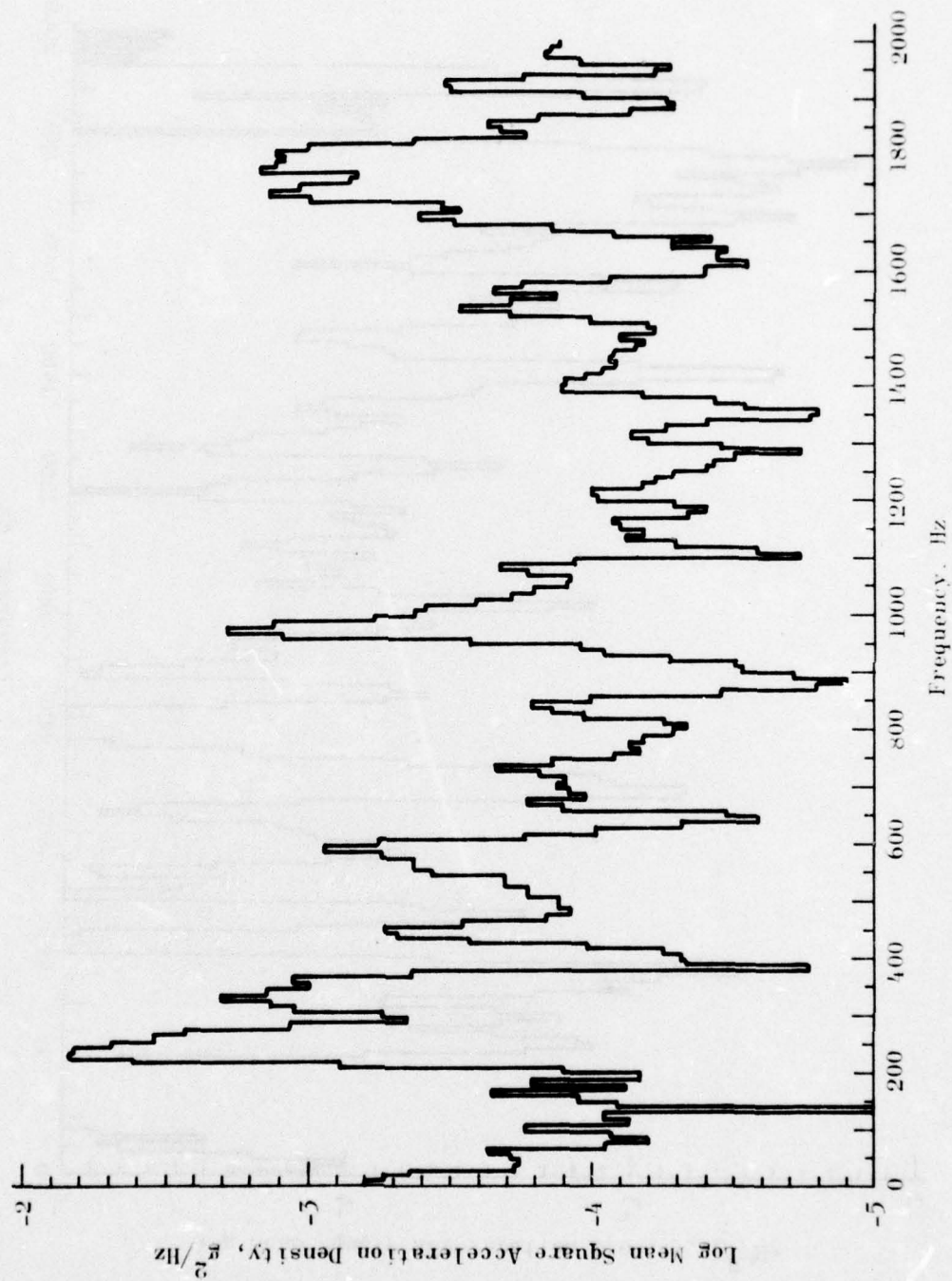
Figure 166. Mean Square Acceleration Density vs Frequency, Test 1, Cut 14, cg Z-Axis Accelerometer (AFRPL Data)

235
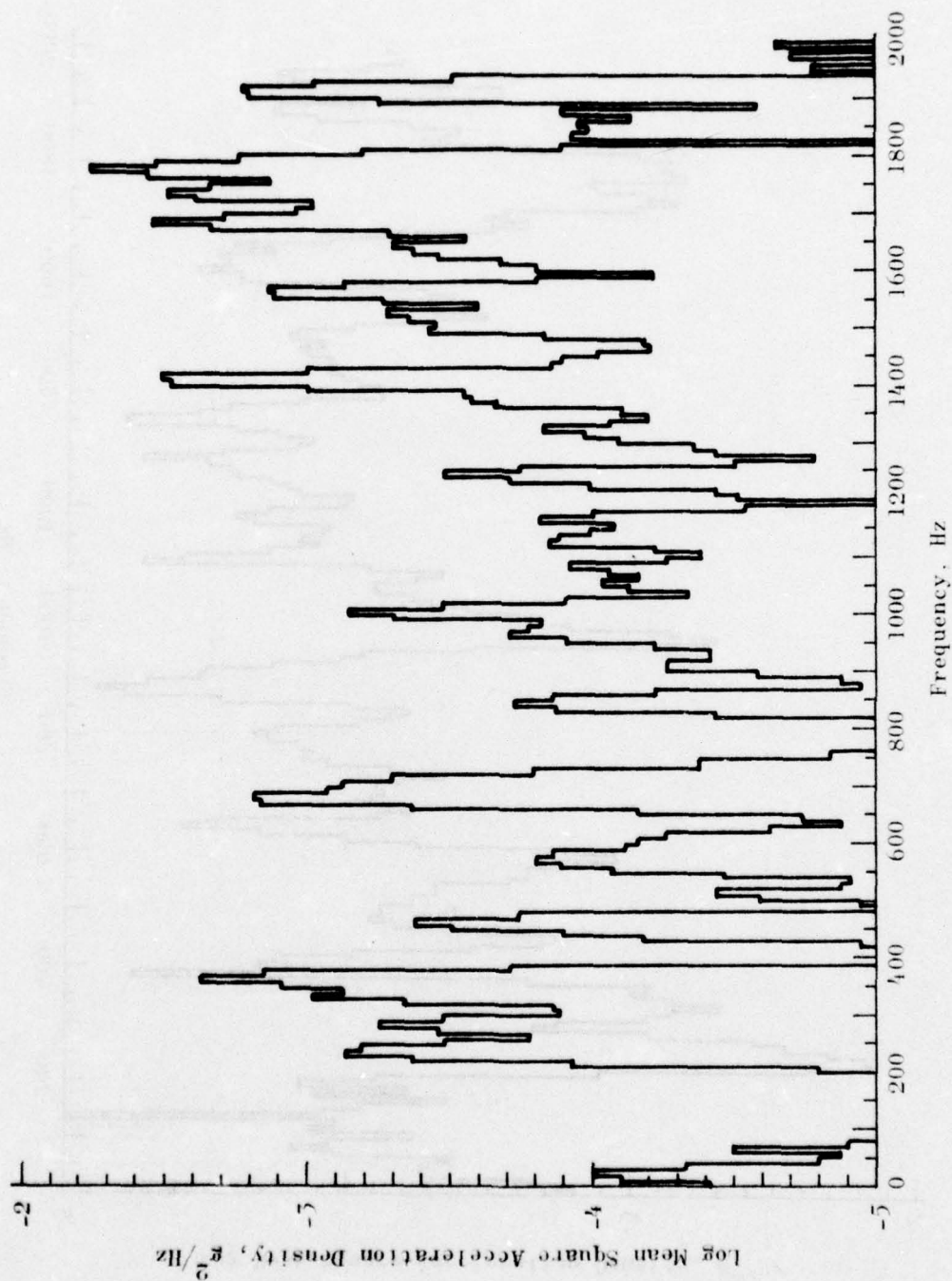
Figure 167. Mean Square Acceleration Density vs Frequency, Test 1, Cut 14, Aft Lug Z-Axis Accelerometer (AFRPL Data)

236
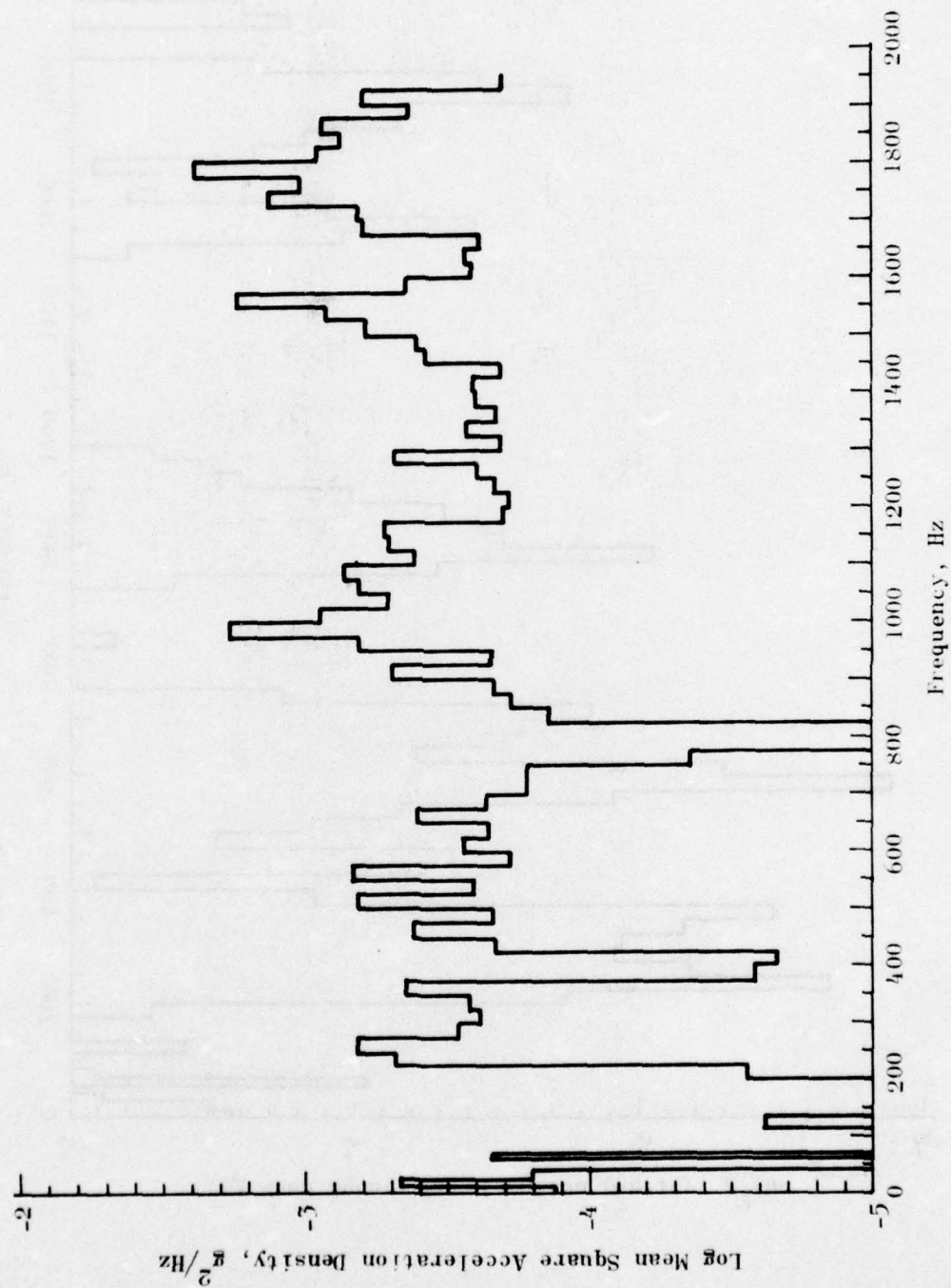
Figure 168. Mean Square Acceleration Density vs Frequency, Test 2, Fwd Lug Control Accelerometer (Rocketdyne Data)
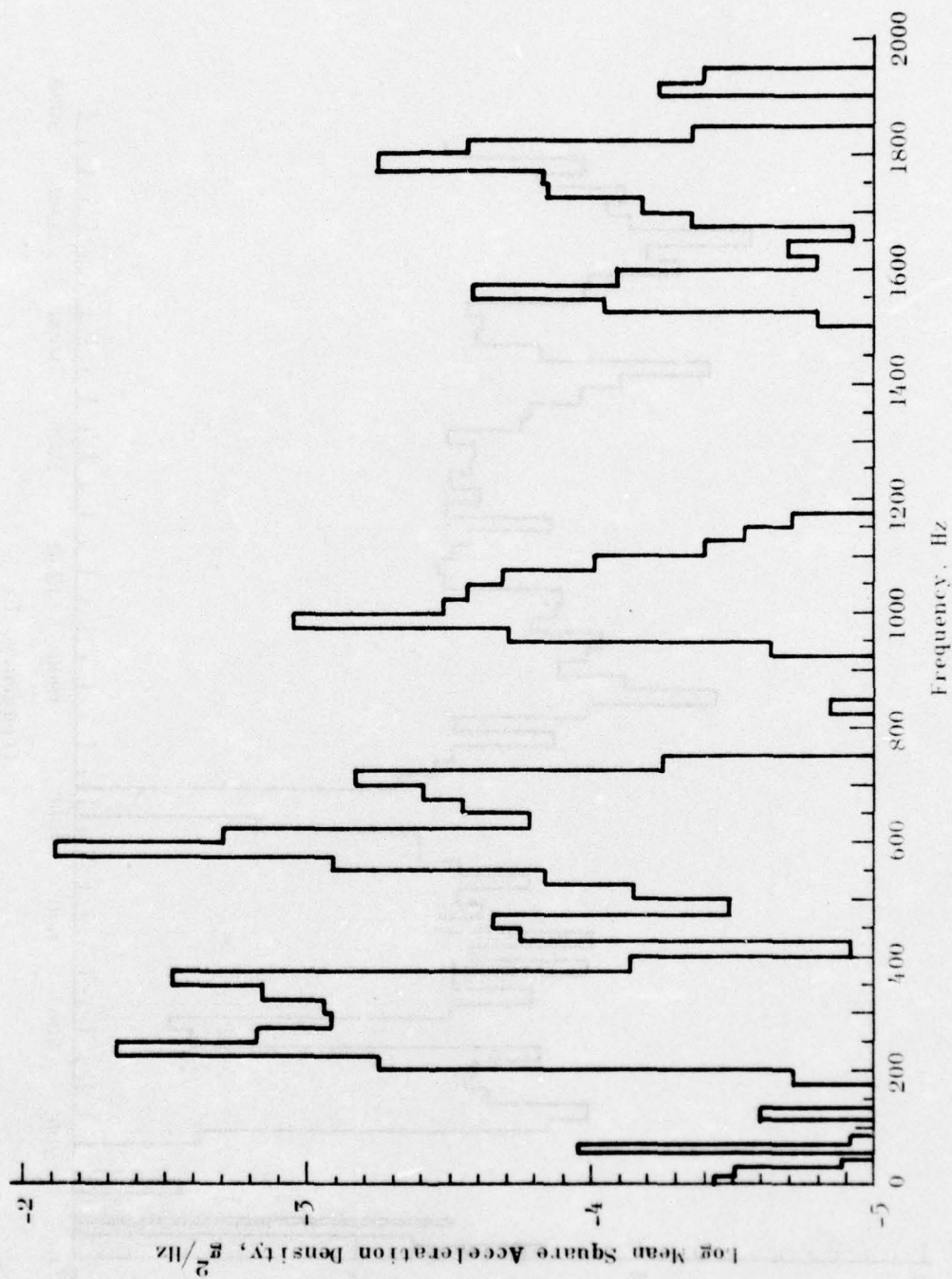
Figure 169. Mean Square Acceleration Density vs Frequency, Test 2, cg Z-Axis Accelerometer (Rocketdyne Data)

238
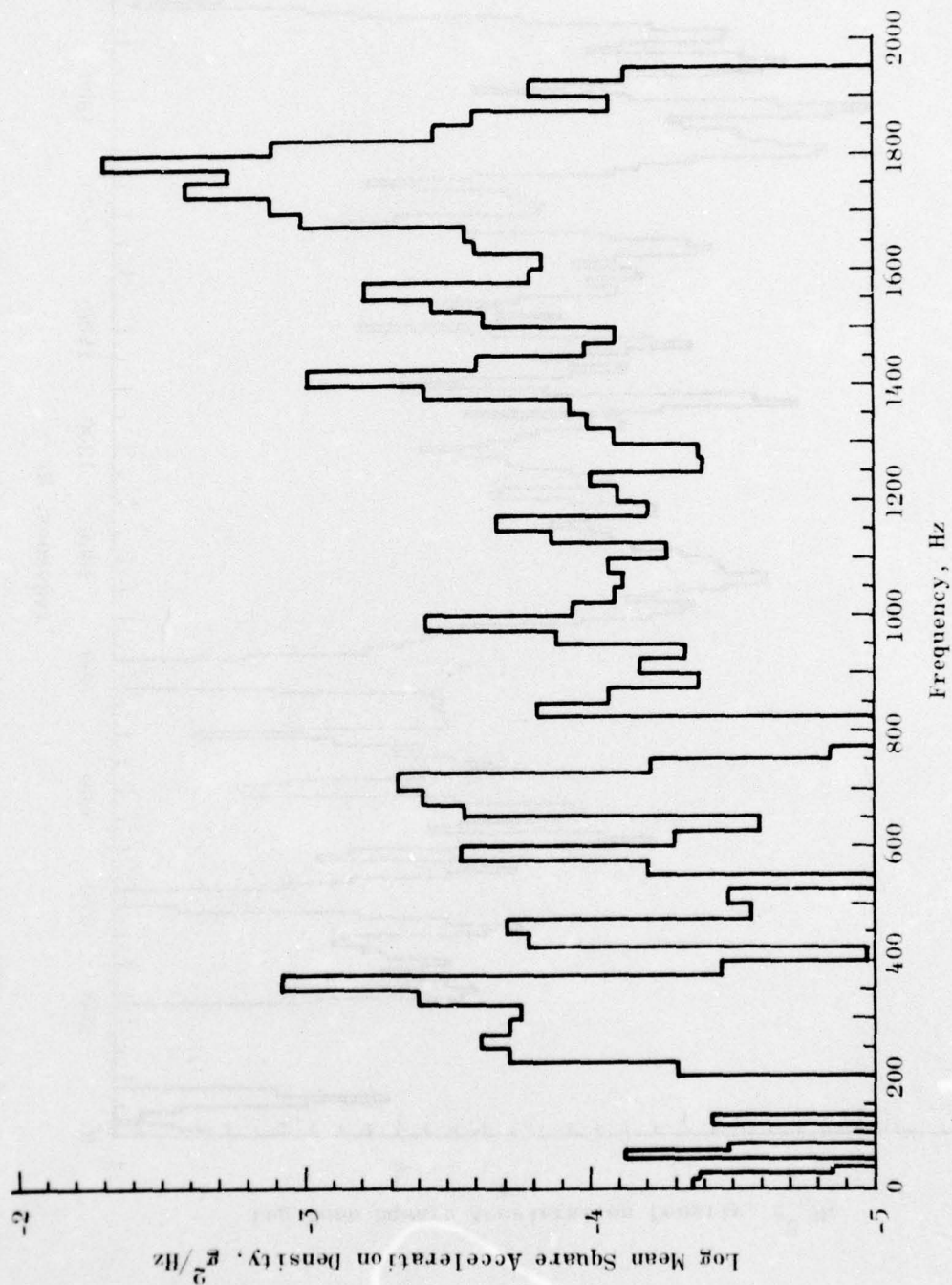
Figure 170. Mean Square Acceleration Density vs Frequency, Test 2, Aft Lug Z-Axis Accelerometer (Rocketdyne Data)

239
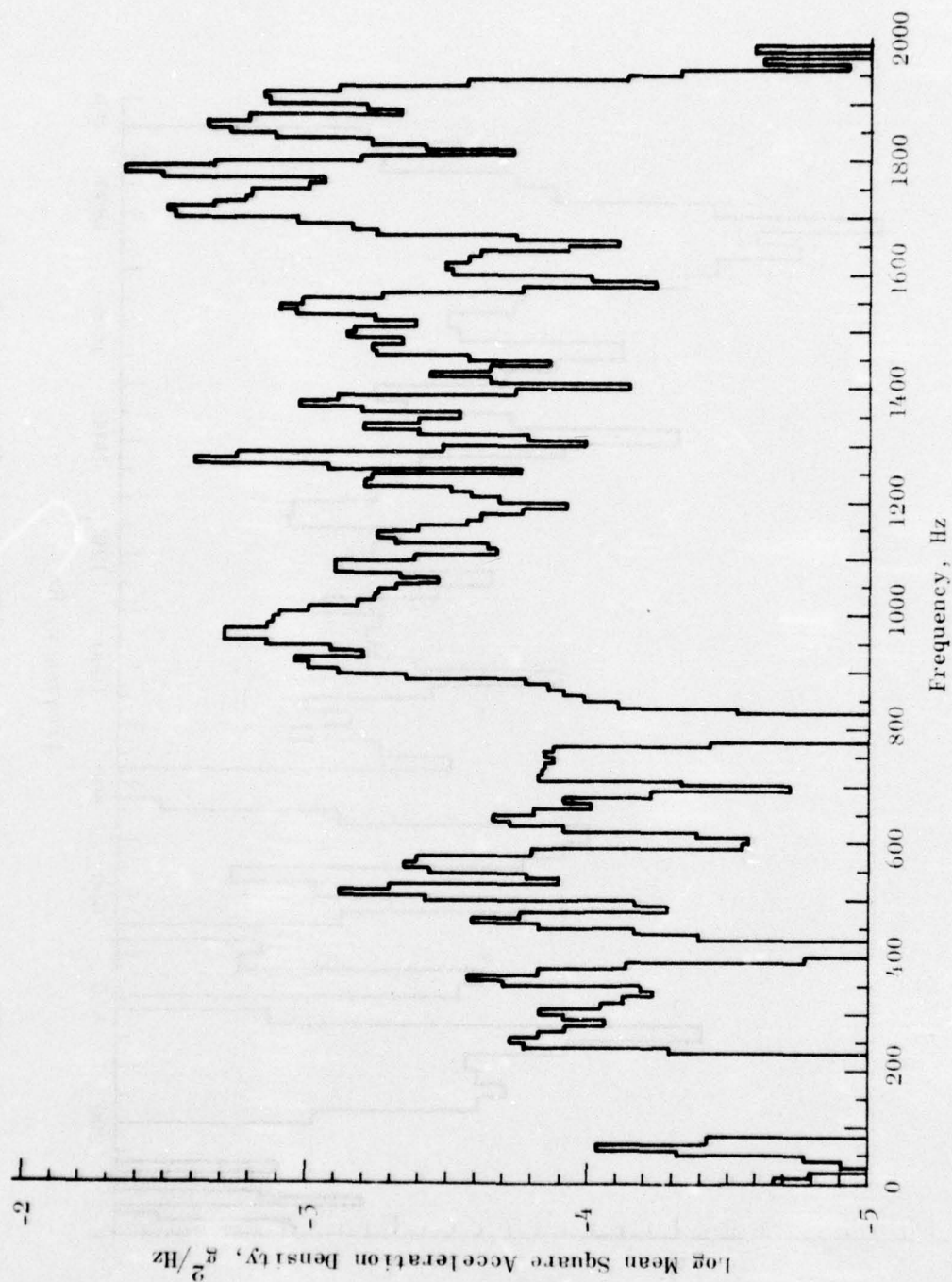
Figure 171. Mean Square Acceleration Density vs Frequency, Test 2, Cut 8, Fwd Lug Z-Axis Accelerometer (AFRPL Data)

240
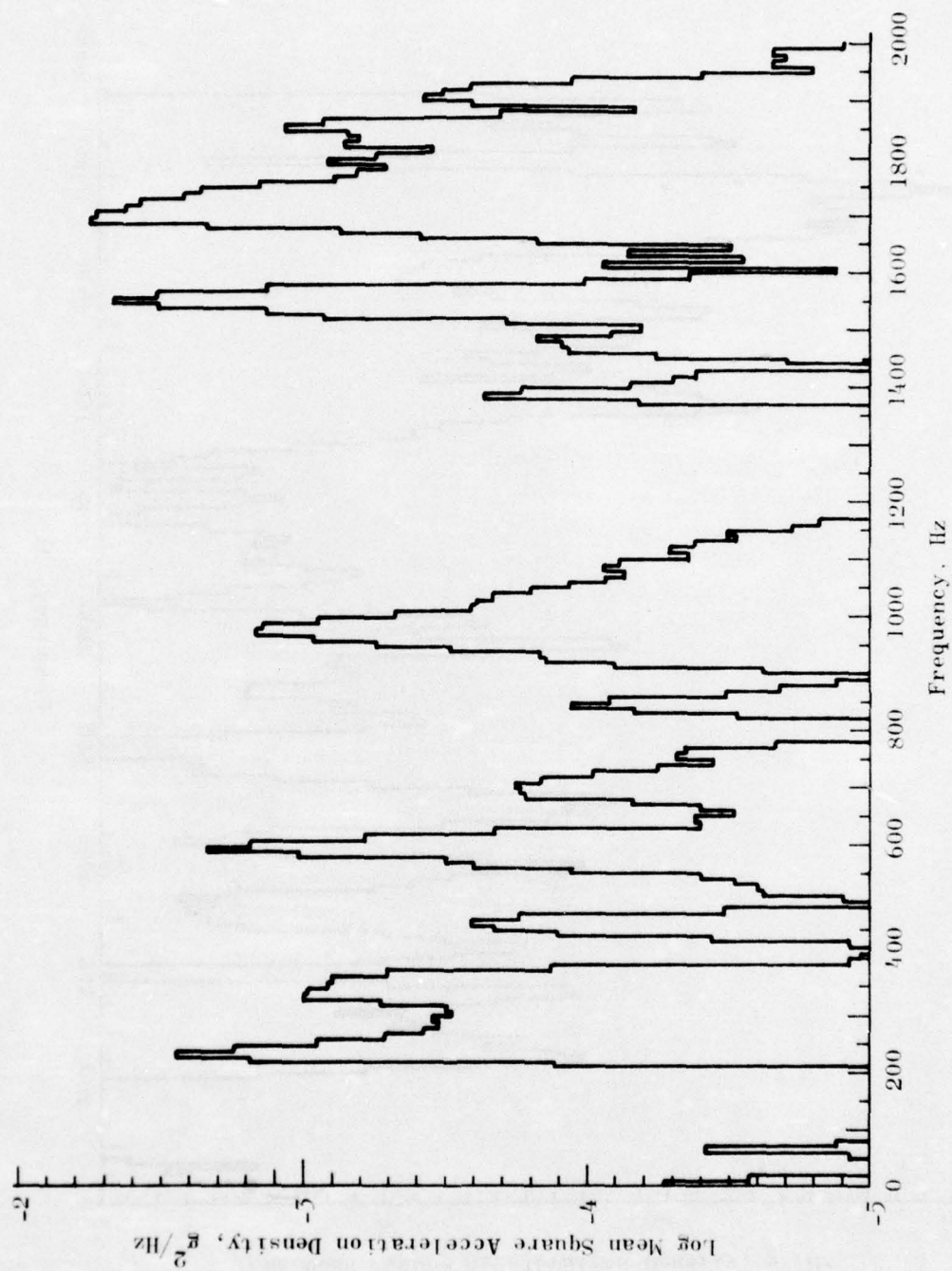
Figure 172. Mean Square Acceleration Density vs Frequency, Test 2,
Cut 8, αg Z-Axis Accelerometer (AFRPL Data)

241
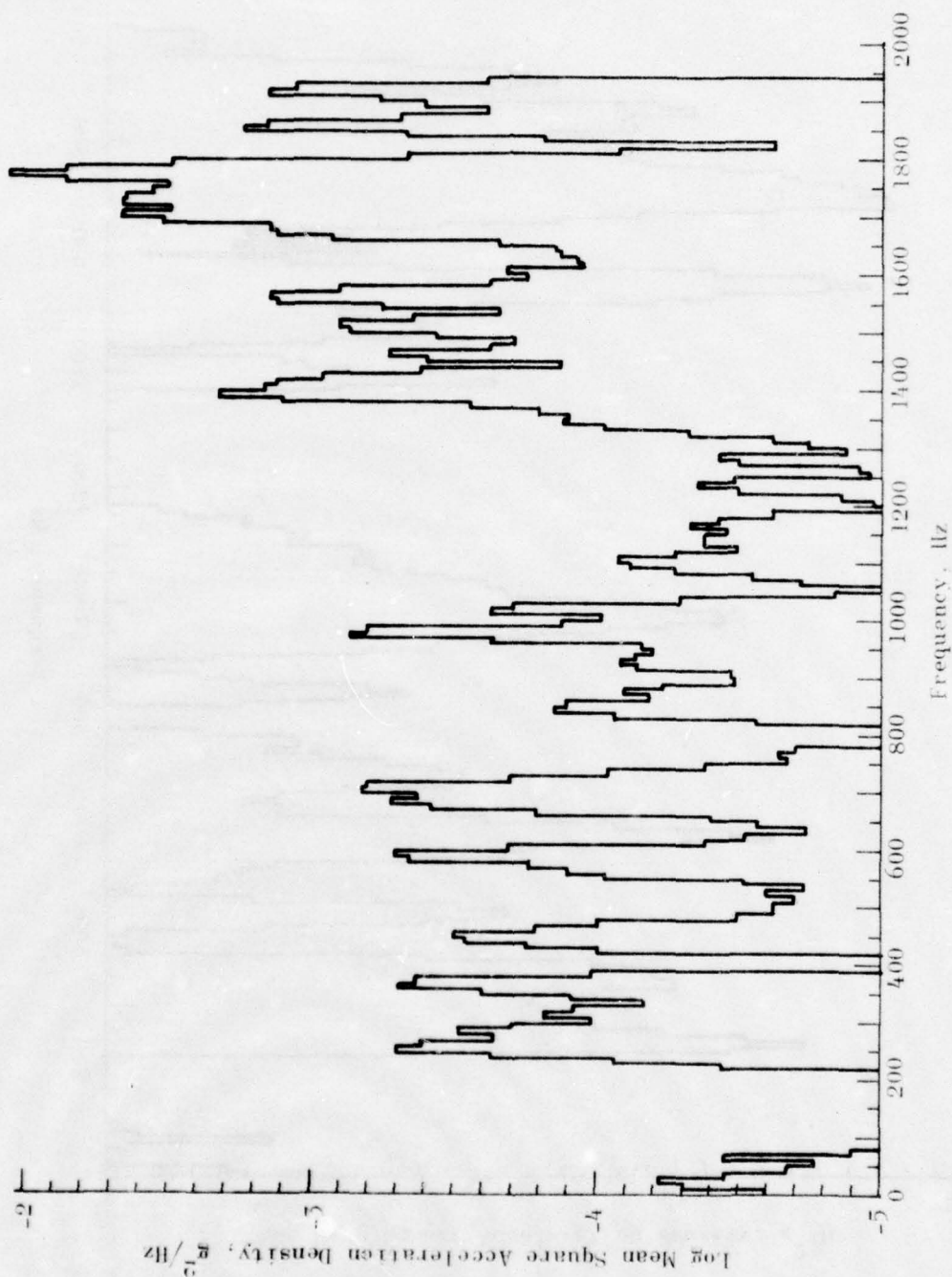
Figure 175. Mean Square Acceleration Density vs Frequency, Test 2,
Cut 8, Aft lug Z-Axis Accelerometer (AFRPL Data)

242

TABLE 30. MEAN SQUARE ACCELERATION (g^2)
FOR GROUND SIMULATION TESTS

	Test 1, Cut 14	Test 2, Cut 8
Aft End X-Axis[1,2]	0.045	0.035
Aft End Z-Axis[1,2]	0.016	0.010
cg X-Axis	0.408	0.311
cg Z-Axis	0.792	0.853
Fwd Lug Z-Axis	0.987	0.955
Aft Lug Z-Axis	0.837	1.003

$$\text{Mean Square Value} = \frac{1}{1000} \sum_{i=1}^{1000} x_i^2$$

x_i = digital data points (g) sampled at
4000 points/sec

[1] Major axes of accelerometers are rotated 45°
to major axes of motor.

[2] Cable to aft end accelerometer was broken;
values are noise level only.

243

For a particular test, data were best presented by normalizing all responses to zero at the initial condition. This was accomplished by subtracting the initial stress level from all subsequent readings. In addition, for the flight tests, it was necessary to reduce measured stress levels by an amount equal to the change in ambient pressure at the motor. This pressure was determined by the altitude of the test vehicle and the Mach number of the aircraft. Altitude-pressure corrections may be obtained from meteorological data for the flight area at standard atmosphere tables. The velocity correction was taken from data supplied by AEDC (Mr. Dick Matthews) as shown in Figure 174.

Normalized thermal responses of the normal stress gages for two simulations are shown in Figures 175 and 176. These data were obtained from the analog display (oscillographs). For subsequent discussion, attention will focus on the response of Gage N-23, located near the mid-plane of the BDU.

The uncertainty in the reduced data is influenced by several factors including:

1. Accuracy of Reduction method
2. System recording noise combined with diaphragm response
3. For flight data, knowledge of local pressure

The response of Gage N-23 for the two methods of data reduction is portrayed in Figure 177 for Simulation Test 1 and Figure 178 for Test 2. The two methods generally agree within a spread of uncertainty on the order of $\pm$ 0.6 psi.

The corresponding (dc normal stress) data from Flights 9 and 10 are shown in Figures 179 and 180, respectively. These plots show the gage response corrected for altitude and aircraft velocity. Results between simulation and flight test compare satisfactorily.

244
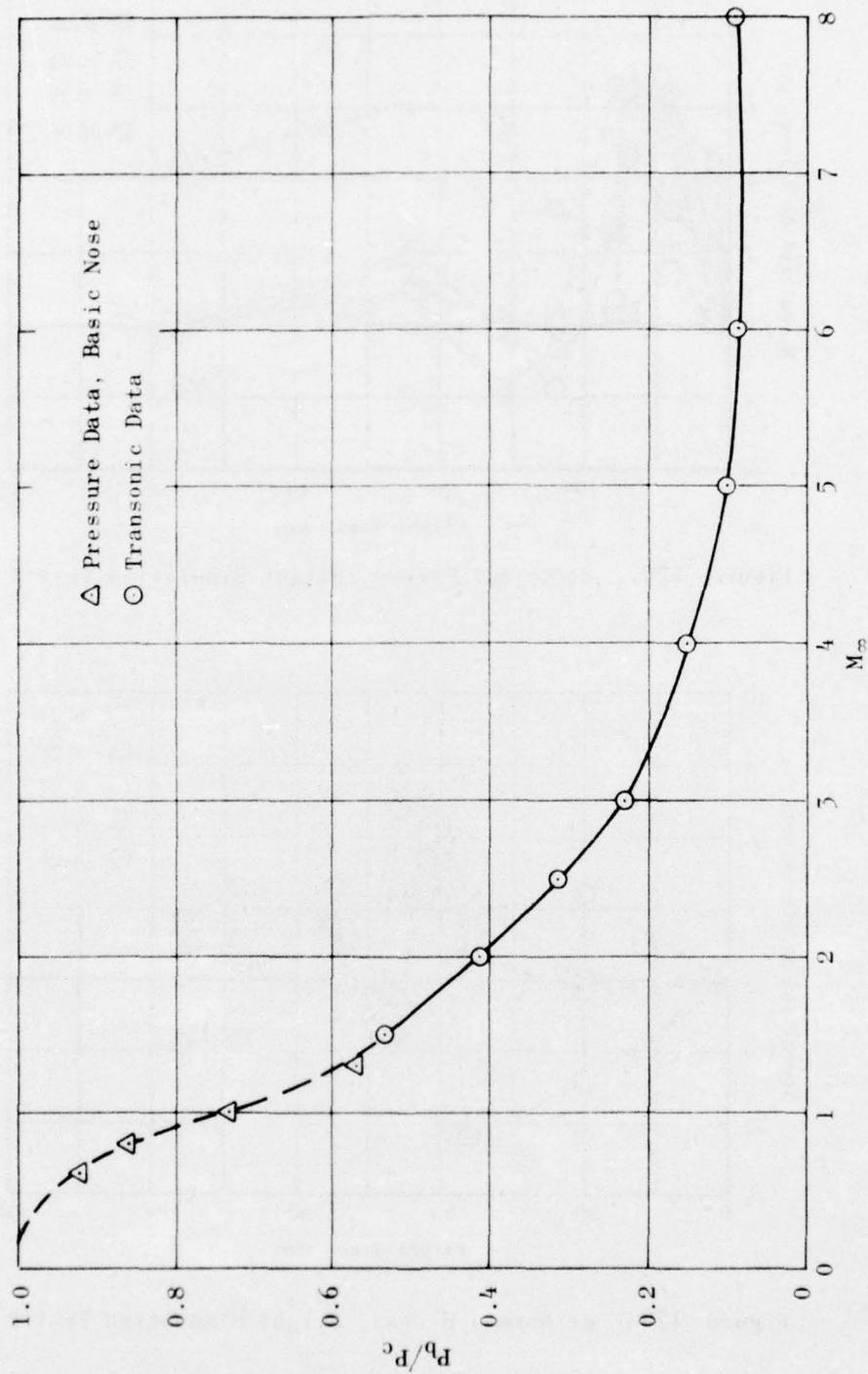
Figure 174. Ratio of Base Pressure to Cone Pressure vs Free-Stream Mach Number
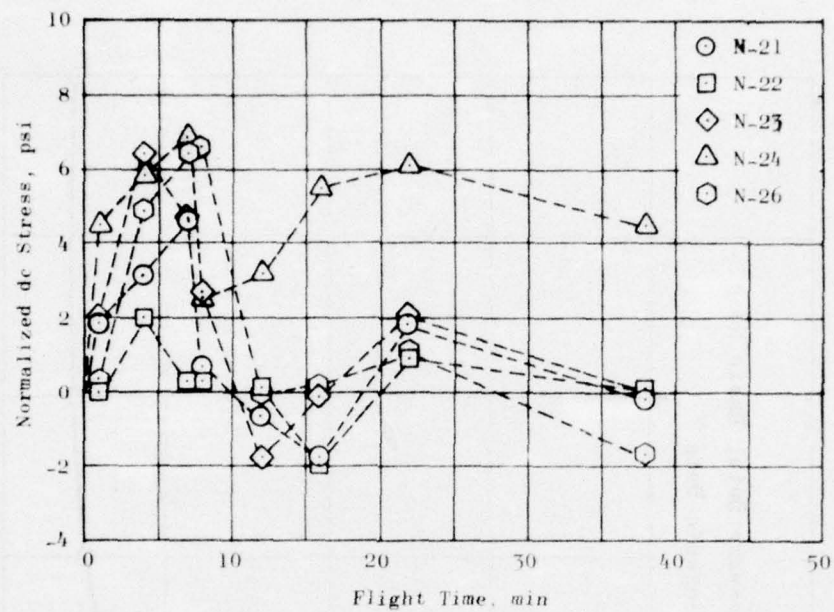
Figure 175. dc Normal Stress, Flight Simulation Test 1
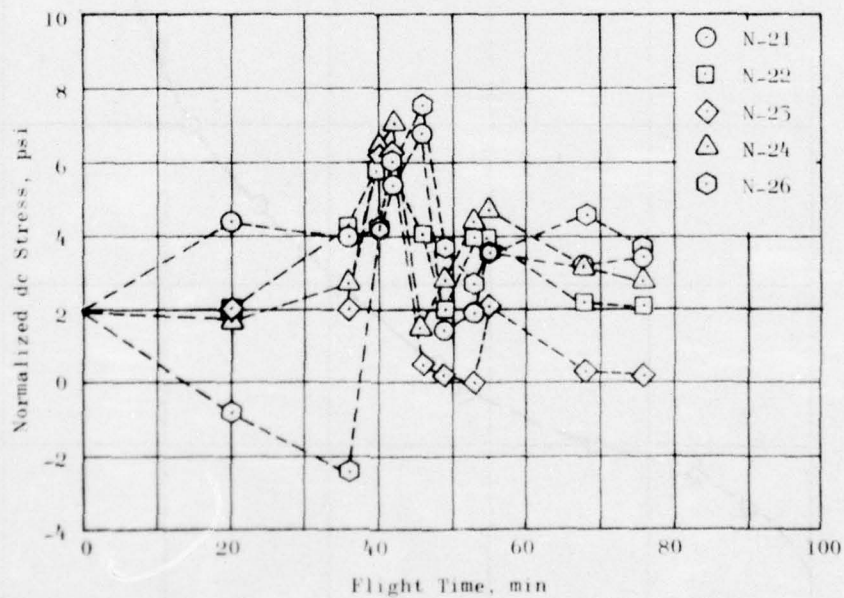
Figure 176. dc Normal Stress, Flight Simulation Test 2

246
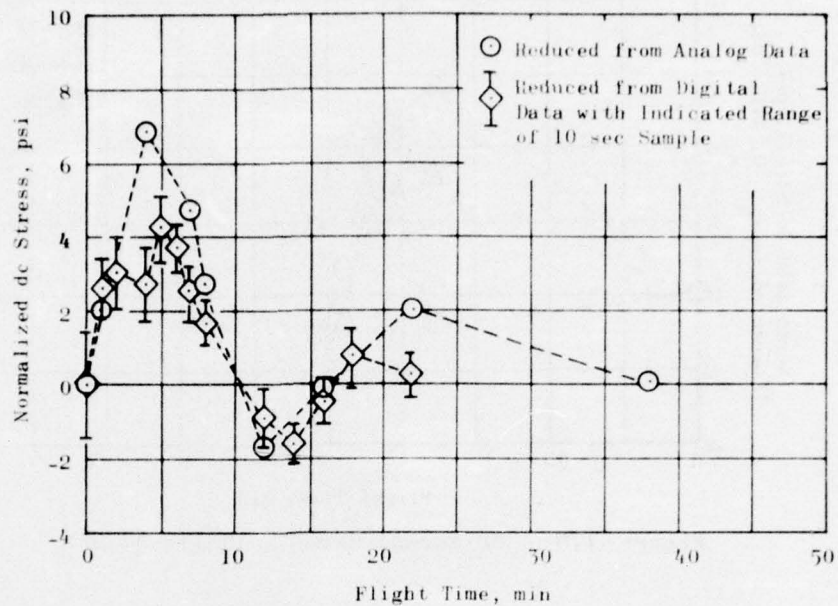
Figure 177. dc Normal Stress, N-23
Flight Simulation Test 1
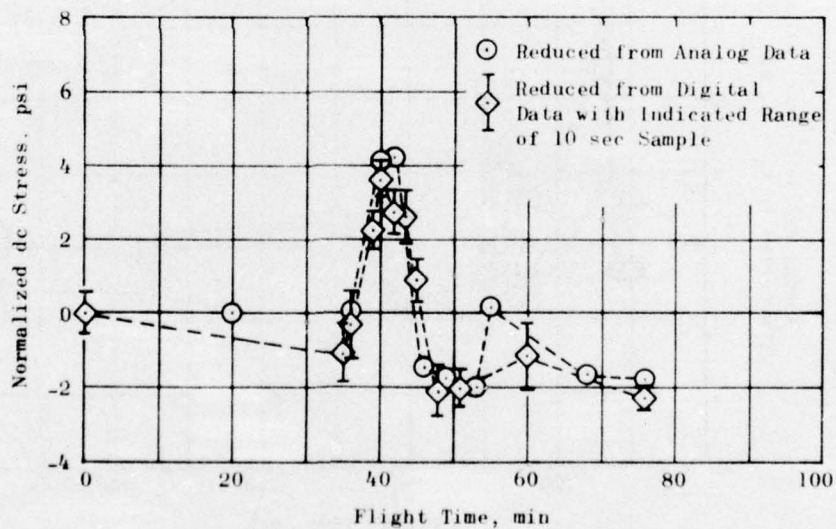
Figure 178. dc Normal Stress, N-23,
Flight Simulation Test 2

247
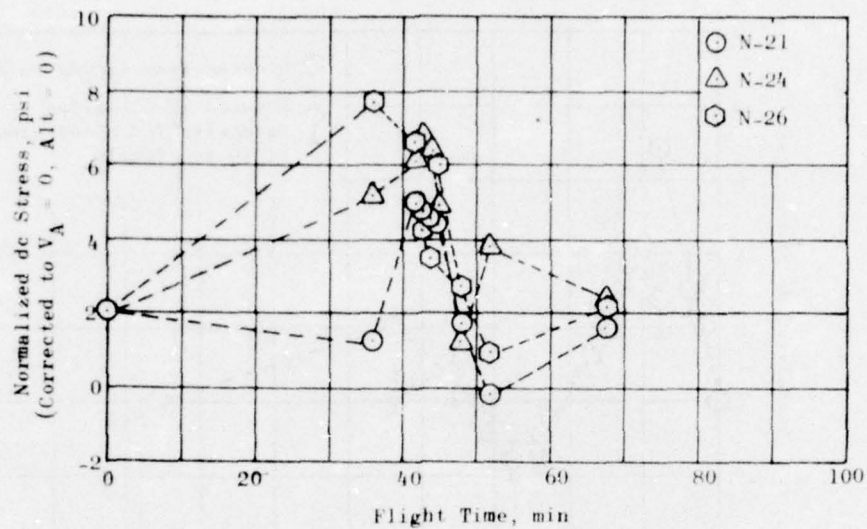
Figure 179. dc Normal Stress, Flight Test 9
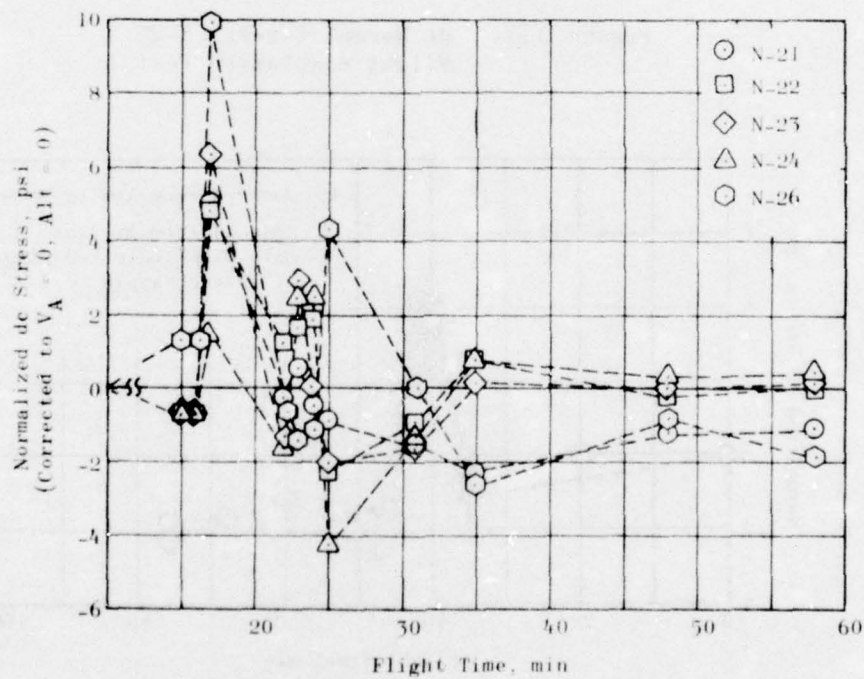
Figure 180. dc Normal Stress, Flight Test 10

248

POSTFLIGHT GROUND SIMULATION

Following the twentieth flight test, the BDU was returned to Rocket-
dyne for a final round of ground simulation of the flight environments.
Two basic flight profiles from captive flight testing--loiter/dash and
low-speed/high-altitude cruise--were selected for simulation. Dynamic
inputs were the highest level random signals recorded during supersonic
dash and TFR. These levels were essentially the same. The objective of
these tests was to establish the degree to which the captive flight en-
vironment can be simulated in ground test equipment using motor grain
response as the evaluation criterion.

Four tests were run to simulate the captive-flight environment.
Temperature profiles shown in Figures 181 and 182 represent the two
extreme thermal environments. The control random vibration levels are
shown in Figure 183 and 184 for the X-axis (in the plane of the aircraft
wing) and Z-axis (perpendicular to the plane of the wing), respectively.
The control accelerometer was located at the center of gravity of the
missile where the derived levels were obtained during flight. A direct-
connecting port to the shaker driver was used for the Z-axis test. The
missile was mounted in the launcher/ejector as in flight and the launcher
was driven by the shaker for the X-axis test. Summary data plots, Figures
185 through 188, show that the temperature and stress gage histories were
well simulated. The hoop-direction clip gage gave much lower response
than during flight, but the fact that it gave no reasonable response
during Simulation Test 2 raises doubts concerning its functionality during
these tests.

Dynamic response is summarized in Table 31. Data for Test 4, Condi-
tion 1A, are obviously not for a static condition. These data were
actually recorded after test start-up. Condition 1A for the other three
tests reflect system response to a static condition and define the noise
level of the overall system. The true dynamic gage response is most
nearly reflected in the ac component record and is seen to be on the
order of < 0.5 psi.
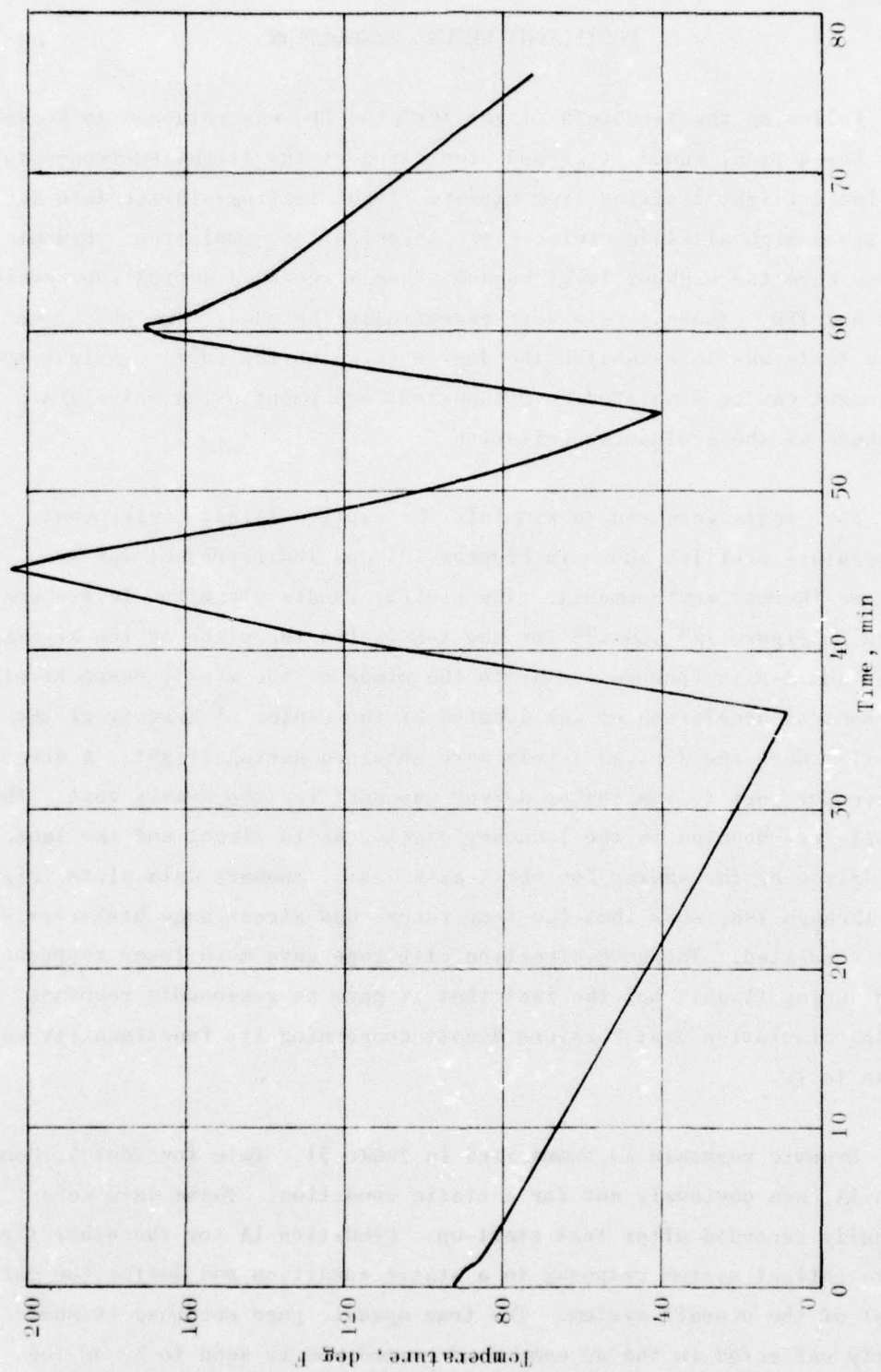
Figure 181. Mission 9, Type Aeroheat Driving Function
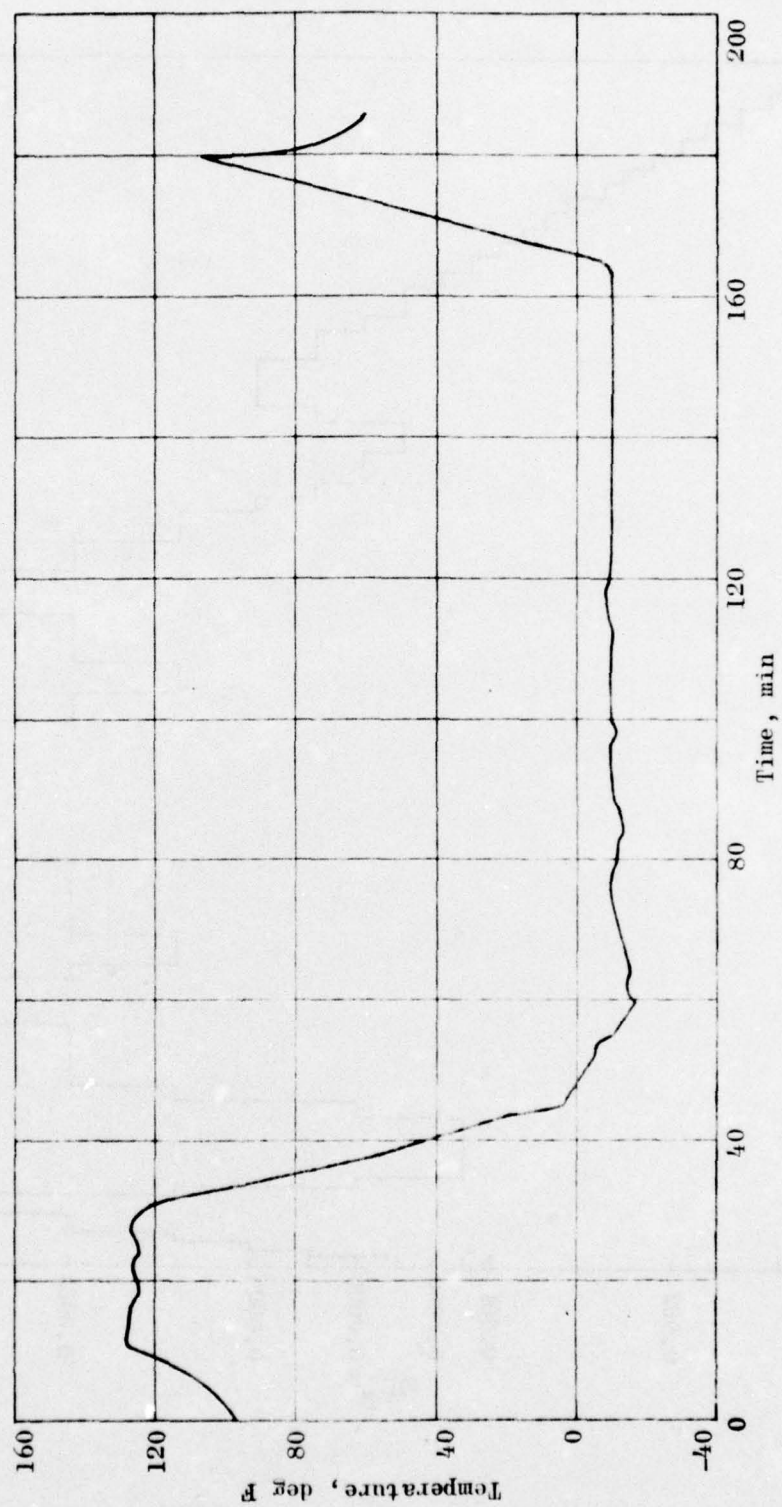
Figure 182. Mission 15, Type Aeroheat Driving Function

251
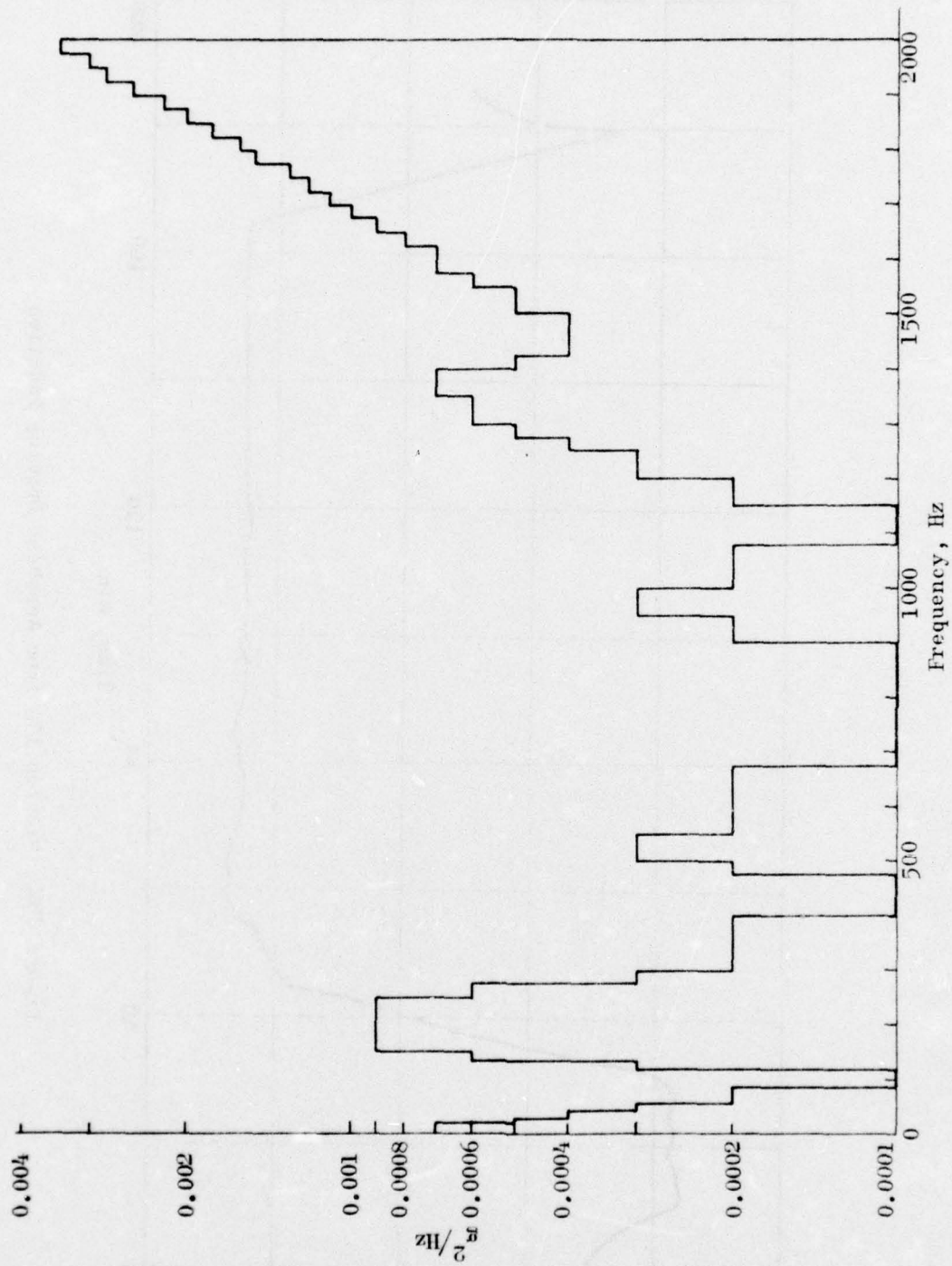
Figure 183. Random Vibration, X-Axis cg Driving Function
Power Spectral Density, Softmount

252
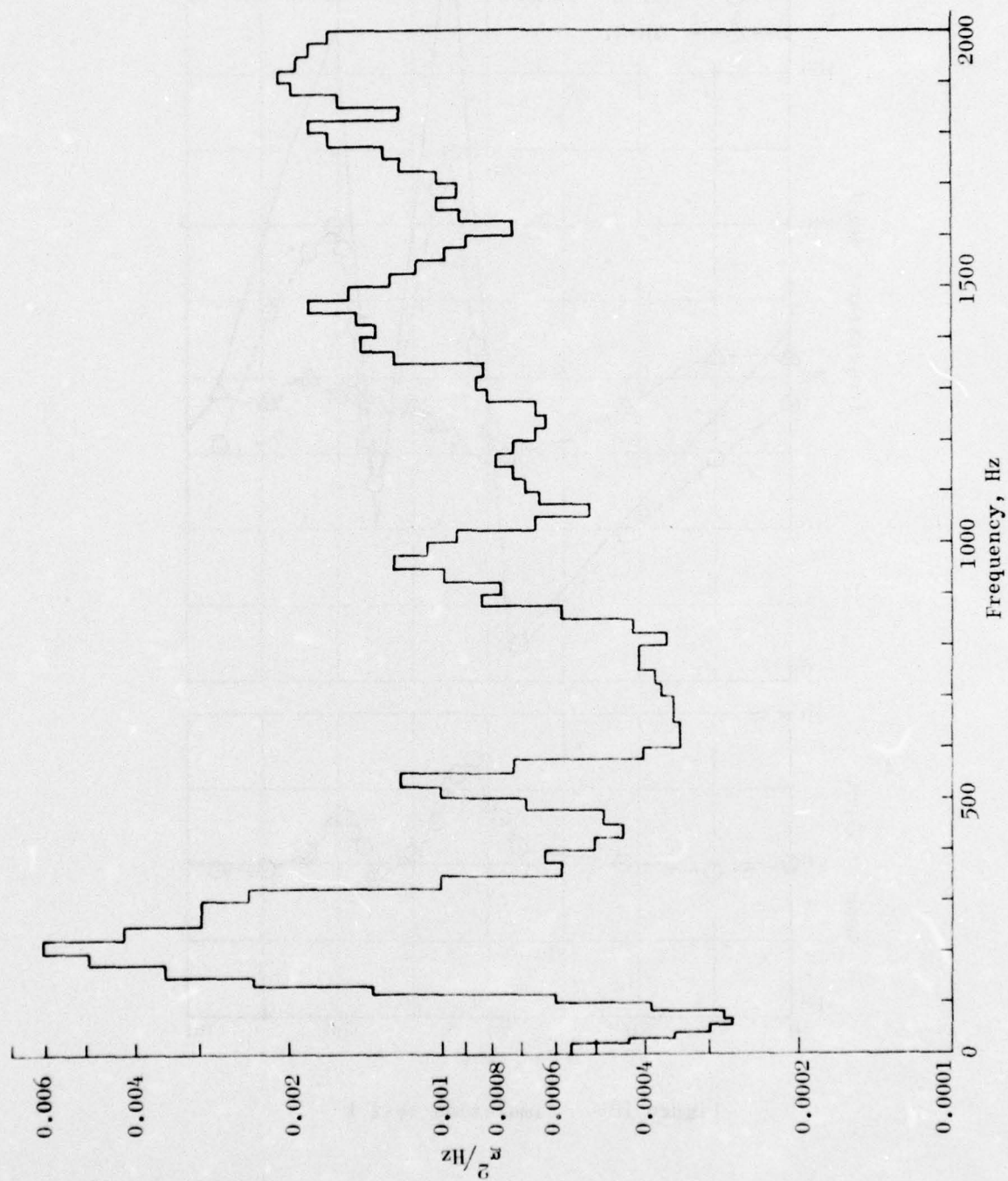
Figure 184. Random Vibration, Z-Axis cg Driving Function
Power Spectral Density, Hardmount
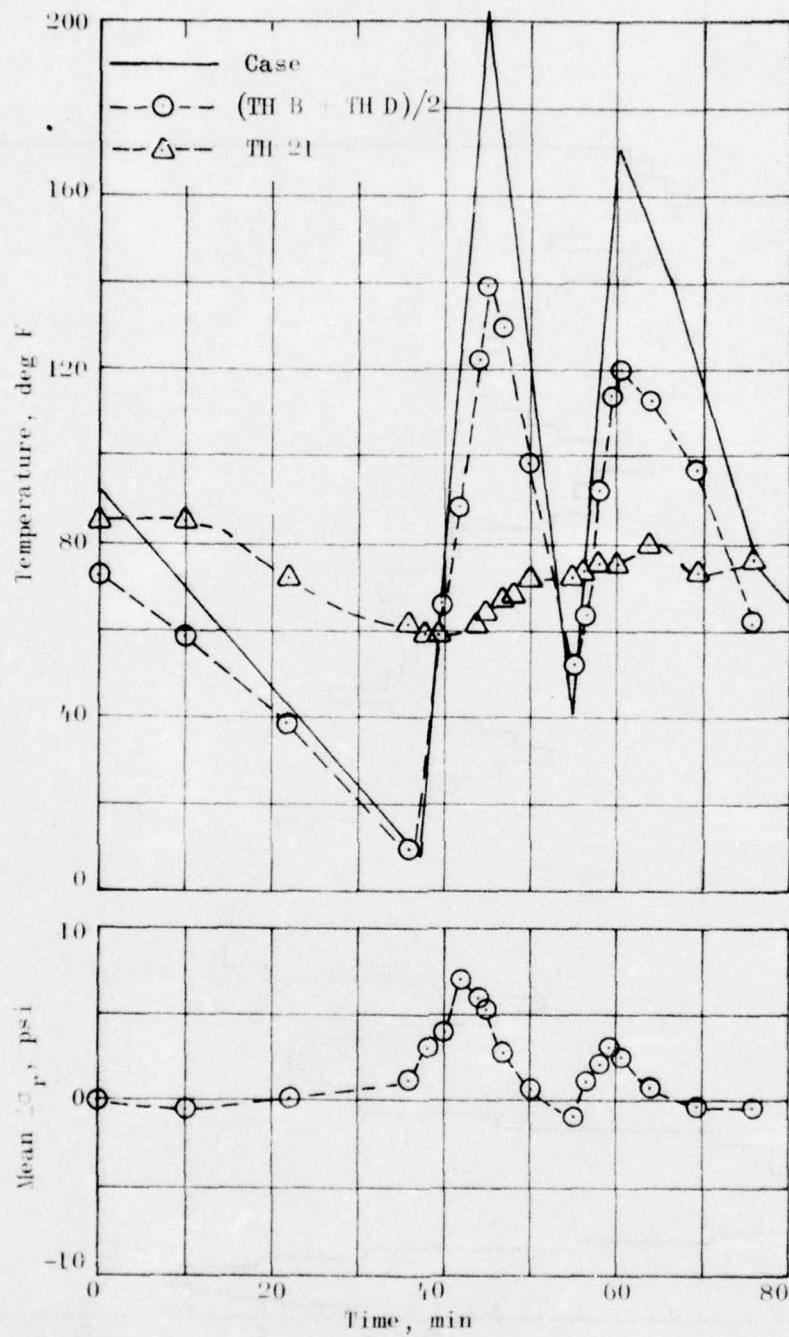
Figure 185. Simulation Test 1

254
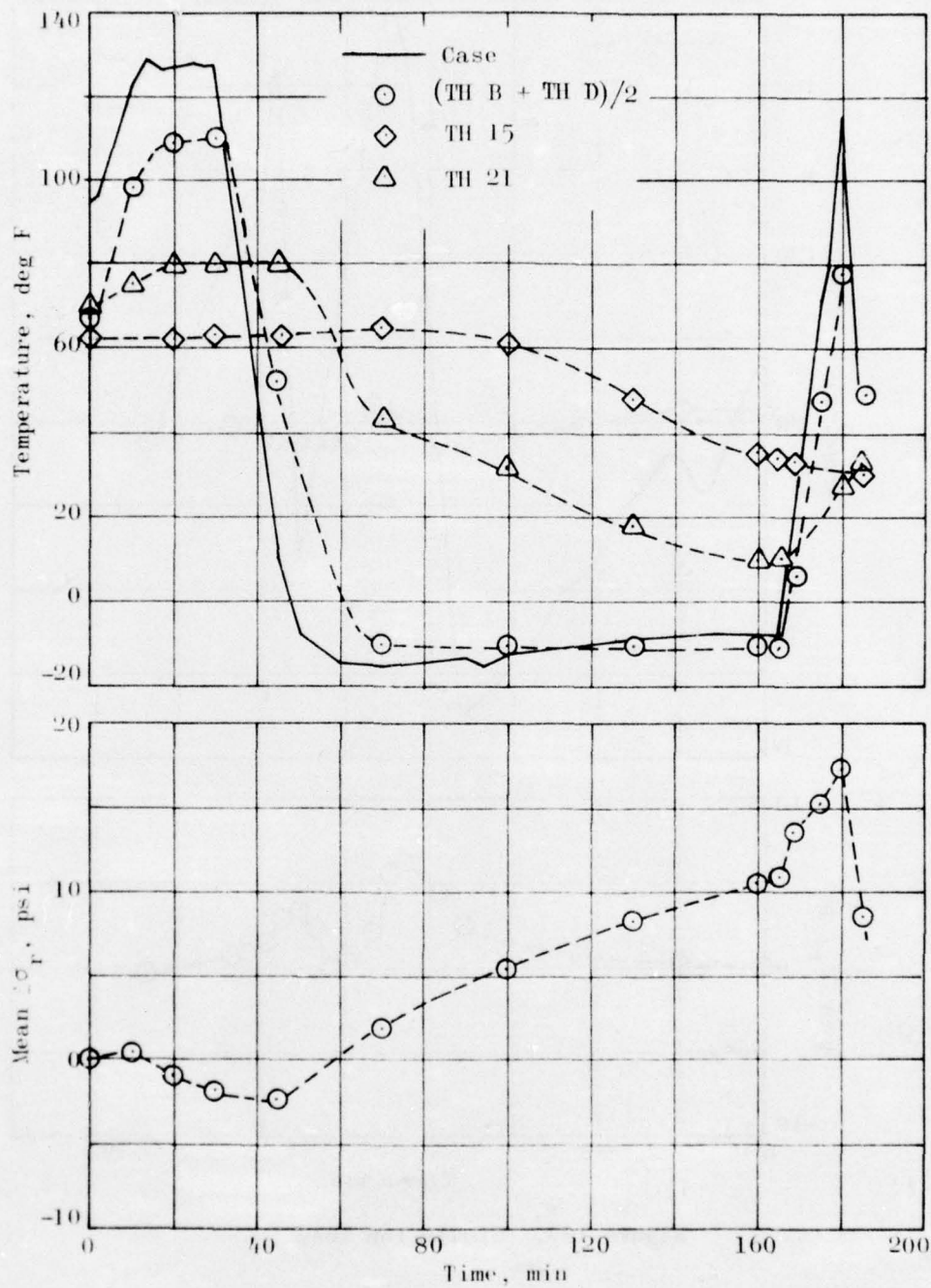
Figure 186. Simulation Test 2

255
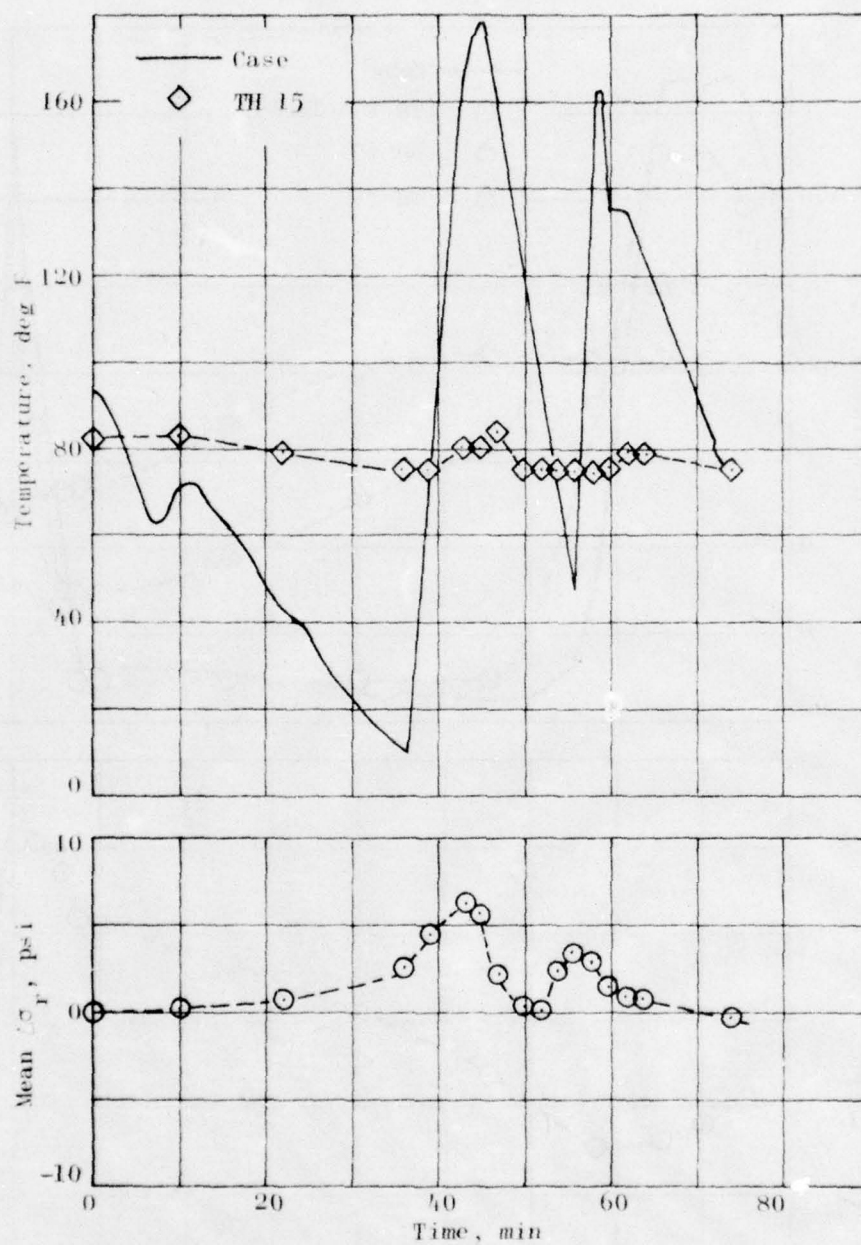
Figure 187. Simulation Test 3

256
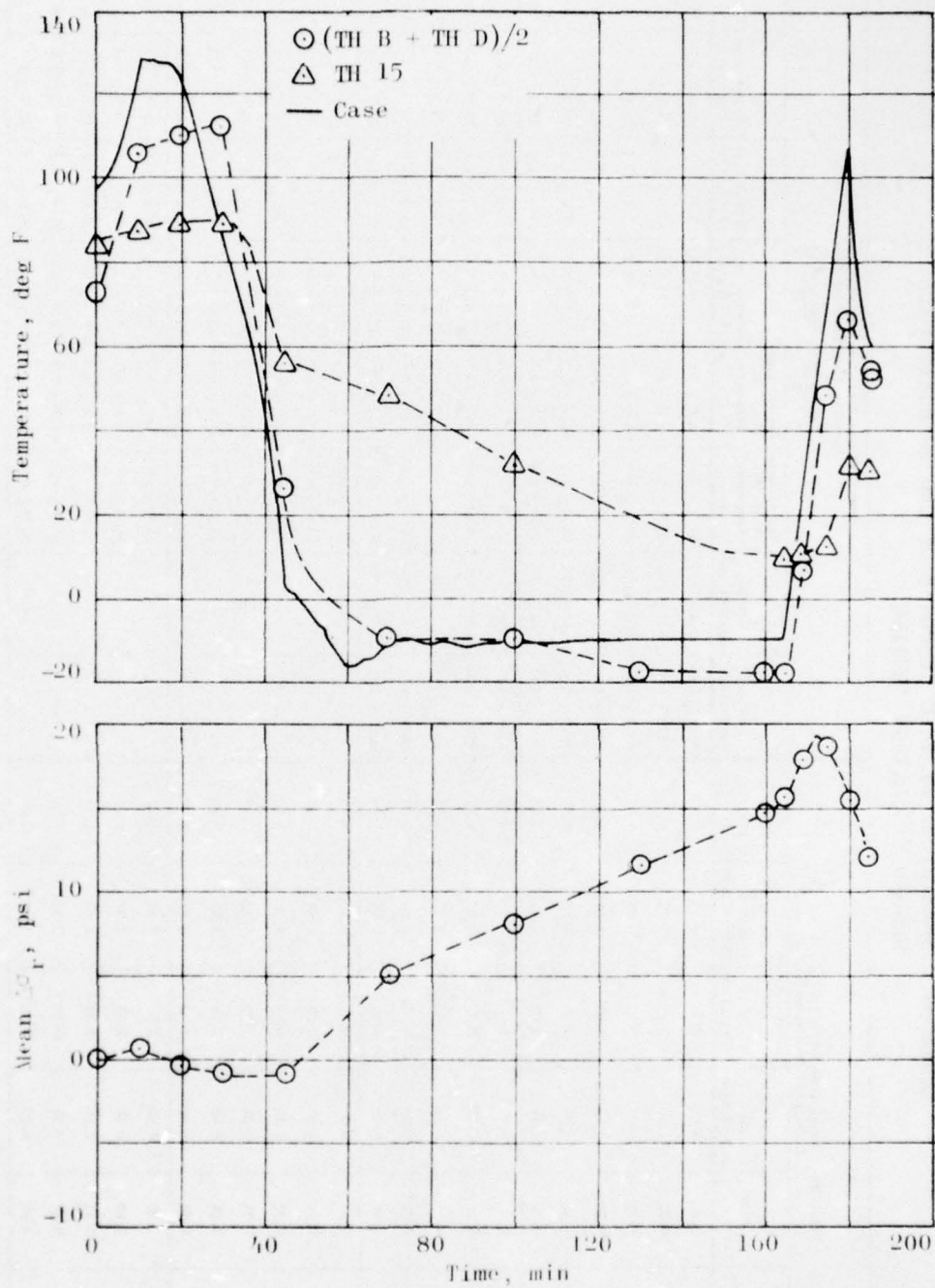
Figure 188. Simulation Test 4

TABLE 51. SUMMARY OF DYNAMIC RESPONSE OF BDU TO POSTFLIGHT GROUND SIMULATION TESTING

Test	Condition	Total RMS g Level from Power Spectral Analysis of Selected Accelerometers						Aft Lug Tension, lb	Fwd Lug Tension, lb	Mean Response Histogram Analysis of 4000 Point Sampling from Selected Gages $\frac{Max - Min}{2} + \frac{Max - Min}{2}$					
		Aft Z (Axis 45°)	Aft X (Axis 45°)	CG X-Direction	CG Z-Direction	Fwd Lug Z-Direction	Aft Lug Z-Direction			Normal Gage N-18, AC Component psi	Normal Gage N-23, AC Component psi	Normal Gage N-18, psi	Normal Gage N-22, psi	Normal Gage N-25, psi	Normal Gage N-24, psi
Sim Test X-Axis, Softmount, Flt 9	1A	0.33	0.0	0.0	0.0	0.10	0.10	8850 ± 650	2700 ± 250	14.7 ± 0.1	-2.8 ± 0.1	4.7 ± 3.5	3.4 ± 2.1	20.0 ± 5.0	5.5 ± 2.5
	1B	0.52	0.22	1.19	3.03	3.02	4.53	8850 ± 600	2675 ± 200	15.3 ± 0.5	-3.0 ± 0.3	4.4 ± 4.0	3.6 ± 2.0	20.0 ± 6.0	5.3 ± 2.7
	3B	0.54	0.24	0.35	3.27	3.24	4.45	8850 ± 600	2550 ± 200	18.8 ± 0.4	-4.8 ± 0.3	5.0 ± 4.1	3.8 ± 2.3	20.0 ± 5.0	5.5 ± 2.9
	3G	0.52	0.20	1.42	3.42	3.54	4.62	8950 ± 500	3350 ± 150	17.6 ± 0.5	-3.3 ± 0.4	12.0 ± 3.4	7.1 ± 2.1	25.0 ± 5.0	10.8 ± 2.5
	5J	0.55	0.22	1.42	3.58	3.62	4.53	8900 ± 550	2650 ± 200	14.2 ± 0.5	-2.2 ± 0.3	5.5 ± 3.7	3.9 ± 1.9	20.0 ± 5.0	5.8 ± 5.6
	5D	0.46	0.14	1.34	3.25	3.42	4.48	8900 ± 550	3000 ± 200	15.0 ± 0.4	-2.5 ± 0.3	7.8 ± 4.5	5.6 ± 2.0	22.0 ± 5.0	8.5 ± 3.0
Sim Test X-Axis, Softmount, Flt 15	1A	0.22	0.0	0.0	0.0	0.17	0.10	8900 ± 600	2550 ± 200	16.1 ± 0.1	-3.5 ± 0.1	7.1 ± 4.0	4.5 ± 2.0	20.3 ± 5.2	5.3 ± 2.6
	1B	0.50	0.14	0.73	3.37	3.77	4.47	8900 ± 550	2600 ± 250	16.1 ± 0.4	-3.5 ± 0.5	7.1 ± 3.6	4.3 ± 2.1	20.0 ± 4.4	5.5 ± 2.7
	3B	0.46	0.14	1.17	3.32	3.33	4.56	8900 ± 550	2700 ± 200	12.5 ± 0.5	-1.9 ± 0.3	4.4 ± 3.7	3.5 ± 2.8	20.4 ± 5.2	4.8 ± 3.5
	5F	0.37	0.22	0.56	2.81	3.84	3.94	8900 ± 450	2200 ± 150	27.2 ± 0.6	-7.7 ± 0.5	15.2 ± 2.9	14.0 ± 2.5	30.0 ± 4.0	18.3 ± 2.7
	5E	0.45	0.24	0.52	3.31	4.44	3.99	8850 ± 600	2600 ± 250	23.6 ± 0.5	-6.7 ± 0.6	23.0 ± 3.3	14.8 ± 1.8	35.7 ± 3.6	21.6 ± 2.2
Sim Test Z-Axis, Softmount, Flt 9	1A	0.10	0.0	0.0	0.0	0.10	0.10	---	---	14.7 ± 0.1	-3.5 ± 0.1	3.9 ± 4.4	3.5 ± 1.9	18.0 ± 5.5	4.2 ± 2.5
	1B	0.39	0.20	1.04	2.59	4.04	4.15	---	---	15.0 ± 0.3	-3.0 ± 0.5	4.0 ± 4.4	3.3 ± 2.0	19.5 ± 6.2	3.3 ± 6.5
	3B	0.37	0.33	1.21	2.45	4.20	3.59	---	---	19.8 ± 0.3	-4.5 ± 0.3	5.7 ± 4.4	3.6 ± 1.7	18.2 ± 5.0	6.0 ± 2.4
	3E	0.40	0.32	1.82	2.57	3.82	3.97	---	---	17.4 ± 0.5	-3.5 ± 0.5	11.1 ± 3.4	7.6 ± 1.7	25.0 ± 5.0	10.7 ± 2.4
	5A	0.36	0.24	0.49	2.76	3.62	3.99	---	---	17.1 ± 0.5	-4.0 ± 0.4	5.1 ± 3.6	3.8 ± 1.8	18.0 ± 4.5	4.6 ± 2.4
	5E	0.40	0.32	1.82	2.57	3.82	3.97	---	---	12.1 ± 0.4	-1.3 ± 0.5	4.9 ± 3.5	4.5 ± 1.9	20.0 ± 4.8	6.5 ± 2.9
Sim Test Z-Axis, Hardmount, Flt 9	1A	0.36	0.26	0.51	2.57	3.91	4.03	---	---	13.9 ± 0.3	-2.8 ± 0.5	3.1 ± 4.0	2.9 ± 1.8	17.1 ± 7.0	3.1 ± 3.8
	1B	0.37	0.22	0.54	2.63	3.91	4.22	---	---	14.0 ± 0.3	-2.8 ± 0.4	3.6 ± 3.7	2.8 ± 1.7	17.6 ± 6.0	4.4 ± 3.7
	3B	0.28	0.17	0.50	2.49	4.07	4.11	---	---	11.2 ± 0.3	-0.9 ± 0.4	2.0 ± 5.0	2.6 ± 1.9	18.0 ± 5.5	4.1 ± 3.0
	4F	0.49	0.30	0.54	2.79	3.81	1.52	---	---	27.9 ± 0.5	-7.8 ± 0.4	18.2 ± 6.6	15.4 ± 2.3	30.0 ± 4.2	18.1 ± 2.5
Sim Test Z-Axis, Hardmount, Flt 15	5E	0.30	0.42	0.53	2.45	3.61	2.07	---	---	23.9 ± 0.4	-6.6 ± 0.4	23.4 ± 4.1	15.8 ± 2.1	37.1 ± 5.1	22.7 ± 2.1

Again, the data show an adequate simulation of the flight environment. Testing in either axis yielded significant loading. The system is such that the primary loading may be presumed to be vertical with cross-axis response resulting from the "looseness" in the mounting. Comparison of ground test data with that from the flight tests shows higher response (acceleration) at the lugs and lower response at the aft end of the missile during ground simulation with missile center of gravity as the control location. This suggests that the primary source of dynamic load is from the air flow around the missile with loads transmitted from the missile to the aircraft wing. The ground simulation is based on driving through the missile hanger into the missile.

MOTOR SECTION SIMULATION TESTING

From the standpoint of propulsion unit qualification, the test article is the motor rather than the entire missile. For purposes of translating flight test results into a type test for a rocket motor, simulation testing was conducted on the motor section. A local data record of the stress sensors and duplicate accelerometers was made. The test and results are discussed here.

TEST SET-UP

On the BDU, the aft section, which simulates the solid rocket motor propulsion unit of a tactical missile, is located behind all missile support points. Thus, in flight, all load transference between the motor and the rest of the missile is through the clamp that attaches the motor section to the missile. For ground simulation testing, a vibration fixture was modified to permit driving the motor in a transverse direction through the mating clamp. Input vibration control levels were measured at the clamp plane that nearly coincides with the center of gravity of the BDU. Thus center-of-gravity vibration levels were used as input. The test set-up is shown in Figure 189.

TESTING

All testing (vibration) was conducted at ambient temperature (70 to 80 F) since thermal load simulation was adequately demonstrated during the all-up missile simulation testing. A 0.5-g sine sweep from 10 to 2000 Hertz was conducted to identify peak grain response frequencies. Random vibration was conducted using the input levels at the center of gravity as shown in Figure 183. These levels were subsequently doubled and quadrupled to measure linearity of response and to identify noise vs true response. All input control was in the Z-axis of the motor (corresponding to vertical loading on the wing-mounted missile).

261
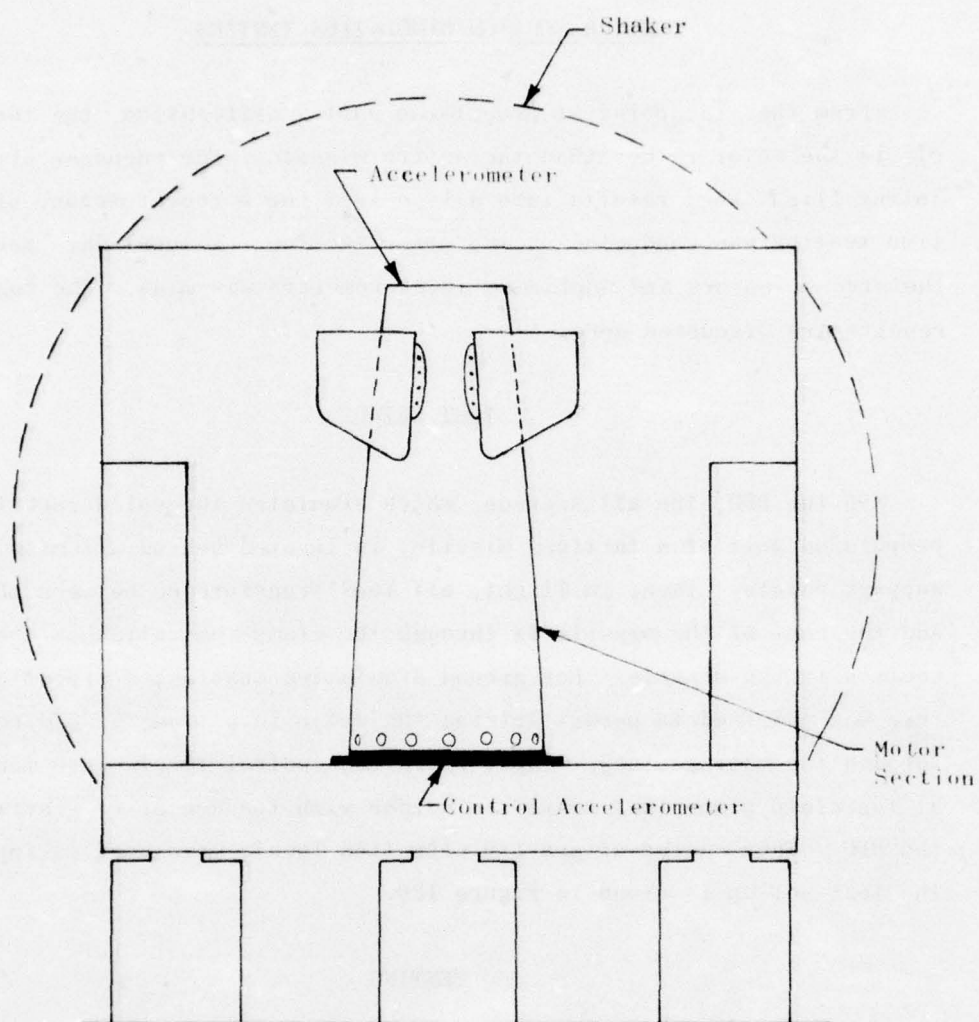
Figure 189.   Motor Section Test Set-up

TEST RESULTS

The 0.5-g sine sweep indicated three frequencies of significant response for the grain stress gages. From a nominal level of 0.1 to 0.2 millivolts, the stress gage responses rose to the values listed at the indicated frequencies in Table 32. Accelerometers mounted in the aft end of the motor section (top end) confirm this response. The amplitude ratios (top to control) for the driven (Z-axis) and cross (X-axis) accelerometers are listed in Table 33.

TABLE 32. 0.5-g SINE SWEEP RESULTS

Frequency, Hz	Output, mv				
	N-18	N-22	N-23	N-24	N-26
88	0.94	0.60	1.76	0.76	1.36
150	0.52	0.29	0.63	0.70	0.52
264	0.52	0.42	0.85	0.33	0.45

TABLE 33. ACCELEROMETER RESPONSE –
0.5 g SINE SWEEP

Frequency, Hz	Amplitude Ratio	
	Z-Axis	X-Axis
88	32	6.8
150	6.5	2.7
264	7.2	1.0
Non-Resonance	1.0	0.2

Because of shaping of the random input, the peak control level in the grain response frequency range was on the order of 200 Hertz. Identifiable response at the three resonant frequencies was nonetheless

observed in the random tests. The rms millivolt response of each of the five functional stress gages at the three key frequencies are listed in Table 34. Within the vagaries of random vibration response, the 88- and 264-Hertz excitations produce an approximately linear stress response with input level. The 150-Hertz stress gage response is less directly coupled to the input level at that frequency.

TABLE 34.   MOTOR-ONLY SIMULATION TEST RESULTS

| Frequency, Hz | Control Level | rms Response, mv * | | | | | rms g Input |
		N-18	N-22	N-23	N-24	N-26	
	1	0.07	0.04	0.14	0.06	0.11	0.077
88	2	0.08	0.05	0.14	0.06	0.10	0.079
	4	0.16	0.09	0.36	0.14	0.26	0.150
	1	0.09	0.08	0.14	0.14	0.12	0.208
150	2	0.10	0.08	0.12	0.14	0.12	0.224
	4	0.12	0.11	0.18	0.19	0.14	0.442
	1	0.17	>0.17	>0.17	0.14	>0.17	0.285
264	2	0.24	0.23	0.38	0.17	0.22	0.367
	3	0.33	0.32	>0.57	0.25	0.30	0.592

*Gage sensitivities are ~ 1.0 mv/psi, therefore, rms mv readings are approximate dynamic stresses.

MOTOR QUALIFICATION TEST SPECIFICATIONS

Whereas extensive studies of motor storage environments have given a plausible foundation to motor qualification test simulation for the storage environment, no similarly extensive data set exists for the captive flight environment.

The external pylon carriage is a relatively severe environment and is well characterized by Project DAME. Since DAME is conducted in a semi-tropical-to-temperate environment, the thermal extremes (aeroheating) measured must be taken as relative and applied to possible starting points in the other climatological regions. Observations over a variety of conditions generally yield the same result--a 200 F temperature rise in 6 to 12 minutes of high-speed flying. The maximum rate of cooling (and its effect on the propellant grain) has been measured. The cooling rate does not appear to significantly influence grain response of this system.

Dynamic levels measured at the missile center of gravity are somewhat lower than those inferred from general statements of captive-flight environment. They are, nonetheless, realistic and provide a distribution over the frequency range of interest (2 to 2000 Hertz). A generous amount of flight time, 1000 hours in 5 years of service, has been postulated. It would be prohibitively expensive to conduct this amount of testing. Acceleration is achieved by emphasizing the extreme--in this case by raising the rms level of random vibration input while maintaining peak levels near their actual values. Since this is basically a fatigue problem, an application of a hypothetical S-N curve would provide the necessary ratio to reduce the desired vibration time from 1000 to ~ 100 hours. In the absence of an S-N curve for the DAME-BDU inert propellant, the relaxation modulus-vs-log time curve substitutes. The log-log slope of log E_r vs log t is about 0.194. To obtain the same damage

in $(1/N)$ of the number cycles one would need an amplitude A' relative to actual amplitude A_0 of:

$$\left(\frac{A'}{A_0}\right) = \left(\frac{1}{N}\right)^{-0.194} = N^{0.194}$$

For a $1/10$ reduction, $N = 10$ and the amplitude must be enhanced about 1.6 times.

Since, for a given system, the exact shaping of the dynamic load is determined only in flight, a somewhat conservative approach to qual testing would involve determining the characteristic response for frequencies of the motor (resonances) by use of a sine survey. Random vibration bands inclusive of these resonances would be further enhanced by a factor equal to the amplification ratio; while non-resonance bands would be suppressed to achieve a constant rms g level total (constant total area under the PSD-vs-frequency curve).

SPARROW QUAL TEST

As a means of comparing the result of the BDU program with the requirements of MIL-STD-810C, which defines the vibration environment for most tactical air-launched rockets, we present two examples.

The BDU and Sparrow both fall into the category of External Stores Carried on Airplanes and are treated in accordance with Part 514.2, Procedure IIB of MIL-STD-810C. From Table 514.2IV of that document, we obtain the governing equations:

Cut-off frequency for high end, $f_1 = 10^5 \, (t/R^2)$ Hz   (1)

where t = case thickness, in. and R = motor radius, in.

$$\text{Low frequency amplitude } W_1 = (5)(10^{-3})(N/3T)^{1/4} \ g^2/Hz \qquad (2)$$

where N = maximum number of anticipated service missions and
  T = test time per axis in hours (for functional test,
  N = 3, T = 1)

$$\text{High frequency amplitude: } W_2 = (5)(10^{-5})(q/\rho)^2(N/3T)^{1/4} \ g^2/Hz \qquad (3)$$

where q = maximum flight dynamic pressure in lb/sq ft and ρ = average
store weight density in lb/cu ft. For endurance test, q is
taken to be 1200 lb/sq ft and for the functional test, q is
taken to be 1800 lb/sq ft. Special adjustments require multiply-
ing the result from Eq. 3 by 4 when testing the motor section.

For the two systems, we obtain the following basic results:

TABLE 35. VIBRATION ENVIRONMENT COMPARISON[a]

	BDU		SPARROW			
	ρ = 88 lb/cu ft R = 6.75 in.		ρ = 86 lb/cu ft N = 200 R = 4 in.			
	t = 0.2 in. (est)		t = 0.074 in. T = 100			
	Functional		Functional		Endurance	
	SPEC	DAME	SPEC	DAME	SPEC	DAME
W_1	0.005 g^2/Hz	0.004 g^2/Hz	0.005 g^2/Hz	0.004 g^2/Hz	0.006 g^2/Hz	0.0064 g^2/Hz
W_2	0.009 g^2/Hz	0.0006 g^2/Hz	0.010 g^2/Hz	0.0006 g^2/Hz	0.007 g^2/Hz	0.0010 g^2/Hz[b]
f_1	439 Hz	410 Hz[b]	462 Hz	410 Hz[b]	462 Hz	410 Hz[b]

[a]In both cases, the DAME observation and the MIL-STD-810C requires enhancement of
the random curve according to observed resonances for the unit. Testing under
MIL-STD-810C is at constant temperature; DAME includes aeroheat response.

[b]In the BDU data, a second cut-off occurs at about 800 Hertz. From 800 to 2000
Hertz, the PSD level rises from W_2 to approximately equal to W_1.

The essence of the comparison is that for frequencies below 400 Hertz,
little change is observed between the two environments. For frequencies
above 400 Hertz, however, the MIL-STD-810C requires a significantly
higher input. In terms of effect on a case-bonded solid propellant motor,
the difference is not critical. For components sensitive to high-
frequency, the differences could become important.

CONCLUSIONS

Success of the BDU program must be measured with a view to its impact on future environment definition and, ultimately, rocket motor cost/quality improvement.

Through effort expended on this program advances were made in the areas of rocket motor loads definition and determination of captive-flight response. It was also demonstrated that these loads and responses can be simulated with vibration and aeroheat facilities to the extent that flight loads can be imposed on the rocket motor.

From the multiplicity of flights flown to basic conditions (altitude and aircraft velocity) representative of "typical" missions, an average response can be elicited as shown in Figures 190, 191, and 192. Figure 190 depicts a temperature profile for a mission that includes loiter at 35,000 feet, dash to Mach 2 at about 40,000 feet, and TFR at 500 feet above ground level. Approximate extremes are indicated on the figure.

Figure 191 depicts, in general terms, the vibration response at the center of gravity of the missile. An application of this spectrum is discussed in MOTOR QUALIFICATION TEST Section.

Figure 192 depicts the nominal BDU grain response to flight conditions. Stress/strain levels to which the BDU was subjected in flight were not critical—the motor has exhibited no failure through the years of testing.

The investigation begun here should be extended to emcompass flying actual motors to accumulate a reserve of data that will permit reliable characterization of the captive-flight environment to permit realistic ground simulation during future motor development efforts. The potential

269

for significantly higher dynamic loads exists with aircraft of the 70s such as the F-15. As a potential test vehicle, an inert instrumented SPARROW (Mk 38 Mod 4) has been fabricated and will be flight tested in the future to build on the information presented here.
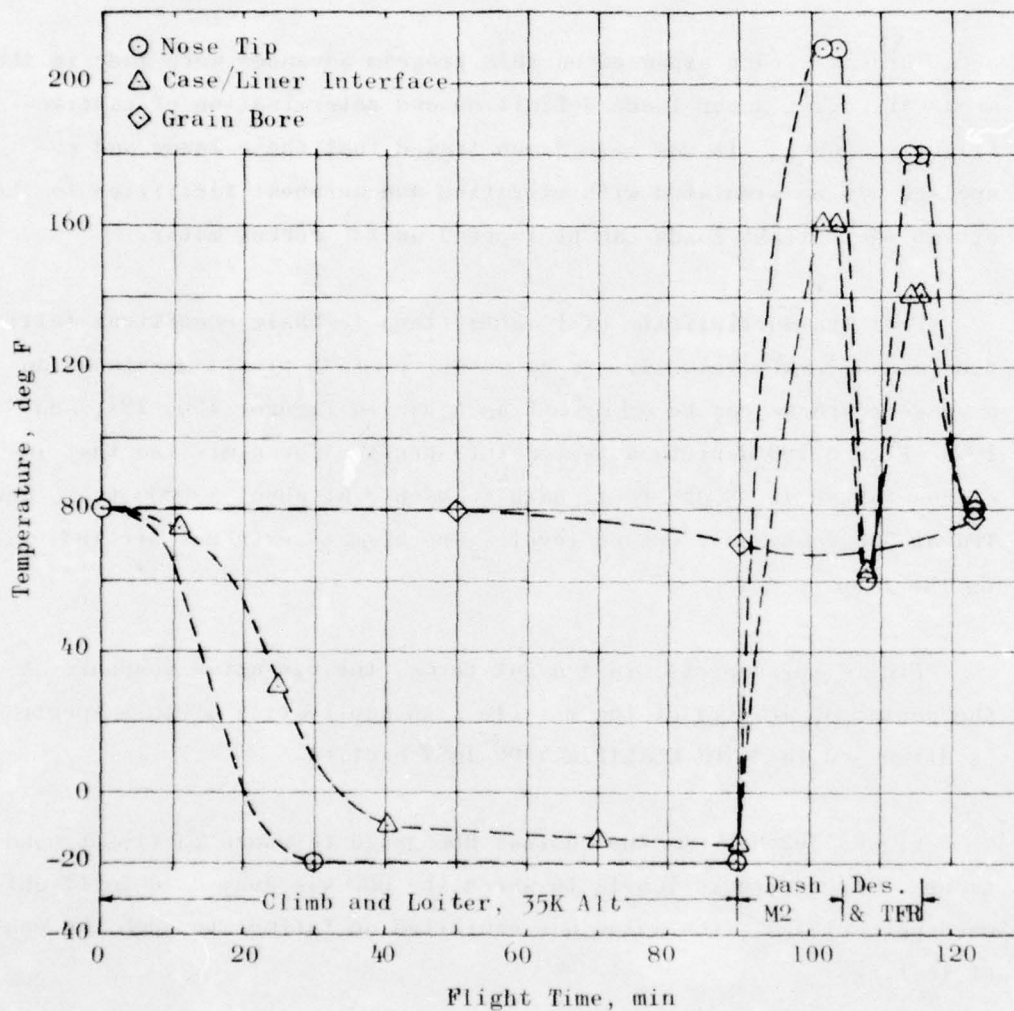
Figure 190. Nominal BDU Thermal Environment
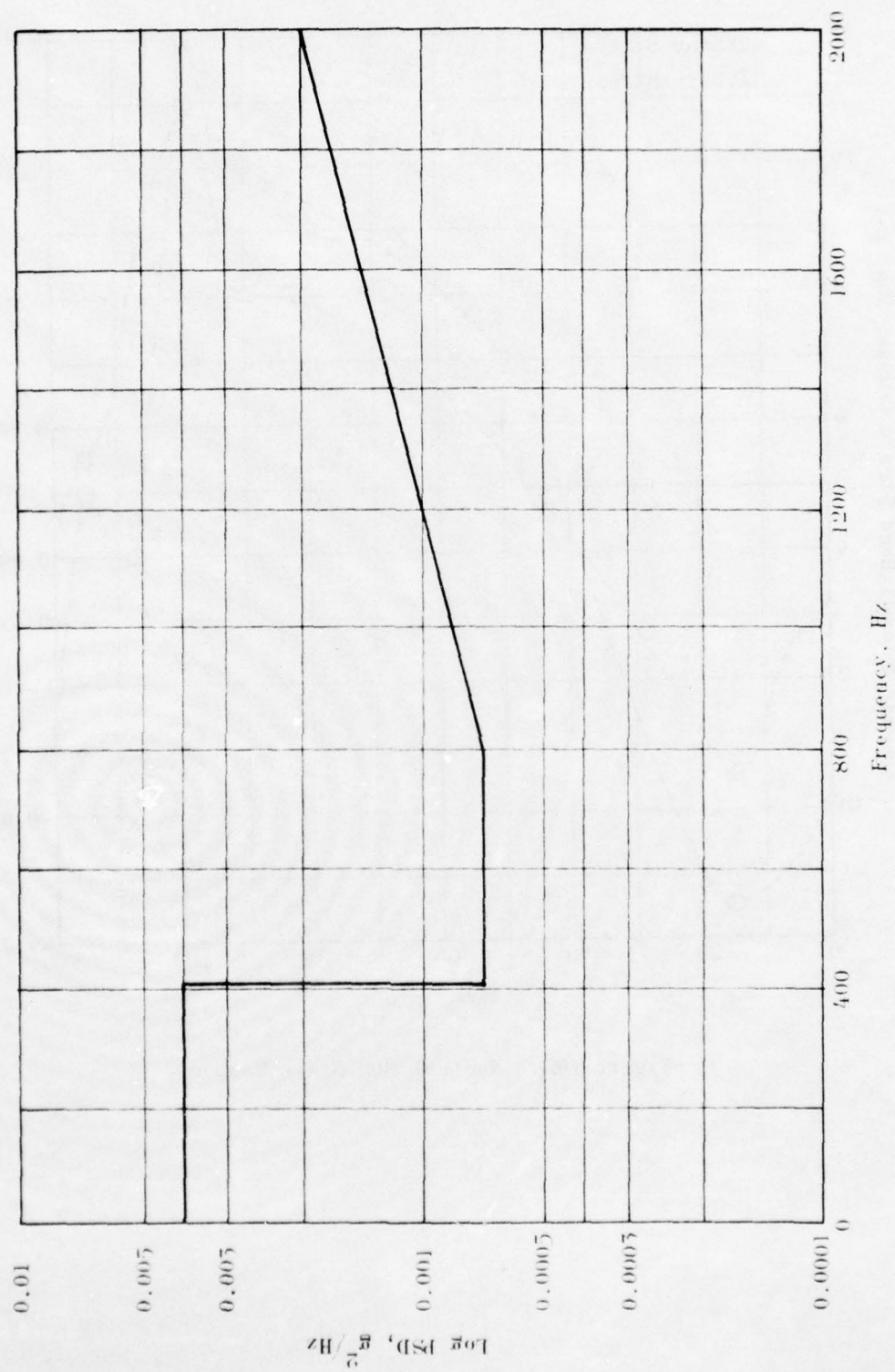
Figure 191. Vibration Response at Missile Center of Gravity
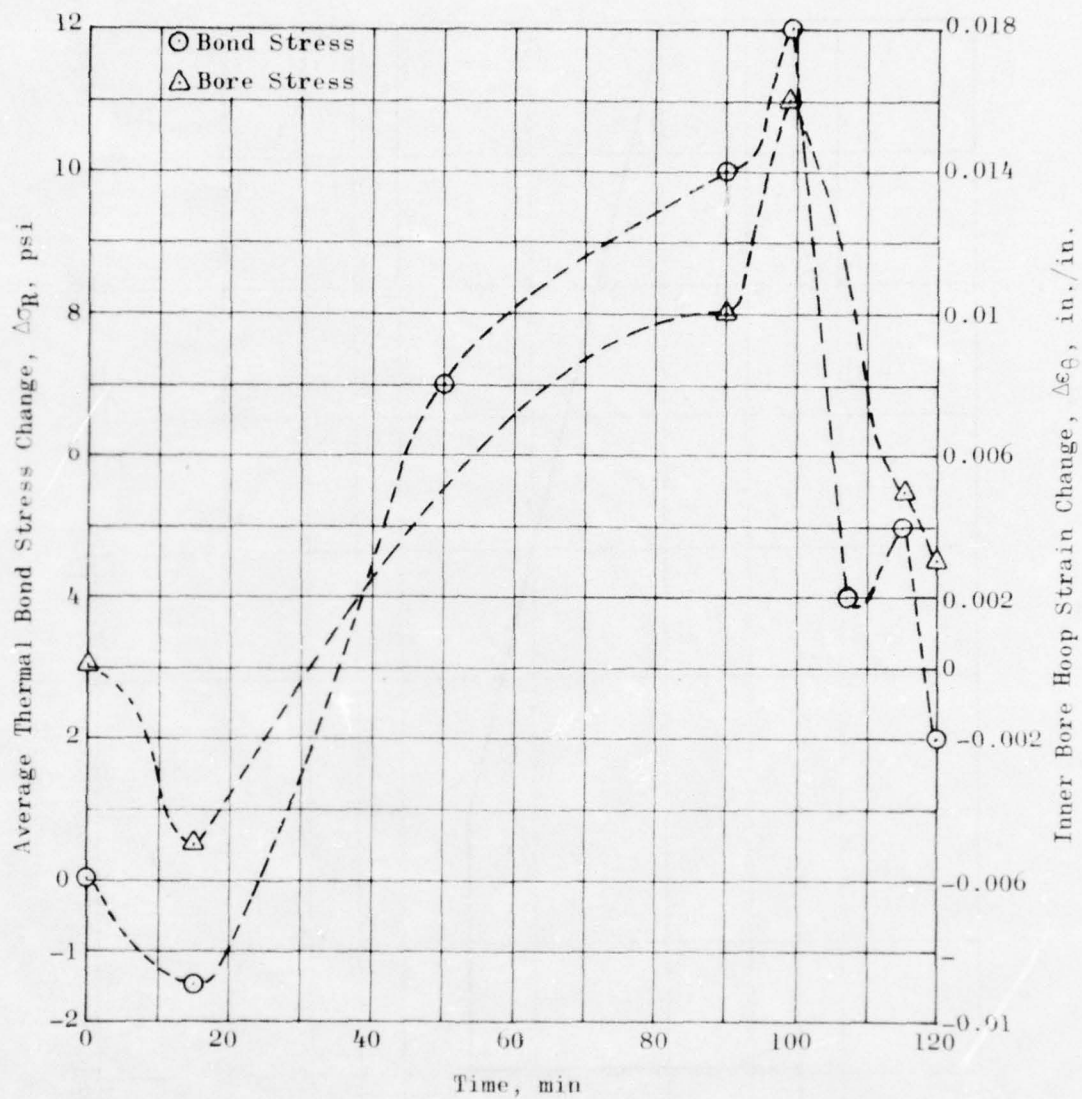
Figure 192. Nominal BDU Grain Response

272

CALIBRATION

GAGE CALIBRATION DATA

Thermistors

Thin film thermistors or "thinistors" on a nickel foil substrate were used in the BDU to monitor temperature at a precise radial location within the grain and to obtain an extremely rapid response time. Thermistors in the grain were 1000-ohm VECO FM3C22. Higher resistance 5000-ohm VECO FN3C23 thermistors were used to monitor case/liner interface temperature.

The thermistors were connected with three resistors to form a bridge circuit as shown in Figure A-1 (a) and (b). The bridge circuit was supplied from the 28-volt regulated voltage supply through a dropping resistor. The circuit for the grain thermistors was arranged to yield an output between ~ 50 and 250 millivolts for the expected temperature range of -70 to 160 F.

The circuit for the case thermistors was arranged to measure high temperatures (above 100 F) and still yield an output in the same range (-300 to 100 millivolts). The devices were, however, calibrated over the entire range from -70 to 160 F and produced a large negative output (~ 1.0 volt) at the lower temperatures.

Data obtained during isothermal tests with the grain cast in place are presented in Tables A-1 and -2 and in Figures A-2 through -6. Generally, the data were consistent and good, i.e., thermistor circuits gave similar outputs at given temperatures. Interpretation of thermistor output was straightforward and unambiguous. Output signals in millivolts may be read directly in terms of temperature from the curves in Figures A-2 through -6.

END

DATE
FILMED

2-77
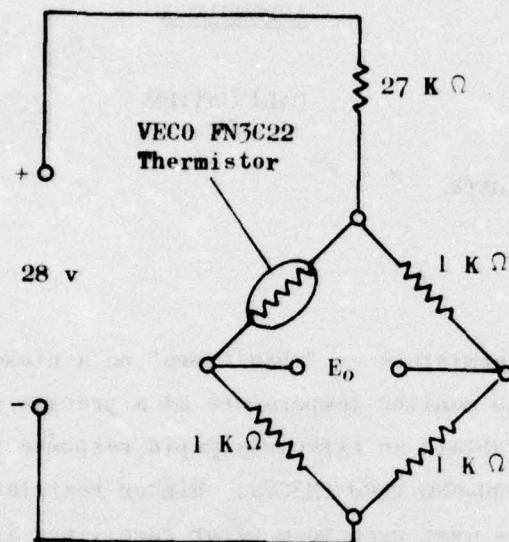
(a) Bridge Circuit for Grain Thermistors
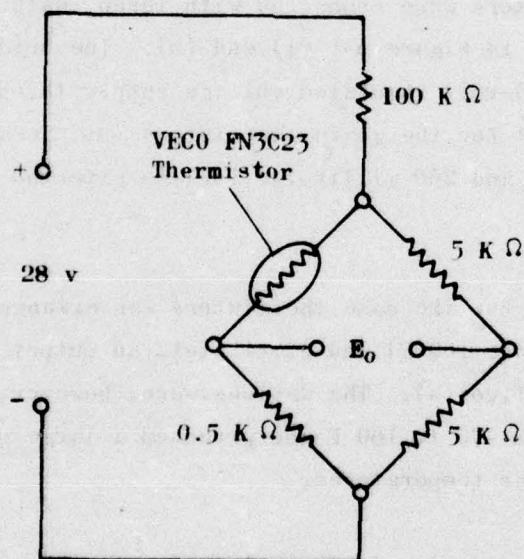
(b) Bridge Circuit for Case Thermistors

Figure A-1. Thermistor Circuit Diagrams

TABLE A-1. THERMISTOR CIRCUIT OUTPUT SIGNALS AS
FUNCTION OF TEMPERATURE

	Output, mv						
	160 F	114 F	65 F	60 F	36 F	-21 F	-69 F
Grain Thermistors							
1	64.5	38.6	-36.1	-43.2	- 98.0	-209	-253
2	54.6	17.6	-62.1	-71.9	-118.0	-227	-258
3	55.6	25.9	-68.6	-76.1	-120.0	-221	-258
5	67.3	46.5	-20.1	-24.9	- 71.0	-193	-246
6	45.3	0.39	-85.0	-92.7	-150.0	-230	-253
9	56.3	19.9	-48.2	-56.5	-114.0	-219	-249
10	65.6	44.0	-26.5	-33.8	- 74.0	-182	-228
11	49.2	16.2	-61.2	-69.8	-119.0	-207	-238
12	68.8	44.1	-17.5	-24.5	- 71.0	-186	-233
13	65.8	38.2	-30.6	-37.6	- 88.0	-198	-239
16	66.3	44.5	-25.8	-28.0	- 76.0	-184	-231
17	68.8	49.6	-14.6	-17.6	- 62.9	-174	-224
18 19 20	See Table A-2						
21	47.6	10.3	-74.8	-75.2	-133.0	-216	-238
22	59.0	31.5	-23.3	-26.1	- 46.5	- 75.2	- 85.3
23	60.1	30.5	-42.3	-47.7	- 97.1	-201	-237
Case Thermistors*							
A	81.0	195	495	536	680	1000	1125
B	71.1	203	447	484	645	991	1097
C	91.5	209	527	564	692	1042	1144
D	89.1	227	493	538	675	995	1098

*Note change in sign

TABLE A-2. THERMISTOR CIRCUIT OUTPUT SIGNALS AS FUNCTION OF
TEMPERATURE (Revised Data for Thermistors 18,
19, and 20)

Thermistor Number	Output, mv							
	160 F	123 F	100 F	75 F	30 F	20 F	-20 F	-42 F
18	20*	-11.4	-43	- 92.7		-191	-238*	-253*
19	20*	-12.7	-42	- 94.3	-193.8	-202	-244	-256
20	12.5*	-19.8	-60	-114.9	-208	-223	-257	-270

*Estimated values

A-4
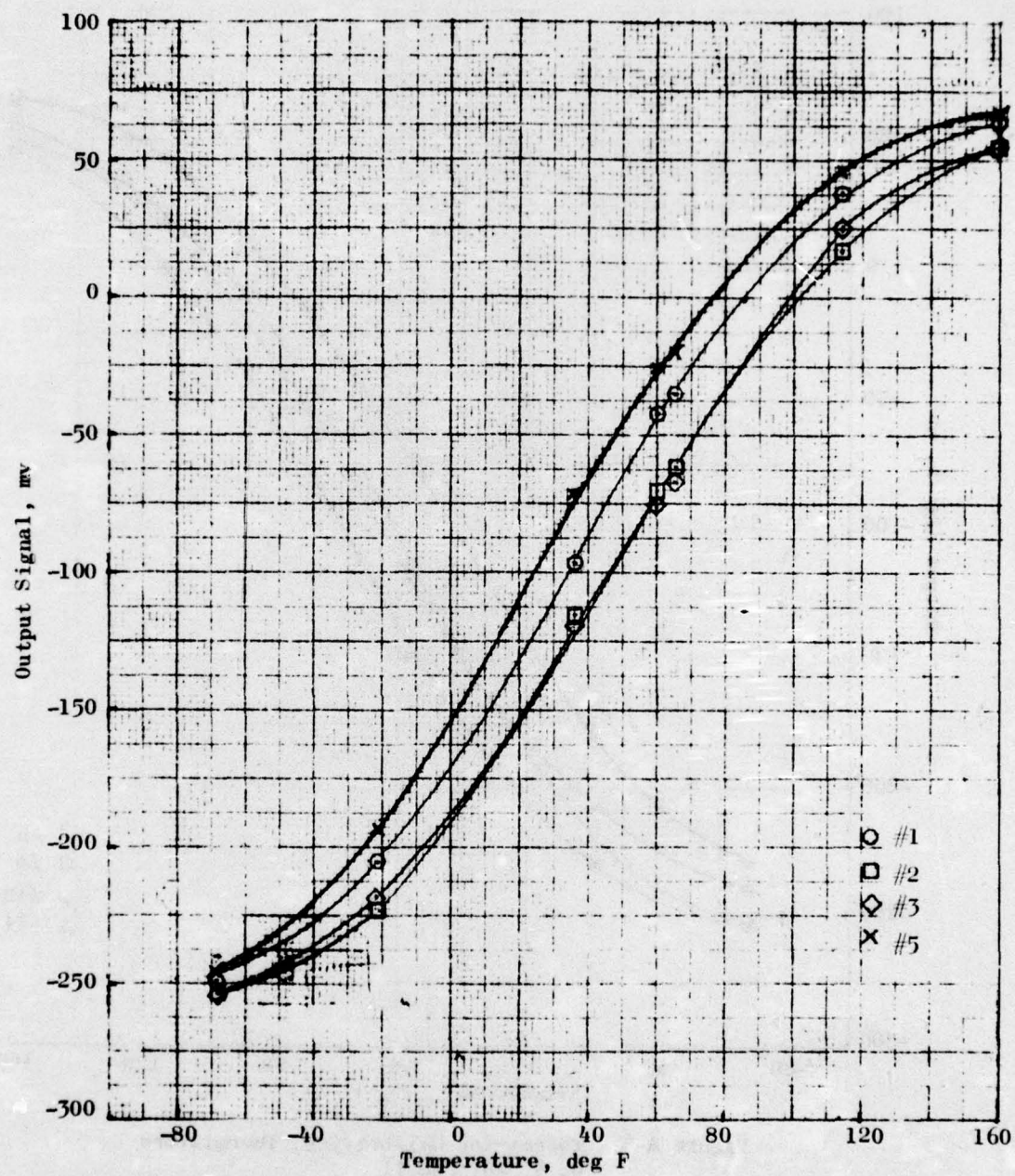
Figure A-2. Thermistor Calibration, Thermistors
1, 2, 3, and 5

A-5
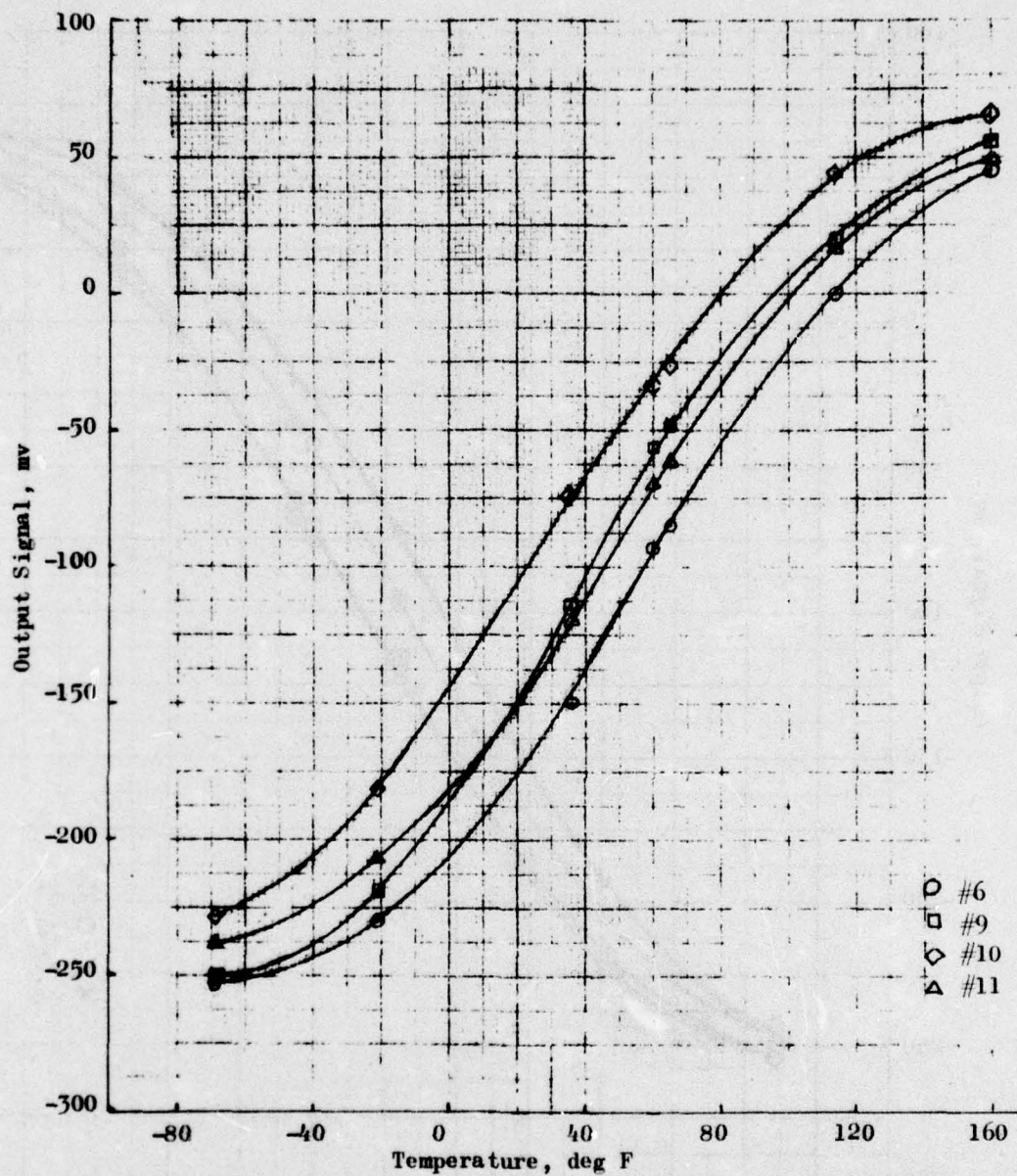
Figure A-3. Thermistor Calibration, Thermistors
6, 9, 10, and 11

A-6
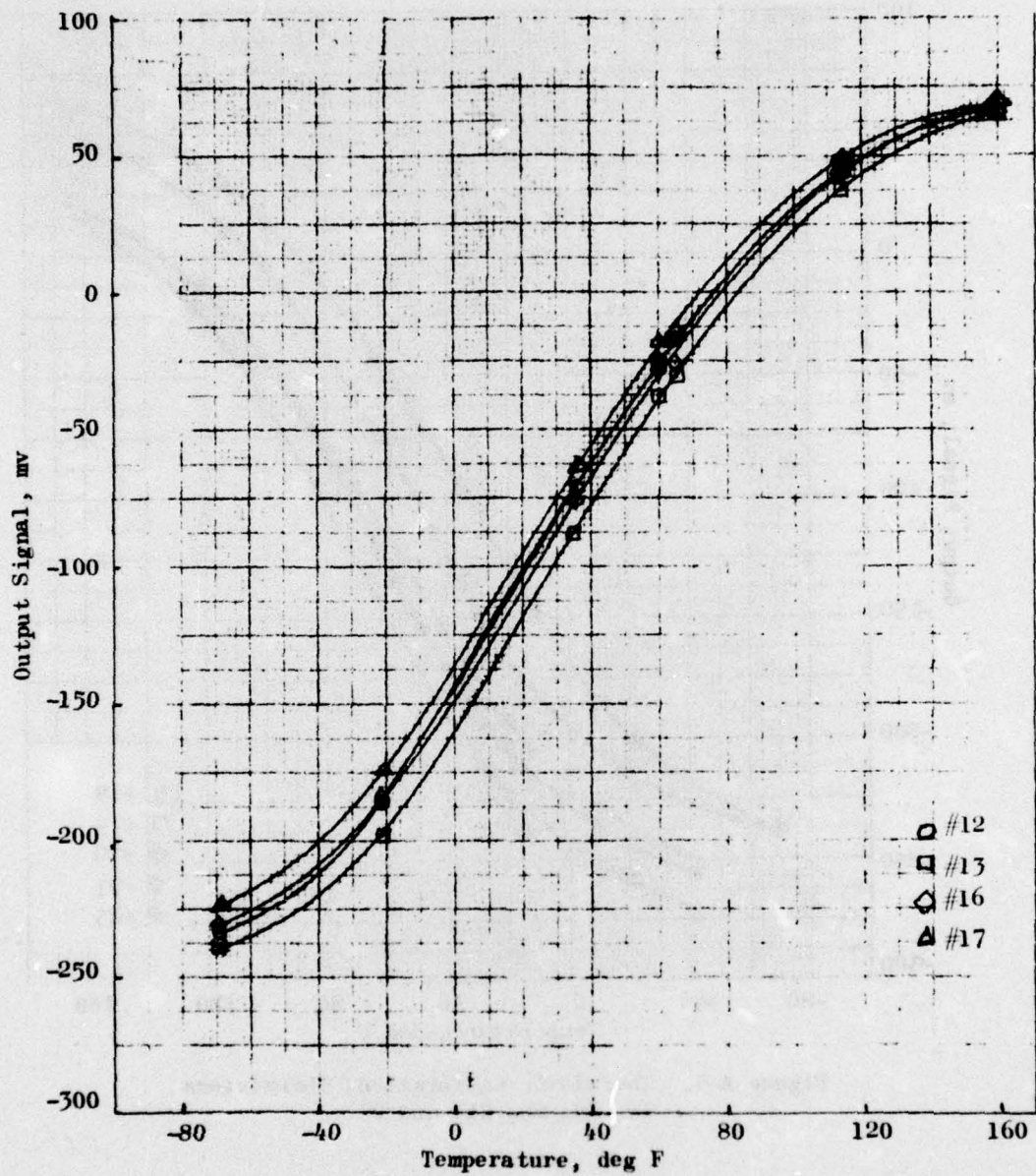
Figure A-4. Thermistor Calibration, Thermistors
12, 13, 16, and 17
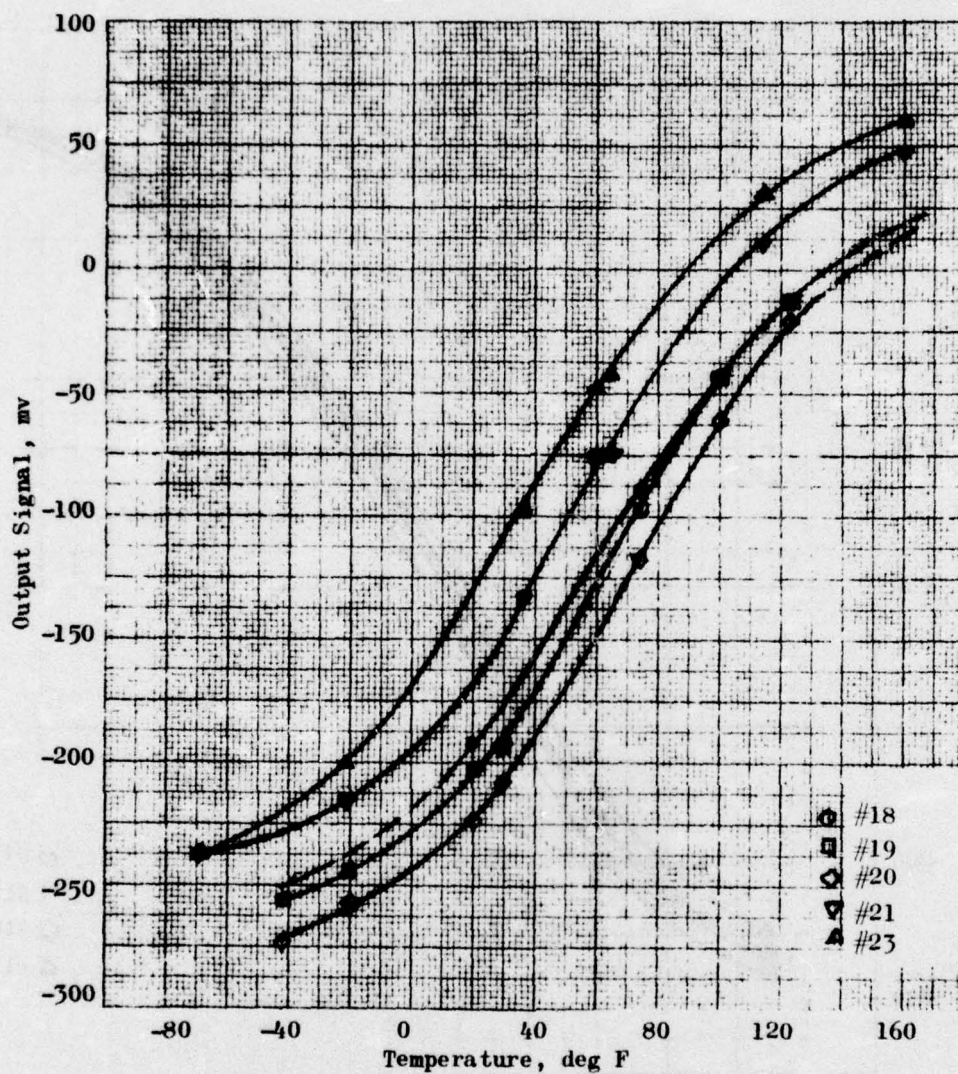
Figure A-5. Thermistor Calibration, Thermistors
18, 19, 20, 21, and 23
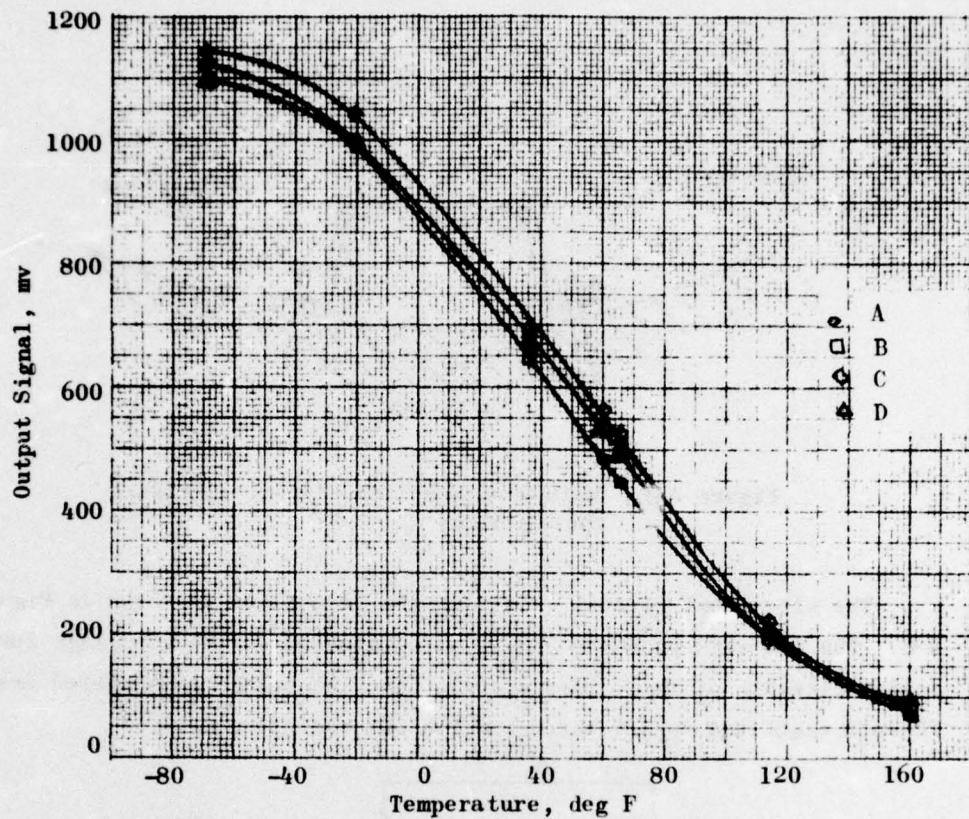
Figure A-6. Case Thermistor Calibration Curves
A, B, C, and D

Surface Strain Sensors

Two clip-type gages using semiconductor elements were mounted in the middle of the bore of the inert propellant grain, one gage to measure hoop strain and the other to measure longitudinal strain. The mounting system is shown in Figure A-7. Two steel mounting pins for each gage were pushed into the bore of the grain and bonded in place. The clip gages were then fitted over the pins and secured with small amounts of epoxy adhesive.

A-9
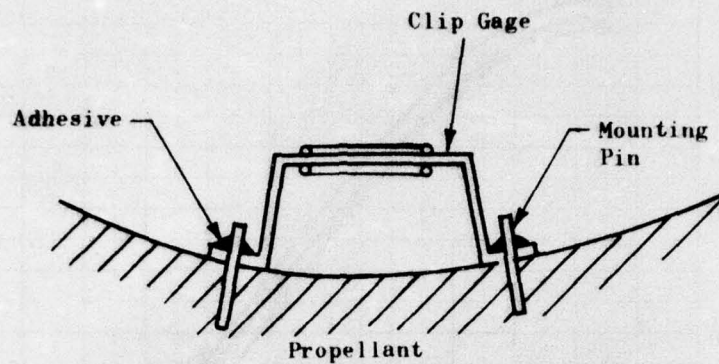
Figure A-7. Method of Mounting Clip-Type Surface
Strain Gages

The electrical circuit used with the clip gages is shown in Figure
A-8. The two semiconductor strain gages mounted on the clip gage form two
active elements of the bridge circuit, and the bridge is supplied from the
28-volt regulated supply through a 13K ohm resistor.
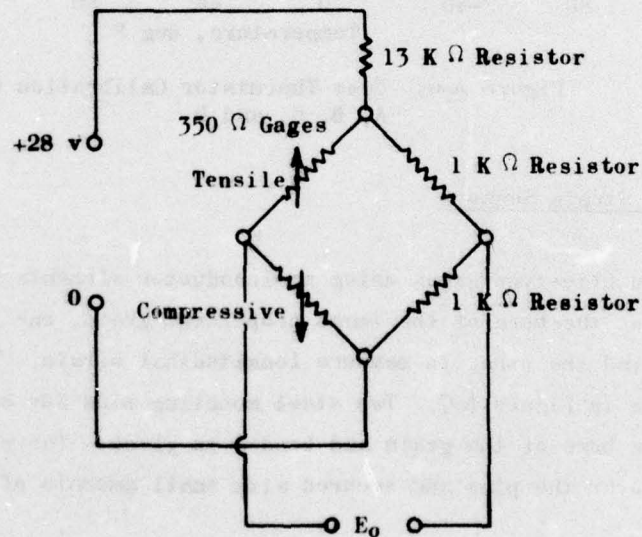
Figure A-8. Surface Strain Gage Circuits

Case Strain Gages

Standard 120-ohm foil strain gages were bonded to the interior surface of the aluminum case before the grain was cast. Two gages were mounted in the hoop direction and two in an axial direction. The gages were connected in a bridge circuit. These gages are not influenced by changes in propellant modulus and, therefore, will operate without significant change at low temperatures. Thus, the case strain gage bridge output may be used to determine pressure on the case at low temperatures when the propellant grain becomes rigid.

Figure A-9 shows the circuit used with the case strain gages. A four-arm active bridge circuit was used and was supplied from the 28-volt supply through a 510-ohm dropping resistor.

Surface Strain Gage Calibration Data

Table A-3 shows calibration data obtained by subjecting the clip gages to known deformations at a series of temperatures. The data are plotted as gage output vs gage length in Figures A-10 and -11. These curves show that the clip gages did not work properly at the higher temperatures. Apart from this high-temperature problem, the clip gages were extremely sensitive although output signal-gage length curves are not precisely linear over the wide range of strains adapted during the calibration tests. However, bore strains in the BDU were not expected to approach the ± 25% strain to which Gage 1 was subjected nor the ± 17% strain to which Gage 2 was subjected. Calibration curves over the strain range of interest (0 to 10%) are essentially linear in form.

Again, interpretation of gage output signals is straightforward if the temperature of the gage is known. The gage length corresponding to a given signal may be found by using the correct temperature curve interpolated from Figures A-12 and -13.
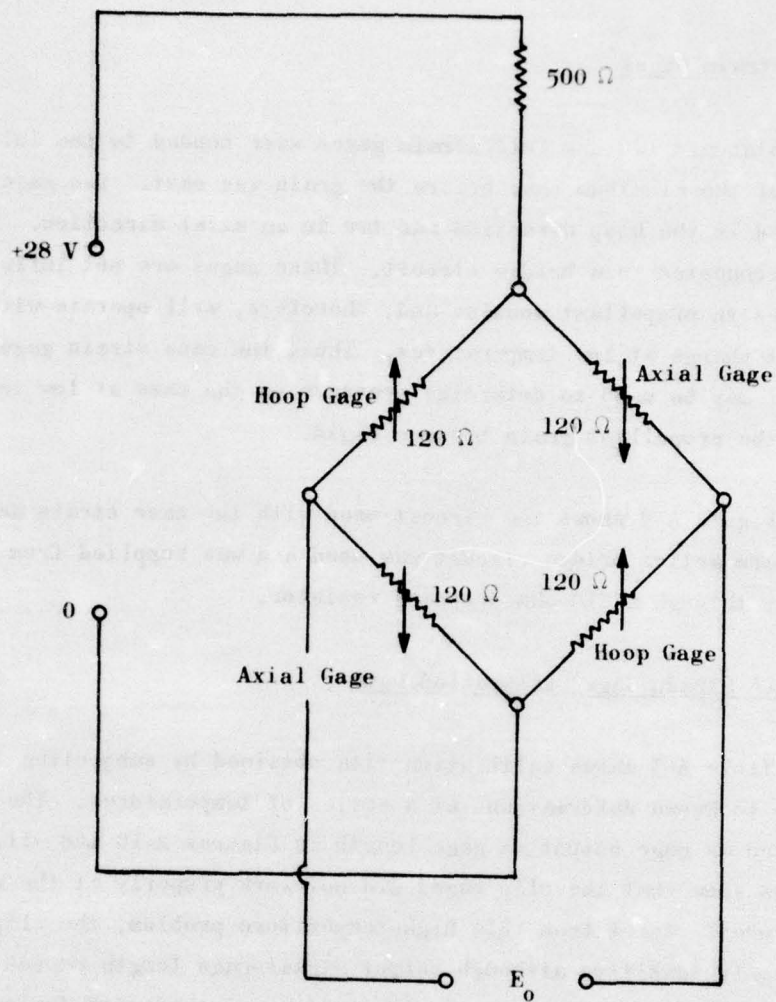
Figure A-9.   Case Strain Gage Circuit

TABLE A-3. CLIP-TYPE SURFACE STRAIN GAGE CALIBRATION DATA

Temp, deg F	Distance Between Pins, in.										
	0.460	0.465	0.470	0.475	0.480	0.485	0.490	0.495	0.500	0.505	0.510
Surface Clip Gage 1, Output, mv											
151	-120.0	- 95	- 66	- 45	- 24	0	27	53	80	---	136
70	-128	- 98	- 70	- 38	- 10	25	60	94	133	169	202
10	-116	- 89	- 58	- 29	0	33	67	106	142	174	212
-35	-106	- 77	- 49	- 18	10	45	82	117	155	184	232
-61	- 98	- 70	- 41	- 21	17	53	86	119	157	193	235
Surface Clip Gage 2, Output, mv											
151	-248	-227	-204	-184	-166	-143	-119	- 95	- 73	---	- 22
70	-227	-208	-189	-169	-148	-123	-102	- 78	- 55	- 38	- 11
10	-215	-202	-182	-161	-142	-114	-100	- 67	- 56	- 33	0
-35	-201	-181	-161	-148	-132	-102	- 84	- 54	- 47	- 25	0
-61	-192	-176	-158	-141	-123	-103	- 79	- 59	- 37	- 19	8
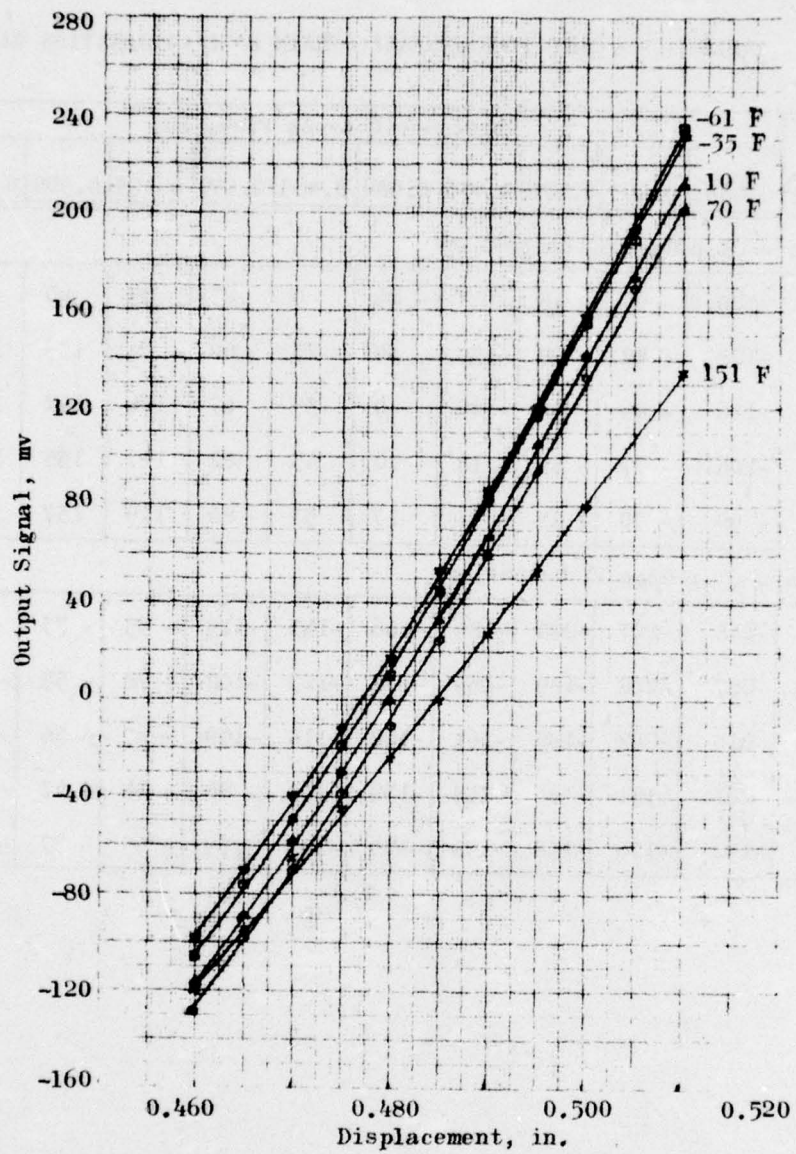
Figure A-10.   Surface Clip Gage 1, Millivolts vs
Displacement
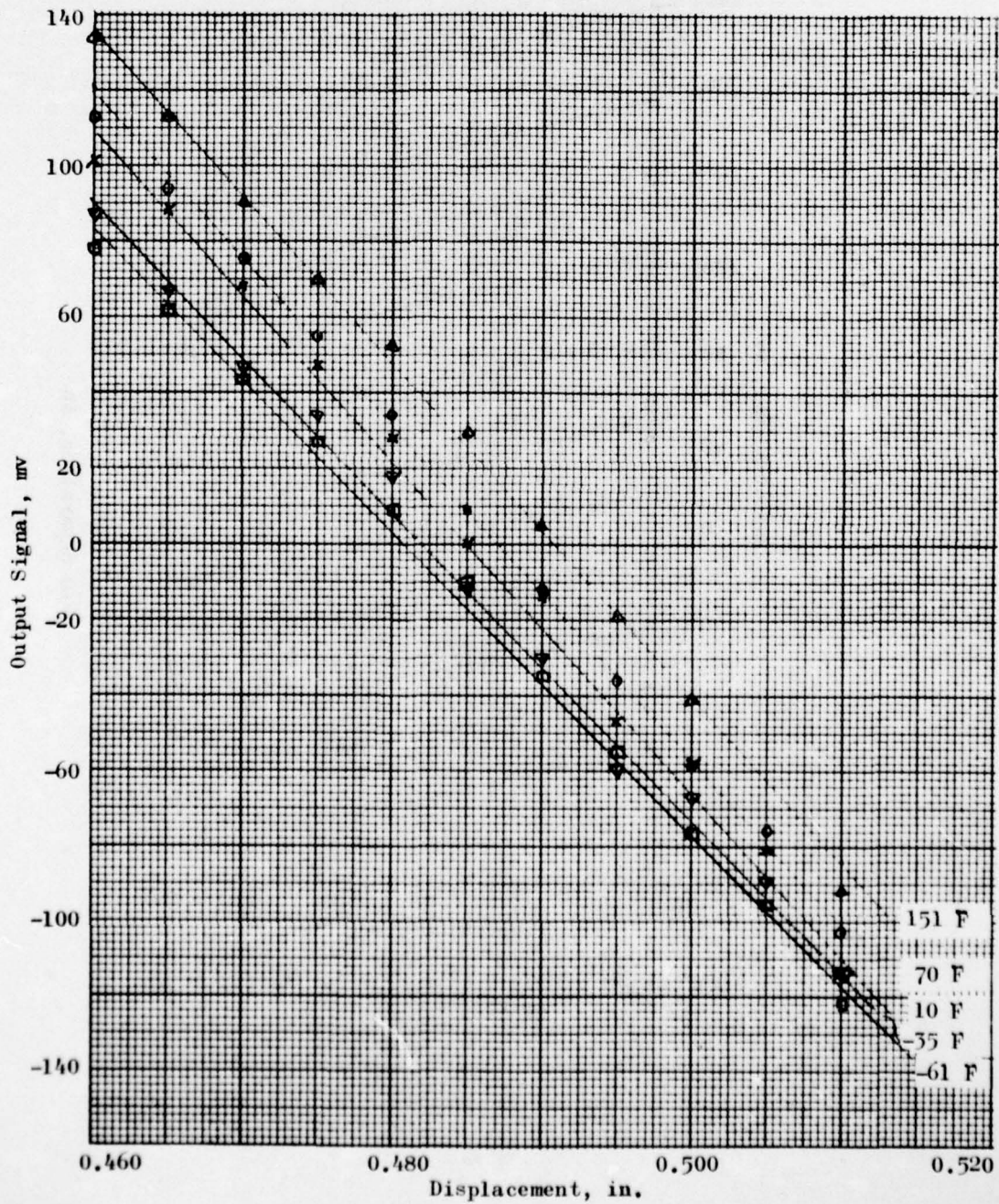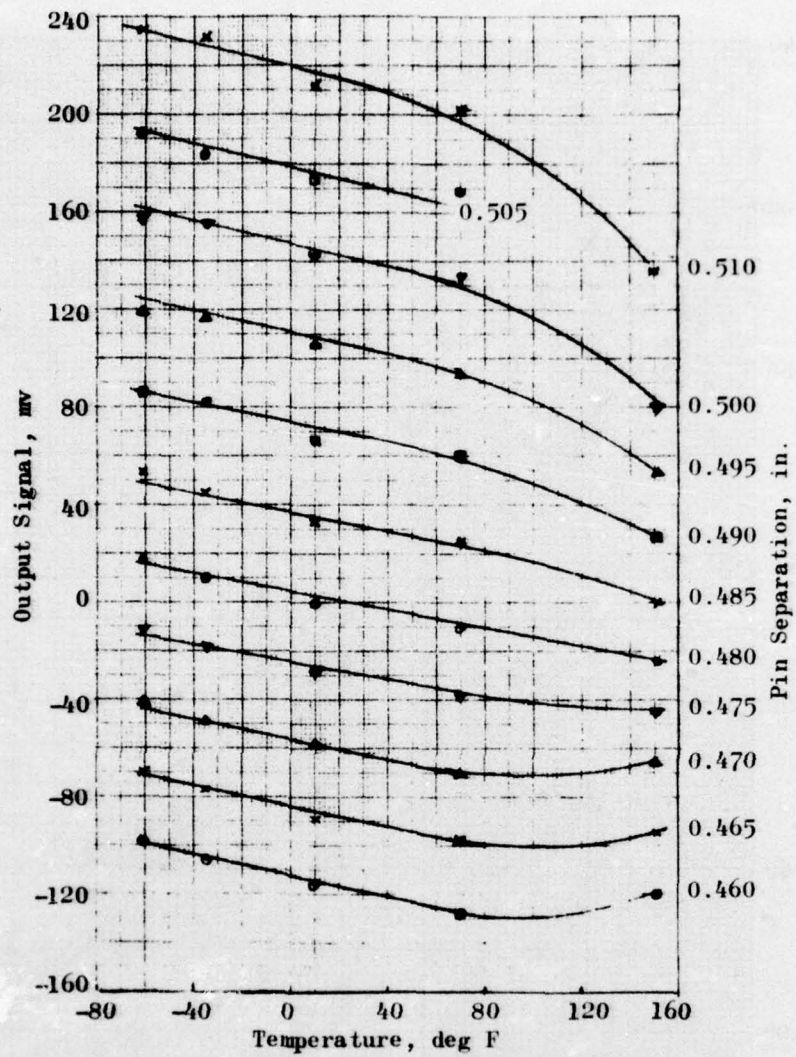
Figure A-12. Surface Clip Gage 1, Millivolts vs
Temperature
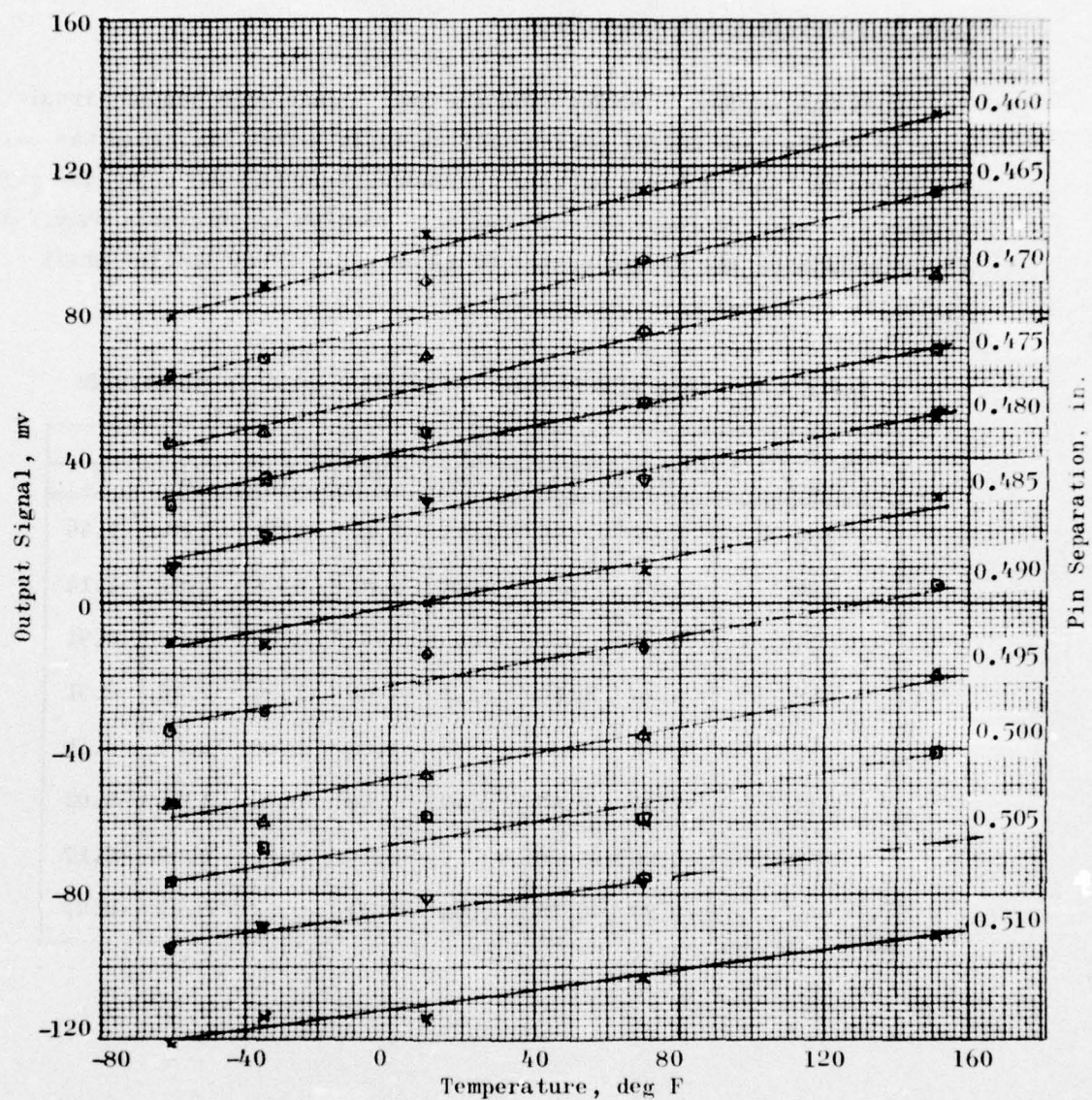
Figure A-13.   Surface Clip Gage 2, Millivolts vs
Temperature

Case Strain Gage Calibration Data

Calibration data obtained from the foil strain gage bridge circuit mounted on the case during pressurization tests before the grain was cast are given in Table A-4 and plotted in Figures A-14 (a) and (b). The gages appeared to give rational data at moderate-to-high temperatures only. At low temperatures the bridge output became progressively smaller until virtually no signal was obtained at -60 F.

TABLE A-4. CASE STRAIN GAGE CALIBRATION DATA IN MILLIVOLTS

Temperature, deg F	Pressure, psi						
	0	10	20	30	40	50	0
154	1.75	1.86	2.43	3.17	3.75	3.84	1.46
122	1.21	--	2.08	2.81	3.58	4.01	1.14
74	0.93	--	--	--	3.20	3.82	0.91
48	0.46	0.66	1.12	1.66	2.34	2.95	0.51
17	0.14	--	0.57	1.08	1.68	2.25	0.30
-11	-0.07	-0.07	0.19	0.48	0.90	1.34	-0.02
-52	-0.26	-0.29	-0.29	-0.19	-0.11	0.04	-0.17
-62	-0.27	-0.38	-0.48	-0.54	-0.52	-0.47	-0.27
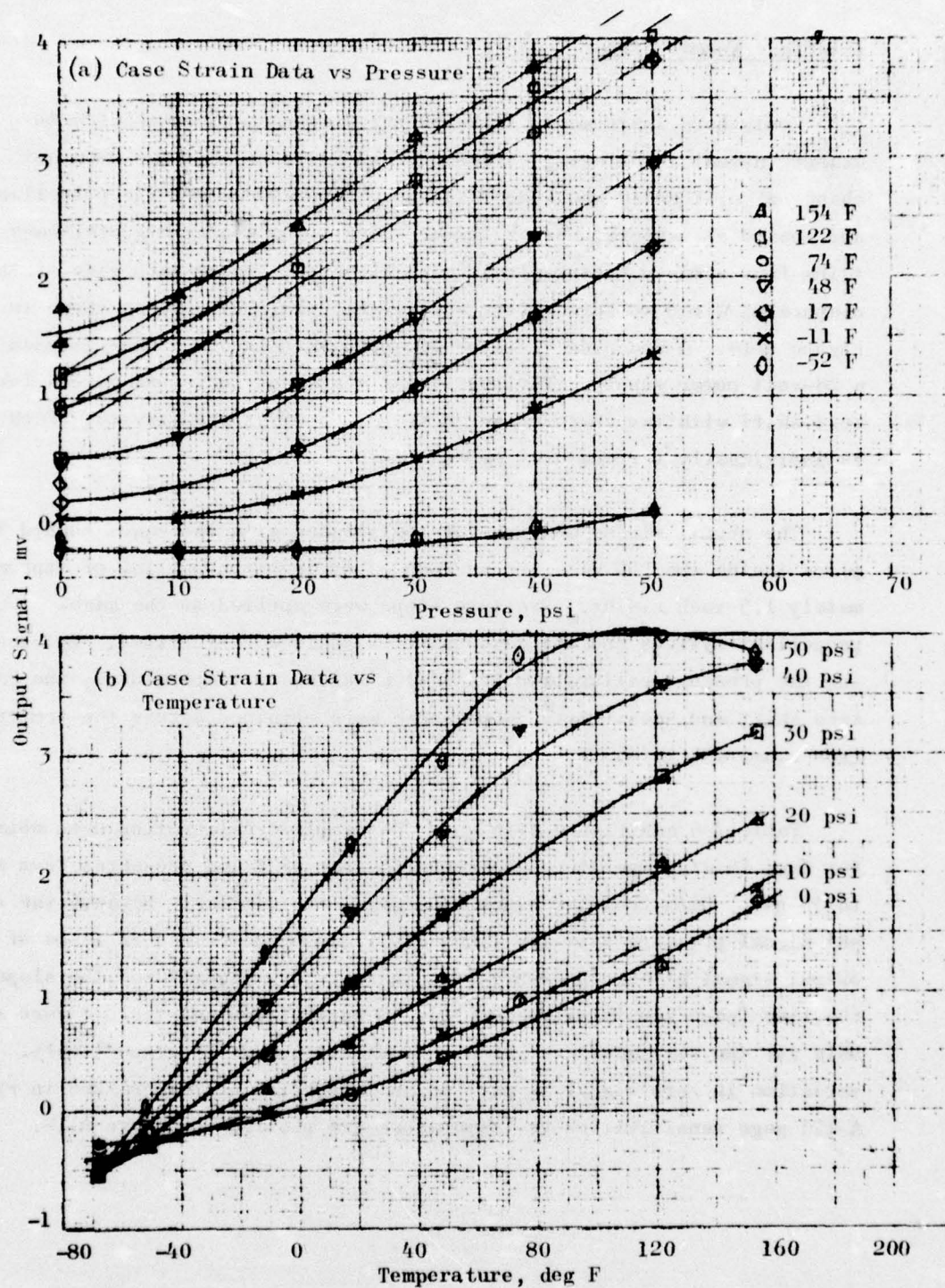
Figure A-14. Case Strain Gage Calibration Data

A-19

Interface Normal Stress Sensors

Konigsberg Instruments P14B-150-psi diaphragm gage was used to measure normal interfacial stress. Sensitivity of the gage does not change significantly when embedded in rubber-based composite propellants and tested at temperatures as low as -65 F. The Konigsberg P14B gage contains four semi-conductor strain gage elements, two on each side of the diaphragm, wired to form a four active-arm bridge circuit as shown in Figure A-15. A dropping resistor of approximately 3.6 K ohms is used with a 28-volt power supply. Various series and shunt resistors give a low zero shift with temperature and an almost constant sensitivity. Each gage is individually temperature-compensated.

The normal stress sensors were calibrated with the gages bonded in place inside the BDU case and surrounded by inert propellant of approximately 1.5-inch radius. Pressure steps were applied to the gage-propellant systems and the gage output signals were recorded. By conducting the pressure calibration tests at a series of temperatures, the gage zero shift and sensitivity to pressure were obtained across the temperature range 154 to -68 F.

Table A-5 and Figure A-16 show the complete calibration data obtained for Gage 18 at temperatures between 154 and -68 F and pressures from zero to 50 psi. Data from the other five gages are similar. Because the output signal-pressure data are linear they may be described in terms of the output signal at zero pressure (the thermal zero signal) and the slope of the line (gage sensitivity, mv/psi). Sensitivities and thermal zero signals for the six gages are given in Tables A-6 and -7, respectively. The variation in zero signal is plotted as a function of temperature in Figure A-17; gage sensitivities vs temperature are plotted in Figure A-18.
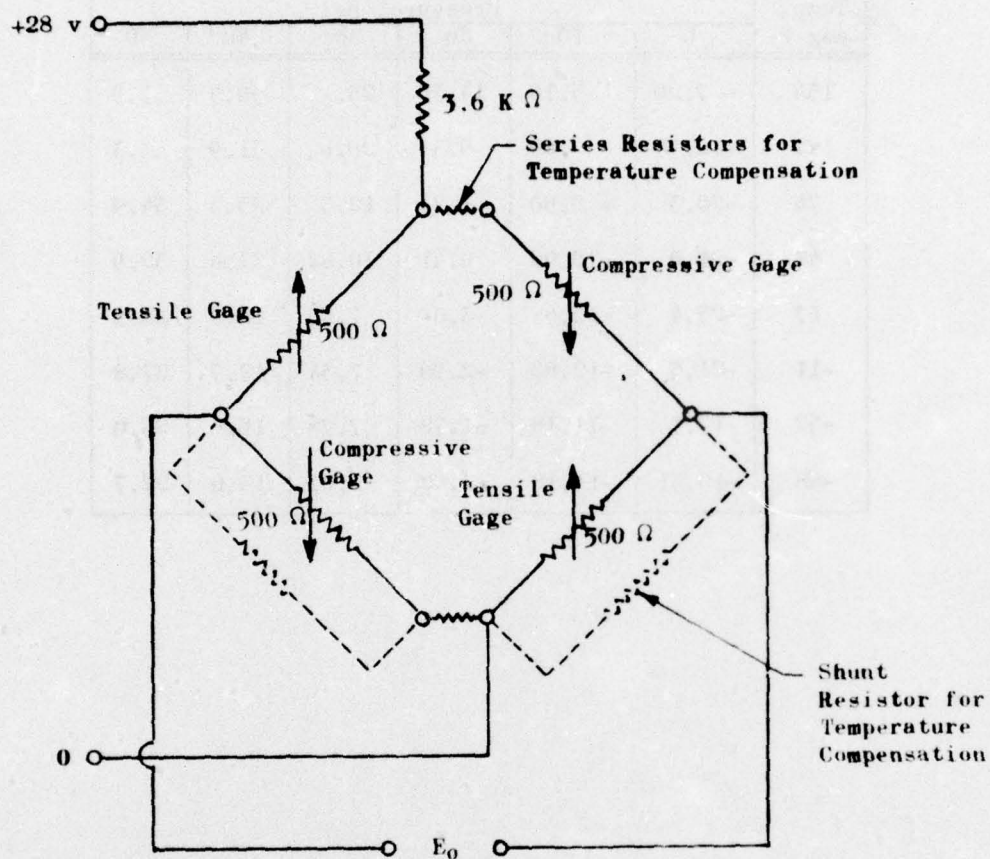
Figure A-15. Typical Konigsberg P14B, 150-psi Diaphragm
Gage Circuit

TABLE A-5. PRESSURE CALIBRATION DATA (IN MILLIVOLTS)
FOR 150 PSI NORMAL STRESS GAGE 18

Temp, deg F	Pressure, psi					
	0	10	20	30	40	50
154	- 7.20	3.10	14.30	25.1	36.5	47.9
122	-12.36	- 2.09	9.33	20.6	31.9	43.3
74	-20.3	- 9.90	1.21	12.5	23.3	34.9
48	-21.0	-10.90	0.41	10.82	21.6	32.9
17	-23.4	-13.68	-3.08	7.53	18.0	28.9
-11	-21.5	-12.82	-2.90	7.34	17.7	27.8
-52	-17.7	-11.18	-1.78	7.78	16.6	26.0
-68	-19.31	-11.18	-3.42	5.07	13.6	22.7
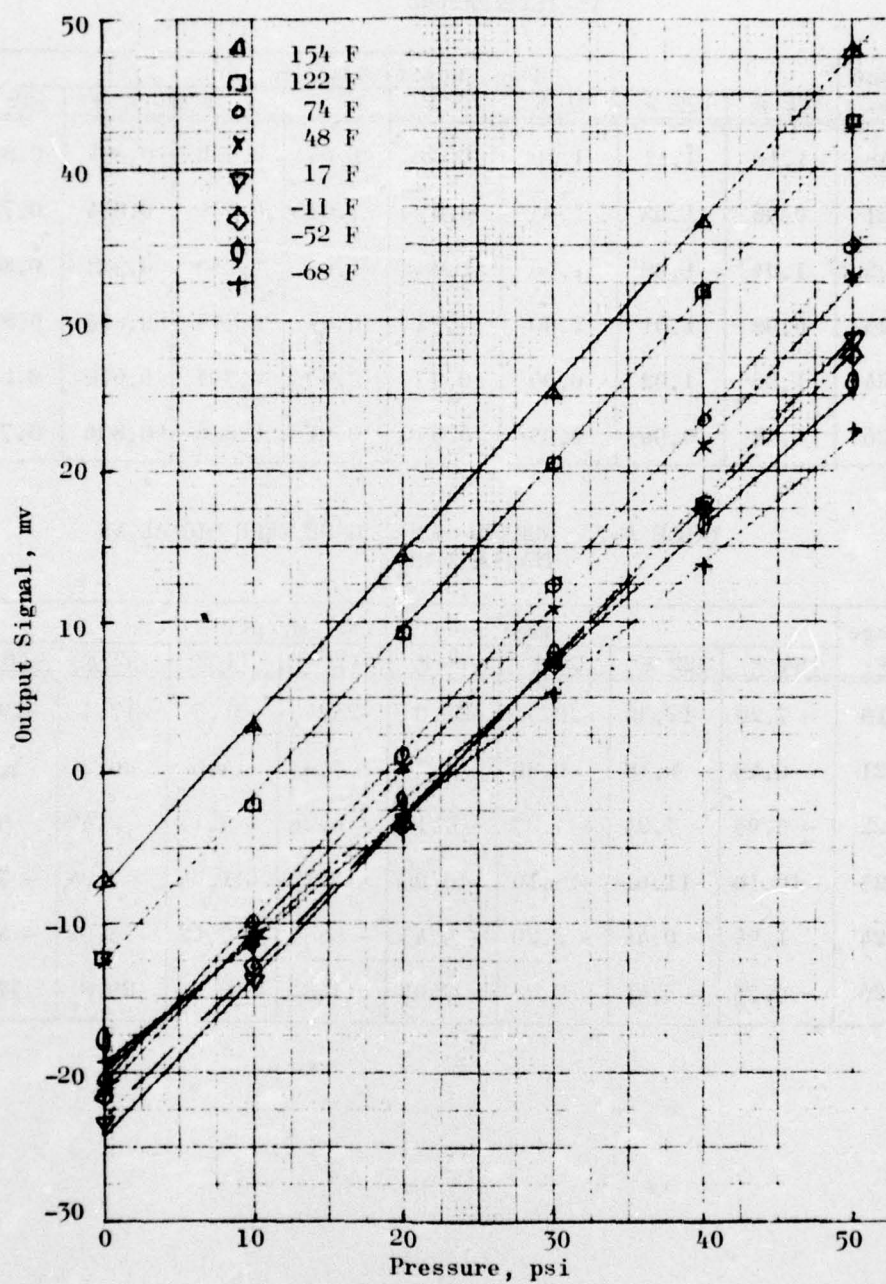
Figure A-16. Pressure Calibration Data for 150-psi
Normal Stress Gage 18

TABLE A-6. NORMAL STRESS GAGE SENSITIVITY VS TEMPERATURE

Gage No.	Gage Sensitivity, mv/psi							
	154 F	122 F	74 F	48 F	17 F	-11 F	-52 F	-68 F
18	1.10	1.11	1.10	1.08	1.05	0.986	0.894	0.840
21	0.96	1.03	1.05	1.03	1.01	0.946	0.834	0.776
22	1.04	1.08	1.06	1.06	1.04	1.030	0.982	0.822
23	0.98	1.01	1.00	0.99	0.97	0.943	0.873	0.854
24	1.00	1.02	0.99	0.93	0.89	0.794	0.670	0.642
26	0.92	0.96	0.95	0.93	0.91	0.886	0.836	0.790

TABLE A-7. NORMAL STRESS GAGE ZERO SIGNAL VS TEMPERATURE

Gage No.	Gage Sensitivity, mv/psi							
	154 F	122 F	74 F	48 F	17 F	-11 F	-52 F	-68 F
18	- 7.20	-12.36	-20.3	-21.0	-23.4	-21.5	-17.7	-19.31
21	0.43	0.18	0.30	4.35	7.85	14.6	26.2	30.8
22	- 5.95	- 7.24	- 7.27	- 7.10	- 6.26	- 5.17	- 2.42	0.74
23	-10.10	-11.61	-13.10	-13.09	-13.13	-11.64	- 7.24	- 7.24
24	1.94	- 0.44	- 2.20	- 5.43	- 6.81	- 7.42	- 5.52	- 4.88
26	- 7.73	- 3.41	2.28	7.04	11.92	19.2	29.8	37.0
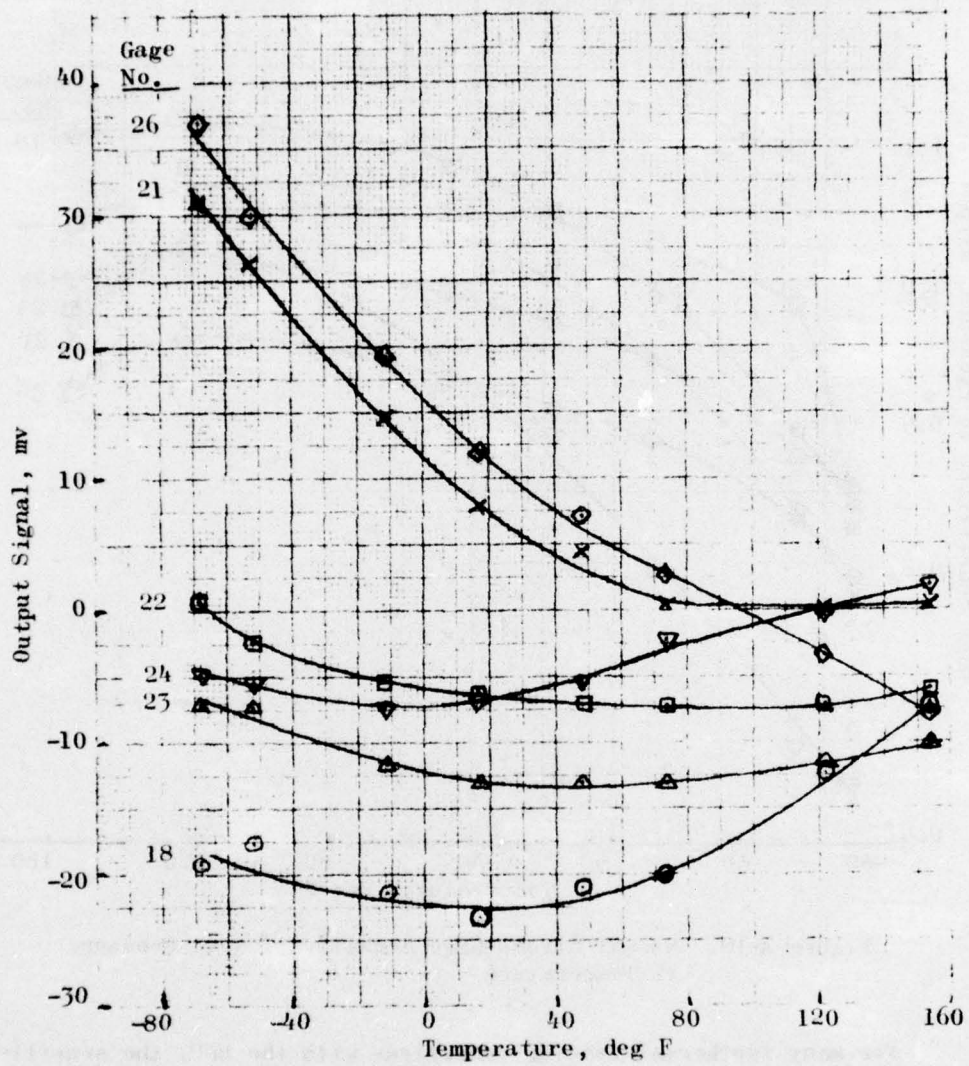
Figure A-17. Normal Stress Gage Zero Signal vs Temperature
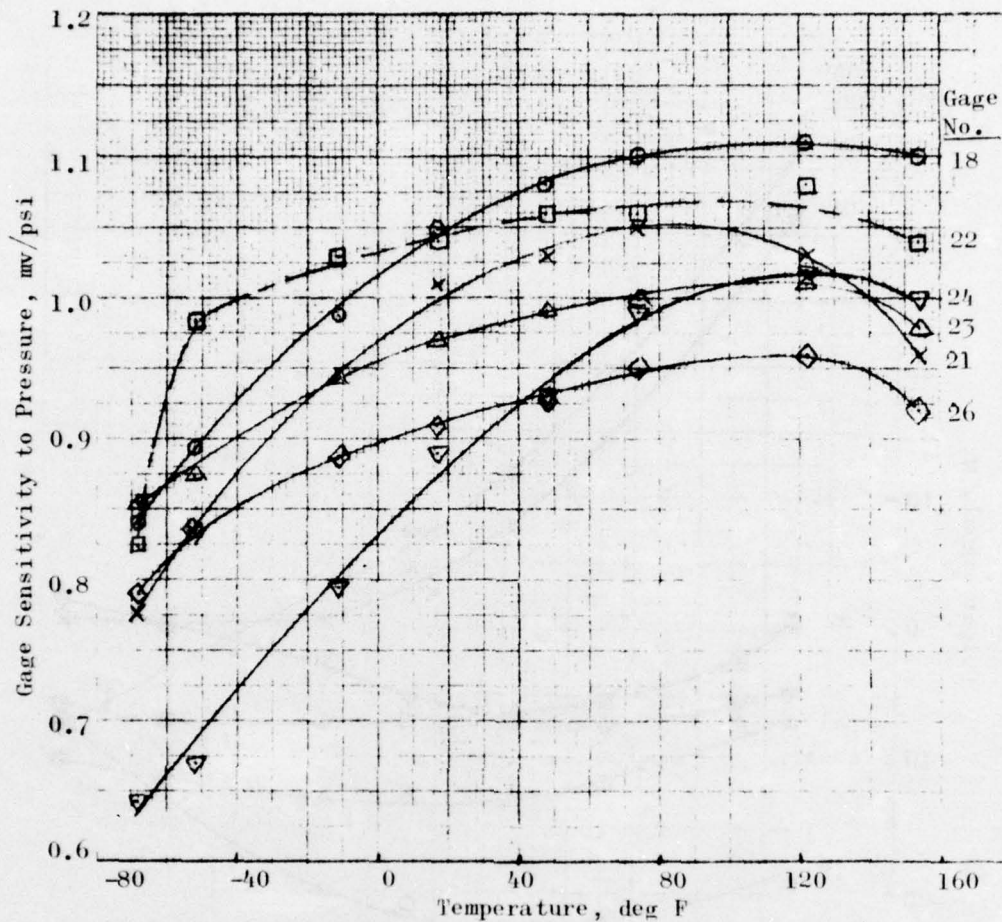
Figure A-18. Normal Stress Gage Sensitivities to Pressure
vs Temperature

For many isothermal loading conditions with the BDU, the sensitivity-
temperature curves of Figure A-18 will enable the gage signals to be
interpreted directly as stress. It is essential to measure the gage out-
put signal from the zero reading for the particular temperature being con-
sidered, i.e., the zero signal curves of Figure A-17. The difference
between the measured output and the zero signals represents the signal due
to stress, which is then divided by the sensitivity (from Figure A-18) to
obtain stress.

For such long-term problems as cooling or heating or for the higher frequency dynamic tests, the gage sensitivity curves as a function of temperature should not be used to interpret the gage data. Because of the viscoelastic propellant response, both temperature and time (or frequency) must be considered in the data analysis. The use of sensitivity curves plotted against log reduced time $(\log t/a_T)$ or reduced frequency (ωa_T) is recommended for these problems.

A reasonably accurate conversion between the temperature curves and the reduced time curves may be made by assuming that the time interval involved in applying the step pressure was 1 minute (reasonably close to reality). Then the value of $\log t = 0$ and, therefore, $\log (t/a_T)$ becomes simply $- \log a_T$.

The correlation between temperature and reduced time is given in Table A-8 where the values of $\log a_T$ for the inert propellant batch used in the BDU are those obtained in a Structural Test Vehicle (STV) program. These values were obtained during isothermal calibration tests of a 150-psi diaphragm gage in a simple uniaxial test fixture.

TABLE A-8. APPROXIMATE CONVERSION OF TEMPERATURE TO LOGARITHMIC REDUCED TIME

Temp, deg F	$\text{Log}_{10} a_T$*	Log t**	Log t/a_T, min
154	-1.80	0	1.80
122	-1.10	0	1.10
74	0	0	0
48	0.75	0	-0.75
17	1.75	0	-1.75
-11	2.85	0	-2.85
-52	5.10	0	-5.10
-68	6.50	0	-6.50

*Loading time assumed to be 1 minute
**Data from STV program

Figure A-19 shows the normal stress gage sensitivities as functions of reduced time, using the conversion of Table A-8.

The STV tests on a 150-psi normal stress sensor embedded in a uni-axial test fixture showed that the gage is slightly more sensitive to hydrostatic pressure than to uniaxial tension. This was also determined by analyses. It appears that if the gage sensitivity to pressure is 1.15 mv/psi, then its sensitivity to uniaxial tension is 1.10 mv/psi, i.e., $\simeq$ 95% of the hydrostatic pressure sensitivity. Therefore, the gage sensitivities to pressure plotted in Figures A-18 and -19 should be reduced by 5% to determine the normal tensile stress component at the BDU case-grain interface.

Interface Shear Stress Sensors

Two types of embedded shear stress measuring gages were used in the BDU: the shear cube and the bending beam shear gage. Two of the shear cubes (120A and 120B) contained foil strain gages as active elements while the third shear cube (SH2) contained semi-conductor strain gage elements. The fourth shear gage (101) contained a metal foil bending element with semi-conductor strain gages attached to both sides. Under shear, the foil beam bends, producing an elongation in one gage element and a contraction in the other element.

The magnitude of the shear stresses to be obtained as a result of thermal loads plus flight loads cannot be estimated with any precision. Consequently, the comparatively insensitive foil gage shear cubes and the bending beam shear gage were included in the BDU to measure large shock stresses that could break the more sensitive semi-conductor type gages. (Another semi-conductor gaged shear cube (SH1) broke during the casting and mandrel extraction operations.)
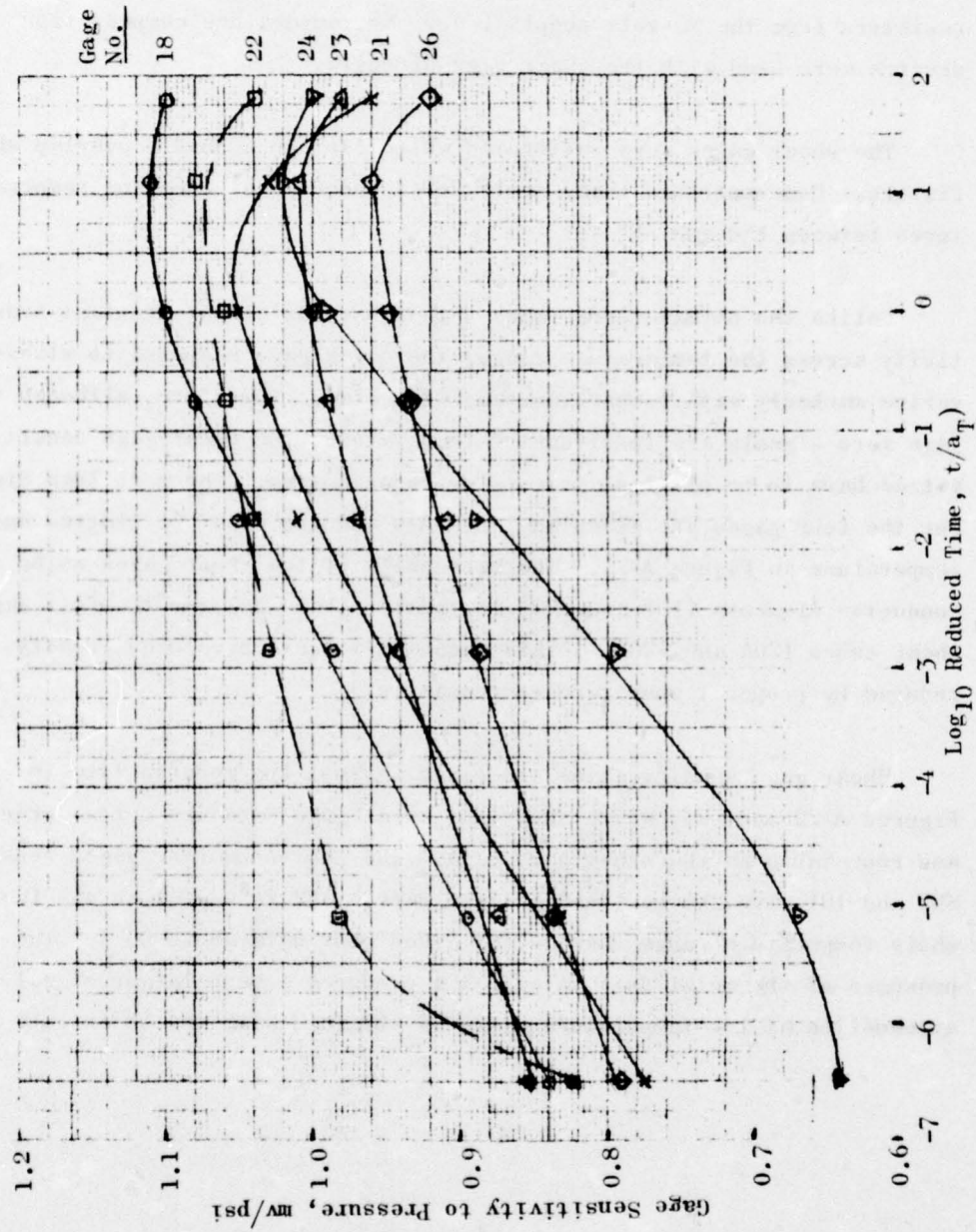
Figure A-19. Normal Stress Gage Sensitivities to Pressure vs Log, Reduced Time

Bridge circuits for the three types of shear gages used in the BDU are given in Figure A-20. All three circuits are powered through dropping resistors from the 28-volt supply line. No temperature compensation devices were used with the shear gage circuits.

The shear gages were calibrated while cast in a double overlap shear fixture. Constant-load creep tests were conducted at constant temperatures between 150 and -47 F.

Unlike the normal stress gages, that have an almost constant sensitivity across the temperature range, the shear gage response to stress varies markedly with temperature and with time. Therefore, although the gage zero signals are functions of temperature, the shear gage sensitivities have to be plotted against log reduced time. The zero load signals for the four gages are given in Table A-9 and the data are plotted against temperature in Figure A-21. The zero shift of the shear gages using semiconductor elements (101 and SH2) is greater than that for the foil gage shear cubes 120A and 120B. (This zero shift could have been greatly reduced by proper temperature compensation.)

Shear gage sensitivities are given against log reduced time in Figures A-22 and -23, which show that shear gage data are not as precise and repeatable as the other gage data. The semi-conductor gaged sensors SH2 and 101 give the best calibration data. SH2 is useful across the whole temperature range whereas 101 gives poor data above 96 F. The presence of the metal foil in gage 101 produces a much larger signal attenuation at low temperatures than is obtained with the shear cube SH2.
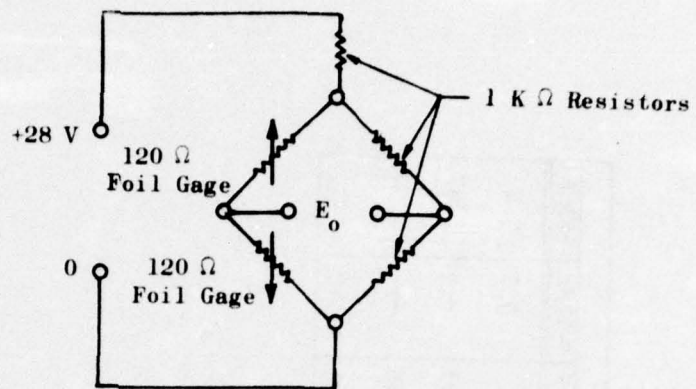
(a) Foil Gage Shear Cube Circuit (120A and 120B)
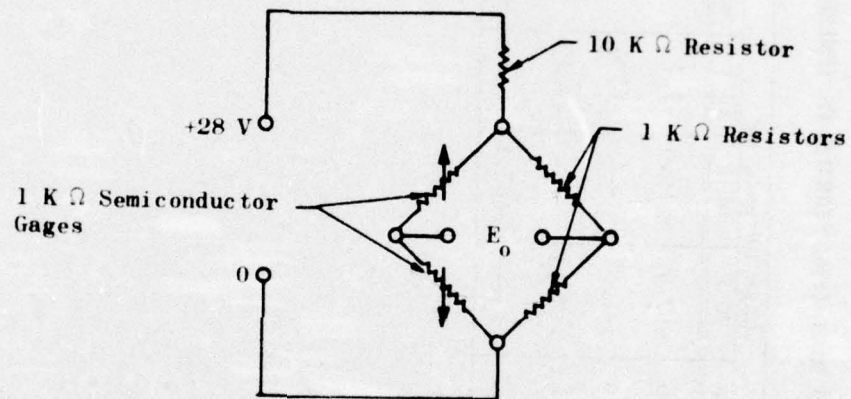
1 K Ω Resistors

+28 V

120 Ω
Foil Gage

E_o

0

120 Ω
Foil Gage

(b) Semiconductor Gage Shear Cube Circuit (SH2)

10 K Ω Resistor

+28 V

1 K Ω Resistors

1 K Ω Semiconductor
Gages

E_o

0

(c) Bending Beam Shear Gage Circuit (#101)

18 K Ω Resistor

+28 V

3.3 K Ω Resistors

1 K Ω Semiconductor
Gages

0
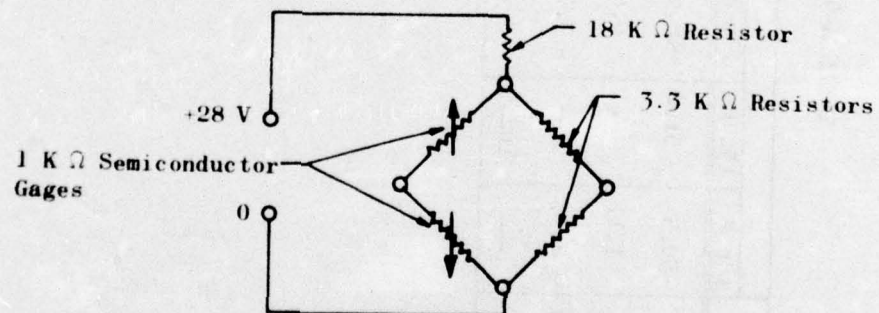
Figure A-20. Shear Gage Circuits

A-31

TABLE A-9. SHEAR GAGE ZERO SIGNALS VS TEMPERATURE

Gage No.	Gage Output, mv										
	156 F	150 F	156 F	96 F	70 F	66 F	46 F	-8 F	-17 F	-47 F	-63 F
101	-50.5	- 51.2	-48.0	-32.6	-19.9	- 16.3	-7.7	6.8	5.4	5.7	3.4
120A	1.11	---	0.86	0.95	1.63	---	1.99	---	2.93	---	3.63
120B	- 2.97	---	- 3.78	- 3.98	- 3.43	---	-3.27	---	-2.58	---	-2.56
SH2	---	-102.2	---	---	---	-105.1	---	-85.4	---	-79.4	---
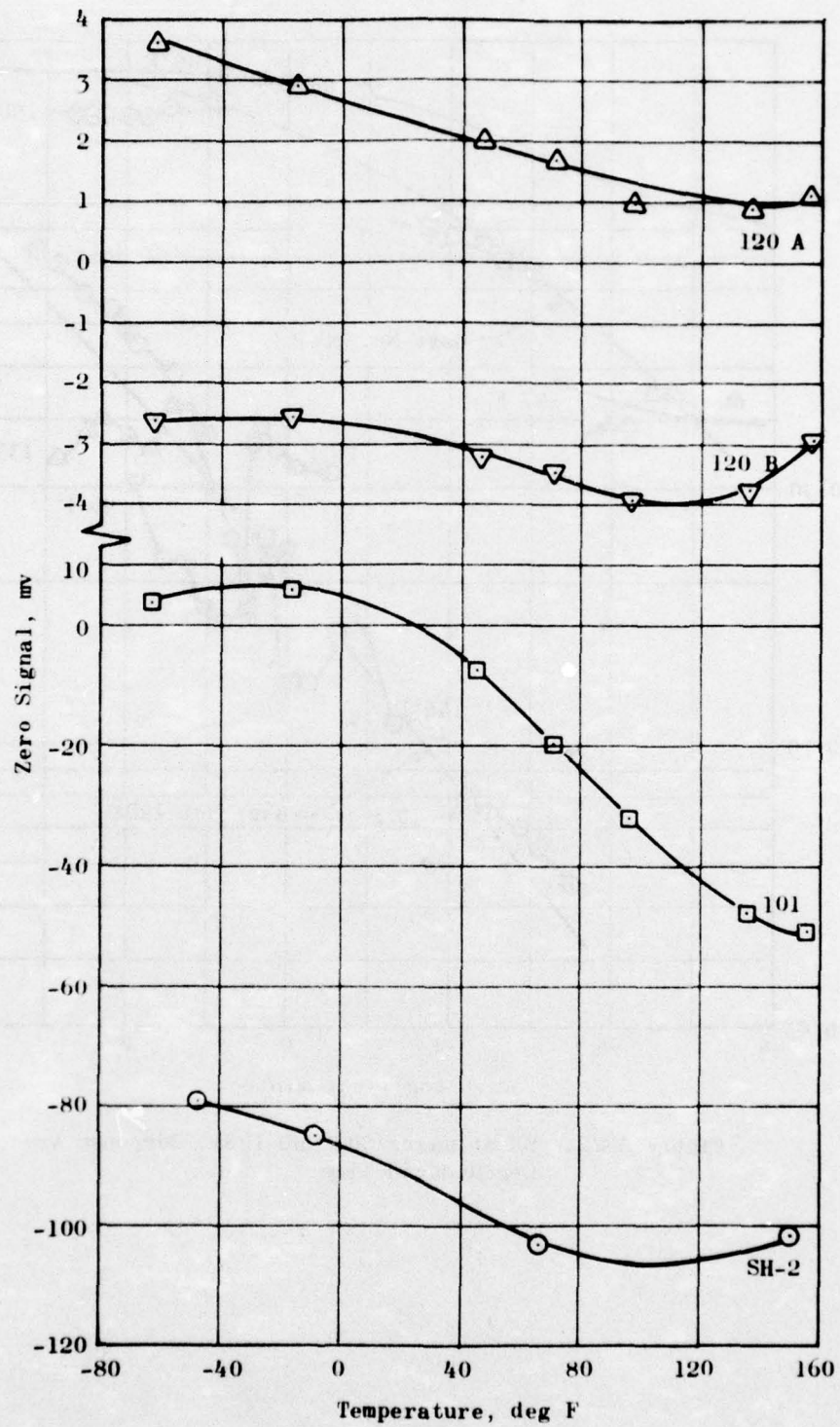
Figure A-21. Gage Signal vs Temperature

A-33
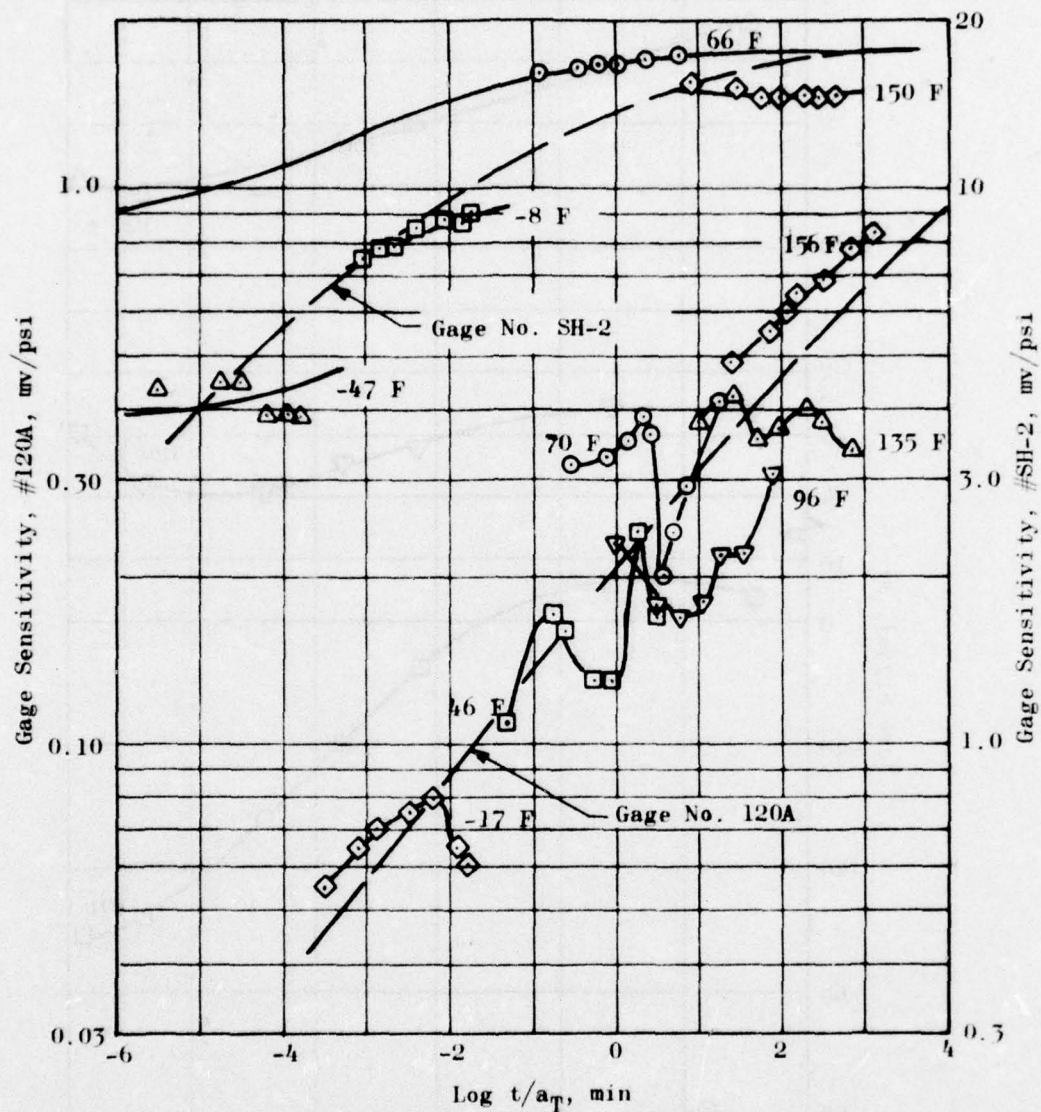
Figure A-22.   Shear Gages SH2 and 120A, Response vs
Log Reduced Time

A-34
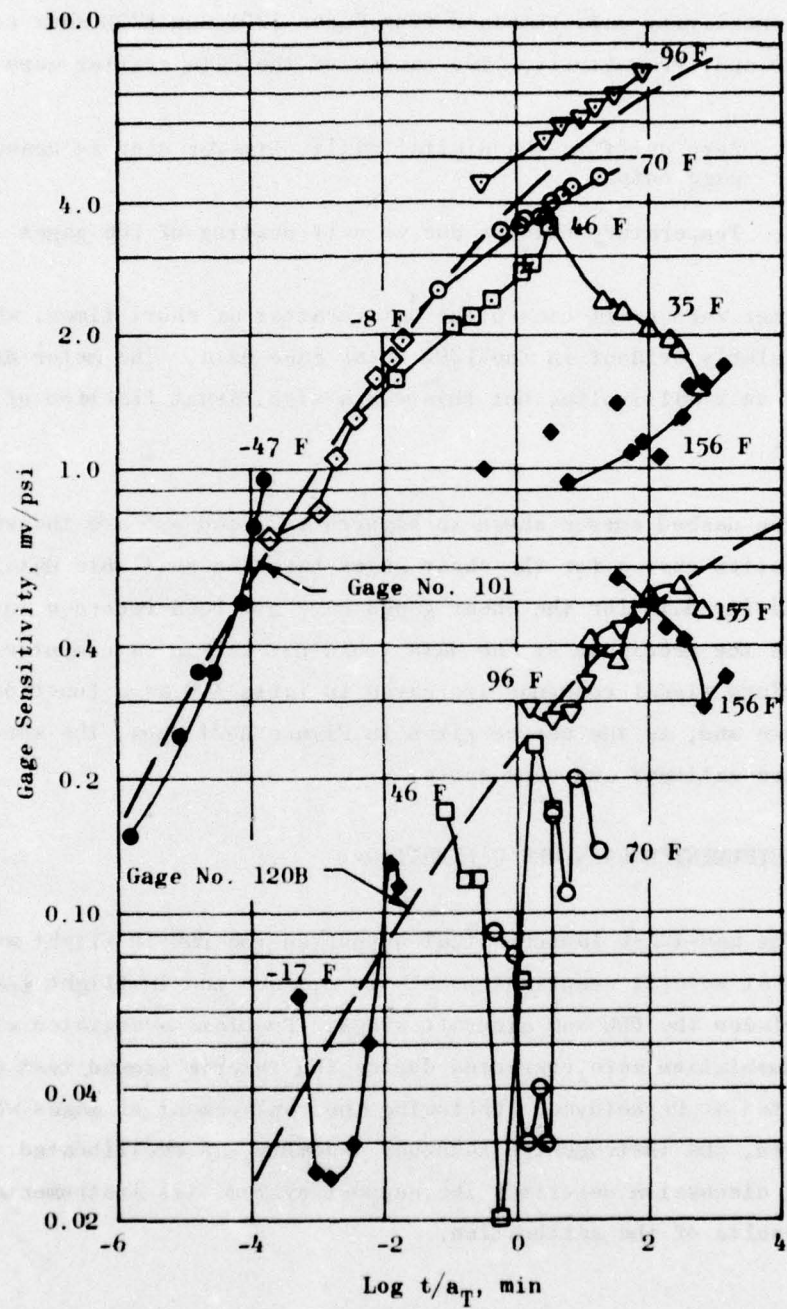
Figure A-23. Shear Gages 101 and 120B, Response vs
Log Reduced Time

Sensitivity data obtained from Gages 120A and 120B show considerable scatter and irregularity. Two causes of the data scatter were determined:

1. Zero drift in the digital millivoltmeter used to measure gage output

2. Temperature changes due to self-heating of the gages

The meter zero drift caused the data scatter at short times, which is particularly evident in the 120B shear gage data. The meter drift was only 1 to 2 millivolts, but this was a significant fraction of the output signal.

The dashed curves shown in Figures A-22 and -23 are the suggested calibration curves for the shear gages based on available data. Gage sensitivity data for the shear gages have not been recorded in a table because the precision of the data would not warrant a computer program fit. Zero signal readings are given in Table A-9 as a function of temperature and, as the curves given in Figure A-21 show, the zero signal data are rational and repeatable.

BDU INSTRUMENTED LAUNCHER CALIBRATION

The MAU-12A/C launcher that supported the BDU in flight was instrumented at several compliant points to measure the in-flight load transfer between the BDU and aircraft wings. Problems associated with this instrumentation were corrected during the interim ground test effort conducted at Rocketdyne. Following the replacement of gages where required, the instrumented launcher assembly was recalibrated. The following discussion describes the support system, its instrumentation, and the results of the calibration.

Launcher Support System

The BDU support consisted of a two-lug/hook system for transferring motor weight to the launcher and two sway braces to provide lateral stability. Locations of the contact points are indicated in Figure A-24. The forward lug was pivoted to allow motion along the missile longitudinal axis; while the aft lug was rigidly attached to the BDU. Descriptive sketches of the lugs are shown in Figure A-25. The sway braces, fore and aft, were identical (Figure A-26) and maintained contact with the BDU by friction between the missile skin and threaded pads of the braces. When the motor was attached to the launcher, the sway brace pads were tightened from one-half to one turn beyond initial contact. This loading resulted in an additional tension in the load lugs.
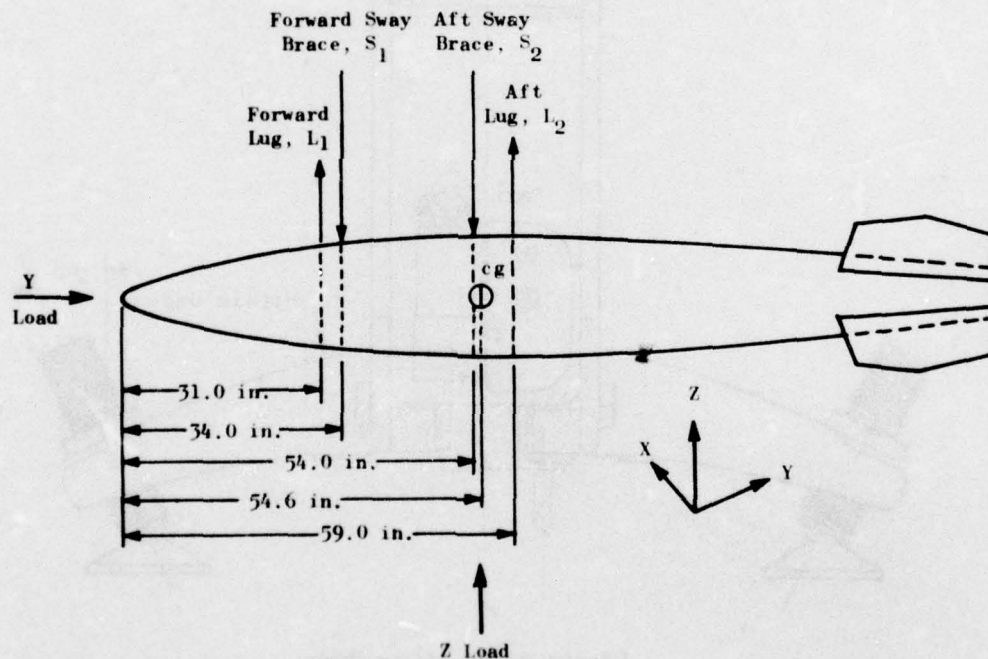
Figure A-24. BDU/Launcher Load Transfer Points

a. Forward Lug   b. Aft Lug
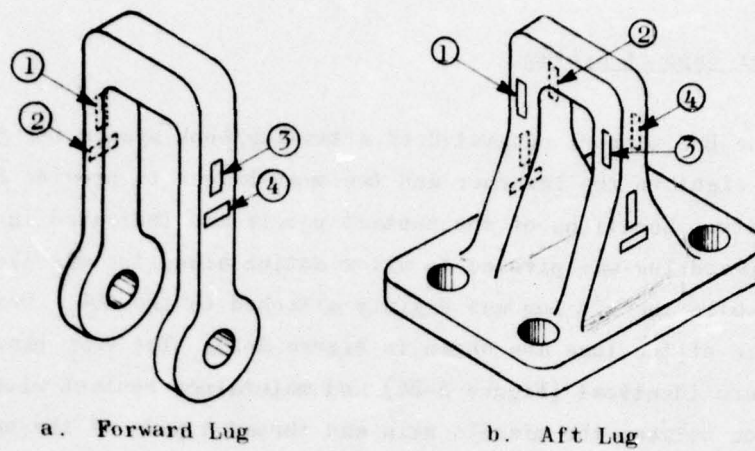
Figure A-25. BDU Launcher Lugs

Strain Gages

25°
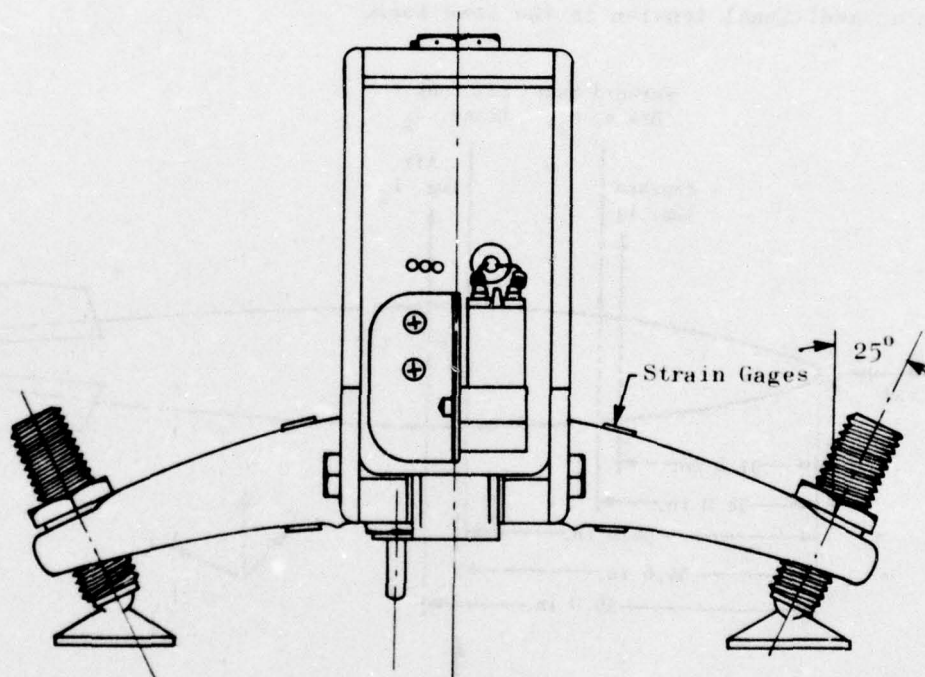
Figure A-26. Sway Brace

With the sway braces thus tightened, load transfer to the launcher became quite complex. Load in the horizontal (X) direction transverse to the missile longitudinal axis (Y direction) should have been reacted almost entirely by the sway braces although the linearity of response depended on continuous contact between the sway brace feet and the missile skin. The possibility for Y-axis load by the lugs existed because of the manner of contact between the lugs and hooks. Loads in the longitudinal (Y) direction were reacted primarily by bending of the aft launch lug with some reaction of the sway braces and the potential for tensile load in the forward lug (which was pivoted about the X axis). Gravitational loads (Z direction) were reacted by tension in the lugs and compression relief in the sway braces. These load conditions are discussed in detail with results of the calibration.

Both launcher lugs were instrumented with a four-gage tensile load circuit as shown in Figure A-27. The two gages oriented in the direction of pull and the two gages oriented at right angles to that axis provided for lateral contraction (Poisson effect) correction and minimal response to bending. The aft lug was also instrumented to measure bending as shown in Figure A-28. This gage arrangement enhanced the bending response of the gages while cancelling response to tensile loads. The sway braces were also gaged with four-gage bridges that, like the bending circuit, provided high sensitivity to unequal or side loads while minimizing response to brace preload when applied equally to both arms. The arrangement is shown in Figure A-29.

The lugs were gaged with foil-type strain gages, and the sway braces were gaged with semi-conductor gages. The aft sway brace was also instrumented with a foil gage circuit as a backup for the semi-conductor circuit (the reliability of which was somewhat suspect).
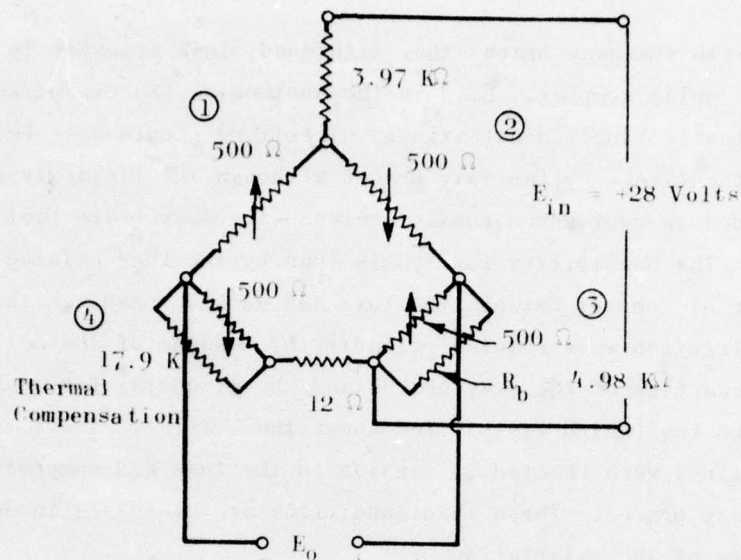
Figure A-27. Mechanical and Electrical Circuit
Forward Lug Tensile Load Measuring
Elements
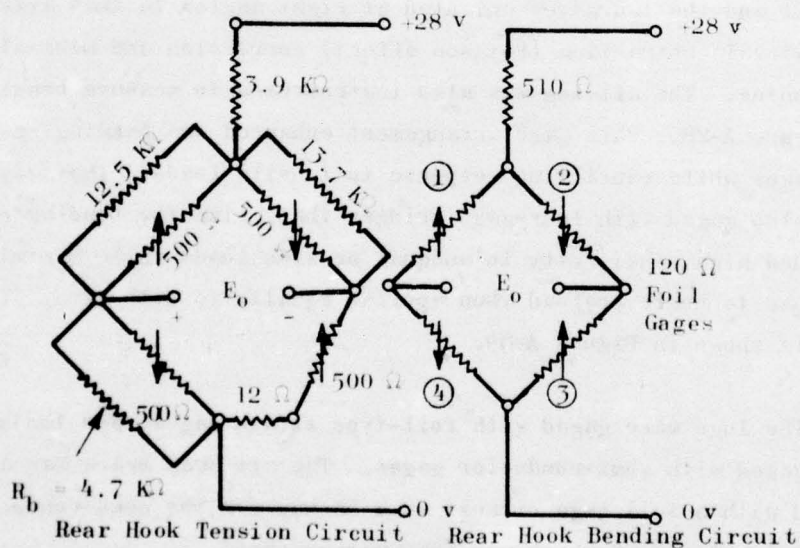
Figure A-28. Aft Lug Circuits

a. Aft Sway Brace Circuit (Semi-conductor) **b.** Front Sway Brace Circuit
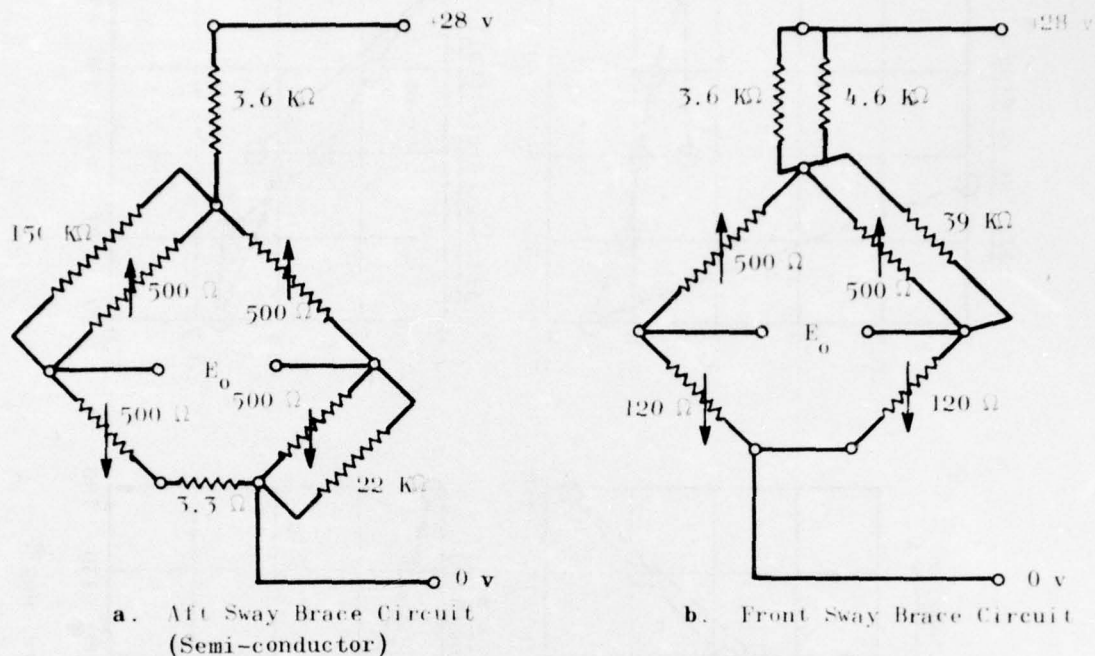
Figure A-29. Sway-Brace Bridge Circuit

In addition to gages located to minimize cross-axis sensitivity, compensating resistors were introduced to minimize gage no-load response change with temperature. In general, the foil gage circuits can be thermally compensated to a high degree. The semi-conductor gages are more temperature sensitive and as a rule must be paired as to thermal response to achieve a reasonable thermal compensation. The thermally induced response of the five gaged elements on the BDU are shown in Figure A-30. Data were recorded at near-equilibrium temperatures during conditioning of BDU/launcher assembly. In addition to gage output resulting from a temperature change, the output may also vary with time during a temperature change (i.e., a thermal gradient may alter the gage output). This is exemplified by the data shown in Figure A-31 for the sway braces on cooldown from 180 to $\sim$ 135 F. The response of the aft sway brace semi-conductor gage appeared to be time dependent though it possibly was responding

A-41
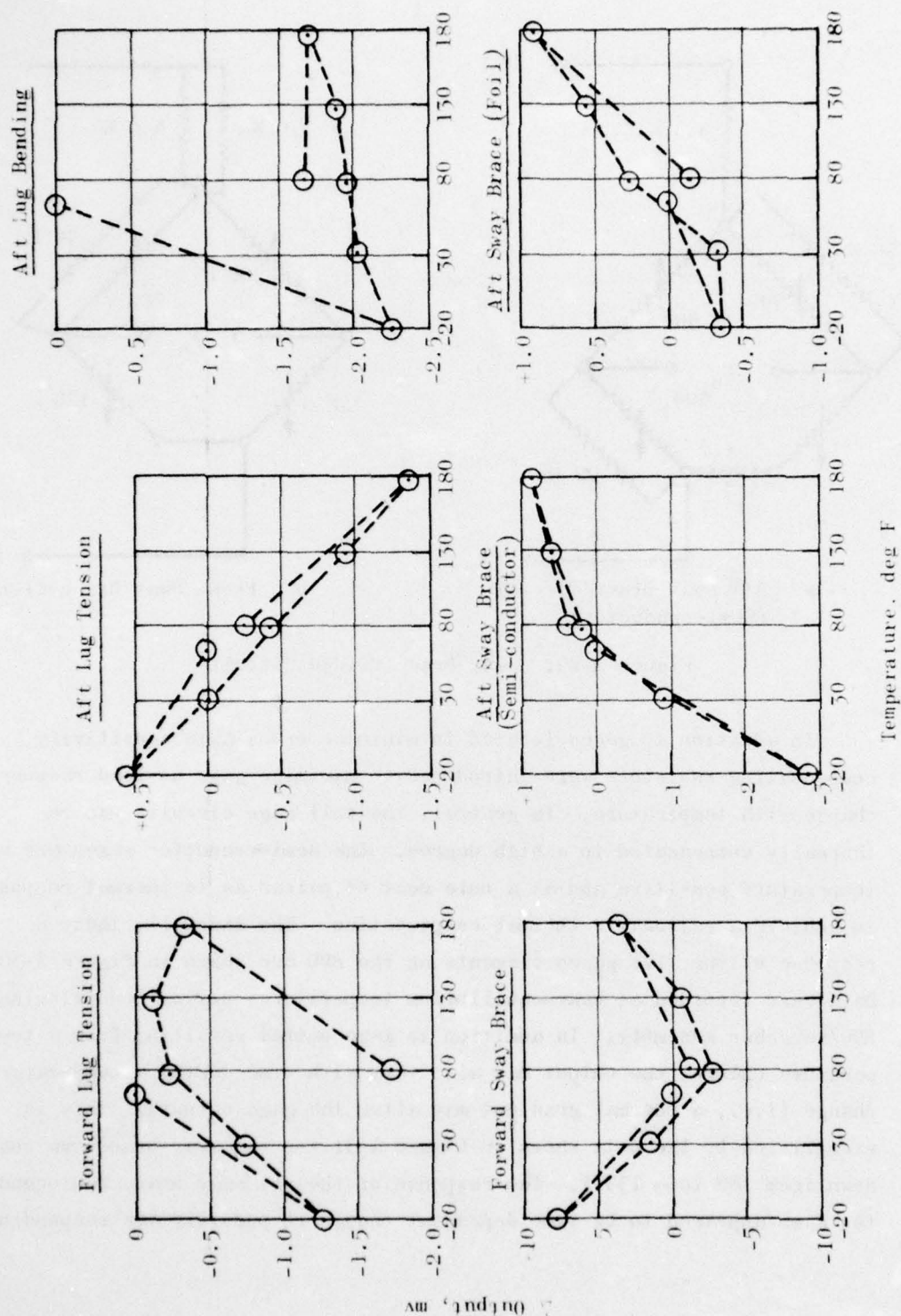
Figure A-30. Thermally Induced Shift in Output, All-Up Calibration
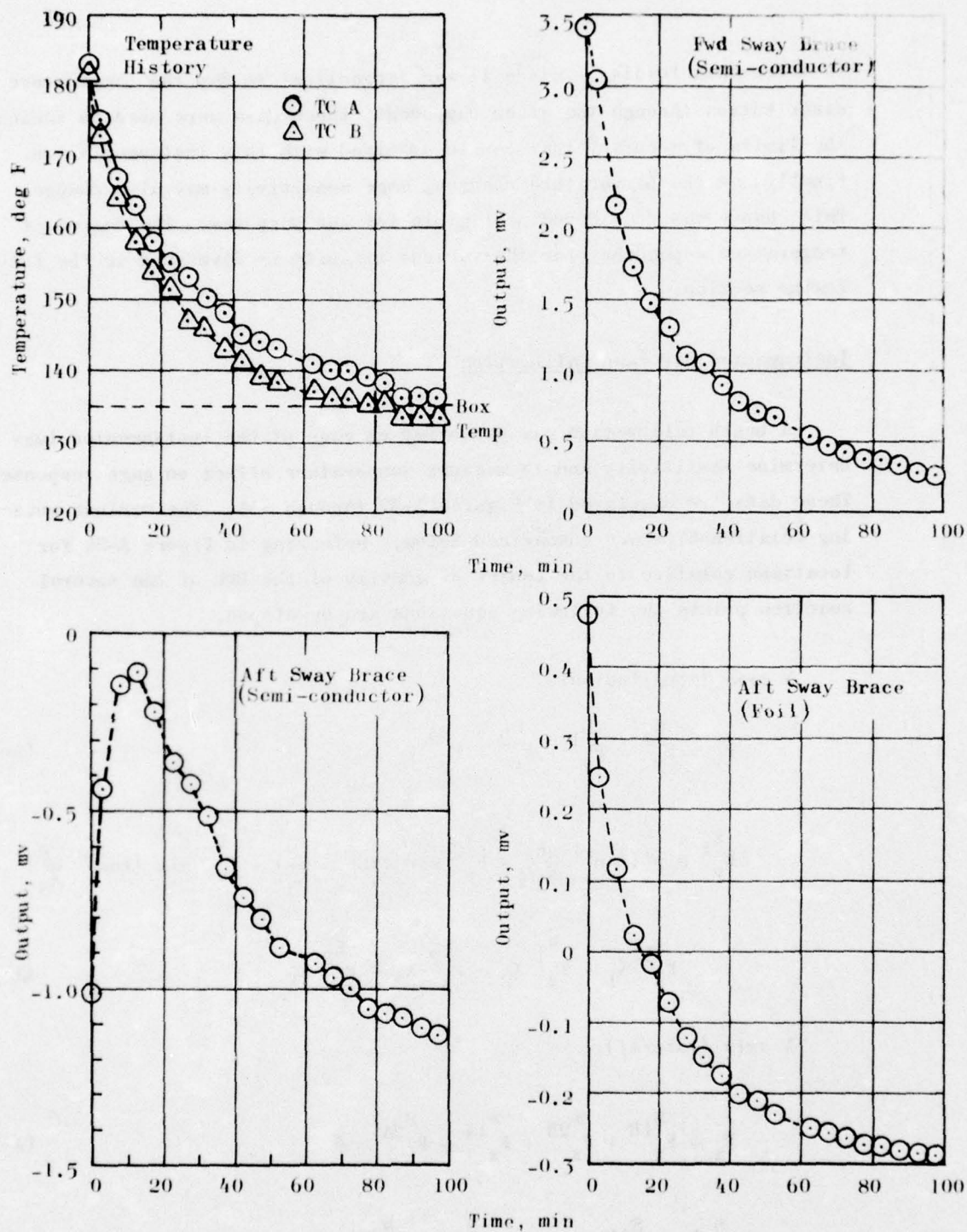
Figure A-31. Sway-Brace Cool-Down Transient Response

to cross-axis loading. Since it was impractical to map the temperature distribution through the given component, these data were used to indicate the limits of accuracy that can be obtained with this instrumentation. Finally, as the temperature changes, gage sensitivity may also change. This change was considered negligible for our purposes. The degree of temperature dependency for the various circuits is discussed in the following section.

Instrumented Launcher Calibration

A bench calibration was performed on each of the instrumented lugs to determine sensitivity and to measure temperature effect on gage response. These data are displayed in Figures A-32 through -34. The various governing relationships are summarized below. Referring to Figure A-24 for locations relative to the center of gravity of the BDU of the several reaction points the following equations are developed:

Y axis (longitudinal):

$$F_y = F_y^{S_1} + F_y^{L_1} + F_y^{S_2} + F_y^{L_2} \tag{A-1}$$

$$F_y^{S_1} \sin\left(\tan^{-1}\frac{8}{X_2}\right) + F_y^{S_2} \sin\left(\tan^{-1}\frac{8}{X_3}\right) + F_y^{L_2} \sin\left(\tan^{-1}\frac{8}{X_4}\right) =$$

$$F_z^{L_1} X_1 - F_z^{S_1} X_2 - F_z^{S_2} X_3 - F_z^{L_2} X_4 \tag{A-2}$$

X axis (lateral):

$$F_x + F_x^{S_1B} + F_x^{S_2B} + F_x^{S_1A} + F_x^{S_2A} = 0 \tag{A-3}$$

$$\left(F_x^{S_1A} - F_x^{S_1B}\right) X_2 = -\left(F_x^{S_2A} - F_x^{S_2B}\right) X_3 \tag{A-4}$$

A-44
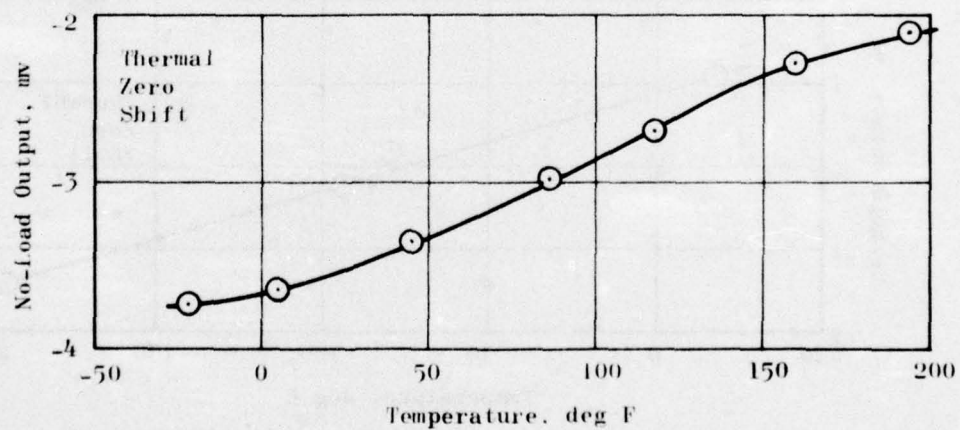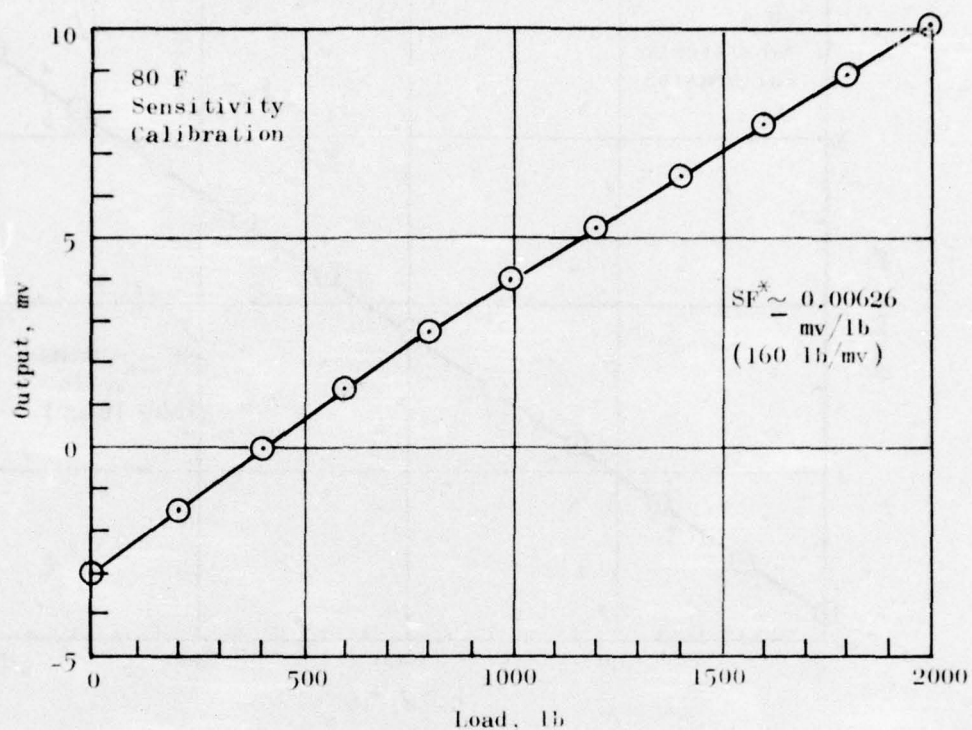
*Sensitivity Factor

Figure A-32. Forward Lug (Tension Gage) Bench Calibration
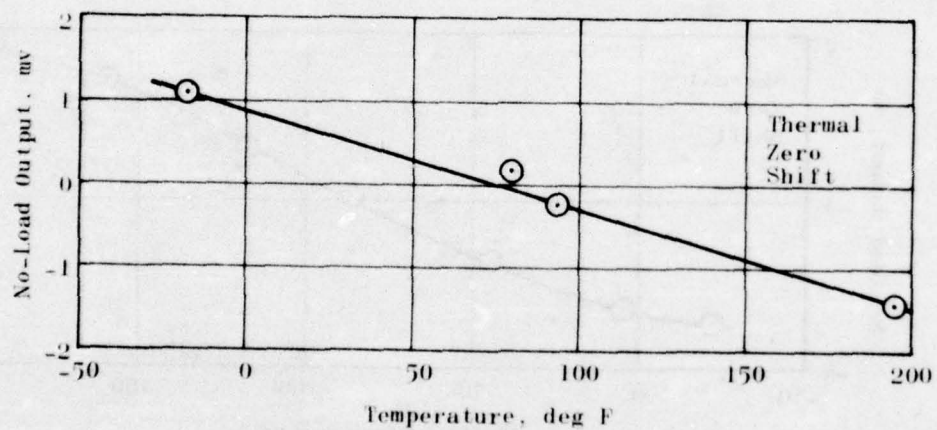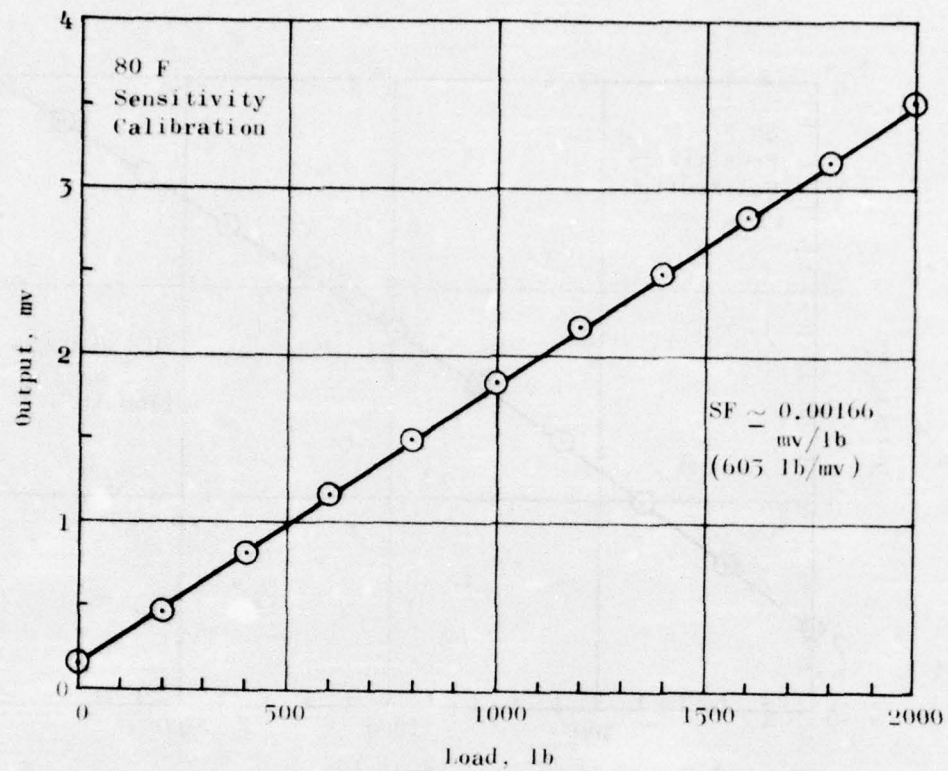
Figure A-33. Aft Lug (Tension Gage) Bench Calibration
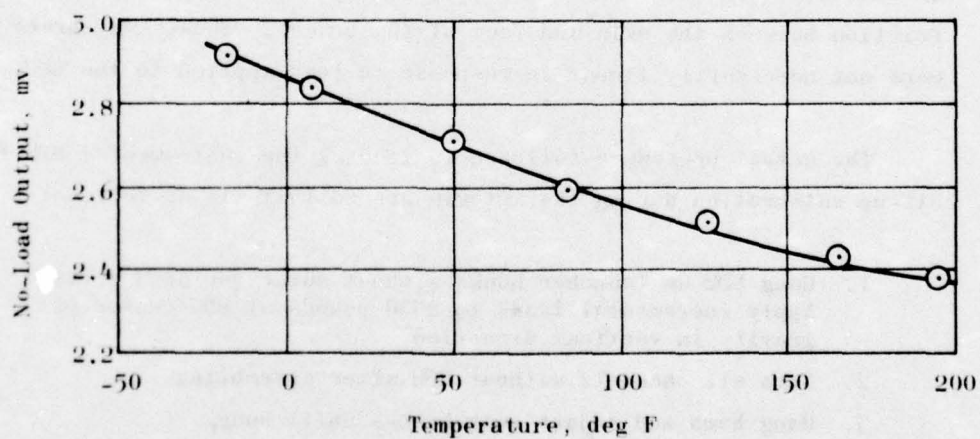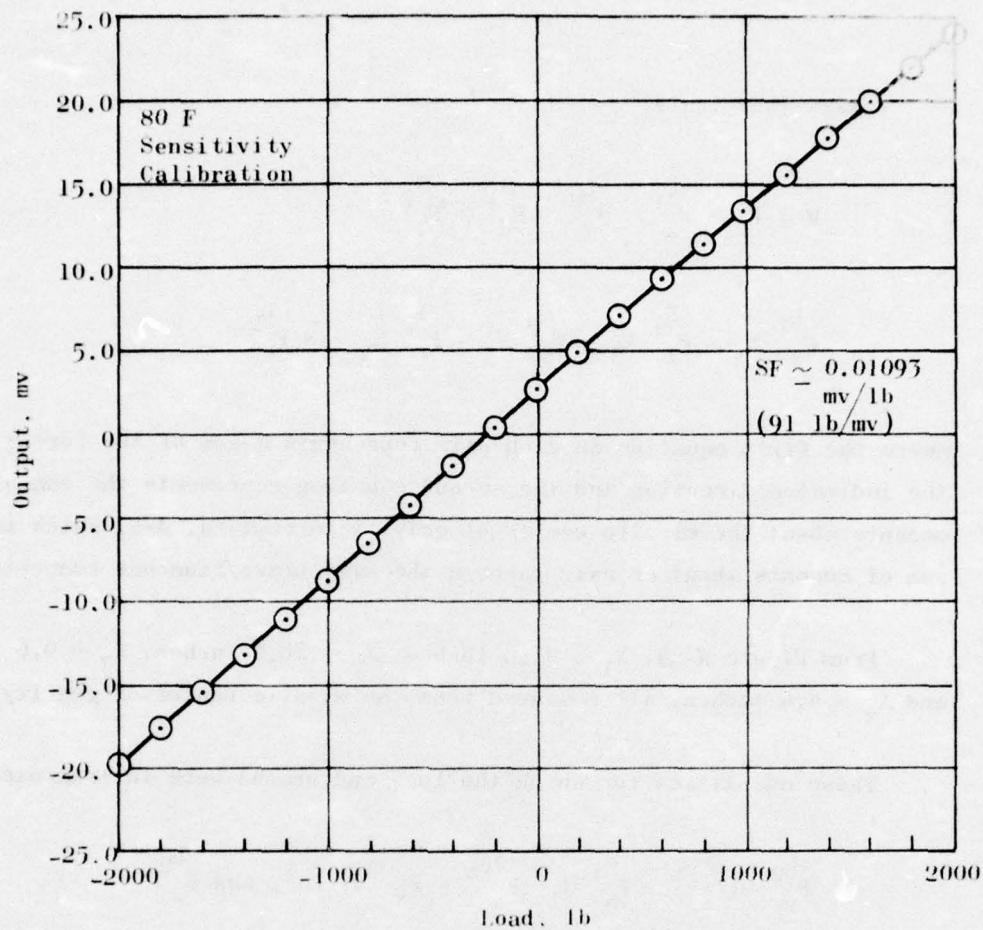
Figure A-34. Aft Lug (Bending Gage) Bench Calibration

Z axis (vertical):

$$W + F_z = F_z^{L_1} + F_z^{L_2} + F_z^{S_1} - F_z^{S_2} \qquad \text{(A-5)}$$

$$F_z^{L_1} X_1 - F_z^{S_1} X_2 - F_z^{S_2} X_3 - F_z^{L_2} X_4 = 8 F_y^{L_2} \qquad \text{(A-6)}$$

Where the first equation in each pair represents a sum of the forces in the indicated direction and the second equation represents the sum of moments about the missile center of gravity (except Eq. A-4, which is the sum of moments about an axis through the sway brace/launcher connector).

From Figure A-24, $X_1 = 23.6$ inches, $X_2 = 20.6$ inches, $X_3 = 0.6$ inch, and $X_4 = 4.4$ inches, all measured from the missile center of gravity.

Those quantities for which the lugs and braces were instrumented are:

$$F_y^{L_2}, \ (F_x^{S_{1A}} - F_x^{S_{1B}}), \ (F_x^{S_{2A}} - F_x^{S_{2B}}), \ F_z^{L_1}, \ \text{and} \ F_z^{L_2}$$

In addition, the basis of contact between the BDU and the sway braces was friction between the skin and feet of the braces. Thus, sway-brace forces were not necessarily linear in response to load applied to the BDU.

The actual procedure followed in loading the instrumented BDU for all-up calibration during the interim ground test was as follows:

1. Hang BDU on launcher hooks without motor (or aft) section. Apply incremental loads to 2000 pounds at BDU center of gravity in vertical direction.

2. Zero all channels without BDU after assembling.

3. Hang bomb and adjust sway braces until snug.

4. Apply 200-pound loads in Z and Y directions.

5. Tighten sway braces in 1/4 turn steps to one full turn then loosen 1/4 turn.

6. Apply 100-pound loads in Z and X directions at three stations along BDU.

7. Apply ± 1500-pound loads in Z direction in 300-pound increments at BDU center of gravity and repeat.

8. Apply ± 1000-pound loads in X direction in 200-pound increments at BDU center of gravity and repeat.

9. Apply 1800-pound load in Y direction (aft) in increments. Apply 1000-pound load in Y direction (aft) in increments. Retorque launcher (retighten sway braces). Apply 1000-pound load in Y direction (aft) in 200-pound increments at BDU nose and repeat.

The voluminous amount of data thus generated is summarized graphically and discussed in the following paragraphs.

Step 1 – Lug Tension Calibration. Step 1, performed with the forward section of the BDU and without the sway braces in contact with the motor, represents a calibration of the lugs in tension. Equations A-5 and -6 are not applicable to this case because of the two above-mentioned conditions. Rather, we have

$$W' + F_z = F_z^{L_1} + F_z^{L_2} \tag{A-7}$$

$$F_z^{L_1} X_1 = W' X' + F_z^{L_2} X_4 \tag{A-8}$$

where

W' – weight of the forward section only

X' = distance from cg of the forward section to cg of the BDU

A-49

Considering the two extremes, $F_z = 0$ and $F_z = 2000$ pounds, respectively, we obtain:

$$\left[F_z^{L_1} (2000) - F_z^{L_1} (0) \right] X - \left[F_z^{L_2} (2000) - F_z^{L_2} (0) \right] X_4 = 0 \quad (A-9)$$

$$\left[F_z^{L_1} (2000) - F_z^{L_1} (0) \right] + \left[F_z^{L_2} (2000) - F_z^{L_2} (0) \right] = 2000 \quad (A-10)$$

Data recorded for both cycles during Step 1 are shown in Figure A-35. Using these results in Eq. A-9 and -10 we obtain:

> Fwd lug tension sensitivity = 123 lb/mv
>
> Aft lug tension sensitivity = 1393 lb/mv

Step 2 - Zero All Channels. The launcher, in preparation for hanging the assembled BDU, was read to establish zero readings. The comparison between ambient no-load readings during bench calibration on the lugs and prior to hanging the BDU is of interest. Table A-10 summarizes this comparison. The readings are comparable for all three channels.

Steps 3 and 4 - Hang BDU, Snug Sway Braces; Apply 200-Pound Loads in Z and Y Axes. The complexities of the analysis of data from the all-up systems rapidly become obvious with the exercise of Steps 3 and 4. Gage output with each indicated condition is summarized in Table A-11. The spread between initial and final free-hanging response is of the same order as the load response itself in every case but one; the bending response of the aft lug is significant and indicates a sensitivity of about 110 lb/mv, which compares favorably with the bench-calibration result of 90 lb/mv. As an approximation

> Aft lug bending sensitivity = 100 lb/mv

A-50
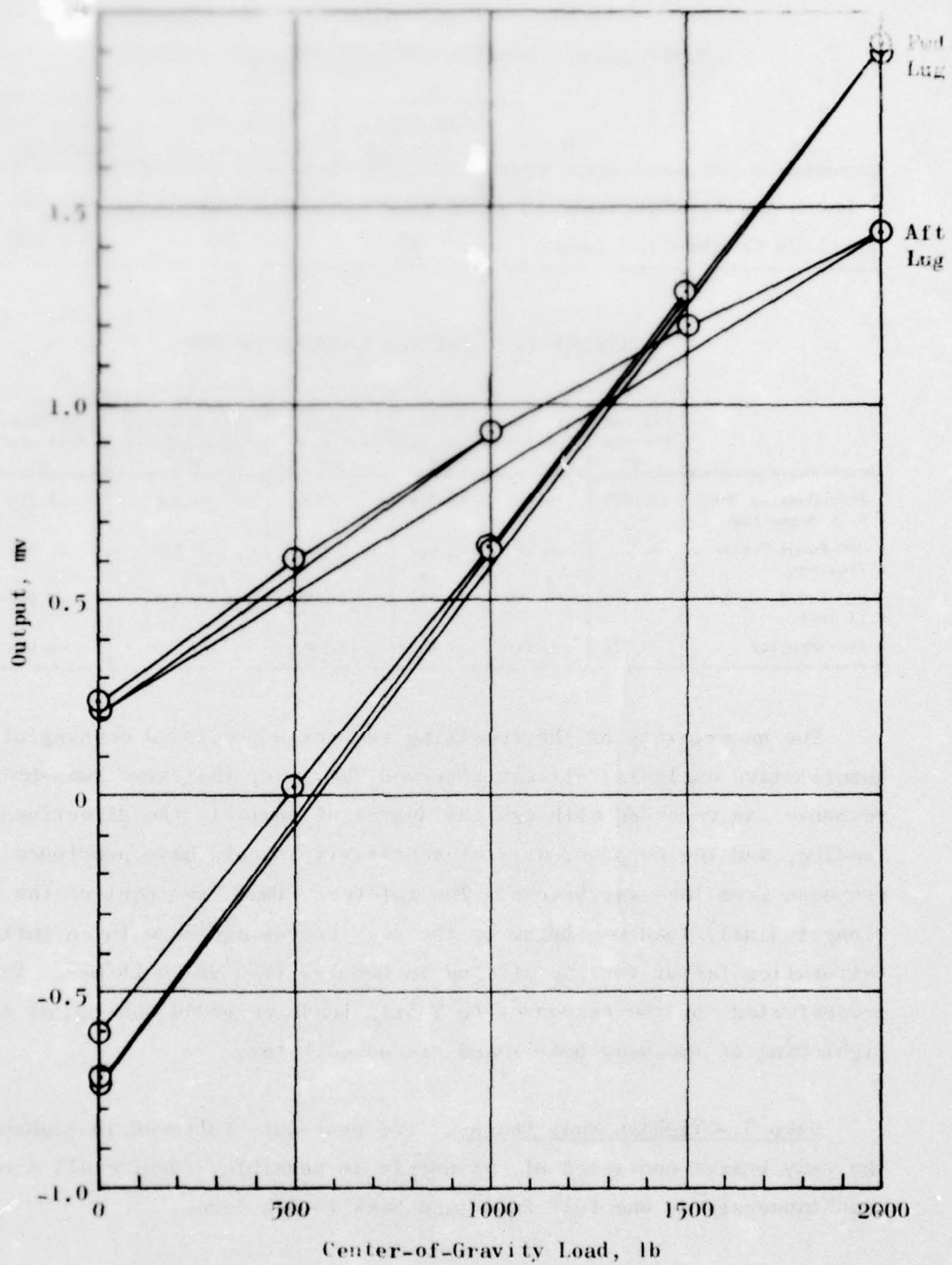
Figure A-35. Lug Response to Applied Vertical Load
(Without Sway Braces)

TABLE A-10.   INSTRUMENTED LUG NO-LOAD OUTPUTS

	Fwd Lug Tension, mv	Aft Lug Tension, mv	Aft Lug Bending, mv
Bench Calibration Zero	-3.031	+0.145	+2.607
All-Up Calibration Zero	-3.003	+0.188	+2.752

TABLE A-11.   INITIAL LOADING OF BDU

	Fwd Lug Tension, mv	Aft Lug Tension, mv	Aft Lug Bending, mv	Fwd Sway Brace, mv	Aft Sway Brace ① Semiconductor, mv	Aft Sway Brace ② Foil Gage, mv
Free-Hanging Bomb Sway Brace Lug	-2.205	+0.412	+2.576	+1.378	-0.526	-0.710
200-Pound Vertical Tension	-2.166	+0.489	+2.622	+1.166	-0.470	-0.686
208 Pounds on Nose (Y Axis)	-2.170	+0.425	+4.607	+1.252	-0.358	-0.667
Free-Hanging	-2.511	+0.441	+2.844	+1.166	-0.370	-0.684

The uncertainty of the remaining responses precluded meaningful quantitative analysis. It was observed, however, that some sway-brace response was recorded although the degree of contact, the directions of loading, and the supposed axis of sensitivity should have precluded response from the sway braces. The inference that some part of the Y-axis (longitudinal) load was borne by the sway braces agrees with an inflated calibration factor for the aft lug in bending (110 vs 90 lb/mv). This is demonstrated by the responses to Y-axis loads recorded subsequent to the tightening of the sway braces and discussed below.

Step 5 - Tighten Sway Braces. The procedure followed in tightening the sway braces consisted of, as nearly as possible, turning all screws simultaneously to one full turn then back to 3/4 turn.

A-52

Outputs of the various gages are shown in Figures A-36 and -37 for the lugs and sway braces, respectively. Summary observations, based on the calibrations determined above yielded the following results: Tension induced by tightening the sway braces full turns amounted to 4400 pounds in the forward lug and 3900 pounds in the aft lug. In addition, a bending moment was generated in the aft lug equivalent to a 110-pound force in the longitudinal direction. The forward-sway-brace response indicated either an imbalance of loading in the X direction or a sensitivity to force in the Z direction (or a combination thereof). The aft-sway-brace semi-conductor gage circuit went through a perturbation but remained reasonably near zero, indicating a balance of forces in the X direction and a very low level of sensitivity to Z-direction forces. The aft-sway-brace foil-gage circuit showed a greater millivolt excursion than did the semi-conductor and recalled that the sensitivity should have been significantly lower with attendant reduction in gage output for the same load. One would thus infer that the foil-gage circuit was more sensitive to vertical load components.

Step 6 - Apply 100-Pound Loads in Z and X Directions at Three Stations. Step 6 represented a mini-calibration in which the moments induced by loadings away from the center of gravity of the BDU were used to generate response. Loading Points A, B, and C were at about 4, 30, and 63.5 inches aft of the BDU nose, respectively. The center of gravity was located about 52.6 inches aft of the nose. The aft sway brace was very nearly in a fulcrum position (Ref. Figure A-24), located only 0.6 inch forward of the center of gravity.

Table A-12 indicates the response, in millivolts, of the various channels to the loads in the Z direction.
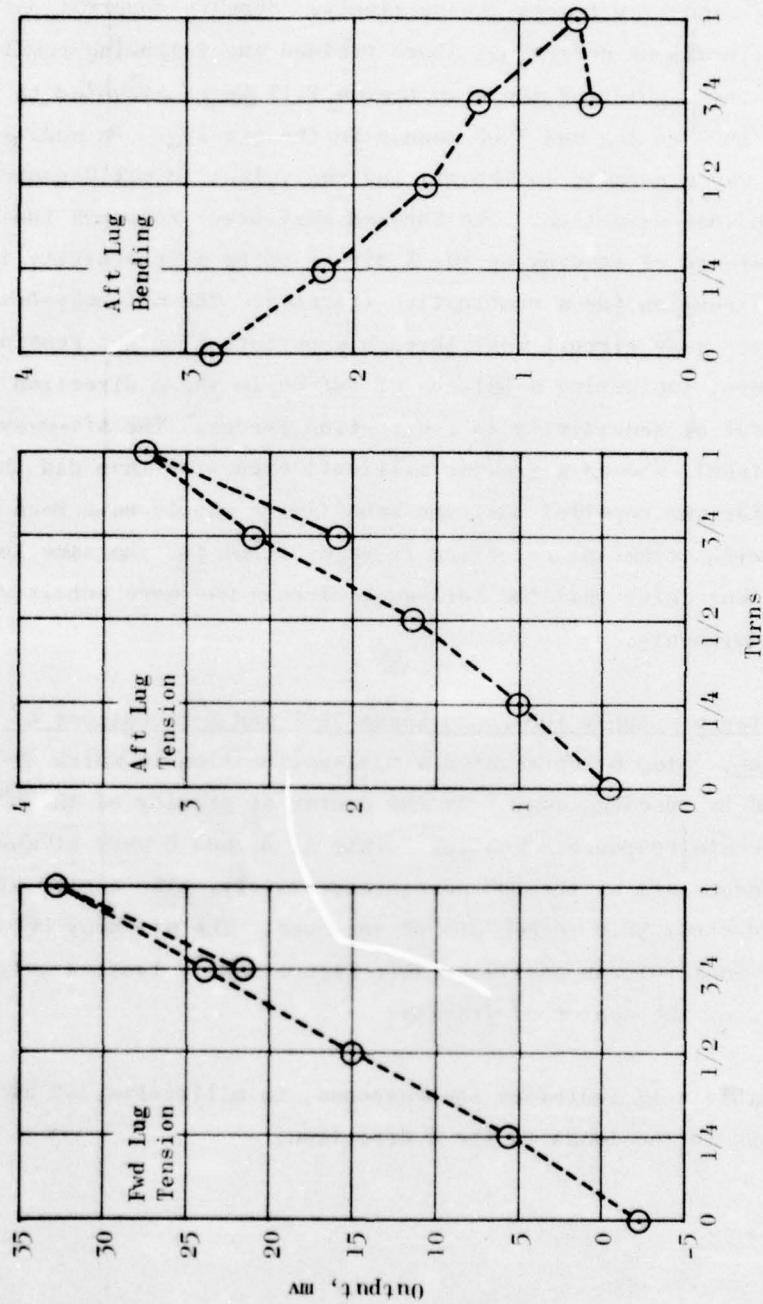
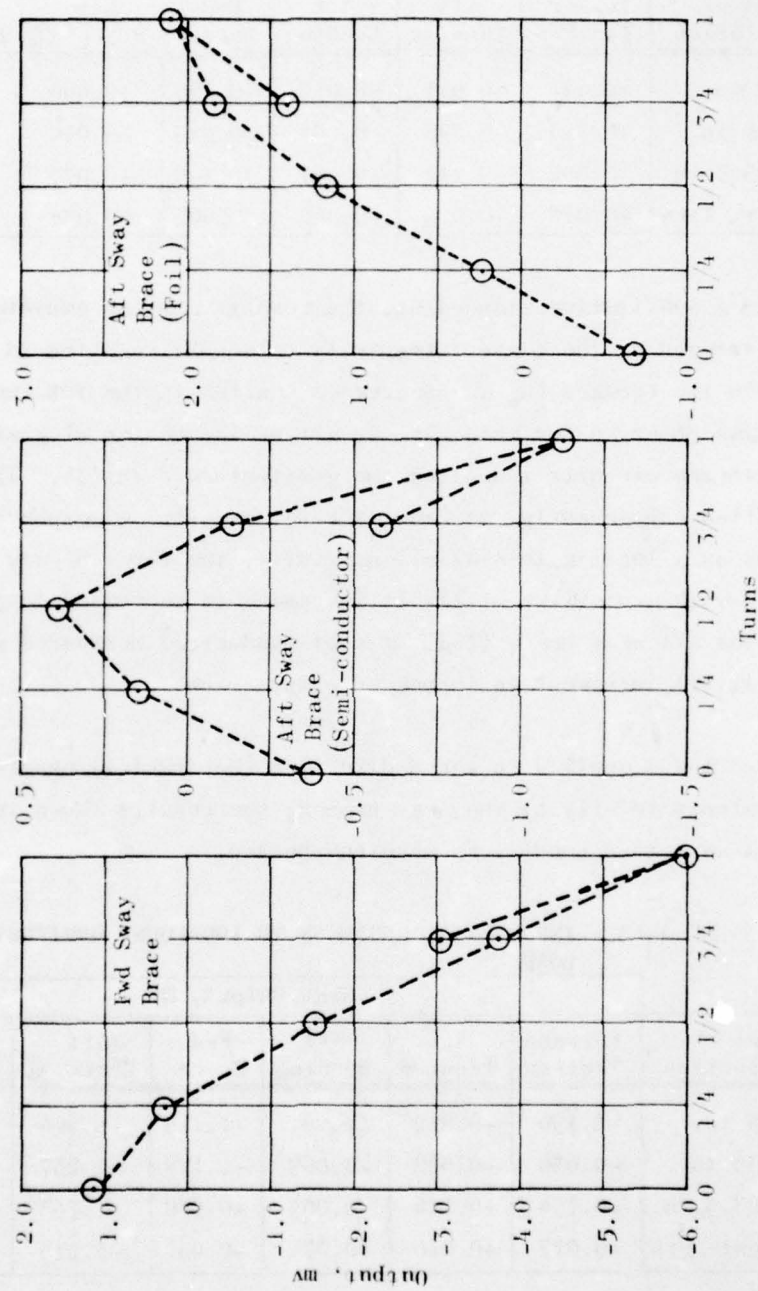Figure A-36. Lug Response to Sway Brace Torquing

Figure A-57. Sway-Brace Response to Sway-Brace Torquing

A-55

TABLE A-12.   INCREMENTAL RESPONSE TO 100-POUND VERTICAL LOAD

Point of Application	Gage Output, mv					
	Forward Tension	Aft Tension	Aft Bending	Fwd Brace	Aft Brace ①	Aft Brace ②
Ⓐ - 4 in.	+0.441	-0.043	-0.010	+0.199	+0.066	+0.044
Ⓑ - 30 in.	+0.213	-0.008	-0.009	+0.083	-0.044	-0.011
Ⓒ - 63.5 in.	-0.302	+0.111	+0.197	-0.149	-0.077	-0.063
Posttest Zero	+0.010	+0.005	-0.008	-0.003	+0.038	+0.031

From a qualitative standpoint, the results were as expected. Loads applied forward of the center of gravity (A and B) resulted in increased tension in the forward lug and decreased tension in the aft lug. The reverse was observed for Load Case C, aft of the center of gravity. The aft-sway-brace circuits indicated the greatest zero shifts. If, as will be amplified subsequently, we can interpret sway-brace response to vertical loads as a legitimate Z-axis sensitivity, the forward sway brace responded with a positive millivolt increment to decreased compression; whereas the aft sway brace (foil or semi-conductor) responded with a positive millivolt increment to increased compression.

Since loads applied in the X direction (horizontal) should have been carried almost totally by the sway braces, the results shown in Table A-13 for the X-axis load conditions were unexpected.

TABLE A-13.   INCREMENTAL RESPONSE TO 100-POUND HORIZONTAL LOAD

Point of Application	Gage Output, mv					
	Forward Tension	Aft Tension	Aft Bending	Fwd Brace	Aft Brace ①	Aft Brace ②
Ⓐ - 4 in.	-0.156	-0.082	+0.061	+1.113	-0.984	-0.502
Ⓑ - 30 in.	-0.056	-0.022	+0.069	+1.128	-1.257	-0.486
Ⓒ - 63.5 in.	+0.154	+0.116	-0.005	+0.930	-1.755	-0.484
Posttest Zero	-0.017	+0.010	+0.074	-0.034	-0.113	+0.004

The indicated response of the aft lug (tension) was ± 130 pounds. The sway braces responded essentially the same whether the applied load was forward or aft of the BDU center of gravity. Since both sway braces were forward of the center of gravity a yaw moment should have been induced by the brace reactions. Obtaining the same direction of reaction for all load cases implied that the unbalanced moment was taken out in one or both lugs. While this is feasible, it was unexpected and unaccounted for in either Eq. A-3 and -4 or in the instrumentation. Without knowledge of the division of X-axis load between sway braces and lugs it was impossible to provide a sway-brace calibration.

Step 7 - Z-Axis Calibration. Step 7 consisted of applying load to the center of gravity (through a bolt in the locator hole) in the vertical direction. The load range of 1500 pounds was applied in 300-pound increments, reduced to zero in one step, and repeated. Following two cycles with the load applied downward, the test was repeated with the load applied upward. Data from each of the six channels are shown in Figures A-38 through -43.

Recalling Eq. A-5 and -6, we expected a complex response; and on examination, the data indicated a complex response. On application of vertical tension (downward Z force) the forward lug exhibited tension relief. This surprising result occurred because the net force supported by the launcher rack was the combination of tension in the lugs and compression in the sway braces. From the initial readings we surmised a net tension in the lugs of about 7700 pounds (~ 3200 pounds forward, ~ 4500 pounds aft) composed of 635 pounds due to the weight of the BDU and 7000 pounds due to compression loading in the sway braces. The application of an additional 1500-pound load resulted in a net increase of only about 600 pounds tension in the lugs (with an implied reduction of 900-pound compression in the sway braces). Load distribution was such that the forward lug supported about 30 pounds less tension with the 1500-pound load

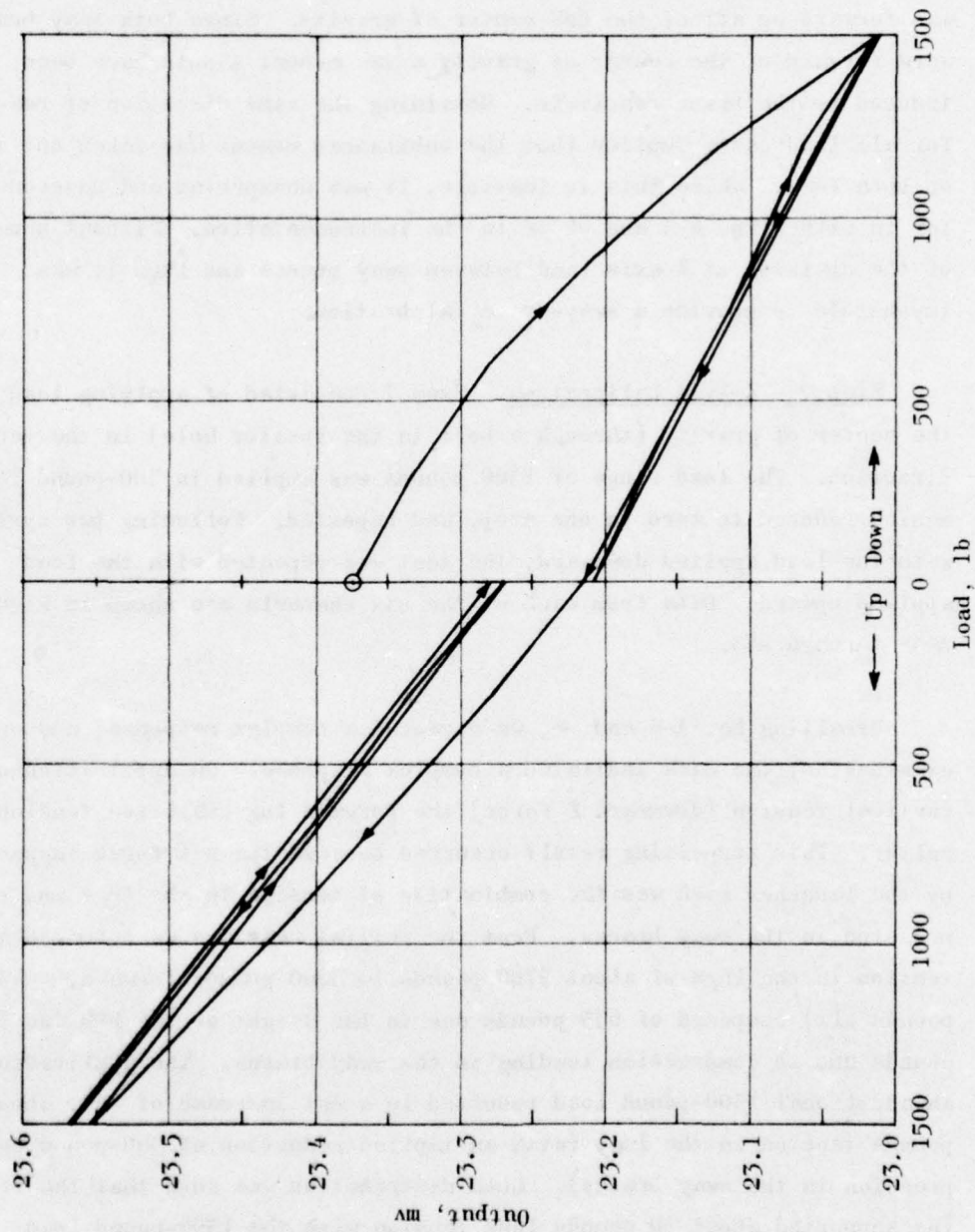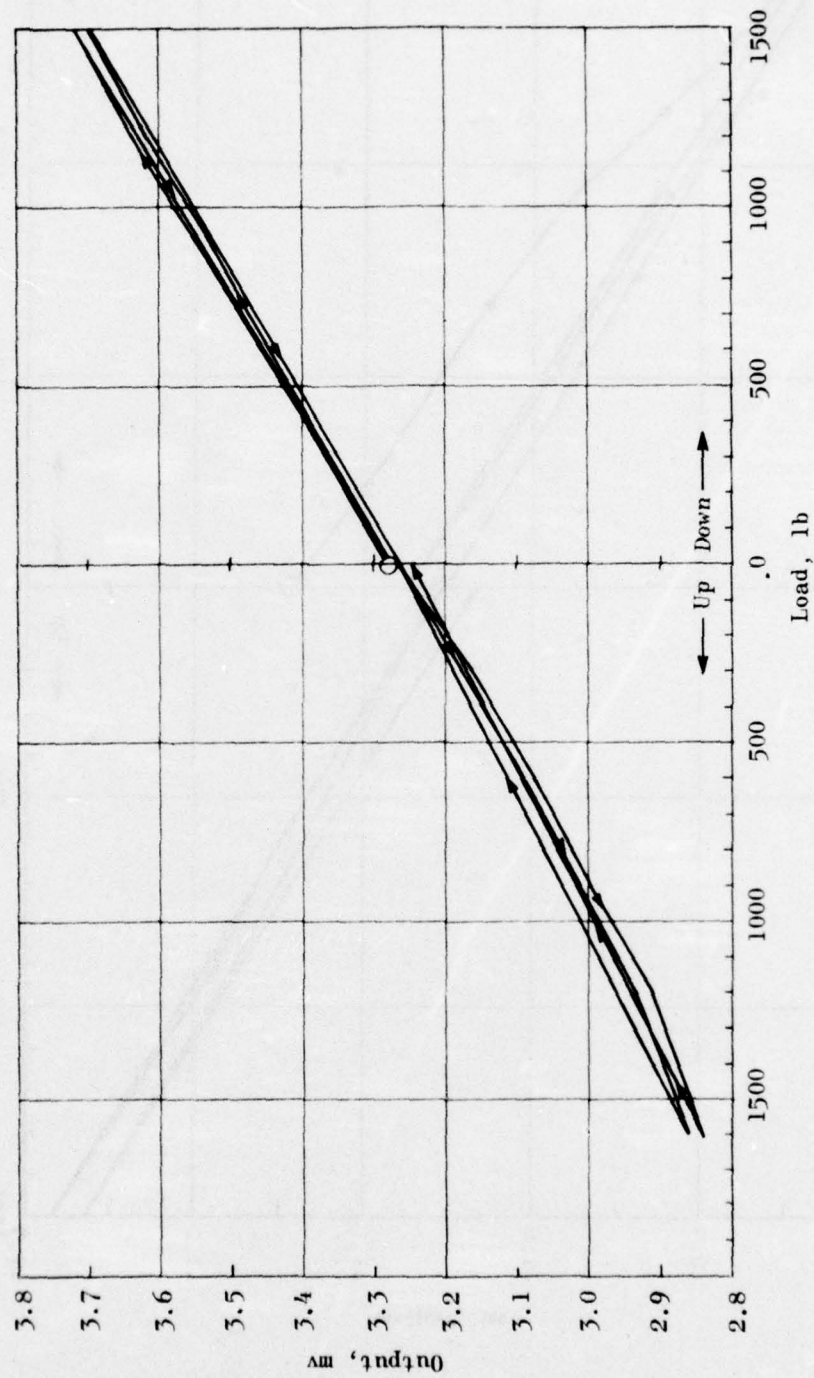Figure A-58. Forward Lug Tension, All-Up Calibration, Z-Axis Force

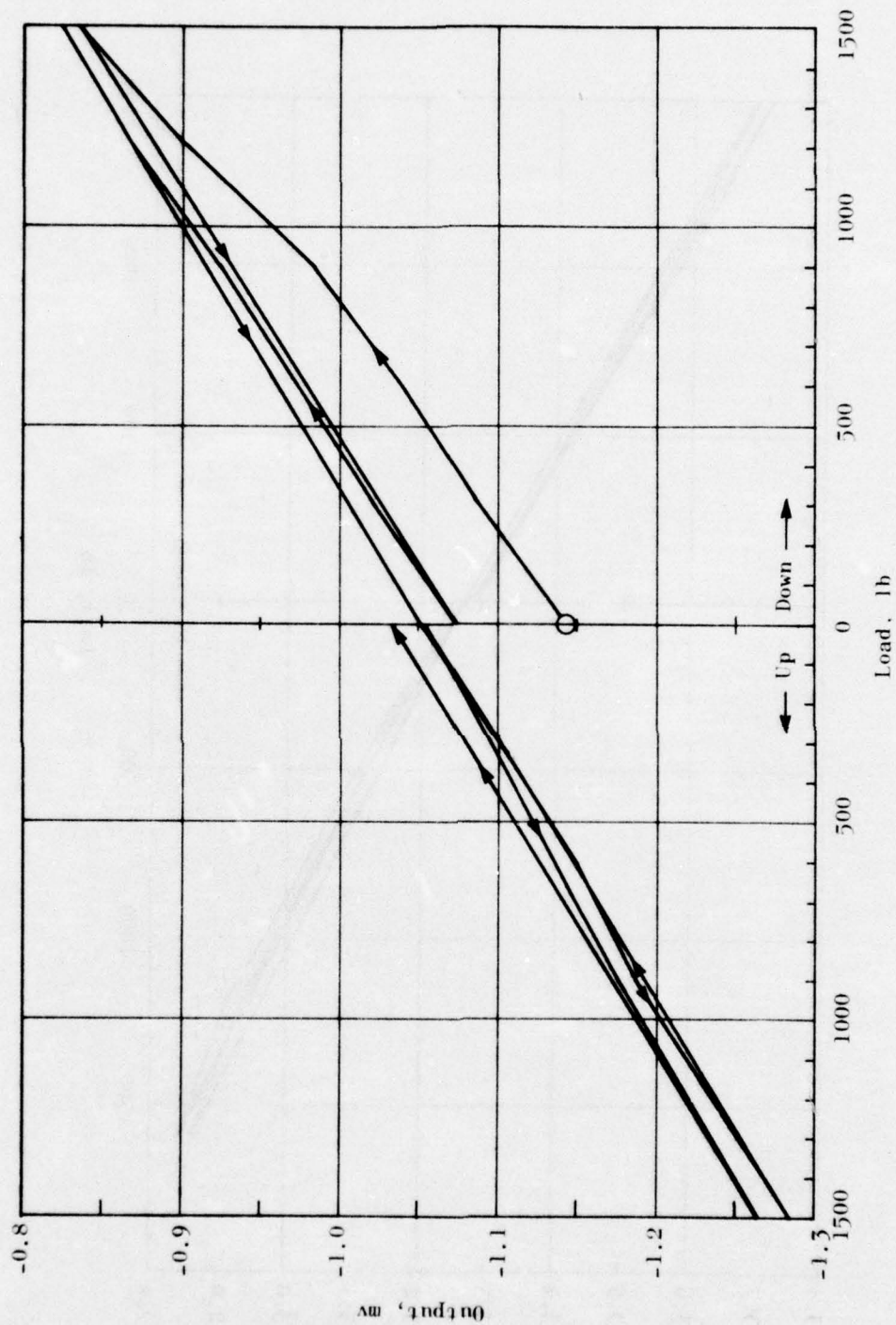Figure A-59. Aft Lug Tension, All-Up Calibration, Z-Axis Force

A-59

Figure A-40. Aft Lug Bending, All-Up Calibration, Z-Axis Force
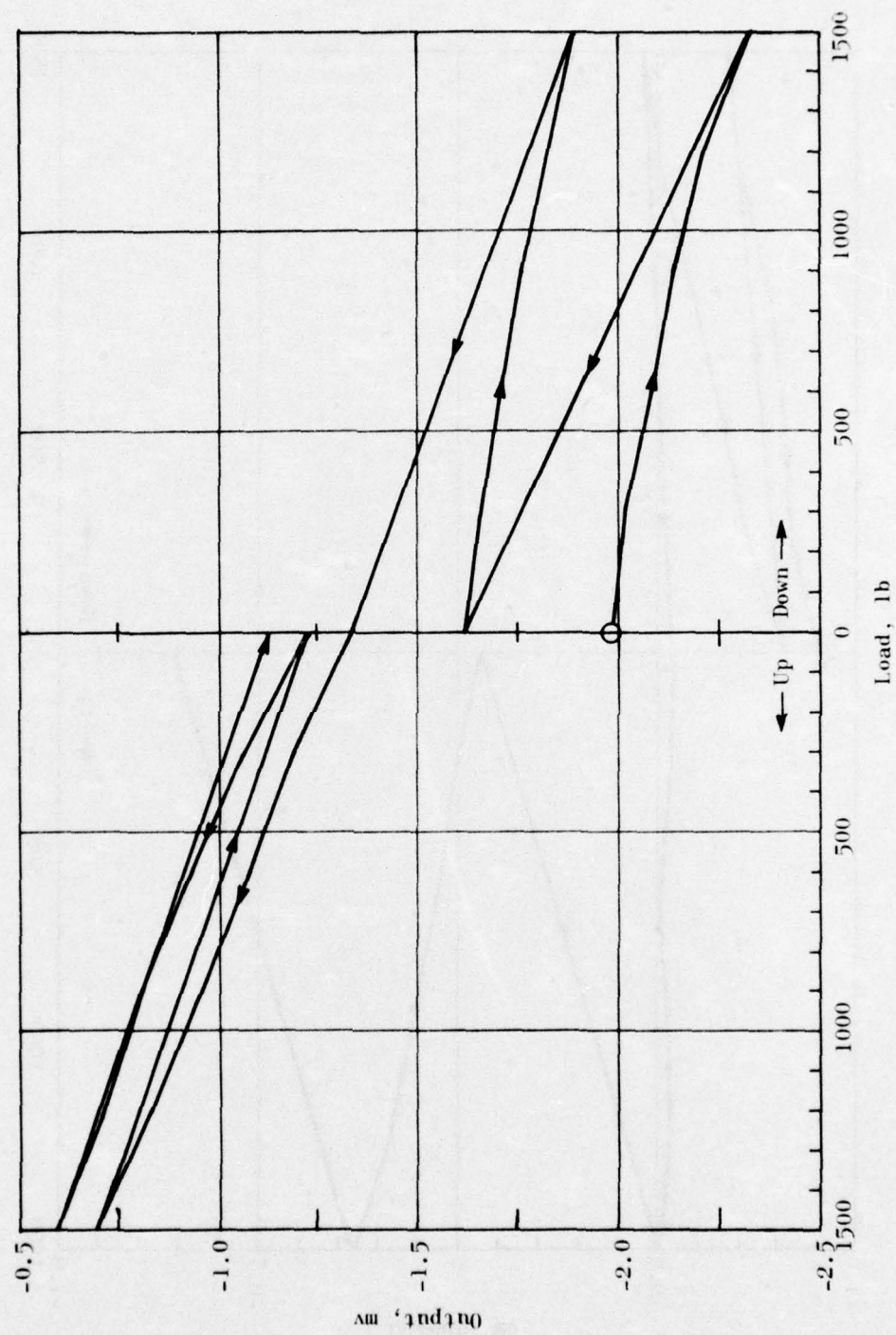
A-60

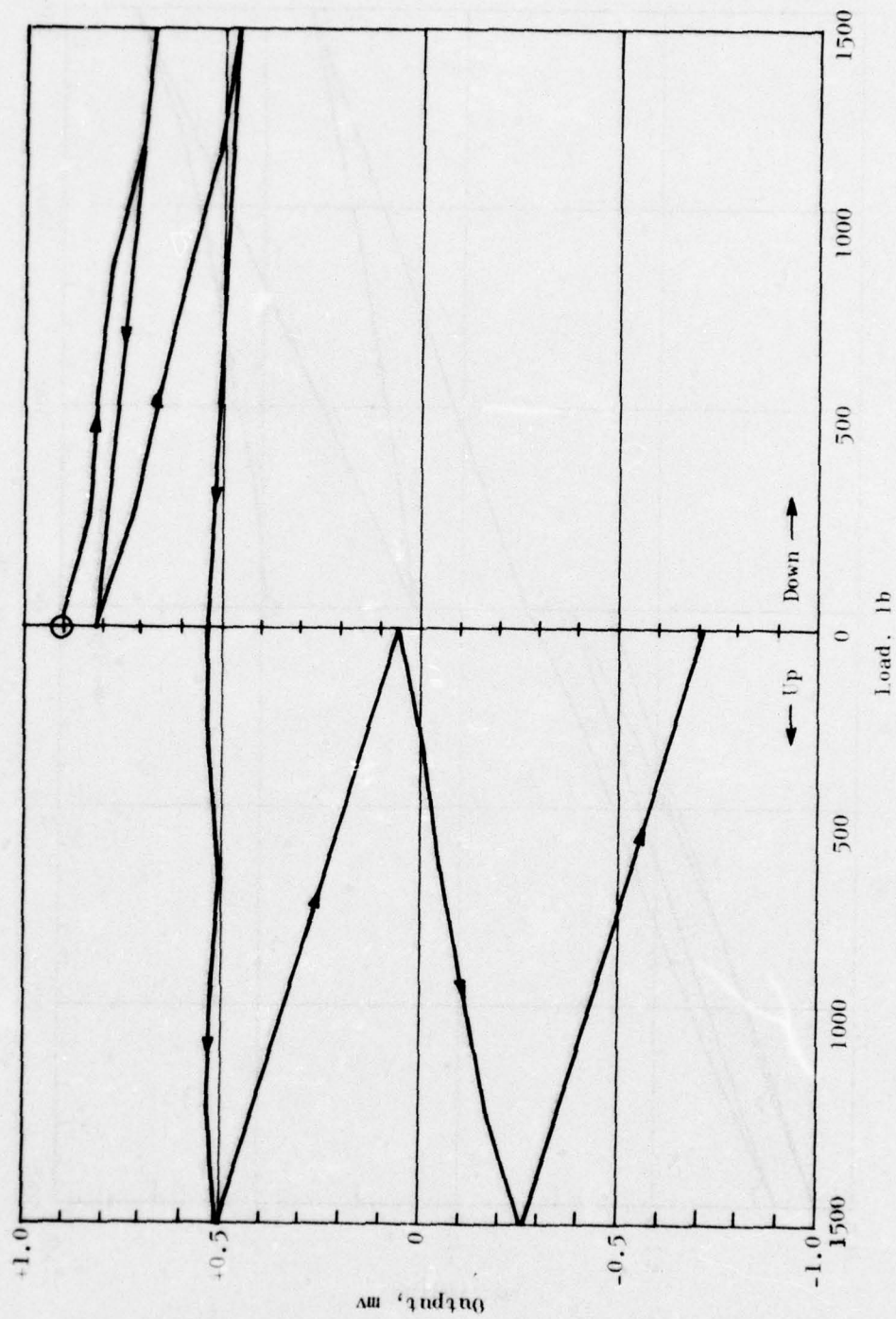Figure A-41. Forward Sway Brace, Z-Axis Force

A-61

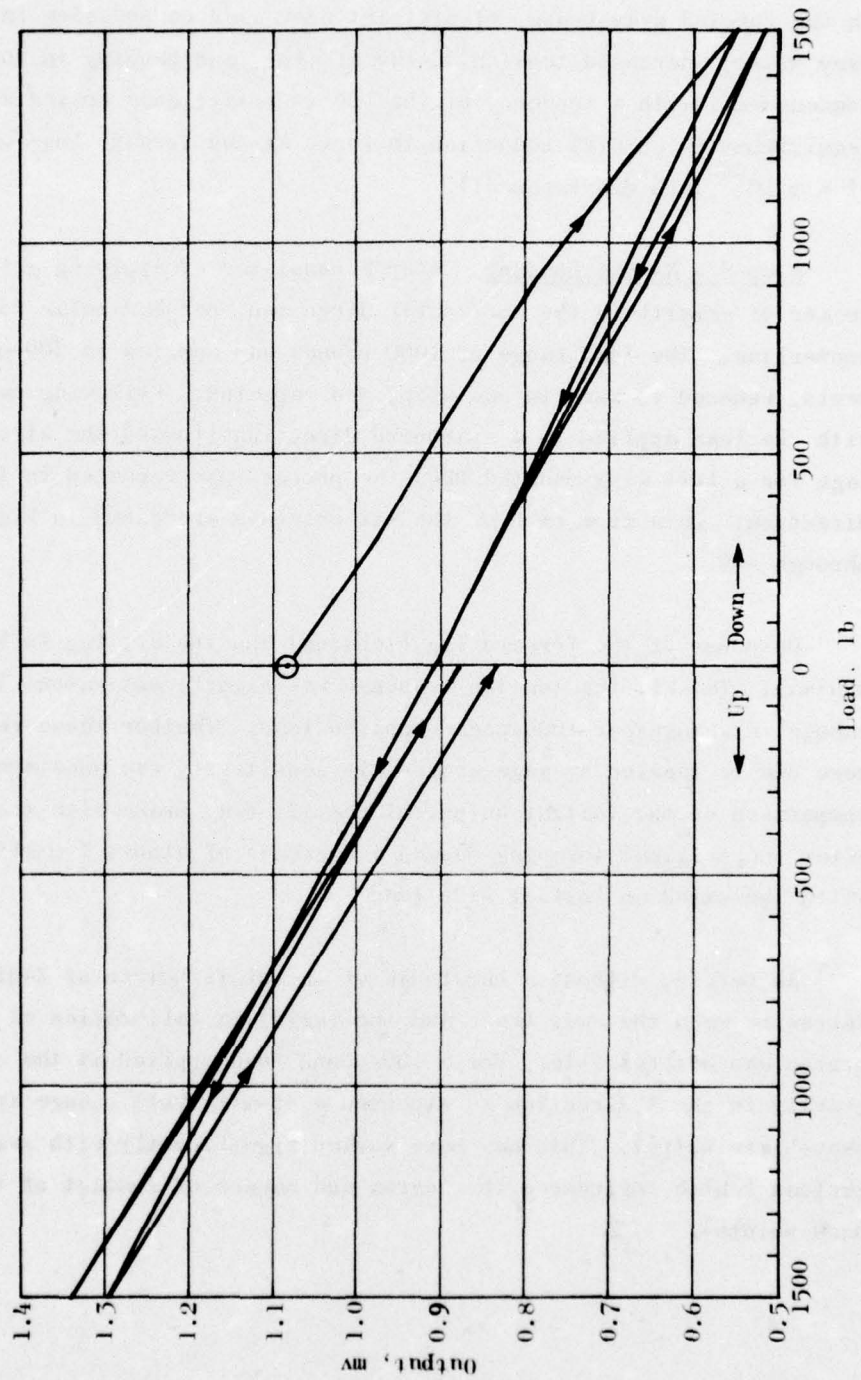Figure A-42. Aft-Sway-Brace Semi-conductor Bridge, All-Up Calibration, Z-Axis Force

A-62

Figure A-43. Aft-Sway-Brace Foil Bridge, All-Up Calibration, Z-Axis Force

applied. Qualitative examination indicated slightly increased compression in the forward sway brace, significant decreased compression in the aft sway brace, increased tension in the aft lug, and bending in the aft lug commensurate with a tendency of the BDU to rotate nose upward slightly (equivalent to an 0.8% reduction in force at the forward lug--on the order of 8×10^{-6} inch displacement).

Step 8 - X-Axis Loading. Step 8 consisted of applying a load to the center of gravity in the horizontal direction, perpendicular to the BDU centerline. The load range of 1000 pounds was applied in 200-pound increments, reduced to zero in one step, and repeated. Following two cycles with the load applied in a starboard direction (toward the aircraft fuselage for a left-wing-mounted BDU) the process was repeated in the port direction. Data from each of the six channels are shown in Figures A-44 through -49.

Response of the forward lug (tension) and the aft lug in bending was minimal. The aft lug tension response was significant--about 380-pound change in change-per-1000-pound applied load. Whether these responses were due to tension or gage cross-axis sensitivity was undetermined. A comparison of the initial output of the aft sway brace with the output after the original torquing showed a decrease of almost 5 millivolts, which indicated an initial side load.

As before, without a knowledge of the distribution of X-direction forces between the sway brace and the lug(s), a calibration of the sway braces was not feasible. For a 100-pound load applied at the center of gravity in the X direction we expected a +1-millivolt change in the aft-sway-brace output. This may have varied significantly with sway brace preload (which influenced the degree and manner of contact of the lug/hook points).
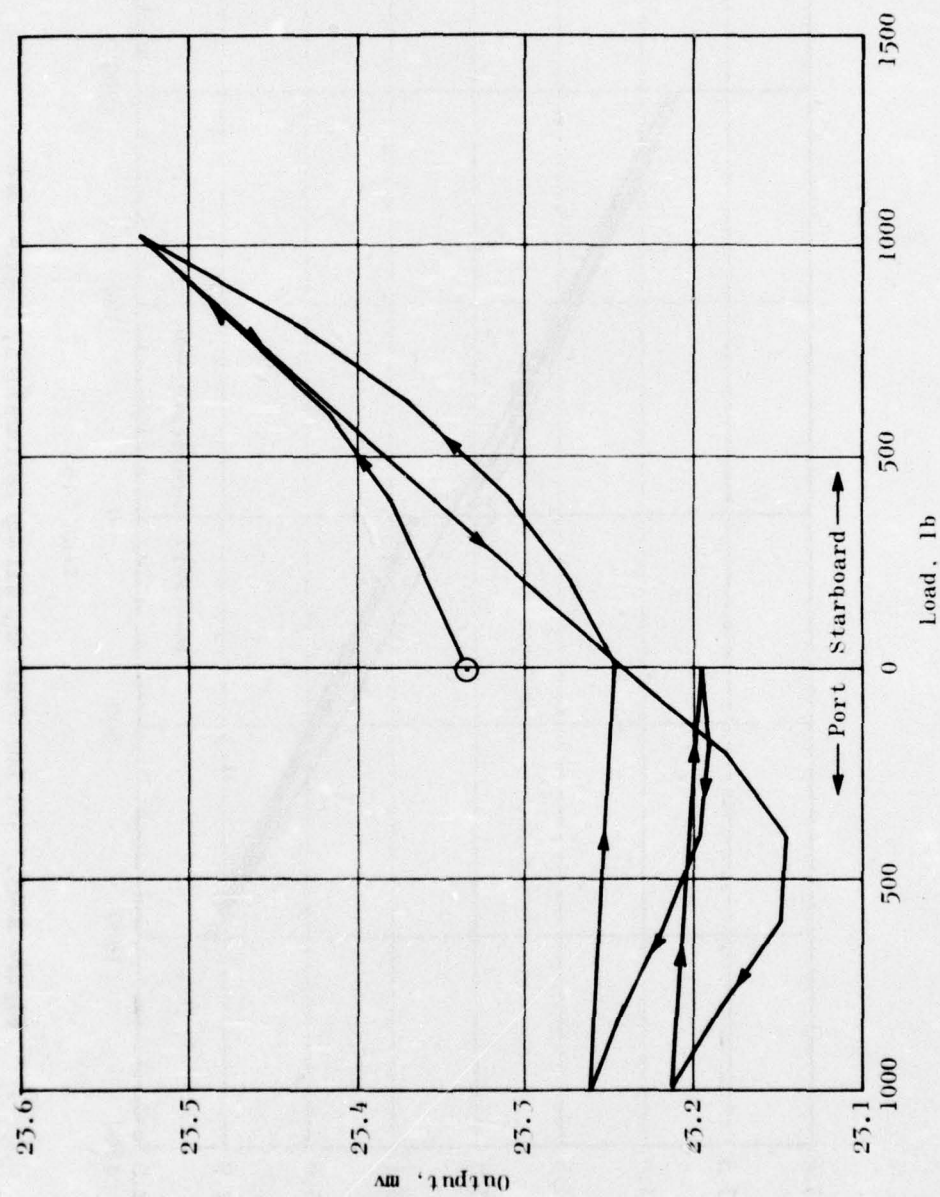
Figure A-44. Forward Lug Tension, All-Up Calibration, X-Axis Force

A-65

Figure A-45. Aft Lug Tension, All-Up Calibration, X-Axis Force

A-66
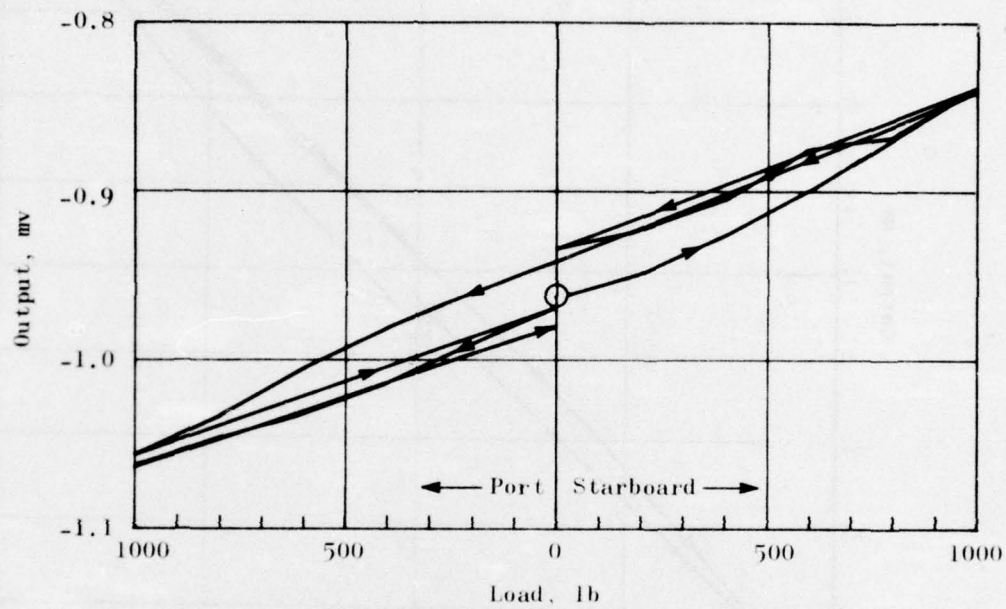
Figure A-46. Aft Lug Bending, All-Up Calibration, X-Axis Force

A-67

Figure A-47. Forward Sway Brace, All-Up Calibration, X-Axis Force

A-68

Figure A-48. Aft Sway Brace (Semi-conductor Gages),
All-Up Calibration, X-Axis Force

A-69

Figure A-49. Aft Sway Brace (Foil Gages), All-Up
Calibration, X-Axis Force

Step 9 - Y-Axis Loading. Step 9 was performed in two parts. After
three cycles to about 1000 pounds (applied at the nose of the BDU) the
sway braces were retorqued and two cycles to 1000 pounds were run. Data
obtained are presented in Figures A-50 through -55.

Significant shift occurred on the first test cycle (to 1800 pounds).
The remaining two cycles on the first run were highly linear for all
gages. Retorquing the sway braces added about 1900 pounds tension to the
lugs (300 pounds forward, 1600 pounds aft). The forward lug and aft sway
brace foil gage responded linearly following this retorquing. The forward
sway brace, aft lug bending, and aft sway brace semi-conductor gages
showed similar responses on the second run. The initial slope on the

Figure A-50. Forward Lug Tension, All-Up Calibration,
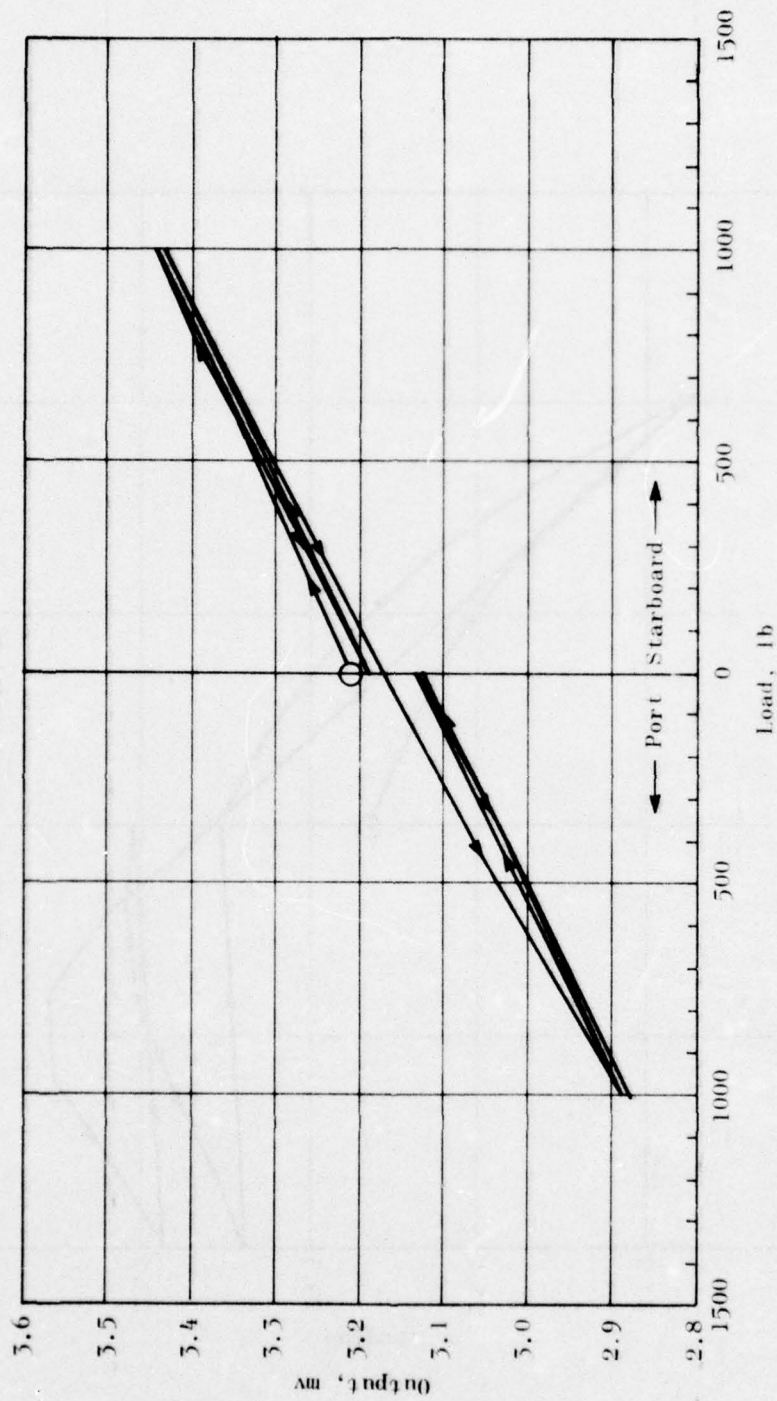Y-Axis Force

A -71
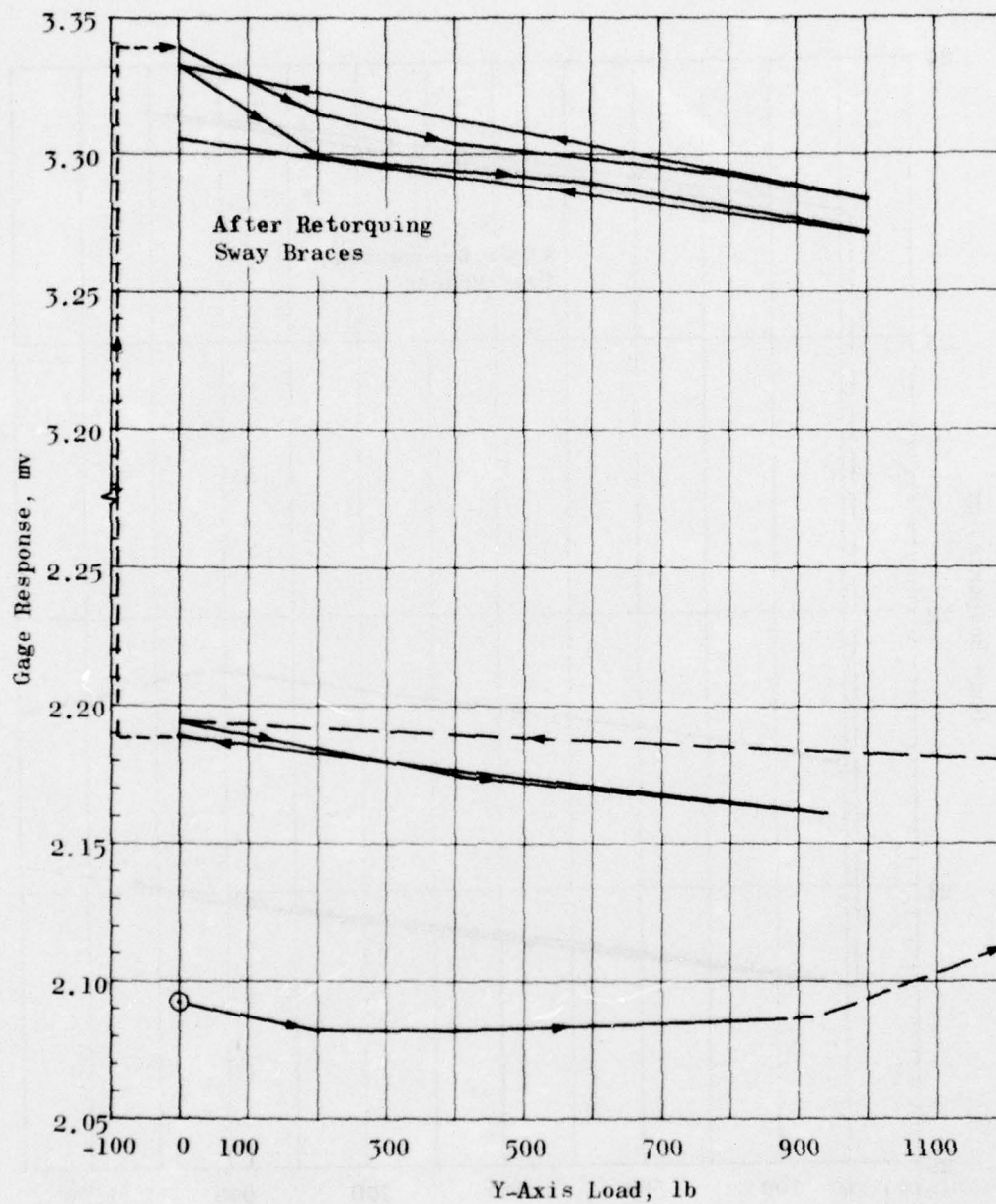
Figure A-51. Aft Lug Tension, All-Up Calibration,
Y-Axis Force

A-72
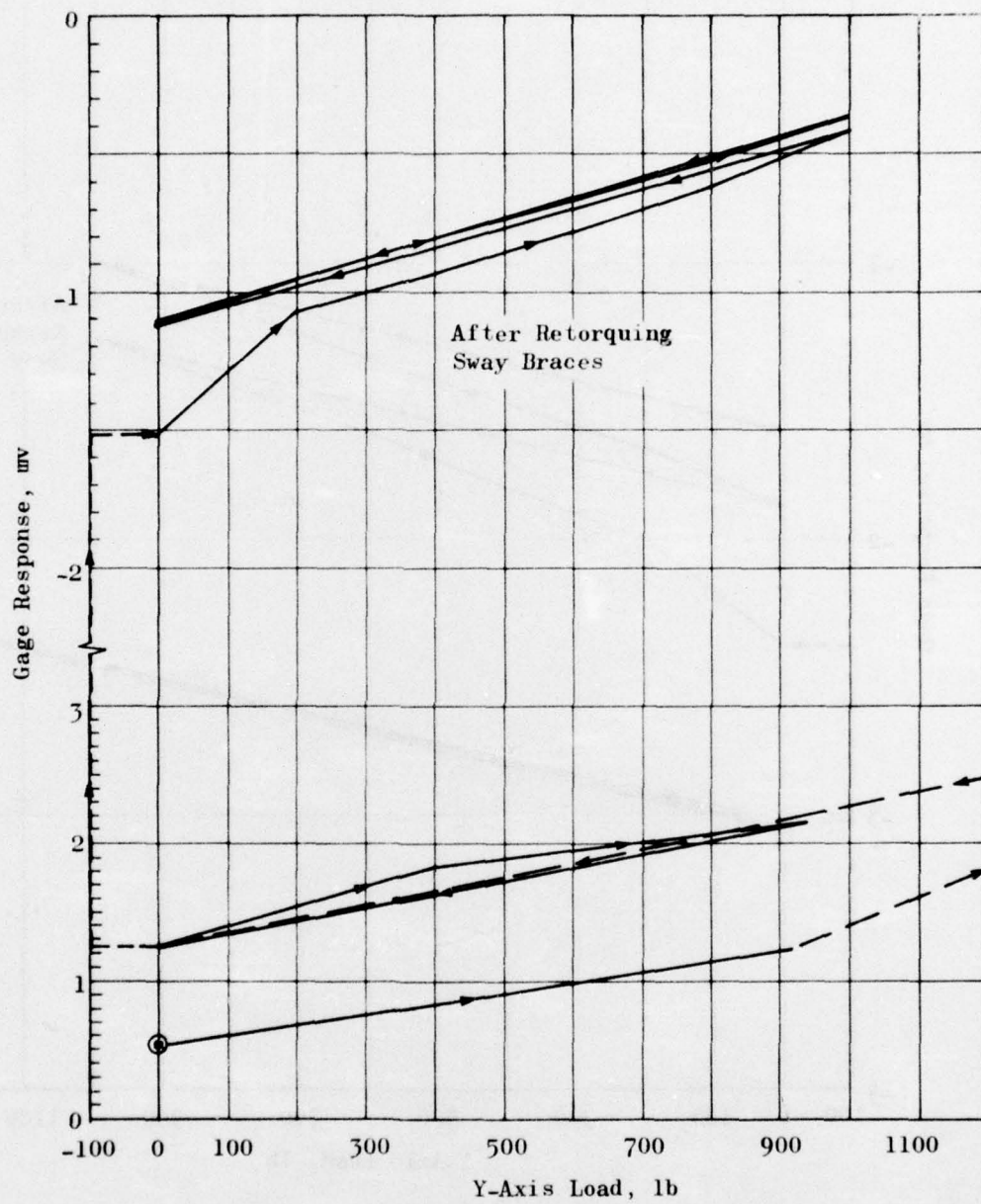
Figure A-52. Aft Lug Bending, All-Up Calibration,
Y-Axis Force
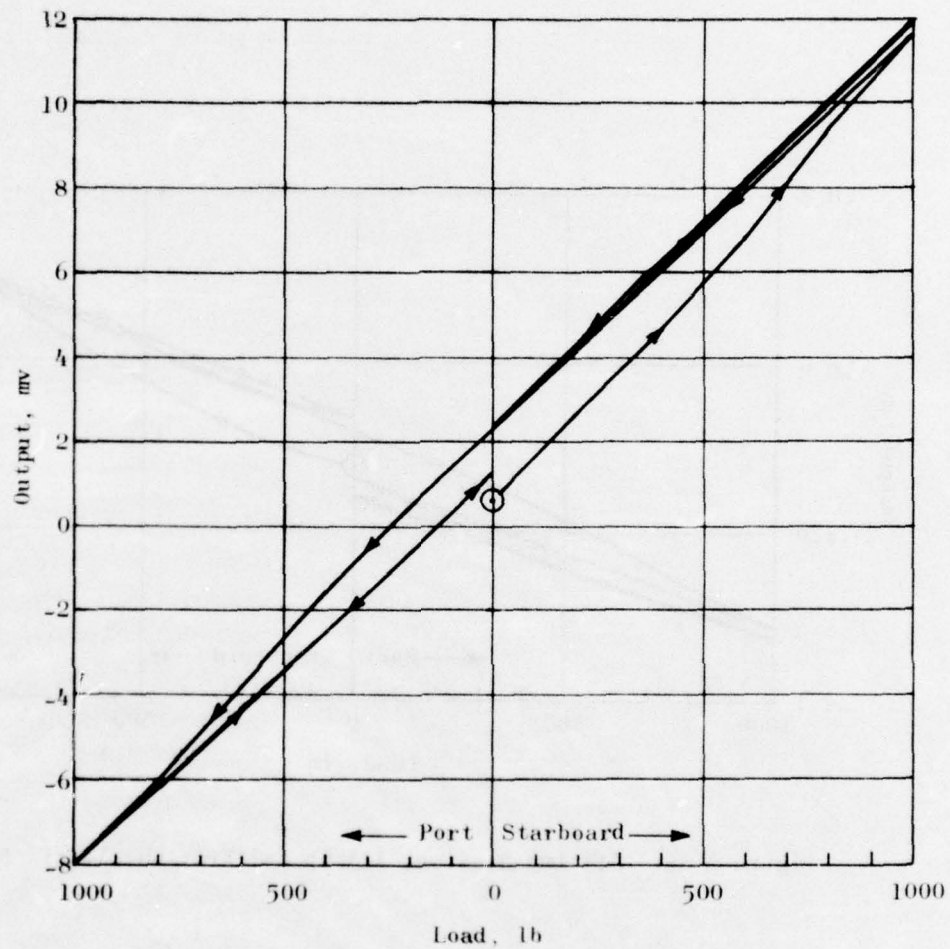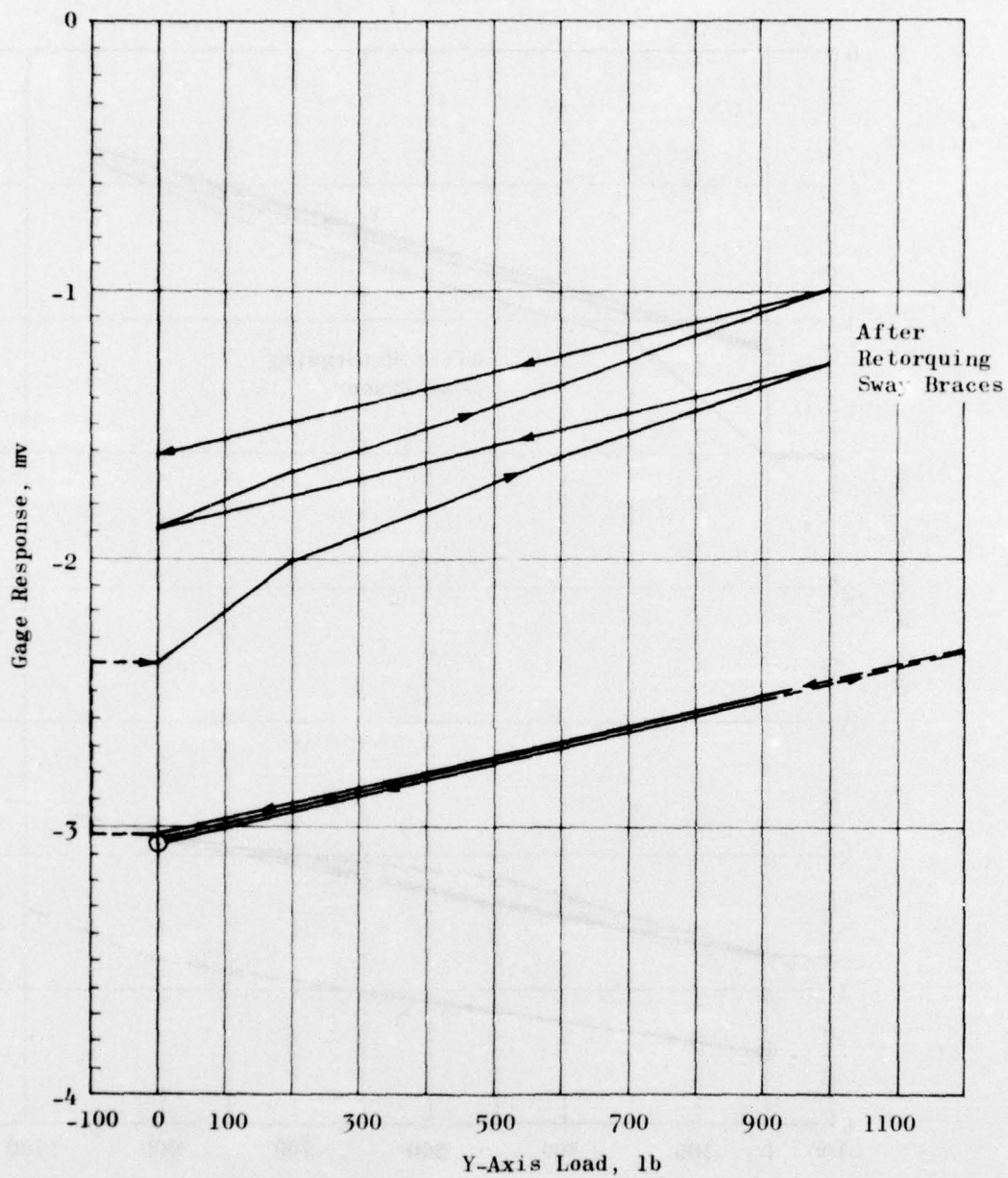
Figure A-53. Forward Sway Brace, All-Up Calibration,
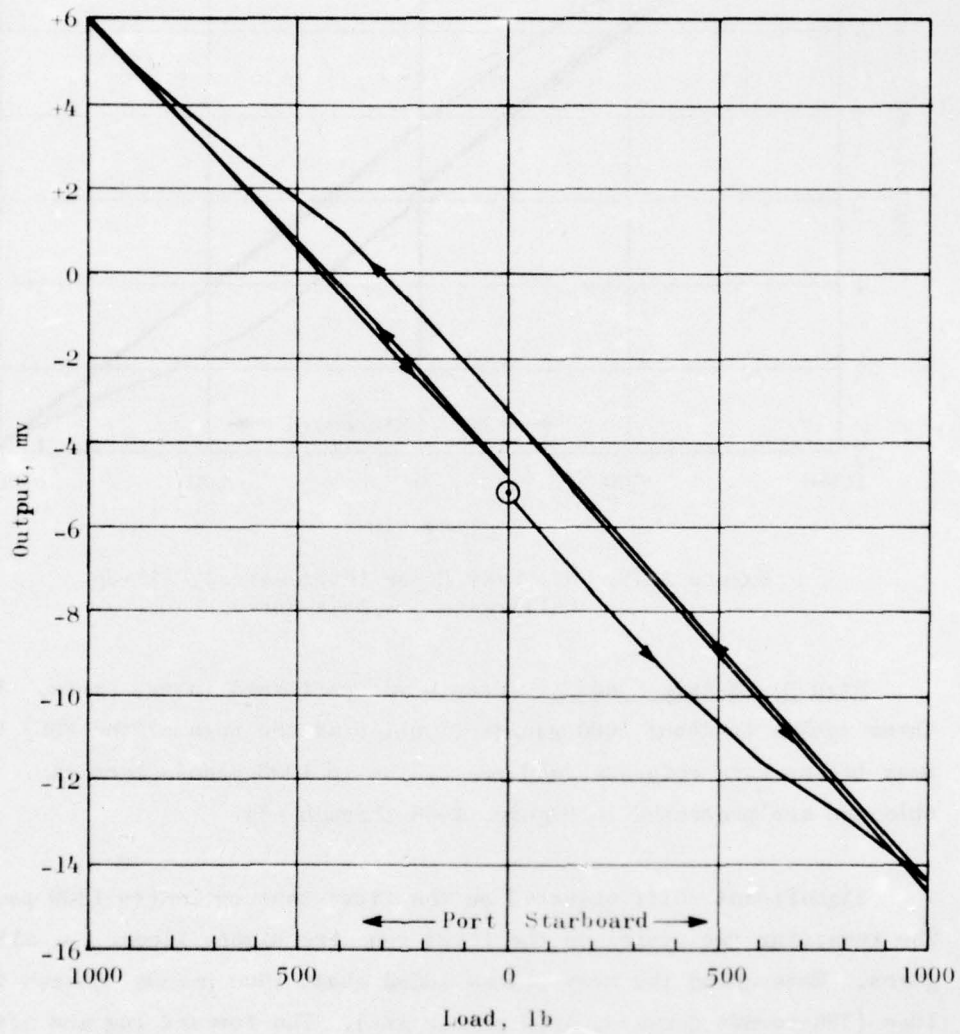Y-Axis Force
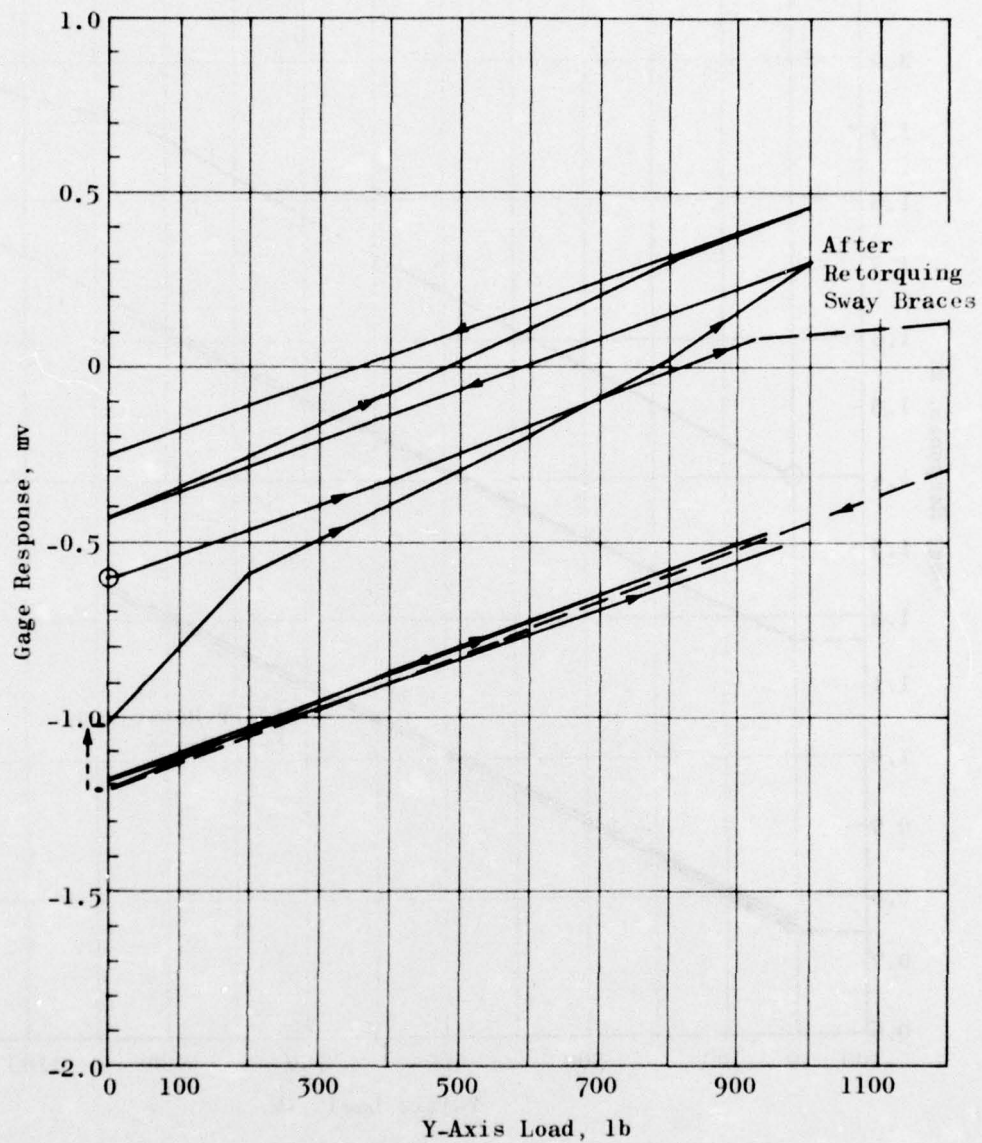
Figure A-54. Aft Sway Brace (Semi-conductor), All-Up Calibration, Y-Axis Force

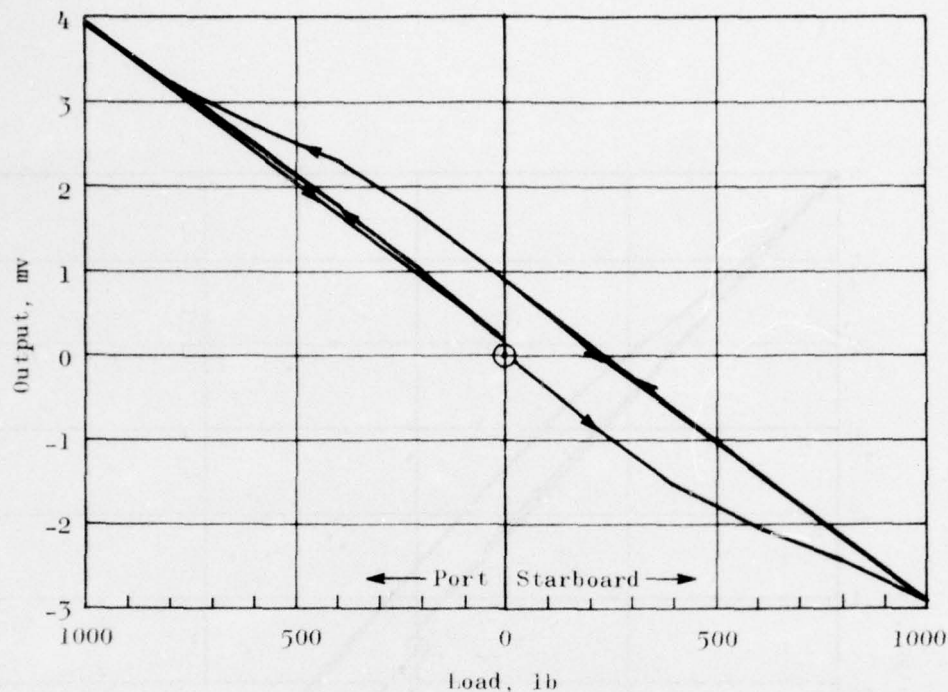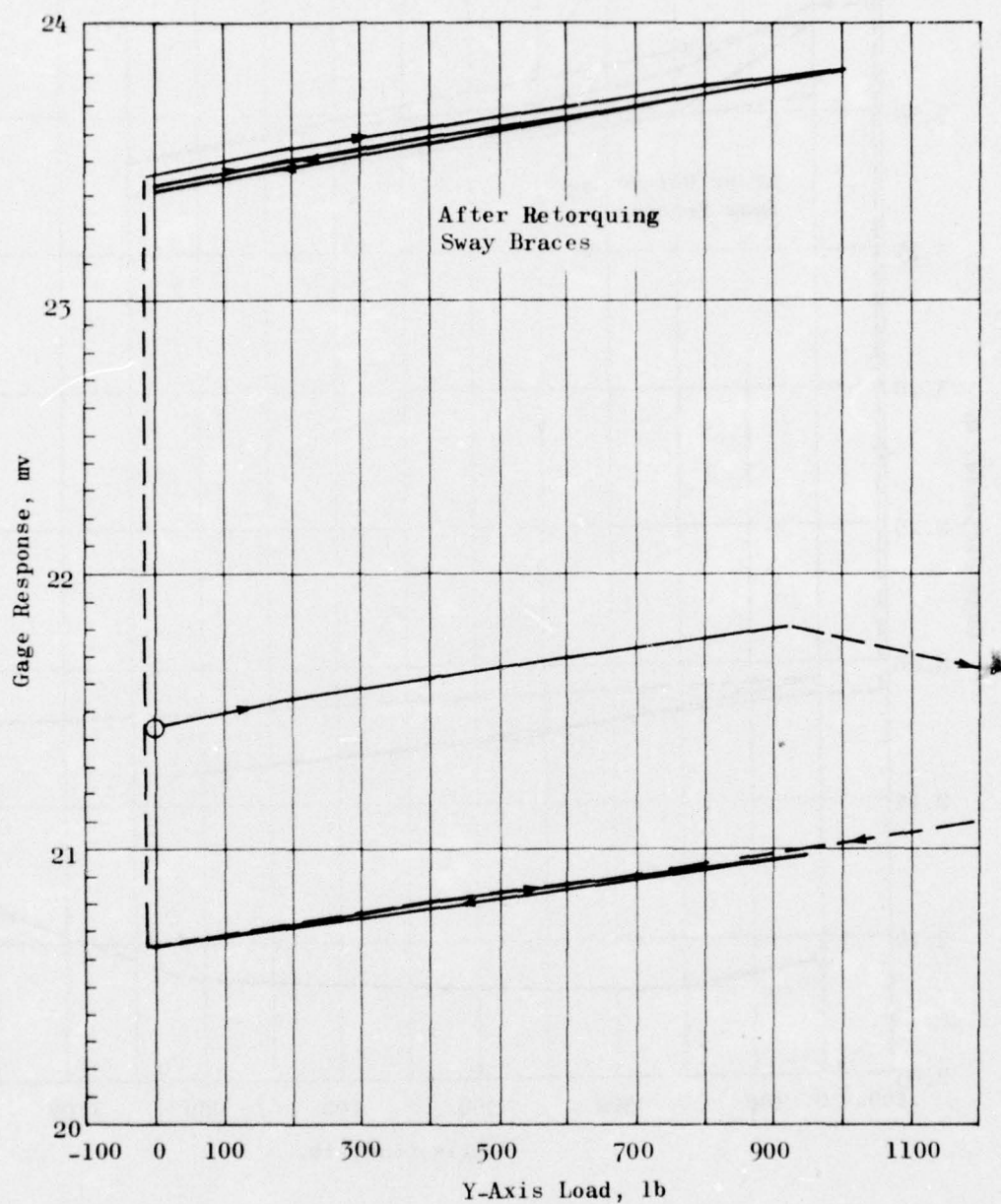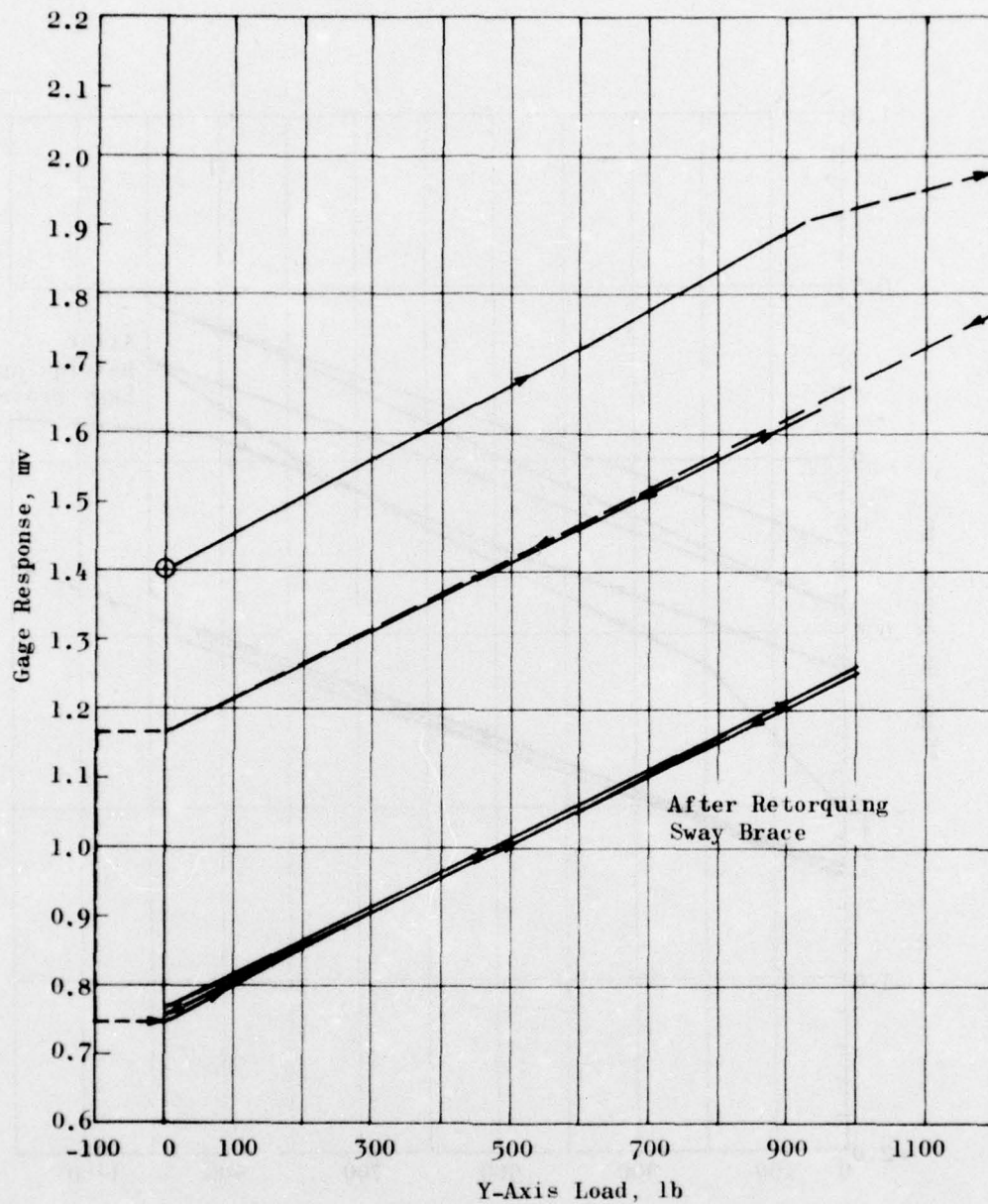**Figure A-55.** Aft Sway Brace (Foil), All-Up Calibration, Y-Axis Force

first loading step was high, and the two loading cycles indicated some
hysteresis. The aft lug tension gages exhibited some hysteresis, but this
was due primarily to a high slope response for the first loading step in
both cycles of the second run. The slope of the aft lug bending response
was about 0.7 millivolt for 1000 pounds force at the nose. This compares
with about 9.1 millivolts per 1000 pounds with the sway braces loose. It
was, therefore, concluded that 90 to 95% of the longitudinal load was
absorbed in the sway braces.

Launcher Calibration Factors. Bench calibrations of the lugs along
with the test data accumulated without the sway braces in contact with the
motor yielded the only gage sensitivity data of importance. Recognizing
that even these results are subject to significant uncertainty (perhaps ±
30%) the following calibration factors are submitted:

Forward lug tension	= 130 lb/mv
Aft lug tension	= 1400 lb/mv
Aft lug bending	= 100 lb/mv

Because of its low sensitivity, the thermal no-load effect was significant
for the aft lug tension gage. This correction is -1 mv/100 deg F.

Accelerometers

The accelerometer cables were repaired and the connectors cleaned.
All the crystal accelerometers were removed from the BDU and calibrated
using an electrodynamic vibrator. The output characteristics were
slightly different from those determined in the initial calibration. The
new values were incorporated into the data analysis routines.

High-Gain Amplifiers

High gain amplifiers were used for six propellant instruments such that the ac component of the signal from the instrument was amplified (x 1000) to a level easily recovered from the tape record. The total signal (both ac and dc components) was also recorded through low-gain amplifiers. Earlier during the program difficulties were encountered with the high-gain amplifiers and with filtering the low-frequency and dc component from the channels they serve. Progressive improvements were made, and it was believed these channels were functioning properly during Flights 9, 10, and 11.

Analysis of data from these last three flights showed the signals through the high-gain amplifiers were very low; while oscillations in signals from the same instruments through low-gain amplifiers were moderately high. That is, whenever calibration factors and signal conditioning equipment characteristics were considered, data processed through high-gain and low-gain circuits were not consistent.

Consequently, new amplifier assemblies were fabricated and installed. The circuits were carefully checked during the interim test period, and the wiring and electrical components were checked and characterized. Oscillatory signals were then inserted in lieu of the signal from individual gages, and the gain levels from the dual-range arrangement were determined correct. Oscillatory signals were then inserted parallel to the gage signals through $1/2$ uf capacitors. In these tests, the gages shunted the input signal such that the gain levels were reduced. This attenuation is characteristic of the test circuit and can be disregarded. Data from these tests showed consistency between the high-gain and low-gain channels.

A-78

As a final check, the BDU propellant section (which contained the dual-ranged gages) was tapped with a mallet and the signals monitored from the VCO plugs. During these tests the high-gain channels were clearly functional.

Although the reason for the inconsistent flight data was not determined, it was decided to proceed with ground simulation tests.

BDU Chamber Pressure Measurement

Having recognized that the influence of atmospheric pressure on the normal stress diaphragm gage becomes significant at flight altitudes, it was decided to install a pressure sensor in the BDU chamber. A diaphragm normal stress gage was mounted on the grain surface. The gage had a sensitivity of about -4.2 mv/psig with a zero shift at ambient of about -11.2 millivolts.

APPENDIX B

DYNAMIC RESPONSE MEASUREMENT CHARACTERISTICS
OF THE NORMAL STRESS DIAPHRAGM GAGE

Sensitivity of the 150 psi gages used on the BDU is in the range of 0.6 to 1.0 mv/psi. Bond stresses of up to 20 psi during captive flight are expected, and stresses induced by vibration are expected to be on the order of 0.5 to 1.0 psi. Hence, two parallel records of gage output are made. The first is a direct record of gage output; the second records only dynamic response. Because of the expected low dynamic stresses, the second record is amplified 10 times more than the first, or direct, record. Dynamic stresses recorded on the second, amplified, record during flight tests were about as expected, i.e., 1 to 2 psi. Corresponding data from the first record, however, indicated much higher dynamic response, up to 20 psi. An additional complicating factor arose from intermittently faulty operation of the data track carrying the amplified dynamic response.

To resolve the conflict, several tests of the various elements in the instrumentation system were conducted. Results of the investigation supported the accuracy of the amplified data and revealed a noise problem that produced the apparent dynamic stress signals. The source of the noise was traced to beats between the carrier frequencies for the FM data records. In the course of the overall investigation, available data on the dynamic characteristics of the normal diaphragm gage were studied and some limited tests were conducted to extend the earlier work. The tests, the data obtained, and the inferences made from these data are described below.

EXPERIMENTAL EFFORT

The test specimen, Figure B-1, was fabricated from the specimen used in the original calibration.[1] The 2-inch-diameter propellant rod was cut to a length of 2 inches. The base of the rod was bonded to a steel end plate with the diaphragm gage embedded in the propellant rod at the base plate interface. Static calibration was accomplished by mounting weights on the specimen to achieve bondline compressive stresses up to about 10 psi. The DC voltage supply to the gage circuitry was overridden with AC excitation to evaluate the influence of possible power-supply noise on the gage response. Finally, with the 2-pound weight on the rod, the specimen was subjected to sinusoidal vibration from 10 to 2000 Hertz at 1-, 3-, and 10-g inputs. At the 10-Hertz frequency, displacement limitations on the shaker permitted a peak level of 5 g. All mechanical tests were run at 0 F, ambient, and 140 F. Data obtained are discussed along with those from Ref. 1 in the following paragraphs.
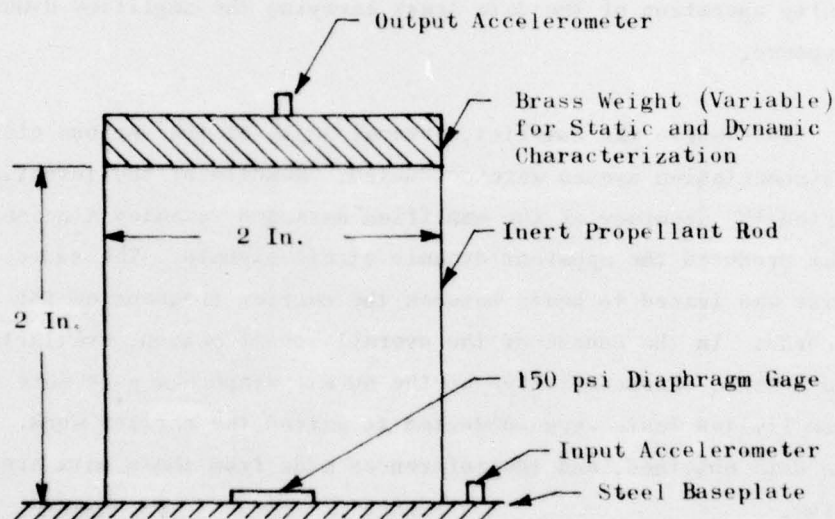

Figure B-1. Dynamic Characterization Test Specimen

---

[1] Leeming, H., et al: Solid Propellant Structural Test Vehicle Program – Final Report, AFRPL-TR-72-29, April 1972.

Static Calibration

Gage sensitivity data measured in compression are presented in Table B-1 below. Sensitivity has apparently decreased and flattened out, as might be expected from experience with this system.

TABLE B-1. GAGE SENSITIVITY IN COMPRESSION

Temp, deg F	Sensitivity, mv/psi	
	Ref. 1 (1972)	Current Test (1975)
140	0.90	0.71
74	0.80	0.78
0	0.80	0.74

Effect of Noise in Power Supply

As shown in Table B-2 below, a variety of AC voltages were super-imposed on the bridge power supply. Since the bridge circuitry is linear in design, no significant effect was expected; and in fact, none was observed. On the table, all sensitivities are normalized to a 28-volt supply level. It is apparent from these data that power input variations cause a linear response variation, as would be expected. Further, a feeling for expected data scatter was established for the next step of mechanical testing.

Dynamic Testing

Vibration tests were conducted in a fixed-free mode as opposed to the fixed-fixed mode used in Ref. 1. This shifted the resonant frequency of the test specimen. The mass of the added weight and the propellant rod resulted in a nominal 0.67 psi at the gage interface for 1-g input. As the specimen passed through resonance, phase shifts between the top and

TABLE B-2. EFFECT OF POWER SUPPLY ON GAGE RESPONSE

DC Power, v	AC, v	Frequency, Hz	DC Sensitivity, mv/psi/28 v	AC Sensitivity, mv/psi/28 v
28	--	--	0.78	--
20	20	60	0.69	0.66
20	20	120	0.70	0.73
20.3	20	440	0.68	0.72
19.8	19	1200	0.70	0.69
28	2	60	0.67	0.66
28	2	120	0.71	0.73
28	2	440	0.70	0.59
28	2	600	0.69	0.66
28	2	800	0.74	0.73
28	2	1200	0.75	0.88

bottom of the specimen resulted in lesser peak stress at the bondline interface. This stress can vary from almost zero to greater than twice the weight/area being supported as the frequency is increased. Indicated sensitivities, normalized to 1 g, assume that the full load is borne at the interface. Data obtained at each test temperature are given in Tables B-3, -4, and -5. Amplitude ratios are plotted in Figure B-2, from which resonance at each temperature can be identified.

DISCUSSION AND CONCLUSIONS

The diaphragm gages used in these tests and on the BDU are designed to measure pressures up to 150 psi. We are using them to measure stresses on the order of 10 psi and are attempting to resolve dynamic components on the order of 0.5 psi. As with any measuring device, when trying to resolve data below 1% of full-scale, significant data scatter is bound to occur. Data shown in the five tables above are remarkably consistent in view of the low level of operation.

The diaphragm gage is shown to have a reasonably flat response up to the expected response frequency limit of a case-bonded propellant grain (< 400 Hertz). There is certainly no enhancement of sensitivity that would result in a tenfold increase in output due to vibration. Based on the data shown, the diaphragm gage is a useful indicator of dynamic stresses as well as those induced by pressurization and temperature cycling. The dynamic stresses as indicated on the amplified record are probably valid at frequencies below about 500 Hertz. The higher (especially near 1000 Hertz) responses are attributable to cross talk between channel carrier frequencies.

TABLE B-3. DYNAMIC GAGE RESPONSE AT 140 F

Frequency, Hz	Apparent Gage Sensitivity, mv/psi/g		
	1 g	3 g	10 g
10	0.68	0.73	0.71*
20	0.68	0.70	0.67
40	0.72	0.76	0.79
100	0.67	0.69	0.72
200	0.70	0.70	0.69
400	0.43	0.43	0.44
1000	0.24	0.24	0.22
1400	0.56	0.46	0.46
2000	0.32	0.31	0.36

*Test input limited to 5 g at 10 Hertz

TABLE B-4. DYNAMIC GAGE RESPONSE AT 61 F

Frequency, Hz	Apparent Gage Sensitivity, mv/psi/g			
	Ref. 1*	1 g	3 g	10 g
10	0.89	0.73	0.76	0.72**
20	0.72	0.67	0.64	0.69
40	0.98	0.64	0.70	0.77
100	0.82	0.61	0.65	0.70
200	0.77	0.63	0.69	0.73
400	0.50	0.59	0.60	0.60
1000	1.22	0.25	0.20	0.20
1400	--	0.18	0.13	0.18
2000	--	0.31	0.22	0.24

* Derived from data acquired at 75 and 40 F
** Test input limited to 5 g at 10 Hertz

TABLE B-5. DYNAMIC GAGE RESPONSE AT 0 F

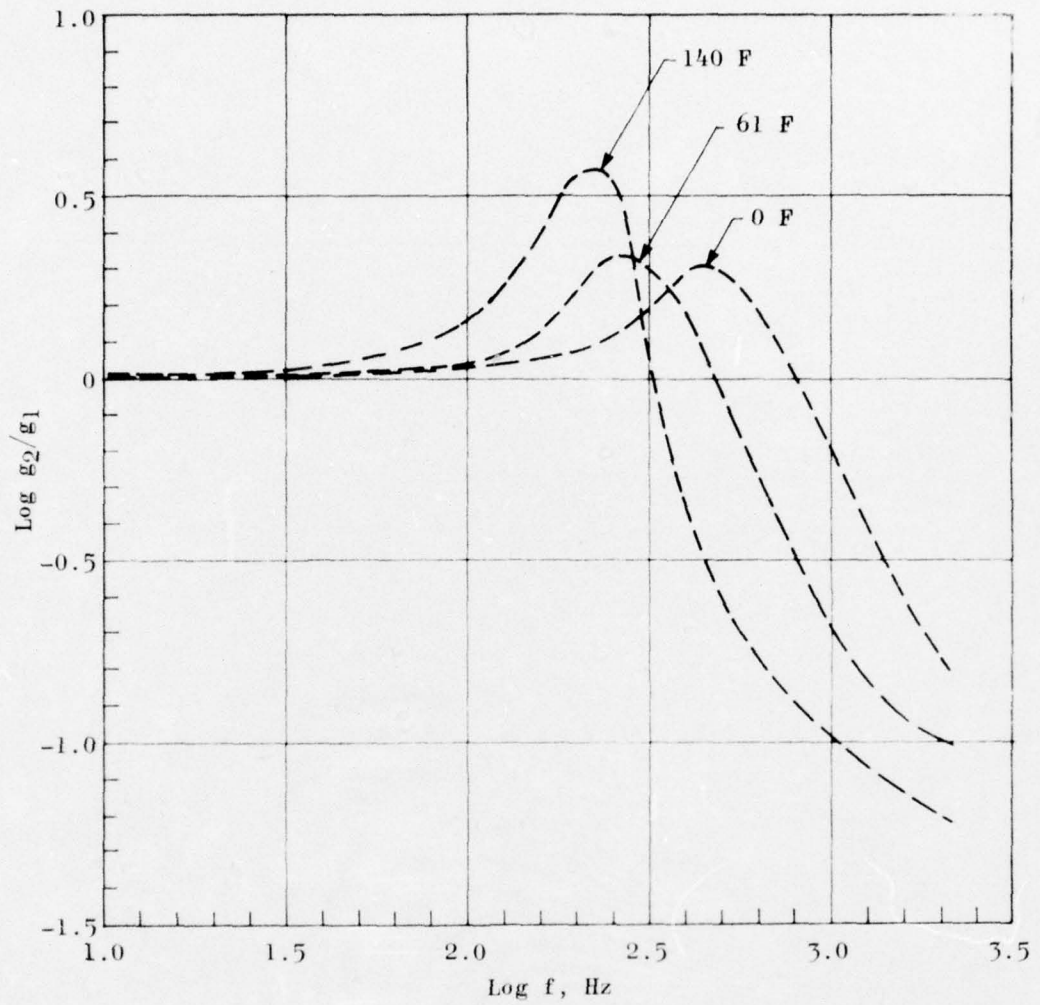| Frequency, Hz	Apparent Gage Sensitivity, mv/psi/g			
	Ref. 1*	1 g	3 g	10 g
10	0.68	0.61	0.70	0.58**
20	0.79	0.61	0.62	0.66
40	0.78	0.56	0.68	0.60
100	0.79	0.75	0.70	0.60
200	0.77	0.55	0.56	0.55
400	0.45	0.54	0.54	0.56
1000	0.44	0.44	0.44	0.40
1400	--	0.33	0.31	0.30
2000	--	0.23	0.16	0.17

* Data taken at -10 F
** Test input limited to 5 g at 10 Hertz

Figure B-2. Vibration Response of Inert Propellant Rod

Page B-8 is blank